

TWO-PHASE FLOW BOILING IN SMALL- TO MICRO- DIAMETER TUBES

A thesis submitted for the degree of Doctor of Philosophy

by

Dereje Shiferaw

School of Engineering and Design
Brunel University
West London, Uxbridge, UB8 3PH

May 2008

“Occurrences in this domain are beyond the reach of exact prediction because of the variety of factors in operation, not because of any lack of order in nature.”

Albert Einstein

“And beyond all questions, great is the mystery of godliness...”

1 Timothy 3:16

Abstract

This thesis is dedicated to the experimental and theoretical study of flow boiling in small to micro diameter tubes using R134a. Flow pattern, heat transfer and pressure drop studies were conducted in stainless steel cold drawn tubes with internal diameter 2.88, 1.1, and 0.52 mm using an existing facility that was designed with a long term research objective of improving the fundamental understanding of flow boiling in small metallic tubes. The facility was moved to the present location from London South Bank University and re-commissioned before carrying out the experiments. The test sections were heated by a direct passage of alternating current and wall temperatures were measured at 15 axial locations by miniature thermocouples that were directly spot-welded at the tube outer wall. A digital high-speed camera was used to simultaneously observe the flow patterns (during the heat transfer tests) directly at a borosilicate glass tube located immediately downstream of the heat transfer test section. The purpose of the flow visualization study was to support understanding of the heat transfer characteristics and development of flow regime-specific models. The heat transfer and pressure drop data of X. Huo (2005) in the 4.26 and 2.01 mm tubes and the flow visualization results of Chen (2006) for the tubes of diameter 4.26, 2.88, 2.01, and 1.1 mm were included with the new data in an extensive analysis of flow boiling heat transfer and pressure drop in five vertical tubes with internal diameters 4.26, 2.88, 2.01, 1.1 and 0.52 mm. The wide range of tube diameter was chosen to investigate the influence of tube size and possibly identify the threshold where the effect of small or micro diameter effects become significant. In the experiments, parameters were varied in the ranges: mass flux 100 to 700 kg/m²s; heat flux 1.6 to 150 kW/m²; pressure 6 to 14 bar; quality up to 0.9 and the inlet temperature was controlled at a subcooling of 1 – 5 K. There was no clear significant difference between the characteristics and magnitude of the heat transfer coefficients in the 4.26 mm and 2.88 mm tubes but the coefficients in the 2.01 and 1.1 mm tube were higher. The heat transfer results suggested that a tube size of about 2 mm might be considered as a critical diameter to distinguish small and conventional tubes. Further differences have now been observed in the 0.52 mm tube. These differences, both in flow patterns and heat transfer, indicate a possible second change from small to micro behaviour at diameters less than 1 mm for R134a. Also, the results showed axial variations in heat transfer characteristics marking the importance of

surface conditions on heat transfer. This calls for a further detail investigation to understand the underlying physics in the initiation of boiling, effect of surface condition on nucleation, and structure of newly emerging flow patterns, particularly in very small tubes.

Existing correlations were examined using the results of the five tubes and indicated that these correlations do not predict the present small diameter data to a satisfactory degree. Therefore, two new correlations that take into account both magnitude and characteristic effect of tube diameter have been proposed covering the 4.26 mm-1.1 mm and the smallest 0.52 mm tube, respectively. A detailed comparison was also made with the state-of-the-art flow regime-specific model of Thome et al. (2004) and verified that the mechanistic modelling approach has a promising capability of predicting two phase heat transfer in small diameter tubes, although it still requires further development. Some improvements have been proposed and tested against the current data. Using a similar approach, a new two phase pressure drop model has been proposed and compared with the current data with encouraging results.

Declaration

The research presented in this thesis is the original work of the author except where otherwise specified, or where acknowledgements are made by references. This project was carried out at the School of Engineering and Design, Brunel University, under the supervision of Prof. T. G. Karayiannis and Prof. D.B.R. Kenning.

The work has not been submitted for another degree or award to any other institution.

Acknowledgments

I would like to express my gratitude to Professor T.G. Karayiannis for his support and encouragement throughout this study. His guidance and advice were indispensable for the successful completion of the work. He prioritized research meetings and availed himself for discussion at any time although he has other important responsibilities.

To Professor D.B.R. Kenning, whose devotion and rich experience in boiling are immeasurable. I had a great privilege of working with him. His profound comments and advices shaped the realization of the work in this form.

I am grateful to the technicians Mr. M. Richards and Mr. C. Xanthos for their support in the installation and construction of the facility and test sections. I also acknowledge the technical team of South Bank University, especially Mr. R. Mills for their help in the dismantling of the facility.

To Dr X. Huo and Dr. L. Chen for providing their data and offering their kind and constructive advises. I also thank Mr. M. Mahmoud for his friendship and involvement in the experiments of the smallest tube.

To the School of Engineering and Design, Brunel University, for providing me the scholarship and the opportunity to compile this study.

To my parents, for their love and encouragement. Special thanks to Yeneye for her love and care. To the bible study group, for their prayer and fellowship.

Above all, to God and His only Son Jesus Christ, words are not enough to praise Him for his comfort, strength and courage. His presence is the source of my inspiration. I dedicate this work to His glory.

**PAGE
NUMBERING
AS ORIGINAL**

Contents

Abstract	iii
Declaration	v
Acknowledgments	vi
List of Figures	xiv
List of Tables	xxvii
Nomenclature	xxx
1. Introduction	1
1.1 Brief review on microchannel application.....	1
1.2 Research background.....	4
1.3 Objectives.....	7
1.4 Overview.....	8
2. Fundamentals of Two Phase Flow Study and Definitions	10
2.1 Introduction.....	10
2.2 Flow patterns and flow maps.....	10
2.2.1 Flow patterns.....	11
2.2.2 Flow pattern maps.....	12
2.2.3 Flow pattern transitions.....	14
2.3 Two phase flow model and pressure drop.....	16
2.3.1 Homogeneous two phase model.....	17
2.3.2 Separated flow model.....	20

2.3.3	Drift flux model.....	22
2.3.4	Annular flow model.....	23
2.4	Fundamentals of two phase flow boiling heat transfer.....	24
2.4.1	Boiling incipience, growth and departure.....	25
2.4.2	Pool boiling.....	27
2.4.3	Flow boiling heat transfer.....	28
2.4.4	Heat transfer mechanisms.....	31
2.5	Channel size classifications.....	33
2.6	Summary.....	36
3.	Two Phase Flow Study in Small- to Micro-Passages: State-of-the-art Review	38
3.1	Introduction.....	38
3.2	Flow patterns and flow maps.....	39
3.2.1	Flow patterns.....	39
3.2.2	Flow pattern maps.....	49
3.3	Two phase pressure drop.....	59
3.4	Flow boiling heat transfer.....	66
3.4.1	Onset of nucleate boiling.....	66
3.4.2	Heat transfer characteristics and mechanisms.....	76
3.4.3	Pressure and temperature oscillations.....	96
3.4.4	Critical Heat Flux (CHF) and dryout.....	103
3.5	Heat transfer predictions.....	111
3.5.1	Heat transfer correlations.....	111
3.5.2	Heat transfer models.....	111
4.	Experimental Methods and Validation	127
4.1	Introduction.....	127
4.2	Experimental facility and procedure.....	128

4.2.1	Heat transfer test section.....	136
4.2.2	Flow visualization test section.....	147
4.3	Measurement accuracy.....	148
4.4	Experimental data reduction.....	159
4.4.1	Local heat transfer coefficient.....	159
4.4.2	Boiling two phase pressure drop.....	161
4.5	Experimental validation.....	163
4.5.1	Single phase pressure drop.....	163
4.5.2	Single phase heat transfer.....	166
4.5.3	Thermocouple connection method.....	168
4.6	Repeatability of the experiments.....	172
4.7	Summary.....	176
5.	Boiling Heat Transfer Results and Discussion	178
5.1	Introduction.....	178
5.2	Experimental time-averaged local heat transfer coefficient.....	178
5.2.1	Effect of heat flux.....	179
5.2.2	Effect of mass flux.....	197
5.2.3	Effect of pressure.....	203
5.2.4	Effect of tube diameter.....	209
5.2.5	Dryout heat transfer.....	213
5.3	Discussion of results using flow pattern transitions.....	215
5.3.1	Small diameter tube results (4.26 – 1.1 mm).....	216
5.3.2	Micro-tube results (0.52 mm).....	234
5.4	Comparison with existing correlations.....	243
5.4.1	The 1982 Lazarek – Black correlation.....	243
5.4.2	The 1986 Gungor – Winterton correlation.....	246

5.4.3	The 1991 Liu – Winterton correlation.....	248
5.4.4	The 1996 Tran et al. correlation.....	250
5.4.5	The 2004 Kandlikar – Balasubramanian correlation.....	252
5.4.6	The 2004 Zhang et al. correlation.....	254
5.4.7	The 2007 Saitoh et al. correlation.....	257
5.5	New proposed correlation.....	259
5.6	Summary.....	265
6.	Boiling Two Phase Pressure Drop Results and Discussion	269
6.1	Introduction.....	269
6.2	Total pressure drop.....	269
6.2.1	Effect of heat flux.....	270
6.2.2	Effect of mass flux.....	272
6.2.3	Effect of pressure.....	273
6.2.4	Effect of tube diameter.....	276
6.2.5	Contributions of the three pressure drop components.....	276
6.3	Comparison with existing prediction methods.....	281
6.3.1	Homogeneous flow model.....	281
6.3.2	Separated flow model of Lockhart – Martinelli.....	283
6.3.3	Existing pressure drop correlations.....	285
6.4	Summary.....	294
7.	Models for Two Phase Flow Boiling Heat Transfer and Pressure Drop	297
7.1	Introduction.....	297
7.2	Three – zone evaporation heat transfer model.....	298
7.2.1	Presentation of the model.....	299
7.2.2	Comparison with current results.....	303
7.2.3	Parametric sensitivity of the three – zone model.....	318

7.2.4	Summary.....	320
7.3	Annular two phase flow model.....	320
7.4	New improvements to the heat transfer models.....	324
7.4.1	Incorporating nucleate boiling region.....	324
7.4.2	Improving effect of heat flux on heat transfer coefficient.....	326
7.4.3	Film thickness predictions.....	327
7.4.4	Summary.....	330
7.5	New pressure drop predicting model.....	331
7.6	Summary.....	347
8.	Conclusions and Future Work	350
8.1	Conclusions.....	350
8.1.1	Heat transfer and flow visualization.....	350
8.1.2	Boiling two phase pressure drop.....	352
8.1.3	Correlations and modelling.....	353
8.2	Future work.....	355
	Bibliography	358
A	Operating Instructions for the Experimental Facility	381
B	Single Phase Heat Transfer Correlations Used for Validation	387
C	Selected Existing Flow Boiling Heat Transfer Correlations Used for Comparison with the Current Data	389
D	Selected Existing Two Phase Pressure Drop Correlations Used for Comparison with the Current Data	392
E	R134a Physical Properties	394
	Curriculum Vitae	399
	Publications from the work covered in this thesis	402

List of Figures

2.1.	Flow patterns in vertical gas flow, (Collier and Thome,1994).....	12
2.2.	Flow pattern map for vertical flow for air- water and steam (D =10-30 mm), Hewitt and Roberts, 1969).....	13
2.3.	Flow patterns and heat transfer regions in vertical tube (Collier and Thome, 1994).....	29
2.4.	Heat transfer coefficient as a function of quality with increasing heat flux (Collier and Thome, 1994).....	31
2.5.	The various channel size classification criteria.....	36
3.1.	Flow patterns in capillary tubes (Mishima and Hibiki, 1996).....	40
3.2.	Flow patterns in small tubes, diameter: (a) 1.1 (b) 2.01 (c) 2.88 and (d) 4.26 mm (Chen et al. 2006).....	42
3.3.	Two-phase flow patterns in a microchannel, D=100 μm : (a) $U_{ls} = 0.15 \text{ m/s}$, $U_{gs} = 6.8 \text{ m/s}$; (b) $U_{ls} = 0.56 \text{ m/s}$, $U_{gs} = 20.3 \text{ m/s}$; (c) $U_{ls} = 3.96 \text{ m/s}$, $U_{gs} = 19.0 \text{ m/s}$; (Kawahara et al. 2002).....	45
3.4.	Two phase flow patterns: (a) air–water flow in a 25 μm silica tube, (b) steam–water flow in a 50 μm silica tube and (c) air–water flow in a 100 μm quartz tube, (Serizawa et al. 2002).....	46
3.5.	Flow regime map and transition lines predictions for air-water flow, Mishima and Hibiki (1996).....	50
3.6.	Air-water flow regimes for the 1.1 mm tube of Triplett et al. (1999) and comparison with the experimental flow regime transition lines of (a) Damianides and Westwater (1988) and (b) Fukano and Kariyasaki (1993).....	51
3.7.	Flow regime maps of Xiong and Chung (2007) for: (a) $D_h = 0.622 \text{ mm}$, (b) $D_h = 0.412 \text{ mm}$ (C) $D_h = 0.209 \text{ mm}$	53

3.8.	Flow pattern maps for 0.51 mm tube using R134a at ~ 8 bar, (a) experimental data, (b) Transition boundary correlation; Revellin and Thome (2007b).....	55
3.9.	Flow regime transition boundary lines, P = 6 bar: (a) U_{ls} vs. U_{gs} , (b) G vs x , data of Chen (2006).....	57
3.10.	Wall temperature at the onset of nucleate boiling, Hapke et al. (2000).....	69
3.11.	Comparison of measured wall superheat with correlations, Hapke et al. (2000).....	70
3.12.	Pressure drop versus mass flux characteristic curve for a uniformly heated channel, (Ghiaasiaan and Chedester, 2002).....	72
3.13.	Degree of wall superheat with tube diameter, (a) experimental value varying with different mass flux and heat flux at each tube size, (b) comparison with correlation taking only the maximum value for each tube, Yen et al. (2003).....	73
3.14.	Heat transfer coefficients versus quality for various heat flux (q''_T , W/m ²) at constant mass flux of: (a) $G = 50$ kg/m ² s, (b) $G = 100$ kg/m ² s, (c) $G = 150$ kg/m ² s, (d) $G = 200$ kg/m ² s, (e) $G = 242$ kg/m ² s, (f) $G = 300$ kg/m ² s, Wambsganss et al. (1993).....	77
3.15.	Experimental data for the circular tube (2.46 mm): (a) local heat transfer coefficient for various combination of mass flux at three constant values of heart flux and $\Delta T_{sup} > 2.75K$, P = 8.25 bar , (b) boiling curve showing convection dominant heat transfer at low wall superheat $\Delta T_{sup} < 2.75K$, Tran et al. (1996).....	78
3.16.	Heat transfer coefficient versus quality: (a) $d= 1.1$ mm, $G=505$ kg/m ² s, (b) $d= 1.8$ mm, $G=570$ kg/m ² s, (c) $d= 2.8$ mm, $G=130$ kg/m ² s, (d) $d= 3.6$ mm, $G=130$ kg/m ² s, (e) 2×2 mm, square tube, 342 kg/m ² s, (f) generalised sketch of heat transfer coefficient vs. quality for small tubes and channels, Lin et al. (2001b).....	81

3.17.	Local heat transfer coefficient versus superficial velocity and flow regime transition lines from Triplett et al. (1999) (SF: slug flow, SAF: slug-annular flow, AF: annular flow).....	83
3.18.	Heat transfer coefficient versus quality for the 0.51 mm tube: (a) effect of heat flux at a mass flux of 295 kg/m ² s, (b) effect of mass flux, and (c) comparison with the 0.19 mm tube result and Ravigururajan, 1998 cited in Yen et al. (2003).....	84
3.19.	Effect of heat flux and mass flux on heat transfer coefficient for three different diameter tubes of: (a) 3.1 mm; (b) 1.12 mm and (c) 0.51 mm, Saitoh et al. (2005).....	88
3.20.	Heat transfer coefficient as a function of vapour quality with various trends of heat flux and mass flux effect, Thome (2006).....	89
3.21.	Heat transfer coefficient as a function of vapour quality: (a) Water, G = 400 kg/m ² s; (b) Ethanol, G = 300 kg/m ² s, Cortina Diaz and Martin (2007).....	91
3.22.	Pressure fluctuations at 134 kg/m ² s, 53 kW/m ² , Kenning and Yan (2001): (a) low inlet compressibility; (b) high inlet compressibility.....	97
3.23.	Wall temperature fluctuations for R141b, G = 510 kg/m ² s, Lin et al. (2001a).....	98
3.24.	Wall temperature fluctuations, Sumith et al. (2003): z = 90 mm for water, at G = 106.5 kg/m ² s.....	98
3.25.	Wall temperature behaviour at various heat fluxes: (a) 47 kg/m ² s, (b) 124 kg/m ² s, Owhaib et al. (2006).....	110
3.26.	Comparison of the Kew and Cornwell (1997) model to their sample data.....	114
3.27.	Sketch illustrating the annular two phase flow model of Boye et al. (2007).....	120
4.1.	Schematic diagram of the experimental system (the R22 Cooling system is not shown).....	130
4.2.	Photograph of the R134a experimental facility.....	131

4.3.	Schematic diagram of the R22 cooling system.....	133
4.4.	Photograph of the R22 cooling system.....	134
4.5.	Schematic diagram of the test section.....	138
4.6.	Photograph of the actual test sections.....	138
4.7.	Schematics showing positions of roughness measurement (Taylor Hobson Ltd.).....	140
4.8.	The high resolution non-contact roughness measuring instrument (Hommel) at the Institute for Thermodynamics, University of Hannover, Germany, (with permission, Prof. A. Luke).....	141
4.9.	Sample preparation of the 0.52 mm tube (Institute for Thermodynamics, University of Hannover, with permission, Prof. A. Luke).....	142
4.10.	Picture showing the 0.52 mm sample with its dimensions: (a) isometric view, (b) top view. (Institute for Thermodynamics, University of Hannover, Germany).....	143
4.11.	Sketch showing how average roughness is calculated.....	146
4.12.	Sketch describing how peak to valley parameters are evaluated.....	147
4.13.	Photograph of the high-speed camera positioned to take pictures.....	148
4.14.	Comparison of the measured friction factor with well-known correlations for $D = 4.26$ mm and $P=7.9$ bar.....	164
4.15.	Measured friction factor as a function of Re for the 0.52 mm tube at 8 bar pressure.....	165
4.16.	Comparison of single phase heat transfer results with well-known large tube correlations for $D = 4.26$ mm at $P= 7.5$ bar.....	166
4.17.	Single phase heat transfer results for $D = 0.52$ mm in the turbulent region.....	168
4.18.	Single phase heat transfer for $D = 0.52$ mm in the laminar region.....	168
4.19.	Rough sketch showing electric and thermocouple wire connections.....	170

4.20.	The measured wall temperature difference between different ways of thermocouple attachment, at different vapour quality.....	172
4.21.	Repeatability results of 4.26 mm tube: (a) single phase experiments at pressure of 11 bar; (b) two phase boiling results at a mass flux of 300 kg/m ² s and pressure of 8 bar.....	174
4.22.	Reproducibility of the 1.1 mm tube experiments at a mass flux of 300 kg/m ² s and 8 bar pressure.....	175
5.1.	Local time-averaged heat transfer coefficient, for D = 4.26 mm, G = 400 kg/m ² s and P = 8 bar, as a function of: (a) local quality, (b) axial position.....	180
5.2.	Local time-averaged heat transfer coefficient, for D = 2.88 mm, G = 400 kg/m ² s and P = 8 bar, as a function of: (a) local quality, (b) axial position.....	182
5.3.	Local time-averaged heat transfer coefficient, for D = 2.01 mm, G = 400 kg/m ² s and P = 8 bar, as a function of: (a) local quality, (b) axial position.....	184
5.4.	Local time-averaged heat transfer coefficient, for D = 1.10 mm, G = 400 kg/m ² s and P = 8 bar, as a function of: (a) local quality, (b) axial position.....	186
5.5.	Local time-averaged heat transfer coefficient as a function of local quality for D = 1.10 mm: (a) G = 200 kg/m ² s, P = 8 bar (b) G = 400 kg/m ² s, P = 6 bar.....	189
5.6.	Local time-averaged heat transfer coefficient, for D = 0.52 mm, G = 400 kg/m ² s and P = 8 bar, as a function of: (a) local quality, (b) axial position.....	192
5.7.	Local time-averaged heat transfer coefficient, for D = 0.52 mm, G = 300 kg/m ² s and P = 6 bar, as a function of: (a) local quality, (b) axial position.....	194
5.8.	Degree of wall superheat as a function of heat flux for the D = 0.52 mm tube G= 300 kg/m ² s, P= 6 bar.....	196

5.9.	Local time-averaged heat transfer coefficient as a function of local quality for $D = 1.10$ mm, $G = 200$ kg/m ² s and $P = 6$ bar.....	197
5.10.	Effect of mass flux on heat transfer coefficient versus quality at $P = 8$ bar: (a) $D = 4.26$ mm, $q = 54$ kW/m ² ; (b) $D = 2.88$ mm, $q = 54$ kW/m ² ; (c) $D = 2.01$ mm, $q = 54$ kW/m ² ; (d) $D = 1.1$ mm, $q = 54$ kW/m ² ; (e) $D = 0.52$ mm, $q = 58$ kW/m ²	201
5.11.	Effect of mass flux on heat transfer coefficient versus axial position at $P = 8$ bar: (a) $D = 1.10$ mm, $q = 54$ kW/m ² ; (b) $D = 0.52$ mm, $q = 58$ kW/m ²	202
5.12.	Local heat transfer coefficient as a function of vapour quality for different system pressure, $G = 300$ kg/m ² s: (a) $D = 4.26$ mm, (b) $D = 2.88$ mm, (c) $D = 2.01$ mm, (d) $D = 1.10$ mm, and (e) $G = 400$ kg/m ² s, $D = 0.52$ mm.....	206
5.13.	Reproducibility of the 0.52 mm tube experiments at a mass flux of about 500 kg/m ² s and pressure ~6 bar.....	208
5.14.	The degree of wall superheat versus heat flux at conditions corresponding to figure 5.13.....	209
5.15.	Local heat transfer coefficient as a function of heat flux for different tube diameters at a mass flux of 400 kg/m ² s and 8 bar pressure.....	211
5.16.	Local heat transfer coefficient as a function of system pressure for different tube diameters at a mass flux of 400 kg/m ² s and heat flux 54 kW/m ²	212
5.17.	Sketch showing typical heat transfer characteristics for tubes of 1.1 mm internal diameter and larger.....	213
5.18.	Flow regime transition lines of Chen et al. (2006) for $D = 4.26$ mm, $G = 300$ kg/m ² s and $P = 8$ bar pressure superimposed: (a) on a local heat transfer coefficient versus vapour quality plot, (b) relative axial position versus heat flux plot.....	217
5.19.	Sketch showing anticipated heat transfer coefficient trend in various flow regimes.....	218

5.20.	Flow pattern photos showing interface instability due to trails of small bubbles for $D = 4.26$ mm tube.....	219
5.21.	Flow regime transition lines of Chen et al. (2006) for $D = 2.88$ mm, $G = 300$ kg/m ² s and $P = 8$ bar pressure superimposed: (a) on a local heat transfer coefficient versus vapour quality plot, (b) relative axial position versus heat flux plot.....	220
5.22.	Flow patterns for the 2.88 mm tube at $G = 300$ kg/m ² s and 8 bar pressure.....	222
5.23.	Flow regime transition lines of Chen et al. (2006) for $D = 2.01$ mm, $G = 300$ kg/m ² s and $P = 8$ bar pressure superimposed: (a) on a local heat transfer coefficient versus vapour quality plot, (b) relative axial position versus heat flux plot.....	224
5.24.	Flow patterns observed for the 1.1 mm tube at a mass flux of 300 kg/m ² s and 6 bar pressure.....	226
5.25.	Flow regime transition lines of Chen et al. (2006) for $D = 1.1$ mm, $G = 300$ kg/m ² s and $P = 8$ bar pressure superimposed: (a) on a local heat transfer coefficient versus vapour quality plot, (b) relative axial position versus heat flux plot.....	228
5.26.	Flow patterns images at the exit of the 1.1 mm diameter tube corresponding to the heat transfer experiments at a mass flux of 300 kg/m ² s and 8 bar pressure.....	229
5.27.	Influence of mass flux on the local heat transfer coefficient and flow regime transition boundaries of Chen et al. (2006) at 8 bar pressure for the four tubes of diameter: (a) 4.26 mm, (b) 2.88 mm, (c) 2.01 mm and (d) 1.1 mm.....	231
5.28.	Influence of pressure on the local heat transfer coefficient and flow regime transition boundaries of Chen et al. (2006) at a mass flux of 400 kg/m ² s and heat flux 54 kW/m ² for the four tubes of diameter: (a) 4.26 mm, (b) 2.88 mm, (c) 2.01 mm and (d) 1.1 mm.....	234
5.29.	Flow pattern in the smaller tube of 0.52 mm internal diameter at different heat flux, for mass flux, $G=400$ kg/m ² s and pressure, $P=8$ bar.....	236

5.30.	Sequence of flow patterns showing coalescence, $G=300 \text{ kg/m}^2\text{s}$, $P=6 \text{ bar}$ and $q =3.7 \text{ kW/m}^2$	236
5.31.	Flow regime transition boundaries using Revellin and Thome (2007) correlation superimposed on heat transfer results at a mass flux of $300 \text{ kg/m}^2\text{s}$ and 6 bar pressure: (a) heat transfer coefficient versus quality, (b) axial distance versus heat flux.....	239
5.32.	Flow patterns for a mass flux of $300 \text{ kg/m}^2\text{s}$ and 6 bar pressure at different heat flux in kW/m^2	240
5.33.	Transition boundaries using correlation of Revellin and Thome (2007) superimposed on the plot showing influence of: (a) mass flux at $P = 6 \text{ bar}$, (b) pressure at $G = 400 \text{ kg/m}^2\text{s}$, both for a nominal heat flux of 58 kW/m^2	242
5.34.	Comparison with Lazarek and Black (1982) correlation for tubes of diameter: (a) 4.26 mm , (b) 2.88 mm , (c) 2.01 mm , (d) 1.10 mm and (e) 0.52 mm	245
5.35.	Comparison with Gungor and Winterton (1986) correlation for tubes of diameter: (a) 4.26 mm , (b) 2.88 mm , (c) 2.01 mm , (d) 1.1 mm and (e) 0.52 mm	247
5.36.	Comparison with Liu and Winterton (1994) correlation for tubes of diameter: (a) 4.26 mm , (b) 2.88 mm , (c) 2.01 mm , (d) 1.1 mm and (e) 0.52 mm	249
5.37.	Comparison with the Tran (1996) correlation for tubes of diameter: (a) 4.26 mm , (b) 2.88 mm , (c) 2.01 mm , (d) 1.1 mm and (e) 0.52 mm	251
5.38.	Comparison with Kandlikar (2004) correlation for tubes of diameter: (a) 4.26 mm , (b) 2.88 mm , (c) 2.01 mm , (d) 1.1 mm and (e) 0.52 mm	253
5.39.	Comparison with Zhang et al. (2004) correlation using Cooper (1984) for nucleate boiling term at different tubes of diameter: (a) 4.26 mm , (b) 2.88 mm , (c) 2.01 mm , (d) 1.1 mm and (e) 0.52 mm	255

5.40.	Comparison with Zhang et al. (2004) correlation using Rohsenow (1952) correlation for the nucleate boiling contribution at different diameter of tubes: (a) 4.26 mm, (b) 2.88 mm, (c) 2.01 mm, (d) 1.1 mm and (e) 0.52 mm.....	256
5.41.	Comparison with Saitoh et al. (2007) for different tubes of diameter: (a) 4.26 mm, (b) 2.88 mm, (c) 2.01 mm, (d) 1.1 mm and (e) 0.52 mm.....	258
5.42.	Comparison with the new proposed correlation for different tubes of diameter: (a) 4.26 mm, (b) 2.88 mm, (c) 2.01 mm, (d) 1.1 mm and (e) 0.52 mm.....	263
6.1.	Effect of heat flux on the total measured two phase pressure drop at a system pressure of 8 bar and various mass fluxes for different internal tube diameters: (a) 4.26 mm, (b) 2.88 mm, (c), 2.01 mm, (d) 1.1 mm and (e) 0.52 mm.....	272
6.2.	Effect of system pressure on the measured two phase total pressure drop at various system pressures and a mass flux value of 400 kg/m ² s for different tube internal diameter: (a) 4.26 mm, (b) 2.88 mm, (c) 2.01 mm, (d) 1.1 mm and (e) 0.52 mm.....	275
6.3.	Effect of system pressure on liquid to vapour density ratio for R134a.....	276
6.4.	Effect of tube internal diameter on two phase total pressure drop gradient as a function of exit quality at 8 bar system pressure and 400 kg/m ² s mass flux.....	277
6.5.	Contribution percentages from the three pressure drop components to the total measured value and the deducted friction pressure drop component at a mass flux of 400 kg/m ² s and 8 bar system pressure for different tube diameters: (a) 4.26 mm, (b) 2.88 mm, (c) 2.01 mm, (d) 1.1 mm and (e) 0.52 mm.....	280
6.6.	Comparison with the homogeneous flow model pressure drop for different tube diameters: (a) 4.26 mm, (b) 2.88 mm, (c) 2.01 mm, (d) 1.1 mm and (e) 0.52 mm.....	282

6.7.	Comparison with the separated flow model pressure drop for different tube diameters: (a) 4.26 mm, (b) 2.88 mm, (c) 2.01 mm, (d) 1.1 mm and (e) 0.52 mm.....	284
6.8.	Comparison with the Chisholm et al. (1983) pressure drop correlation for different tube diameters: (a) 4.26 mm, (b) 2.88 mm, (c) 2.01 mm, (d) 1.1 mm and (e) 0.52 mm.....	286
6.9.	Comparison with the Tran et al. (2000) pressure drop correlation for different tube diameters: (a) 4.26 mm, (b) 2.88 mm, (c) 2.01 mm, (d) 1.1 mm and (e) 0.52 mm.....	288
6.10.	Comparison with the Mishima and Hibiki (1996) pressure drop correlation for different tube diameters: (a) 4.26 mm, (b) 2.88 mm, (c) 2.01 mm, (d) 1.1 mm and (e) 0.52 mm.....	290
6.11.	Comparison with the Muller-Steinhagen and Heck (1986) pressure drop correlation for different tube diameters: (a) 4.26 mm, (b) 2.88 mm, (c) 2.01 mm, (d) 1.1 mm and (e) 0.52 mm.....	292
7.1.	Diagram illustrating the three zones: a liquid slug, an elongated bubble and a vapour slug, redrawn from original, Thome et al. (2004).....	300
7.2.	Comparison of the local heat transfer coefficient versus vapour quality with the Thome et al. (2004), three-zone model, for various heat fluxes at 8 bar pressure and 300 kg/m ² s mass flux.....	305
7.3.	Comparison of the local heat transfer coefficient versus vapour quality with the Thome et al. (2004) three-zone model for D=4.26 mm tube: (a) P = 8 bar, (b) P = 12 bar.....	306
7.4.	Comparison of the local heat transfer coefficient versus vapour quality with the Thome et al. (2004), three-zone model, for D = 2.01 mm and various heat fluxes at 8 bar pressure and 300 kg/m ² s mass flux.....	307
7.5.	Comparison of the local heat transfer coefficient versus vapour quality with the Thome et al. (2004) three-zone model for D = 2.01 mm tube at various mass and heat flux values: (a) P = 8 bar, (b) P = 12 bar.....	309
7.6.	Experimental results and predictions for continuous dry out cases when the critical film thickness value $\delta_{min} = 1.75 \mu\text{m}$, $C_{\delta 0} = 0.43$ and the	

	frequency of bubble generation, f equals 1.5 times that recommended by Dupont et al. (2004).....	310
7.7.	Comparison of the local heat transfer coefficient versus vapour quality with the Thome et al. (2004), three-zone model, $P=6$ bar: (a) $G=200$ kg/m ² s, (b) 400 kg/m ² s.....	312
7.8.	Comparison of the 1.1 mm experimental data with the results of three-zone model: (a) effect of pressure at 300 kg/m ² s and 68 kW/m ² (b) effect of mass flux at a pressure of 8 bar and 69 kW/m ²	314
7.9.	Comparison of the local heat transfer coefficient versus vapour quality of the 0.52 mm tube with the Thome et al. (2004), three-zone model, for various heat fluxes at 6 bar pressure and 300 kg/m ² s mass flux.....	315
7.10.	Effect of diameter on local heat transfer coefficient in comparison with that predicted by the three-zone model at 8 bar pressure and 300 kg/m ² mass flux.....	317
7.11.	Sensitivity of the heat transfer coefficient to the three optimized parameters given by the model using the 1.1 mm tube results: (a) frequency of bubble generation (b) Correction factor to the initial film thickness, (c) critical film thickness to dryout, (d) prediction of dryout when the critical film thickness is same as roughness of the tube and the other two parameters are adjusted as shown.....	319
7.12.	Comparison of the local heat transfer coefficient versus vapour quality of the 0.52 mm tube with the Boye et al. (2007), annular two phase model, for various heat fluxes at 6 bar pressure and 300 kg/m ² s mass flux.....	324
7.13.	Comparison of local heat transfer coefficient for 2.01 mm tube at a mass flux of 300 kg/m ² s and 8 bar pressure with: (a) original three-zone model, (b) modified by including nucleate boiling term in the bubbly flow regime.....	326
7.14.	Comparison of the average heat transfer coefficient ($x \leq 0.25$) as a function of heat flux at a mass flux of 300 kg/m ² s, 8 bar pressure for the 2.01 mm tube data.....	327

7.15.	Comparison of various film thickness relations for 1.1 mm tube at a mass flux of 300 kg/m ² s and 6 bar pressure.....	330
7.16.	Sketch of the three zones and their respective lengths.....	333
7.17.	Comparison of the various velocity relations as function of heat flux for 1.1 mm tube at a mass flux of 300 kg/m ² s and 6 bar pressure.....	335
7.18.	(a) forces in the liquid film control volume, (b) momentum exchanges in the liquid film control volume, (c) forces acting on the control volume in the elongated bubble, and (d) momentum exchanges for the control volume in the elongated bubble.....	337
7.19.	Total pressure drop as a function of exit quality as predicted by the model, at 8 bar pressure: (a) 2.01 mm, (b) 1.1 mm.....	341
7.20.	Pressure gradients in the three zones as a function of exit quality for the 2.01 mm tube at 8 bar pressure and mass flux of 300 kg/m ² s.....	341
7.21.	Total pressure drop as a function of exit quality as predicted by the model, at 8 bar pressure: (a) 2.01 mm, (b) 1.1 mm.....	344
7.22.	Comparison with the current pressure drop data for the different tube diameters: (a) 4.26 mm, (b) 2.88 mm, (c) 2.01 mm, (d) 1.1 mm and (e) 0.52 mm.....	346

List of Tables

3.1.	Flow patterns observed in small passages of (hydraulic) diam. ($D \geq 1\text{ mm}$).....	48
3.2.	Flow patterns observed in micro tubes of diameter ($D < 1\text{ mm}$).....	48
3.3.	Summary of the experimental heat transfer characteristics.....	92
4.1.	The calming section and hydrodynamic development lengths.....	139
4.2.	Heated length and wall thickness for each tube.....	139
4.3.	Summary of the measured roughness of the tubes.....	145
4.4.	Glass tube dimensions.....	148
4.5.	Range of experimental parameters.....	150
4.6.	Uncertainty results for the internal diameter of the stainless steel tubes (4.26 – 1.1 mm, Chen 2006).....	151
4.7.	Uncertainty results of the internal diameter of the borosilicate glass tubes (4.26 – 1.1 mm, Chen 2006).....	151
4.8.	Uncertainty results of the heated length measurements.....	152
4.9.	Uncertainty values for temperature sensors.....	153
4.10.	Uncertainty values for pressure transducers, (Chen, 2006).....	154
4.11.	Uncertainty results of mass flux.....	156
4.12.	Uncertainty values of heat flux for the different tubes.....	158
4.13.	Uncertainty results of vapour quality determination.....	159
4.14.	Overall uncertainty results for determining local heat transfer coefficient.....	161
4.15.	Properties heat transfer compounds used in attaching thermocouple wires (both properties taken from RS Ltd. online catalogue).....	171
5.1.	Mean average error (MAE) and percentage of data within $\pm 30\%$ (β) for the comparison results of various correlations shown above.....	263

6.1. Mean average error (MAE) and percentage of data within $\pm 30\%$ (β) for the comparison results of various correlations shown above.....	293
B.1. Single phase heat transfer correlations used for validation.....	386
C.1. Selected existing flow boiling heat transfer correlations used for comparison with the current Data.....	387
D.1. Selected Existing Two Phase Pressure Drop Correlations Used for Comparison with the Current Data.....	391
E.1. R134a Physical Properties.....	393

Nomenclature

Latin

<i>Symbol</i>	<i>Parameter</i>	<i>SI unit</i>
A	Cross sectional area	m^2
A	Empirical constant, Eq. 3.4	-
AC	Alternating current	-
Bo	Boiling number	-
Bo	Bond number	-
C	Chisholm parameter	-
C	Single phase heat loss coefficient	$W K^{-1}$
Ca	Capillary number	-
C_a	Emperical constant	-
	for heat transfer coefficient, Eq. 5.16	
C_{Cooper}	Cooper (1984) emperical coefficient	-
$C_{\delta 0}$	Constant for initial film thickness	-
CHF	Critical Heat Flux	$W m^{-2}$
Co	Confinement number	-
Co	Convective number	-
C_p	Specific heat capacity	$J kg^{-1} K^{-1}$
\bar{C}_v	Constant volume specific heat	$J kg^{-1} K^{-1}$

<i>Symbol</i>	<i>Parameter</i>	<i>SI unit</i>
D	Tube diameter	m
D_b	Bubble departure diameter	m
D_h	Hydraulic diameter	m
DNB	Departure from nucleate boiling	-
e	Tube internal roughness	m
$Eö$	Eötvös number	-
G	Mass flux	$\text{kg m}^{-2} \text{s}^{-1}$
g	Gravitational acceleration	m s^{-2}
E	Enhancement factor to - - convective heat transfer component	-
F	Non-dimensional tube radius	-
F	Enhancement factor to - - convective heat transfer component	-
f	Friction coefficient	-
f_b	Bubble frequency	Hz
F_{Fl}	Fluid-Surface parameter	-
Fr	Froude number	-
h	Specific enthalpy	J kg^{-1}
h_{lg}	Latent heat of vapourization	J kg^{-1}
I	Electrical current	Ampere
j	Drift flux velocity	m s^{-1}
J_a	Jakob number,	-
L	Length	m
L	Live electrical line	-
L_B	Bubble length	m
L_{dry}	Dryout length	m

<i>Symbol</i>	<i>Parameter</i>	<i>SI unit</i>
L_{film}	Film length	m
L_p	Pair (tripplet) length	m
M	Molecular weight	kg kmol ⁻¹
MAE	Mean absolute error	-
\dot{m}	Mass flow rate	kg s ⁻¹
N	Number of active nucleation sites	-
N	Number of samples	-
N	Neutral electrical line	-
n	Exponent to heat flux	-
N_b	Boiling number	-
N_{mb}	Non-dimensional microchannel - - Boiling number	-
Nu	Nusselt number	-
OFI	Onset of flow instability	-
ONB	Onset of nucleat boiling	-
OSV	Onset of significant void	-
P	Pressure	Pa
P_e	Perimeter	m
P_R	Reduced pressure	-
Pr	Pradtl number	-
q	Heat flux	W m ⁻²
Q	Heat flow rate	W
r	Radial coordinate	-
r_n	Radius of bubble nucleus	m
r_c	cavity radius	m

<i>Symbol</i>	<i>Parameter</i>	<i>SI unit</i>
R	Tube radius	m
$R_b(t)$	Radius of growing bubble	m
R_B	Slug bubble radius	m
Re	Reynolds number	-
R_G	Gas constant	J mol ⁻¹ K ⁻¹
S	slip ratio	-
S	Suppression factor to nucleate- - boiling heat transfer coefficient	-
S_m	Modified suppression factor	-
S_t	Stanton number	-
S_x	Standard deviation	-
T	Temperature	⁰ C
t	Time	s
t_{dry}	Time for dry vapour to pass a fixed location	s
$t_{dry, film}$	Time required for film to dry out	s
t_{film}	Residence time for liquid film	s
t_{95}	95 % confidence limit	-
U	Velocity	m s ⁻¹
U_B	Slug bubble velocity	m s ⁻¹
U_{ra}	Random error	-
U_s	Relative/slip velocity	m s ⁻¹
U_{sys}	Systematic error	-
V	Voltage	Volts
V	Volume	m ³

<i>Symbol</i>	<i>Parameter</i>	<i>SI unit</i>
W	Weight	kg
W_e	Weber number	-
X	Martinelli parameter	-
x	Vapour quality	-
x_{cr}	Quality at critical heat flux	-
x_e	Exit quality	-
y	Transverse coordinate	-
z	Axial coordinate	-
Z_c	Non-dimensional axial distance ratio	-

Greek

<i>Symbol</i>	<i>Parameter</i>	<i>SI unit</i>
α	Area void fraction	-
α	Heat transfer coefficient	$\text{W m}^{-2} \text{K}^{-1}$
α_{film}	Heat transfer coefficient durring passage - - confined bubble with film.	$\text{W m}^{-2} \text{K}^{-1}$
β	Percentage of data within $\pm 30\%$	-
δ	Liquid film thickness	m
δ_0	Initila film thickness	m
δ_{end}	End film thickness	m
δ_{is}	Laminar thermal sublayer thickness	m
δ^*	Non-dimensional film thickness	-
ΔP	Pressure drop	Pa
ΔT	Temperature difference	K
ε	Volumetric void fraction	-
ϕ	Two phase multiplier	-
κ	Thermal diffusivity	$\text{m}^2 \text{s}^{-1}$
λ	Conductivity	$\text{W m}^{-1} \text{K}^{-1}$
μ	Viscosity	N s m^{-2}
ν	Specific volume	$\text{m}^3 \text{kg}^{-1}$
θ	Inclination angle	rad
θ	Contact angle	rad
θ_r	Receding contact angle	rad
ρ	Density	kg m^{-3}

<i>Symbol</i>	<i>Parameter</i>	<i>SI unit</i>
σ	Surface tension	N m^{-1}
τ	Shear stress	N m^{-2}
τ_b	Bubble generation period	s
τ^*	non-dimensional bubble generation period	-
τ_i	Interfacial shear stress	N m^{-2}
ν	Kinematic viscosity	m s^{-2}

Subscripts

<i>Symbol</i>	<i>Meaning</i>
<i>a</i>	Air
<i>a</i>	Acceleration
<i>b</i>	Bulk fluid
<i>B</i>	Bubble
<i>CB</i>	Confined bubble
<i>CBD</i>	Convective boiling dominant
<i>crit</i>	Critical
<i>df</i>	Drift flux
<i>dry</i>	Dryout zone
<i>ex</i>	Exit
<i>exp</i>	Experimental value
<i>f</i>	Friction
<i>fi</i>	Interfacial friction
<i>film</i>	Film
<i>FC</i>	Forced convective
<i>g</i>	Gas
<i>g</i>	Gravitational
<i>go</i>	Gas-only
<i>gs</i>	Superficial gas
<i>h</i>	Homogeneous mixture
<i>i</i>	Internal
<i>i</i>	Index
<i>i</i>	Iteration number

<i>Symbol</i>	<i>Meaning</i>
<i>i</i>	Interface
<i>in</i>	Inlet
<i>l</i>	Liquid
<i>lf</i>	Liquid film
<i>LS</i>	Liquid slug
<i>lg</i>	Liquid to vapour change
<i>LM</i>	Lockhart-Martinelli
<i>lo</i>	Liquid-only
<i>ls</i>	Superficial liquid
<i>m</i>	Mean
<i>M</i>	Martinelli
<i>max</i>	Maximum
<i>min</i>	Minimum
<i>nb</i>	Nucleate boiling
<i>NBD</i>	Nucleate boiling dominant
<i>net</i>	Net
<i>o</i>	Outer
<i>ONB</i>	Onset of nucleate boiling
<i>opt</i>	Optimum
<i>p</i>	Pair
<i>Pred</i>	Predicted
<i>ref</i>	Reference
<i>sat</i>	Saturation
<i>sub</i>	Subcooled
<i>sup</i>	Superheat
<i>t</i>	Turbulent
<i>tot</i>	Total

<i>Symbol</i>	<i>Meaning</i>
<i>tp</i>	Two phase
<i>tt</i>	Turbulent liquid and turbulent gas
<i>tv</i>	Turbulent liquid and laminar gas
<i>sp</i>	Single phase
<i>v</i>	Vapour
<i>VS</i>	Vapour slug
<i>vt</i>	Laminar liquid and turbulent gas
<i>vv</i>	Laminar liquid and laminar gas
<i>w</i>	Wall
<i>wi</i>	Inner wall
<i>wo</i>	Outer wall
<i>0</i>	Initial

Chapter 1

Introduction

1.1 Brief review on microchannel applications

Boiling two phase flow is a very efficient way of removing high heat flux and has been applied for a very long time in many different systems including the petrochemical and nuclear industries. In recent years, the automotive industry, motivated by the small refrigerant charging, low weight and small overall volume that will provide environmental and fuel efficiency benefits, has pushed the development of compact heat exchangers for air-conditioning and fuel vaporizers. A second significant deriving force for the application of microchannel in heat transfer comes from the increasing demand for the efficient cooling by high performance micro-electronic devices in a limited space. This has challenged the conventional method of cooling, mainly because of higher local heat fluxes leading to hot spots and smaller system enclosure. High dissipation rates in the order of 1000 kW/m^2 (for computer chips) and heat fluxes beyond 140 MW/m^2 (x-ray radiation sources, magnetrons used for radars, fusion reactors) are required, Mudawar (2001), Kenny et al. (2006). These demands cannot be met by conventional cooling systems (heat pipes, air-convective heat sinks, or vapour chambers). Multiple heat pipes and vapour chambers have been attractive solutions for micro processing cooling. However, they are not capable of heat power above tens of watts partly because of their limitation in rejecting their heat to the ambient, Upadhyaya (2005). A number of other cooling solutions have been proposed to alleviate the increasing demand for high cooling capacity in electronics and space craft controllers.

These include but are not limited to micro-refrigeration, micro-heat sinks, single and two phase microchannels, jet-impingement, spray cooling, pool boiling.

Single phase water microchannel cooling was first proposed by Tuckerman and Peas (1981) for very large scale integrated (VLSI) circuits. They demonstrated microchannel heat sinks of $50 \mu\text{m} \times 300 \mu\text{m}$ can remove 7900 kW/m^2 with substrate to coolant temperature difference of 71 K. Water flow rate exceeding 500 ml/min ($\sim 30 \text{ kg/hr}$) was required. Since then, micro cooling technology has been studied intensively. Emerson Network Power designed an active microstructure cooling system capable of providing an average heat flux of nearly 1500 kW/m^2 , keeping the junction temperature below 55°C . They reported that the main practical challenges in introducing these cooling systems are high pressure drop and the attachment of the heat sinks to the processors. In addition, the main drawback of single phase cooling systems is the non-uniform cooling temperature, i.e. stream-wise temperature increase in the coolant temperature and heat dissipating device, which is not desirable for temperature sensitive devices such as electronic chips. Consequently, two phase boiling flow is preferred for its lower flow rate requirement, better performance and improved temperature uniformity.

A closed-loop two phase microchannel cooling system using electro osmotic pumping was developed by Jiang et al. (2002). The system has silicon heat exchangers that can achieve junction-fluid resistance near 0.1 K/W with 40 plasma etched channels of $100 \mu\text{m}$ hydraulic diameter. Mudawar (2001) assessed various high heat flux thermal management schemes such as pool boiling-thermosyphon, detachable heat sinks, channel flow boiling, microchannel (ten to several hundred micrometers) and minichannel (order of one or few millimetres) heat sinks, jet-impingement and spray cooling. Two main configurations of the micro- and mini-channel two phase cooling application were demonstrated. These were direct cooling, i.e. direct immersion of the device surface in the liquid coolant, and indirect cooling using metallic heat sinks between the device and the coolant. Both techniques have their pros and cons. The former method shortens the thermal resistance between surface and coolant, but the system needs to ensure electrical and chemical compatibility between the coolant and the device. The latter provides flexibility in the coolant choice; however, it increases the thermal resistance and suffers from relatively low CHF. Agostini et al. (2007) conducted a review on the application of three different methods for cooling high heat flux computer chips. These are liquid cooling in copper or silicon micro geometry heat

dissipation elements, impingement of liquid jets directly on the silicon surface chips and two phase flow boiling copper or silicon microchannels. After assessing the advantages and disadvantages of the different cooling options, they concluded that two phase flow boiling in microchannels is the most promising approach for the cooling demands of 3000 kW/m^2 heat flux and chip temperature below $85 \text{ }^\circ\text{C}$.

On the other hand, Schmidt (2000) proposed refrigeration systems for electronics cooling because of their various advantages. These include, maintaining low device temperature while dissipating high heat fluxes, faster switching time (due to increase electron mobility), better device performance and reduced current leakage. However, one of the drawbacks to such systems is the fact that high operating pressure is required to overcome their low saturation temp (below subfreezing point). This will add complexity in connector design (mechanical strength of devices) and sealing issues. Lee and Mudawar (2006) implemented microchannel evaporators into refrigeration systems. This was initiated mainly to attain a device temperature below $55 \text{ }^\circ\text{C}$ while dissipating rates in the order of 1000 kW/m^2 . They were able to test evaporator inlet pressure as low as 1.44 bar, since a vapour compression refrigeration flow loop using R134a were used. However, such systems also require dry vapour at the compressor inlet. Slightly superheated exit conditions at the microchannel evaporator outlet means that localised high wall temperature near the exit, which could cause large local thermal stresses. Some proposed methods to alleviate this problem include developing wet compression tolerant compressors with adaptive flow control systems to maintain the required evaporator outlet quality.

Various coolants have been proposed for high heat flux cooling applications, particularly in electronic cooling, which require the use of coolant that boils at 10 to 40 K below the desired device's operating temperature. The high saturation temperature of water and poor dielectric properties preclude it from electronic cooling, if low device temperature is sought. Operating at sub atmospheric pressure for low temperature applications causes complications such as undesirable bubble nucleation and air inclusions if the system leaks. For two phase electronic cooling, fluorinerts such as FC 72, FC 87, PF 5052 are most promising and preferred, mainly due to their dielectric fluid property and appropriate saturation temperature (56.6 , 32 and $50 \text{ }^\circ\text{C}$ respectively). However, their thermal properties (specific heat and latent heat) are far inferior to water. Therefore application of these fluids particularly in immersion or spray cooling (pool

boiling) most often requires surface enhancements for better performance, Mudawar (2001). In addition, they have global warming potential although their ozone depletion ability is minimal.

The fast popularity of microchannel cooling technology is also mainly due to the advancement in material technology and fabrication methods. Sunden et al. (1995) who reviewed fabrication methods of microchannels stated that the microchannel fabrication have progressed in few years from precision cutting using diamond blades to micro machining such as photolithography and anisotropic, electro discharge machining, laser machining and plasma etching. The suitability of silicon wafers for chemical etching and their use in the semi-conductor industry have made them first choice for micorchannel applications, particularly for electronics cooling. However, their brittleness and surface characteristics (wettability and surface smoothness) are some of the drawbacks in two phase boiling systems, although they are commonly used with single phase microchannels. Therefore, most often they need surface treatments to improve the surface thermal nucleation characteristics, which otherwise will require high initial superheat for onset of nucleate boiling (ONB). Frieser and Reeber (1980) investigated the physical characteristics and three means of treating silicon surfaces (chip backside of IBM mounts) to provide reliable nucleation sites for boiling in perflourinated coolants. They reported that without treating the surface, it was not possible to obtain nucleation. Alternatively, copper microchannels have also been demonstrated, Qu and Mudawar (2003a), Agostini et al. (2007) in two phase cooling systems.

1.2 Research Background

As briefly reviewed above, the increasing demand for high cooling capacity and meeting environmental targets such as reducing global warming and ozone layer depletion imposes a limit on the conventional ways of designing cooling systems. The much-favoured alternative is therefore to use compact heat exchangers and microchannels. They are preferred for their minimum requirement of material during their manufacturing, enhanced heat transfer performance and small refrigerant inventory used in the system. Moreover, advances in high performance micro-devices, micro-systems including electronic chips and the miniaturization of electronic circuits demand the development of efficient heat removal techniques. Microchannel two phase boiling is one of the promising methods suggested for cooling of high power electronics

circuits. However, modelling and design of the thermal management of micro-devices of high thermal performance, including electronic chips and other systems containing compact and ultra-compact heat exchangers, require a fundamental understanding of thermal transport phenomena for the ultra-compact systems. Therefore, fundamental studies of flow patterns, void fraction, pressure drop and heat transfer are all required for the understanding of the heat transfer mechanism and developing accurate design method for thermal management of micro-devices. Despite the fact that there is an intense research in two phase flow boiling in small to micro passages, the heat transfer research community has yet to conclude on several issues related to flow boiling in small-to-micro passages. These are briefly reviewed below.

Identifying the channel diameter threshold, below which the macroscale heat transfer phenomena do not fully apply, is important in validating and developing predictive methods for the thermal-hydraulic performance of small to microscale channels. However, there is no clear and common agreement on the definition and classification criterion for the size ranges in small/mini/microchannel two-phase flow study. Although different definitions have been given by various researchers, Brauner and Maalem-Maron (1992), Cornwell and Kew (1993), Mehendale et al. (2000), and Kandlikar and Grande (2003), most of the ways used to classify the various size ranges do not consider the physical mechanisms and other effects involved when varying the size of the channels. One reason could be the lack of comprehensive heat transfer data covering a wide range of channel diameters.

The number and type of flow patterns observed in small tubes is diverse among different researchers, although most flow pattern studies in small/micro tubes have clearly shown that there is a considerable difference in the flow pattern characteristics compared with conventional size channels. These include the predominance of surface tension force over gravity, the absence of stratified flow pattern in horizontal channels and the appearance of additional flow patterns that are not common in normal diameter tubes, Barnea et al. (1983), Mishima and Hibiki (1996), Kew and Cornwell (1997), Chen et al. (2006), and Revellin et al. (2006).

There is also no common agreement on the mechanism of heat transfer in small-to-micro passages. Based on conventional way of interpreting flow boiling mechanism, nucleate boiling, forced convection and a combination of both were the main mechanisms repeatedly reported in the literature. Some researchers concluded that

nucleate boiling is the dominant heat transfer mechanism, since it was observed that heat transfer coefficient is more or less independent of vapour quality and mass flux, while it is strongly dependent on heat flux, e.g. Lazarek and Black (1982), Wambsganss et al. (1993), Tran et al. (1996), Bao et al. (2000), Yu et al. (2002), Fujita (2002). On the other hand, some experimental studies have also observed effects of mass velocity and vapour quality on heat transfer but not heat flux. This is interpreted as forced convective boiling is dominant heat transfer mechanism, e.g. Carey et al. (1992), Oh et al. (1998), Lee and Lee (2001), Qu and Mudawar (2003a). Others have reported a combined effect of both mechanisms, i.e. nucleate boiling at low quality and forced convective boiling at high quality region in a similar way as that observed in large tubes, e.g. Kuznestov and Shamirzaev (1999), Lin et al. (2001a), Sumith et al. (2003), Saitoh et al. (2005).

Flow boiling studies have also showed a decrease in heat transfer coefficient with increasing quality, often accompanied by fluctuating wall temperatures, e.g. Lin et al. (2001a), Yan and Lin (1998), Wen et al. (2004), Huo et al. (2007). Such deterioration of heat transfer associated with sudden rise in wall temperature can affect the integrity of cooling devices and lead to irreversible damage. These have been attributed to transient dryout, particularly at low mass flux, and relatively high heat flux. Other studies have also indicated fluctuations in pressure and wall temperature in the order of magnitude of the mean superheat causing evaporation, assumed to be caused by the acceleration of liquid slugs by expanding confined bubbles, Kew and Cornwell (1996), Yan and Kenning (1998).

There are a limited number of experiments that have tested a wide range of tube diameter to investigate the heat transfer trend with channel size. Most studies have reported that the heat transfer coefficient increases with decreasing tube diameter, Yan and Lin (1998), Oh et al. (1998), Huo et al. (2007), Owhaib et al. (2004). On the other hand some researchers found little or no significant effect of tube diameter on the magnitude of heat transfer, Kuwahara (2000), Baird et al. (2000), Khodabandeh (2003), Saitohi et al. (2005). Therefore, there is no clear trend on the effect of tube diameter on flow boiling.

There is also a need for validated prediction methods for two phase heat transfer and pressure drop that will facilitate the design and optimization of compact heat exchangers for use with refrigerants and other fluids. Several correlations have been proposed, most of which are extensions of large tube correlations, which are empirically formulated from a rigorous data analysis. However, they did not predict well the heat transfer

coefficient in small diameters, Qu and Mudawar (2003a), Owhaib and Palm (2003) and Huo et al. (2007). A promising approach is made in developing regime based models, Qu and Mudawar (2003b), Thome et al. (2004).

Although there are a large number of experimental studies inside tubes of 1 mm and above there are only limited heat transfer data in metallic tubes of size below 1 mm. The effect on heat transfer characteristic and flow pattern when the tube size is decreased much below 1 mm is not well understood. The few research studies indicated that flow boiling in very small diameter tubes is usually associated with high initial liquid superheat required to initiate boiling, Yen et al. (2003), Hapke et al. (2000), Peng and Wang (1993) and Peng et al. (1998). The unusually high superheat in micro tubes was also reported to be related to the reduction of active nucleation sites and vapour nucleation inside very small channels, Zhang et al. (2002) and Brereton (1998). Flow pattern studies of very small diameter tubes reported further differences in the flow pattern characteristics as the tube size decreased below 1 mm, Serizawa et al. (2002), Kawahara et al. (2002), Xiong and Chung (2007). These include the emergence of additional features to those observed in small diameter tubes, e.g. the appearance of a symmetrical liquid ring that no longer bridges the tube and liquid lump flow (flow of liquid lumps sliding on the wall) and diminishing appearance of dispersed and churn flows.

1.3 Objectives

The above brief overview indicates that there is a great practical interest for research in micro passages and suggest needs for systematically measured boiling heat transfer data to understand the mechanisms of flow boiling in small to micro diameter passages and developing models. The work presented in this thesis is part of a long-term study of flow boiling patterns, heat transfer and pressure drop in small to micro diameter metallic tubes. X. Huo (2005) studied heat transfer and pressure drop in 4.26 and 2.01 mm tube and L. Chen (2006) completed a flow visualization study for tubes 4.26, 2.88, 2.01, and 1.1 mm in diameter. The current work includes the heat transfer (with simultaneously observed flow patterns) and pressure drop work in the 2.88, 1.1 and 0.52 mm tubes. The data obtained in the previous studies of the group are also included in parts of the thesis to provide a complete picture of the various phenomena discussed. Most often flow pattern studies have been conducted and reported separately from heat transfer studies and are mainly carried out using adiabatic flows. However, the

promising success of newly emerging regime-based models require a simultaneous investigation of flow pattern and heat transfer in order to support understanding and modelling of heat transfer characteristics. This thesis, which covers flow boiling data over a wide range conditions, tubes with internal diameters 4.26, 2.88, 2.01, 1.1 and 0.52 mm, heat flux 1.6 – 150 kW/m²; mass flux 100 – 700 kg/m²s, pressure 6 – 14 bar and exit quality 0 to 0.9, addresses the above issue by conducting simultaneous study of flow visualization and heat transfer. The present study also investigates the effect of tube diameter on heat transfer trend and magnitude, which will aid the effort to identify the thresholds for distinguishing macro, small and microscale characteristics. In addition, by assessing the effect of various parameters, the thesis contributes to the clarification of heat transfer mechanism and on the development of heat transfer and pressure drop prediction methods.

1.4 Overview

This thesis is organised as follows. Chapter 2 presents the fundamental background for two phase flow boiling studies in conventional tubes. It discusses the basic theories that could also be transferred to the study of microscale systems. In chapter 3, a detail state-of-the-art review on flow boiling in small to micro passages is provided. A wide range of subjects in flow boiling studies are covered. The experimental facility used in the present study is described in Chapter 4. Chapter 5 presents the heat transfer results of the five tubes and discusses these results using the simultaneously obtained flow patterns. In this Chapter, the experimental results are compared with existing correlations. Also new correlations that take account the influence of tube diameter on heat transfer are developed based on the present experimental data. Chapter 6 presents the boiling two phase pressure drop results and compares these results with existing correlations. In chapter 7, existing theoretical models are investigated using a detailed comparison with the present data. Also, some features of the models that require modification are demonstrated. At the end of the chapter, a new pressure drop model based on the “three-zone modelling” approach using slug flow regime is developed. Finally, conclusions and recommendations for future work are presented in Chapter 8.

Chapter 2

Fundamentals of Two Phase Flow Study and Definitions

2.1 Introduction

A brief introduction to the fundamentals of two phase flow pattern, pressure drop and heat transfer is given in this chapter in order to identify the new features of two phase flow boiling in small diameter tubes and relate and understand what can be borrowed from the macroscale theory. The chapter also serves as a theoretical background section for the main study. It is organised as follows: Section 2.2 describes the two phase flow regimes that exist in conventional vertical tubes and the mechanisms of flow pattern transition. Section 2.3 introduces two phase pressure drop and void fraction. Section 2.4 covers boiling two phase flow heat transfer, where the fundamentals of phase change heat transfer and their mechanisms as well as methods proposed to determine the heat transfer rate are discussed.

2.2 Flow patterns and flow maps

The respective distribution of the two phases (liquid and vapour), which take a particular configuration, defines the type of flow patterns. In many cases, these patterns have some distinct characteristics that allow the use of simple descriptive phrases to designate each. The dynamics and pattern of these phases are also influenced by physical parameters and forces such as gravity and surface tension. In normal tubes, gravity acts to separate the phases and pull the liquid to the bottom of the channel, i.e. it causes directional influence or tends to form stratified flow in horizontal channels. Surface tension keeps the channel surface wet and tends to form spherical gas bubbles and liquid droplets. This section provides a brief introduction to the definitions of various flow configurations, description of flow pattern maps and flow pattern transitions, particularly in conventional size vertical tubes.

2.2.1 Flow patterns

The flow pattern names are designated from the various shapes that the phase interface attains based on subjective and objective criteria. Identifying the type of flow pattern(s) expected during the actual working conditions is important for heat exchanger design. Based on the prevailing flow pattern(s), a suitable heat transfer and hydrodynamic theory can be selected. Also, knowledge of the flow pattern during operation is very helpful in troubleshooting heat exchanger problems. The common technique used to study the flow patterns in channels is using high speed visualization through transparent channels. Such a method is associated with an unquantifiable uncertainty and open to subjective judgements. Alternative methods have been developed to address this issue. Researchers have proposed x-radiography that allowed visualization of heated channels which are opaque (Hewitt 1978, Derbyshire et al. 1964). Others have also used transparent glass tubes with a thin conductive metallic layer that is used to provide the required heat flux, Owhaib et al. (2006). However, lack of standard methods for identifying various flow patterns have led to a number of different names for flow configurations and classifications.

In boiling two phase flow cases, the particular flow regime is dependent on pressure, flow rate, heat flux, and channel geometry. The most common flow patterns observed in vertical upward two-phase flow are bubbly, slug, churn, wispy-annular and annular. Figure 2.1 shows schematics of the various flow patterns.

The qualitative definition of these flow patterns as described in Collier and Thome (1994) are given below.

- a) Bubbly flow: flow of discrete gas or vapour flows in a continuous liquid phase
- b) Slug flow: a flow of bullet shaped (Taylor) bubbles. The size of the vapour/gas bubble is nearly equal to the internal diameter of the tube, which is only separated from the wall by a slowly descending film of liquid. The liquid flows as liquid slugs that separate the successive gas bubbles. In some cases, the liquid slug may contain small entrained gas bubbles.
- c) Churn flow: flow of gas or vapour in a chaotic manner through the liquid, which is mainly displaced to the channel wall. The flow has an oscillatory or intermittent behaviour.

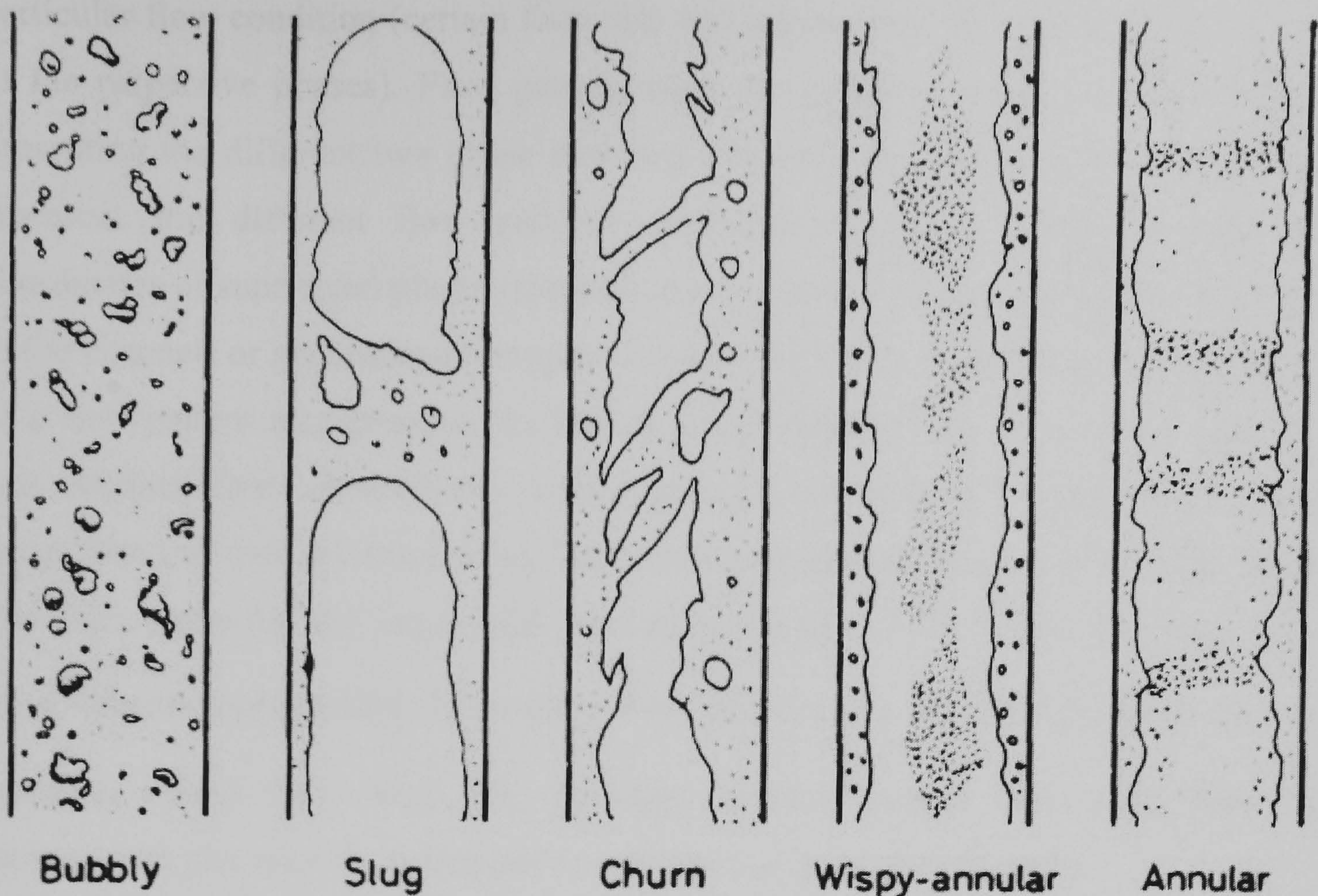


Figure 2.1 Flow patterns in vertical gas flow, (Collier and Thome, 1994).

- d) Wispy-annular flow: a flow with relatively thick liquid film on the walls and a large liquid entrainment in the central gas or vapour core. The liquid in the film is aerated by small gas bubbles and it takes its name from the fact that the entrained liquid phase appears as large droplets which have agglomerated in to long irregular wisps.
- e) Annular flow: a flow in which liquid phase flows as annular film coating the wall of the tube, while the gas or vapour flows in the core. The film interface is mostly covered by ripple waves (short wave length and small amplitude) and disturbance waves (longer wave length and large amplitude), Hewitt and Hall-Taylor (1970). A continuous break up of the large amplitude waves forms a source of droplet entrainment which occurs in varying amounts in the central gas core. The annular flow pattern is the dominant flow pattern in conventional channels existing from vapour mass fraction of low percentage to values close to unity.

2.2.2 Flow pattern maps

Flow pattern maps are prepared that clearly indicate transition lines between the flow patterns in order for designers to be able to identify the flow patterns corresponding to a

particular flow condition (certain flow rate and vapour fraction or superficial velocities of the respective phases). Flow pattern maps are probably the most useful tools for presenting the different two phase flow regimes and their transition boundaries. They represent the different flow patterns allocating respective areas on plots with coordinates of superficial phase velocities (mean velocity of each phase if flowing alone in the channel) or generalised parameters containing these velocities. A typical example of a flow pattern map prepared by Hewitt and Roberts (1969) is shown in Fig. 2.2. It was obtained from observations on low pressure air-water and high pressure steam-water flows in vertical round tubes with internal diameters ranging from 10 to 30 mm. The axes represent the superficial momentum fluxes of the liquid ($\rho_l j_l^2$) and vapour ($\rho_g j_g^2$) phases respectively. Generally, flow patterns are affected by more than two variables (mass flux, heat flux, pressure, surface tension, tube size) thus two-dimensional plot may be inadequate to represent an inclusive influence.

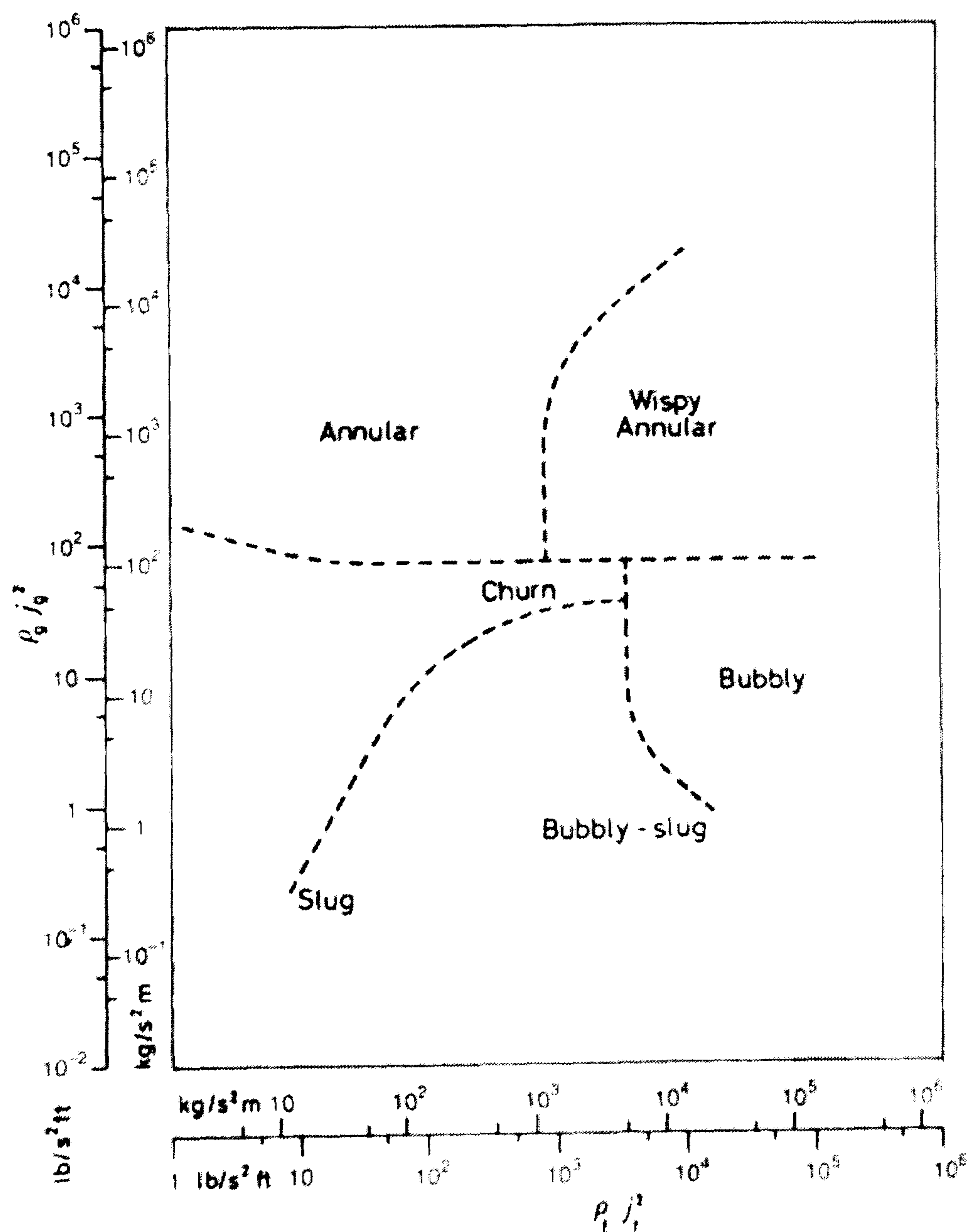


Figure 2.2 Flow pattern map for vertical flow for air- water and steam ($D = 10-30$ mm), Hewitt and Roberts, (1969).

2.2.3 Flow pattern transitions

Flow pattern boundaries are defined after classifying the flow pattern with established criteria. Most of the flow pattern classifications have involved subjective decisions, since visual observation was used to identify the flow pattern boundaries. Other ways of establishing flow pattern boundaries involve measurement of mean density across the tube or local average void fraction and phase velocities. In the past, an intensive research has also been dedicated to developing models that predict flow pattern transition boundaries. A brief introduction of flow pattern transition boundaries for conventional vertical tubes is presented below.

Bubbly to slug flow transition

The flow pattern transition criterion suggested by many researchers is related to the critical void fraction. As the gas flow increases the bubbles get closer to each other resulting in collision. Some of the collisions eventually lead to coalescence of bubbles to form slugs. The bubble collision frequency increases exponentially with void fraction (Radovich and Moissis, 1962). A large increase in collision frequency was obtained at a void fraction of about 0.3, which indicated flow pattern transition to slug flow tends to occur approximately near this point. Taitel et al. (1980) and Mishima and Ishii (1984) suggested a critical void fraction $\epsilon_{crit} = 0.25$ and $\epsilon_{crit} = 0.30$, respectively. Lu and Zhang (1994), who also suggested $\epsilon_{crit} = 0.30$ using R-12 for adiabatic condition, hypothesized that transition from bubbly to slug takes place when the interfacial surface area per unit volume reaches a maximum. This was proposed based on the one-dimensional steady state, frictionless, fully developed momentum equation for both phases.

Slug to churn flow transition

There are several theories developed to provide transition criteria from slug to churn flow in vertical tubes. When the superficial gas velocity increases, the average void fraction in the liquid slug reaches a critical value, which corresponds to coalescence of the successive bubble slugs, which result in the collapse of the liquid slugs, Brauner and Barnea (1986). They suggested transition to churn flow takes place when the void fraction in the liquid slug is greater than the “bubble maximum volumetric package” ($\epsilon_{max} = 0.52$). On the other hand, Dukler and Taitel (1986) considered churn flow as unstable slug flow (short liquid slug and long Taylor bubbles), which could develop into a stable slug flow further down stream through coalescence of gas slugs. Others

treated the transition from slug to churn to occur as a result of the collapse of relatively short highly aerated liquid slugs due to instabilities in the wake of Taylor bubbles, (Mishima and Ishii, 1984). According to Mishima and Ishii, the transition takes place when the mean void fraction, ε_{df} , evaluated using a drift flux model (Eq. 2.1) is greater than the mean void fraction, ε_{gs} , Eq. (2.2).

$$\varepsilon_{df} = \frac{U_{gs}}{CoU_h + 0.35 \left(\frac{gD\Delta\rho}{\rho_l} \right)^{0.5}} \quad (2.1)$$

where, $Co = 1.2 - 0.2 \left(\frac{\rho_g}{\rho_l} \right)^{0.5}$ for round tubes

$$\varepsilon_m = 1 - 0.813 \left[\frac{(Co - 1)U_h + 0.35 \left(\frac{\Delta\rho g D}{\rho_l} \right)^{0.5}}{U_h + 0.75 \left(\frac{\Delta\rho g D}{\rho_l} \right)^{0.5} \left(\frac{\Delta\rho g D^3 \rho_l}{\mu_l^2} \right)^{1/18}} \right]^{0.75} \quad (2.2)$$

Slug to churn transition has also been related to flooding of the liquid film surrounding the bubble, (McQuillan and Whalley, 1985 and Jayanti and Hewitt, 1992). At a certain defined flow rate, the gas velocity will suddenly disrupt the liquid film so that the slug flow will break down to give churn flow. Since, the gas velocity is not high enough to reverse the film flow direction, counter current flow is encountered in which the liquid film flows downward.

Churn to Annular transition

The most commonly used criterion for transition is the flow reversal condition, which is related to flooding, Hewitt (1982). As the gas flow rate or superficial gas velocity increases the interfacial shear stress becomes significant to support the liquid film on the tube walls. Therefore, the flow reversal characteristic of the churn flow does not exist anymore and the liquid film gets thinner. The flooding criterion proposed by Hewitt and Wallis (1963) uses the correlation,

$$\sqrt{U_{gs}^*} + \sqrt{U_{ls}^*} \approx 1, \quad (2.3)$$

where,

$$U_{gs}^* = U_{gs} \sqrt{\frac{\rho_g}{gD\Delta\rho}} \quad \text{and} \quad U_{ls}^* = U_{ls} \sqrt{\frac{\rho_l}{gD\Delta\rho}}$$

The characteristics of entrained droplets were also considered to govern the transition to annular flow, Taitel et al. (1980). The gas velocity required to suspend entrained droplets was given by:

$$U_{gs} = 3.2 \left[\frac{g\sigma(\rho_l - \rho_g)}{\rho_g^2} \right]^{1/4} \quad (2.4)$$

Annular to wispy annular flow transition

The wispy annular flow is mostly considered as a subcategory of annular flow, which occurs at high mass flux when the entrained droplets are seen to appear as elongated droplets. The wispy-annular region is assumed to occur when $U_{gs}^* > 1$ and $U_{ls}^* > 2.5 - 3$, Collier and Thome (1994). A criterion for transition from annular flow to wispy-annular flow was also suggested by Wallis (1969) based on an experiment using electrical probe measurement of liquid wisps in the gas core. The criterion for transition was given as

$$U_{gs} = \left(7 + 0.06 \frac{\rho_l}{\rho_g} \right) U_{ls} \quad (2.5)$$

Corresponding to the case when $U_{ls}^* > 1.5$.

2.3 Two phase flow model and pressure drop

Although there are a number of empirical equations to predict various two phase flow parameters, there are different assumptions in treating the distribution of the phases in a two phase flow modelling. This section introduces the fundamental approaches of two phase flow modelling in predicting the pressure drop and provides the theoretical background for the two phase pressure drop investigation of the current study. In addition, the pressure drop equations presented here are required later when comparing with the present experimental data; hence the fundamental equations and correlations will not be repeated further.

There are a large number of empirical and semi-empirical methods employed to determine the different two phase thermal hydraulic parameters. However, there are also different basic models used in two phase flow studies, which vary in the way the dynamics of each phase and their interaction is treated. These include:

- (a) **Homogenous two phase flow model:** the model assumes the two phase mixture as a single phase with average physical properties.
- (b) **Separated two phase flow model:** treats the phases as separately segregated into two streams with (not necessarily) different velocities.
- (c) **Drift flux model:** a type of separated flow model that correlates phase velocities in terms of relative velocities.
- (d) **Annular two phase flow model:** calculates phase parameters based on the annular flow pattern.

This section briefly introduces the fundamentals of the above two phase flow models and empirical methods used to predict two phase flow pressure drop and void fraction. All the models will be introduced in light of predicting the pressure drop.

2.3.1 Homogenous two phase model

The model basically assumes that the two phases are well mixed and more particularly travel with the same phase velocity. Therefore, it is expected that this model is best suited for bubbly (dispersed bubble) and wispy-annular flow patterns. However, several two phase flow studies in the literature have often applied homogenous model for various flow regimes with acceptable accuracy. The basic conservation equations for a one-dimensional steady homogenous flow as given in most fundamental two phase flow books, Whalley (1987), Collier and Thome (1994), Tong and Tang (1997).

From the continuity equations in the gas and liquid phases and the basic assumption of homogenous flow, i.e. the two phases flow with the same velocity, $U_g = U_l$, the area void fraction is given as,

$$\alpha_h = \frac{1}{1 + \left(\frac{1-x}{x} \frac{\rho_g}{\rho_l} \right)} \quad (2.6)$$

As can be seen from Eq. (2.6), the homogenous flow assumption simplifies the calculation of void fraction. If the density ratio (ρ_l/ρ_g) is less than 10 or $G > 2000$ kg/m²s, the homogenous void fraction is considered as a better estimate of the actual void fraction. However, this corresponds to high pressure systems. In conditions of (ρ_l/ρ_g) greater than 10, the homogenous flow assumption is expected to under-predict the actual void fraction by a factor of 5 to 10, Whalley, (1987).

Pressure gradient in homogeneous flow

Generally, the total pressure gradient during two phase flow boiling in vertical tubes is the overall contribution of three components, namely: acceleration, gravitational, and frictional, i.e.

$$\left(\frac{dp}{dz}\right)_{tot} = \left(\frac{dp}{dz}\right)_a + \left(\frac{dp}{dz}\right)_g + \left(\frac{dp}{dz}\right)_f \quad (2.7)$$

In homogeneous flow, the two phases are treated as a single phase flowing with a single velocity, it is therefore appropriate to define a homogenous average density and viscosity.

The homogenous average density is given as

$$\rho_h = \rho_g \alpha_h + \rho_l (1 - \alpha_h) \quad (2.8)$$

Using Eq. (2.6) for α_h (homogenous void fraction), Eq. (2.8) can be re-written as,

$$\frac{1}{\rho_h} = \frac{x}{\rho_g} + \frac{1-x}{\rho_l} \quad (2.9)$$

Various expressions were proposed for the average homogenous viscosity

$$\frac{1}{\mu_h} = \frac{x}{\mu_g} + \frac{1-x}{\mu_l} \quad (\text{McAdams et al. 1942}) \quad (2.10)$$

$$\mu_h = \mu_g \frac{x\rho_h}{\rho_g} + \mu_l \frac{(1-x)\rho_h}{\rho_l} \quad (\text{Dukler et al. 1964}) \quad (2.11)$$

$$\mu_h = \mu_g \alpha_h + \mu_l (1 - \alpha_h) (1 + 2.5 \alpha_h) \quad (\text{Beattie and Whalley, 1981}) \quad (2.12)$$

The **acceleration pressure gradient** is determined as; see Collier and Thome (1994)

$$-\left(\frac{dp}{dz}\right)_a = G^2 \frac{d}{dz} \left(\frac{x^2 v_g}{\alpha} + \frac{(1-x)^2 v_l}{1-\alpha} \right) \quad (2.13)$$

Considering homogeneous flow assumptions,

$$-\left(\frac{dp}{dz}\right)_a = G \frac{dU_h}{dz} = G^2 \frac{dv_h}{dz} \quad (2.14)$$

$$\frac{dv_h}{dz} = v_{lg} \frac{dx}{dz} + x \frac{dv_g}{dp} \left(\frac{dP}{dz} \right) \quad (2.15)$$

The **gravitational pressure gradient** is expressed as:

$$-\left(\frac{dp}{dz}\right)_g = \rho_h g \sin \theta = [\rho_g \alpha_h + \rho_l (1 - \alpha_h)] g \sin \theta \quad (2.16)$$

The **friction pressure gradient** arises from the shear stress effects. In single phase flow the wall shear stress is usually expressed in terms of friction factor, (Eq. 2.23). The friction factor is usually given empirically as a function of Re and (in some cases for turbulent flow) tube roughness.

$$f_f = \frac{\tau}{\frac{1}{2} \rho U^2} = \frac{\tau}{\frac{1}{2} \frac{G^2}{\rho}} \quad (2.17)$$

In a similar way, the total wall shear stress in the momentum equation can be expressed using the friction factor, see also Collier and Thome (1994), Whalley (1987).

Therefore,

$$-\left(\frac{dp}{dz}\right)_f = f \frac{P_e}{A} \left(\frac{\rho_h U_h^2}{2} \right) \quad (2.24)$$

where, $\frac{P_e}{A} = \frac{4}{D}$, for the case of circular channels

Collecting the above terms for each contribution, the total pressure gradient based on homogeneous flow assumption can be represented as,

$$-\left(\frac{dp}{dz}\right)_{tot} = \frac{-\frac{2fG^2v_l}{D}\left[1+x\left(\frac{v_{lg}}{v_l}\right)\right] + G^2v_l\left(\frac{v_{lg}}{v_l}\right)\frac{dx}{dz} + \frac{g}{v_l\left(1+x\frac{v_{lg}}{v_l}\right)}}{1+G^2x\left(\frac{dv_g}{dp}\right)} \quad (2.25)$$

If we consider evaporation in a vertical tube (diameter (D), length (L) and inlet condition at saturation temperature, $x = 0$ to a vapour-liquid mixture with mass quality x) and assuming the quality varies linearly with the axial length, the two phase multiplier integral over the length can easily be evaluated and given as; see Collier and Thome (1994), Whalley (1987).

$$-\Delta p = \left(\frac{2f_{lo}L}{d}G^2\frac{1}{\rho_l}\right)\left(1+\frac{x}{2}\right) + (\rho_l g L)\left(\frac{\ln(1+x)}{x}\right) + G^2\frac{x}{\rho_l} \quad (2.26)$$

Normally, the most common approach is to express the two phase friction pressure gradient in terms of the two phase multiplier,

$$-\left(\frac{dp}{dz}\right)_f = \left[\frac{2}{D}f_{lo}\frac{G^2}{\rho_l}\right] \cdot \left[\frac{f_h}{f_{lo}}\frac{\rho_l}{\rho_h}\right] = -\left(\frac{dp}{dz}\right)_{f_{lo}} \cdot \phi_{lo}^2 \quad (2.27)$$

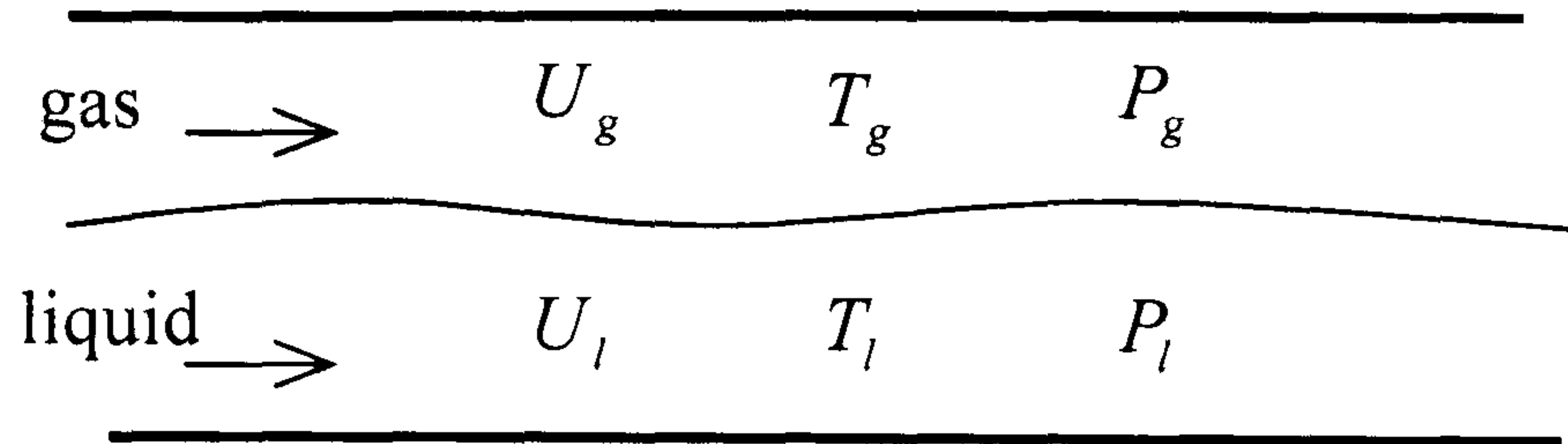
where $-\left(\frac{dp}{dz}\right)_{f_{lo}}$ is the friction pressure gradient calculated from a liquid single phase

flow assuming that mass flux is the total mass flux, i.e. the sum of mass fluxes of liquid and gas in two phase flows. ϕ_{lo}^2 , is the two phase multiplier corresponding to the liquid only friction pressure gradient.

2.3.2 Separated flow model

Separated flow model is quite often used in the literature to predict two phase flow pressure drop. It is a more comprehensive approach of treating two phase flow than homogeneous flow assumption. For instance, the separated flow model equations will reduce to homogenous model if the phase velocities become equal. The basic assumptions of the separated flow model include: phases flow physically separated with a constant but not necessarily equal velocities; there is a thermal and hydrodynamic equilibrium between the phases, i.e. $T_g = T_l$; $P_g = P_l$. The later is considered, because it is usually felt that the rates of mass and energy exchange are large enough to promote

equilibrium. The void fraction is given in Eq. (2.8) with U_g/U_l referred to as the slip ratio (S), which is greater than 1, since gas moves faster than liquid. In case of homogenous flow, it is equal to unity.



Pressure gradient in separated flow model

The total pressure gradient derived from the steady state momentum equation is given as:

$$-\left(\frac{dp}{dz}\right)_{tot} = \frac{4\tau}{D} + [\alpha\rho_g + (1-\alpha)\rho_l]g + G^2 \frac{d}{dz} \left[\frac{x^2}{\alpha\rho_g} + \frac{(1-x)^2}{(1-\alpha)\rho_l} \right] \quad (2.28)$$

On the other hand, the same approach of expressing two phase pressure drop based on a single phase result and corresponding two phase multiplier, is quite often used for the separated flow model as well. Therefore, the frictional contribution to the total pressure gradient is treated in the same way as the homogenous model, and is given as: see Collier and Thome (1994), Whalley (1987), Tong and Tang (1997).

$$-\left(\frac{dp}{dz}\right)_f = -\left(\frac{dp}{dz}\right)_{f_l} \phi_l^2 = \left[\frac{2f G^2 (1-x)^2}{D} \frac{1}{\rho_l} \right] \phi_l^2 \quad (2.29)$$

or

$$-\left(\frac{dp}{dz}\right)_f = -\left(\frac{dp}{dz}\right)_{f_{lo}} \phi_{lo}^2 = \left[\frac{2f_{lo} G^2}{D} \frac{1}{\rho_l} \right] \phi_{lo}^2 \quad (2.30)$$

In the separated flow model, the void fraction (which is required to determine the acceleration and gravitational pressure gradients) and the two phase multiplier need to be determined in order to calculate the total pressure gradient. Unlike the case for homogeneous flow model, the void fraction is not straight forward to calculate. The

most widely applicable method of determining these parameters (void fraction and two phase multiplier) is empirically from experimental data. The void fraction is measured using methods such as quick-closing valve, gamma ray densometer, x-rays, Hewitt (1977), Collier and Thome (1994). Experimentally, the friction component can be deducted from the measured total pressure drop, after calculating the gravitational term and the acceleration components. The gravitational and acceleration components can be evaluated from the measured void fraction and momentum flux, respectively. A large number of two phase pressure drop correlations have been proposed for conventional tubes in the open literature, including: Lockhart-Martinelli, (1949), Martinelli-Nelson (1948), Thom (1964), Chisholm (1983), Freidel (1979).

2.3.3 Drift flux model

The model is first developed by G. B. Wallis (Wallis 1969). It defines the various parameters using the relative velocity of the phases. The drift flux model is more appropriate when there is a well defined velocity of the gas phase, e.g. bubbly, slug. One of the features of drift flux model is the fact that it uses several phase velocity definitions, which are slightly confusing to identify. Some of the velocities applicable to the model are defined below for the sake of completeness.

U_{gs} and U_{ls} are defined as superficial phase velocities, which are phase velocities treating each phase as flowing alone in the whole channel.

j_g and j_l are referred to as the drift flux velocities of the gas and liquid, respectively.

U_s is defined as the relative velocity (also called the slip velocity), which is the difference between the velocities of the phases ($U_g - U_l$). The slip velocity is given as;

$$U_s = \frac{j_g}{\alpha} - \frac{j_l}{1 - \alpha} \quad (2.31)$$

j_{gl} , is defined as the drift flux velocity of the gas relative to the liquid and is given by:

$$j_{gl} = \alpha (1 - \alpha) U_s \quad (2.32)$$

For bubbly flow, U_B is the bubble rising velocity defined from equating the drag and buoyancy forces and considering the dynamic nature of the interface and is given by (Batchelor, 1967):

$$U_B = \frac{D^2 g (\rho_l - \rho_g)}{18 \mu_l} \left(\frac{3 \mu_g + 3 \mu_l}{3 \mu_g + 2 \mu_l} \right) \quad (2.33)$$

Thus the slip velocity is given as $U_s = U_B (1 - \alpha)$

and the drift flux (j_{gl}), is therefore

$$j_{gl} = U_b \alpha (1 - \alpha)^2 \quad (2.34)$$

In summary, the drift flux model provides an estimate of the void fraction, if the various gas velocities are known. For instance, Zuber and Findlay (1965) suggested Eq. (2.35) for plug flow.

$$\alpha = \frac{U_{gs}/j}{Co + U_{gj}/j} \quad (2.35)$$

where, Co is the distribution parameter proposed as $Co=1.13$

For bubbly flow they suggested,

$$U_{gj} = 1.4 \left[\frac{\sigma g (\rho_l - \rho_g)}{\rho_l^2} \right]^{1/4} \quad (2.36)$$

2.3.4 Annular flow model

Normally annular flow is the dominant flow type that exists over a wide range of quality in conventional tubes. Although, mostly a smooth liquid film is considered in calculations, actually the liquid film has ripples on its surface. It is also associated with large disturbance waves, which are assumed to cause substantial amount of liquid entrainment as droplets in the vapour core. The realistic approach requires understanding of the droplet generation and deposition process in order to develop hydrodynamic and heat transfer model for annular flow. These have been extensively studied by G.F. Hewitt and co-workers (Hewitt and Hall-Taylor, 1970).

In an ideal case, it is assumed that there is no entrainment and deposition. Considering one-dimensional steady flow, the force balance on an annular liquid film and gas core with outer radius (r), inner radius (r_i) and axial distance (Δz) can be given as, see also Whalley (1987).

Liquid film

$$-2\pi r \tau \Delta z + 2\pi r_i \tau_i \Delta z - \rho_l g \Delta z 2\pi (r^2 - r_i^2) + \left[P - \left(P + \frac{dP}{dz} \Delta z \right) \right] \pi (r^2 - r_i^2) = 0 \quad (2.37)$$

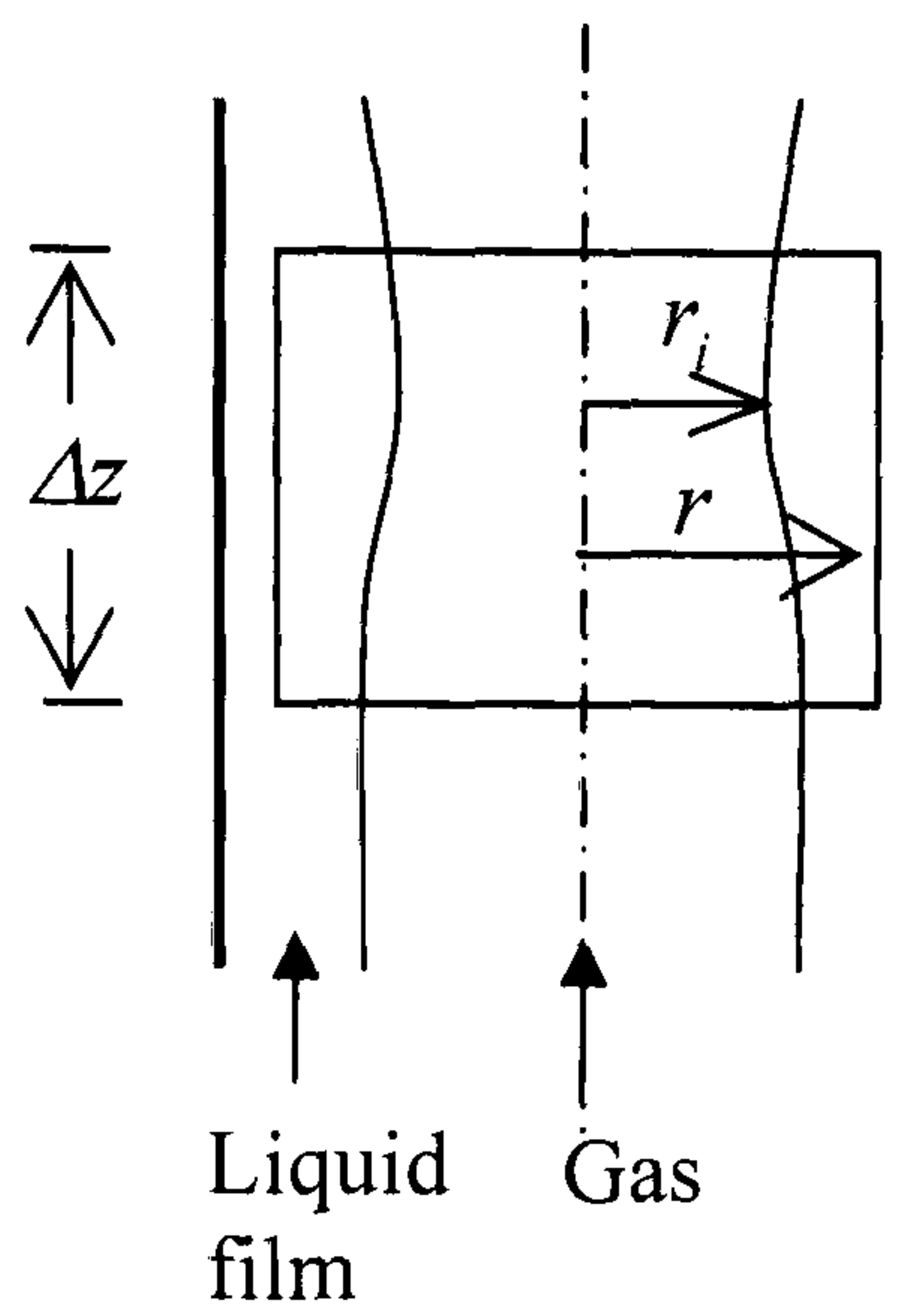
Gas core

$$-2\pi r_i \tau_i \Delta z - \rho_l g \Delta z 2\pi r_i^2 + \left[P - \left(P + \frac{dP}{dz} \Delta z \right) \right] \pi r_i^2 = 0 \quad (2.38)$$

where,

τ - shear stress at radius at r

τ_i - interfacial shear stress at r_i ,



The velocity profile in the liquid film and pressure drop can be evaluated considering the simple assumptions that the liquid film flow is laminar (Eq. 2.39) and defining interfacial shear stress using the interfacial friction factor (Eq. 2.40), Wallis (1970), i.e.

$$\tau = \mu_l \frac{du}{dy} \quad (2.39)$$

$$f_{fi} = \frac{\tau_i}{\frac{1}{2} \rho_g U_g^2} \quad (2.40)$$

where, the friction factor is given by

$$f_{fi} = f_g \left(1 + 360 \frac{\delta}{D} \right) \text{ and } f_g = 0.079 Re_g^{-\frac{1}{4}}$$

2.4 Fundamentals of two phase flow boiling heat transfer

The process of phase change in which vapour is formed from a liquid state is governed by the fundamental mechanisms of nucleation and evaporation. Nucleation, as defined by Dhir (1998), is a phase change process in which vapour bubbles are formed either on a heated surface or in a superheated liquid layer adjacent to a heated surface. On the other hand, evaporation requires a pre-established liquid-vapour interface. This section provides introduction to the fundamentals of phase change heat transfer covering briefly

boiling incipience and the basic types of boiling (pool and flow). The heat transfer mechanisms during phase change processes that are generally mentioned are presented in the last section. A particular attention is given to nucleate pool boiling features and flow boiling heat transfer in vertical heated conventional size channels. Since, this is of interest in the present study.

2.4.1 Boiling incipience, growth and departure

A certain degree of superheat is necessary to initiate nucleation from unstable equilibrium state. There are two kinds of nucleation processes, homogeneous and heterogeneous nucleation. Homogeneous nucleation occurs in a metastable liquid away from the heated surfaces by a probabilistic process, in which a number of energetic molecules come together to form a small much localized vapour region referred to as vapour nuclei, Whalley, (1987). On the other hand, heterogeneous nucleation will easily occur if a surface or foreign bodies provide active nuclei. In such case, non-condensable and dissolved gasses can exist of nucleation underneath the liquid in cavities. The reason for the much lower superheat required for nucleation on solid surfaces compared with that required for homogeneous nucleation can be explained using free energy of formation and presence of cavities, (Collier and Thome, 1994). The pressure of the gases minimizes the degree of superheat required to maintain a certain bubble diameter. This sub-section will mainly focus on the later type of nucleation.

The degree of superheat required for initiation is predicted from combining the Young's Laplace equation, Clausius-Clapeyron equation, the perfect gas law and taking in to account the additional partial pressure due to the pre-existence of dissolved gases, like air inside the cavity. It is given by Collier and Thome (1994) as,

$$T_g - T_{sat} = \frac{R_G T_{sat} T_g}{h_{lg} M} \ln \left[1 + \left(\frac{2\sigma}{P_l r_n} \right) \left(1 + \frac{\rho_g}{\rho_l} \right) - \frac{P_a}{P_l} \right] \quad (2.41)$$

The minimum radius of cavity required for initiating nucleation from a site can be obtained from defining the mechanical equilibrium equation for a spherical vapour nucleus of radius (r_n) in a liquid of constant pressure (P_l), and partial pressure of air in cavities, which is usually given as:

$$r_n = \frac{2\sigma}{P_l - (P_g + P_a)} \quad (2.42)$$

During nucleation, the surrounding liquid is considered to form presumably a linear temperature gradient across the thermal boundary layer. Hsu (1962) theoretically studied the mechanism of boiling incipience on a heated surface and suggested that the condition for incipience of nucleation is the existence of a higher temperature in the liquid surrounding the nucleus. He provided a relation for the temperature profile and the size of the active nucleation site using a transient conduction model for the super heated liquid layer. His criterion for the onset of nucleation is given by.

$$\frac{\delta_{ts} (T_w - T_{sat})^2}{T_w} \leq \frac{8\sigma T_{sat} C}{\rho_g h_{lg}} \quad (2.43)$$

where, $C = 1.6$ and δ_{ts} is the thickness of thermal laminar sublayer.

Although Hsu (1962) was the first to formulate a theoretical condition for boiling incipience, subsequently, other researchers have also provided various criteria for incipience of nucleation theoretically and experimentally; Davis and Anderson (1966), Bergles and Rohsenow (1964), Kenning and Cooper (1965), Marsh and Mudawar (1989) are among the earlier studies cited elsewhere.

Once the bubble is initiated, its growth is controlled initially by the inertia of the liquid, during which the bubble radius increases proportionally to the time elapsed from formation. Later, the hot liquid surrounding the bubble supplies latent heat of vaporization by thermal diffusion through the vapour liquid interface. In the second period, the bubble growth radius is proportional to the square root of time elapsed since bubble formation (Whalley, 1987). Mikic, et al. (1970) proposed a relation for bubble growth based the above two mechanisms, given in Eq. (2.44) and Eq. (2.45), respectively for inertia and thermal diffusion dominant periods.

$$R_b(t) = \left[\frac{2}{3} \frac{\Delta T_{sat} h_{lg} \rho_g}{T_{sat} \rho_l} \right]^{1/2} \cdot t \quad (2.44)$$

$$R_b(t) = \left[\frac{12}{\pi} Ja^2 \kappa_l \right] \sqrt{t} \quad (2.45)$$

Hsu's hypothesis, which suggests bubble nucleation will not grow unless the surrounding liquid temperature is higher than the bubble temperature, reinforces the assumption that a waiting period should be introduced for the bubble to gain enough heat of vaporization to begin the rapid growth.

After the size of the bubble reaches a critical radius, being compelled by buoyancy and hydrodynamic drag forces, it begins to detach from the surface, although surface tension and inertia force acts against that. The bubble departure frequency is equal to the reciprocal of the sum of bubble growth, which can be estimated by solving the bubble growth equation, and waiting periods (Collier and Thome, 1994). Zuber (1963) formulated an equation for the product of bubble departure frequency and diameter given as,

$$f_b D_b = 0.59 \left[\frac{\sigma g (\rho_l - \rho_g)}{\rho_l^2} \right]^{1/4} \quad (2.46)$$

2.4.2 Pool boiling

The case when boiling takes place from heated surface submerged in a stagnant liquid, is referred to as pool boiling. The classical way of discussing the various attributes of pool boiling is to go through the typical pool boiling curve, which is the graph of surface heat flux versus surface wall temperature (or degree of wall superheat). However, only a brief introduction which is related to the present study will be given here.

When a certain wall superheat enough to commence nucleation is achieved, the onset of nucleate boiling (ONB) occurs. For fluids with low reduced pressure, ONB happens at higher superheat followed by a sudden drop in wall superheat suggesting a hysteresis effect. The nucleate pool boiling region comprises of two features: the isolated bubble region (at low heat flux) and the vapour patches and columns region (at relatively high heat flux), Collier and Thome, (1994).

The maximum heat flux limit, in which further increase in heat flux beyond this limit results in a sudden enormous increase of wall temperature, is referred to as the Critical Heat Flux (CHF). Also, it is generally believed that CHF in pool boiling occurs during a process, in which the heat flux is high enough to cause a high rate of vapour patches leaving the surface inhibiting incoming liquid. Various mechanisms and related predictions have been given in literature, (Collier and Thome, 1994), which will not be discussed here.

Accurate modelling of overall pool boiling process is difficult as a consequence of the stochastic and non-linear nature of the phenomenon plus the fact that active nucleation sites depend on physical conditions and preparation of surfaces. Also, 'how well the

liquid wets the surface?’ and ‘how effectively the liquid displaces air from the cavities?’ affect heat transfer performance. Therefore, most of the methods used to predict nucleate boiling correlations are based on the empirical correlations.

It is apparent experimentally that as the heat flux increases the surface temperature changes slowly in the nucleate boiling region; therefore the heat flux is expressed using power law relation as

$$q \propto C \Delta T_{sat}^a \quad (2.47)$$

where, C and a are constants that depend on physical properties of liquid and nucleation site density. The exponent a is usually found from experiments and is a = 3. Since the heat transfer coefficient can also be written in terms of heat flux as,

$$\alpha \propto q^{a-1/a} \quad (2.48)$$

$$a - 1/a = 0.67 \text{ for } a=3$$

There are two basic attempts of empirically correlating nucleate boiling heat transfer: one takes account the surface effects, while the other ignores this effects and evaluate heat transfer coefficient at a particular heat flux, Whalley (1987).

A large number of correlations in the literature also undertake analogical relationship as that of forced convection in single phase, i.e. $Nu = f(Re, Pr)$. Although the physical properties of single phase liquid can be taken in evaluating the non-dimensional parameters, length scale (L), and velocity (U) requires appropriate definition.

2.4.3 Flow boiling heat transfer

The various attributes of a case of a uniform low heat flux applied to a liquid flowing in a vertical tube with subcooled inlet condition and totally evaporated exit condition, is found in a mostly referred figure in Collier and Thome (1994), Fig. 2.3. The sketch shows the various heat transfer regimes along with the corresponding flow patterns expected.

If a subcooled liquid is fed at the inlet, a single phase heat transfer proceeds in the first section. Subsequently, the temperature of the wall increased to slightly above the saturation temperature attaining a nucleate condition at the wall. However, the bubbles formed collapse as they detach from the wall and reach the core of the stream, where subcooled liquid still exists. This region is referred to as *subcooled nucleate boiling*

region. In this region, thermodynamic quality is less than 0, indicating that although nucleation has begun, the liquid core temperature is still below saturation temperature. This corroborates the existence of thermodynamic non-equilibrium in this region. In the process, the collapsing of the bubbles will eventually increase the mean bulk fluid temperature to the saturation temperature. Following this region, the bulk liquid is thermodynamically assumed to reach saturation temperature marking the onset of *saturated nucleate boiling region* ($x = 0$). As the quality increases from $x = 0$ to 1, the various flow configurations (such as bubbly, slug, annular) evolve. Subsequently, the liquid film of the annular region is completely evaporated (which is also known as dryout) resulting in an abrupt increase in the wall temperature. The liquid deficient region follows the dryout point, which includes entrained droplet up to a point further down stream where $x = 1$ (superheated vapour).

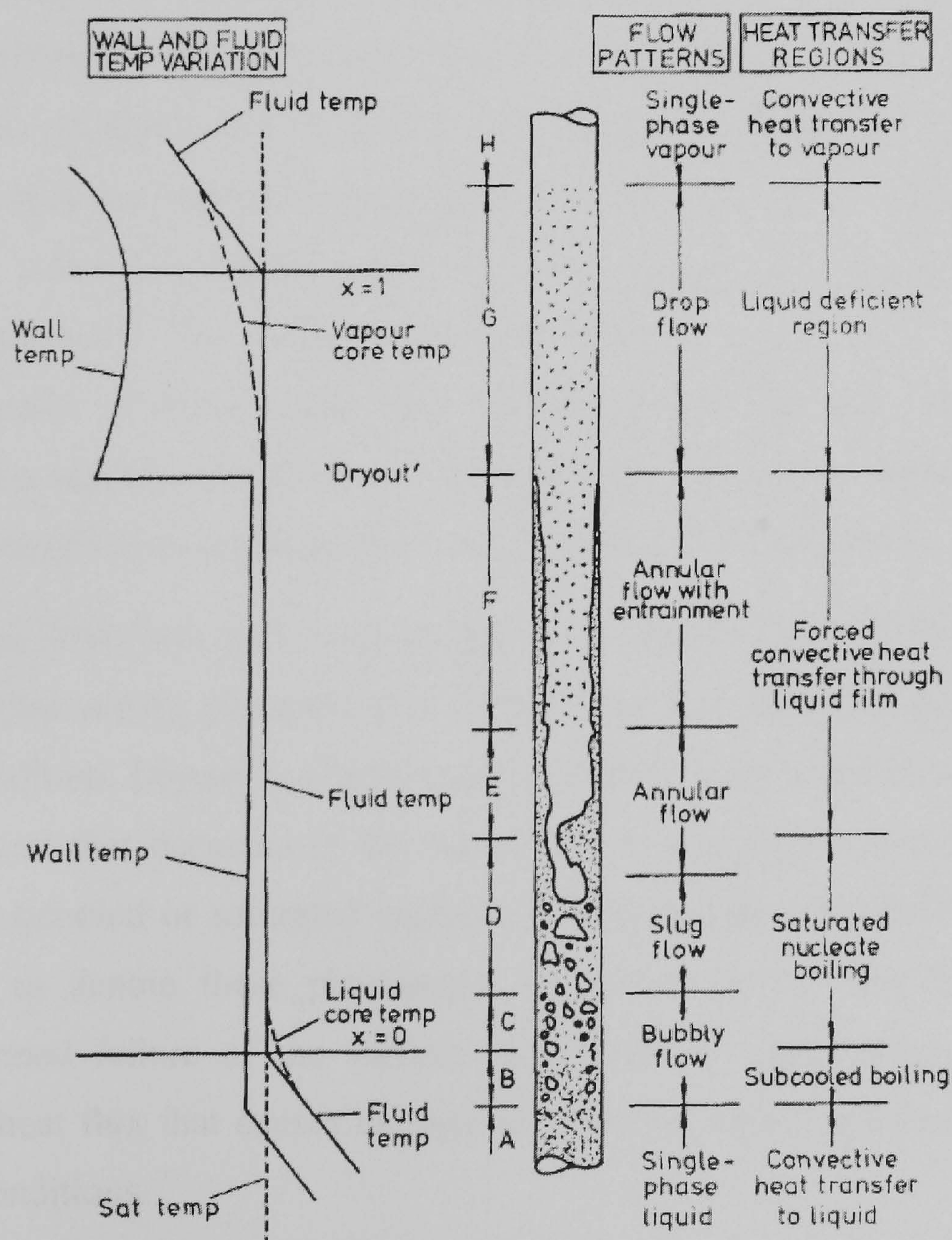


Figure 2.3 Flow patterns and heat transfer regions in vertical tube (Collier and Thome, 1994)

The saturated boiling covers the typical flow patterns from bubbly to annular flow. The classical assumption in this region is that the thermodynamic equilibrium exists between the phases of a single component. However, it is also reported that the phase non-equilibrium has been observed with refrigerants by Gouse and Dicksom (1966) and liquid metals by Chen (1965).

The axial development of heat transfer coefficient with tube length or mass quality is described in Fig. 2.4. The figure also includes the progressive variation as constant heat flux increases from (i) to (vii) according to Collier and Thome (1994). In the single phase convective heat transfer region, the heat transfer coefficient changes slightly with axial length. Near the point, where $x = 0$, i.e. in the subcooled nucleate boiling region, the coefficient increases linearly with the axial length. This is caused by decrease in the temperature difference between the wall and the bulk fluid. Conventionally, saturated nucleate boiling region is identified by a uniform heat transfer coefficient with mass quality. The coefficient increases monotonically with quality in the two phase forced convective region, related to the decrease in the liquid film thickness. Dryout results in a sudden decrease in the heat transfer coefficient. Increasing the heat flux (from i to ii) initiate an early subcooled boiling region and a higher heat transfer coefficient in the nucleate boiling region. The forced convective region is not influenced except the dryout occurs early at lower mass flux. Further increasing heat flux evades the convective boiling region, a phenomenon called departure from nucleate boiling (DNB). This marks the transition to an abrupt decline of heat transfer coefficient.

At high heat flux, DNB begins to occur as early as in the subcooled boiling region. The DNB in boiling has similar phenomena as critical heat flux corresponding to saturated pool boiling condition. Dryout is a term usually referred to as deterioration in the heat transfer coefficient that occurred in the convective boiling region, where as DNB is related to the subcooled or saturated nucleate boiling regime. The CHF term can be generally used to denote these phenomena. However, Collier and Thome (1994) distinctively termed failure of the surface as a result of rapid surface temperature increase or the heat flux that causes damage as 'burnout' unlike apparently use of the term for CHF conditions.

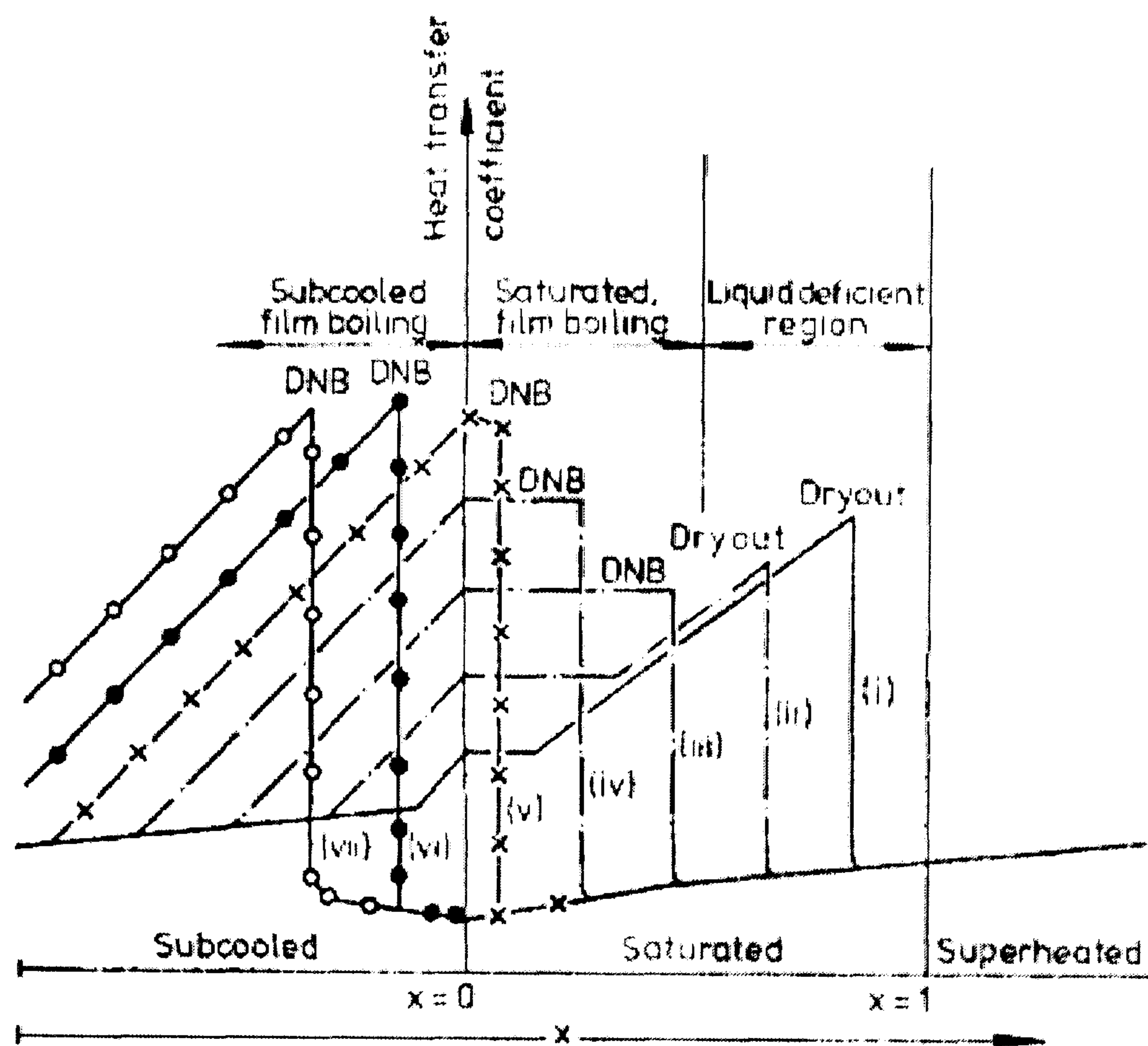


Figure 2.4 Heat transfer coefficient as a function of quality with increasing heat flux (Collier and Thome, 1994)

2.4.4 Heat transfer mechanisms

In general, understanding the physical phenomena and defining the mechanisms for heat transfer in various types of boiling and regimes is still a controversial subject.

In nucleate pool boiling, although there is no definite consensus, the possible explanations given to the mechanism of heat transfer include (Hsu and Graham, 1976):

- Microconvection in the thermal boundary layer (this is more prominent in the subcooled boiling in which case bubbles leaving the heated surface and condense in the cold bulk liquid will induce convection).
- The transient conduction across a thin microlayer of liquid adhering to the surface under the bubble become the main source of heat of vapourization with a result of rapid removal of heat from the surface.
- Bubble agitation enhancing the natural convection in the liquid phase.

Although later confirmed by many other studies, probably Dengler and Addoms (1956) are the first to realise at least two different heat transfer mechanisms could be responsible for phase change from liquid to vapour in a tube. The two mechanisms, suggested, based on the experimental heat transfer coefficient dependence on local

quality, were nucleate boiling and forced convective boiling. At low qualities, a thin layer of liquid near to the heated surface is superheated to a sufficient degree that allows nucleation, i.e. dominance of nucleate boiling. In this region, heat transfer rate is independent of quality and mass velocity, which was experimentally verified by Collier and Pulling, Sterman and Styushin, (both cited in Collier and Thome, 1994). On the other hand, at high qualities, the forced convective heat transfer mechanism is dominant. The later heat transfer phenomenon is related to the existence of the annular flow regime, where heat is transferred by conduction and convection through the liquid film and vapour generated continuously at the interface. The liquid film is thin enough to suppress nucleation by preventing superheat using effective thermal conduction.

The existence of the above mechanisms has been represented in various forms using enhancement and suppression factors employed with nucleate and convective boiling, respectively. However, in various correlations and methods predicting flow boiling heat transfer, there is no common agreement on the quantitative combination between nucleate boiling and convective boiling.

Moreover, the classical interpretation that heat transfer mechanism in flow boiling system is nucleate boiling dominant at low qualities and forced convective evaporation at high qualities were also dissented by other alternative interpretations. Some researchers believe the existence of nucleate boiling at high qualities, (Beattie and Lawther, 1979, Standiford 1978, Beattie and Green 1984). However, many other studies supported the fact that nucleation is suppressed at high quality flow (Hewitt et al. 1965, Aounallah et al. 1982, Kandlikar et al. 1995). This later group of researchers argue that at constant heat flux, if the heat transfer coefficient increases with quality and mass flux particularly during forced convective boiling, the degree of wall superheat decreases. If it does decrease below the value required for incipience of nucleation as shown by the previous equations in section 2.4.1, nucleate boiling will completely be suppressed.

The belief that nucleation might take place even if bubble generation is suppressed at the heated wall opened a way to other alternative explanations to the argument, whether the nucleate boiling mechanism still exists at high quality in annular flow. This was favoured by Mesler (1977) who observed the deposition of droplets in a thin falling film, which were ejected from the surface of the film causing entrainment of gas bubbles in the liquid film. The gas bubbles may reach the supersaturated liquid region and act as nucleation sites maintaining the nucleation process. They also observed that

the disturbance in the film at bubble rupture becomes a condition for bubble growth. Marsh and Mudawar (1989) postulated that waves in the film could trigger bubble nucleation. Based on their observations, they stated that more favourable conditions may occur for nucleation by large waves than thin films between waves during nucleate boiling causing larger wall superheat. This was also mentioned by Hewitt et al. (1965) from their direct observation that disturbance waves in annular flow were observed to trigger nucleation sites rather than suppress nucleation. The gradual suppression of the nucleate boiling may lead to a temporarily reduction of heat transfer coefficient with increasing quality. Therefore, it could be possible that the two mechanisms, i.e. nucleate and convective boiling can coexist at the same time for a certain conditions.

Various flow boiling correlations were also proposed in the literature, such as Chen (1966), Shah (1982), Gungor and Winterton (1986), Kandlikar (1990), Liu and Winterton (1991) and Steiner and Taborek (1992).

2.5 Channel size classifications

Classification of channel sizes based on flow structure and heat transfer characteristics is one of the subjects where the heat transfer community do not have an established agreement yet. However, identifying the threshold where the macroscale heat transfer phenomena do not apply to the microscale is important in developing and validating tools to predict thermal hydraulics of small and microchannels. One of the reasons for the lack of clear and generally acceptable understanding on the definition and classification criterion for the size range small/mini/microchannel in two-phase flow studies could be the limited number of researches and heat transfer data over a wide range of diameters at the same experimental conditions.

Shah (1986) characterized compact heat exchangers as exchangers with surface-to-volume ratio $> 700 \text{ m}^2/\text{m}^3$. These are heat exchangers constructed from tubes or channels with passages of size corresponding to hydraulic diameter $< 6 \text{ mm}$. Mehandale et al. (2000) defined channel size ranges from compact heat exchanger application point of view as:

- Conventional ($d_h > 6 \text{ mm}$)
- Macrochannel ($1 - 6 \text{ mm}$)
- Mesochannel ($100 \mu\text{m} - 1 \text{ mm}$)
- Microchannel ($1 - 100 \mu\text{m}$),

Kandlikar and Grande (2003), after reviewing several flow boiling studies in various tube sizes, categorized channel dimensions as given below:

- Conventional channels: $D_h \geq 3 \text{ mm}$
- Minichannels: $200 \mu\text{m} \leq D_h < 3 \text{ mm}$
- Microchannels: $10 \mu\text{m} \leq D_h < 200 \mu\text{m}$

The above classifications do not consider the physical mechanisms and other effects involved when varying the size of the channels. Hence, there is no effect of operating parameters and thermophysical properties on classifying the size ranges.

The predominance of the different forces that exist during two phase flow in channels varies with channel size thereby affecting the flow pattern types and transitions. As the diameter of the channel decreases, surface tension and viscous forces become important. For instance, under reduced gravitational force, conventional channels showed similar characteristic as that of small channels, Brauner and Moalem-Maron (1992). Moreover, the absence of stratified flow in horizontal microchannels and hence the fact that the orientation of the channel has no effect on two phase flow pattern indicates the prevalence of surface tension force over gravity, (Triplett et al. 1999, Daminanides and Westwater, 1988). Consequently, a number of attempts to define macro-micro transition have used surface tension force as a base to formulate a non-dimensional criterion.

Brauner and Maolem-Maron (1992) proposed a non-dimensional number known as Eötvös number ($E\ddot{o}$), given in Eq. (2.59). This was based on their observation and linear stability analysis that considers the disturbance wavelength in the order of channel diameter.

$$E\ddot{o} = \frac{(2\pi)^2 \sigma}{(\rho_l - \rho_g) D_h^2 g} \quad (2.49)$$

They recommended ($E\ddot{o} > 1$) as threshold for small channel effect. They observed that surface tension force dominates when $E\ddot{o} > 1$. However, this limit was observed to vary among different researchers. Triplett et al. (1999) could not observe stratified flow for $E\ddot{o} > 100$ in their experiments.

On the other hand, Cornwell and Kew (1993) defined a commonly used threshold criterion where macroscale heat transfer modeling becomes unreliable for predicting flow boiling heat transfer coefficients, which is referred to as the confinement number (Co). This non-dimensional number is the ratio of surface tension and gravity forces

given by Eq. (2.60), which is again the square root of the reciprocal of the Bond number (Eq. 2.61). As the diameter decreases or the Co number increases above the threshold given by this criterion, i.e. $Co = 0.5$ ($Bo = 4$), bubble growth is assumed to be confined by the channel to the point where individual bubbles grow in length rather than in diameter.

$$Co = \frac{[\sigma / (g(\rho_l - \rho_g))]^{1/2}}{D_h} \quad (2.50)$$

$$Bo = D \frac{g(\rho_l - \rho_g)}{\sigma} \quad (2.51)$$

The confinement criterion is found to roughly agree with the experiment of Fukano and Kariyasaki (1993), who investigated the effect of diameter using air-water flow in 1 to 9 mm at atmospheric conditions, and Chen et al. (2006) experiments for 1.1 to 4.26 mm using two phase flow boiling of R134a.

Jacobi and Thome (2002) assumed the microchannel effect to take place when channel diameter is small enough such that the diameter of the bubble fills the size of the passage before detachment. Such criterion requires proper prediction of bubble departure diameter during flow boiling in small channels, which is dependent on several factors including surface conditions and thermophysical properties. Most often, it is taken to be the same as the departure diameter for nucleate pool boiling neglecting the effect of shear force on the nucleating bubble. Several correlations have been proposed (mainly for large diameter tubes) to determine the bubble departure diameter, (Mikic et al. (1970), Jensen and Mammel, 1986). Following that, Thome (2004) in his review of boiling in microchannels, indicated the importance of considering physical mechanism in classifying channel size and recommended the use of bubble departure diameter as preliminary criterion. He also mentioned the effect of shear on bubble departure diameter and reduced pressure on bubble size that need to be considered in addition to surface tension forces.

The various criteria discussed above are also shown in figure 2.1 as a function of saturation pressure. Only the Confinement and Eötvös number vary with pressure.

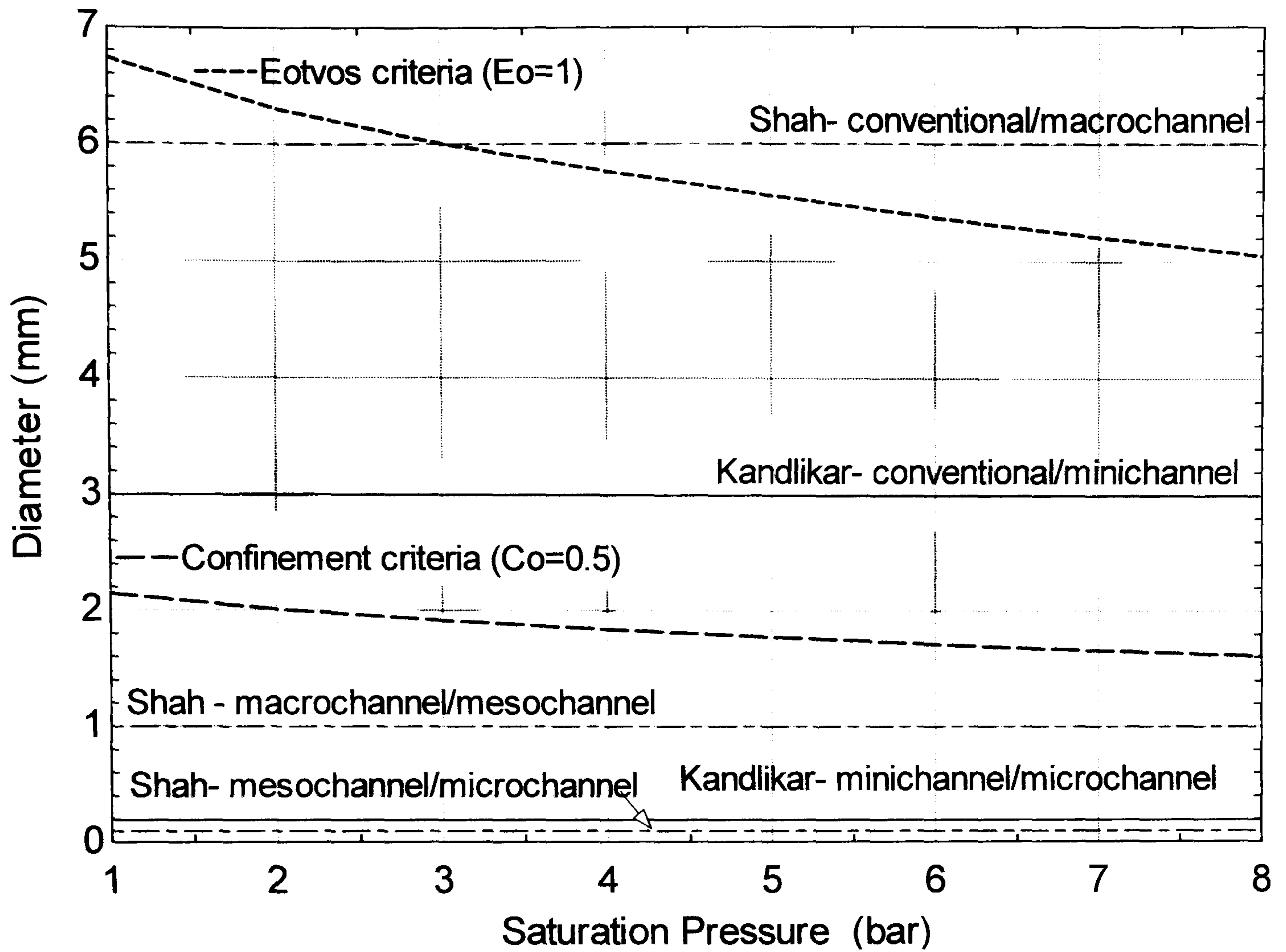


Figure 2.5 The various channel size classification criteria.

2.6 Summary

The fundamental theories of flow boiling in conventional channels are briefly discussed knowledge that can be related to the microscale boiling processes, such as flow pattern transition mechanisms, pressure drop predicting models, onset of nucleate boiling, general heat transfer mechanisms are also briefly introduced. Finally, channel size classification theories are reviewed and indicated the need for a comprehensive definition that considers the fundamental phenomena and mechanism to classify normal and small size tubes. For this purpose experimental data that consider a wide range of diameters is necessary. This research is also aimed to address this issue by testing five different diameter tubes.

Chapter 3

Two Phase Flow Study in Small- to Micro-Passages: State-of-the-art Review

3.1 Introduction

An overview of the fundamentals of two phase flow studies in conventional size tubes was presented in chapter 2. This chapter provides the state-of-the-art review on various subjects related to the two phase flow studies in small- to micro– passages. In recent years there has been increased research activity in flow boiling in small diameter tubes, mainly driven by the demand for compact cooling systems. A better heat transfer performance is widely expected for small diameter tubes compared with the conventional tubes. However, several new features have also been observed in microscale two phase flows, which are not typical characteristics of conventional systems.

This chapter is organised as follows. Section 3.2 presents flow patterns and flow map studies covering the changes identified as the passage size decreases. Section 3.3 covers the subject of two phase flow pressure drop. Section 3.4 provides a review of the heat transfer characteristics observed in small diameter tubes. The heat transfer prediction methods and their features are discussed in section 3.5. Finally, a short summary of the overall trends observed as cooling systems become compact is given in section 3.6.

3.2 Flow patterns and flow maps

This section will mainly focus on the studies of flow patterns and maps that are relevant to small diameter tubes. The review presents the studies of flow patterns and flow pattern transition maps separately.

3.2.1 Flow patterns

Many studies have reported different new flow pattern features in small diameter tubes compared with conventional tubes. Some researches have investigated the tube diameter effect on the type of flow pattern by testing a wide range of tube size and indicated that the surface tension force is dominant over gravity during two phase flow inside small diameter tubes. This was mostly deduced from the fact that the orientation of the tube has insignificant effect to the type of flow patterns and there is a relatively uniform distribution of liquid and vapour phases. Damianides and Westwater (1988) studied two phase flow of air-water at atmospheric condition for horizontal tubes of 1-5 mm internal diameter. They identified dispersed bubble, bubbly, plug, slug, pseudo slug, wavy and annular flows. Plug and pseudo slug are terms usually used in horizontal tubes to represent elongated bubble and flows that have wavy interface with large amplitude that reaches the top of the tube wall during stratified flow, respectively. Mishima and Hibiki (1996) studied experimentally air-water flow in tubes of internal diameter 1 to 4 mm. In addition to the typical flow patterns found in conventional tubes (bubbly, slug, churn, annular and annular-mist flow), they observed flow patterns that are specific to small tubes, which are marked with asterisk in Fig. 3.1. The new features observed corresponding to the normally categorised as bubbly flow include the appearance of spiral and intermittent bubble trails as large as the diameter of the tube. Corresponding to the conventional slug flows, the bubbles (in case of small tubes) have smooth spherical top, longer in length and surrounded with thin liquid film. Mishima and Hibiki (1996) considered the long slug bubbles followed by trails of fine bubbles as churn flow. Conventionally, this was categorised as slug flow and it is not clear that the churn flow (if at all existed) was a main flow or a transition regime. Tripplet et al. (1999) conducted an adiabatic two phase flow experiment using air-water inside circular tubes of diameter 1.1 and 1.45 mm and semi-triangular (triangular with one corner smoothed) channels of hydraulic diameter 1.09 and 1.49 mm. They reported churn flow at high liquid and gas superficial velocity. This was in some cases related to unstable flow of elongated bubbles and was occasionally described as an aerated slug flow. In general,

Trippliet et al. identified five distinct flow patterns: bubbly, slug, churn, slug-annular and annular type flow patterns. Fukano and Kariyasaki (1993) noticed relatively different flow regime characteristics in small diameter tubes of 1, 2.4 and 4.9 mm using an air-water flow. These were: diminishing of the separated bubble flow regime, uniform circumferential distribution of film thickness (axisymmetric flow pattern), absence of trails of small bubbles following the gas slug and lower relative velocity of bubble to liquid slug. Fukano and Kariyasaki (1993) also observed that the liquid film thickness decreases with decreasing the diameter of the tube from 4.9 to 1 mm. Coleman and Garimella (1999) conducted adiabatic two phase flow experiments using an air-water mixture inside a wide range of small diameter tubes. It was stated that they did not observe stratified flow in any of their tubes. The channels were of 1.30, 1.75, 2.60 and 5.50 mm internal diameter tubes and rectangular channels with hydraulic diameter of 5.36 mm.

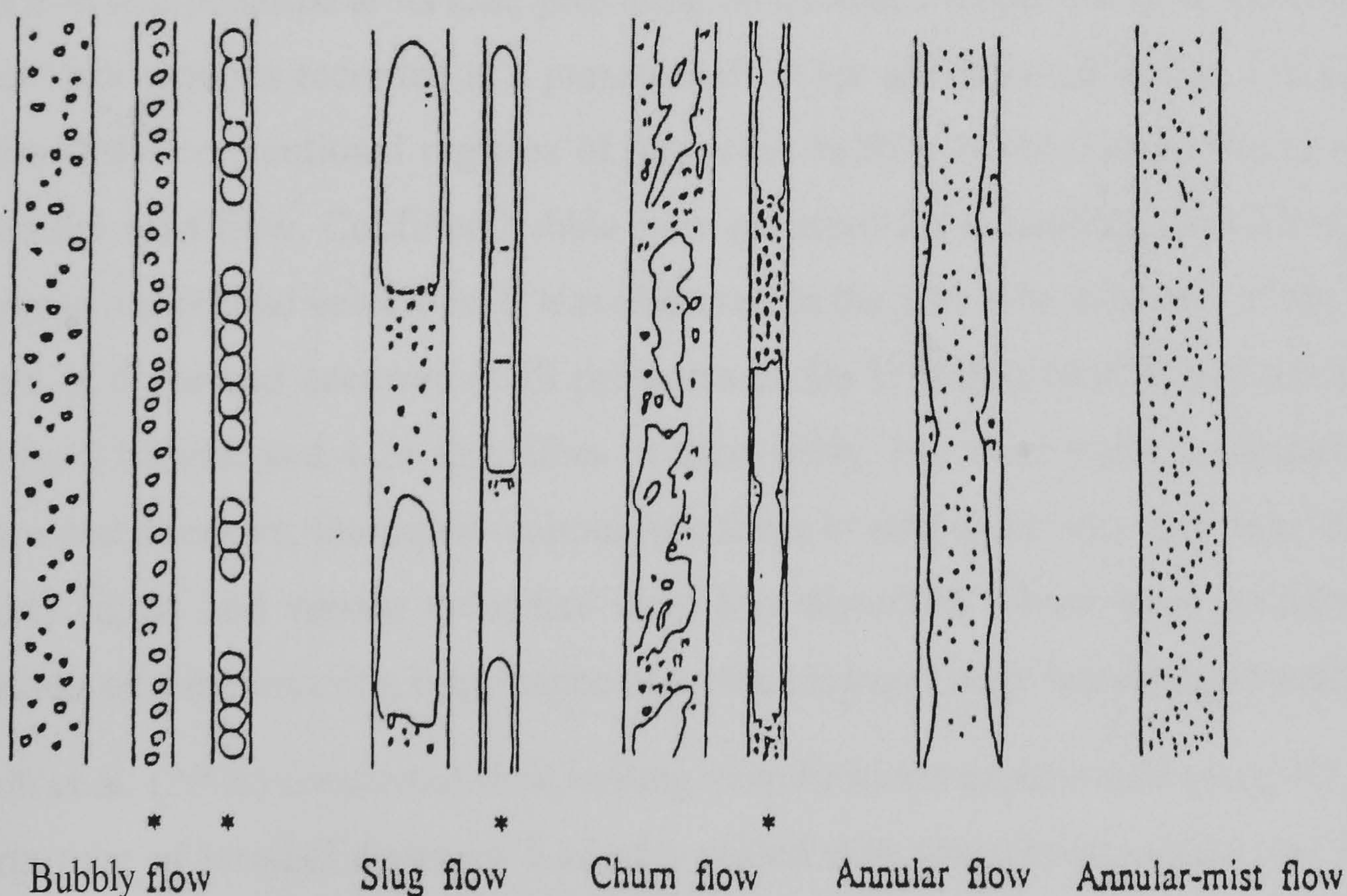


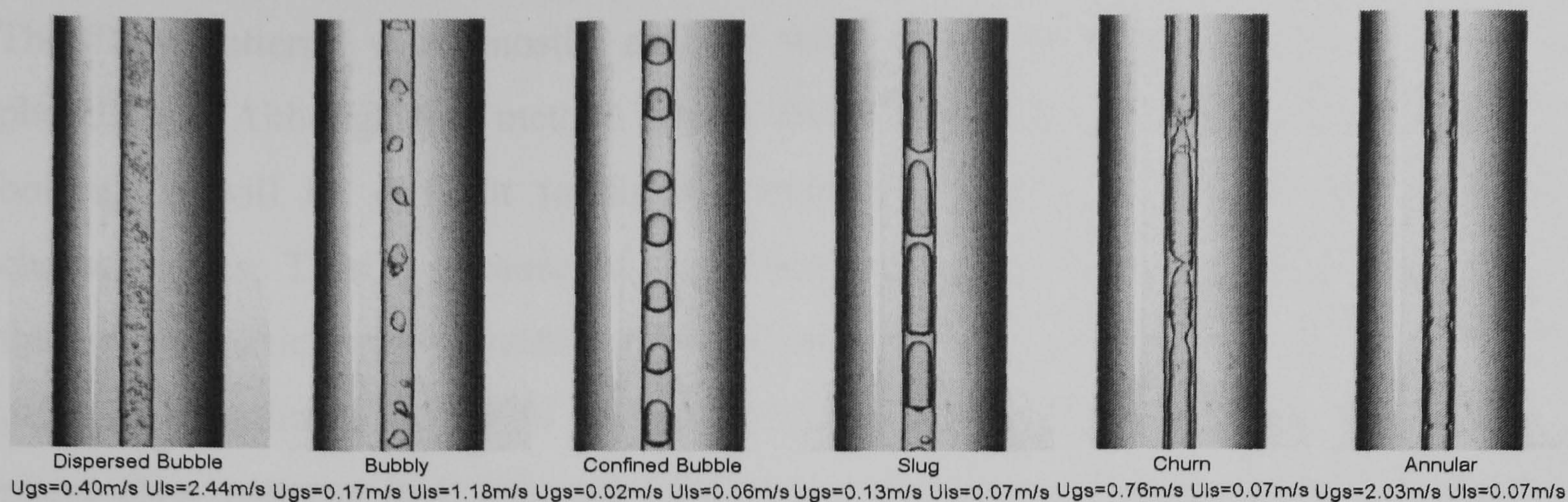
Figure 3.1 Flow patterns in capillary tubes (Mishima and Hibiki, 1996).

Kew and Cornwell (1997) conducted flow boiling tests in small diameter tubes of 1.39, 3.69 mm using R141b and observed three flow regimes: isolated bubbles, confined bubble and slug/annular flow. These flow patterns were slightly different from those

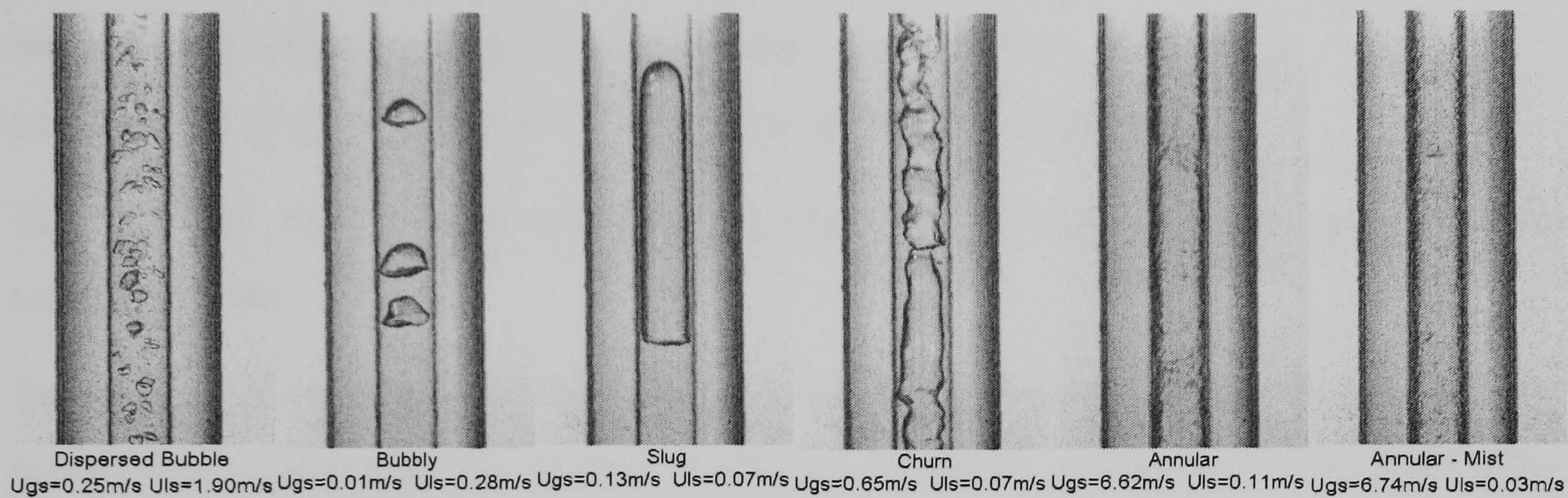
observed in normal tubes. Specifically, the appearance of confined bubble flow was considered as typical feature in small diameter tubes. These are bubbles regular in shape with spherical top constrained by the size of the passage begin to grow in length than in diameter. Various terminologies have been given to denote these flows. Following classical interpretation, they were also referred to as plug flow (horizontal tubes), elongated bubble and slug flow. It is difficult to clearly put a distinction among these flow patterns, however some researchers identify confined flow from the rest similar regimes by its relatively shorter length and having spherical cap and bottom, (Chen et al. 2006). In their case, slug flow was distinguished as bullet shaped bubbles with sharp corners and a fluctuating surface at the rear.

Similarly, Chen et al. (2006) examined the flow patterns at qualities $x > 0$ leaving tubular boiling test sections ranging in diameter from 4.26 mm down to 1.1 mm for R134a over the pressure range 6-14 bar. The flow patterns were observed by a digital high-speed camera in a borosilicate glass tube with an internal diameter matched to the test section and installed at its exit, providing an adiabatic length for flow development. Typical flow patterns recorded at a pressure of 10 bar are depicted in Fig. 3.2. Chen et al. defined the conventional regimes of dispersed bubble, bubbly, slug, churn, annular and annular-mist flow. Confined bubble flow occurred for a combination of low liquid and vapour superficial velocities. It was observed in the 2.01 mm tube only at the lowest pressure of 6 bar and occurred at all pressures in the 1.10 mm tube. It was not seen in the larger 2.88 mm and 4.26 mm tubes of their study. For these same combinations of pressure and diameter, the liquid–vapour interfaces in slug and churn flow that occurred at higher liquid and vapour velocities were less disturbed. These were considered as indications of the increasing importance of surface tension with decreasing diameter.

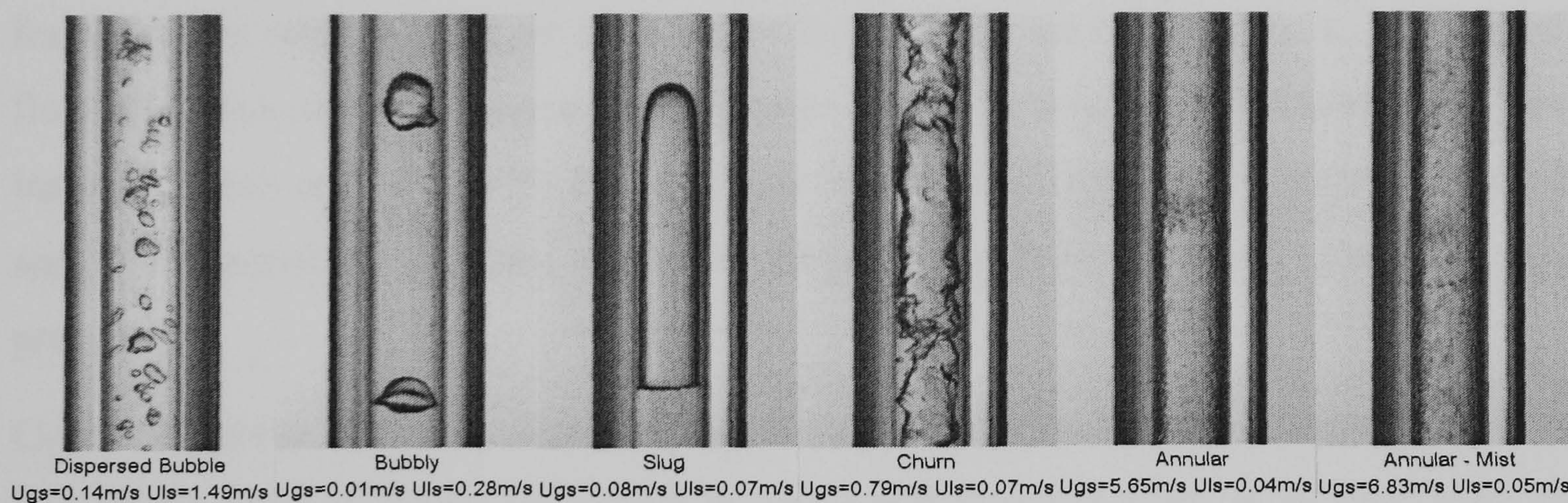
Owhaib et al. (2006) conducted flow boiling visualizations experiments using R134a inside a quartz tube of internal diameter 1.33 mm coated with transparent conductive film. They observed bubbles growing and coalescing into elongated bubbles leaving the liquid film wavy. Two mass fluxes of 47 and 124 kg/m²s were tested at a pressure of 6.4 bar. The corresponding range of heat flux was 5 -13.6 kW/m² and 20 - 32.4 kW/m² for the lower and higher mass flux values, respectively.



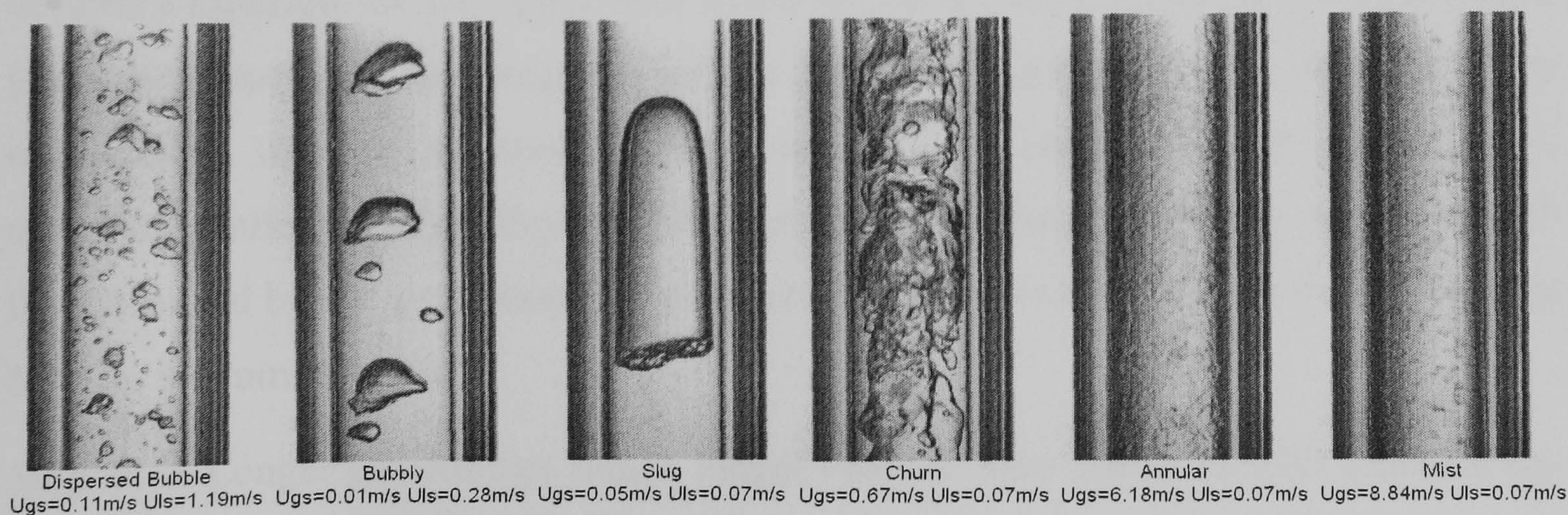
(a)



(b)



(c)



(d)

Figure 3.2 Flow patterns in small tubes, diameter: (a) 1.1 (b) 2.01 (c) 2.88 and (d) 4.26 mm (Chen et al. 2006).

The flow patterns were mostly annular with droplet entrainment and deposition phenomena. Although this method allows direct visualization flow conditions during boiling, it will be difficult to directly relate the results with local heat transfer characteristics. This is because of the difference in the surface condition and wall thermal properties with conventional metal tubes, consequently altering the nucleation process. Revellin et al. (2006) and Revellin and Thome (2007a, 2007b) studied two phase flow patterns in 0.509 and 0.790 mm tubes using R134a and R245fa. They observed mainly bubbly, slug, semi-annular (annular flow disrupted by gradually disappearing churning liquid-vapour zone) and annular flows with sometimes a combination of more than one of these types at the same condition.

The different flow pattern characteristic observed in small diameter tubes can be summarised as:

Bubbly flow: flow of discrete bubbles travelling along the centre of the passage usually comparable in size with the passage. Different variations of this flow were given other descriptive names as: dispersed bubble flow and separated bubbly flow. The former is formed when relatively bigger bubbles are broken into fine bubbles due to high liquid flow rate. However, these were reported to be absent in very small diameter tubes. For instance, Zhao and Bi (2001) did not observe dispersed bubble flow pattern for their smallest channel (0.87 mm), while all the other typically flow patterns were still present.

Confined bubble: flow of bubbles regular in shape with spherical top constrained by the size of the passage, which are typical in very small diameter tubes. Kew and Cornwell defined a criterion for the appearance confined bubble flow, which is a dimensionless parameter based on the ratio of surface tension to gravity forces, referred to as confinement number, equation (2.50) discussed in Chapter 2. Chen et al (2006) observed confined bubble flow at a diameter of 2.01 mm, which was consistent with that predicted by the confinement number criterion (for R134a it ranged from 1.7 mm at 6 bar to 1.4 mm at 14 bar).

Slug flow: Longer gas bubbles (much longer than the tube diameter) with spherical top and surrounding by thin liquid film, usually followed by trails of fine bubbles.

Churn flow: In case of churn flow in small diameter tubes, a number of studies indicated that the liquid-vapour interface was not as chaotic as in conventional tubes. In some

studies, it was not considered as main flow regime, Revellin and Thome (2007a, 2007b).

Annular flow: occurs at high gas flow rate. Unlike conventional tubes, entrainment of liquid droplets in the gas core is not a common phenomenon. However, mist flow was observed occasionally at very high vapour velocity. In case of small diameter tubes, the liquid–gas interface is usually wavy (Damianides and Westwater, 1988). Wavy annular flow is created when the liquid superficial velocity decreased to a level that initiates coalescence of elongated bubbles, (Triplett, 1999). In contrast, Coleman and Garimella, 1999, reported that the wavy-annular flow regime was observed to die out with decreasing tube diameter.

Most of the two phase flow studies discussed above are for small passages, with hydraulic diameter down to 1.0 mm. They have clearly shown that there is a considerable difference in the flow pattern characteristics compared with that of the conventional size channels. These include the predominance of surface tension force over gravity, the absence of stratified flow pattern in horizontal channels and the appearance of additional flow patterns, which are not common in normal tubes. However, a question still remains ‘What happens to the flow pattern characteristic, if the diameter decreases further below 1 mm to micrometer range?’

Flow patterns in micro passages

Kawahara et al. (2002) investigated the nitrogen-de-ionized two phase flow characteristics in a 0.1 mm diameter tube made of fused silica. Flow patterns observed from their video recording did not include bubbly and churn flows. Besides, they exhibited additional flow characteristics than those observed in small diameter tubes. These were described as gas core flows with ring-shaped film referred to as liquid-ring flow and a ‘serpentine-like gas core’ surrounded by deformed liquid film. The special flow patterns are shown in Fig. 3.3. Mostly intermittent and semi-annular flows were observed in their experiments. The absence of bubbly and churn flows were related to dominant effect of surface tension and low liquid velocity (laminar liquid flow).

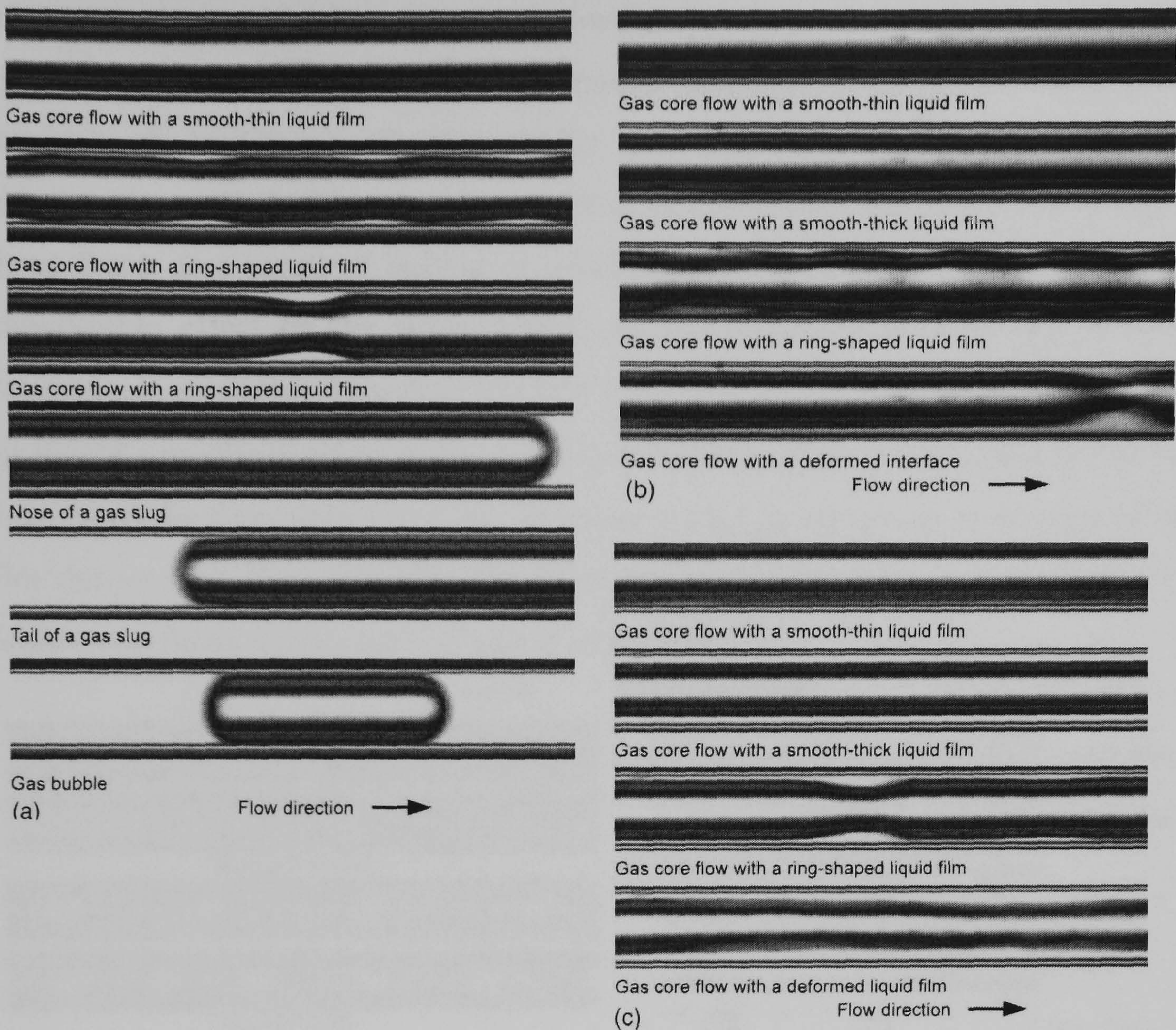


Figure 3.3 Two-phase flow patterns in a microchannel, $D=100 \mu\text{m}$: (a) $U_{ls} = 0.15 \text{ m/s}$, $U_{gs} = 6.8 \text{ m/s}$; (b) $U_{ls} = 0.56 \text{ m/s}$, $U_{gs} = 20.3 \text{ m/s}$; (c) $U_{ls} = 3.96 \text{ m/s}$, $U_{gs} = 19.0 \text{ m/s}$; (Kawahara et al. 2002).

Serizawa et al. (2002) studied two phase flow and reported the visualization results for air-water and steam-water flows in circular tubes of 20, 25 and 100 μm and 50 μm internal diameter, respectively. Figure 3.4 depicts their flow patterns. For air-water two phase flow in a 25 μm silica tube (Fig. 3.4a), the special flow pattern features include the observation of liquid-ring flow and liquid-lump flows. The liquid-ring flow was described as the appearance of a symmetrical liquid ring with long gas slugs passing in the middle. They hypothesised that the liquid-ring flow could develop from slug flow when the gas slug velocity is too high and the liquid slug is too short to form a stable liquid bridge between consecutive gas slugs. Liquid-lump flows developed with further increase in the gas flow rate at this condition. The authors described this as an entrainment of the liquid phase by high-speed gas core into liquid lumps that slide across the inner wall. Similar flow patterns, with that of air-water flow for 25 μm silica

tube, were observed in the case of steam-water flow in a 50 μm silica tube, Fig. 3.4b. The only difference exhibited was the absence of liquid lump flow in the later case. However, the existence of other similar flow patterns including liquid-ring flow indicates the method of forming the two phase flow has little effect. In other words, two phase flows as a result of boiling or adiabatic mixing of air-water seem to have no considerable effect on the type of flow patterns observed at least for these sizes. Experiments using the same fluid but in a 100 μm quartz tube gave the same results as for the 25 μm silicon tubes except the small liquid droplets in the gas slug flow were sticking on the tube wall, Fig. 3.4c. This was related to the temporal absence of liquid film during slug flow. Nevertheless, they also observed stable liquid-ring flow and liquid-lump flows for the 100 μm quartz tube as well.

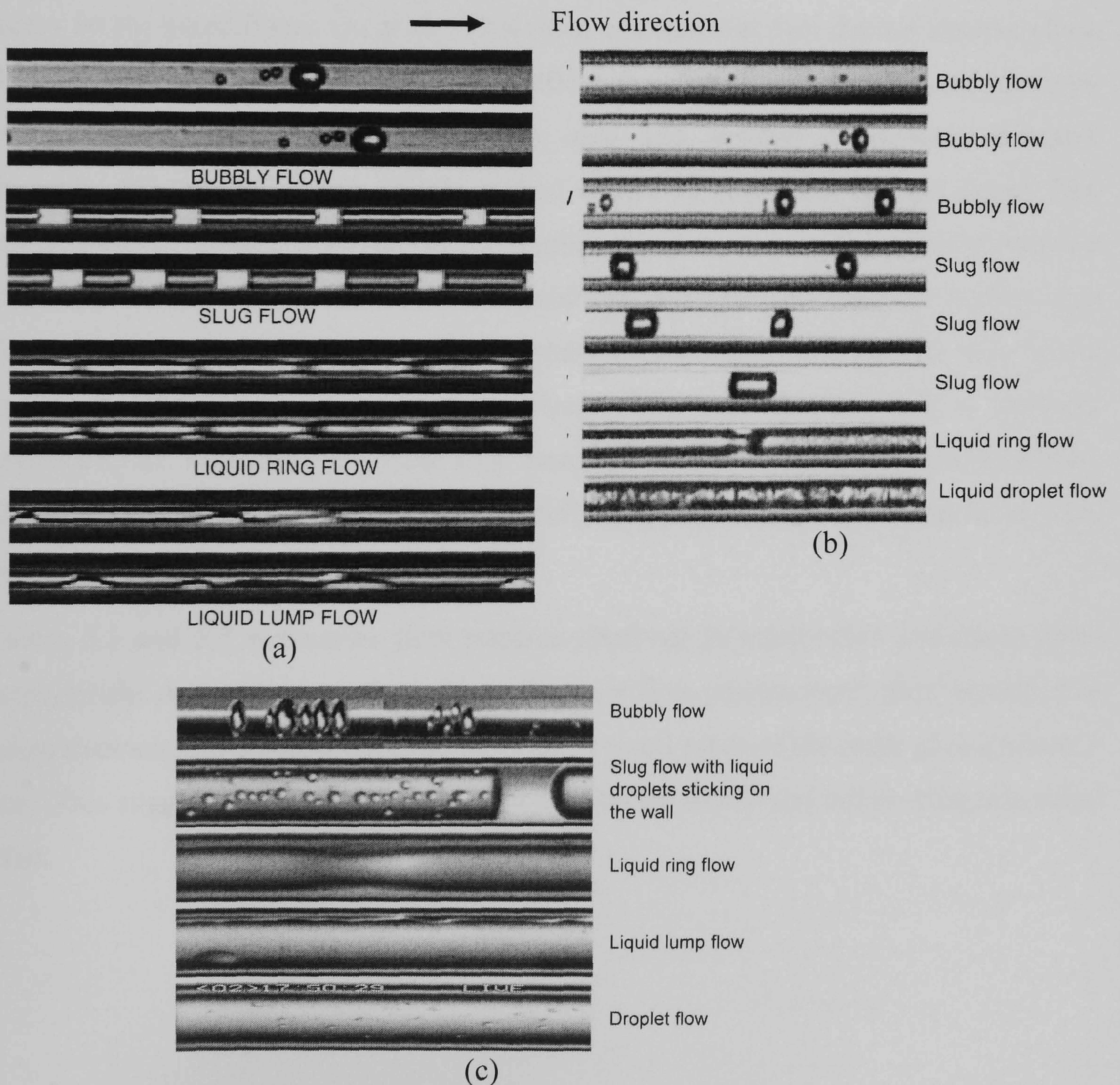


Figure 3.4 Two phase flow patterns: (a) air-water flow in a 25 μm silica tube, (b) steam-water flow in a 50 μm silica tube and (c) air-water flow in a 100 μm quartz tube, (Serizawa et al. 2002).

Chung and Kawaji (2004) studied two phase flow pattern inside tubes of diameter 530, 250, 100 and 50 μm using a mixture of nitrogen gas and water. For the 530 and 250 μm , in addition to bubbly, churn, slug-annular and annular flows, they observed gas core flows with thin-smooth or wavy liquid film (also called liquid-ring and serpentine-like gas core flows). They related churn flow with the “streaks and swirls” that trail the gas slug, not with the highly irregular gas-liquid interfacial structure observed in relatively large channels. On the other hand, for 100 and 50 μm , they could not identify bubbly, churn, slug-annular flow (asymmetric waves of large amplitude) and annular flows. However, only variants of slug flow regime, where a long gas core that resemble annular flow with smooth liquid film and round nose and tail were observed. This was attributed to the higher viscous and surface tension effects than gravitational and inertia forces on the liquid flows. Qu et al. (2004) also reported that they did not observe churn flow in their rectangular channel with 0.406 mm hydraulic diameter using nitrogen-water, while bubbly flow (occasionally), slug and annular flows were obtained. Recently, Xiong and Chung (2007) studied experimentally adiabatic gas-liquid flow patterns using nitrogen and water in rectangular microchannels with hydraulic diameter of 0.209, 0.412 and 0.622 mm. They observed four different flow patterns: bubbly, slug flow, slug-ring flow (liquid-ring flow), dispersed-churn flow, and annular flow in the 0.412 and 0.622 mm microchannels. Churn flow was characterised as periodic appearance of “disruption tail of the slug” usually followed by some very small bubbles. The bubbly-slug flows were developed to fully slug, while dispersed-churn flows were absent in the 0.209 mm channel.

Tables 3.1 and 3.2 summarise flow patterns observed in small tubes and micro tubes respectively. As can be seen from the tables, new flow pattern types were identified in microchannels, which have not been reported in small tubes of the order of magnitude 1 mm. This suggests that another classification between small- and micro- channels could exist.

Table 3.1 Flow patterns observed in small passages of (hydraulic) diameter ($D \geq 1$ mm)

Reference	Passage size and Fluid type	Flow patterns
Damianides and West water (1988)	1 – 5 mm tubes Air-water	Dispersed bubble, Bubbly, Plug, slug, Pseudo slug, wavy and annular
Mishima and Hibiki (1996)	1 – 4 mm tubes Air-water	Bubbly (with spiral and intermittent bubble trails), slug (with smooth spherical top), churn (long slug bubble followed by trails of bubbles), annular and annular-mist flow
Triplett et al. (1999)	1.1 and 1.45 mm (tubes and semi-triangular channels) Air-water	Bubbly, churn (unstable elongated bubble flow or aerated slug flow), slug, slug-annular and annular type flow patterns.
Kew and Cornwell (1997)	1.39 and 3.69 mm R141b flow boiling	Isolated bubble, confined bubble and slug/annular flow
Chen et al. (2006)	1.1 – 4.26 mm R134a flow boiling	Dispersed bubble, bubbly, slug, churn, annular, mist flow.

Table 3.2 Flow patterns observed in micro tubes of diameter ($D < 1$ mm)

Reference	Passage size and Fluid type	Flow patterns
Kawahara et al. (2002)	0.1 mm fused silica tube Nitrogen – De-ionized water	Intermittent (slug flow), gas core flow with smooth-thin liquid film, gas core flow with ring shaped liquid film, semi-annular flows. (bubbly and churn flows were absent)

Serizawa et al. (2002)	0.02, 0.025 mm (silica tubes) and	Bubbly, slug, liquid ring flow, liquid lump flow.
	0.1 mm (quartz tube) – Air-water	Lump flow was not observed when using steam-water.
	0.05 mm (silica tube) – Steam-water	
Chung and Kawaji (2004)	0.05 to 0.53 mm tubes	Bubbly, churn (slug flow with streaks and swirls that trails it), gas core flow with smooth thin liquid film, gas core flow with wavy liquid film (liquid ring flow), slug-annular, annular.
	Nitrogen-water	Churn- observed only in 0.25 and 0.53 mm at certain conditions.
Xiong and Chung (2007)	0.209, 0.412 and 0.622 mm	Bubbly, slug, slug-ring (liquid-ring flow), dispersed-churn flow and annular flows microchannels. Dispersed-churn flows were absent in the 0.209 mm channel.
	Nitrogen-water	Churn featured as periodic appearance of “disruption tail of the slug” usually followed by some very small bubbles.

3.2.2 Flow pattern maps

One of the first flow pattern studies in small diameter tubes was presented as early as 1964 by M. Suo and P. Griffith, (Suo and Griffith, 1964). They studied adiabatic two phase flow of heptane/N₂ and water/N₂ in horizontal tubes of internal diameter 1.028-1.59 mm. They provided a flow map using coordinates of liquid Capillary number ($U_l \mu_l / \sigma$) versus liquid volumetric ratio ($Q_l / (Q_l + Q_g)$). In their map, bubbly-slug, slug and annular flows were identified with their transition boundaries. Since then a number of flow pattern maps have been proposed in the open literature.

Fukano and Kariyasaki (1993) suggested a flow map from their experiments for three tubes that provided three flow pattern types: bubbly, intermittent and annular. The comparison of their data with the transition lines proposed by Barnea et al. (1983) showed agreement only for the 4.0 mm internal diameter tubes. The Barnea et al. flow map was developed based on a data from 4 mm vertical tube and identified three flow regimes as: dispersed bubble, intermittent flow (elongated bubble, slug, and churn) and annular flows. On the other hand, Mishima and Hibiki (1996) produced flow patterns maps for tubes of 2.05 and 4.08 mm internal diameter using superficial phase velocities as coordinates and compared them with the transition lines predicted by Barnea et al. (1983), Kariyasaki et al. (1992) (cited in Mishima and Hibiki, 1996) and Mishima and Isshi (1984). As it can be seen from Fig. 3.5, their results were better predicted by Mishima and Isshi model, for example at the bubbly-slug and slug-churn transition lines.

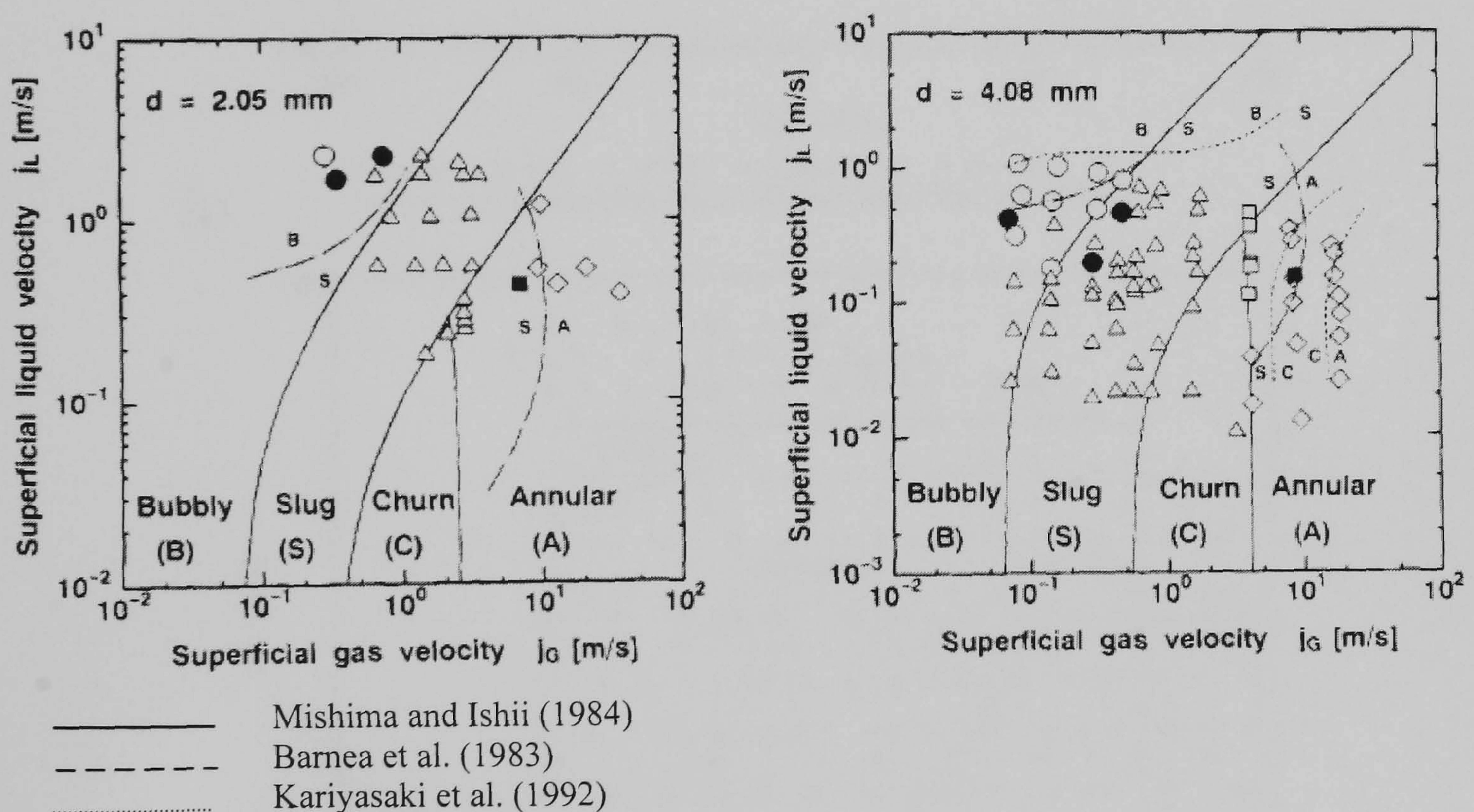


Figure 3.5 Flow regime map and transition lines predictions for air-water flow, Mishima and Hibiki (1996).

Tripplet et al. (1999) compared their flow pattern map with the correlation of Suo and Griffith (1964), and models of Taitel et al. (1980), Barnea et al. (1983) and Taitel and Dukler (1976). None of these prediction methods agreed with the results. However, in figure 3.6, a relatively better agreement was found when they compared their results with other experimental flow pattern maps of Damianides and Westwater (1988) and Fukano and Kariyasaki (1993). Similarly, Coleman and Garimella (1999) showed their

results agreed with the experiment results of Damianides and Westwater (1988) and Fukano et al. (1989). However, comparison with the model of Taitel and Duckler (1976) did not well predict their data. This suggests, models and correlations developed for relatively large tubes cannot predict well flow pattern results from small diameter tubes as they did not account the new flow pattern features observed.

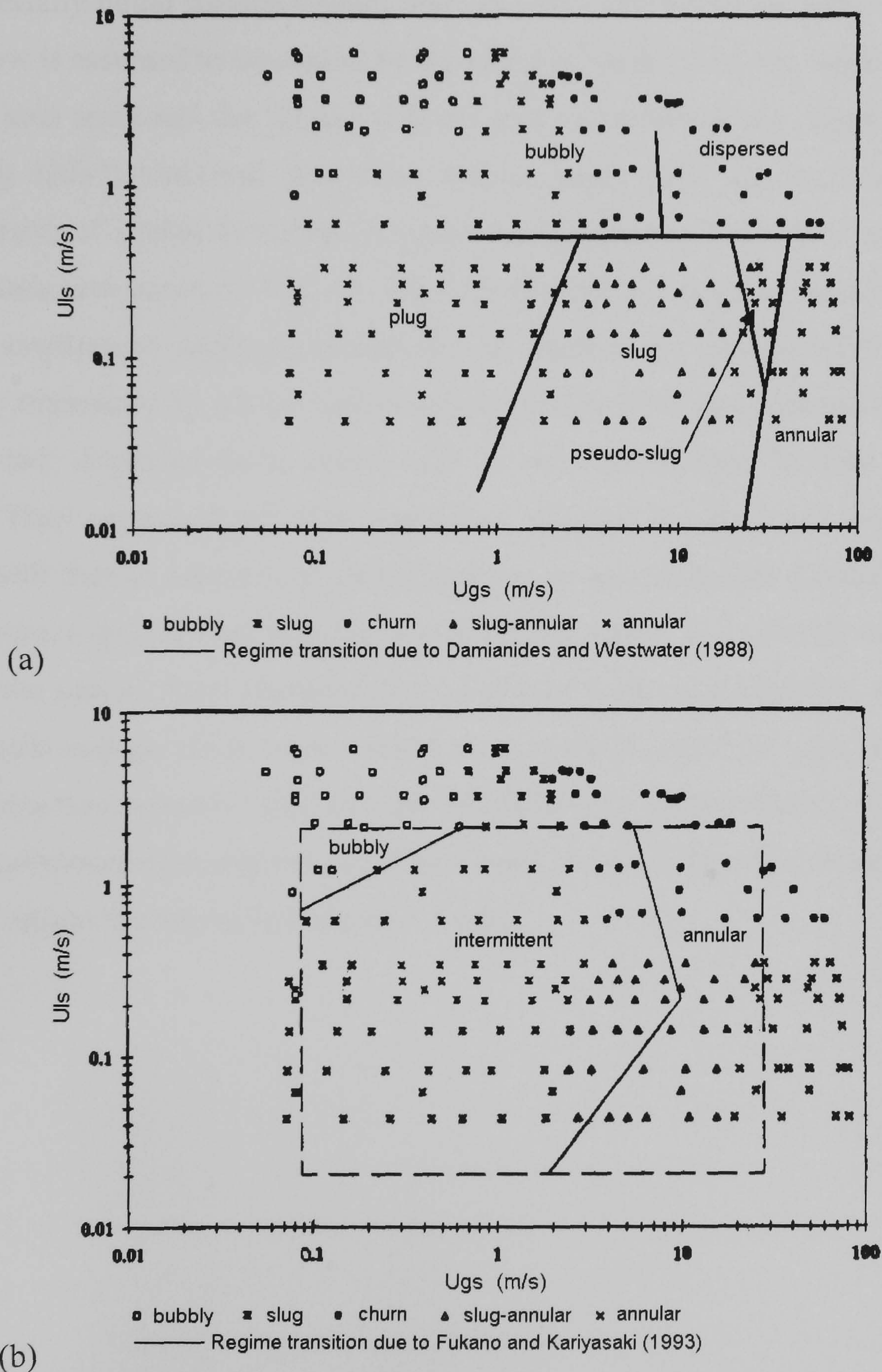


Figure 3.6 Air-water flow regimes for the 1.1 mm tube of Triplett et al. (1999) and comparison with the experimental flow regime transition lines of (a) Damianides and Westwater (1988) and (b) Fukano and Kariyasaki (1993).

Yang and Shieh (2001) studied two-phase flow patterns using two different fluids in horizontal tubes of diameter 1- 3 mm. The flow pattern map obtained for air-water mixture agreed well with Diamandes and Westwater (1988). However, a similar experiment using R134a gave different results, particularly at the slug/annular and bubble/slug transition lines. This was attributed to the fact that the property of the fluids, especially liquid surface tension, was different. The transition delay from slug to annular flow is assumed to be caused by the effect of surface tension, which minimizes interfacial area and coats the liquid along the wall circumferentially. Therefore, Xiong and Chung (2007) predicted their flow regime maps using gas and liquid Weber numbers (ratio of inertia to surface tension) as coordinates. Their flow maps for the three channels are shown in Fig 3.7. The fact that bubbly-slug and annular flows are located at smaller and larger gas Weber number respectively implied bubbly slug flow was highly dominated by surface tension while annular flow was dominated by inertia. Slug-ring and dispersed-churn flows exist in the intermediate between these two extremes. They compared the flow maps they obtained for the 0.622 mm hydraulic diameter with that of Akbar et al. developed for ~1 mm hydraulic diameter based on Weber numbers and reported that the results did not agree. The possible reasons were related to the special flow characteristics associated with microchannels, and the fact that the liquid and gas flows were laminar even at higher gas flow rates resulting in a weaker interaction between liquid and gas interfaces than minichannels (~1mm). In the end, they concluded flow regime maps developed for minichannels (~1mm) could not predict the results for microchannels ($D < 1$ mm).

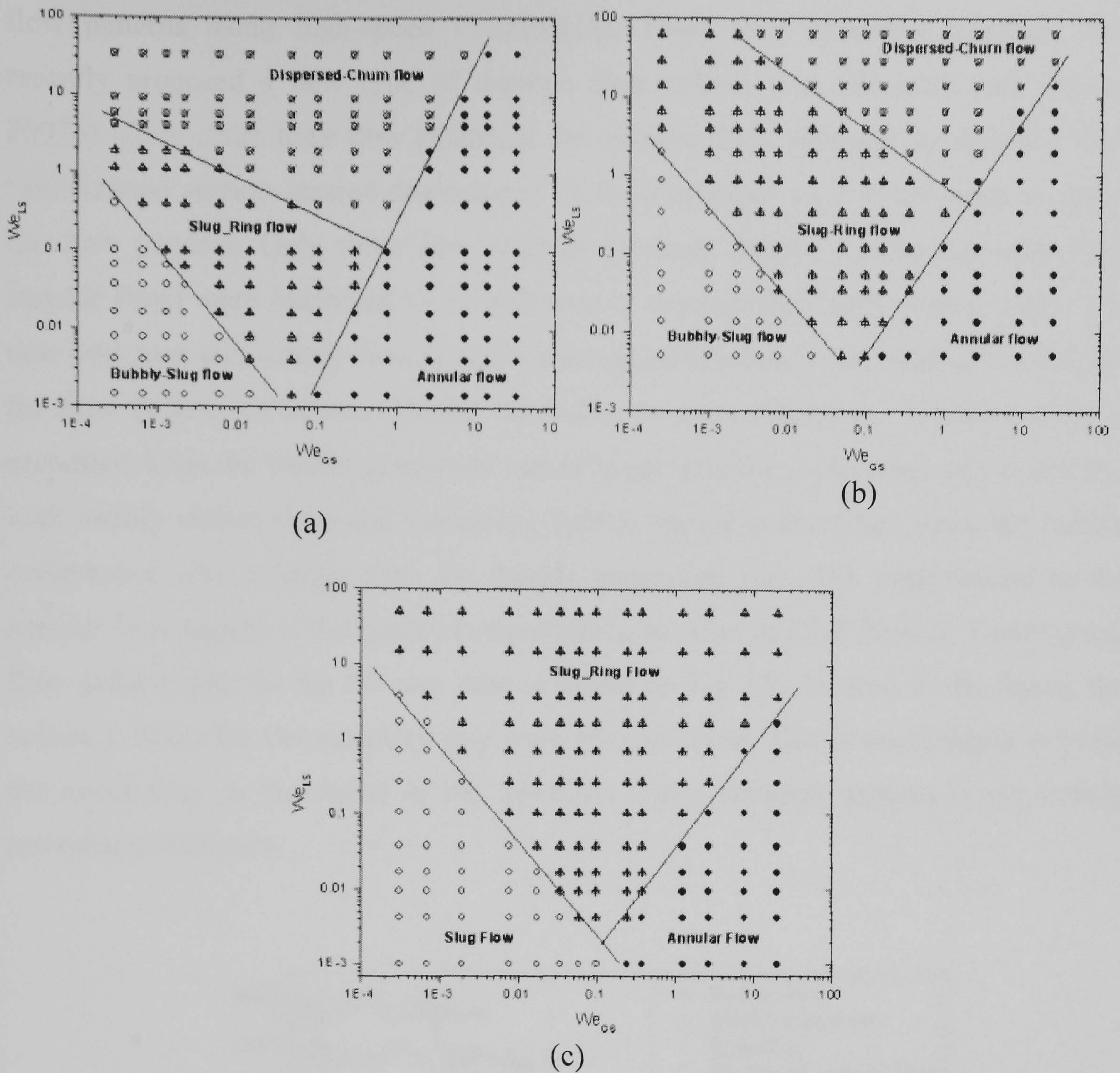
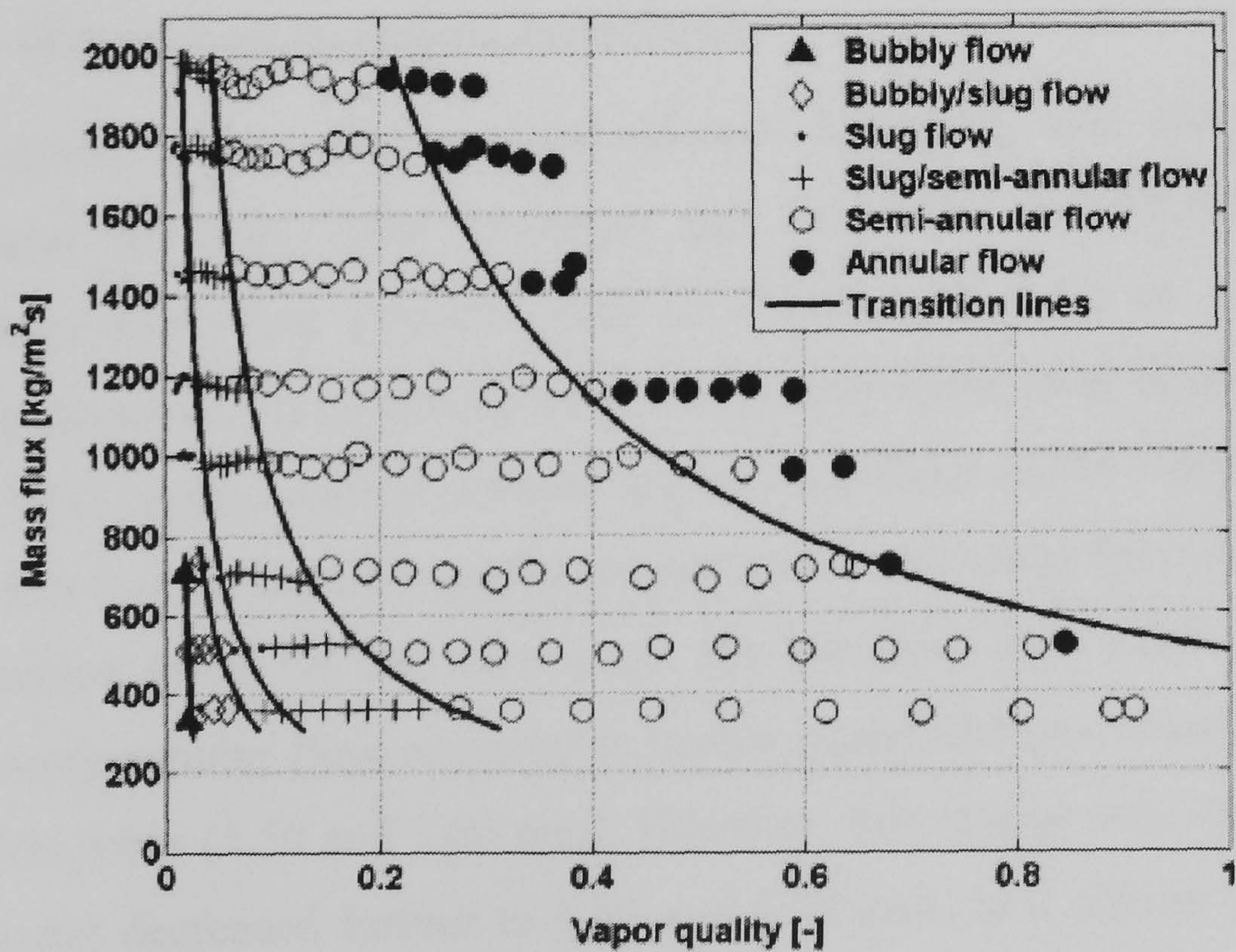


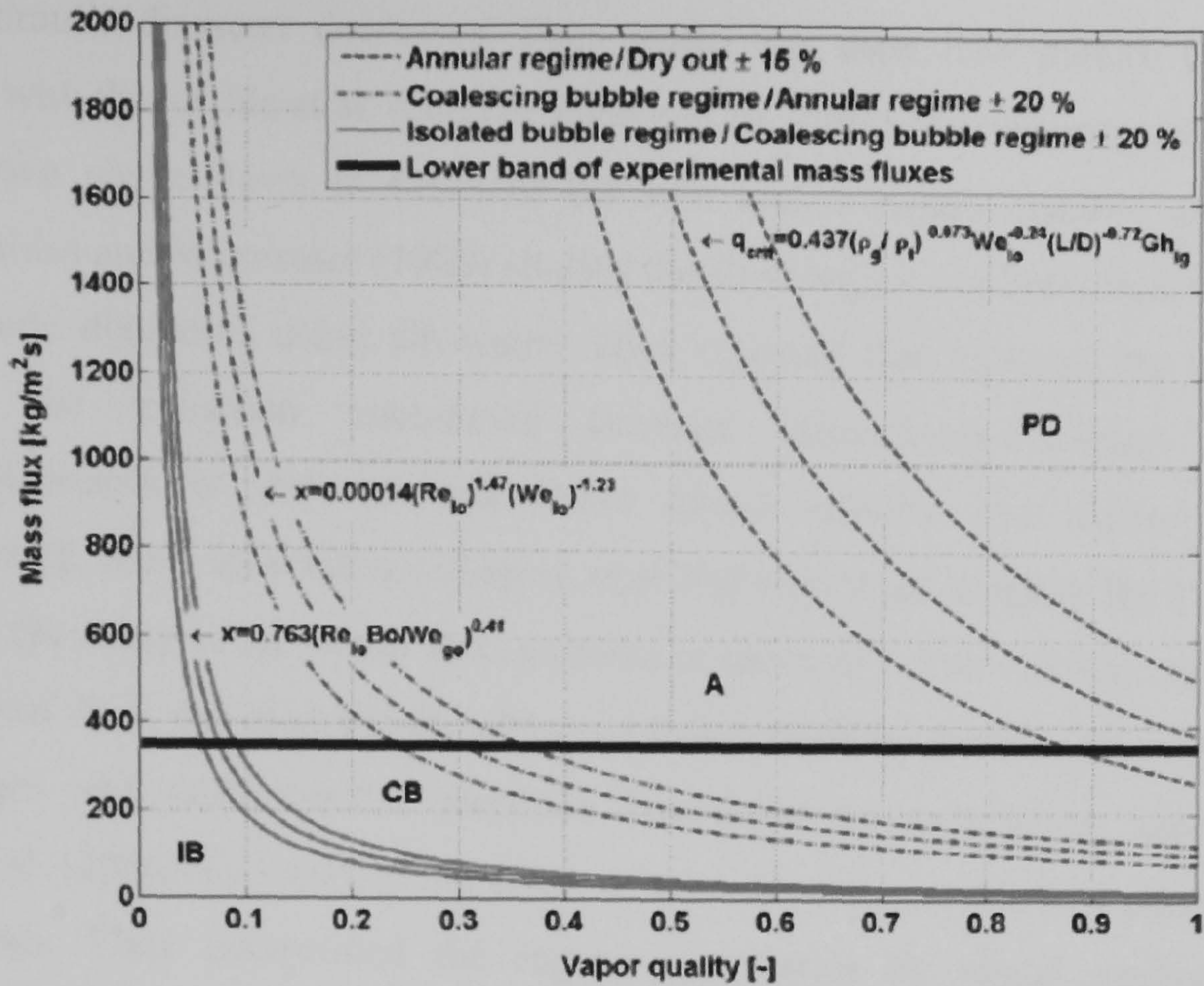
Figure 3.7 Flow regime maps of Xiong and Chung (2007) for: (a) $D_h = 0.622$ mm, (b) $D_h = 0.412$ mm (c) $D_h = 0.209$ mm.

Most of the flow patterns reported so far were obtained by a direct observation in a transparent tube using high speed visualization. Hence, identifying flow pattern types and determining the transition boundaries involve subjective judgement. Revellin et al. (2006) employed an optical technique (using laser beam and photo diodes) to segregate the flow patterns in addition to the high speed visualization made at the exit of the evaporator section. The signals from their optical measurement were also used to determine bubble frequency, length and velocity. It might be difficult to merely use the signal outputs to identify the flow regimes and transitions due to similarity in signals from some flow pattern types (for instance elongated bubble and annular) and lack of distinct signal characteristics in some flow cases (e.g. semi-annular). However, coupled with high speed visualization, the method was unique in its approach and has additional advantages. Most importantly, it reduces the subjectivity involved in differentiating

flow patterns using high-speed visualization. From their extensive research, they recently proposed a new type of diabatic flow pattern map (Revellin and Thome, 2007b). They claim their flow pattern is for diabatic flow, although an adiabatic flow visualization section located downstream of the evaporator section was used to obtain the flow patterns. Only three flow regimes (isolated bubble, coalescing bubble and annular flow) were identified to be sufficient to develop their flow pattern maps. The new flow map was mainly developed considering coalescence as the leading mechanism for flow pattern transitions. Hence, according to their definition; isolated bubble is presented when the bubble generation rate is larger than the coalescence rate (including both bubbly and/or slug) and coalescing bubble regime is identified when the bubble coalescence rate is larger than the bubble generation rate. The upper-bound to the annular flow regime is the quality corresponding to onset of CHF /dryout. Their typical flow pattern map for the 0.5 mm tube is shown in Fig 3.8. As seen in the figure, the accuracy limits for the transition line were also provided. This is encouraging because the uncertainty in the width of the transition zones between regimes is not mostly provided in literature.



(a)



(b)

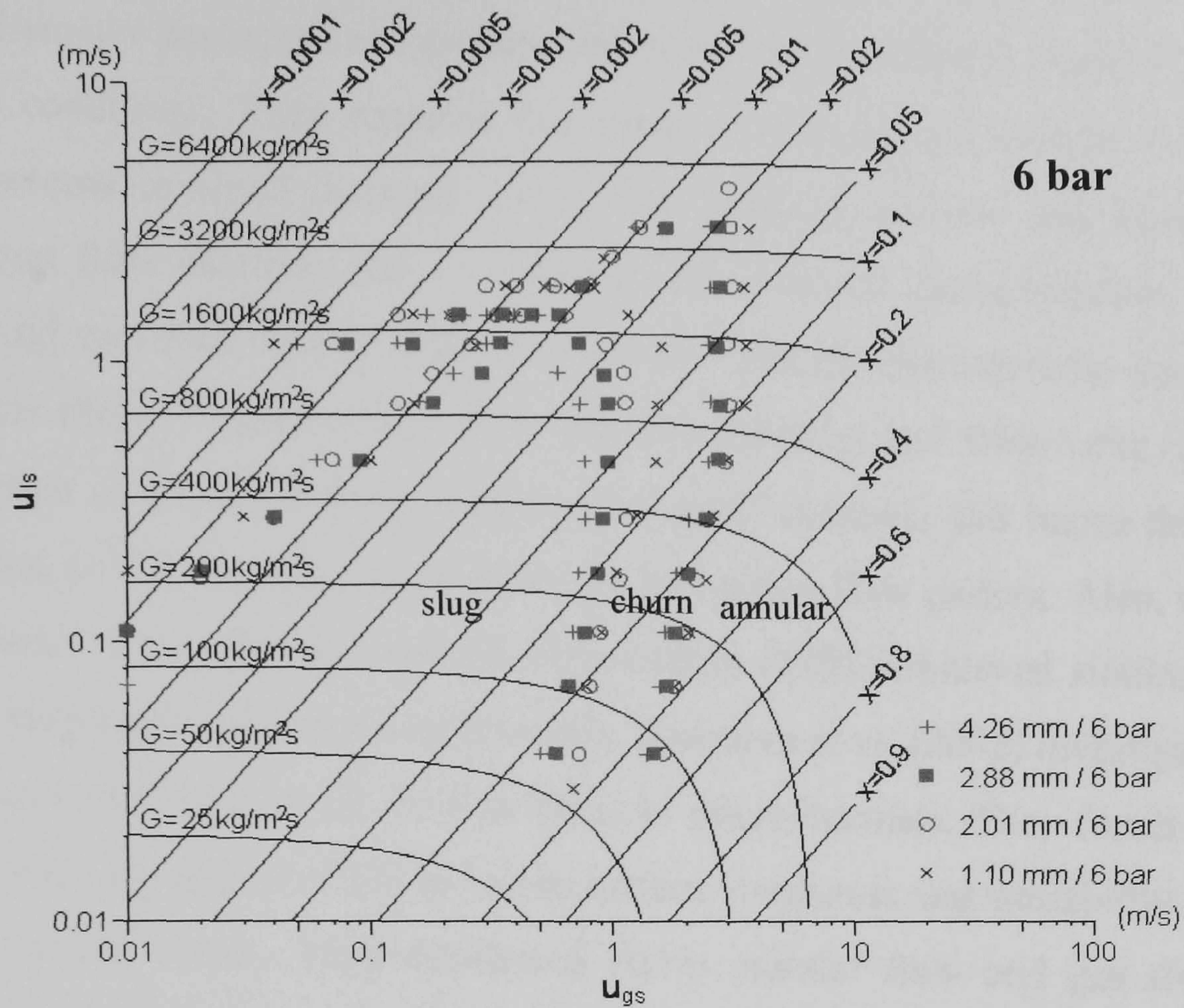
Figure 3.8 Flow pattern maps for 0.51 mm tube using R134a at ~ 8 bar, (a) experimental data, (b) Transition boundary correlation; Revellin and Thome (2007b).

Effect of tube diameter on transition boundaries

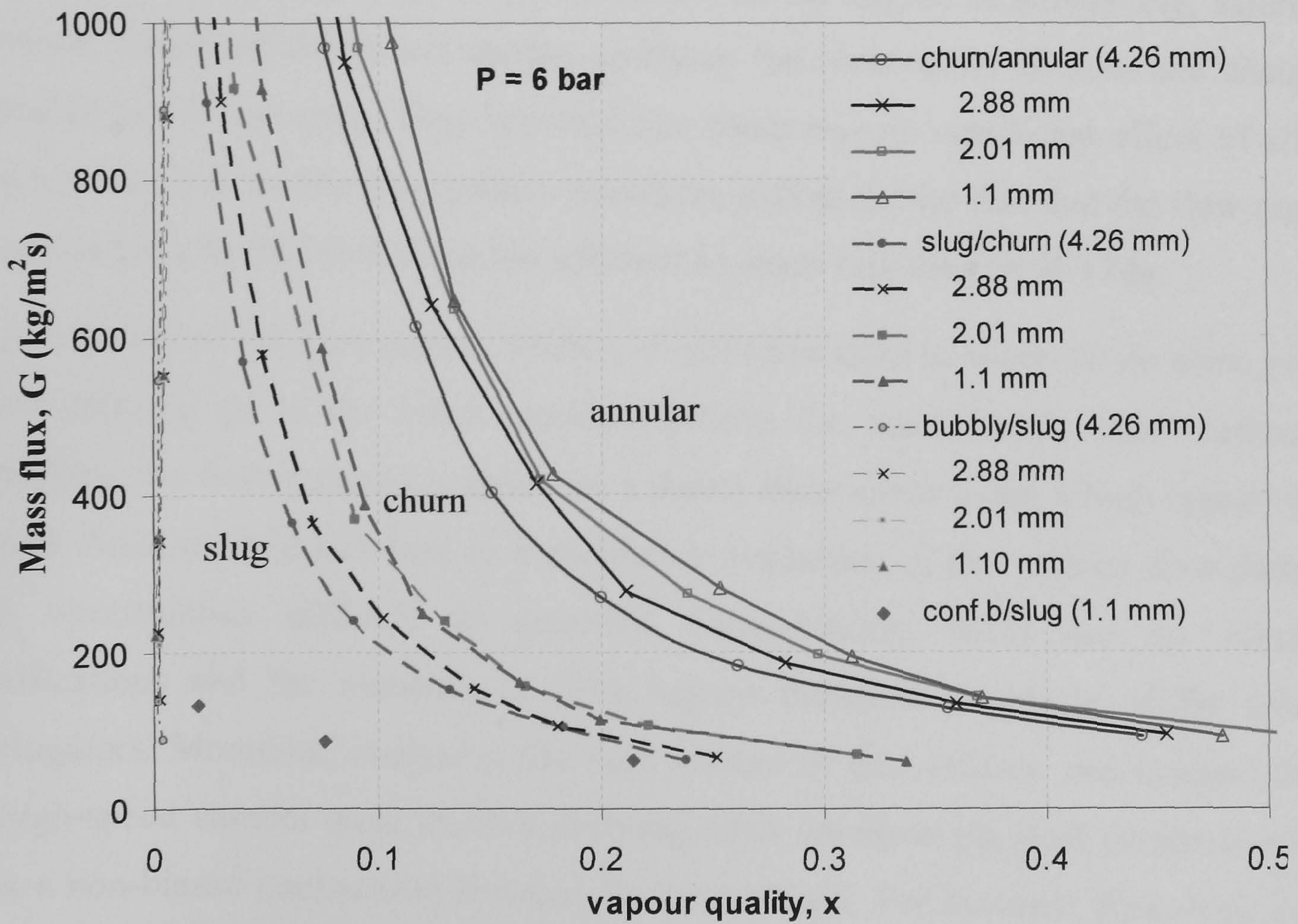
A number of studies have investigated the effect of decreasing tube diameter on flow pattern transition boundary lines. Coleman and Garimella superimposed the flow patterns obtained from four circular tubes of different diameter in a single map. Decreasing the diameter, the transition from intermittent flows (slug or plug) to bubbly (dispersed bubble) regime shifted towards higher superficial liquid velocity. This was related to the fact that the liquid is readily pushed to the wall along the circumference by the surface tension force. On the other hand, the transition from intermittent flow to annular and wavy annular flow occurred at higher superficial gas velocity for the two larger diameters tubes (5.50 and 2.60 mm). However, this change was not consistent as the tube diameter decreased further to 1.75 and 1.30 mm. In a similar experiment by Zhao and Bi (2001), for three different triangular channels of hydraulic diameter (2.9, 1.4, 0.87 mm), found the dispersed bubble-to-slug flow transition line to shift towards higher superficial liquid velocity as the hydraulic diameter decreased from 2.9 to 1.4 mm. Besides, slug-churn and churn-annular transition lines were observed to shift towards higher superficial gas velocity. The churn flow regime is shown to diminish as

the hydraulic diameter decreases. They stated that their flow pattern transition lines agreed with that of Ide et al. (cited in Zhao and Bi, 2001) who investigated adiabatic air-water two phase flows in tubes of 0.9 mm and a square channel of side 1 mm. Damianides and Westwater (1988) studied the flow regimes in horizontal tubes of 1 to 5 mm inside diameters using air-water. They reported that reducing the tube diameter shifted the transition boundaries between intermittent-dispersed bubbly and intermittent-annular flow towards lower liquid velocity and higher gas velocity respectively. Also, they did not observe stratified flow regime inside the 1 mm diameter tube. In the study of air-water flow patterns in tubes of 0.5 to 4.0 mm inside diameter, for vertical flow, Lin et al. (1998) observed that decreasing the tube diameter shifted the slug-churn and churn-annular transition boundaries towards lower vapour velocity. Chen et al. (2006) also studied the effect of tube diameter on the flow pattern transition boundaries. They determined the regime boundaries by visual analysis of video recordings at fixed total mass flow rate for increasing vapour flow created by small increments in the heat input to the test section. Figure 3.9 (a) shows their dimensional regime map for different diameters at pressures of 6 bar using the superficial velocities of the liquid and vapour phases as coordinates. Constant mass flux and constant quality lines are superimposed on the maps in Chen's thesis, Chen (2006). The flow pattern transition data of Chen is also plotted in mass flux versus quality graph in Figure 3.9 (b) for a pressure of 6 bar. As shown in the figure, when the diameter is reduced, the slug/churn and churn/annular transition lines shift towards higher quality. There is no obvious effect on the bubbly/slug transition line. The flow regime boundaries are shifted to significantly lower qualities as the mass flux increases. At higher quality, the transition lines for different tubes merge into a single line. Chen et al. (2006) also showed that maps for different diameters collapsed onto a single map in a non-dimensional plot employing the liquid and vapour Weber numbers. It is difficult to make a direct comparison between the regime transition boundaries of Chen et al. (2006) and Revellin and Thome (2006) because of the fact that different flow pattern classification were used. However, making a rough assumption that isolated bubble and coalescing bubble regimes of Revellin and Thome (2007) correspond to slug and churn flow regimes of Chen et al. (2006), there is an interesting agreement for mass flux values larger than about $650 \text{ kg/m}^2\text{s}$. However, below this mass flux value, the churn-annular boundary quality becomes lower than the coalescing bubble-annular boundary quality.

It is worth to note that for mass flux values below about $350 \text{ kg/m}^2\text{s}$, the transition boundary lines of Revellin and Thome (2006) are approximate extrapolations.



(a)



(b)

Figure 3.9 Flow regime transition boundary lines, $P = 6 \text{ bar}$: (a) U_{ls} vs. U_{gs} , (b) G vs x , data of Chen (2006).

Other effects on flow patterns

Few studies have also assessed other secondary effects on two phase flow patterns in small diameter passages such as flow direction, channel shape, channel orientation and surface conditions. They reported that these effects are not significant on two phase flow patterns in small diameter tubes. For instance, Fukano and Kariyasaki (1993) found that flow direction has no effect on flow pattern characteristics. Tripplet et al. (1999) did not observe any difference in flow pattern characteristic due to change in geometric shape. Triplet et al. (1999) and Daminanides and Westwater (1988) reported the absence of stratified flow in horizontal small channels and hence the fact that the orientation of the channel has no effect on two phase flow pattern. Also, under reduced gravitational force, Brauner and Moalem-Maron (1992) observed similar flow regime characteristics with conventional channels. Serizawa et al. (2002) investigated the effect of surface conditions on the flow patterns in microchannels. They found that the flow patterns were equally sensitive to inside surface roughness and wettability in addition to surface tension forces. They confirmed stable annular flow and gas slug flow with stable thin liquid film occurred under carefully treated clean surface conditions. Revellin and Thome (2007) studied the effect of the degree of subcooling, saturation pressure, length of the heated section upstream the observation section, and changing diameter to 0.8 mm tube. They reported that there was no significant effect of all the above parameters on the flow pattern transition, except for the fact that the flow regime transition lines for R-245fa were less affected by mass flux than for R-134a.

As a summary of the flow pattern studies, it will be prudent to comment on some points before moving on to the other sections. Firstly, the most widely used method of identifying the flow patterns is based on a direct observation using a high-speed video camera. Such method can lead to a subjective evaluation of the various flow patterns with uncertainties difficult to quantify. Consequently, there are no standard classifications and the numbers of flow regime divisions sometimes differ among investigators. Moreover, analysing the vast amount of data (videos and images) from the high-speed camera must involve deriving other common physical parameters that allow a non-biased comparison between flow conditions. For instance, Kawahara et al. (2002) developed their flow pattern maps based on the probability appearance of each type of flow. It will be tenable to also consider other techniques along with direct observation that enable measurements of different related flow parameter such as void

fraction and bubble frequency. Secondly, flow regimes may also transform gradually, rather than have sharp boundaries. Besides, some flow patterns are intermittent in nature, i.e. differences may be observed in time. Thirdly, since different transitions are governed by different balance of forces, the use of single parameter to suitably represent all the flow pattern transition is unlikely. Hence, a more appropriate approach seems to separately treat each transition and provide criteria based on phenomenological aspects of that particular transition. Finally, in the past, flow pattern studies were made independent of heat transfer and are mainly focussed on adiabatic two-phase flows (mostly air-water mixing). However, heat transfer processes and pressure drop are closely related to local flow structure. This has not been the case until recently when flow pattern based heat transfer models emerged. Also, identifying flow pattern types is necessary to define the range validity of mechanistic models that are regime-specific, although explicit information about flow regime boundaries may not be required for heat transfer correlations. Therefore, the objectives of flow pattern studies should include integrating the results with the heat transfer process so as to contribute to mechanistic heat transfer and pressure drop modelling attempts.

3.3 Two phase pressure drop

Accurate predictions of pressure drop are necessary for design of compact heat exchangers or any cooling system. Hence, most flow boiling studies have made a parallel experimental investigation of pressure drop along with the heat transfer studies. Here the effect of various parameters on the two phase pressure drop is reviewed below. In addition, the performance of several correlations to predict the pressure drop results of small diameter tubes is discussed. Although, two phase pressure drop predictions could depend on the local flow structure, general correlations based on empirical multipliers seem to perform better compared with the corresponding classical heat transfer correlations. For instance, predictions based on the two phase multiplier, a method proposed by Lockhart-Martinelli back in 1949, which is adopted by large number of studies still works fairly well for some of the current results. The most widely used classical models are based on homogenous, separated flow, and annular two phase flow models. Brief introduction of these models was given in Chapter 2.

Effect of mass flux, heat flux and system pressure

Tong et al. (1997) studied pressure drop during highly subcooled flow boiling of water in smaller diameter tubes of 1.05 to 2.44 mm. Mass flux ranged from 25×10^3 to 45×10^3 kg/m²s, inlet temperature from 22 to 66 °C. The experimental pressure drop results showed an increase in the value with mass flux, which was assumed to be the result of shear-stress enhancement with higher mass flux. On the other hand, Kureta et al. (1998) conducted boiling two phase pressure drop experiment using water at atmospheric pressure. They used vertical tube with 6 mm internal diameter, 680 mm heated length, 800 mm pressure drop measuring length. The pressure drop versus mass flux had a negative slope in the two phase region followed by a positive slope at high mass flux. Tran et al. (2000) analysed two phase saturated boiling pressure drop in small diameter tubes using their extensive data collected at Argon National Laboratory. The various ranges of parameters were: channel size 2.46 and 2.92 mm circular tubes and a rectangular channel with hydraulic diameter 2.4 mm; fluids R-134a, R-12 and R-113; pressure 1.38 to 8.56 bar. The total test section lengths were 412, 881 and 914 mm for the test fluids of R113, R12 and R134a, respectively. The experimental results for R134a and R12 at 8.35 bar indicated that pressure drop increased with mass flux. On the other hand, Kaminago et al. (2003) conducted pressure drop experiments during water flow boiling in capillary tubes of 1.45 mm, for the range of 0.01 to 1 bar pressure. In the sub-atmospheric pressure range, there was no effect of mass flux on pressure drop. However, the pressure drop slightly increased with mass flux at atmospheric pressure. Huo et al. (2007) conducted boiling two phase pressure drop experiment using R134a inside 4.26 and 2.01 mm stainless steel tubes and found that the pressure drop increased with mass flux. In general, as confirmed by all the studies above, the pressure drop increases with mass flux.

Kureta et al. (1998) reported that the boiling two phase pressure drop increased with heat flux, but the slope slightly decreased at high heat flux. The test section they used for this experiment was a horizontal tube with 2 mm internal diameter, 100 mm heated length, and 120 mm pressure drop measuring length. As the heat flux increased, the minimum point in the ΔP Vs G curve shifted towards the high mass flux and pressure drop. Tran et al. (2000) also found that the two phase pressure drop at 8.35 bar saturation pressure, for R134a and R12 increased with exit quality, which is almost directly proportional to heat flux. Wen and Kenning (2004) studied two phase pressure

drop of water during flow boiling in vertical channels with a cross-section of $2 \times 1 \text{ mm}^2$. They measured the local pressure variation at five different axial locations. The pressure drop versus length curves indicated pressure drop increased with heat flux for various mass fluxes but the trend was not consistent for all the mass fluxes. Also, Wen and Kenning (2004) reported a two phase pressure drop distribution along the channel acquired at 200 Hz sampling frequency. Pressure fluctuations that propagate with liquid slugs having amplitude as large as 5 kPa, were plotted against axial length at various mass flux and heat flux. The oscillation amplitude (5 kPa) was comparable to the time averaged two phase pressure drop along the channel. Comparing the results for different inlet compressibility conditions, the pressure drops at low inlet compressibility were larger than at high inlet compressibility. Huo et al. (2007) also observed the two phase pressure drop increased with heat flux. Revellin and Thome (2007c) presented results of adiabatic two phase frictional pressure drop in two very small horizontal tubes of 0.509 and 0.790 mm in diameters for R134a and R245fa. The measurements were taken from a visualization transparent glass tube, which was 100 mm long. The plot of the two phase pressure drop gradient against vapour quality (calculated near the end of the evaporator section, which was located upstream of the pressure drop measuring section) showed a similar common characteristics of increasing pressure drop with quality and mass flux. They noticed, however the flow pattern transition affects the trend of pressure drop gradient versus quality curve, i.e. the existence of smooth and wavy annular flows. However, the change in the trend was observed only at $G = 1000$ and $1200 \text{ kg/m}^2\text{s}$ and is not consistent with other mass fluxes or related flow patterns. Therefore most of these studies indicate that the two phase pressure drop increases with heat flux

Tong et al. (1997) found that the pressure drop increased with decreasing exit pressure at constant internal diameter and mass flux. Tran et al. (2000) for R134a at 8.35 bar system pressure also indicated pressure drop increased with decreasing saturation pressure. Recently, Revellin and Thome (2007c) also reported that the pressure drop increased with decreasing saturation temperature. Huo et al. (2007) also observed the two phase pressure drop decreased with increasing system pressure from 8 to 12 bar. Generally, the reason for the pressure effect is attributable to the influence of the liquid-to-vapour density ratio on the system pressure.

Effect of tube diameter

Tong et al. (1997) obtained a higher pressure drop for the smaller tube and the value decreased with increasing internal tube diameter. This was explained using boundary layer theory. Based on the theory, the total apparent shear stress (turbulent plus viscous) is directly proportional to the transverse direction velocity gradient within the turbulent boundary layer (Kays, 1980). As the tube internal diameter changes, the boundary layer thickness also changes, more specifically the boundary layer or bubbly layer becomes thinner for small diameter tubes. Consequently, a higher velocity gradient establishes that in turn result in a larger pressure drop. Huo et al. (2007) also found that the two phase pressure drop in the 2.01 mm tube was higher than the 4.26 mm tube. Recently, Revellin and Thome (2007c) reported that the measured friction pressure drop was higher for the 0.51 mm tube compared with the 0.790 mm. In contrast, Lee and Lee (2001), in rectangular channels of various gap sizes, reported the two phase friction pressure drop of R113 decreasing with decreasing gap size from 2 to 0.4 mm.

Other effects on two phase pressure drop

Tong et al. (1997) assessed the effect of length to diameter ratio on the two phase pressure drop and stated that the pressure drop increased with increasing length to diameter ratio. Tran et al. (2000) showed the two phase pressure drop results presented in the form of ΔP Vs G were approximately 30 % higher for R134a (compared with R12), in the mass flux range of (60 to 300 kg/m²s), at an exit quality of 0.7 and saturation pressure of 8.35 bar. In contrast, in the ΔP Vs q graph, the pressure drop results of R134a were 30 to 45 % higher than R12 for heat flux range of (5 to 30 kW/m²). There was no explanation given for this. They also reported that there was no significant effect of channel geometry on two phase pressure drop results. Revellin and Thome (2007c) also stated that R-245fa exhibited a higher pressure drop than R134a. This could be due to the difference in their fluid properties particularly the liquid to vapour density ratio. Tong et al. (1997) also reported that the two phase pressure drop decreases with increasing degree of inlet subcooling, while Revellin and Thome (2007c) did not observe any significant effect of the degree of inlet subcooling on the saturated two phase friction pressure drop.

On the contribution of the various pressure drop components

As discussed in Chapter 2, the total two phase pressure drop is comprised of three main contributions: friction, acceleration and gravitational pressure drop components. Lazarek and Black (1982) performed experiments to determine the three different contributions (friction, acceleration, and gravity) separately. For instance for the friction pressure drop measurement, an adiabatic section was used with positive inlet quality, and a small correction made for the hydrostatic pressure loss using Zuber-Findley (1965) void fraction model. They compared the two phase pressure drop with Martinelli-Lockhart correlation. The results indicated that a better prediction can be obtained for Chisholm constant ($C = 30$). Moreover, the acceleration pressure loss was deduced from dual tube heating experiment then subtracting the friction and hydrostatic contributions. The results were reasonably predicted by multiplying the separated flow momentum change of Martinelli and Nelson (1948) with an empirical coefficient. Assessing the contribution of pressure drop components (acceleration and friction loss), interesting results were reported for the smaller diameter tube by Kureta et al. (1998). The acceleration loss, which was assumed to be negligible in many other studies, was found to be comparable with the friction loss. Furthermore, using Martinelli-Nelson correlation (1948) for the friction pressure drop, they compared the acceleration contribution of the total measured pressure drop with that of homogeneous flow and annular flow models. In the comparison, Akagawa's (1970) correlation was also included. In the annular flow model case, the exit void fraction was calculated using Smith (1969) correlation. The comparison result indicated that their acceleration pressure drop contribution was best predicted by the annular flow model.

Pressure drop correlations

Tran et al. (2000) assessed the capability of large tube pressure drop correlations to predict their small tube pressure drop data. It was stated that five large tube correlations (Freidel, 1979, Chisholm, 1983 (C-coefficient method), Jung and Radermacher, 1989 and Souza and Pimenta, 1995) under-predicted their experimental results, while Chisholm, 1986 (B-coefficient method) slightly over-predicted the data. The divergence was attributed to the difference in the flow patterns between normal tubes and small channels. In the end, they developed a new correlation to predict the two phase friction pressure drop. This was based on the B-coefficient method of Chisholm, 1986. They modified the B-coefficient to take into account the surface tension and channel size

effects. This was made by introducing the confinement number proposed by Kew and Cornwell (1995). The modified correlation predicted their data within 20% for all the test conditions. Later, Yu et al. (2002) from the same laboratory conducted water flow boiling experiments in a horizontal tube of 2.98 mm with almost the same heated length (0.91 m). The two phase friction loss was calculated using Lockhart –Martinelli correlation (1949) and compared with the prediction of the Chisholm correlation (1967). However, their data were over-predicted consistently by about 30 %. The reason was again related to the fact that the prevailing flow pattern in small diameter tubes being slug flow (considered to have a lower pressure gradient) instead of annular flow (which Chisholm's correlation is mainly based). They modified the two phase multiplier using their experimental data. On the other hand, Lee and Lee (2001) reported that their experimental results for the two phase friction loss were predicted by Lockhart-Martinelli correlation within 20 %. They used the modified Chisholm constant for both laminar and turbulent regime and considered the effect of quality varying along the flow direction. Warriar et al. (2002) proposed a correlation for the two phase pressure drop based on experiment on parallel rectangular channels of 0.75 mm hydraulic diameter using FC-84 as working fluid. The two phase pressure drop was calculated using the separated flow model with the void fraction equation of Lockhart-Martinelli. For relatively short tubes, the effect of flashing on the vapour quality is mostly assumed negligible. Nevertheless, they have considered the vapour quality change as a result of flashing. This was based on an assumption that flashing occurred when the liquid temperature is higher than the saturation temperature corresponding to the local pressure. Kaminago et al. (2003) compared the measured friction pressure drop with the correlations of Chisholm (1967), Mishima and Hibiki (1996) and Beattie and Whalley (1982). However, none of the correlations provided satisfactory agreement. Finally, they proposed a correlation that identified total pressure drop into three contributions as: liquid-only, interfacial interaction and gas-only components. They claim their major development was the consideration of the influence of vapour phase in capillary tubes by introducing an additional parameter in the two phase multiplier equation of Chisholm. Wen and Kenning (2004) compared their pressure drop results with the correlations of the Lockhart-Martinelli method with a modified constant Chisholm constant C from Mishima et al. 1993, Chisholm (1973), Tran (2000) and the homogeneous model. The acceleration and the hydrostatic components were calculated using the one-dimensional separated flow model. A relatively better agreement was

obtained with the Lockhart-Martinelli correlation (within 35% scatter). Similarly, Saitoh et al. (2005) compared the measured pressure drop with the homogeneous model and the Lockhart-Martinelli correlation. For the relatively larger tube (3.1 mm), the Lockhart-Martinelli correlation performed better than the homogeneous model. In the homogeneous model, the acceleration component was neglected (since it was less than 10% of the friction loss). However, as the diameter of the tube decreased to 0.51 mm, the homogeneous flow model performed better. Zhang and Webb (2001) compared their results with the Freidel (1979) correlation that failed to fairly predict their data. Hence, they modified the correlation by neglecting the Weber and Froude numbers, i.e. assuming the two phase multiplier is only weakly dependent on these parameters. They also replaced the density and viscosity ratios by the reduced pressure. Eventually, their data for R22, R134a and R404a in tubes of 6.25 and 3.25 mm diameter and channels of 2.13 mm (hydraulic diameter), were compared with the modified correlation and were predicted within $\pm 11\%$. Revellin and Thome (2007c) compared their two phase friction pressure drop data with several correlations. Only the Muller-Steinhagen and Heck correlation were observed to predict their turbulent regime data to an acceptable degree (62 % of data within $\pm 20\%$). A phenomenological model proposed by Garimella et al. (2002) for intermittent flows of R134a was also considered. However, only 20% of the data fall within $\pm 20\%$ and there was a large scatter. Eventually, they modified the homogeneous flow model using a new two phase friction factor correlation developed from a least square curve fitting of their experimental data. The new modified correlation predicted their data and the data from other laboratories (Cavallini et al. (2005) Zhang and Webb, 2001 and Tran, 2000) fairly well. Based on the two phase friction factor versus Reynolds plot, they observed a similar flow regime transition thresholds with the classical theory, i.e. laminar ($Re < 2000$), transition ($2000 < Re < 8000$) and turbulent ($Re > 8000$) regimes, except for the Reynolds range for transition regime being significantly large. It is worth noticing that their measurements were taken from a glass tube with a different surface finish conditions, (much smoother than conventional metal tubes). Besides, the total pressure drop was not measured using a differential pressure transducer mounted between inlet and exit plenum. Rather, it was deduced from the fluid temperature measurements (saturation pressures). The method may introduce unnecessary error, in cases of phase non-equilibrium conditions (at very low and very high quality regions). Also, depending on the scanning rate and the type of data logger, a time lag or lead may occur as the inlet and exit measurements were not

taken at the same real time (advantage of installing a pressure differential transducer to acquire the difference at the same moment).

In general there is a divergence among researchers as to which prediction method can accurately be used for small diameter tube results. Some small channel data have been predicted well by correlations for conventional size channels (Lazarek and Black, 1982; Lee and lee, 2001; Wen and Kenning, 2004; Revellin and Thome, 2007c). Where as other studies indicated their small tube data could not be predicted by large tube correlations (Tran et al. 2001; Yu et al. 2002; Kaminago et al, 2003; Zhang and Webb, 2001). The need for further research in this area is clear.

3.4 Flow boiling heat transfer

There is an increasing number of researches on flow boiling heat transfer in small- to micro- passages, and most of them are experimental studies. However, there are not as yet conclusive remarks on several issues that relate small diameter/micro tubes. Literature reviews made by Palm (2001), Bergles (2003), Kandlikar (2003), and Thome (2004, 2005) have pointed out some of the open questions that need further study. This section will provide a state-of-the-art review on the flow boiling heat transfer characteristics in small size passages and broadly covers issues such as, onset of nucleate boiling, microscale heat transfer mechanisms, associated fluctuations of temperature, pressure, and flow, critical heat flux /dryout phenomena, and heat transfer rate prediction methods.

3.4.1 Onset of nucleate boiling

The underlying physics of nucleate boiling incipience from a pool boiling perspective was introduced in a concise way in Chapter 2. However, the phenomena become different as the size of the channel decreases. This is related mainly to the effect of confinement, number and distribution of active nucleation sites and other effects yet not understood clearly. This section reviews some of the new features of boiling incipience in small diameter tubes. One of the most arguable concepts regarding the onset of nucleate boiling in very small channels is that which was reported by Peng and Wang (1994). They investigated experimentally flow boiling in microchannels (0.15 – 0.42 mm) hydraulic diameter using water and ethanol and reported that it was not possible to observe vapour bubbles inside their heated microchannel, although from the results of wall superheat measurements, they confirmed that fully developed nucleate boiling

condition was achieved. The authors believed the reason for not observing bubbles in the heated channels were related to a new hypothesis they developed. The hypothesis assumes there should be a critical minimum liquid bulk scale, enough to allow evaporation or support bubble growth, which was referred to as “evaporating space”. If the liquid bulk size is smaller than the “evaporating space”, fictitious boiling may occur and will not be possible to observe actual bubbles growing in the channel (even with a magnification tool). However, they did observe strings of small bubbles in the exit liquid mixing chamber at the same condition. No explanation was given for the appearance of the fine bubbles in the exit chamber. Further, they suggested that the flow boiling in microchannels might be associated with quasi- /non- equilibrium of liquid near the saturation point, i.e. the liquid could take considerably higher heat energy than possible for liquid sensible heat. Bergles et al. (2003) questioned the results of their measurement (e.g. uniform flow distribution, accurate heat flux calculation and wall temperature measurements) and suggested the reason for not observing vapour bubbles could be due to the high degree of subcooling, which would result in very small bubbles during forced subcooled boiling. Peng et al. (1998) further analysed theoretically the notion of fictitious boiling and thermodynamic aspects of phase change in microchannels. The basic assumption for the theoretical analysis was that bubble initiation and growth is physically constrained by the channel walls and upstream and downstream liquid inertia. They used the phase instability criteria for pure substance (Carey, 1992), which was given as,

$$\bar{C}_v > 0 \text{ and } \left(\frac{\partial P}{\partial V} \right)_T < 0 \quad (3.1)$$

The first condition is almost true for all substances. Therefore, they pursue algebraically re-arranging the second condition to set a criterion for nucleation in confined space. Re-arranging the second part of Eq. (3.1) and from the Clausius-Clapeyron equation (3.2), they defined a non-dimensional number referred to as N_{mb} (Eq. 3.3), which is dependent on heat flux, and physical properties of the fluid. Therefore, according to their analysis, nucleation is assumed to occur in microchannels, if $N_{mb} \leq 1$.

$$\left(\frac{\partial P}{\partial T} \right)_s = \frac{dP}{dT} = \frac{h_{lg}}{T_{sat} (v_g - v_l)} \quad (3.2)$$

$$N_{mb} = \frac{h_{lg} \alpha_g}{C \pi (v_g - v_l) q'' D_h} \quad (3.3)$$

where C is a correction factor introduced by the authors.

The wall superheat for onset of nucleation was given as,

$$\Delta T_{sup} \geq \frac{4 A T_{sat} (v_g - v_l) \sigma}{h_{lg} (D_h)} \quad (3.4)$$

where A is an empirical constant obtained from their experiment ($A=280$) and introduced because of the fact that the pressure difference across the bubble interface would be greater than that given by Young's Laplace equation due to the restriction by the channel walls on bubble growth.

The above analysis of nucleation criteria was again commented by Bergles (2003) using the relation for radius of cavity at incipient boiling (Eq. 3.7) recommended by Bergles and Rohsenow (1964)

$$r_c = \left(\frac{2 T_{sat} v_g \sigma \lambda_l}{h_{lg} q N} \right)^{0.5} \quad (3.7)$$

Bergles et al. argued that the channel size should not affect initiation of boiling and must be possible to commence nucleation from natural cavities even for very small channels. Finally, Bergles et al. proposed the ONB to be evaluated from the intersection of forced convection, Eq. (3.8) and nucleation heat transfer, Eq. (3.9).

$$q = \alpha (T_w - T_b) = \alpha [(T_w - T_{sat}) + (T_{sat} - T_b)] \quad (3.8)$$

$$q_{ONB} = \frac{h_{lg} (T_w - T_{sat})^2 \lambda_l}{8 T_{sat} v_g \sigma} \quad (3.9)$$

Unlike Peng et al.'s wall temperature measurement, which showed boiling initiated at wall superheats (2-8 K), Lin et al (cited in Peng et al. 1998) found liquid superheat temperature in the same order of magnitude required for homogenous nucleation was measured at the onset of nucleate boiling in microchannels. The corresponding heat flux was reported to reach 10^5 kW/m².

Hapke et al. (2000) investigated experimentally the onset of nucleate boiling and wall superheat for de-ionized water in a vertical tube with 1.5 mm internal diameter using a thermographic measurement technique. The liquid temperature was observed to reach a maximum just before commencing nucleation. This liquid superheat is relatively higher than that measured for conventional tubes, see figure 3.10. Oscillation of wall

temperature was observed at the onset of nucleate boiling (initial high wall superheat region). This was related to the increase in pressure drop due to blockage of the channel by the growing bubble (channel size in the same order of magnitude as bubble diameter). This resulted in a transient pressure and flow rate oscillation inducing local temperature fluctuation at the onset of nucleate boiling. As seen in figure 3.10, the wall temperature was also observed to fall after the first maxima due to high heat transfer rate at the onset of bubble formation, and then the temperature rise back. They compared their experimental initial wall superheat value with the model of Sato and Matsumura (1963) and empirical equation of Bergles-Rohsenow (1964) given in Eq. (3.10) and Eq. (3.11), respectively. As seen in figure 3.11, both equations under-predicted their experimental result at the higher heat flux values except for $q = 50 \text{ kW/m}^2$, at which a better agreement was obtained.

$$(T_w - T_{sat})_{ONB} = 2 \left(\frac{2T_{sat} (v_g - v_l) q \sigma}{h_{lg} \lambda_l} \right)^{1/2} \quad (3.10)$$

$$(T_w - T_{sat})_{ONB} = \frac{5}{9} \left(\left(\frac{q}{1120} \right)^{0.463} P^{-0.535} \right)^{P^{0.0234}} \quad (3.11)$$

where, the unit for pressure, P, should be in bar.

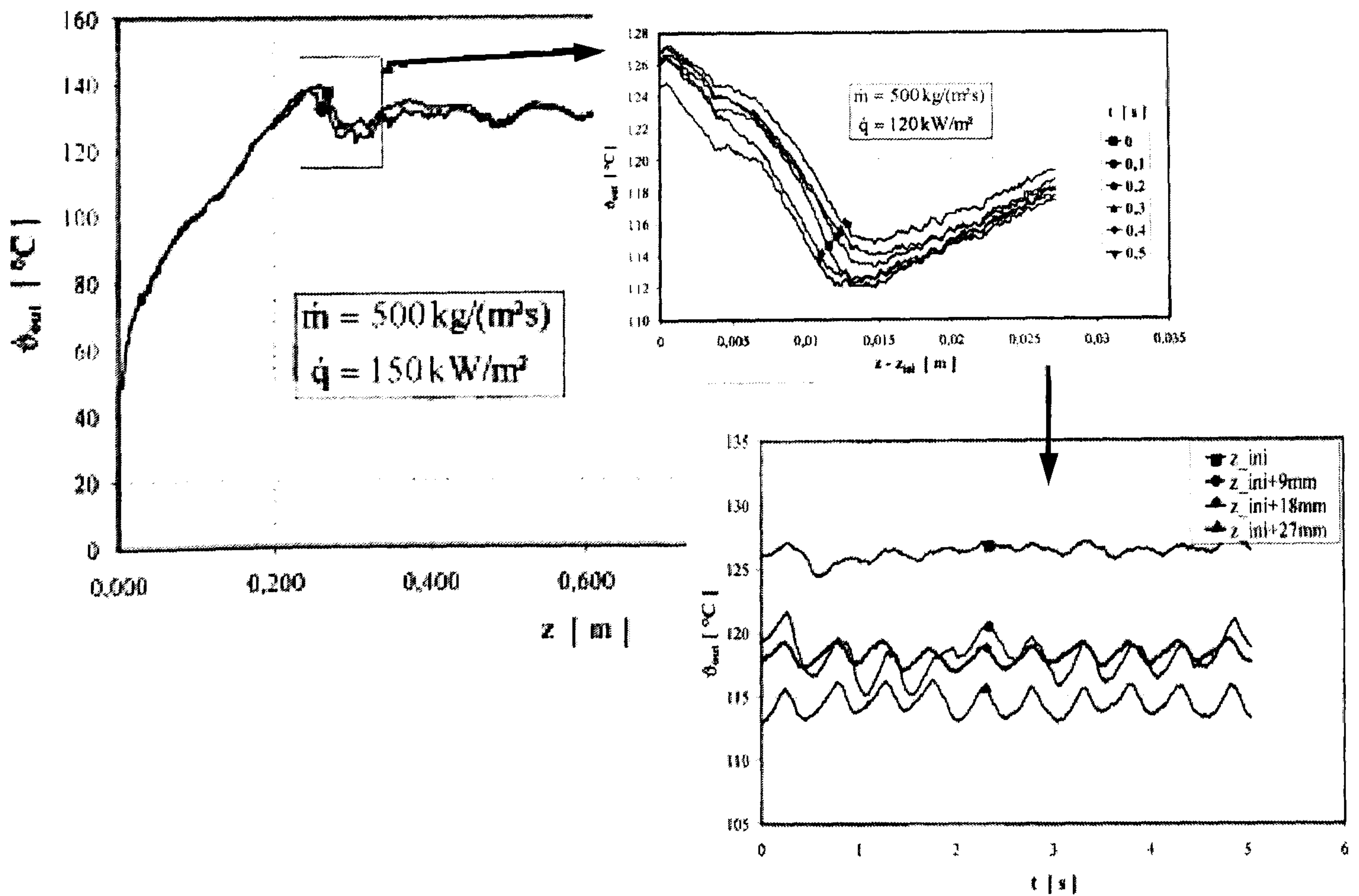


Figure 3.10 Wall temperature at the onset of nucleate boiling, Hapke et al. (2000).

Their experimental initial wall superheat was found to depend on mass flux, i.e. wall superheat decreased with increasing mass flux at constant heat flux. Based on this, they formulated their own semi-empirical equation for determining the initial wall superheat at the onset of nucleate boiling (for vertical tubes only) given in terms of boiling number (N_b), Stanton number ($Nu/(Re Pr)$) and fluid temperature as

$$\left[1 - \left(\frac{T_w - T_{sat}}{T_w - T_l} \right)_i \right] \frac{1}{St} = 5.1557 N_b^{-0.555} \quad (3.19)$$

The use of the above equation requires iteration (refer Hapke et al. 2000 for the iteration procedure). They also briefly investigated the effect of neglecting the axial conduction term and calculating the inner wall temperature using only one-dimensional steady state conduction. They also introduced axial conduction and treated the two-dimensional conduction equation. However, they found no significant difference between the two methods (maximum deviation being only ± 0.1 K, which is less than the uncertainty limit reported by many studies).

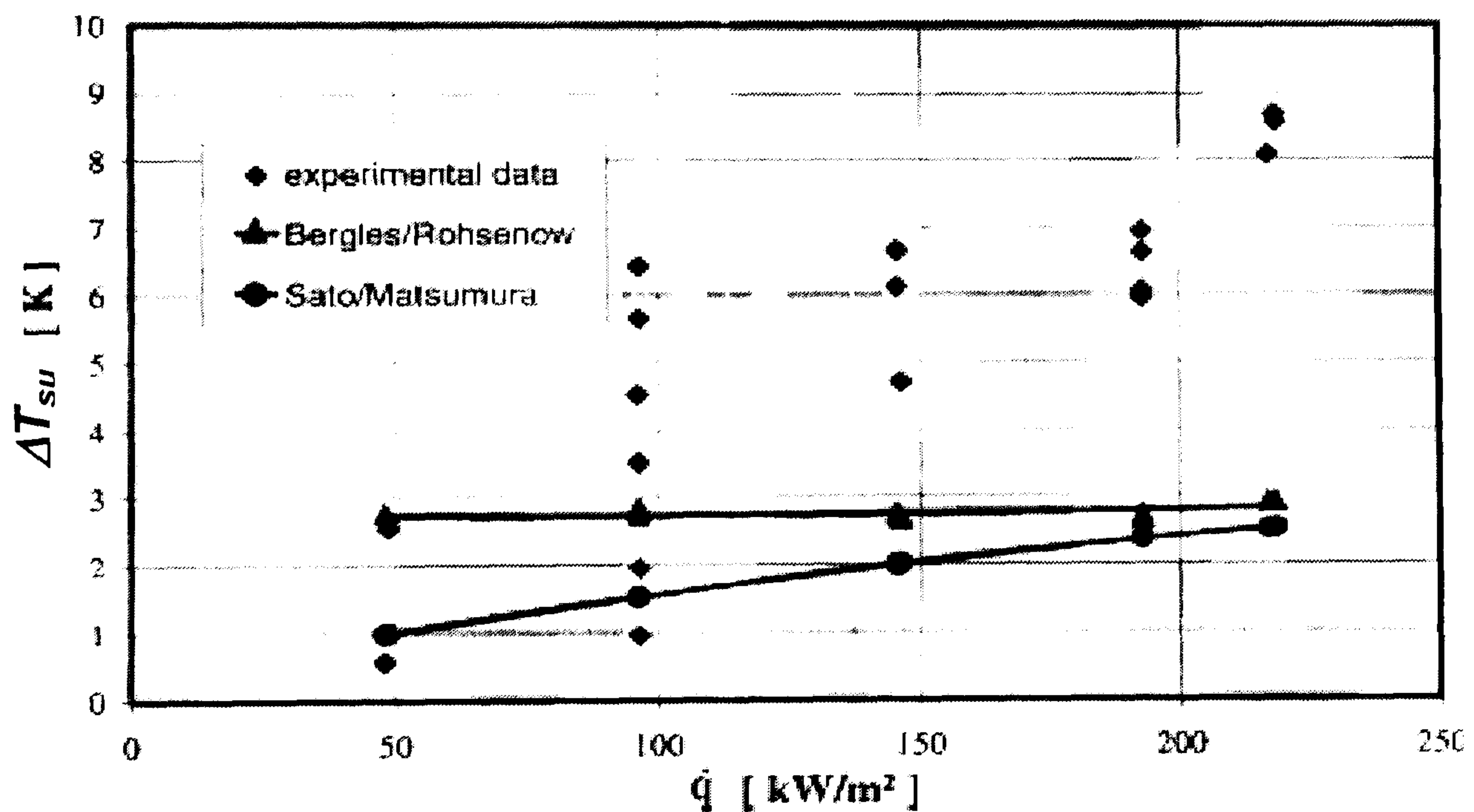


Figure 3.11 Comparison of measured wall superheat with correlations, Hapke et al. (2000).

Zhang et al. (2002) studied the wall superheat conditions of de-ionized water with and without surfactant using plasma etched silicon microchannels with hydraulic diameter of 113 μm . They observed a bubble initiated and developed into annular flow in the channel causing local uniform wall temperature with heat input, referred to as “partial boiling” region. The wall temperature then increases at the onset of “fully developed boiling” followed by a two phase annular flow, which gave rise to a second relatively

uniform wall temperature and high heat transfer coefficient. Conditions differed when the channel size decreased to 44 μm (hydraulic diameter). They observed eruption of vapour with more than 20 K wall superheat right before ONB. Besides, they did not observe the second uniform wall temperature trend in the two phase region, instead the wall temperature increased monotonically with heat transfer rate. This was attributed to the appearance of mist flow with relatively low heat transfer coefficient resulting in an increase in wall superheat. They introduced surfactant to investigate the effect of surface tension force on the later phenomenon. However, the wall superheat behaviour in the smaller channel was not affected by the addition of surfactant. On the other hand, changing the surface roughness, by varying the etch parameters and enhancing the wall channels with notches and cavities, resulted in a very significant effect. Consequently, they obtained nucleate boiling in very small channels ($\sim 28 \mu\text{m}$) with wall superheat values much lower than that required for natural channel (without surface treatment). Therefore, they suggested that the unusual high superheat required in very small channels could be caused by the smoothness of the tube and lack of enough active nucleation sites, which can significantly be improved by surface enhancement. In general, they concluded that boiling incipience in microchannels is different from that of the conventional channels because of the fact that firstly microchannels may have smooth surface depending on the fabrication and manufacturing process.

Ghiaasiaan and Chedester (2002) analysed the onset of nucleate boiling (ONB) for water using data available in the literature. The commonly used method to identify the ONB and the onset of significant void (OSV), i.e. using the characteristic curve of pressure drop versus mass flux were employed, Fig. 3.12. ONB was located at the point where single phase pressure drop line (linear curve) deviated from the ΔP Vs. G curve. The equation of Bergles and Rohsenow (1964) and Sato and Matsumura (1963) presented above under-predicted the collected data for 1, 1.17 and 1.45 mm tubes up to slightly higher than 30%. The reason was assumed to be caused by the fact that the thermo-capillary forces in microchannels were dominant in suppressing micro-bubbles at nucleation sites. They proposed a semi-empirical method for estimating boiling incipience heat flux and were reported to be dependent on turbulence characteristics of the micro-tube.

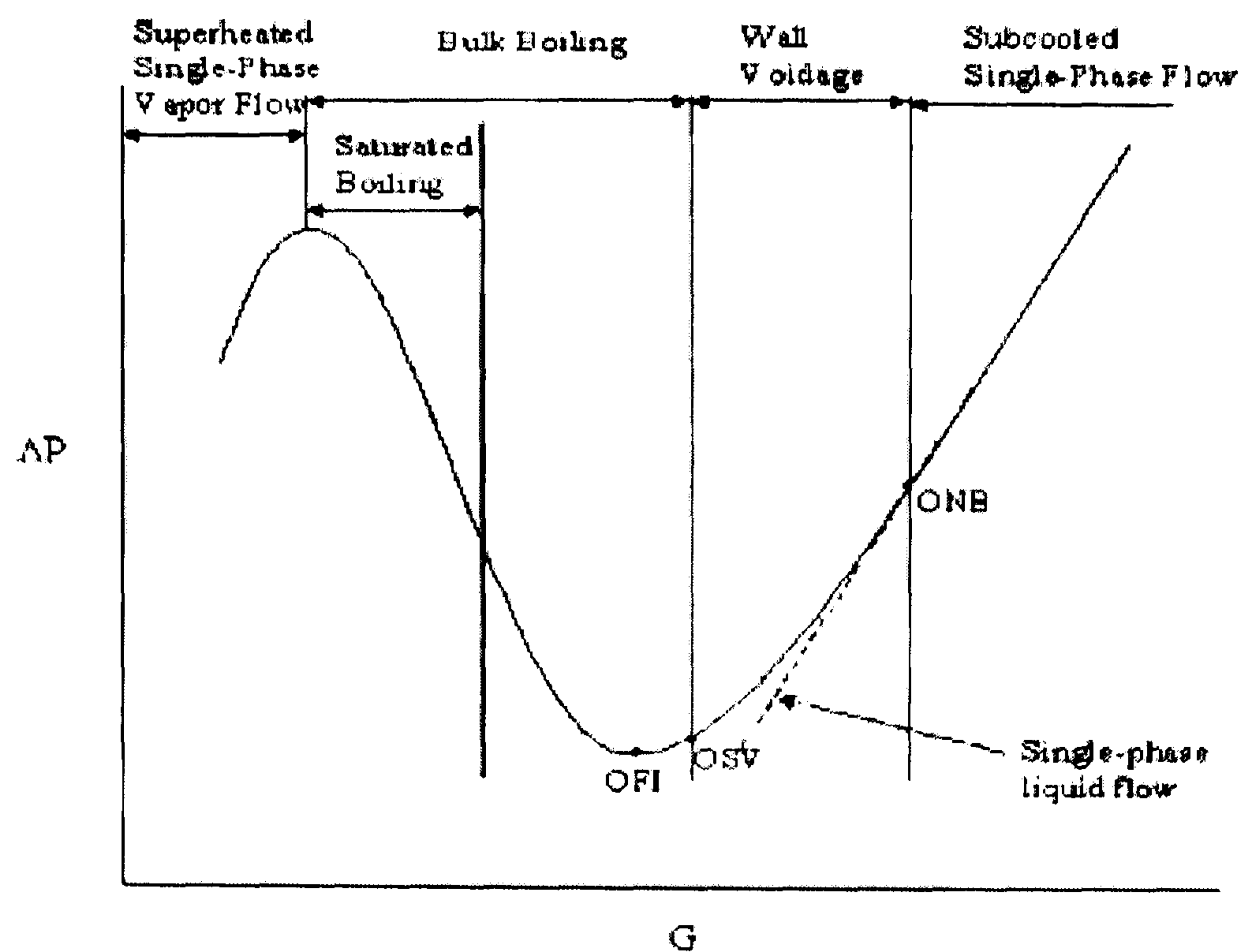


Figure 3.12 Pressure drop versus mass flux characteristic curve for a uniformly heated channel, (Ghiaasiaan and Chedester, 2002).

Qu and Mudawar (2002) studied boiling incipience in microchannel heat sinks. They measured the incipient boiling heat flux for microchannels of 231 μm wide and 713 μm deep ($\sim 350 \mu\text{m}$ hydraulic diameter). Their visualization confirmed incipience of boiling in microchannels is different with that of conventional channels. For low inlet velocity, the bubble detachment size was in the order of magnitude of the channel size and decreased with increasing inlet liquid velocity. Drag force due to bulk fluid flow and surface tension force was found to control bubble departure size. They proposed a mechanistic numerical model for bubble departure, which was based on force balance on the detaching bubble and thermal conditions (i.e. bubble can only detach, if the liquid temperature near the lowest temperature point along the bubble interface is at least equal to the saturation temperature). This theory was adopted from the classical bubble detachment theory.

Numerical calculation of the velocity and temperature field along the channel near the exit (where they observed small number of nucleation sites) was also carried out to analyse the hydrodynamic and thermal conditions for bubble growth and detachment. The experimental results indicated incipient boiling heat flux increased with increasing inlet velocity and decreasing inlet temperature. On the other hand, Peng and Wang (1994) stated that liquid velocity and subcooling did not to influence the fully developed nucleate boiling. However, they observed little effect on initiating nucleate boiling, i.e. high inlet degree of subcooling seemed to promote the increase of the effect of the inlet velocity in suppressing the onset of nucleated boiling.

Yen et al. (2003) studied flow boiling in R123 and FC-72 in tubes with internal diameter of 0.19 and 0.51 mm and reported that degree of wall superheat as high as 100 K was required to initiate boiling, see figure 3.13. Initially they stated the superheat was observed to depend on the mass flux and Boiling number, i.e. as the mass flux increased the critical Boiling number required for onset of boiling decreased. However, when they compared their results with Brereton et al. (1998) correlation, they considered only the maximum value for each tube size, as shown in Figure 3.13 (b). Finally, they concluded that the wall superheat required for onset of boiling should only depend on tube size and cavity distribution on the tube wall. The reason for the fact that the superheat required increased as the tube diameter decreased was attributed to the number of active site distribution, i.e. the number of nucleation sites became limited as the tube diameter decreased due to confined space limits.

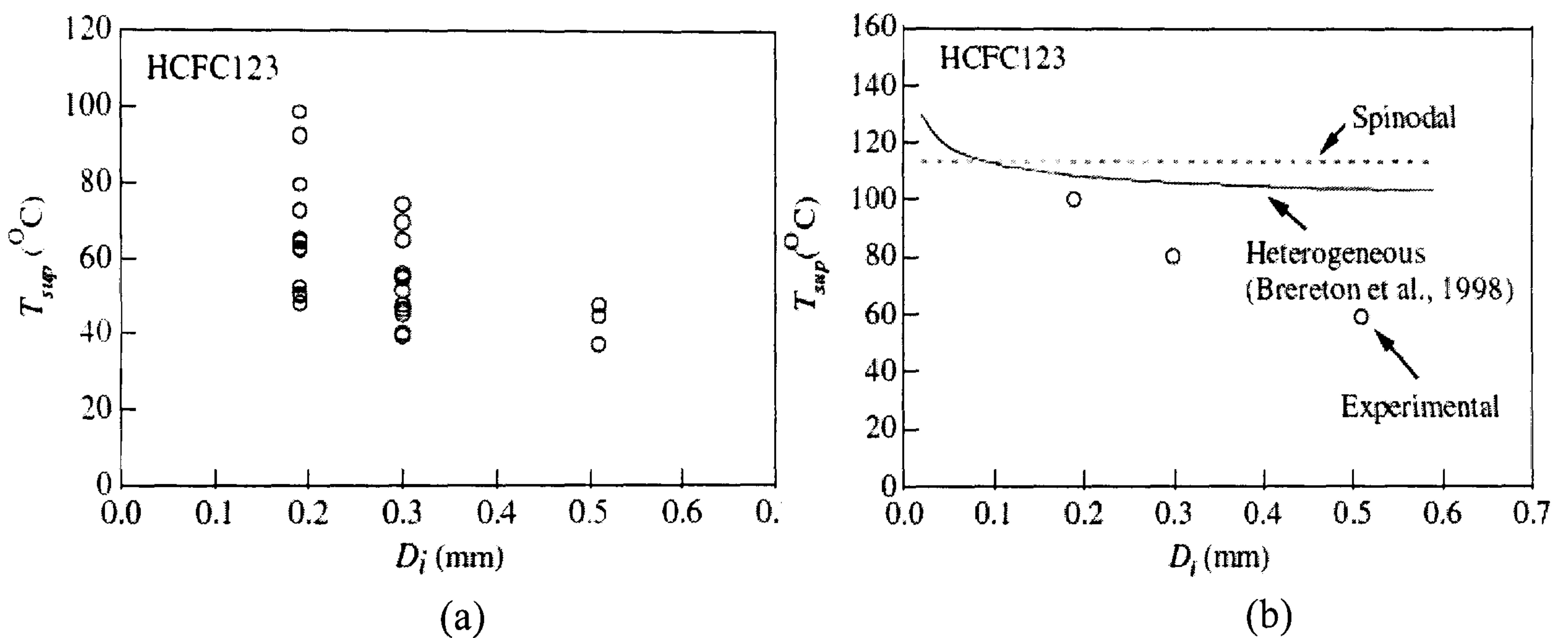


Figure 3.13 Degree of wall superheat with tube diameter, (a) experimental value varying with different mass flux and heat flux at each tube size, (b) comparison with correlation taking only the maximum value for each tube, Yen et al. (2003).

Li and Cheng (2004) investigated the effect of channel size, mass flow rate and heat flux on boiling incipience during water flow in silicon microchannels. They studied the effect of contact angle, dissolved gas and pre-existing active nucleation sites on bubble nucleation based on the model by Hsu (1962) for boiling incipience and laminar convection heat transfer. Their result indicated existence of dissolved gasses, large contact angle, and microcavities with trapped residual gasses could significantly lower the wall superheat required for initiating nucleation even in very small size channels. Also, large flow rate was found to suppress bubble generation in microchannels.

Lee et al. (2004) investigated experimentally bubble dynamics of water in a single silicon microchannel of 41.3 μm hydraulic diameter. They compared their data for ONB with the boiling incipience heat flux proposed by Hino and Ueda (1985) given in Eq. (3.20)

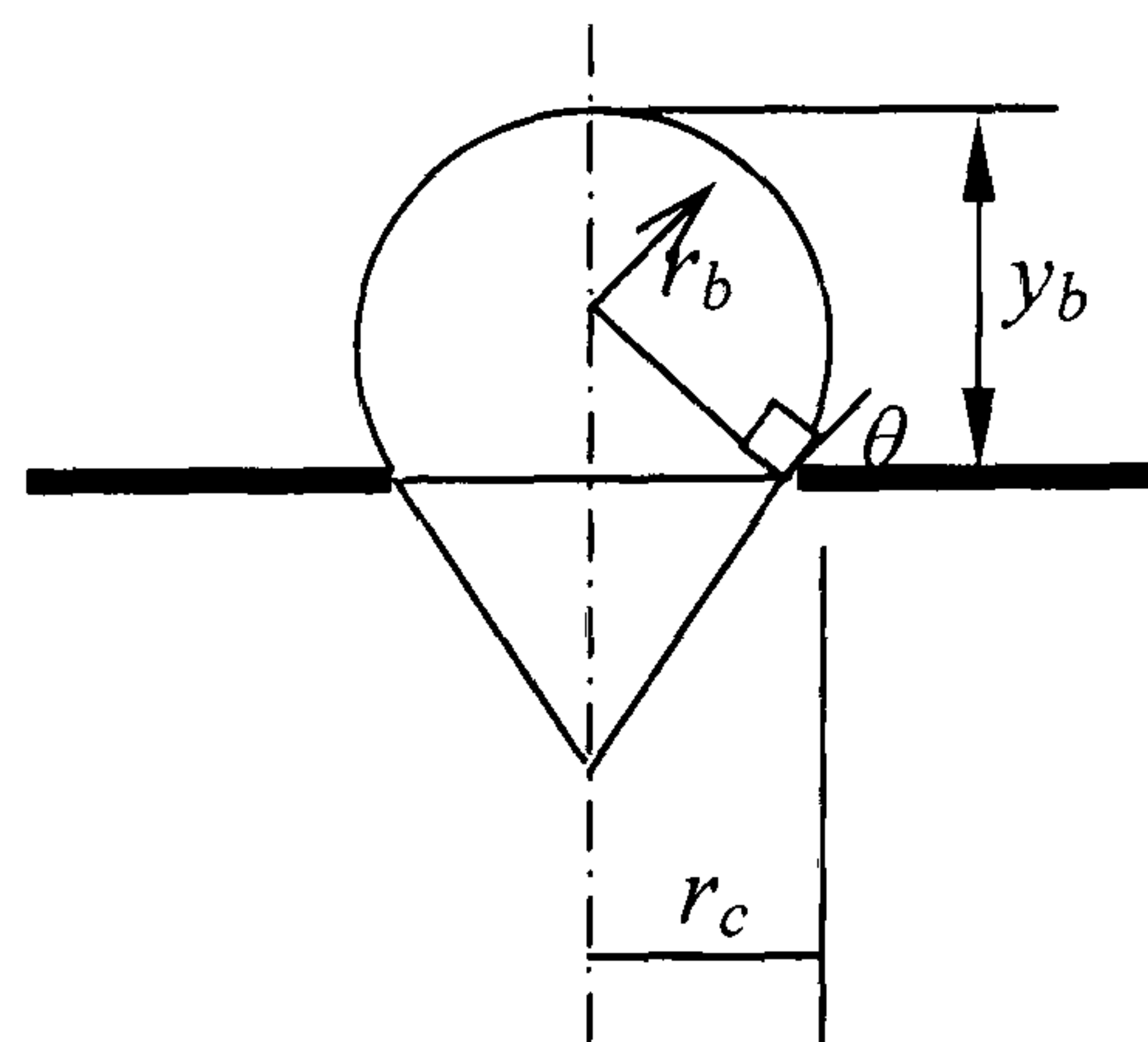
$$q_{ONB} = \frac{\lambda_l}{r_{c,max}} \Delta T_{sat,ONB} - \frac{2\sigma \lambda_l T_{sat} \nu_{lg}}{h_{lg} r_{c,max}^2} \quad (3.20)$$

where, the maximum cavity radius was assumed to be much smaller than that given by Collier and Thome (1994) critical radius relation (Eq. 3.21)

$$r_{c,crit} = \left(\frac{2\sigma \lambda_l T_{sat} \nu_{lg}}{h_{lg} q_{ONB}} \right)^{1/2} \quad (3.21)$$

They used Eq. (3.20) to evaluate the cavity radius based on measured heat flux and wall superheat. The results agreed approximately with the maximum roughness measured on the side walls.

Liu et al. (2005) used a high speed visualization to identify the onset of nucleate boiling in a microchannel 275 μm wide by 630 μm deep. They also developed an analytical model to predict the onset of nucleate boiling and studied the effect of various parameters (flow rate, exit pressure, channel aspect ratio) on the incipient heat flux. Their model was based on the theory of Davis and Anderson (1966), and assumed truncated sphere for bubble nucleus, which does not affect the temperature distribution of the surrounding liquid. The superheat equation was given as:



$$T_g - T_{sat} = T_g \frac{2\sigma C}{\rho_g h_{lg} y_b} \quad (3.22)$$

Or

$$T_g = T_{sat} \left/ \left(1 - \frac{2\sigma C}{\rho_g h_{lg} y_b} \right) \right. \quad (3.23)$$

where $C = 1 + \cos \theta$

A linear liquid temperature profile assumption near the wall provided the fluid temperature to be evaluated as

$$T_l(y) = T_w - \frac{q y}{\lambda_l} \quad (3.24)$$

ONB could occur when $T_l \geq T_g$, at the tip of the bubble nucleus (the lowest temperature across the bubble interface). Therefore, considering at least ($T_l = T_g$) for ONB and solving the quadratic equation for y_b , the superheat criterion was given as:

$$T_w - T_{sat} = \frac{2 \sigma C}{\rho_g h_{lg}} \frac{q}{\lambda_l} + 2 \sqrt{T_{sat}} \sqrt{\frac{2 \sigma C}{\rho_g h_{lg}} \frac{q}{\lambda_l}} \quad (3.25)$$

Varying the contact angle θ in the above relation showed a weak effect on the incipient heat flux. The active radius range was highly dependent on wall temperature. They also found increasing flow rate, exit pressure and microchannel height produced higher incipient heat flux, where as increasing the fluid inlet temperature and microchannel width resulted in a lower incipient heat flux.

Kandlikar (2006) commented on streamlines and stagnation on upstream of a truncated spherical bubble attached to a cavity at a given contact angle. The investigation was made by Kandlikar et al. 1997 (*cited in Kandlikar 2006*). Considering the stagnation point liquid temperature as a condition for nucleation incipience, they derived a range of active cavity radius as,

$$\{r_{c,min}, r_{c,max}\} = \frac{\delta_t \sin \theta_r}{2.2} \left(\frac{\Delta T_{sat}}{\Delta T_{sat} + \Delta T_{sub}} \right) \cdot \left[1 \pm \sqrt{1 - \frac{8.8 \sigma T_{sat} (\Delta T_{sat} + \Delta T_{sub})}{\rho_g h_{lg} \delta_t \Delta T_{sat}^2}} \right] \quad (3.26)$$

where, θ_r is receding contact angle, δ_t thermal boundary layer thickness. They reported that the location of the stagnation point from the wall surface can be given by a simple relation as $y_s = 1.10 * R_b$, where R_b is the bubble radius.

The local wall superheat at the boiling inception was given as

$$\Delta T_{sat,ONB} = \sqrt{8.8 \sigma T_{sat} q / (\rho_g h_{lg} \lambda_l)} \quad (3.29)$$

The corresponding local liquid subcooling based on the single phase heat transfer relation is written as:

$$\Delta T_{sub,ONB} = \frac{q}{\alpha} - \Delta T_{sat,ONB} \quad (3.30)$$

They indicated that ΔT_{sat} and ΔT_{sub} at ONB could be quite small for small channels due to the highest single phase heat transfer coefficient just before ONB. They mentioned the bulk liquid sometimes could be superheated resulting in rapid bubble growth.

3.4.2 Heat transfer characteristics and mechanisms

Heat transfer mechanisms proposed by different experimental studies are broadly discussed here. The effect of various parameters: heat flux, mass flux, vapour quality and pressure on the experimental heat transfer coefficient for these studies are also summarised in a table at the end of the section. Among one of the first reports of boiling in small diameter tubes was that of Lazarek and Black (1982). They measured the local heat transfer coefficient for flow boiling of R113 in a vertical tube with an internal diameter of 3.15 mm and heated length 126 mm. They used the direct electric heating method. The experimental parameters covered a range of heat flux 14-380 kW/m², mass flux 125-750 kg/m²s and pressure 1.3-4.1 bar. The fluid inlet condition was highly subcooled (~35 K). The local heat transfer coefficient was observed to increase with heat flux for both the subcooled and the saturated boiling regime. The saturated flow boiling heat transfer coefficient was independent of quality. Relating these with the knowledge of macroscale heat transfer characteristics, they suggested that nucleate boiling was the dominant heat transfer mechanism. Using the same fluid and method of heating in a small horizontal tube with diameter of 2.92 mm, Wambsganss et al. (1993) measured the local heat transfer coefficient for a range of heat flux 8.8 -90.75 kW/m², mass flux 50-300 kg/m²s, exit saturation pressure 1.24-1.60 bar and exit quality 0-0.9. The test section was stainless steel tube with a heated length of 368 mm (more than double that used by Lazarek and Black). Again, the heat transfer coefficient was mostly dependent on heat flux, and weakly dependent on mass quality, Fig 3.14. However, there was no effect of heat flux on the coefficient at their lowest mass flux (50 kg/m²s). It is worth to note that at this mass flux, the flow was laminar (Re ≈ 360). The heat flux effect became significant as the mass flux increased. They superimposed the flow pattern transition lines, obtained for air-water flow in tubes with diameter of 3 mm from Damianides and Westwater (1988), with local heat transfer coefficient versus local quality plots. Although the flow pattern transition lines were developed originally for adiabatic flow of different thermo-physical properties (surface tension), the dominant

flow regime was deduced to be the slug flow up to a quality of 0.6-0.8. In addition, the wave flow observed at low mass flux developed into annular flow as the mass flux increased. Based on this and the effect of heat flux, nucleate boiling was assumed to dominate the heat transfer mechanism.

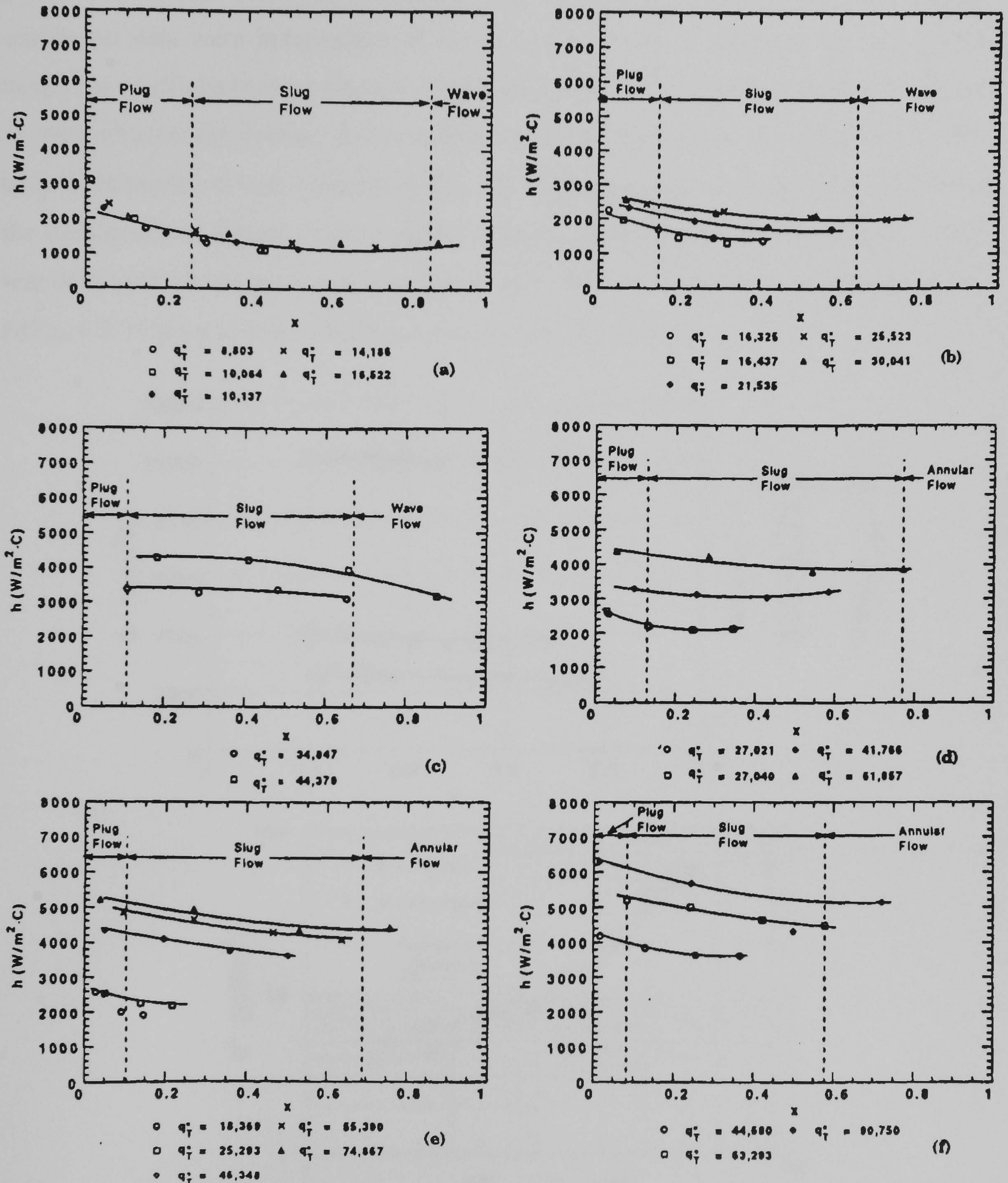


Figure 3.14 Heat transfer coefficients versus quality for various heat flux (q''_T , W/m²) at constant mass flux of: (a) $G = 50$ kg/m²s, (b) $G = 100$ kg/m²s, (c) $G = 150$ kg/m²s, (d) $G = 200$ kg/m²s, (e) $G = 242$ kg/m²s, (f) $G = 300$ kg/m²s, Wambsganss et al. (1993).

Later, Tran et al. 1996 using the same facility conducted boiling experiment in circular and rectangular channels with diameters of 2.46 and hydraulic diameters of 2.40 mm, respectively. The fluid was R12. The local heat transfer coefficient was reported for a range of parameters: heat flux $7.5 - 59.4 \text{ kW/m}^2$, mass flux $44-700 \text{ kg/m}^2\text{s}$ and a pressure 8.25 bar . The results showed that for quality $x \geq 0.2$, the heat transfer coefficient data were independent of quality up to $x \sim 0.8$, see figure 3.15 (a). In this range, the coefficients were strongly dependent on heat flux. Again, there was no effect of mass flux on the average heat transfer coefficient for a mass flux range 44 to $700 \text{ kg/m}^2\text{s}$. However, at wall superheat ($\Delta T_{sup} < 2.75 \text{ K}$), they observed a mass flux effect on the boiling curve, figure 3.15 (b). Based on their analysis, they stated nucleate boiling was dominant for the quality range of $(0.2 - 0.8)$, while in the low wall superheat region ($\Delta T_{sup} < 2.75 \text{ K}$) was dominated by convective boiling process.

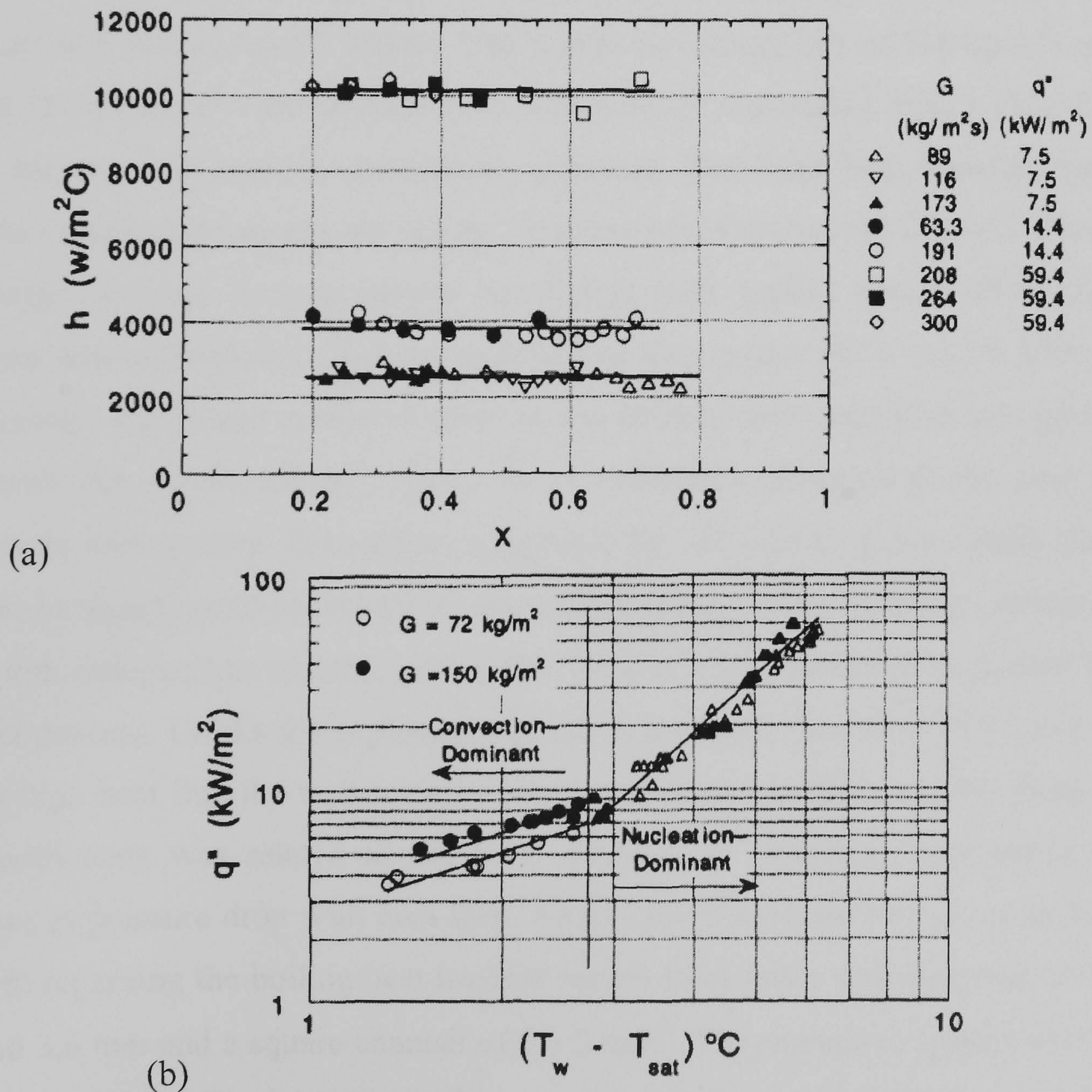


Figure 3.15 Experimental data for the circular tube (2.46 mm): (a) local heat transfer coefficient for various combination of mass flux at three constant values of heart flux and $\Delta T_{sup} > 2.75 \text{ K}$, $P = 8.25 \text{ bar}$, (b) boiling curve showing convection dominant heat transfer at low wall superheat $\Delta T_{sup} < 2.75 \text{ K}$, Tran et al. (1996).

Kew and Cornwell (1997) studied flow boiling heat transfer in small single tubes with diameter of 1.39, 2.87 and 3.69 mm using R141b. The test section was 500 mm long and heated using direct electric heating (DC). The results of their measurement showed, for the 3.69 and 2.87 mm tubes, the heat transfer coefficient increased with heat flux up to a quality of $x \sim 0.20$ and $x \sim 0.15$, respectively. Beyond these quality limits, the coefficients increased monotonically with quality and were independent of heat flux. The trends were reported to be similar to those observed in conventional tubes. However, different trends were observed in the smaller tube of 1.39 mm. At higher mass flux, the heat transfer coefficient decreased sharply with quality. They inferred temporary local dryout of the wall during confined bubble flow and annular-slug flow regimes from temperature measurements. This was assumed to be the reason for the rapid fall in the heat transfer coefficient. Lin et al. (2001a) investigated the two phase heat transfer in a 1.1 mm diameter vertical tube using a similar experimental facility (same fluid and test section heated length). The results for a mass flux of 510 kg/m²s and heat flux of 18-72 kW/m² were reported. The inlet pressure was varied from 1.35 to 2.20 bar, while the exit was kept at atmospheric pressure. The local heat transfer coefficient showed varying dependence on quality. At lower heat flux ($q \leq 42$ kW/m²), there was a monotonic increase in heat transfer coefficient with quality after a short region of decrease near zero quality. At intermediate heat flux values ($42 \leq q \leq 53$ kW/m²), the heat transfer coefficient remained more or less uniform after a peak at low quality. For high heat flux ($q > 59$ kW/m²), there was a monotonic decrease in the heat transfer coefficient with quality. The authors suggested that the results at low quality (heat flux dependent region) were dominated by nucleate boiling process. Whereas, at high quality (heat flux independent region), convective boiling was considered to govern the heat transfer process. Unlike the explanation given in Kew and Cornwell (1997) and the fact that at high heat flux the wall temperature was observed to fluctuate, the sharp drop in the coefficients was related to the axial decrease in saturation temperature due to increase in pressure drop with heat flux. An extensive analysis was given on Lin et al. (2001b) regarding the boiling heat transfer results from tubes with diameter of 1.1, 1.8, 2.8 and 3.6 mm and a square channel of 2×2 mm². The respective typical heat transfer plots are shown in Fig 3.16(a)–(e). Flow pattern transition lines obtained for air/R141b were superimposed with the local heat transfer coefficient plots. Based on the results, most of the saturated boiling region is dominated by annular flow regime. The confined bubble regime, which is taken as “small tube effect”, covered only very small range of

quality. They identified three boiling regions: nucleate boiling region (heat flux dependent region), convective boiling region (heat flux independent and quality dependent region) and partial dryout region (heat transfer coefficient decreased sharply with quality). According to their flow pattern transition qualities, the nucleate boiling region was assumed to cover confined bubble, slug and churn flow regimes. The decrease in heat transfer coefficient with quality in the heat flux dependent region was attributed to the increase in liquid film thickness during confined bubble flow, i.e. bubble front velocity increases due to its quick expansion. Following this region, they observed an increase in heat transfer coefficient with quality, which was related to convective boiling phenomena. Their sketch of the expected heat transfer characteristic for small tubes is shown in Fig 3.16 (f). In the region where the heat transfer coefficient increased with quality, the coefficient also increased with mass flux. Moreover, all the flow regime transition lines shifted towards lower quality with increasing mass flux. They reported dryout was influenced by confinement of bubbles and more likely to occur when confinement increased.

Kureta et al. (1998) conducted flow boiling heat transfer tests with diameters of 2 and 6 mm. The experiments were carried out at atmospheric exit pressure using water. Inlet liquid subcooling, mass velocity and heated length were varied 70 to 90 K, 100 to 10170 kg/m²s and 4.0 to 680 mm, respectively. Boiling heat transfer results for the 2 mm tube, at a mass flux of 1000 kg/m²s showed that the Nusselt number (Nu) increased rapidly with quality in the subcooled region due to the onset of subcooled boiling. In the saturated region, ($x > 0$), the Nu showed a local peak at low quality near $x = 0$ followed by a monotonic increase in Nu with quality at a much lower slope. The local peak was assumed to be caused by the stirring effect of the bubbles and the slug flow. On the other hand, the monotonic increase in Nu was attributed to forced convective evaporation effect of a thinner liquid film and higher vapour velocity. They also analysed the effect of tube diameter based on the results of the two tubes. Although, comparison of different tube sizes using Nu was not genuine as the non-dimensional parameter has a diameter term already, larger Nu was observed for the larger diameter tube. The fact that a lower Nu was obtained for the smaller tube was related to flow laminarization and suppression of two phase turbulent mixing in the nucleate boiling region. However, for the smaller tube the Reynolds number was greater than 3000 at 500 kg/m²s.

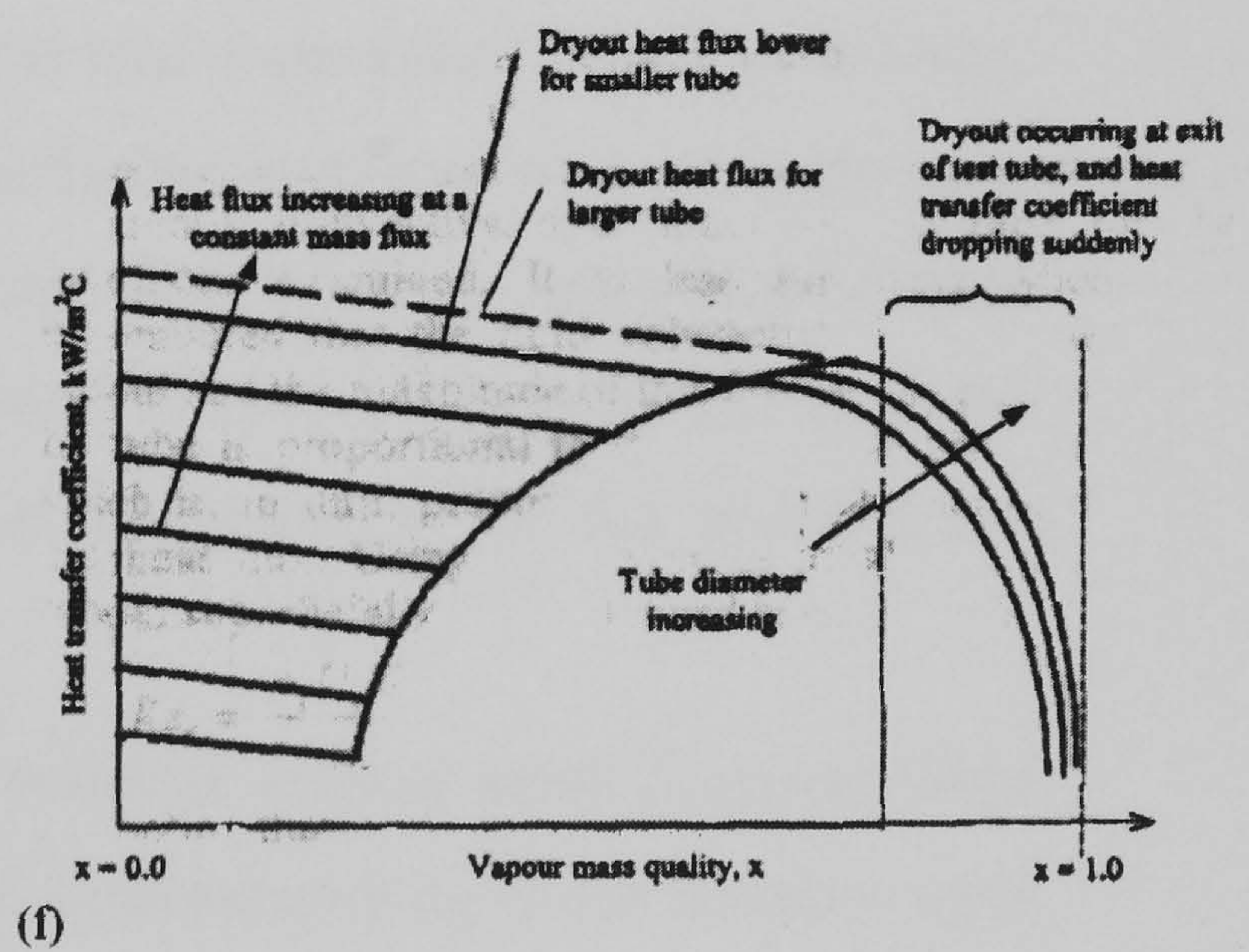
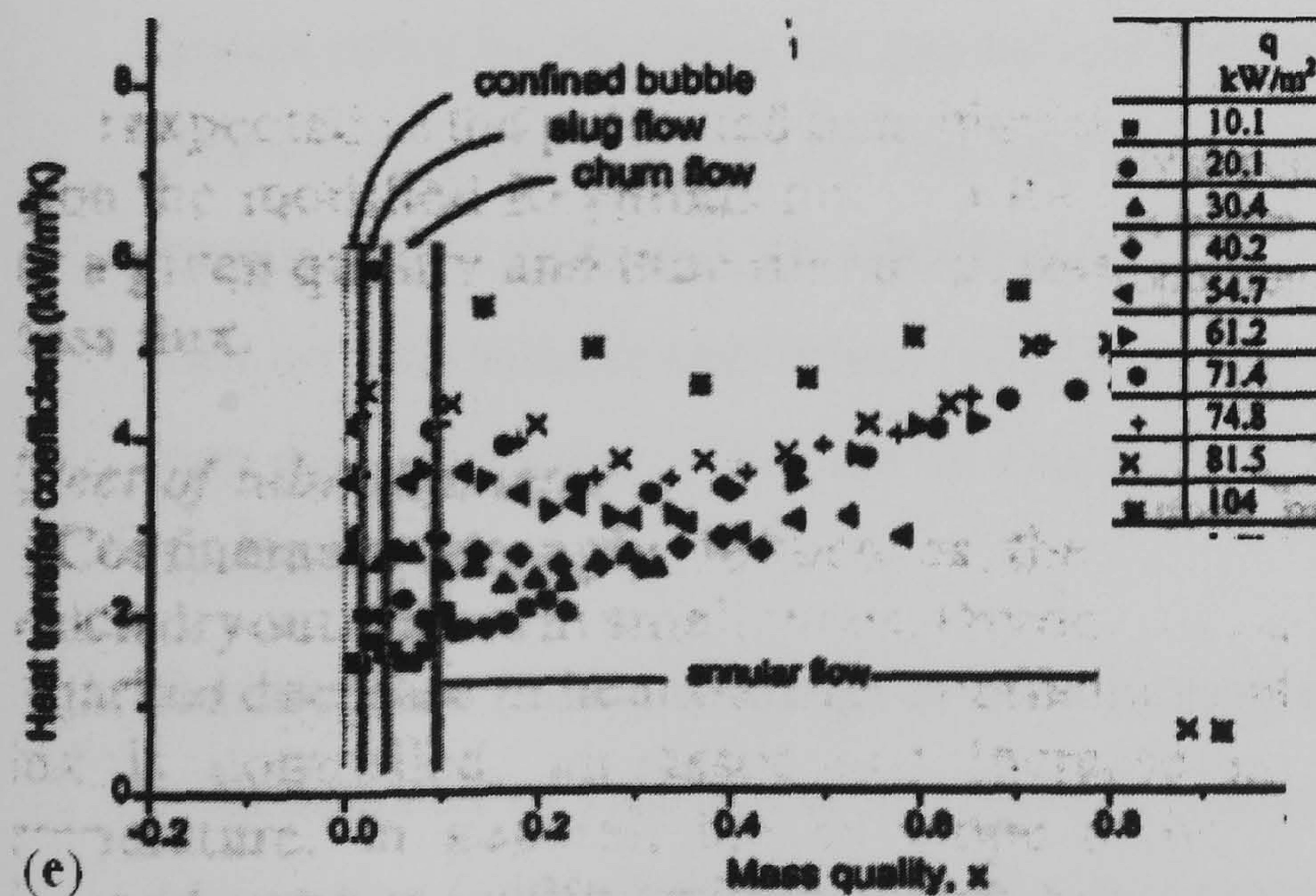
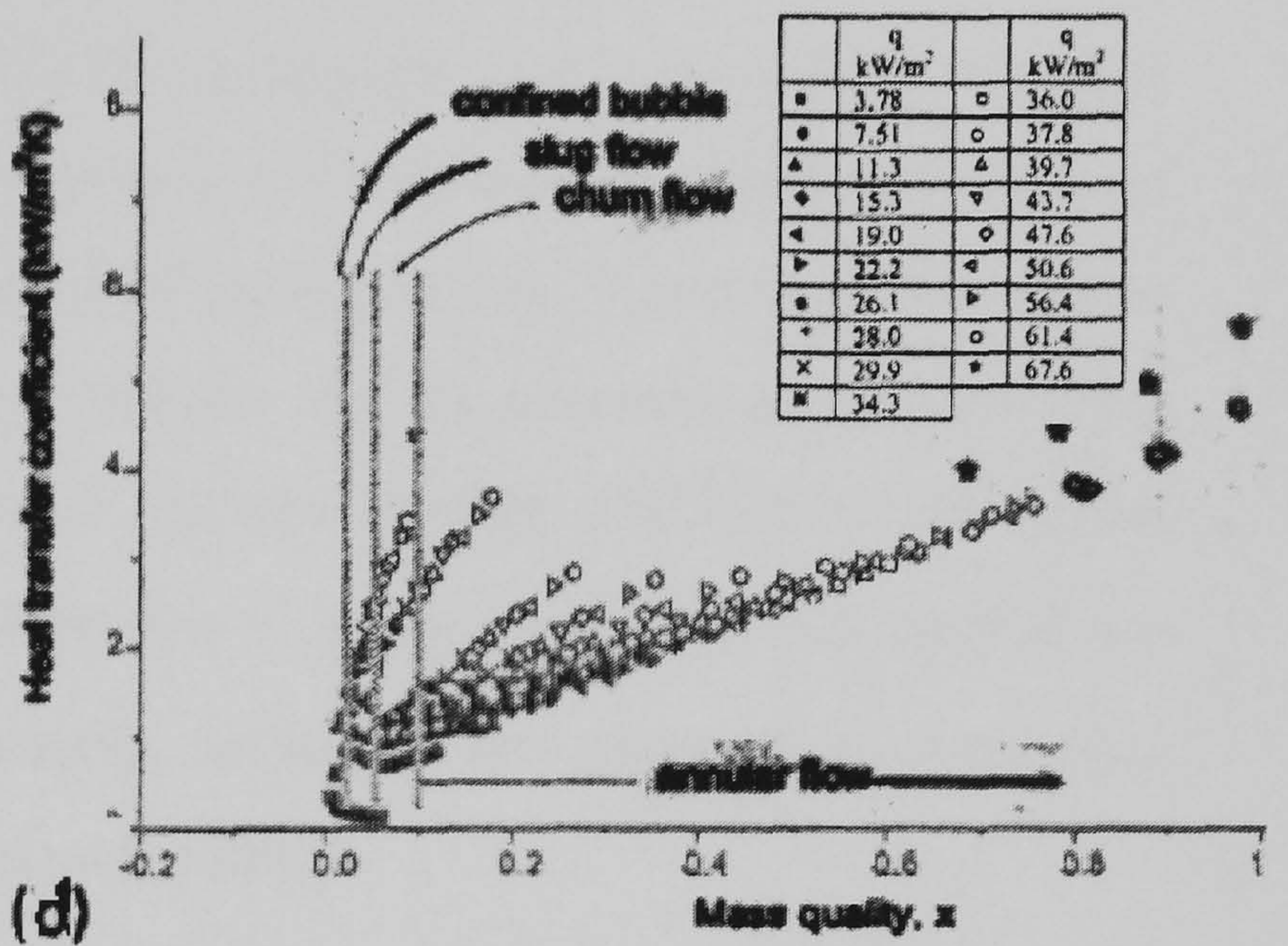
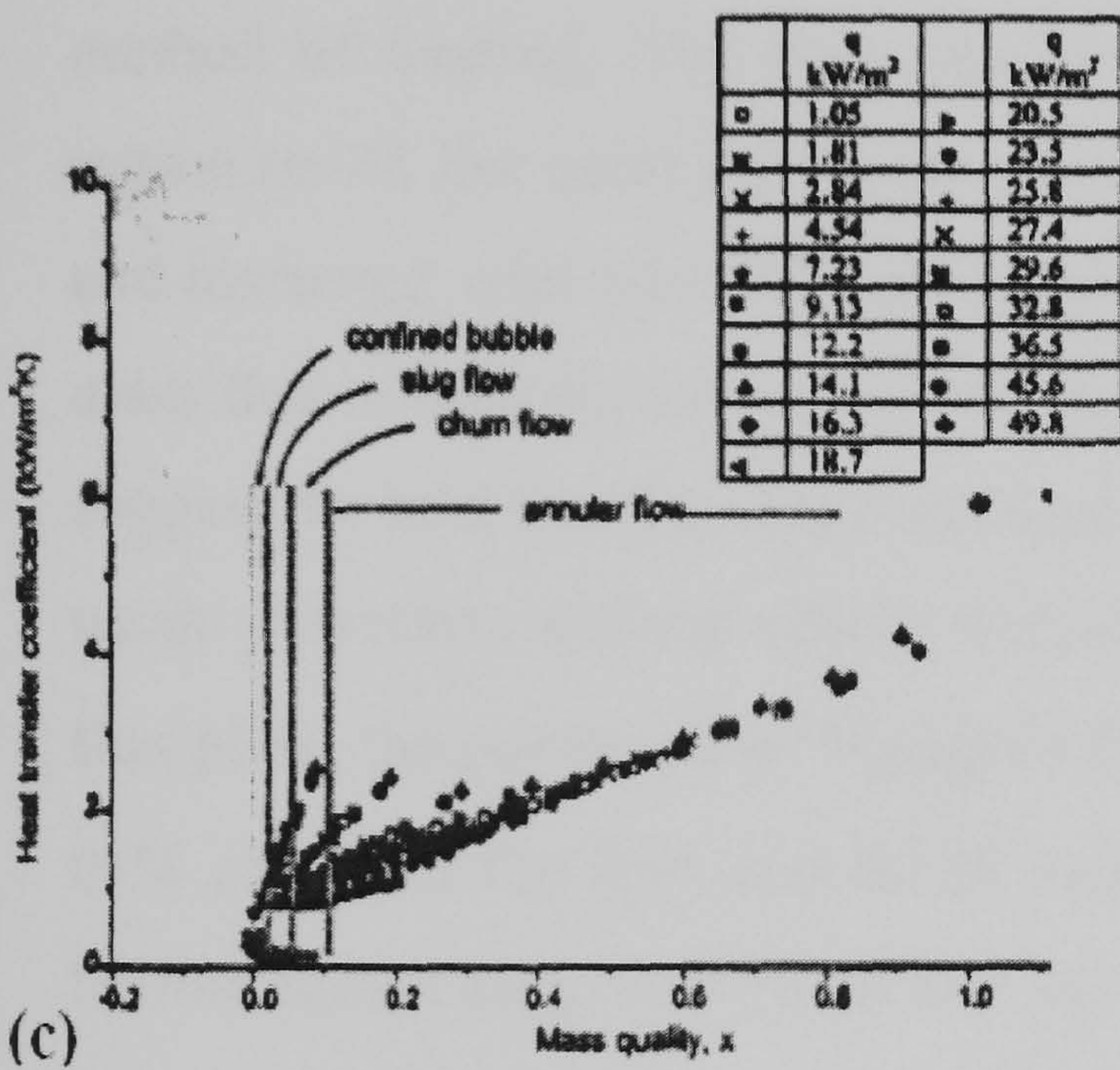
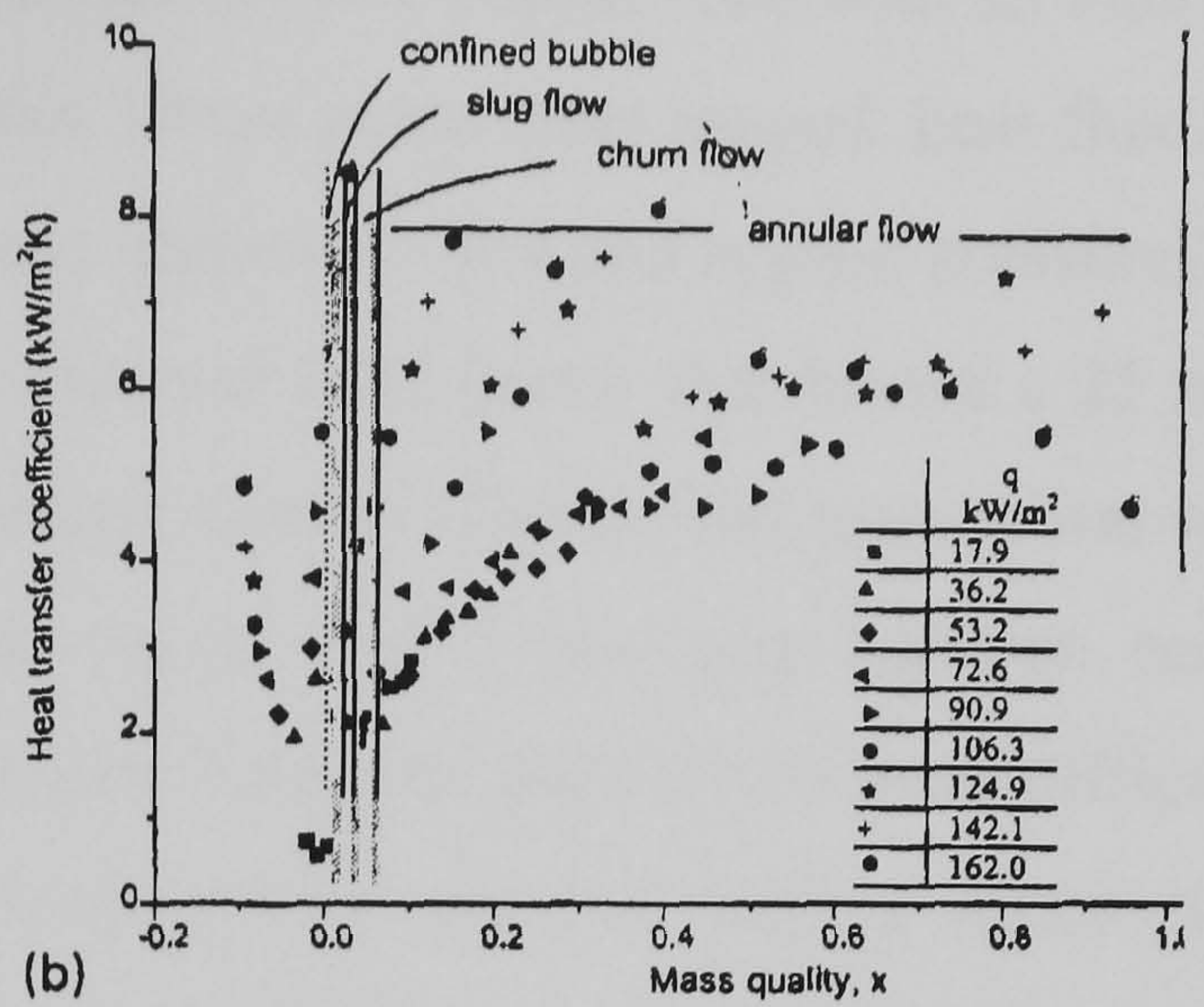
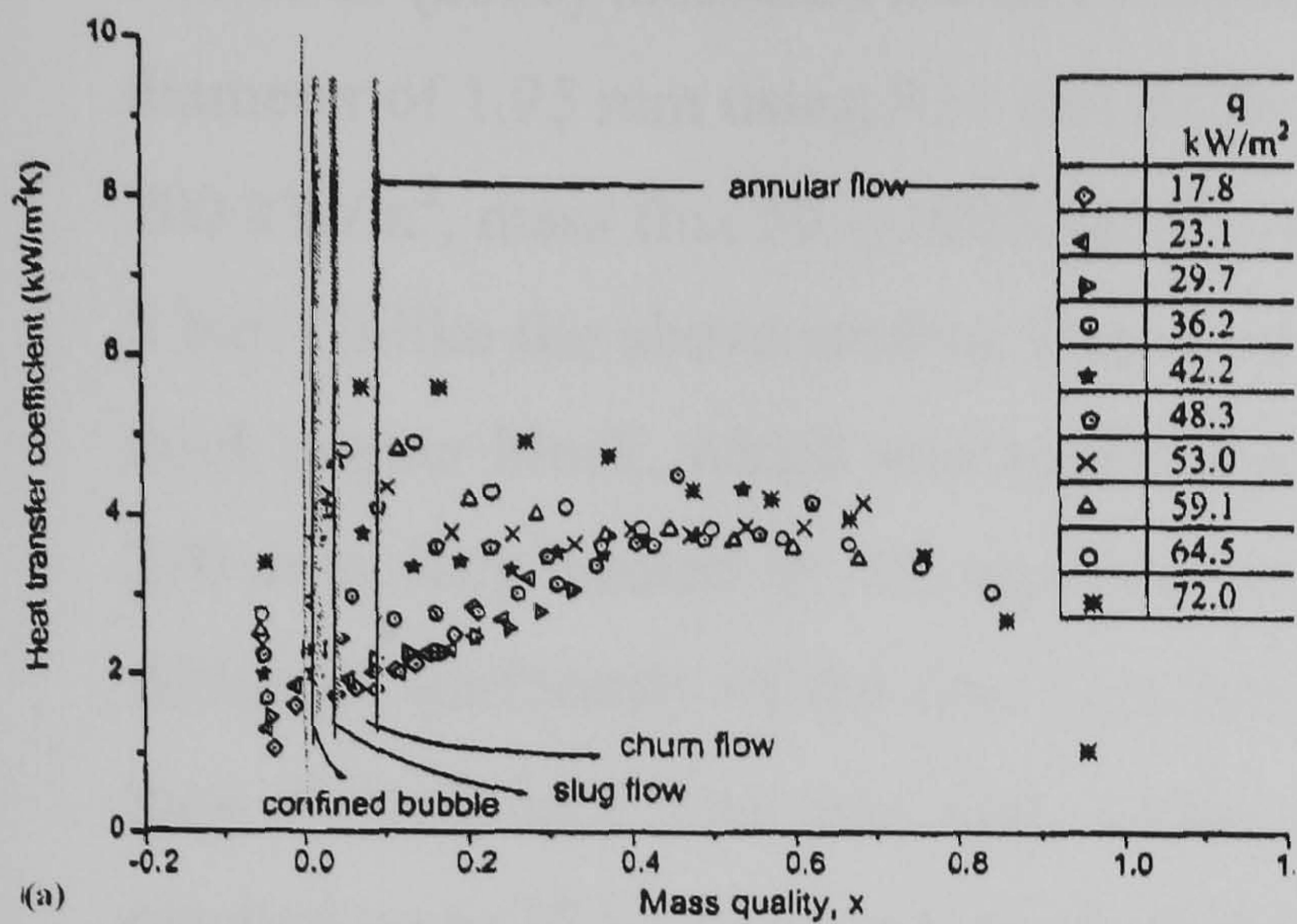


Figure 3.16 Heat transfer coefficient versus quality: (a) $d = 1.1$ mm, $G = 505$ kg/m²s, (b) $d = 1.8$ mm, $G = 570$ kg/m²s, (c) $d = 2.8$ mm, $G = 130$ kg/m²s, (d) $d = 3.6$ mm, $G = 130$ kg/m²s, (e) 2×2 mm, square tube, 342 kg/m²s, (f) generalised sketch of heat transfer coefficient vs. quality for small tubes and channels, Lin et al. (2001b).

Bao et al. (2000) measured the heat transfer coefficient in a copper tube with an internal diameter of 1.95 mm using R11 and R123 fluids. Other parameters ranged: heat flux 5 – 200 kW/m², mass flux 50 – 1800 kg/m²s, vapour quality 0 – 0.9 and system pressure 2 – 5 bar. Unlike the above studies, they used an external band heater that heated a 25 mm thick copper block, which was soldered to the test section. The heated test section was 270 mm long heated in 10 separate heating zones with 2 mm gap between each. Although uniformity of the heat flux and accurate heat loss predictions were difficult, they claimed heat loss was kept within 5 % except for the end heating zones (that reached up to 20%). However, the heat flux was reported to vary within 10 % due to the method of heating. The heat transfer coefficient increased rapidly in the subcooled region ($x < 0$). For quality ($x > 0$), the heat transfer coefficient were independent of quality and increased with heat flux and saturation pressure. There was no significant effect of mass flux in both the subcooled and the saturated boiling region. These have led them to suggest the heat transfer was controlled by a nucleate boiling dominant process and very weak convective boiling effects. Moreover, in the heat transfer coefficient versus heat flux plots, the power curve fitting of the form $h = C \cdot q^n$ resulted in an exponent of $n = 0.74$ and 0.72 for R11 and R123 respectively, falling in the range of nucleate pool boiling region suggested by Steiner and Taborek (1992).

Lee and Lee (2001) studied boiling heat transfer in rectangular channel of various aspect ratios by changing the gap between the upper and lower plates from 2 to 0.4 mm. The working fluid was R113. The heat transfer coefficient increased monotonically with quality while there was no significant effect of heat flux. However, the effect of mass flux on heat transfer coefficient (coefficient increased with mass flux) diminished as the gap size decreased. Convective evaporation was suggested to be the predominant mechanism.

Sumith et al. (2003) investigated flow boiling of water in vertical small diameter tubes with diameter of 1.45 mm at atmospheric pressure. Inlet subcooling to the stainless steel test section (with a heated length of 100 mm) was varied from 2 to 12 K. They reported heat transfer results for various mass fluxes at four different heat fluxes of (36, 101, 209 and 391 kW/m²). The heat transfer characteristics showed varying dependence on mass flux and quality at different heat flux. The gradual increase in heat transfer coefficient with quality at higher quality was attributed to the high heat transfer rate caused by forced convective evaporation thin annular liquid film. At high heat flux, the thin liquid

film evaporation dominant region was assumed to become influenced by partial dryout. Moreover, the transition lines from Triplett et al. (1999) obtained for adiabatic air-water flow with the same tube size were superimposed in the heat transfer coefficient versus superficial vapour velocity plots, Fig. 3.17. Based on this, they reported the dominant flow patterns were slug-annular and annular flow. They also suggested nucleate boiling might partially exist in the slug annular region (for superficial vapour velocity < 7 m/s) because of the fact that the large wave in the liquid film could support nucleation in the thicker part of the wave. However, the heat transfer coefficient was weakly dependent on vapour velocity beyond ($U_g > 7$ m/s), implying convective evaporation dominant effect. Also, their heat transfer coefficient versus Re plots with superimposed flow pattern transition lines indicated the coefficient increased with Re for $Re < 400$. In the range of Re from 400 to 2000, a uniform coefficient with Re was obtained mainly in the slug-annular flow region.

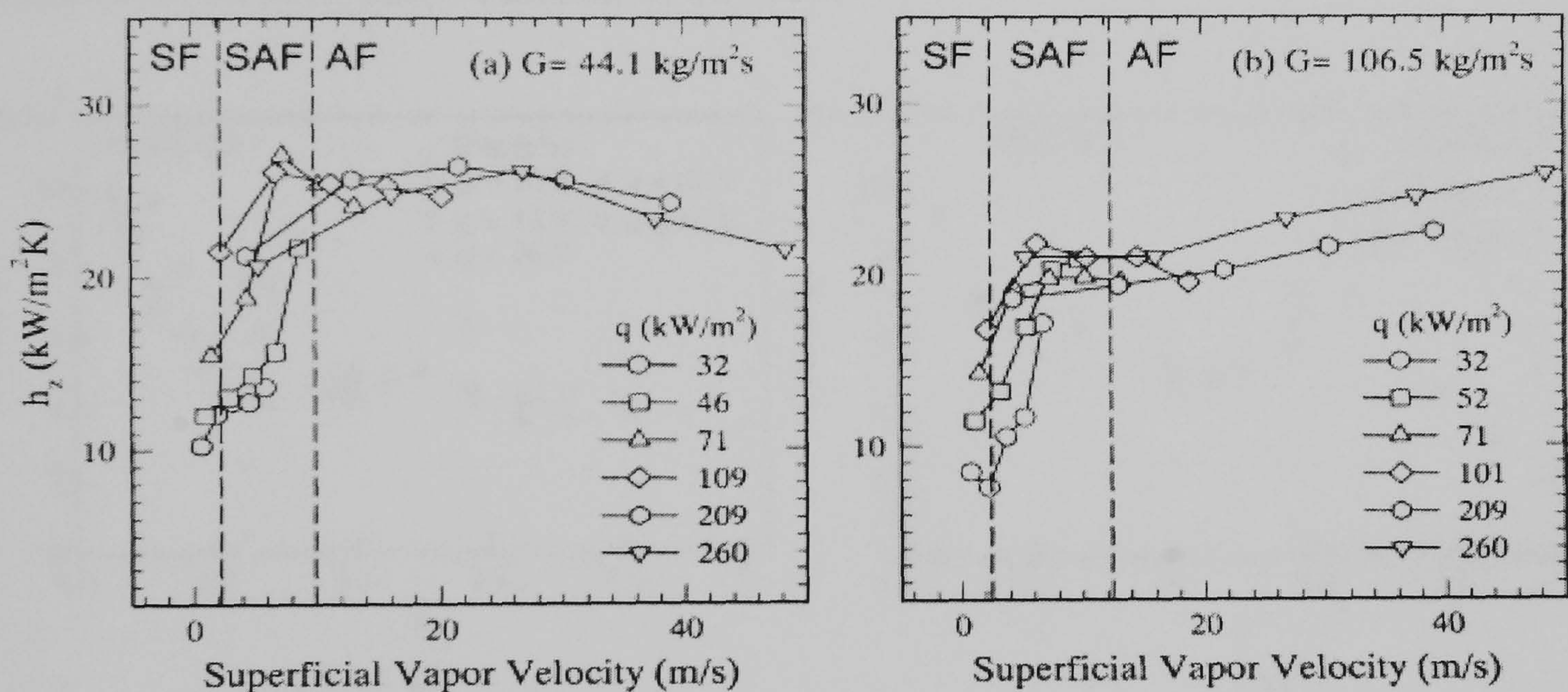


Figure 3.17 Local heat transfer coefficient versus superficial velocity and flow regime transition lines from Triplett et al. (1999) (SF: slug flow, SAF: slug-annular flow, AF: annular flow)

Yen et al. (2003) studied flow boiling in R123 and FC-72 in three very small tubes with internal diameter of 0.19, 0.3 and 0.51 mm and heated length of 280 mm at atmospheric pressure for a range of heat flux $10 - 26.9$ kW/m² and mass flux $50 - 295$ kg/m²s. They stated that the heat transfer measurements with the 0.3 mm tube were unstable due to frequent restarting of the syringe pumps. The heat transfer results of the 0.19 and 0.51 mm tube were reported and are presented in figure 3.18. The heat transfer coefficient decreased with quality at the lower quality region ($x < 0.3$) followed by a uniform coefficient beyond this limit. As seen in figure 3.17 (a), there was no clear effect of heat

flux, especially for $x > 0.3$. However, the highest heat transfer coefficient was obtained for their lowest heat flux (10 kW/m^2). In figure 3.17 (b), no obvious effect of mass flux was observed for quality less than 0.6. Nevertheless, for the lower mass flux ($145 \text{ kg/m}^2\text{s}$), there was a second decrease in heat transfer coefficient with quality (after a peak at about $x = 0.6$) towards the exit to the test section. Comparing the results of both tubes (0.51 mm and 0.19 mm), for $x < 0.3$, there was no clear effect of tube diameter. Beyond this limit, the heat transfer coefficient values for the 0.51 mm tube were higher than that of the 0.19 mm tube. They also compared their results with that of Ravigururajan, 1998 (cited in Yen et al. 2003), which was obtained for $D = 0.425 \text{ mm}$ using R124. However, they did not mention the heat flux value for Ravigururajan, (1998) study, hence it is difficult to make direct comparison. Although, the effect of different inlet geometries is not clearly understood, their experimental setup was an open loop with an inlet and outlet blocks soldered to the test sections, giving rise to sudden contraction and expansion of the flow.

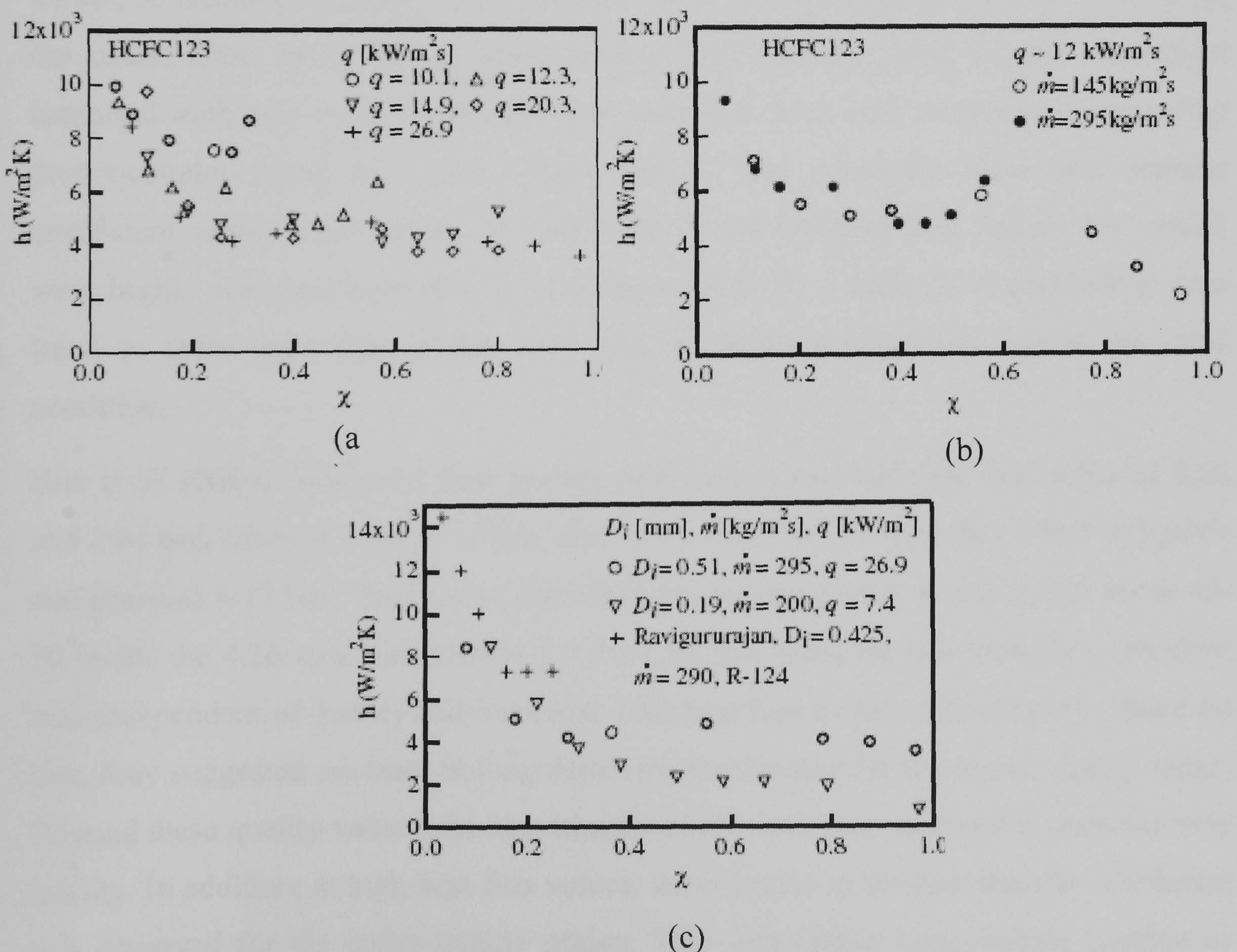


Figure 3.18 Heat transfer coefficient versus quality for the 0.51 mm tube: (a) effect of heat flux at a mass flux of $295 \text{ kg/m}^2\text{s}$, (b) effect of mass flux, and (c) comparison with the 0.19 mm tube result and Ravigururajan, 1998 cited in Yen et al. (2003).

On the other hand, Owhaib et al. (2004) studied flow boiling heat transfer in vertical narrow tubes with diameter, 1.7, 1.224 and 0.83 mm using R134a. They reported heat transfer results for a range of parameters 3 – 34 kW/m², mass flux 50 – 400 kg/m²s, saturation pressure 8.6 and 6.5 bar. The three stainless steel test section tubes had the same heated length of 220 mm (the paper also says 310 mm). Boiling curves for various mass fluxes at different tube diameter were presented. For the 1.7 mm tube, there was a scatter in the data for different mass fluxes mostly indicating an increase in the slope of the boiling curve with mass flux. On the other hand, for the 1.224 mm tube, the scatter in mass flux effect was observed only for $\Delta T_{sat} < 2$ K or $q < 12$ kW/m². There was no obvious effect of mass flux in the boiling curve for the 0.826 mm, except at high heat flux ($q > 27$ kW/m²). Also, the average heat transfer coefficient plotted with mass flux for the 1.7 mm indicated that for $G \leq 100$ kg/m²s, the coefficient decreased with mass flux (only for $q = 5$ and 10 kW/m²). Otherwise, a slight monotonic increase in average heat transfer coefficient with mass flux was obtained for other heat and mass flux values. A similar plot in the 1.224 mm showed a very weak effect of mass flux. In all the cases, there was a strong effect of heat flux (average heat transfer coefficient increased with heat flux). Although, they only had three wall temperature measuring thermocouples along the entire heated length, they presented local heat transfer coefficient versus local quality for each tube at two different heat fluxes. The results were highly scattered especially for the larger tubes. It is difficult to conclude a clear trend as there were data in the same plot of different magnitude but at the same condition.

Huo et al. (2004) conducted flow boiling of R134a in two stainless steel tubes of 4.26 and 2.01 mm tubes at a range of heat flux, 13 – 150 kW/m², mass flux 100-500 kg/m²s and pressure 8-12 bar. They found that when the vapour quality was less than about 40-50 % for the 4.26 mm and 20-30% for the 2.01 mm tube, the heat transfer coefficient was independent of quality and increased with heat flux and system pressure. Based on this, they suggested nucleate boiling dominant mechanism for the above quality range. Beyond these quality values, the heat transfer coefficient was observed to decrease with quality. In addition, at high heat flux values, the decrease in the heat transfer coefficient was observed for the entire quality region. This was related large bubble creation or crowding of bubbles resulting in suppression of nucleate boiling. From a separate flow pattern experiments using the same tubes, but at the exit of the heated section, they

reported that in the continuously decreasing heat transfer coefficient case, the flow regimes at the exit of the sections were churn and annular.

Wen et al. (2004) conducted flow boiling of water using thin walled rectangular channels of cross-section $2 \times 1 \text{ mm}^2$. This was an interesting experiment due to the fact that local pressure measurements were synchronised with high speed video recordings. They used two test-sections of different heated length, and five thermocouples were attached to the middle of the wide side (2 mm) of the channel. The results showed that the heat transfer coefficient increased with quality for $x < 0.3$. Forced convective mechanism was expected based on conventional tube interpretation. They stated that a boiling curve plotted for various mass fluxes of all their data indicated mass flux effects. There was no significant effect of subcooling and inlet compressibility on the average heat transfer coefficient. Nevertheless, strong heat flux effect made them suggest nucleate boiling dominance. They argued that the conflicting results based on the local heat transfer coefficient plots in comparison with that of boiling curves could arise from the fact that nucleate boiling might have existed for a short period. Based on the local video observations combined with wall temperature fluctuations measurements, they identified three heat transfer regimes particularly during confined bubble flow.

- Single phase convection during liquid slug flow with weak or no entrained bubbles
- Thin liquid film evaporation surrounding the confined bubble
- Vigorous nucleate boiling in the film towards the rear of the confined bubble

Time fractions of these regimes were also presented for specific cases. They also suggested that using large channel flow boiling heat transfer conditions for the interpretation of the heat transfer mechanism in microchannels could be misleading.

Saitoh et al. (2005) investigated R134a flow boiling in three horizontal tubes with diameters, 3.1, 1.12 and 0.51 mm and relatively long heated lengths of 3235, 935 and 550 mm, respectively. They measured the pressure drop and local heat transfer coefficient for range of heat flux 5 - 39 kW/m², mass flux 150 - 450 kg/m²s, saturation pressure 3.5-4.88 bar. Moreover, their system pressure was lower than other typical R134a experimental facilities (with indirect cooling and pump, e.g. Huo et al. 2004, Owhaib et al. 2004). Although, their facility was much closer to the practical application, controlling the compressor lubricant oil from mixing with the working fluid or evaluating its effect on the heat transfer and pressure drop measurements is thought

to be the main shortcoming. However, they reported that the concentration of the lubricant oil in their system was less than 0.1 wt %. The local heat transfer coefficient against vapour quality for the three tubes is shown in Fig. 3.19. Based on the results and knowledge of conventional heat transfer mechanisms, they suggested that nucleate boiling at low quality and forced convective evaporation at high quality controlled the heat transfer process. For the larger diameter tube (3.1 mm), there was no significant effect of saturation pressure on the heat transfer results. On the other hand, for the 0.51 mm tube, the heat transfer coefficient increased with saturation pressure particularly at high quality (in the region where heat transfer coefficient falls with quality). The pressure drop along the test tube was relatively large (~ 4.9 bar) due to the fact that they used quite long heated length. This caused a huge saturation temperature drop (~ 20 K) between inlet and outlet ports, which can create a significant flashing effect. Therefore, the local quality was not merely a result of the heat flux, which could have an effect on their heat transfer coefficient characteristics compared to other relatively short tube results. Unlike most other flow boiling studies (which employed indirect cooling loop and a liquid pump in the main circuit), their experimental set up was similar to a typical compression refrigeration cycle with a direct use of compressor and expansion valve (for controlling flow rate and system pressure). Consequently, they had saturated inlet conditions with vapour quality (0 to 0.2). They investigated the effect of inlet quality by plotting the heat transfer coefficient against local quality at different inlet qualities. For low inlet quality ($x_{in} < 0.03$), they observed flow instability and early dryout at relatively low local quality ($x \sim 0.5$). For inlet quality, $x_{in} \geq 0.13$, all the curves showed the same characteristics. In addition, dryout (sharp drop in heat transfer coefficient with quality) occurred late at high quality ($x \sim 0.9$) in this case.

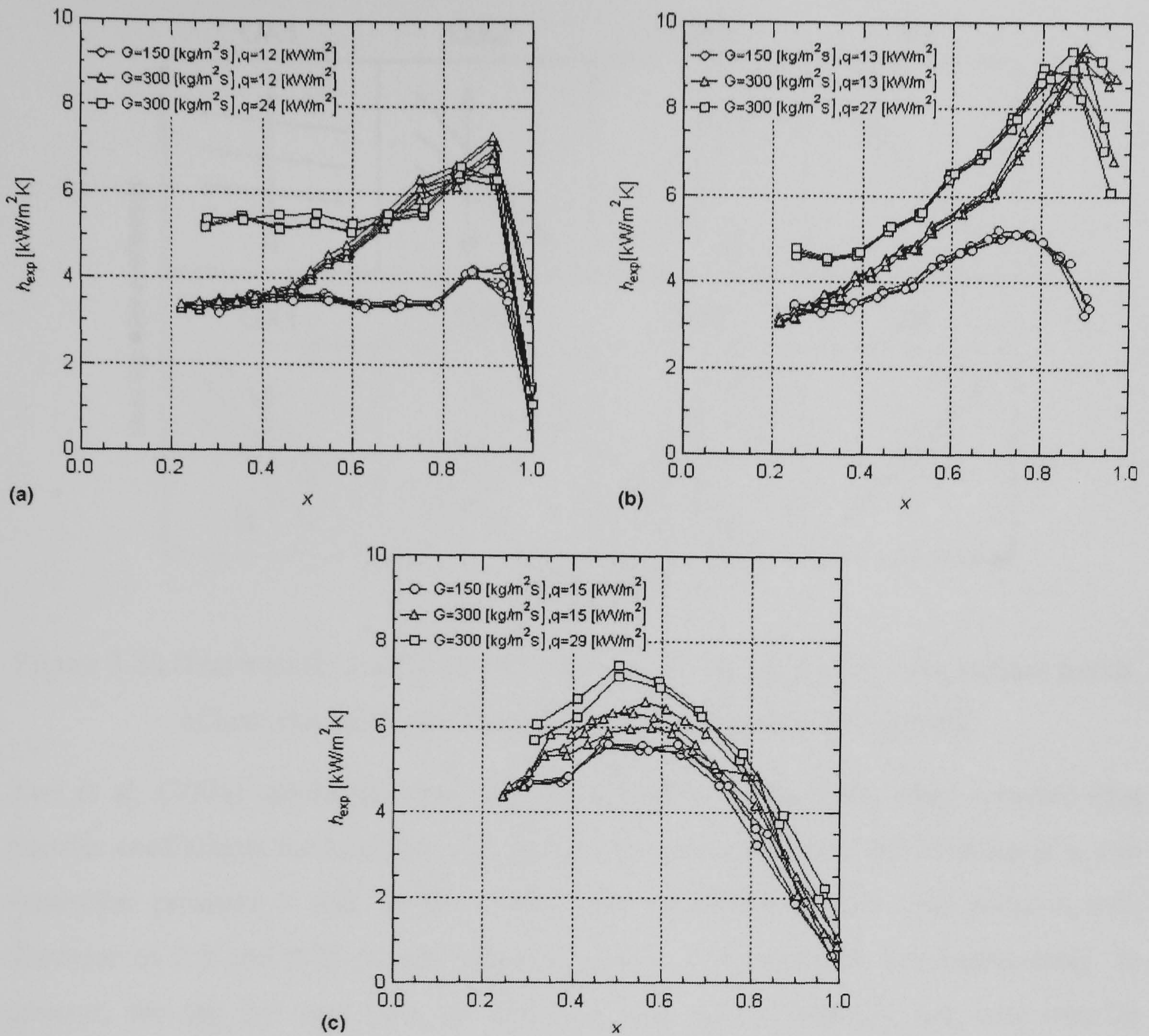


Figure 3.19 Effect of heat flux and mass flux on heat transfer coefficient for three different diameter tubes of: (a) 3.1 mm; (b) 1.12 mm and (c) 0.51 mm, Saitoh et al. (2005).

Agostini and Thome (2005) categorized the trends in the local heat transfer coefficient versus vapour quality and its relation to heat and mass flux after reviewing thirteen different studies. They noted that in most of the cases reviewed (11 out of 13), when vapour quality ($x < 0.5$), the heat transfer coefficient is almost independent or decreases with vapour quality, while it increases with heat flux. Beyond this quality range ($x > 0.5$), the heat transfer coefficient falls sharply with vapour quality and is independent of heat flux or mass flux. Figure 3.20 shows the heat transfer coefficient versus vapour quality with different trends of heat flux (QX1, QX2, and QX3), mass flux (GX1, GX2, and GX3) effects. The trend when the heat transfer coefficient does not depend on heat flux and mass flux is represented as X1 and X2.

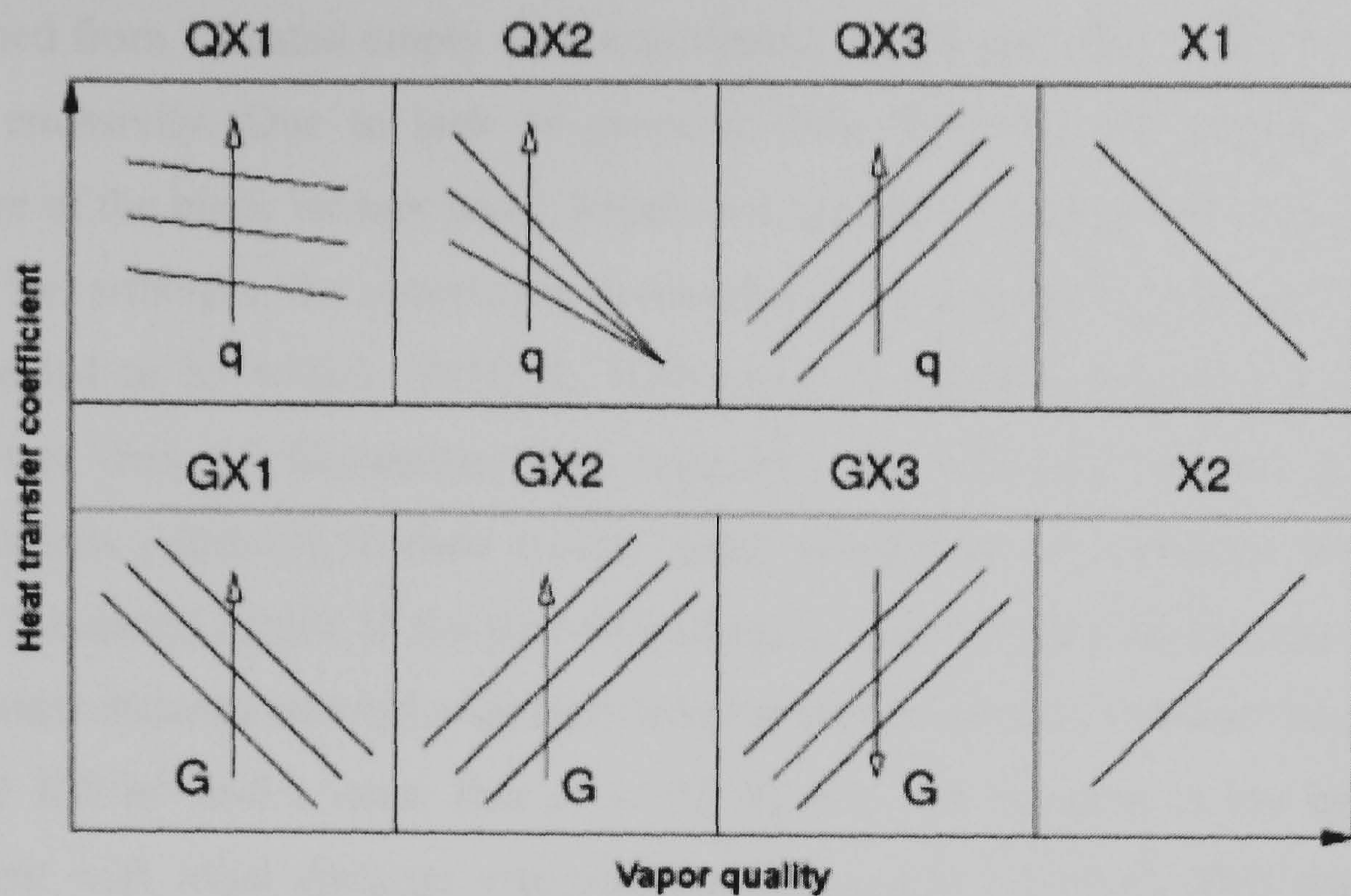
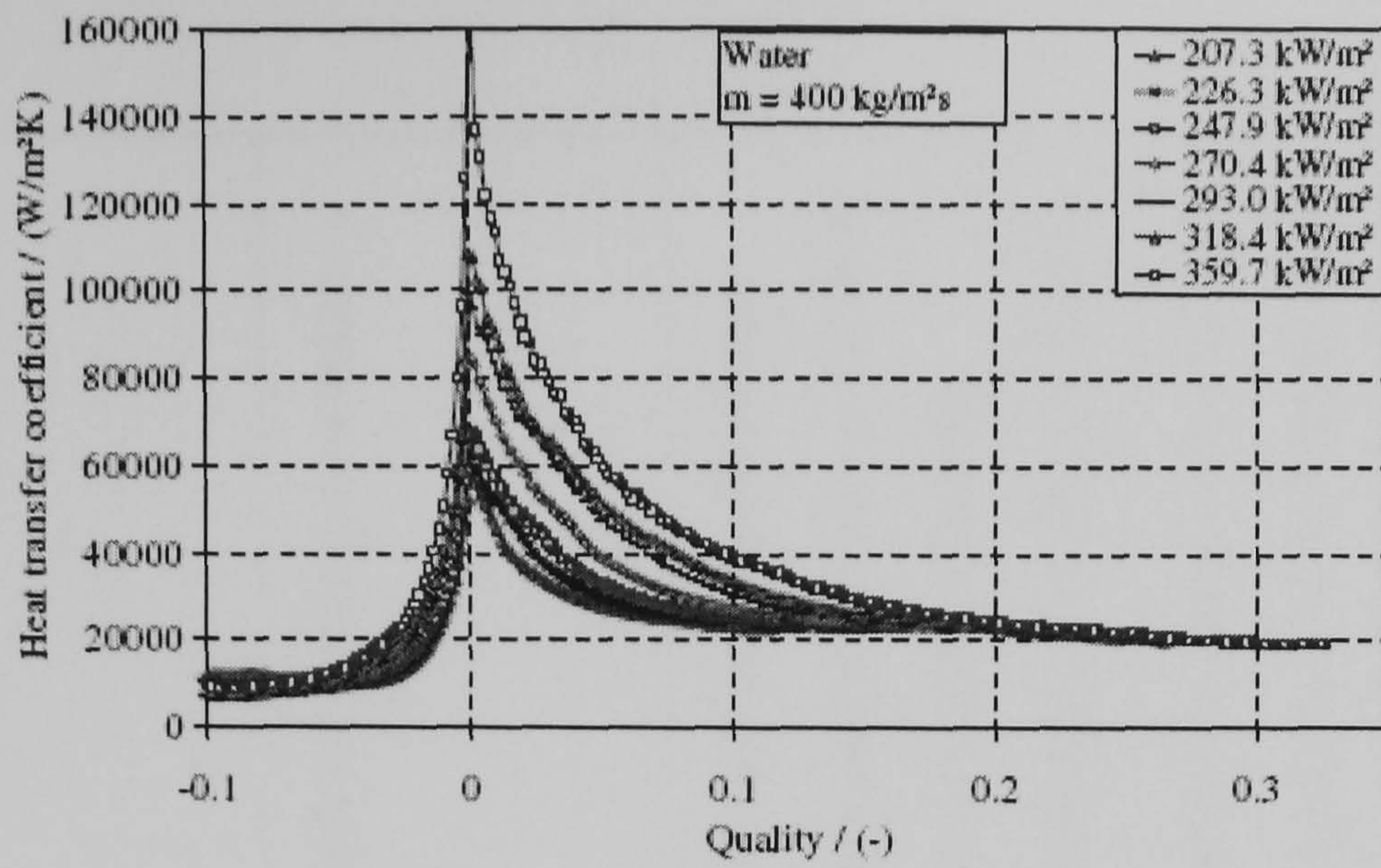


Figure 3.20 Heat transfer coefficient as a function of vapour quality with various trends of heat flux and mass flux effect, Agostini and Thome (2005).

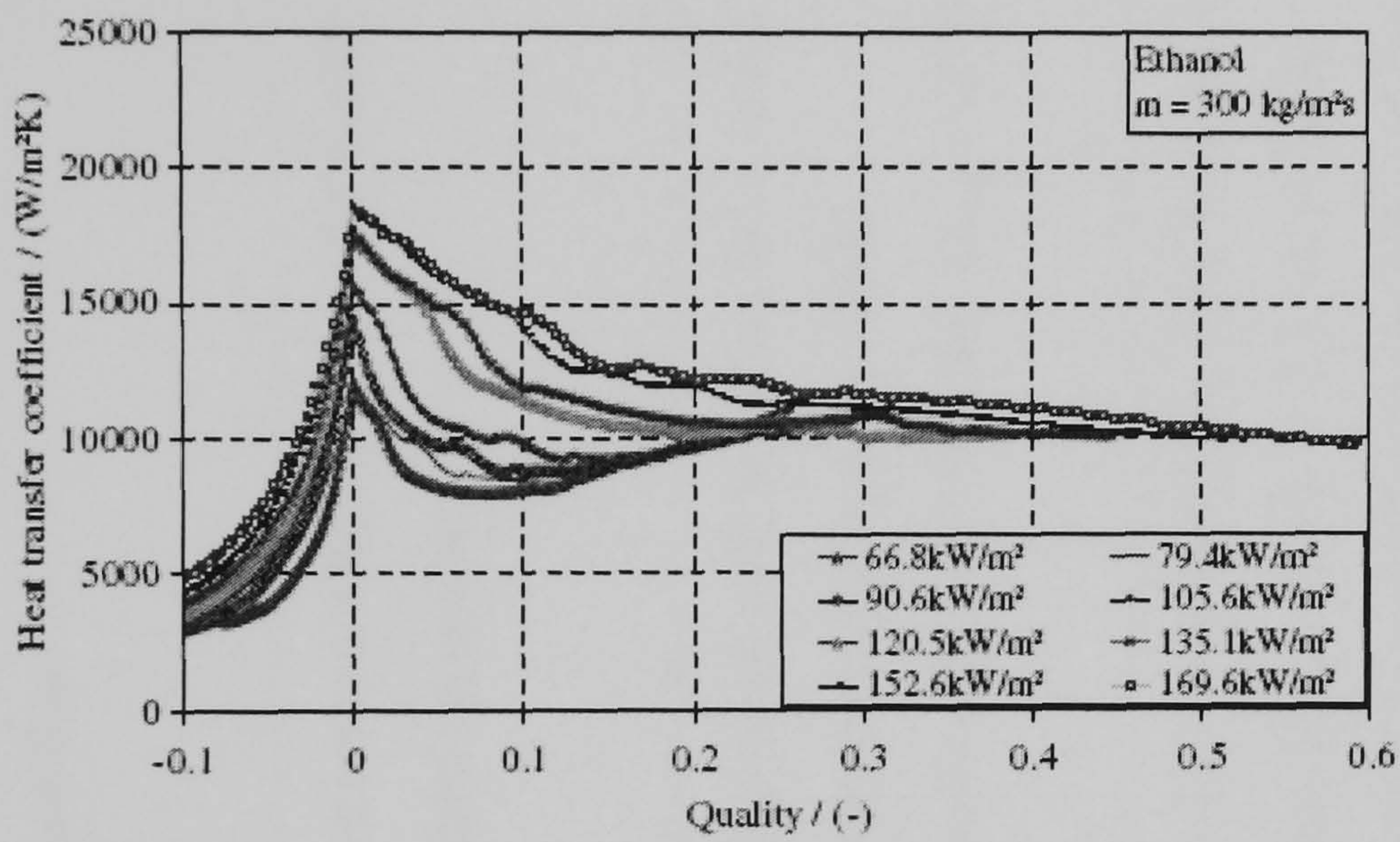
Yun et al. (2005) conducted flow boiling experiment using CO_2 . They reported heat transfer coefficients for heat flux 7 to 48 kW/m^2 , mass flux 1000 and $1500 \text{ kg/m}^2\text{s}$, and saturation pressure 5 and 10 bar. They used horizontal circular test sections with diameter of 2.0 and 0.98 m and heated length of 1200 and 400 mm respectively. In general, for the 2.5 mm tube, at low heat flux ($q \sim 7.5 \text{ kW/m}^2$), the heat transfer coefficient increased slightly with quality. At intermediate heat flux, ($q \sim 15.9 \text{ kW/m}^2$), there was a sudden fall in the heat transfer coefficient at $x \sim 0.55$. This was related to the CHF, although for heat flux $q > 15.9 \text{ kW/m}^2$ there were experimental results of similar behaviour except the quality at which heat transfer dropped shifted to lower quality value. For the range of heat flux 26.5 to 46.5 kW/m^2 , there was no significant effect of heat flux. No similar plots were presented for the 0.98 mm tube at different mass flux. However, the only result of $G = 1500 \text{ kg/m}^2\text{s}$ at two heat fluxes ($q = 20$ and 30 kW/m^2) showed a sharp fall in heat transfer coefficient at quality $x \sim 0.35$.

A few researchers have also used an infrared thermography to measure the wall temperature. Boye et al. (2007) measured flow boiling heat transfer coefficients for water inside circular tube of 1.5 mm diameter and 500 mm heated length. The test section, which was made of nickel alloy (Inconel 600), was open to the ambient with no insulation. The authors believed the heat loss through convection and radiation could be acceptable compared with the extra calibration work required if instead a transparent vacuum chamber was used (to curtail at least the convection loss). The heat loss was

determined from a heated empty tube experiment, which was also used to calibrate the surface emissivity. Due to lack of property data, they did not include conduction resistance of the black lacquer layer, which was applied to increase the emissivity of the surface. Nevertheless, the uncertainty in measuring the average heat transfer coefficient was reported to be within 10-30 %. Although, the actual scanning rate of their IR camera was only 15 frames/sec, they suggested the technique is ideal for transient measurements (claiming in their words “axial profiles can be obtained with no time delay”). Presented results of the ratio of boiling to single phase heat transfer coefficient against axial distance showed a uniform heat transfer coefficient for heat fluxes $q = 25.6$ and 35.1 kW/m^2 and a mass flux of $G=50 \text{ kg/m}^2\text{s}$. An increase in the heat transfer coefficient with axial distance was observed for $q \geq 54.5 \text{ kW/m}^2$. This was taken to indicate forced convective boiling mechanism. The magnitude of the heat transfer coefficient was significantly lower than the corresponding results of Kandlikar and Balasubramanian (2004). The drop in the heat transfer coefficient near the exit of the test section was related to measurement errors caused by radiation emitted from the electrical connection and power supply equipment. However, they did not explain why a similar phenomenon was not observed near the inlet of the test section. In a similar experimental setup, Cortina Diaz and Schmidt (2007) carried out flow boiling of water and ethanol inside a rectangular channel of $0.3 \times 12.7 \text{ mm}^2$. Unlike the results of Boye et al., the heat transfer coefficient was higher at low quality near $x=0$ and sharply fall with quality followed by a uniform value after $x=0.15$. In the heat transfer coefficient decreasing region, the coefficient increased with heat flux. However, they mentioned that these results did not agree with their previous report (Cortina Diaz et al. 2004), which was related to channel geometry effect, and the fact that the later data was limited to low quality ($x=0.3$). Time averaged heat transfer coefficient against vapour quality of their typical plot is shown in Fig. 3.21 (a) for water at $G = 400 \text{ kg/m}^2\text{s}$. On the other hand, the results of ethanol showed an increase in heat transfer coefficient with quality for relatively low heat flux (e.g. for $G = 300 \text{ kg/m}^2\text{s}$, $q \leq 152.6 \text{ kW/m}^2$), see Fig. 3.21 (b). However, there was still a drop in the heat transfer coefficient at low quality followed by an almost constant heat transfer coefficient region. They also found a similar characteristic for n-hexane (Cortina Diaz and Schmidt 2007b).



(a)



(b)

Figure 3.21 Heat transfer coefficient as a function of vapour quality: (a) Water, $G = 400 \text{ kg/m}^2\text{s}$; (b) Ethanol, $G = 300 \text{ kg/m}^2\text{s}$, Cortina Diaz and Martin (2007).

Table 3.3 provides summary of the various heat transfer characteristics reviewed above.

Table 3.3 Summary of the experimental heat transfer characteristics

Reference	Conditions	Heat transfer characteristics	Heat transfer mechanism
Lazarek and Black (1982)	D = 3.15 mm, L = 126 mm q = 14 – 380 kW/m ² G = 125 – 750 kg/m ² s P = 1.3 – 4.1 bar $\Delta T_{\text{sub}} = -35 \text{ K}$; R113	Heat transfer coefficient (HTC) increased with heat flux, but independent of quality and mass flux.	Nucleate boiling dominant.
Wambsganss et al. (1993)	D = 2.92 mm, L = 368 mm; q = 8.8 – 90.75 kW/m ² G = 50 – 300 kg/m ² s P = 1.24 – 1.60 bar; R113	HTC increased with heat flux and weakly dependent on quality.	Nucleate boiling dominant.
Tran et al. (1996)	D = 2.46 mm tube, D _h = 2.40 mm channel q = 7.5 – 59.4 kW/m ² G = 44 – 700 kg/m ² s P = 8.25 bar; R12	HTC increased with heat flux for $x \geq 0.2$ and independent of quality. HTC increased with mass flux for $\Delta T_{\text{sup}} < 2.75 \text{ K}$	Nucleate boiling dominant mechanism for $\Delta T_{\text{sup}} > 2.75 \text{ K}$ and convective boiling dominating for $\Delta T_{\text{sup}} > 2.75 \text{ K}$
Kew and Cornwell (1997)	D = 1.39, 2.87, and 3.69 mm, L = 500 mm q = 9.7 – 90 kW/m ² G = 188 – 1480 kg/m ² s P _{inlet} = 2.5 bar; P _{exit} = 1 bar; R141b	For D = 2.87 and 3.69 mm, HTC increased with heat flux when $x < \sim 0.2$. Beyond this limit, HTC increased with quality and was independent of heat flux.	Nucleate boiling at low quality and convective boiling at high quality. For D = 1.39 mm, local intermittent dryout.

Lin et al. 2001	D = 1.1 mm, q = 18 -72 kW/m ² G = 510 kg/m ² s P _{inlet} = 1.35 – 2.20 bar; P _{exit} = 1 bar R141	At low heat flux, HTC increased with quality after a peak near x=0. At moderate heat flux, HTC is almost independent of quality. At high heat flux monotonic decrease in HTC with quality.	Nucleate boiling at low quality and convective boiling at high quality. At high heat flux partial dryout occurred.
Kureta (1998)	D = 2.0 and 6.0 mm; L = 4 to 680 mm q = 10-2007 kW/m ² G = 100 – 10170 kg/m ² s P = 1 bar; ΔT _{sup} = 70 - 90 K; Water	Sharp increase of Nu in the subcooled region. In the saturated region, Nu increased with heat flux and slightly with elevation distance but not with mass flux.	Nucleate boiling dominance. No obvious effect of heated length
Bao et al. (2000)	D = 1.95 mm, L = 270 mm q = 5 – 200 kW/m ² G = 50 – 1800 kg/m ² s P = 2 – 5 bar; R11, R123	In the subcooled region, rapid increase of HTC. In the saturated region, HTC independent of quality and increased with heat flux and pressure	Nucleate boiling dominant
Lee and Lee (2001)	0.4 to 2.0 mm × 20 mm width channels L = 260 mm, q = 2.95 -15.77 kW/m ² G = 51-209 kg/m, R113	HTC increased monotonically with quality.	Convective boiling
Yen et al. (2003)	D = 0.19, 0.51 mm; L = 280 mm q = 10 – 26.1 kW/m ²	HTC decreased with quality for x < 0.3. For x > 0.3, HTC was almost independent	Nucleate boiling dominant

	$G = 50 - 295 \text{ kg/m}^2\text{s}; \text{R123}$	of quality and mass flux.	
Sumith et al. (2003)	$D = 1.45 \text{ mm}, L = 100 \text{ mm}$ $q = 36 - 391 \text{ kW/m}^2$ $G = 23.4 - 152.7 \text{ kg/m}^2\text{s}; P = 1 \text{ bar}$ $\Delta T_{\text{sub}} = 2 - 12 \text{ K}; \text{water}$	HTC increased with heat flux and superficial vapour velocity for $U_{\text{gs}} < 7 \text{ m/s}$ and beyond this limit, HTC weakly dependent on heat flux and U_{gs} .	Film boiling. For $U_{\text{gs}} < 7 \text{ m/s}$, nucleation could exist in the thicker part of the liquid film
Owhaib et al. (2004)	$D = 1.7, 1.2, 0.83 \text{ mm}; L = 220 \text{ mm}$ $q = 3 - 34 \text{ kW/m}^2$ $G = 50 - 400 \text{ kg/m}^2\text{s}; \text{R134a}$	HTC weakly dependent on mass flux but increased with heat flux.	Nucleate boiling dominant
Huo et al. (2004)	$D = 4.26, 2.01 \text{ mm},$ $L = 500, 211 \text{ mm}$ $q = 13 - 150 \text{ kW/m}^2$ $G = 100 - 500 \text{ kg/m}^2\text{s}$ $P = 8, 12 \text{ bar}; \text{R134a}$	For $x < 0.4-0.5$ ($D = 4.26 \text{ mm}$) and $x < 0.2-0.3$ ($D = 2.01 \text{ mm}$), HTC was independent of quality and mass flux, while it increased with heat flux and pressure. Beyond this quality range, HTC decreases with quality.	Nucleate boiling at low quality.
Wen et al. (2004)	Channel, $2 \times 1 \text{ mm}, L = 280 \text{ mm}$ $Q = 27 - 160 \text{ kW/m}^2$ $G = 57 - 211 \text{ kg/m}^2\text{s}$ $P = 1 \text{ bar}; \Delta T_{\text{sub}} = 1 - 12 \text{ K}; \text{water}$	HTC increased with heat flux and almost independent of mass flux. No effect of inlet compressibility on the time-averaged HTC	Convective boiling. Observation did not support that nucleate boiling is dominant mechanism
Saitoh et al. 2005	$D = 0.51, 1.12, 3.1 \text{ mm}$	At low quality, HTC increased with heat	Nucleate boiling at low quality

	<p>L = 550, 935, 3235 mm respectively q = 5-39 kW/m² G = 100-450 kg/m²s P = 3.5 - 4.88 bar; R134a</p>	<p>flux and independent of quality. At high quality, HTC increased with quality and mass flux but independent of heat flux</p>	<p>and convective boiling at high quality</p>
Yun et al. (2005)	<p>D = 2.0 and 0.98 mm L = 1200 and 400 mm respectively. q = 7 – 48 kW/m² G = 1000 – 1500 kg/m²s P = 5 and 10 bar; CO₂</p>	<p>At low heat flux, HTC increased with quality. At high heat flux, HTC constant up to x ~ 0.45 and then sharply drops</p>	<p>At low heat flux, convective boiling and dryout at high heat flux.</p>
Boye et al. (2007)	<p>D = 1.5 mm, L = 500 mm q = 10 – 115 kW/m² G = 50 – 100 kg/m²s, P = 3 bar; water</p>	<p>HTC decreased with quality for x < 0.2 and then slightly increased with quality. Very little heat flux effect for x > 0.2 HTC increased with heat flux.</p>	<p>Nucleate boiling at low quality and convective boiling at high quality.</p>
Cortina Diaz and Schmidt (2007)	<p>Channel, 0.3 × 12.7 mm², L = 200 mm q = 11 – 400 kW/m² G = 50 – 500 kg/m²s P = 1 bar; water, ethanol</p>	<p>HTC sharply decreased with quality for x < 0.15 and stayed almost constant beyond this limit.</p>	<p>Nucleate boiling at low quality. Convective boiling at high quality.</p>

Geometry, flow direction and heated length effects

Tran et al (1996) also obtained similar results for the rectangular channel, and circular channel indicating no effect of channel geometry. Lazarek and Black (1982) conducted an experiment in a downward flow and at an approximately the same condition as their upward flow experiments. However, there was no significant effect of flow direction, confirming the gravitational force was not dominant as opposed to large diameter tubes. Kureta et al. (1998) conducted flow boiling heat transfer tests with diameters of 2 and 6 mm varying the heated length from 4.0 to 680 mm and found no obvious effect of heated length on heat transfer. There are not enough number of studies to confirm these effects.

3.4.3 Pressure and temperature oscillations

One of the challenges in understanding flow boiling heat transfer characteristics in small/mini tubes is the fact that it is usually associated with fluctuations of flow, pressure and wall temperature. These fluctuations were attributed to various reasons, mostly: periodic flows, bubble confinement, partial dryout, inlet compressibility, high temperature at onset of nucleation. Despite its relevance for safe operation of microcooling systems, there is a relatively limited number of studies that investigated fluctuations related to flow boiling in small channels. This subsection tries to review most of the works (to the best of the author's knowledge) that investigated fluctuations in single channels. Aligoodarz et al. (1998) investigated wall temperature and local pressure fluctuations during flow boiling of water in rectangular channels of cross-section $2 \times 2 \text{ mm}^2$ and $2 \times 1 \text{ mm}^2$. They used the liquid crystal technique for wall temperature measurement with response time of 4 ms, synchronised with a colour video camera with a speed of 200 Hz. Interesting results of wall temperature fluctuation were presented, although difficulties of applying the liquid crystal layer ($\sim 10 \text{ }\mu\text{m}$) uniformly over a long length were reported in addition to the relatively low speed of the camera. For the $2 \times 2 \text{ mm}^2$ channel, at low heat flux relatively large fluctuations in wall temperature were observed related to the unstable confined bubble regime, i.e. local phenomena such as liquid flow, large bubble formation, "stick-creep" bubbles and bubble sliding. As the heat flux increased, the amplitude of fluctuation decreased but the frequency increased. Local pressure fluctuation measurements, which were made only for the $2 \times 1 \text{ mm}$ channel indicated fluctuations corresponding to saturation temperature

variation within ± 2 K. They also observed flow reversal in the single channel. Using a similar experimental facility but with five pressure transducers mounted along the tube, Yan and Kenning (1998) measured fluctuations in local pressure for the 2×1 mm² channel. In this case, a camera with relatively higher frame rate (500 frames/sec) and two thin-foil thermocouples, which were attached at the back of the channel were used. The results of the local pressure measurements indicated fluctuations that propagated along the channel caused by the growth of confined bubbles. The growth was also observed to be affected by the upstream compressibility of the inlet flow. Later, Kenning and Yan (2001) also confirmed that at high inlet compressibility, the confined bubble grew both in the upstream and downstream direction, while the compressibility had no effect on the time-averaged heat transfer coefficient. It was also observed that at the channel exit a decrease in the pressure pulse initiated nucleation in the film especially at the corners, which cause disturbance in the film. A typical feature of the pressure fluctuations for a high and low inlet compressibility conditions is given in Fig. 3.22. As seen in the figure, the pressure curves for the five axial locations (P1 – P5) indicated fluctuations with time corresponding with the various boiling regimes.

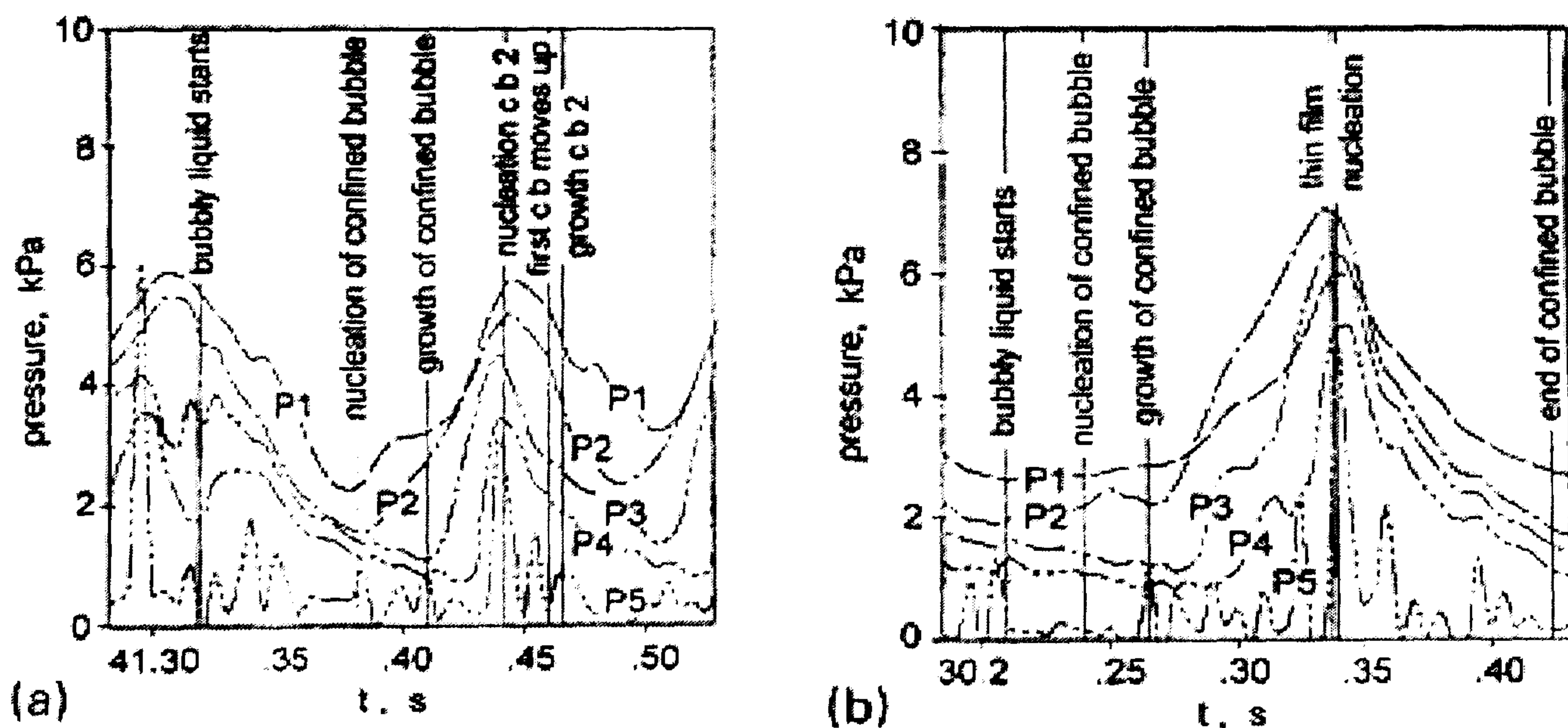


Figure 3.22 Pressure fluctuations at $134 \text{ kg/m}^2\text{s}$, 53 kW/m^2 , Kenning and Yan (2001):
 (a) low inlet compressibility; (b) high inlet compressibility.

As previously mentioned, confined bubble flow (described in various forms as slug, plug, elongated bubble) is the most common flow regime in small diameter tubes. Therefore, as the heat flux increases, the frequency of this periodic flow increases, so is the fluctuation of the wall temperature. Associated with this, the partial dryout and rewetting phenomena are mainly related with high fluctuations in wall temperature. For

instance, Lin et al. (2001a) found that fluctuations in wall temperature increased as the heat flux increase, see Fig. 3.23. This was assumed to be caused by time varying heat transfer coefficient and time varying local pressure and fluid saturation temperature.

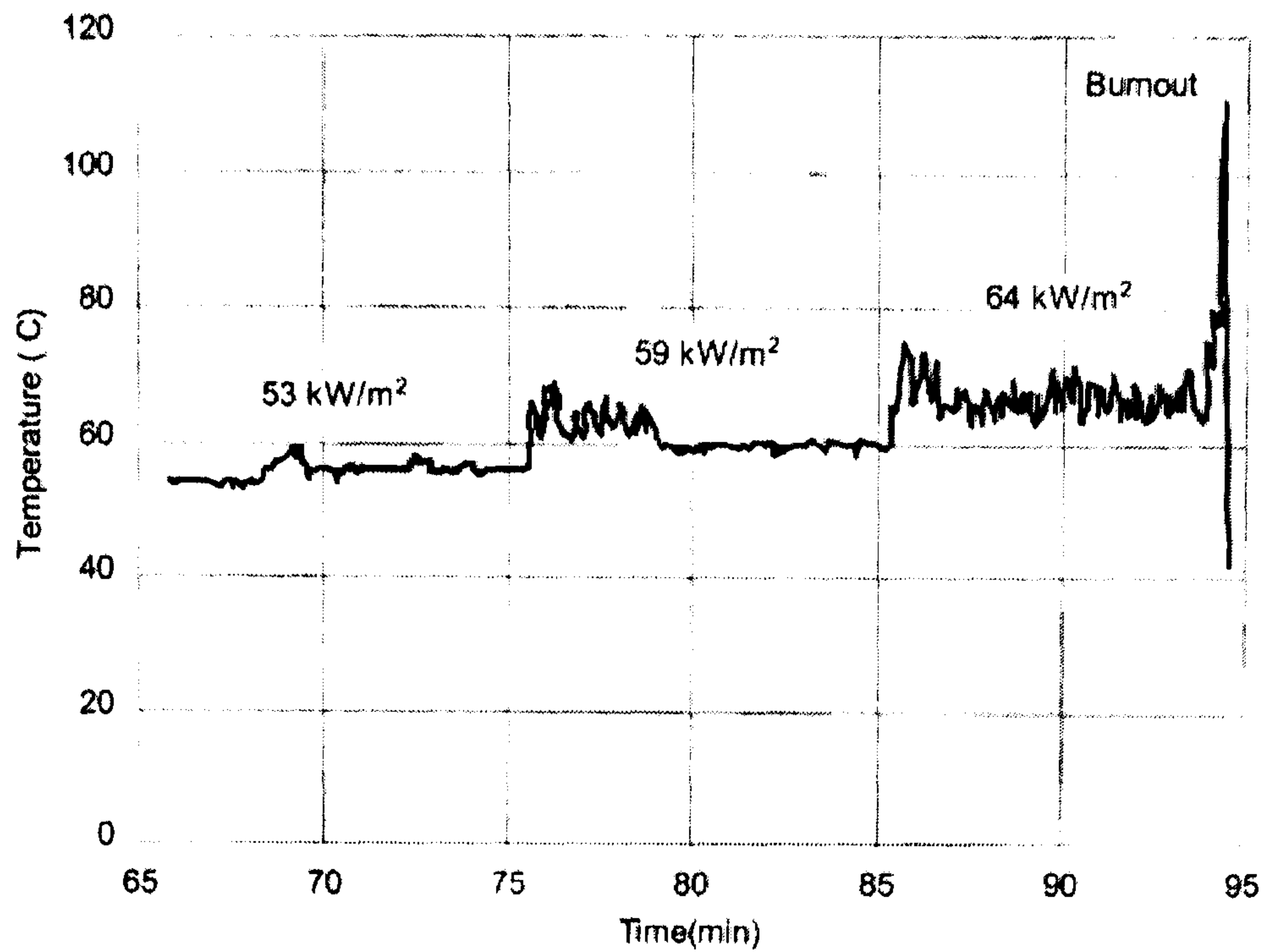


Figure 3.23 Wall temperature fluctuations for R141b, $G = 510 \text{ kg/m}^2\text{s}$ Lin et al. (2001a).

Similarly, Sumith et al. (2003) analysed partial dryout by plotting the wall temperature fluctuation, shown in Fig. 3.24. Again, the fluctuation amplitude increased with heat flux. Although, they mentioned that their measurement setup was not able to detect high frequency (the response time for the inner surface temperature to their data logger was 2 to 3 sec), it was possible to observe high fluctuations with high frequency at high heat flux ($q \sim 589 \text{ kW/m}^2$). This was assumed to be caused by intermittent dryout.

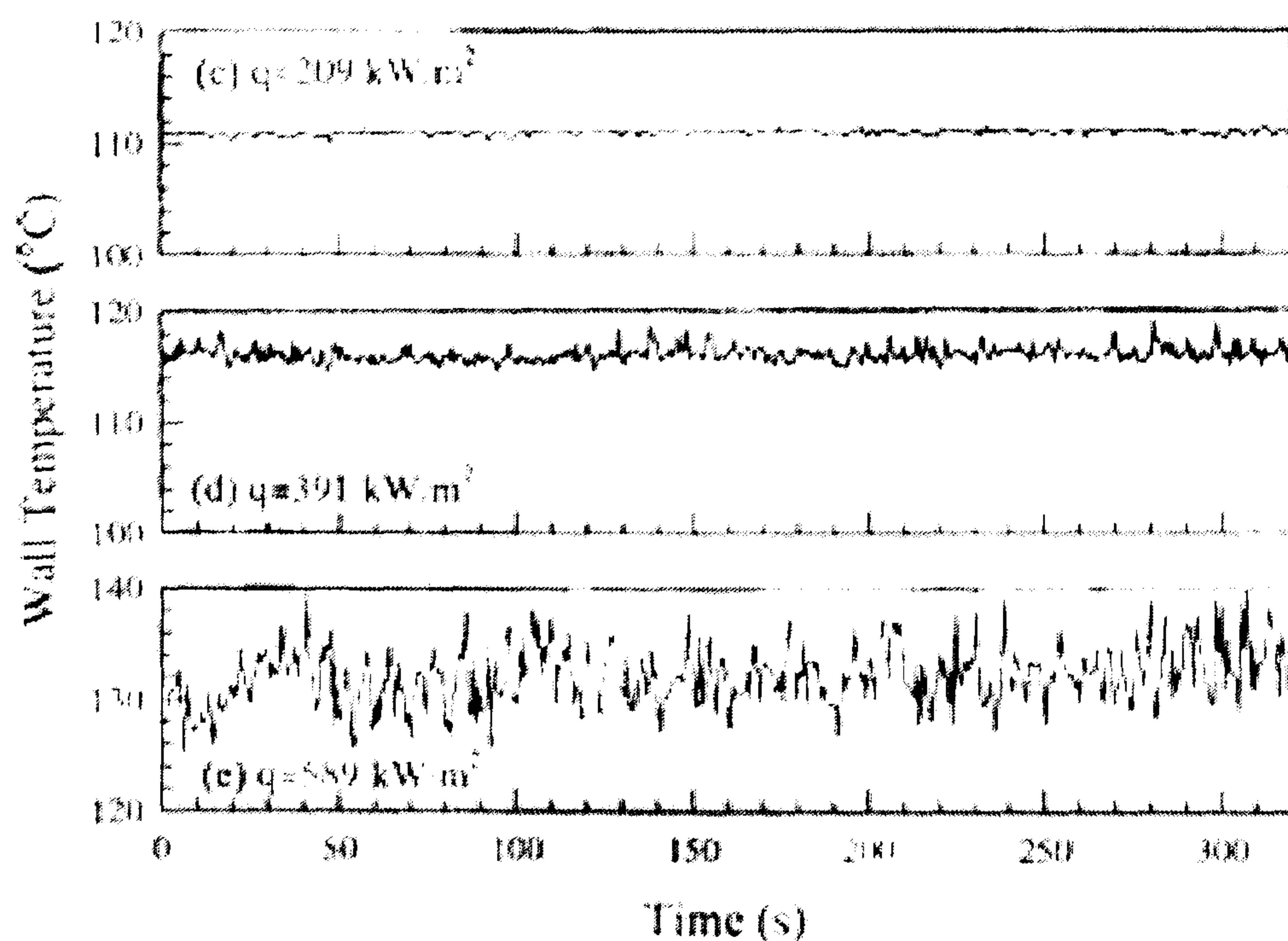


Figure 3.24 Wall temperature fluctuations, Sumith et al. (2003): $z = 90 \text{ mm}$ for water, at $G = 106.5 \text{ kg/m}^2\text{s}$.

Wu and Cheng (2003a) conducted a flow boiling heat transfer experiment using water in silicon microchannels of trapezoidal cross-section with dimensions $427 \times 208 \times 146 \mu\text{m}$ (hydraulic diameter of $186 \mu\text{m}$). Heat flux and mass flux were varied from $135\text{-}226 \text{ kW/m}^2$ and 146 to $112 \text{ kg/m}^2\text{s}$, respectively. They obtained different instabilities after boiling incipience. Different modes of instabilities were reported to be related with three flow regimes based on the various combinations of heat flux and mass flux values. These were liquid/two phase alternating flow, continuous two phase flow and liquid/two phase/ vapour alternating flow. The corresponding conditions were low heat flux/high mass flux, moderate heat flux /moderate mass flux and high heat flux /low mass flux, respectively. At high heat flux and low mass flux, the visualization result indicated a sequence of alternating flows (liquid flow- two phase flow- superheated vapour flow- two phase flow with respective duration of 4, 10, 23 and 16 sec). The corresponding oscillation amplitude in the wall temperature, inlet fluid temperature and exit fluid temperature measurements reached as large as 229, 88, and 176 K, respectively. These are extraordinarily large amplitudes with a long period of fluctuation (~ 1 min) and if they occurred in an application of these systems could result in poor cooling performance and even damage to the device. The exit temperature sometimes fell below saturation level. From the results presented, it seemed that the fact that the inlet temperature was highly subcooled and fluctuating might have an effect on the wall temperature and fluid exit temperature fluctuations. In other words, the inlet condition was not controlled, unless there was flow reversal that affected the inlet conditions. Also, the amplitude of oscillation in the wall temperature measurement increased with axial distance. They carried out a similar experiment on different size microchannels with hydraulic diameter of $158.8 \mu\text{m}$, Wu and Cheng (2003b). At relatively high heat flux and low mass flux, a longer period, large amplitude fluctuation of the inlet temperature (~ 70 K) was obtained, while the exit temperature was almost uniform at the saturation point. Unlike the previous results, the wall temperature near the inlet section fluctuated at a larger amplitude and decreased along the tube towards the exit. In addition, the flow visualization showed alternating flow of two phase and single phase liquid but not superheated vapour. Once the mass flux was adjusted for a steady flow, the fluctuation was observed to decrease with increasing heat flux. This was related to the density variation with temperature. In both cases, the heated length was not provided. For the channel with hydraulic diameter of $82.6 \mu\text{m}$, inlet and exit pressure fluctuations as well as mass flux oscillations were reported. The inlet pressure

fluctuated with amplitude of 13.2 kPa corresponding to the large fluctuation in inlet temperature (± 65 K). They also reported unusual large amplitude mass flux oscillations that reached up to ($500 \text{ kg/m}^2\text{s}$), while the exit pressure again stayed relatively uniform. Later, Wu and Cheng (2004), summarised the results into three kinds of unstable boiling modes: (1) the liquid/two-phase alternating flow at low heat flux and high mass flux, (2) the continuous two-phase flow at medium heat flux and medium mass flux, and (3) the liquid/two-phase/vapour alternating flow at high heat flux and low mass flux. Among the three modes, the first type was found to have large oscillation amplitude of pressure and flow rate, which were not in phase. The second type is associated with relatively small oscillations of pressure and flow rate, which were in phase. All of these are large period oscillations that depend on the value of heat flux and mass flux.

The large amplitude/long period fluctuations of inlet temperature were also observed by Xu et al. (2004), who investigated unsteady flow in a single microtube with $500 \mu\text{m}$ inside diameter and 45 mm heated length using water. However, the fluctuation amplitude varied as the inlet temperature increased between ambient to 80°C . The large amplitude fluctuation was obtained for water tank temperature of 100°C (saturation inlet condition). Again, the results seem to be influenced by the inlet condition, in addition to the fact that they mentioned a decrease in inlet temperature due to heat loss at the connections. This could be related to the relatively short heated length and associated end loss effects. In the later experiment, the heating was made using an external flexible rope heater, unlike most of the studies, which applied direct electric heating. The heater was wrapped around the outer surface of the cylindrical aluminium block (20 mm outer diameter), in which the channel was fitted in the middle of the block. The wall temperature measuring thermocouples were also inserted in the aluminium block few millimetres (not mentioned in the paper) from the outer wall of the test section tube, but they did not directly touch the microtube outer surface. Moreover, the wall thickness of the stainless steel test section tube was 0.5 mm, which brings the question of thermal capacity effect especially for transient investigation.

Brutin and Tadriss (2004) studied the effect of inlet and two phase instability during flow boiling of n-pentene in a rectangular channel of $0.5 \times 4 \text{ mm}^2$. The heating was achieved using a cartridge heater rod inserted in an aluminium block that supported the channel. A buffer tank was installed before the test section inlet for the purpose of altering inlet compressibility conditions. Plots of pressure drop versus inlet Reynolds

number at various conditions were used to identify unsteady and steady state zones. Unsteady conditions of pressure fluctuation were obtained below a certain critical inlet Reynolds number, the actual value depends mainly on heat flux. They investigated two different cases of inlet conditions: (1) constant liquid velocity inlet without a buffer tank and (2) constant velocity at the pump exit but with compressible buffer tank attached. In the first case (without buffer tank), the fluctuation were highly damped with maximum amplitude only 30 Pa^2 (rms value) at a frequency of 17.4 Hz. In the second case, a relatively large amplitude $\sim 1.1 \text{ kPa}^2$ (rms value), of pressure drop oscillation with a frequency of 3.8 Hz were observed both for the inlet and exit with a slight phase shift. It is not surprising that they observed high fluctuation in the second case, as they deliberately introduced a compressible inlet condition. Nevertheless, at low flow rate, a comparable fluctuation was obtained in the unstable region at all heat flux conditions.

Saitoh et al. (2005) observed oscillating flows in some of their test tubes. However, they did not observe fluctuation in the 0.51 mm tube, while their 3.1 and 1.12 mm tubes experienced unstable conditions. This is in contrary to other studies that associate flow instability with phenomena that are typical to very small channels, such as periodic flows, high initial superheat for ONB, rapid flow pattern transition, dryout etc. They identified the region of stable and unstable flows in heat flux versus mass flux plane using their 3.1 mm tube for different heated length (1.62 and 3.24 mm). The neutral stability points were obtained when heat flux decreased and mass flux and inlet vapour pressure remained constant. These points were determined from wall temperature measurements. The flow oscillations coincided with the outer wall temperature fluctuations. Three different types of oscillations were known; pressure drop, density wave and thermal oscillations. As their transit time matched with the period of density wave type oscillation (3 to 20 sec), they concluded the oscillations that were observed could be density wave oscillations. However, they did not explain, why this was not observed for their smallest tube of 0.51 mm tube.

Hetsroni et al. (2006) also studied flow boiling instabilities in parallel microchannels of hydraulic diameter $220 \mu\text{m}$ using water and ethanol at very low vapour quality. Pressure drop oscillations with period about 0.36 s were obtained which was assumed to be caused by the alternating flow of liquid and two phase and channel to channel interactions. The period of the oscillation was much lower than that of Wu and Cheng (2004). Associated fluctuations of exit fluid temperature and wall temperature were

observed at the same frequency and phase. The mean wall temperature was observed to vary within ± 10 K. The amplitude of all fluctuations, i.e. pressure drop, fluid and heater temperature increased with increasing heat flux. The wall temperature large fluctuation was related to dryout phenomena.

Chang and Pan (2007) conducted flow boiling experiments with water inside parallel microchannels with hydraulic diameter of $86.3 \mu\text{m}$ and heated length 20 mm. The channels were heated using heater material inserted in a copper block bonded by silver composition at the back of silicon based channels. The uncertainty of surface heat flux was reported to reach a maximum of 49.7 % for low heat flux conditions. They found different two phase flow patterns for stable and unstable conditions. They observed normal flow patterns (bubbly, slug, and annular flows) at low heat flux. When heat flux increased, alternating slug/annular flows with some channels experiencing reverse flow were obtained indicating unstable situation. The bubble growth plotted as bubble slug length versus time showed approximately an exponential relation, during stable flow. However, a large fluctuation in the slug bubble length with time was observed in the unstable state (high heat flux) associated with large pressure drop oscillations. Only one thermocouple at the middle of the channel was used for wall temperature measurements.

Cortina Diaz and Schmidt (2007a) observed different wall temperature oscillation characteristics for water and ethanol. Relatively large amplitude oscillations ($\pm 30\text{K}$) with a lower frequency were obtained for the case of water, particularly in the subcooled region. However, the fluctuations were damped in the saturated nucleate boiling region and the oscillation amplitude decreased with vapour quality. On the other hand, for ethanol, the large amplitude in the subcooled region was not observed and almost constant wall temperature was measured. The authors expected thermal capacitance effect on phase shift or attenuation of the amplitude, since the wall thickness of their test tube was 0.3 mm and temperature measurements of outer wall were used for unsteady state analysis. Hence, a preliminary analysis of conduction resistance effect, assuming a sinusoidal temperature fluctuation at the inner wall and one-dimensional heat conduction with heat generation, was carried out using FLUENT (commercial code). The results indicated a 6 % reduction in amplitude of the wall temperature, while the phase shift stayed the same.

Different techniques were proposed to control the flow and pressure instabilities during flow boiling in microchannels. Kandlikar (2002) suggested increasing the upstream

pressure drop in order to reduce the flow instability especially as a way to mitigate flow reversal. Extending the idea, Kandlikar et al. (2006) studied the effect of using pressure drop elements at the inlet and artificial nucleation sites for the purpose of controlling flow instability. They concluded that using pressure drop elements alone resulted in partial reduction of instability, while artificial cavities produced opposite effect. However, there was a positive result when the two methods were used in conjunction with each other in an optimised manner. The rapid growth of confined bubbles by the large degree of superheat during nucleation could push the upstream and downstream side vapour/liquid interface causing sometimes reversal of flow, especially in parallel microchannels arrangements (since the excess fluid can be shifted to the neighbour channels affecting the flow distribution).

3.4.4 Critical Heat Flux (CHF) and dryout

Design of heat exchangers or cooling systems require a method of accurately predicting the maximum allowable heat flux for their safe operation. When the heat flux becomes higher than a certain limit, the surface will be covered by a vapour blanket, inhibiting sufficient liquid contact. This maximum heat flux is referred to as Critical Heat Flux (CHF), which is a generic term for dryout, burnout, and departure from nucleate boiling (Collier and Thome 1994). Dryout, particularly intermittent dryout and rewetting is a common phenomenon identified in small diameter tubes during confined bubble flow.

CHF

A number of researchers have studied experimentally CHF in small diameter tubes. A list of CHF data for different combination of parameters was provided by Lazarek and Black (1982). The CHF was identified by the wall temperature measurement at the conditions of onset of dry wall conditions, which was sustained to cause a significant excursion in the wall temperature. The onset of partial dryout, initiated by a slight increase in heating power from a steady state, induced a large progressive oscillation in the wall temperature. This was believed to be due to intermittent rewetting of the inner heated surface. At fully dryout conditions, a significant reduction in heat transfer coefficient led to a large increase in the measured wall temperature. A modified CHF correlation, based on the Stevens and Kirby (1964) empirical model was developed, which was given in terms of the critical vapour quality at CHF condition as

$$x_{cr} = 1 - C_1 G D^{1/4} \left(\frac{D}{L} \right)^{0.59} \left[1 + C_2 \left(\frac{\Delta h_i}{h_{lg}} \right) \right] \quad (3.31)$$

D and L (tube diameter and Length are in cm)

Δh_i - inlet subcooling, $C_1 = 6.075 \times 10^{-3}$, $C_2 = 3.11$

Kataoka et al. (1997) predicted analytically the forced convective critical heat flux in vertical tubes. They employed two-fluid and three-fluid two phase flow models with given critical heat flux conditions. Different mechanisms were assumed depending on the flow regime. For annular flow, film dryout in connection with droplet entrainment and deposition was considered. On the other hand, for bubbly, churn and slug flows, the mechanism of DNB was considered. In the later case, they suggested transition from nucleate to film boiling is controlling the process rather than dryout itself. Analytically, they did not model the DNB case. However, a near wall bubble crowding model and evaporation model of the thin film under a slug bubble were mentioned as accepted models for DNB. In the first case, necessary conditions for DNB occur when the void fraction near the wall region reached a certain limiting value, in which heat transfer from the heated surface deteriorates due to crowding or restriction by a bubble layer formed near the wall region. The wall heat flux at DNB was given as:

$$q_w = h_{lg} G (x_b - x_c) \frac{(h_{sat} - h_l)}{(h_l - h_l)} \psi S \quad (3.32)$$

where, x_b vapour quality near the wall region,

x_c , the quality in the core

h_l , liquid phase enthalpy at net vapour generation

ψ , turbulence anisotropy

S , turbulence intensity

$$x_b = \frac{\alpha_b \rho_g}{(1 - \alpha_b) \rho_l + \alpha_b \rho_g}, \quad (3.33)$$

where, α_b is the void fraction near the wall region. The limiting void fraction near the wall region (α_{limit}) is taken to be 0.82 at $q_w = q_{DNB}$, Weisman and Pie (1983). However, Kataoka et al. (1997) recommended $\alpha_{limit} = 0.9 * \alpha^{0.28}$, where α is the average void fraction.

In the second case (evaporation of thin film underneath a slug bubble), DNB was assumed to occur if the thin liquid film surrounding the slug evaporated during the passage of the slug bubble. Therefore, DNB in this case depends on the liquid film thickness, length of vapour slug and its velocity.

$$q_{DNB} = \delta \rho_l h_{lg} (U_B / L_B) \quad (3.34)$$

δ was given as

$$\delta = \frac{\pi(0.0584)^2}{2} \left(\frac{\rho_g}{\rho_l} \right)^{0.4} \left(1 + \frac{\rho_g}{\rho_l} \right) \left(\frac{\sigma}{\rho_g} \right) \left(\frac{\rho_g h_{lg}}{q_w - q_{FC}} \right) \quad (3.35)$$

where, q_{FC} , heat flux due to single phase forced convection heat transfer,

U_B and L_B are given in terms of void fraction, velocity and turbulence parameters of two phase flow, (Katto and Yoshiwara, 1989 cited in Kataoka et al. 1997).

Comparisons of the small tube CHF data with conventional CHF correlations have also been made. Cheng et al. (1997) investigated experimentally the critical heat flux in uniformly heated vertical tubes with wide range of internal diameter, 2-16 mm, using R12. Exit quality and mass flux ranged from -0.75 – 0.59 and 1000 – 6000 kg/m²s, respectively. The ratio of heated length to diameter was almost the same for all tubes ($L/D \approx 100$). For quality between -0.3 to 0.15, the CHF for all the tubes decreased with exit quality almost linearly. The slope of the curves (CHF Vs quality) decreased with increasing tube inside diameter up to $D=8$ mm. However, there was significant change beyond this limit for larger tubes. In contrast, for the smallest tube (2 mm), at relatively lower pressure (1 MPa) and mass flux (1 and 2×10^3 kg/m²s), the CHF increased with exit quality for ($x=0$ to 0.6). This was related to the effect of heated length. There was a clear effect of mass flux (CHF increased with mass flux) at very low exit quality in the subcooled boiling region. However, the effect diminished at positive exit quality (saturated boiling region) and decreased with increasing exit quality. They assumed that at low exit quality (DNB region) higher mass flux enhanced turbulence and bubble transport there by increasing CHF. Whereas, in the fully developed saturated boiling region, annular flow could prevail such that increasing mass flux would increase the entrainment rate, decrease the film flow rate there by decreasing CHF. Moreover, the CHF was also observed to decrease with increasing system pressure, which was related to the effect of fluid properties (latent heat, vapour density, surface tension). For

instance, lower latent heat and higher evaporation rate or lower surface tension could result in a decrease in CHF with pressure, while higher vapour density could bring an opposite effect. Comparison of the measured CHF with that predicted by five large tube CHF correlations, (Groeneveld et al. 1986; Becker, 1967; Katto and Ohno, 1984; Shah, 1987; Weisman and Pei, 1983), were made. However, their data were not well predicted by any of these correlations. In microchannels, Bergles and Kandlikar (2005) argued that the CHF process could be affected by instabilities, particularly in cases when back flow occurred near the CHF (referring to the phenomenon observed by Qu and Mudawar (2004)). The vapour reverse flows were assumed to likely cancel the subcooling effect disturbing the normal characteristics of the real CHF. Zhang et al. (2006) collected CHF data for water in microchannels from literature and compared it with three correlations of CHF for saturated flow boiling (Bowring, 1972; Katto, 1978; Shah, 1979) and three correlations of CHF in subcooled flow boiling (Inasaka and Nariai, 1987; Celata et al. 1994; Hull and Mudawar, 2000). They suggested Shah and Hull-Mudawar for saturated and subcooled boiling respectively. Finally, they provide a new non-dimensional, inlet condition dependent correlation of CHF for saturated flow.

Wojtan et al. (2006) investigated experimentally saturated critical heat flux in circular tubes of 0.5 and 0.8 mm internal diameter using R134a and R245fa. The heated length was varied from 20 to 70 mm. Maintaining other similar conditions, the CHF was reported to increase with mass flux, which is a common case with other many results. The boiling curves at different inlet subcooling merged in to single lines, since the exit quality was always in the fully developed saturated boiling region. Therefore, there was no significant effect of degree of subcooling. Also the effect of saturation temperature was weak at relatively low mass flux region ($G < 1200 \text{ kg/m}^2\text{s}$). Beyond this mass flux limit, CHF increased slightly with saturation temperature. They compared their results with Katto-Ohno improved correlation and Qu – Mudawar correlation. Their data were predicted within 32.8 % using the Katto-Ohno correlation, while the Qu-Mudawar correlation was reported to slightly over-predict their data. Finally, the Katto-Ohno correlation was modified based on least square fitting to their data.

Effect of heated length-to-diameter ratio on CHF

Lezzi and Niro (1994) investigated the effect of heat length to diameter ratio on CHF inside tubes with diameter of 0.5 and 1.0 mm, using water at high system pressure (30, 50, and 70 bar). CHF values for the smaller diameter were larger than that for the larger

diameter. The degree of inlet subcooling was varied from 0 to 250 K and the corresponding CHF values were also observed to linearly increase with the degree of subcooling. CHF decreased with the heated length, however, for the larger heated length, the quality at which CHF occurred was higher (usually $x > 0.5$). Also, CHF decreased with pressure, while it increased with mass flux. Their experimental CHF data were better predicted by Katto-Ohno correlation (1984). Bowers and Mudawar (1994) conducted a high heat flux flow boiling experiment in minichannels and microchannels of diameter 2.54 and 0.51 mm, respectively with heated length of 10 mm using R113. Degree of subcooling was varied from 10-30 K with a volume flow rate up to 8.6 kg/hr. Like Lezzi and Niro (1994), CHF values for microchannels ($L/D \approx 19.6$) were higher than that of minichannels ($L/D \approx 3.94$). However, they did not observe any effect of subcooling on CHF for both mini and microchannels as opposed to most results of normal tubes. For flow rate ($Q < 8.6$ kg/hr), at lower heat flux than CHF, superheated exit condition were obtained indicating total dryout of the film. Later, Mudawar and Bowers (1999) conducted an extensive experiment on CHF using water and studied the effect of various parameters such as tube diameter, heated length to diameter ratio, pressure, mass flux, degree of subcooling. The experiments were planned to reach the maximum possible CHF using a very large mass flux values, (5000 – 134000 kg/m²s) and short tube length. They claimed that the critical heat flux reached a value of 276 MW/m² (maximum ever reported known to the author). The data were collected for tube diameters of 0.406 – 2.54 mm, heated length to diameter ratio 2.4 – 34.1, inlet temperature 18 – 70 °C and exit pressure 2.5 – 172 bar. For the high mass velocity condition, in which the exit quality could be still in the subcooled region (because of the short heated length), CHF which was more properly related to DNB was attained at very high heat flux. The mechanisms for subcooled CHF or (DNB) were assumed to be either of the mechanisms suggested for normal tubes:

- Intense boiling, which cause liquid/bubble boundary layer to detach from heated wall and stagnant liquid to evaporate, (Kutateladze and Leont'ev, 1966)
- Bubble crowding within the boundary layer restricted replenishment near the surface resulting in vapour blanket, (Weisman and Pie, 1983)
- Dryout of liquid sublayer beneath a large vapour bubble resulting in local wall temperature fluctuation.

The measured CHF was found to increase with increasing mass velocity and subcooling, but with decreasing tube diameter and heated length to diameter ratio. Maintaining the degree of inlet subcooling, for pressure below 30 bar, CHF increased with pressure. However, it remained the same from 30-150 bar and began to decrease as it approached critical pressure. Unlike Bowers and Mudawar (1994) and Lezzi and Niro (1994), Wojtan et al. (2006) found that the CHF for the 0.8 mm tube were higher than that for the 0.5 mm tube, the difference increasing with mass flux. The heated length showed a very significant effect on the magnitude of CHF. For both tubes, the CHF increased significantly with decreasing heated length. The CHF versus heated length plot for the two fluids at the same mass flux and inlet subcooling showed a higher CHF for R245fa. However, the deviation was dependent on heated length. In general, the effect was not significant except at heated length of 30 mm.

Dryout

Groeneveld (1986) identified four different temporal changes of wall temperature that define types of dryout. Sudden large increase in temperature (fast dryout), sudden but moderate increase in temperature with time (stable dryout), fluctuating surface temperature which correspond to the intermittent appearance and disappearance of dry patches (unstable dryout) and gradual monotonic increase in wall temperature with power input (slow dryout). The transition boiling regime with positive temperature slope with time was also called onset of intermittent dryout.

Kew and Cornwell (1997) monitored the wall temperature and overheating of the tube at low heat flux and qualities. This was observed to be associated with the rapid decrease in heat transfer coefficient with quality, which was related to the rapid expansion of the bubble causing expulsion of the liquid. At high heat flux, the rapid expansion of bubbles expels the liquid, creating an intermittent local dryout, until the next liquid is replenished. Wen et al. (2002) observed at very low mass fluxes the downstream propagation of transient high wall temperatures indicative of dryout, even at low heat fluxes. In channels of circular cross-section, in which events in the boiling region cannot be observed directly, decreases in time-averaged heat transfer coefficient with increasing quality, often accompanied by fluctuating wall temperatures, have been attributed to transient dryout, particularly at low mass flux, Huo et al. (2007). There have been few studies that investigated the mechanism of dryout in small channels. Agostini et al. (2005) studied boiling heat transfer in rectangular channels with

hydraulic diameter of 2.01 mm using R134a. They found a sudden fall in the heat transfer coefficient with quality, after $x \sim 0.4$. This was again related to partial dryout due to evaporation of the thin liquid film surrounding the vapour slug. For high mass flow rate, dryout was expected early due to the increased drag force at high flow rate of the film. According to a least square fitting to their data, they suggested a heat transfer coefficient correlation for the deteriorating heat transfer region given as.

$$\alpha = 2.8q^{2/3} \dot{m}^{-0.64} x^{-2.08}, \text{ for } x > 0.43 \quad (3.36)$$

Hetsroni et al. (2005) observed dryout happening as a result of uneven distribution of the initial film thickness over the heated surface and during rapid evaporation of the liquid film. This was associated with an increase in heat flux, while the mass flux is steady or vice versa. At higher heat flux, dryout begins at low quality near the inlet. Later, from a flow boiling experiment in parallel triangular microchannels, they observed the initial film thickness decreased with increasing heat flux. The film then evaporated as the bubble passes by to a certain minimum liquid film thickness; consequently intermittent dryout occurred. Unlike the CHF conditions, the surface temperature does not suddenly increase, instead it fluctuates. This is an indicative of the intermittent nature of the dryout and rewetting of the surface, Hetsroni et al. (2006).

As discussed above, a partial dryout phenomenon is mostly associated with wall temperature fluctuations. This was also confirmed by Owhaib et al. (2006) from the close direct observation of dryout conditions using a transparent tube with electric conductive coating. They reported two different flow structures during dryout at very low and relatively high mass fluxes. At $47 \text{ kg/m}^2\text{s}$ a wavy liquid front with smooth and continuous thin film in between the waves was observed. The fluctuation of the liquid front indicated the intermittent nature of the dryout and rewetting phenomena. This was associated with wall temperature fluctuations, see Fig. 3.25 (a). At $124 \text{ kg/m}^2\text{s}$ a relatively stable liquid front was found, Fig. 3.25 (b). In this case the dryout seemed to be the result of complete evaporation of the stable liquid film causing breakup of the film into droplets exposing the surface. This happened at relatively higher quality than the first case.

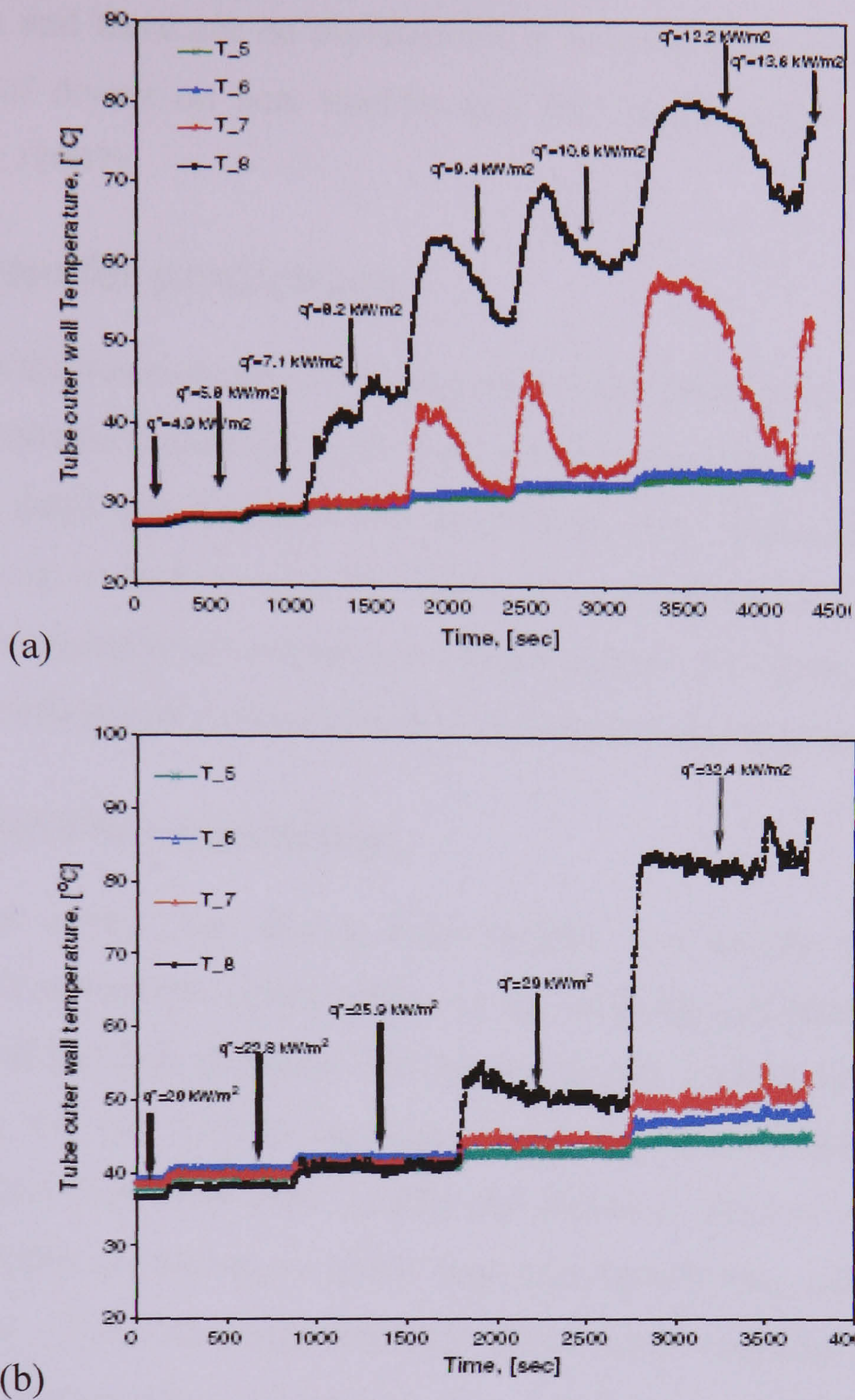


Figure 3.25 Wall temperature behaviour at various heat fluxes: (a) 47 kg/m²s, (b) 124 kg/m²s, Owhaib et al. (2006).

Kenning et al. (2006) suggested that there are two different mechanisms of dryout around individual bubbles in microchannels. These are dryout as a result of depletion of the film thickness below a certain minimum by complete evaporation of the liquid film beneath the confined bubble and dry out due to surface tension driven ‘capillary roll-up’ on partially-wetted surfaces with finite contact angles. There may be two different sorts of partial dryout in the slug flow regime in small tubes. One is a cyclical process caused by regular dryout of the liquid film near the rear of each confined bubble, analogous to dryout of the microlayer under individual bubbles in pool nucleate boiling. The other may involve several bubbles or the expulsion of liquid from the tube, so that it has a longer timescale and is analogous to transition boiling preceding film boiling in pool boiling. Microchannel heat transfer correlations generally do not consider either type of

partial dryout and there are no correlations or models that predict the effects of the second type of dryout on heat transfer and the vapour quality at which it occurs, Shiferaw et al. (2007)

3.5 Heat transfer predictions

Since the classical assumptions to heat transfer rate predictions in conventional systems are briefly introduced in chapter 2, only heat transfer correlations and models, which are developed for small size channels, will be covered here. The range of application of these methods is in many cases limited to the conditions of the data, which the correlation was originally developed from. In this section, flow boiling heat transfer rate prediction methods (empirical correlations and models) will be reviewed separately.

3.5.1 Heat transfer correlations

In conventional tubes, flow boiling heat transfer was mostly expressed either in superposition or asymptotic combinations of the contributions from the two common heat transfer mechanisms (nucleate boiling and forced convective boiling). In some cases either of the two will be dominant based on the inter dependence of some parameters as heat flux, mass flux, quality and pressure. Most of the correlations for small diameter tubes are extensions of the large tube correlations, correcting the various coefficients and exponents using the data from small diameter tubes. The basic development is incorporation of laminar flow conditions (mostly expected for very small tubes), (Zhang et al. 2004; Kandlikar and Balasubramanian, 2004). Some other correlations extended the single phase heat transfer correlation by changing the Prandtl number by the Boiling number and adjusting the coefficient using least square data fitting (e.g. Lazarek and Black, 1982), while others followed the pool boiling correlation power curve fitting (e.g. Tran et al. 1996). In general, as there will not be as such much to discuss regarding each correlation, it is believed that including the list of existing correlations for large and small size channels that are used for comparison with the current data in the appendix, with the corresponding conditions will suffice for the purpose of the thesis.

3.5.2 Heat transfer models

Relatively there are only a few number of two phase flow modelling studies in contrast to the large number of empirical correlations, mainly due to limitations on fully

understanding the various mechanisms and requirement of huge computational time. In particular, the nucleate boiling regime has proved to be difficult to model and therefore, empirical correlations are usually used in this regime. In conventional tubes, annular flow is the dominant flow regime covering a wider range of quality. Consequently, most of the two phase modelling for large diameter tubes were focussed on annular two phase flow, and significant progress have been made in modelling of annular flow (including entrainment and deposition of droplets), Hewitt and Hall-Taylor, 1970, Wallis (1969). However, in small channels, the prevailing flow pattern is not always annular flow, especially for refrigerant flows. Therefore, mechanistic modelling was applied for other flow regimes, especially, slug or confined flows, as well. This section reviews the two phase flow modelling studies for flow boiling in small size passages.

Ishibashi and Nishikawa (1969) proposed a heat transfer model for saturated flow boiling in narrow gaps. This was based on the assumption that 70% of the heat when a confined bubble passes is carried away by transient conduction, the rest being by latent heat. Therefore, they developed a model based on evaporation of the film, taking the time duration of bubble passing to be $t_b = 0.025$ sec and thickness of the film 28-47 μm . However, the temperature fluctuation due to the passing bubble and effect of heat flux on the frequency of the bubble was not considered. Wadekar and Kenning (1990) proposed a model for heat transfer during slug flow based on the length fraction of liquid and vapour slugs. The thickness and flow rate of the liquid film in the vapour slug were based on the method of McQuillan and Whalley (1985). The Chun and Seban correlation (1971) was used for the heat transfer during the vapour slug flow with a surrounding thin liquid film. The Dittus-Boelter equation was used for the heat transfer in the liquid slug region. Later, Wadekar, (1991) incorporated the nucleate boiling effect in the liquid slug, assuming the long bubble could be followed by liquid slug mixed with fine bubbles. This modification was reported to improve the prediction for the slightly higher mass flux than previously used for comparison ($G=90$ $\text{kg/m}^2\text{s}$, $P=3.8$ bar, $D=14.4$ mm, water).

Xia et al. (1992) studied the mechanisms of boiling heat transfer in narrow spaces between parallel plates with gap sizes of 0.8, 1.5, 3.0 and 5.0 mm using R-113. For gap size 3 mm and larger, conventional flow regimes found in larger diameter tubes were observed. Below 3 mm, they obtained a short region of isolated bubbles and a wider region of confined and coalescing bubbles. As the gap size decreased and became

comparable to the bubble departure size, the bubble departure and growth were observed to be influenced by the wall. They also observed a periodic flow of confined bubble with thin liquid film and liquid slug. During flow of the coalescing bubble, the heat transfer region was assumed to be dominated by the mechanism of evaporation, followed by single phase (liquid) convection after the bubble passes. At sufficiently high heat flux, they observed dry patches for the smallest gaps. A theoretical model was proposed based on the above premises, i.e. on the periodic passing of these two flows and transient characteristics of the wall temperature. The local heat flux was assumed to periodically vary with time; hence, the time-averaged heat flux over the heated surface was used. Some limitations to their model include lack of accurate methods to predict the initial film thickness, residence time, bubble length and actual heat flux. In their case, the initial film thickness was taken from the relations given by Grigoriev, 1974 (cited in Xia et al. 1992) as:

$$\delta_0 = K \nu_l \left(\frac{\rho_l D}{\sigma U_g} \right)^{1/3} \quad (3.37)$$

where $K = 96.8$ (empirical coefficient), ν_l is the liquid kinematic viscosity and U_g is the gas velocity.

The major assumption in the emerging mechanistic models for small diameter tubes is that confined bubble flow is the dominant flow, in which transient conduction across the liquid film and evaporation from the surface of the film controls the heat transfer mechanism has also been suggested by Kew and Cornwell (1997). This was first mentioned to explain the reason for the fact that the classical nucleate pool boiling correlations (that of Cooper, (1984) predicted their data better than other known flow boiling heat transfer correlations for larger tubes. A model was proposed that accounted one or combination of the four mechanisms (nucleate boiling, confined bubble, convective boiling and partial dryout). In the isolated bubble regime, nucleate boiling was assumed, while in the confined bubble region either nucleate boiling or confined bubble evaporation was considered. The time fraction for the bubble and liquid slug periodic passages was obtained from the void fraction calculated based on homogeneous flow. However, the heat transfer during the passage of liquid slug was neglected. The film thickness for the confined bubble flow, which was used to evaluate the conduction heat transfer, was adopted from the Taylor (1961) relation for viscous flow. For annular-slug flows, nucleate or forced convective boiling was assumed. It is

important to note that the film thickness during the confined flow was taken to increase with quality regardless of the fact that evaporation was taking place. According to their assumption, when the progressively increasing film thickness reached the value determined for an annular flow, the model switched to apply forced convective boiling in annular flow. Then, the film thickness was considered to decrease with vapour quality. Partial dryout was not incorporated in the model since their attempt to fix a certain minimum film thickness for onset of dryout did not succeed. A typical result of their model prediction is shown in Fig. 3.26.

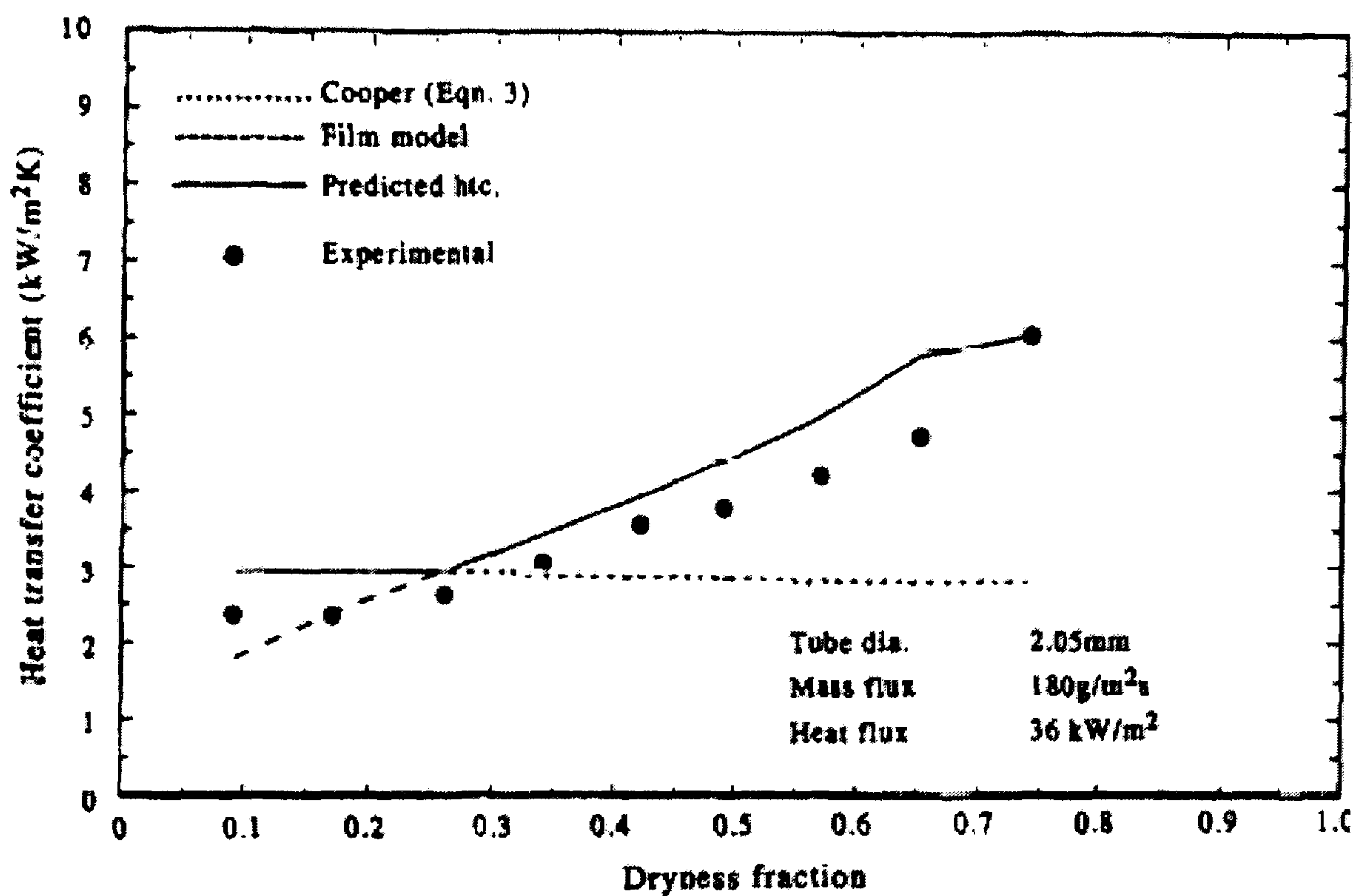


Figure 3.26 Comparison of the Kew and Cornwell (1997) model to their sample data.

Similarly, Jacobi and Thome (2002) proposed a mechanistic heat transfer model that was based on the prevailing flow pattern regime in microchannels. The model utilises the thin film evaporation during elongated bubble flow. The predicted heat transfer coefficient was strongly dependent on heat flux and weakly dependent on mass flux. It was also weakly affected by quality depending on the choice of initial film thickness. The dependence of the model results on heat flux, mass flux and vapour quality showed a similar characteristic with that of conventionally considered as the nucleate boiling dominant mechanism. However, the authors strongly suggested that the heat transfer mechanism in microchannels flow boiling is not nucleate boiling, but it is thin liquid film evaporation of the elongated bubbles. On the other hand, Kew and Cornwell (1997) reasoned out the fact that their boiling heat transfer data were fairly predicted by classical pool boiling correlations instead of flow boiling correlations is due to the similarity in the underlying physics between thin film evaporation and pool nucleate

boiling process. During the periodic flow of elongated bubble there is a pre-assumption that thin liquid film of uniform thickness (referred to as initial film thickness) is formed by the passing of the liquid slug. The value was not theoretically determined in case of Jacobi and Thome (2002). They have also taken into account, the fact that the liquid film thickness gradually decreased due to evaporation, from its initial value until the next liquid slug arrives, unlike that of Kew and Cornwell (1997). The residence time of the elongated bubble was determined using conduction-limited bubble growth model of Plesset and Zwick (1954) that mainly assumes the pre-existence of a uniformly superheated liquid. Nevertheless, they finally assumed the bubble departs the moment it touches the opposite side of the wall and used Jakob number to determine the time period, which was given as.

$$\tau_b = \left(\frac{R \rho_g h_{lg}}{\rho_l C_{p_l} \Delta T_{sup}} \right)^2 \frac{\pi}{12 \kappa_l} \quad (3.38)$$

where τ_b is the period of bubble generation. The above equation did not allow “waiting time” between formation of the consecutive bubbles. Also, other forces (inertia, surface tension) on the growing bubble might have an effect on the detachment period, which was not considered in the above equation. The time varying film thickness at each axial location was determined after evaluating the respective lengths of the bubble and the liquid slug from an energy and mass balance. The heat transfer coefficient was then calculated based on a steady state conduction assumption across the liquid film. The effective liquid superheat, ΔT_{sup} in (Eq. 3.38), which is dependent on the critical cavity radius at the onset of nucleation should be assumed in order to implement the model. The alternative approach is to assume the critical cavity radius, r_{crit} , and evaluate the liquid superheat. Either way, these are parameters that the model requires from elsewhere in addition to the initial film thickness. In the paper, they were varied and were determined after matching the model prediction with an experimental data using least square fitting. This could shed the genuine effects and leads the model to empiricism. A comparison of the model results with the experimental data of Bao et al. 2000 was made. The value of the effective liquid superheat or critical cavity radius and initial film thickness, obtained from least square fitting of the data, were $\Delta T_{sup}=28$ K (or $r_{crit}=0.07$ μm) and $\delta_0 = 1.25$ μm , respectively. Although the model requires the above parameters to be fully functional, it provides a good insight on the possibilities of mechanistic modelling and can be developed in to a more complete prediction tool, if a

model for initial film thickness and confined bubble formation frequency can be proposed. Later, Thome et al. (2004) extended this model into a three-zone evaporation model by incorporating the single phase heat transfers during liquid and vapour slug flows. The model assumed the passage of a liquid slug followed by a confined elongated bubble trapping a thin liquid film against the inner wall, which means the existence of a pair consisting of the liquid slug and the elongated bubble. However, if the liquid film dries out by evaporation before the arrival of the next liquid slug, a vapour slug follows (triplet). The fact that the model considers a dryout zone and exploits the transient evaporation of the film is one of the novelties of the model. The local heat transfer coefficient is then time-averaging of the heat transfer during the three different regimes. The heat transfer coefficient through the evaporating thin liquid film surrounding the elongated bubble was obtained assuming one-dimensional heat conduction in a stagnant thin liquid film. In addition to the above mentioned unknown parameters, a minimum critical thickness of the liquid film at dryout also needs to be determined. Nucleate boiling is not included in the model. Further details of this model will be given in Chapter 7.

Yang et al. (2000) modelled the hydrodynamics of Taylor bubbles in narrow channels using the Lattice-Boltzmann method. A reasonable qualitative agreement was obtained with the experimental observation. An enhancement in heat transfer was predicted in this particular region, compared with the classical theory. Also, the perturbation of the liquid film did not result in any wavy structure in the interface.

Peles and Haber (2000) developed a one-dimensional steady state model for two phase flow in single triangular microchannels. The equation for conservation of mass, energy and Young-Laplace were coupled with the momentum equation and solved numerically. The model exploited the additional advantage of the channel shape relative to a circular tube, i.e. the radius of curvature of the liquid-vapour meniscus decreased gradually along the channel as heat was applied, thereby decreasing the liquid pressure, which became capillary driving pressure. Therefore, the pressure drop in the liquid phase was considered to be the main factor for initiating liquid flow, while the vapour pressure remained almost constant. From their relatively simple one-dimensional model, they were able to predict the liquid radius of curvature, effective dryout length, phase velocities, pressures and film thickness as a function of the hydraulic diameter and fluid properties. Peles et al. (2000) proposed another one-dimensional model in a heated

microchannel, mainly assuming at any given time a single phase either vapour or liquid existed (unlike the concept of two phase mixture).

Hetsroni et al. (2003) conducted an experimental and theoretical study to predict bubble growth in a 1 mm tube using high speed visualisation and infrared radiometer (25 frames/sec) for the wall temperature measurement. A one-dimensional model was also proposed to trace the evolution of the bubble volume (V), thereby predicting the respective lengths of liquid slug, confined bubble and vapour slugs. Their measurement indicated monotonic increase in bubble volume with time. However, at higher time (t), a decrease in the slope (dV/dt) was observed. Two stages of bubble growth were identified: a) initial stage – bubble emerging from a micronucleus with a similar evolution characteristic with that of bubble growing in an infinite medium, b) second stage – radical change in bubble shape and development in to long quasi-cylindrical bubbles with diameter almost same as tube diameter (only separated by a thin liquid film). In the later stage, growth of the bubble was advanced by the liquid evaporation at the surface of the liquid film. The significance of the evaporation from both ends (top and bottom of the bubble) was observed to be dependent on the ratio of bubble length to tube diameter. According to their observation and measurements, for $L_b/D \leq 10$, evaporation from the liquid film surrounding the bubble was considered to be the dominant contributor of bubble growth. On the other hand, evaporation at the end of the bubble become significant portion of the heat transfer, when $L_b/D > \delta \rho_l U^* \lambda / D q_w$ (where U^* is the liquid film velocity). Eventually, if dryout does happen due to complete evaporation of the liquid film, a single phase vapour flow was assumed to follow. A simplified one-dimensional two phase flow model that did not account coalescence of bubbles and flow instability was used to analyse volumetric bubble growth and respective lengths. The model outcome, the volumetric bubble growth for a spherical and long quasi-cylindrical bubble, was correlated as, $V \propto t^{3/2}$ while $V \propto t^{1/2}$ for a very long bubble.

Hetsroni et al. (2006) studied periodic flow of boiling of water and ethanol in a triangular microchannel. Experimental investigation of initial film thickness and frequency was conducted in an attempt to supplement the three-zone model of Thome et al. by addressing the limitations, i.e. prediction of the initial film thickness and frequency of confined bubble formation. They suggested correlations for the frequency of successive events (single phase liquid – confined bubble – vapour single phase) and

initial film thickness based on their experiment results. In their experiments, channels with hydraulic diameters ranged from 100-220 μm , while the mass flux was 32 – 200 $\text{kg/m}^2\text{s}$, heat flux 120 – 270 kW/m^2 and vapour quality 0.01-0.08. However, the experimental data used was for water flow and extremely low vapour quality, which may not represent refrigerant flows with a significant slug flow regime. The results indicated strong dependence of the period of events on Boiling number. The initial film thickness decreased with heat flux up to a minimum value at the onset of dryout. The period of the event cycle (τ_b) was calculated in its dimensionless form as $\tau^* = \tau_b / U D_h$, where U is the mean inlet single phase flow to the microchannel. Therefore, the non-dimensional period (τ^*) was given in terms of Boiling number as; $\tau^* = 3.0 \times 10^5 Bo^{-2}$. The initial film thickness was also represented in its non-dimensional form as $\delta^* = \delta U / \nu$, where ν is kinematic viscosity of the liquid at saturation temperature. The correlation for the non-dimensional initial film thickness is given in terms of Boiling number as $\tau^* = 0.00015 Bo^{-1.3}$.

Numerical simulation of a vapour bubble growth was performed by Mukherjee and Kandlikar (2005). The Navier-Stokes equations together with continuity and energy equations for both phases were solved using the SIMPLER numerical scheme. The simulation was undertaken for water flow in microchannels of 200 μm square cross-section. A level-set approach was used to track the liquid-vapour interface. Their simulation showed qualitative agreement with that of experimentally observed bubble growth process. As the bubble grows, they also obtained a trapped liquid film between the bubble and the channel walls. In addition, the bubble upstream interface moved forward and sometimes backward, which in many cases could induce back flow. Kenning et al. (2006) monitored growth of a confined bubble using high speed visualization and measured the associated pressure oscillation in a capillary tube filled with uniformly superheated liquid. The experiment was designed to provide validation data for their one-dimensional bubble growth model under controlled initial and boundary conditions. The tube was closed at one end to cancel the effects of incoming fluid, while the opposite end was opened to the atmosphere. A growth of a single bubble was initiated by electrical heating of a resistance wire at the closed side of the tube. The resulting longitudinal growth of the bubble in the superheated medium was recorded by high speed video (200/500Hz). The associated pressure wave was also captured by the transducer mounted on the cover that blocked the tube. The bubble length was observed

to rapidly increase after an initial delay, while the pressure increased to a maximum and declined. The bubble growth model was pursued by solving the one-dimensional mass, energy and momentum equation along with the state Clausius-Clapeyron equation. In the model, a uniform initial film thickness with negligible evaporation effect, varied based on liquid film thickness correlations, was used to predict the experimental results. In addition, a constant was introduced in the equation they used for instantaneous heat flux to the bubble interface that was varied in the simulation of the model results. The predicted bubble length and instantaneous bubble pressure with time were compared with the experimental results. The varying parameters were adjusted to reasonably match the model predictions with the experimental data. However, they reported that the overall predicting capability of their one-dimensional model was poor, adding the difficulties of accurately controlled measurements.

Most of the above mechanistic models are based on confined bubble flow. Although, these models could be extended to annular flows with reasonable accuracy, precautions have to be made in some case, particularly during water flow boiling. For instance, due to the high surface tension of water and large contact angle, relatively large bubbles in size will be formed that will get confined at larger tubes compared with refrigerants. Hence, rapid transitions to annular flow (in rare cases, bubble eruption to mist flow) have been observed at very low quality. Following that, annular flow models with and without droplet deposition and entrainment have also been proposed in literature.

Qu and Mudawar (2003b) proposed a one-dimensional steady state annular two phase flow model for predicting heat transfer during saturated flow boiling of water in microchannels. The basic assumptions include laminar liquid and vapour flows, smooth liquid-vapour interface and strong droplet entrainment and deposition effects. The last assumption was made to respond to the common experimental heat transfer characteristics, which is the decrease in heat transfer coefficient with quality. This typical feature of microchannel flow boiling heat transfer is normally believed to be caused by partial dryout. However, no allowance was made for partial dryout, since the main flow is annular. Mass and momentum conservations for the liquid and vapour were solved. The initial mass flow rates of entrained liquid droplet, film flow and vapour core flow at the onset of annular flow were adopted from Whalley et al. (1974), with a modification to account for the effect of surface tension. The correlation developed by Shah and London (1978) were used for interfacial shear stress. The model

results fairly predicted their experimental data, in the range of quality from 0.05 to 0.10. However, the predicted heat transfer coefficient deviated from the data out of this quality range.

Boye et al. (2007) proposed a steady state one-dimensional annular two phase flow model. The model assumes steady-state laminar liquid film and vapour core flow. Short wave length ripples and long wave length disturbances, which are the main features of film interfacial instabilities, are neglected. The liquid film is considered to be uniform across the perimeter at each location. The model assumes laminar liquid film and vapour core flows and neglects capillary and gravitational forces. The equations used in the model are presented below for the fact that these equations are used to predict the current results of the smallest tube in Chapter 7.

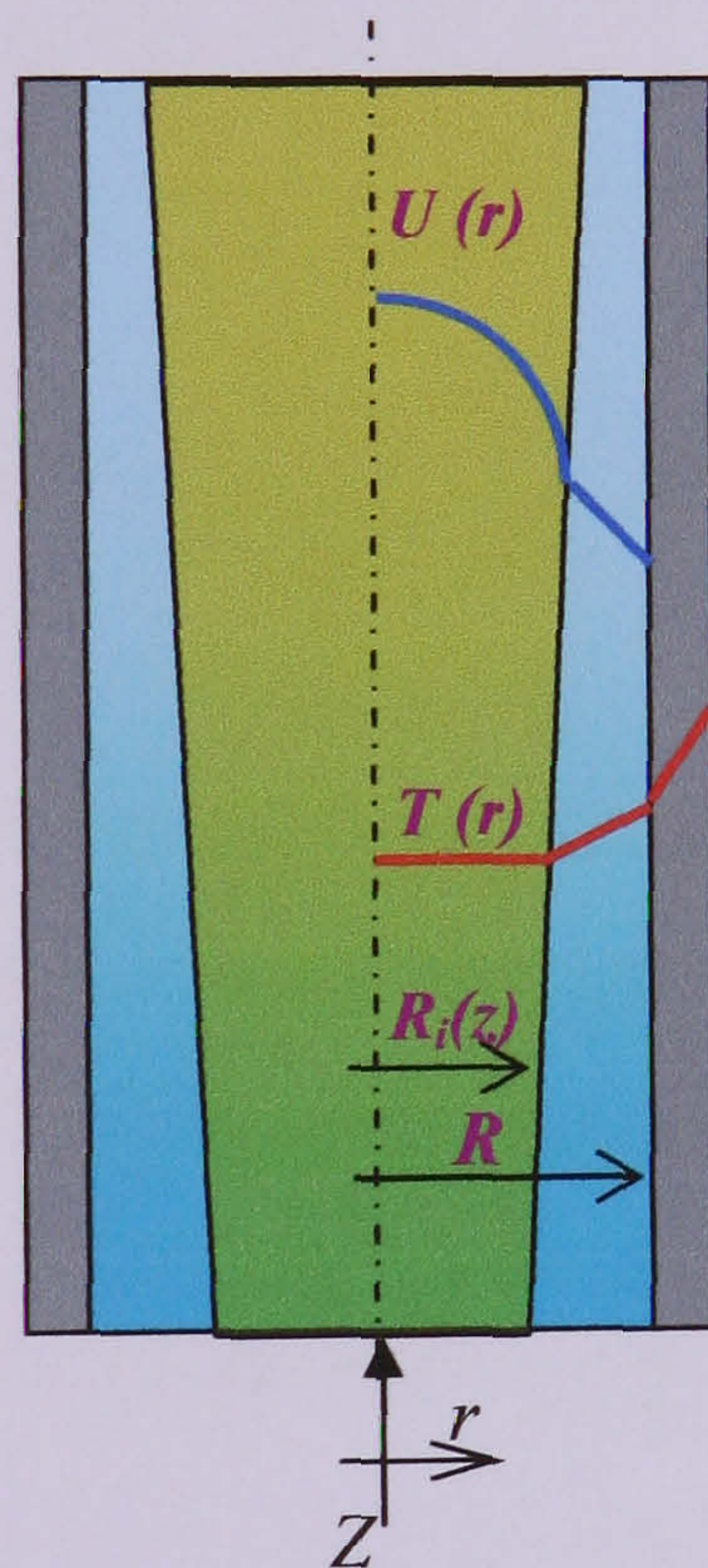


Figure 3.27 Sketch illustrating the annular two phase flow model of Boye et al. (2007)

The momentum equation for the liquid film and vapour core flow, neglecting acceleration in both phases, were given as in equations (3.39) and (3.40) respectively.

$$\frac{1}{r} \frac{d}{dr} \left(r \frac{dU_l}{dr} \right) = \frac{1}{\mu_l} \frac{dP}{dz} \quad (3.39)$$

$$\frac{1}{r} \frac{d}{dr} \left(r \frac{dU_v}{dr} \right) = \frac{1}{\mu_v} \frac{dP}{dz} \quad (3.40)$$

Boye et al. (2007) have also neglected the momentum due to evaporation in both of the above equations. They used the following four boundary conditions,

$$\left. \frac{dU_v}{dr} \right|_{r=0} = 0 \quad (3.41)$$

$$\mu_v \left. \frac{dU_v}{dr} \right|_{r=R_i} = \mu_l \left. \frac{dU_l}{dr} \right|_{r=R_i} \quad (3.42)$$

$$U_v(r = R_i) = U_l(r = R_i) \quad (3.43)$$

$$U_l(r = R) = 0 \quad (3.44)$$

Solving the momentum equations using the boundary equations, the liquid film and vapour velocity distribution were calculated, which were used to determine the mean velocity in the liquid film and vapour core given as,

$$\bar{U}_l(z) = \frac{2}{R^2 \left(1 - \left(\frac{R_i}{R} \right)^2 \right)} \int_{r=R_i}^{r=R} U_l(r, z) r dr = \frac{1}{8\mu_l} \left(\frac{dP}{dz} \right) R^2 \left[1 - \left(\frac{R_i}{R} \right)^2 \right] \quad (3.45)$$

$$\bar{U}_v(z) = \frac{2}{R_i^2} \int_{r=0}^{r=R_i} U_v(r, z) r dr = \frac{1}{8\mu_v} \left(\frac{dP}{dz} \right) R^2 \left[2 \frac{\mu_v}{\mu_l} \left(1 - \left(\frac{R_i}{R} \right)^2 \right) + \left(\frac{R_i}{R} \right)^2 \right] \quad (3.46)$$

One more relation is required to solve the above equations because of the third unknown term, i.e. axial pressure drop. Therefore, Boye et al. used the overall mass conservation equation (3.47) to close the equations. The total mass balance was given as

$$\bar{U}_v \rho_v \pi R_i^2 + \bar{U}_l \rho_l \pi (R^2 - R_i^2) = U_{l,0} \rho_{l,0} \pi R^2 \quad (3.47)$$

Simultaneously solving equations (3.45) – (3.46), the mean vapour core velocity was represented as:

$$\bar{U}_v(z) = \frac{U_{l,0} \frac{1}{R_i^*} \frac{\rho_{l,0}}{\rho_v}}{1 + \frac{\rho_l}{\rho_v} \frac{\mu_v}{\mu_l} \frac{1}{R_i^{*4}} \left(\frac{(1 - R_i^{*2})^2}{1 + 2 \frac{\mu_v}{\mu_l} \frac{1 - R_i^{*2}}{R_i^{*2}}} \right)} \quad (3.48)$$

where $R_i^* = \frac{R_i}{R}$

Introducing the mass quality equation (3.49), the interface radius equation, which has to be solved to determine the local film thickness at a local quality, x , was given in equation (3.50).

$$x = \frac{\bar{U}_v \rho_v \pi R_i^2}{U_{l,0} \rho_{l,0} \pi R^2} \quad (3.49)$$

$$\frac{\rho_l \mu_v x}{\rho_v \mu_l 1-x} = \frac{\frac{R_i}{R} + 2 \frac{\mu_v}{\mu_l} \left(\frac{R_i}{R}\right)^2 \left(1 - \left(\frac{R_i}{R}\right)^2\right)}{\left(1 - \left(\frac{R_i}{R}\right)^2\right)^2} \quad (3.50)$$

Equation (3.50) provides the interface radius, R_i in which the film thickness can easily be calculated as $\delta = R - R_i$. Boye et al neglected the second numerator term in the right hand side of the above equation. Therefore, the final form of the interface radius was given as,

$$\sqrt{\frac{\rho_l \mu_v x}{\rho_v \mu_l 1-x}} = \frac{\frac{R_i}{R}}{1 - \left(\frac{R_i}{R}\right)^2} \quad (3.51)$$

The heat transfer coefficient was obtained by assuming steady state heat conduction across the thin liquid film as,

$$\alpha_p = \frac{k_l}{\delta} \quad (3.52)$$

3.6 Summary

The existing studies presented above in detail covered several issues of flow boiling in small to micro passages such as flow patterns, effect of various parameters on pressure drop and heat transfer, onset of nucleation, heat transfer mechanisms, pressure and temperature fluctuations, dryout and CHF phenomena and heat transfer predicting models. Despite the fact that there is an intense research in two phase flow boiling in small to micro passages, the heat transfer research community has yet to conclude on

several issues related to flow boiling in small-to-micro passages. These include but not limited to the following points.

There are a larger number of flow pattern types probably more than that required for modelling and are diverse among different researchers. However, most flow pattern studies in small/micro tubes have clearly shown that there is a considerable difference in the flow pattern characteristics compared with conventional size channels. These include the predominance of surface tension force over gravity, the absence of stratified flow pattern in horizontal channels and the appearance of additional flow patterns that are not common in normal diameter tubes, Barnea et al. (1983), Mishima and Hibiki (1996), Kew and Cornwell (1997), Chen et al. (2006), and Revellin and Thome (2007a).

Various conclusions have been given on the mechanism of heat transfer in small-to-micro passages. Based on conventional way of interpreting flow boiling mechanism, nucleate boiling, forced convection and a combination of both were the main mechanisms repeatedly reported in the literature. Some researchers concluded that nucleate boiling is the dominant heat transfer mechanism, since it was observed that heat transfer coefficient is more or less independent of vapour quality and mass flux, while it is strongly dependent on heat flux, e.g. Lazarek and Black (1982), Wambsganss et al. (1993), Tran et al. (1996), Bao et al. (2000), Yu et al. (2002), Fujita (2002). On the other hand, some experimental studies have also observed effect of mass velocity and vapour quality on heat transfer but not heat flux. This is interpreted as forced convective boiling is dominant heat transfer mechanism, e.g. Carey et al. (1992), Oh et al. (1998), Lee and Lee (2001), Qu and Mudawar (2003a). Others have reported a combined effect of both mechanisms, i.e. nucleate boiling at low quality and forced convective boiling at high quality region in a similar way as that observed in large tubes, e.g. Kuznestov and Shamirzaev (1999), Lin et al. (2001), Sumith et al. (2003), Saitoh et al. (2005). In the present study, the effect of various parameters on heat transfer and pressure drop are analysed using systematically measured data and the results are discussed with the aide of simultaneously observed flow patterns at the exit of the test tube during flow boiling.

The transient dryout phenomena often reported in small diameter tubes, which is mostly associated with fluctuations in temperature and pressure is not well studied. Such deterioration of heat transfer associated with sudden rise in wall temperature can affect the integrity of cooling devices and lead to irreversible damage. Therefore,

understanding the mechanism of dryout and predicting the condition at which this occurs has a great practical significance.

There is no clear understanding on the influence of channel diameter on heat transfer and hence there is no common theory to identify the threshold below which the macroscale heat transfer phenomena do not fully apply to microscale. Although different definitions have been given by various researchers, Brauner and Maolem-Maron (1992), Cornwell and Kew (1993), Mehendale et al. (2000), and Kandlikar and Grande (2003), most of the ways used to classify the various size ranges do not consider the physical mechanisms and other effects involved when varying the size of the channels. Comprehensive heat transfer data covering a wide range of channel diameters is important in helping solve this issue. However, there are only a limited number of experiments that have tested a wide range of tube diameter to investigate the heat transfer trend with channel size. Most studies have reported that the heat transfer coefficient increases with decreasing tube diameter, Yan and Lin (1998), Oh et al. (1998), Huo et al. (2007), Owhaib et al. (2004). On the other hand some researchers found little or no significant effect of tube diameter on the magnitude of heat transfer, Kuwahara (2000), Baird et al. (2000), Khodabandeh (2003), Saitohi et al. (2005). The current study investigates this by covering a wide range of tube diameters (4.26 – 0.52 mm).

Most of the experimental two phase heat transfer studies inside metal tubes are for internal diameters larger than 1 mm. There are only limited heat transfer data in metallic tubes of size below 1 mm. Therefore, the effect on flow boiling heat transfer characteristic and flow pattern when the tube size is decreased much below 1 mm is not well studied. Few research studies indicated that flow boiling in very small diameter tubes is usually associated with high initial liquid superheat required to initiate boiling, Yen et al. (2003), Hapke et al. (2000), Peng and Wang (1993) and Peng et al. (1998). The unusually high superheat in micro tubes was also reported to be related to the reduction of active nucleation sites and vapour nucleation inside very small channels, Zhang et al. (2002) and Brereton (1998). Piasecka and Poniewski (2004) reported the boiling incipience to be accompanied by nucleation hysteresis, which was related to the stability of few activation sites. Flow pattern studies of very small diameter tubes reported further differences in the flow pattern characteristics as the tube size decreased below 1 mm, Serizawa et al. (2002), Kawahara et al. (2002), Xiong and Chung (2007).

These include the emergence of additional features to those observed in small diameter tubes, e.g. the appearance of a symmetrical liquid ring that no longer bridge the tube and liquid lump flow (flow of liquid lumps sliding on the wall) and diminishing appearance of dispersed and churn flows. In the current thesis the tube size range is decreased down to 0.52 mm to investigate the heat transfer and corresponding flow pattern characteristics in very small tubes.

Several correlations have been proposed, most of which are extensions of large tube correlations, which are empirically formulated from a rigorous data analysis. However, the number of modelling works is relatively scarce. In fact there is also a need for validated prediction methods for two phase heat transfer and pressure drop that will facilitate the design and optimization of compact heat exchangers for use with refrigerants and other fluids. However, they did not predict well the heat transfer coefficient in small diameters, Qu and Mudawar (2003a), Owhaib and Palm (2003) and Huo et al. (2007). A promising approach is made in developing regime based models, Qu and Mudawar (2003b), Thome et al. (2004), Boye et al. (2007). In the current work a new two-phase pressure drop model, correlations for heat transfer for small to micro tubes and improvements on the state-of-the-art flow regime based models are proposed and presented.

Other issues not addressed in this thesis, but worth mentioning include, the effect of physical parameters such as inlet and exit geometries, channel shape, surface finish.

Chapter 4

Experimental Methods and Validation

The state-of-the-art review of two-phase flow boiling in small to microscale passages presented in the previous chapter pointed out a number of issues that require further investigation and understanding. The current study is aimed to address some of these issues using systematically measured flow boiling heat transfer data and flow visualization. In order to achieve this, an experimental facility capable of testing a wider range of parameters such as tube diameter, heat flux, mass flux, pressure, degree of subcooling and type of fluid was constructed. This chapter presents the experimental methods, measurement accuracy, data reduction equations and validation results. It is organised as follows; Section 4.2 describes the experimental facility and details of the test sections design for both heat transfer measurements and flow pattern visualization. Uncertainty analysis and the results of measurement accuracy are reported in section 4.3. Section 4.4 presents the methods of data reduction for both pressure drop and heat transfer. Section 4.5 provides the validation results carried out using single phase friction factor and heat transfer tests and comparison with well-known single phase correlations. Long- and short-term reproducibility of the measured data have been checked frequently at different conditions. Section 4.6 presents the typical repeatability results. Finally, a brief summary of the chapter is given in section 4.7.

4.1 Introduction

The experimental facility was first designed during the Doctorate programmes of Huo (2005) and later Chen (2006) in London South Bank University to investigate flow boiling heat transfer, pressure drop and flow visualization. Huo (2005) conducted flow boiling heat transfer experiments in two tubes of 4.26 and 2.01 mm internal diameter with R134a as a working fluid. Using the same facility, Chen (2006) studied flow

visualization in four borosilicate glass tubes of 4.26, 2.88, 2.01 and 1.1 mm internal diameter. The facility was then dismantled and moved to Brunel University and re-installed and commissioned by the present author. Minor modifications, like replacing the preheater type and location, have been made during the re-construction. After re-construction, single phase validation measurements were conducted for the larger tube to check the intactness of the rig and ensure overall accuracy. The experimental study was then extended by studying the tubes of internal diameter 2.88, 1.1 and 0.52 mm. Moreover, flow pattern experiments were also conducted simultaneously with heat transfer measurements. The design of each component in the experimental facility is reported in the PhD thesis of Huo (2005) and later in Chen (2006). Hence, this will not be repeated here. However, the experimental facility and procedure with the associated uncertainty analysis and validation results will be covered in this chapter. Particular attention will be given to the new test-section design.

4.2 Experimental facility and procedure

Main facility

The schematic diagram and photograph of the R134a main circuit is shown in Figure 4.1 and 4.2, respectively. The main circuit consists of reservoir (1), gear pump (2), line filter drier (3), flow meters (5), subcooler (6), preheater (7), test section (9), separator (12) and condenser (13). Almost all the parts including the pipes are made of stainless steel, which implies the facility is capable of accommodating various kinds of fluids. However, if water were used, the reservoir and pump would need to be replaced, since they are made of mild steel and cast iron, respectively. The reservoir is equipped with a pressure safety valve, liquid level indicator and pressure gauge. A bypass line is fitted at the exit of the pump in order to avoid excessive pressures during increased flow resistance, especially for the smaller tubes. Fouling becomes a major problem as the tube diameter decreases; hence a drier-type line filter capable of removing moisture is installed after the pump. The system pressure is controlled by an immersion heater (14) and a cooling coil (15) inserted inside the reservoir. To attain the required system pressure, the power input to the immersion heater is varied by a variac, which is also monitored by a PID controller. The PID controller also maintains the maximum temperature in the reservoir below the allowable value for a specific pressure. For relatively small heat load conditions (especially for the smaller tubes of 1.1 and 0.52

mm), running the main condenser (13) creates flow and pressure instabilities. This is because of its large cooling capacity compared with the load. In such cases, the cooling coil inside the reservoir is enough to stabilize the system pressure with no need to use the main condenser. The flow rate is measured using two Coriolis flow meters supplied by Micro Motion Ltd. (F_1 and F_2 in Fig. 4.1). The models are CMF010 and CMF025, which work in different flow rate ranges, i.e. (0 – 25 kg/h) and (0 – 500 kg/h) respectively. These flow meters are claimed to be the most accurate flow measuring devices and did not need to be calibrated by other standard instrument. However, they require single phase inlet condition for accurate measurement. Hence, temperature and pressure data are taken just before the flow meter in order to ensure this. The flow rate is controlled by using precise needle valves located downstream of the meters, so that the upstream flow and its measurement are not affected by the valve operation. The inlet conditions (degree of subcooling or inlet quality) to the test section are controlled by adjusting the capacity of the subcooler (6) and heating power to the preheater (7). Originally, the preheater was constructed from six immersion heater rods inserted inside six pipes that are connected to each other in series, (Huo 2005). This was later found to provide heating powers far more than required by the test conditions. It also demands additional cooling due to its large lumped mass, in case of high degree of subcooling inlet conditions (e.g. single phase tests). Therefore, the flow was by-passed and the preheater was replaced by a simple flexible rope heater wrapped around the tube just before the test section.

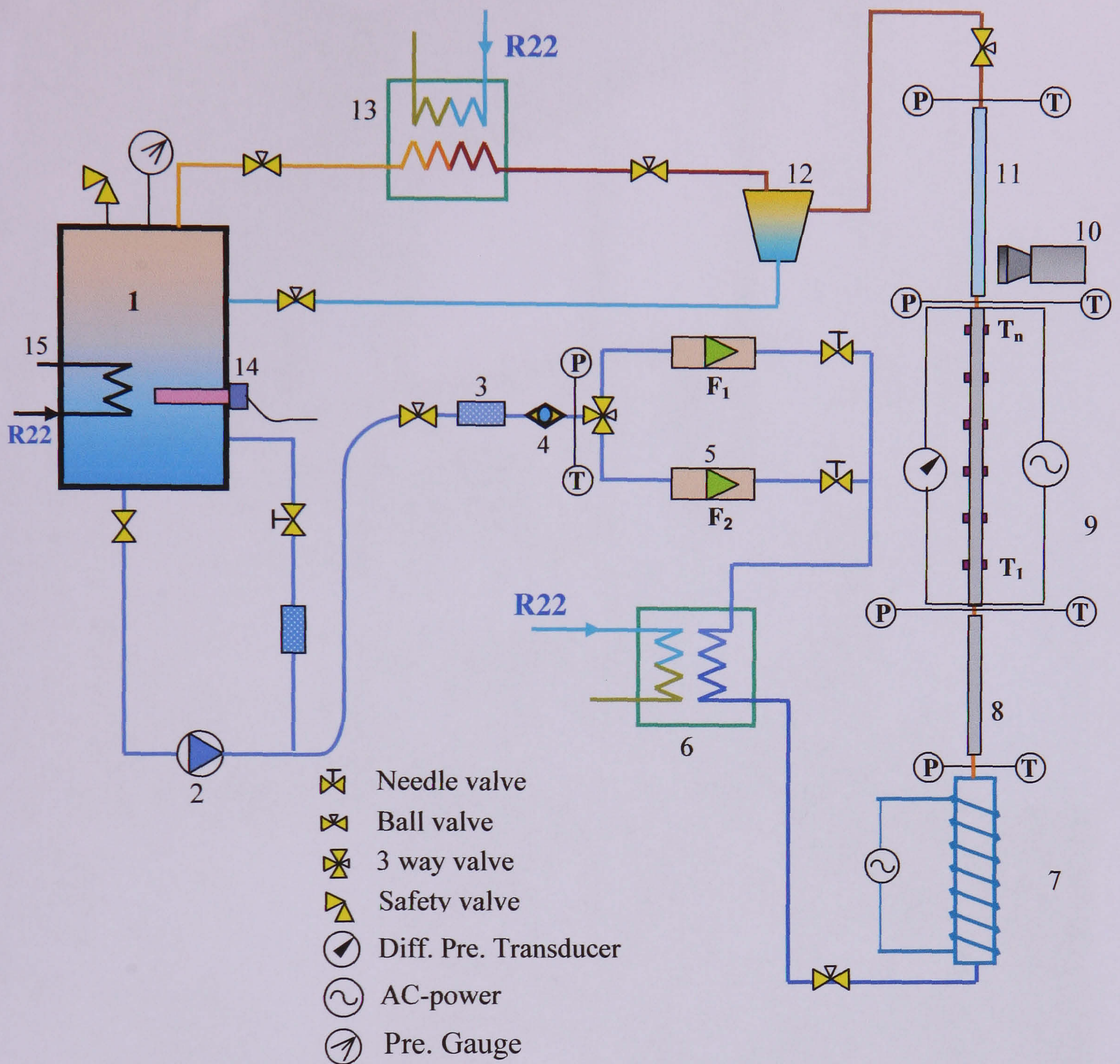


Figure 4.1 Schematic diagram of the experimental system (the R22 Cooling system is not shown)

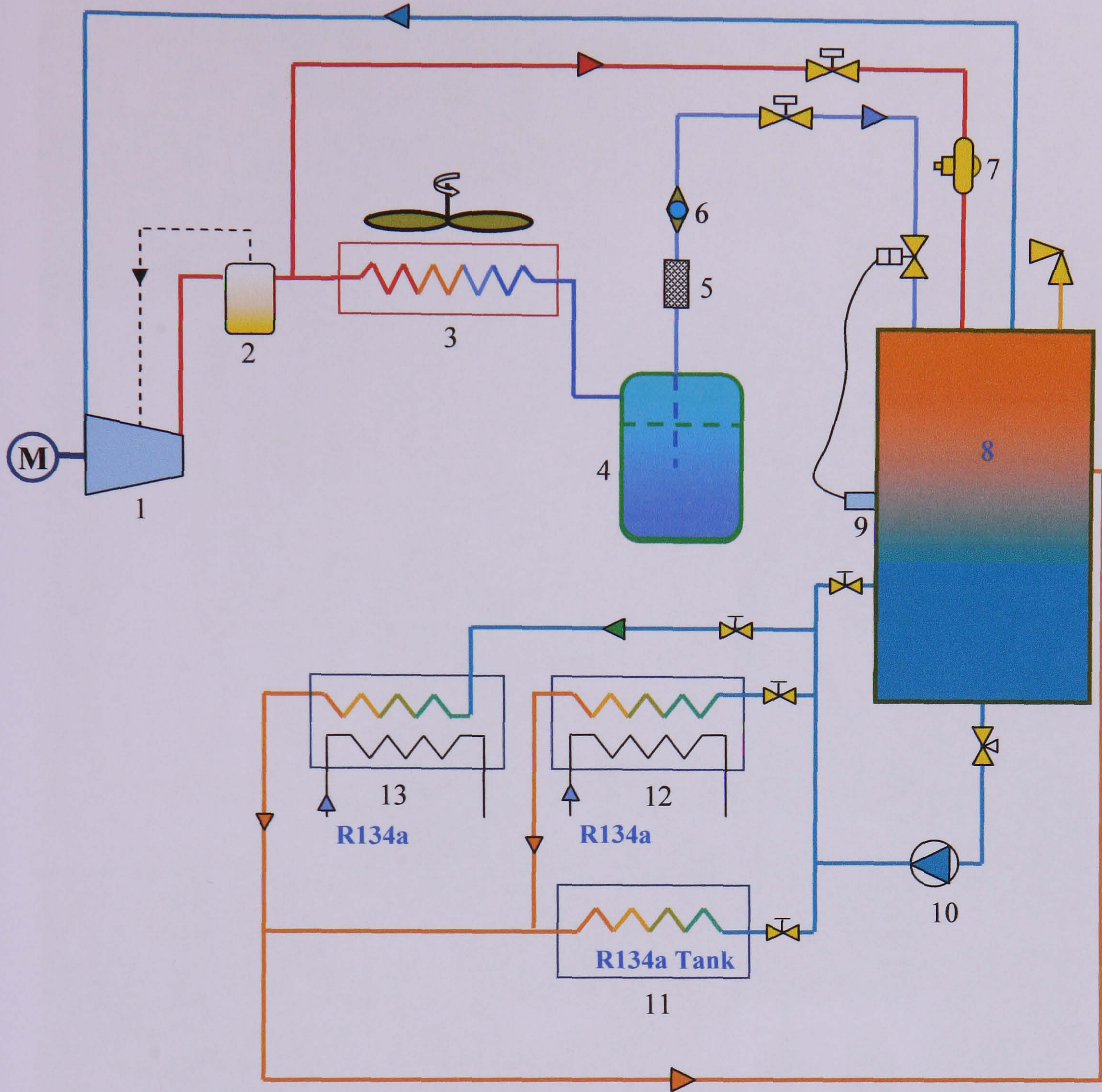


Figure 4.2 Photograph of the R134a experimental facility.

Auxiliary facilities

The indirect cooling at the different heat exchangers (6, 13 and 15 of Fig. 4.1) in the R134a main circuit is achieved using a refrigeration system. The schematic of the cooling system, which uses R22 fluid, is shown in Fig. 4.3. Also, a photograph of this cooling system is presented in Fig. 4.4. The main components of the cooling loop include compressor (1), oil separator (2), air-condenser (3), liquid receiver (4), flooding evaporator tank (8), gear pump (10) and heat exchangers (11, 12 and 13). The

compressor is a Bitzer type with cooling capacity of 12 kW. The high pressure and temperature vapour from the compressor is sent to the air-condenser through the oil separator. From the condenser, the relatively cold but high pressure liquid is collected in the liquid receiver. The liquid is then sucked by the low pressure evaporator tank. The fact that the system uses a flooded type of evaporator helps to have a more flexible and stable cooling system, i.e. there is no direct influence of the heat load (from the main circuit) on the compressor. As a result, the compressor can run continuously without the need to switch on and off depending on the load. The evaporator tank is also equipped with hot gas by-pass regulator (7), thermostatic-liquid level controller (9) and liquid level indicator. The hot gas bypass regulator ensures that there is not wet suction at the compressor inlet and works at a required setting pressure. When the evaporator pressure is lower than the set pressure, the hot gas bypass regulator reacts by opening a valve that by passes the hot gas from the compressor discharge. Incorrect setting of the regulator creates either a short circuit of the compressor, i.e. high pressure inlet to the compressor, or wet suction. The thermostatic liquid level controller controls an expansion valve, which creates freezing temperatures and low pressure. When the liquid level is below the position where the thermostat is installed, the gas in the line expands and acts upon the expansion valve to open and allow more liquid from the receiver. The cold liquid in the evaporator tank is pumped using a gear pump to the various heat exchangers as required. The cooling capacity at these heat exchangers is controlled by regulating the flow rate using needle valves installed in the respective R22 lines, see the schematics.



- | | | | | | |
|----|---------------------------|----|---------------|----|-------------------------|
| 1 | Compressor | 2 | Oil separator | 3 | R22 air-condenser |
| 4 | Receiver | 5 | Filter | 6 | Sight glass |
| 7 | Hot gas by-pass regulator | 8 | R22 tank | 9 | liquid level controller |
| 10 | Pump | 11 | Cooling coil | 12 | Subcooler |
| 13 | R134a condenser | | | | |

Figure 4.3 Schematic diagram of the R22 cooling system

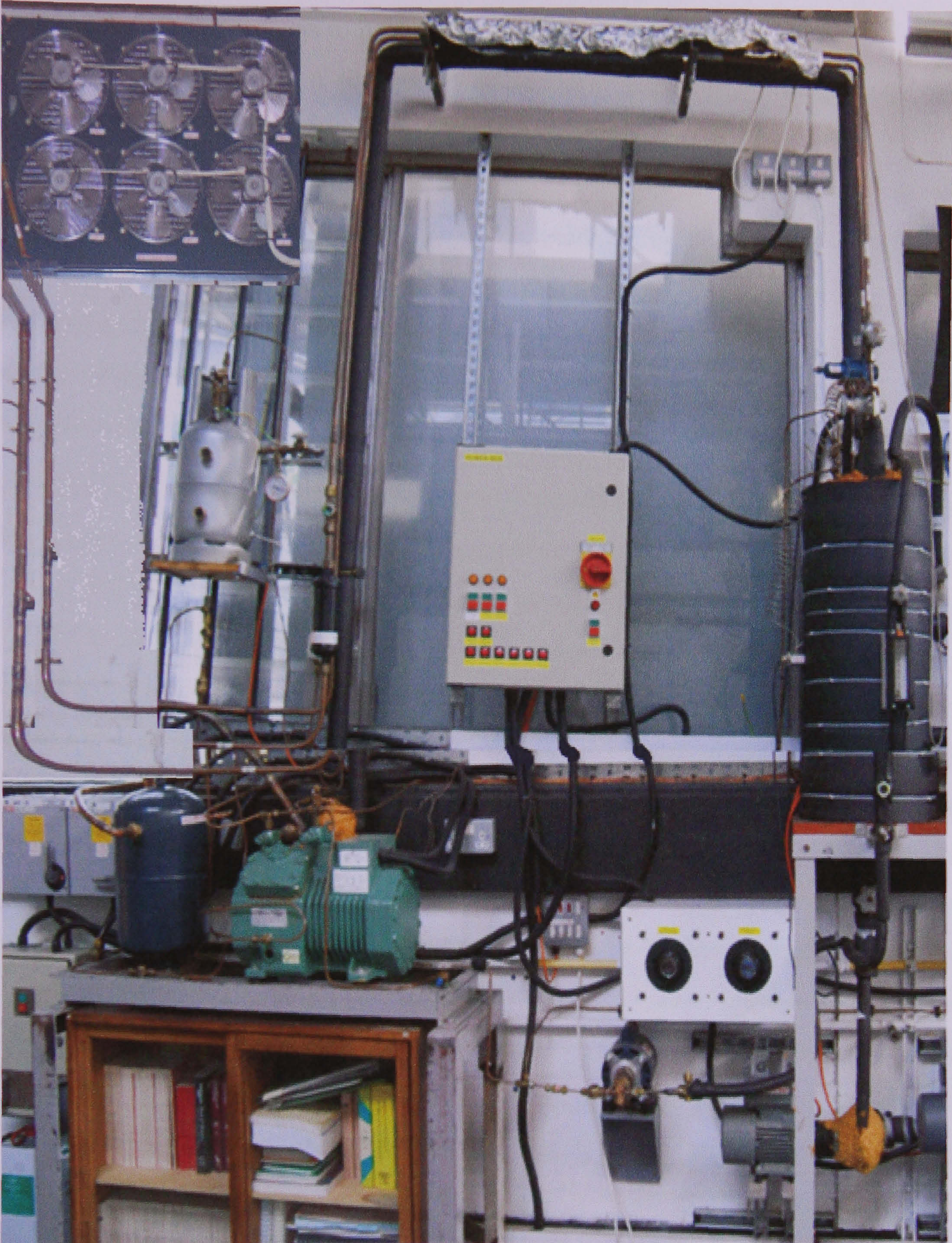


Figure 4.4 Photograph of the R22 cooling system.

In common with most vapour compression cycles, retaining the oil in the compressor is one of the experimental challenges. Hence, an oil-separator matching the compressor's capacity was fitted in the discharge line. This oil separator feeds the returning oil back to the compressor crank case. However, a considerable amount of oil is mixed with the refrigerant in the system. This is mainly because of the fact that the oil-separator is not 100% efficient and the location of the compressor, i.e. it was sitting on a stand with height above the lower part of the rig. One of the options devised to overcome the oil

loss in the compressor was to provide an external oil recovery system, Huo (2005). The oil recovery system has a refrigerant-oil mixture collecting reservoir fitted with an immersion heater and pressure safety valve and gear pump. When the oil in the refrigerant is settled at the bottom of the R22 cooling system, the refrigerant-oil mixture is pumped to the oil reservoir, where the refrigerant is separated from the oil by heating the mixture using an immersion heater. The vapour refrigerant from the reservoir is released to the system, while the oil collected at the bottom of the reservoir is returned to the compressor crank case by gravity. The oil in the compressor crank case is continuously heated to keep the oil viscosity low, even while the system is switched off. The facility was monitored using automatic switches controlled by the PID and data acquisition system. The data acquisition system consists of two data loggers Solartron models SI35951E and SI3535F, which are connected to the various sensors. The input signals to the data loggers include voltages from thermocouples, transducers, flow meters and power meters. For the test section wall and inlet and exit fluid temperature measuring thermocouples, the SI35951E data logger which is capable of withstanding up to 500 Volts difference with the ground, is used. The use of separate data loggers reduces the noise and allows having a separate electrical ground for the heated test section. Moreover, the sensors are connected to the data logger via a cold-junction ice box, which gives a reference temperature of 0 °C. Two personal computers are used to monitor, display the results and save the recorded data. One of these is connected to the high-speed visualisation camera to acquire the flow pattern images and videos. For the heat transfer section, a visual basic computer program written by (Huo, 2005 and Chen, 2006) was used as an interface to view the measured data, check steady state and record the data. On the other hand, the visualization section uses software supplied by Photo-Sonics with the high-speed camera. The software is used for acquiring, recording and processing images. It is also capable of making further analysis such as play backs at different speeds, converting to different file formats and measurements of distance, speed and acceleration between points or scenes.

Experimental Procedure

Once the inlet flow conditions required for a particular test are attained, single phase experiments are carried out for each flow rate and system pressure before commencing the two phase boiling experiments. These were performed in order to determine the loss coefficient, which is later used to predict the heat loss from the test section during two

phase flow boiling. In the current study, the inlet temperature was controlled at a subcooling of 1- 5 K by adjusting the capacity of the subcooler and heating power to the preheater. Subsequently, a series of flow boiling tests were performed by increasing the heat flux in small steps until the exit quality reached about 90 % at fixed mass flux, system pressure and inlet subcooling. The data were recorded after the system was steady at each heat flux, which normally took few hours at the start of the system (from standstill) and a maximum of 20 min between tests. The scanning rate of the data logger is ~ 6 sec, and each recording was the average of 20 consecutive measurements. The next test was then performed at different flow rate and system pressure in order to cover the entire test matrix. High-speed flow visualization is carried out directly at borosilicate glass tubes installed at the exit of the heated test section, simultaneously with the heat transfer tests. The two phase fluid after the visualization section is directed to the separator, where the two phases of R134a are separated. The liquid phase is returned back to the reservoir, while the dry vapour flows via the condenser to the reservoir. The operating instruction for the experimental facility is included in Appendix A.

4.2.1 Heat transfer test section

As mentioned in Chapter 2, there is no clear and common agreement on the definition and classification criterion for the size ranges in small/mini/microchannel in two-phase flow studies. One reason could be the lack of comprehensive heat transfer data covering a wide range of channel diameters. A complete definition for normal and small size tubes is required that considers all the fundamental phenomena, based on experimental data for a wide range of conditions. Therefore, one of the main objectives of this study is the systematic measurement of flow boiling characteristics of R134a over wide ranges of pressures, flow rates and heat fluxes in five tubes with internal diameters of 4.26, 2.88, 2.01, 1.10 and 0.52 mm. This choice of size range was based on an initial assessment using the Confinement number proposed by Cornwell and Kew (1993).

The test sections are made of stainless steel cold drawn tubes. Each test tube has a calming section, heated section and visualization section consecutively arranged as shown in the schematic diagram in Figure 4.5. A photograph of the actual test section is also shown in Figure 4.6 for one of the typical test tube. A calming section made of the same tube as the heated section is connected before the inlet to the heated section to provide a hydrodynamic development length and avoid the disturbance caused by

sudden contraction. The length of the calming section is different for different tube diameters. Table 4.1 presents the length of the calming section in comparison with that required for laminar and turbulent hydrodynamic development length. Hydrodynamic entry lengths for laminar and turbulent flows are given by the Equations (4.1) and (4.2), respectively. In the case of laminar inlet conditions, the hydrodynamic entry length is dependent on Reynolds number. Hence, the values are calculated only for tubes with laminar inlet condition and if the corresponding mass flux is greater than 100 kg/m²s (the minimum mass flux range)

The hydrodynamic entry length for the laminar flow regime is given by Durst et al. (2005) as,

$$\frac{L}{D} = \left[0.619^{1.6} + (0.0567 * Re)^{1.6} \right]^{1/1.6} \quad (4.1)$$

On the other hand, in the turbulent flow regime the entry length depends only of the tube diameter and it is given by Kays (1980) as,

$$10 \leq L/D \leq 60, \quad (4.2)$$

For the calculated values shown in Table 4.1, $L/D = 50$ was taken.

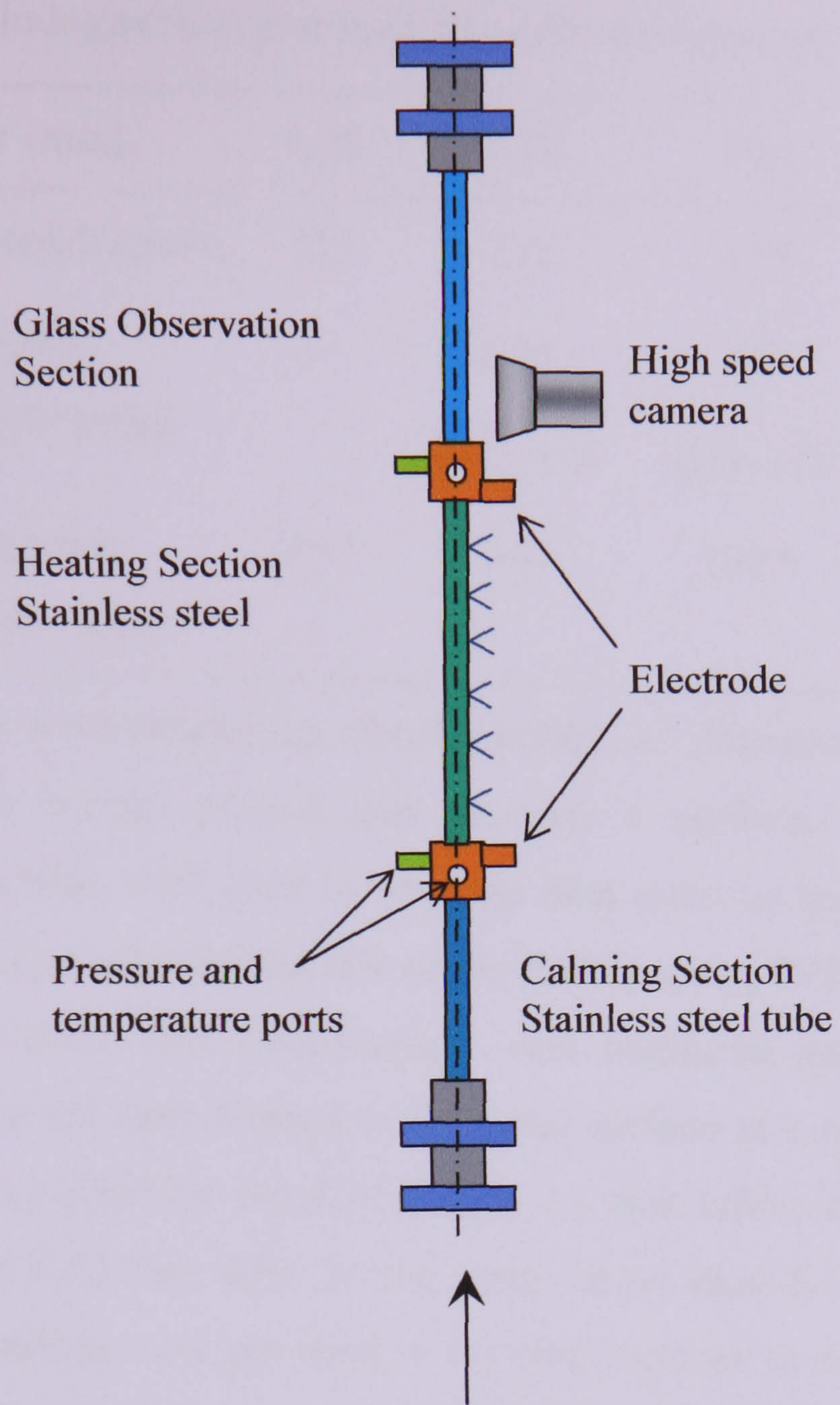


Figure 4.5 Schematic diagram of the test section

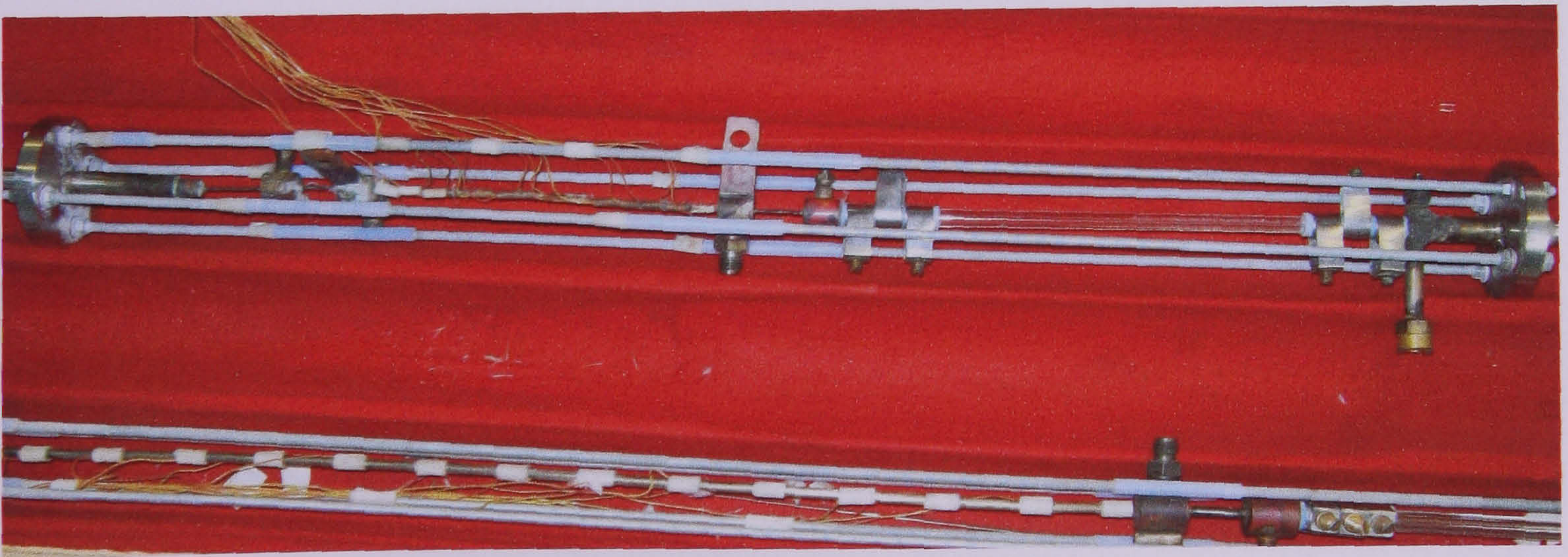
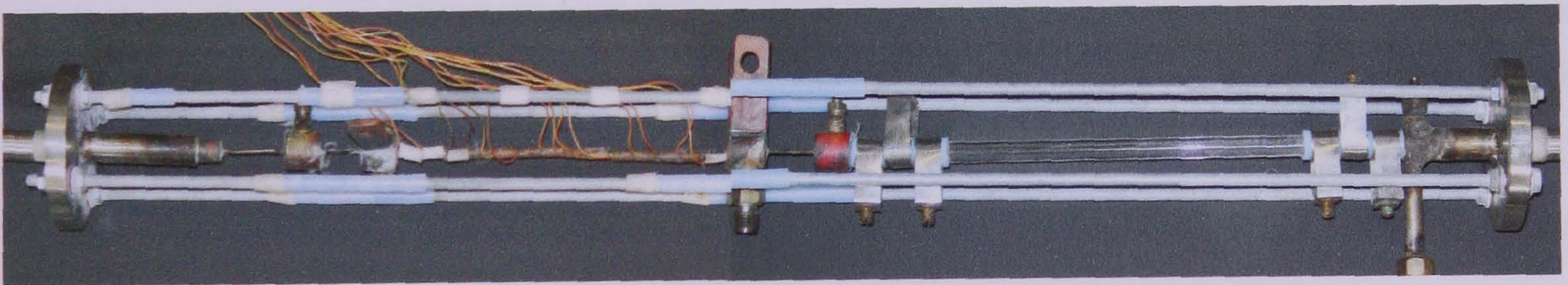


Figure 4.6 Photograph of the actual test section.

Table 4.1 The calming section and hydrodynamic development lengths.

Internal Diameter (mm)	4.26	2.88	2.01	1.10	0.52
calming section length (mm)	235	225	175	100	150
laminar hydrodynamic development length) (mm)	-	326	228	124.8	60
		@G~125	@G~179	@G~327	@G~690
turbulent hydrodynamic development length (mm)	213	144	100.5	55	26

The test sections were heated by direct passage of alternating electric current (low voltage and high current power) that provides a uniform heat flux condition. A transformer and variac were used to vary the heat input or heat flux. The test section was electrically insulated from the rest of the facility using PTFE at the top and bottom of the tube. The outer wall temperatures were measured using ungrounded K-type thermocouples that are spot welded to the outer surface at a uniform spacing. Fifteen thermocouples were used for the 4.26 mm to 1.1 mm tubes, while ten thermocouples were used for the 0.52 mm tube. In the tubes larger than 1.1 mm, the first and last thermocouples readings were not used in the data analysis so as to avoid errors due to thermal conduction to the electrodes. On the other hand, for the 0.52 mm tube, the two thermocouples at each end were located sufficiently far from the electrodes to be included in the analysis. The pressures and temperatures at the inlet and outlet were measured using pressure transducers (PDCR 4010 and PDCR 910-0826) and T-type needle probes (grounded thermocouples). A differential pressure transducer (PX771-100WDI) was installed across the test section to provide the pressure drop measurement. Table 4.2 provides the lengths of the heated section, the pressure drop length and the thickness of each tube.

Table 4.2 Heated length and wall thickness for each tube

Internal diameter	4.26	2.88	2.01	1.1	0.52
Heated length	500	300	211	150	100
Pressure drop length	521	321	233	165	108
Wall thickness	0.245	0.15	0.19	0.247	0.15

All dimensions in mm

In this study the roughness of the test-tubes is considered to have an effect not only on the pressure drop but also on the dryout phenomena and nucleation characteristics especially of the smallest tube (these will be discussed in more detail in the coming chapters 5, 6 and 7). Therefore, it is recommended that internal surface conditions of test tubes should be known. Consequently, roughness measurements were made for all the five test tubes. For the 4.26 mm to 1.1 mm tubes, the roughness was measured by Taylor Hobson Limited, UK. The measurement report stated that the measurement was made using conventional contact stylus with 2 μm stylus tip and 0.8 mm filter cut-off, at four positions nominally 90 degrees apart. The stylus traverses in axial direction along the sample starting at 100 mm in from one end face. The sketch provided by Taylor Hobson Ltd. is included in Fig. 4.7. Although it is not clear how roughness measurements of the above kind will indicate nucleation site characteristics or distributions, it is believed to provide comparative information among the different tubes.

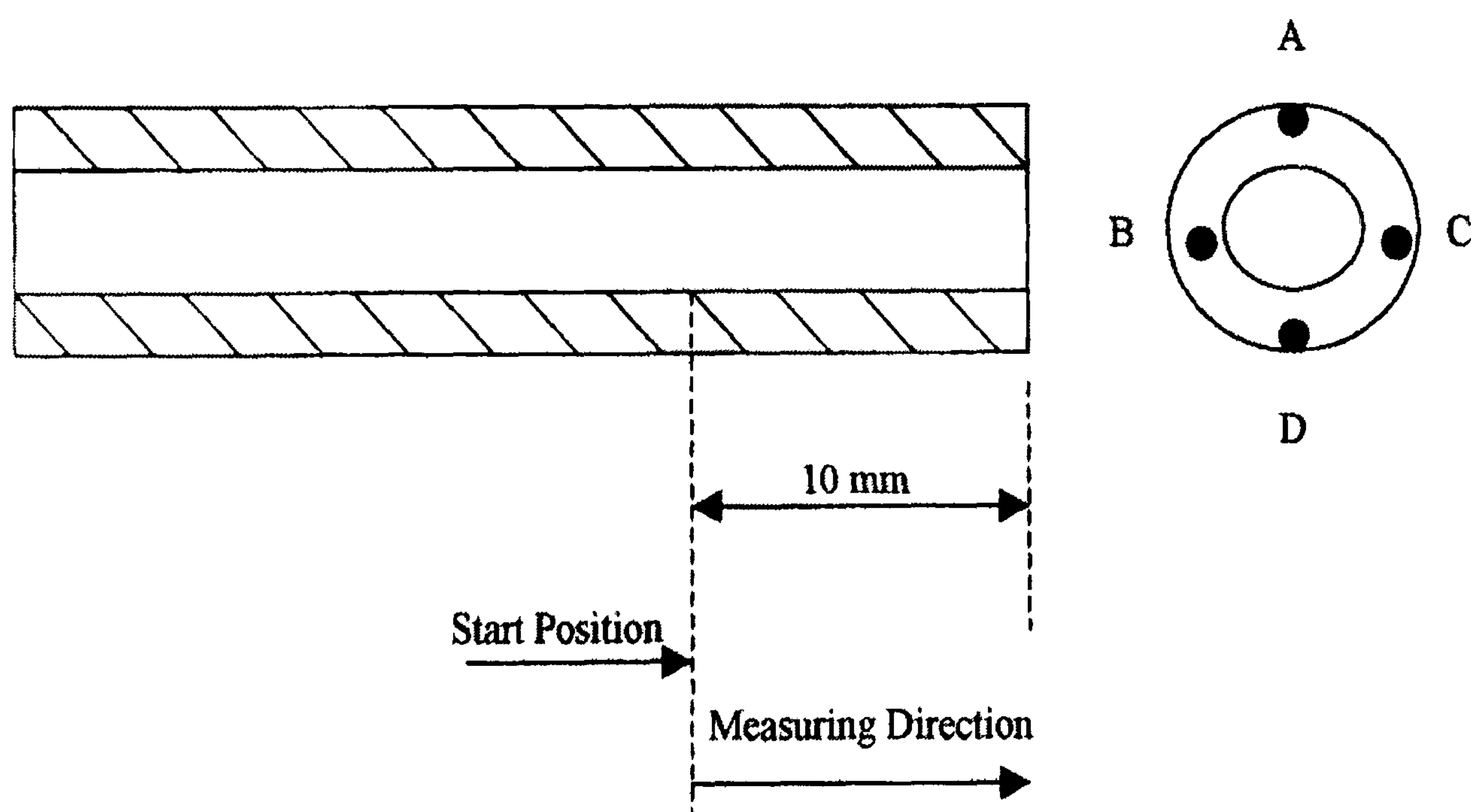


Figure 4.7 Schematics showing positions of roughness measurement (Taylor Hobson Ltd.)

The method of roughness measurement for the 0.52 mm tube is different from the rest of the tubes and was carried out at the Institute for Thermodynamics, University of Hannover, Germany, where they have a long term experience in surface characterization for boiling. Surface characterization of very small tubes is extremely challenging and time consuming. It is difficult to make accurate measurement without interference from the sample preparation technique in such a very small surface. The surface roughness

measurement facility at Hannover University uses a high-resolution non-contact probe, which is a state-of-the-art technique, see Figure 4.8.

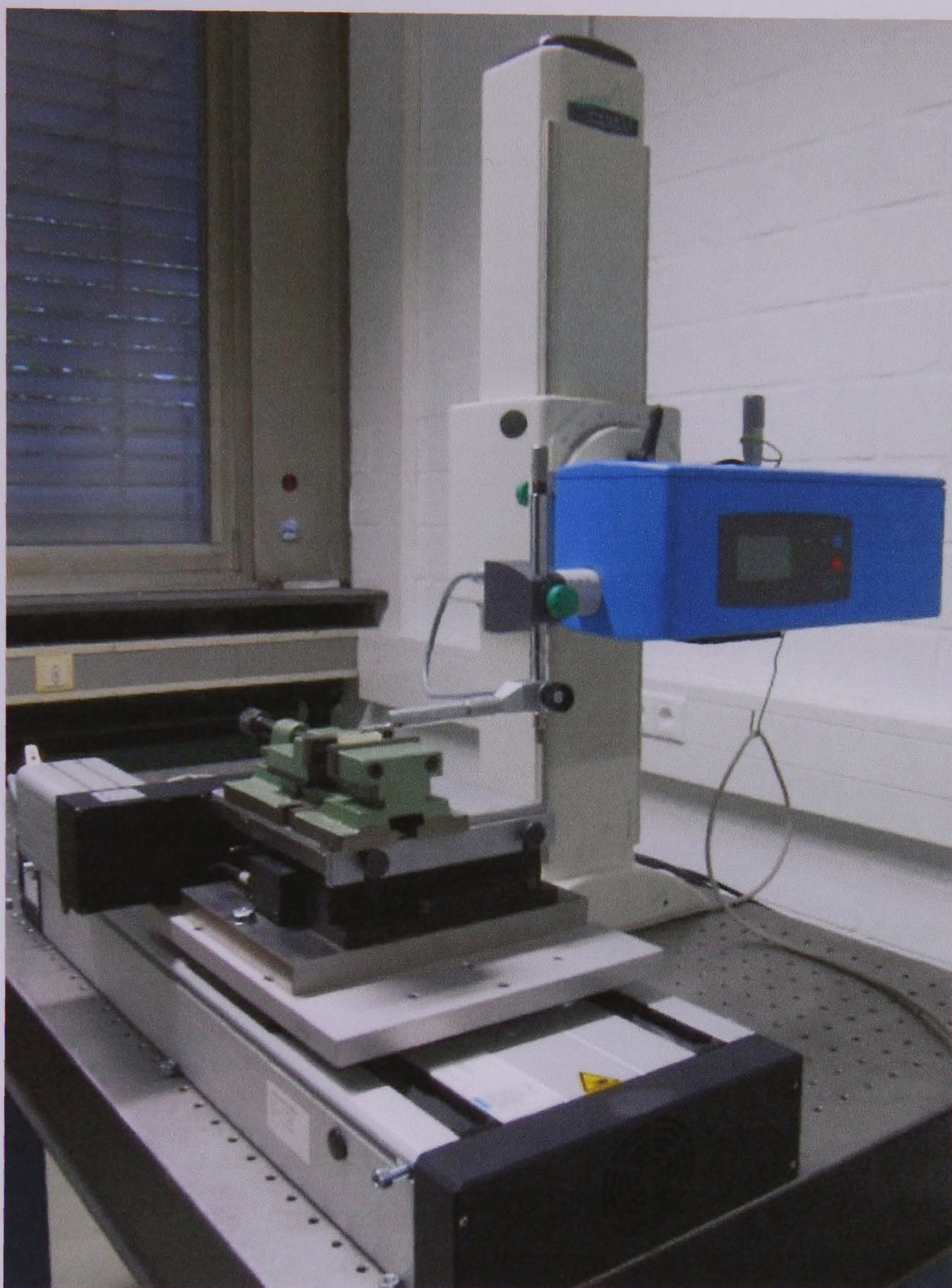


Figure 4.8 The high resolution non-contact roughness measuring instrument (Hommel) at the Institute for Thermodynamics, University of Hannover, Germany, (with permission, Prof. A. Luke).

Figure 4.9 shows a photograph of the 0.52 mm sample, which was prepared by inserting the tube inside a rectangular-block using resin and sectioning the assembly across a chord of ~ 0.187 mm . The 3-D roughness of the sample was then measured.

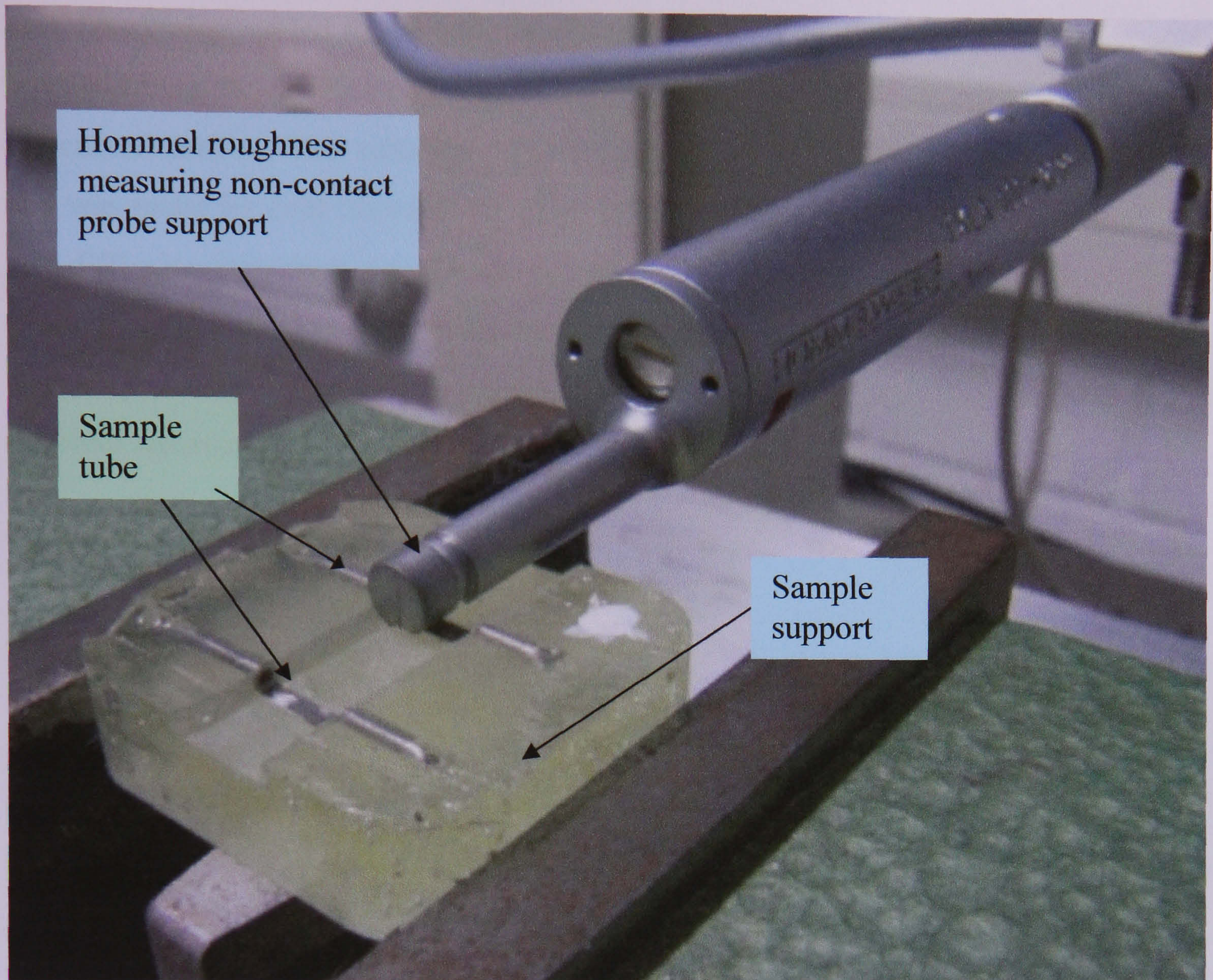
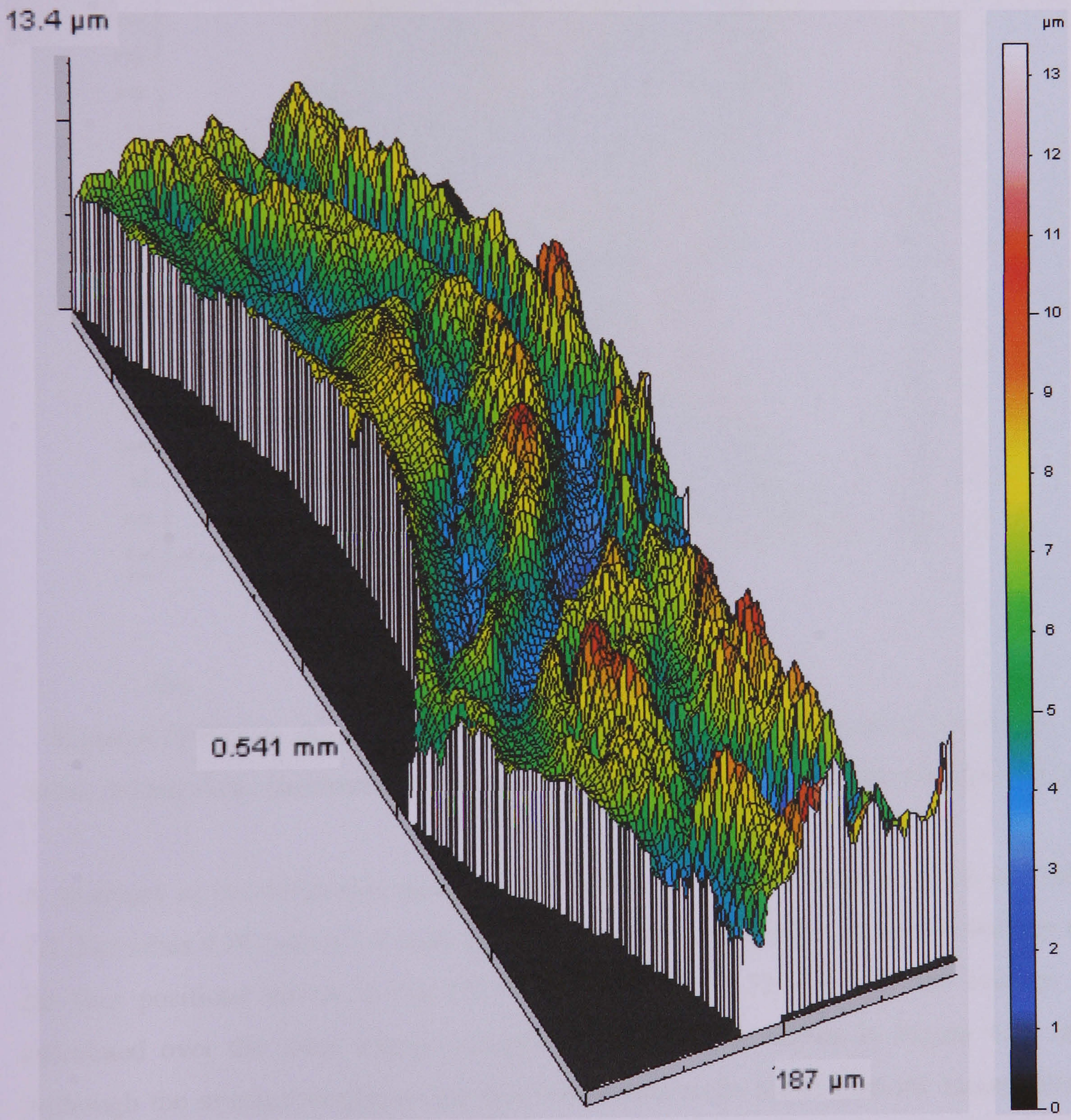


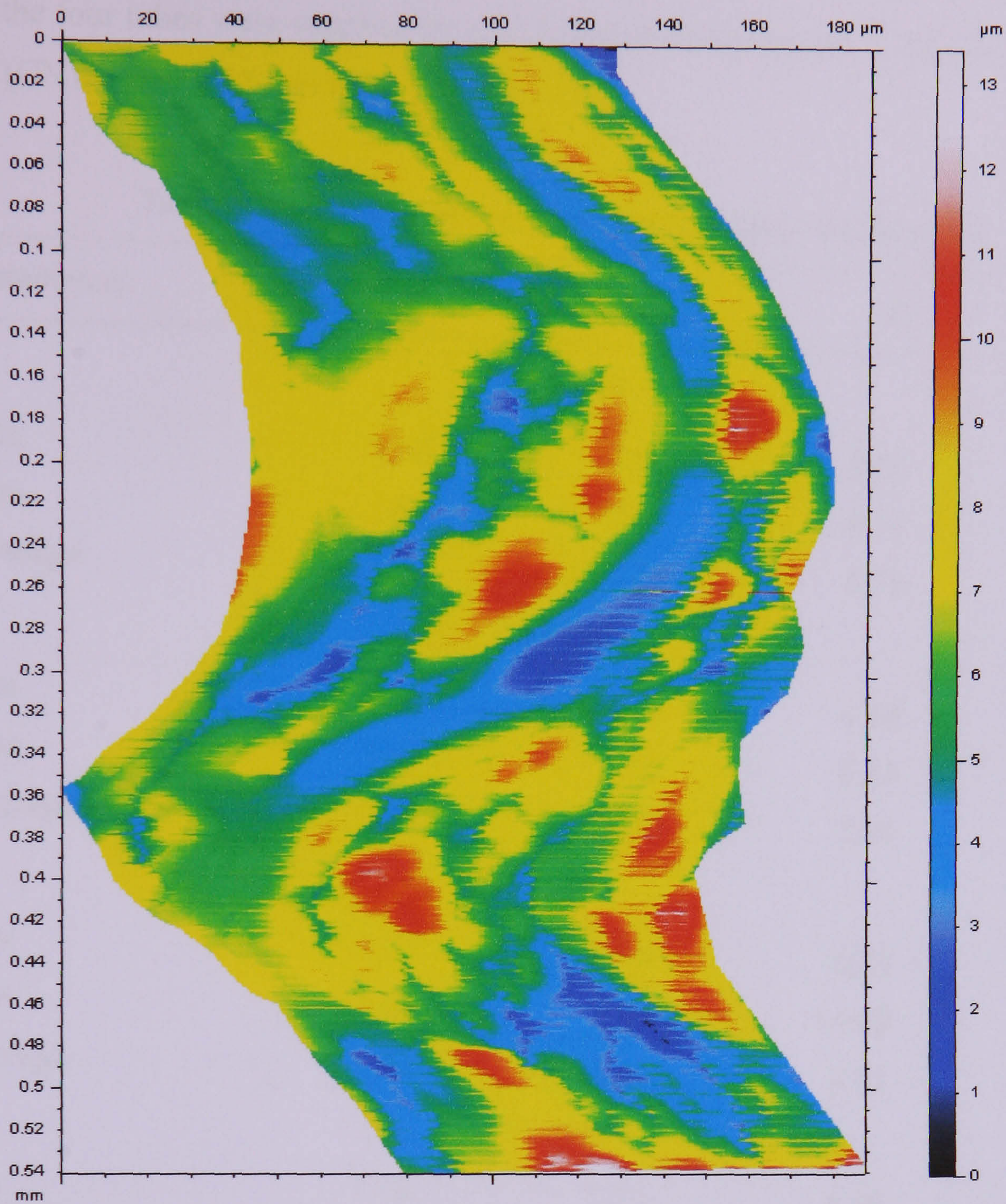
Figure 4.9 Sample preparation of the 0.52 mm tube (Institute for Thermodynamics, University of Hannover, with permission, Prof. A. Luke).

The measurements are still being analysed but preliminary results showing a 3-D isometric view of a sample 0.541mm long and ~ 0.187 mm wide is included in Figure 4.10. The stylus traverses in the radial direction, i.e. across the chord, making 550 measurements over a distance of 0.187 mm. After it finishes the radial motion, it shifts axially by $0.5 \mu\text{m}$, i.e. ~ 1100 runs were made axially. The 3-D figure shows roughness results as high as $11 \mu\text{m}$. Figure 4.10 (b), the top of view of the microtube sample shows the channel does not have a uniform cross section throughout the length. As seen in figure 4.10, a sharp curvature effect with approximate lateral amplitude of $45 \mu\text{m}$ (compared with internal diameter of $520 \mu\text{m}$) with a half wavelength of $360 \mu\text{m}$ is observed over a sample length of $541 \mu\text{m}$. This effect, which is believed to be the result of the manufacturing process may have a significant implication on the results to be presented later, although the sample length is too short to make a general conclusion. As mentioned above, these results are still under investigation, since sample preparation is

time consuming, added to the additional work created by the presence of the curvature in re-adjusting the position of the probe time-to-time to measure the actual roughness in the curved surface. This tube was supplied by a company called Ice Oxford Company and was made by cold drawing. Finding such small size seamless tubes in the market was difficult relatively to welded tubes of same size. Relying on commercially available products with no standard method of controlling the internal surface condition adds another problem to the heat transfer measurements and raises reproducibility issues in different laboratories.



(a)



(b)

Figure 4.10 Picture showing the 0.52 mm sample with its dimensions: (a) isometric view, (b) top view. (Institute for Thermodynamics, University of Hannover, Germany).

A summary of the roughness measurement values for the five tubes is given in Table 4.3. For tubes 4.26 mm to 1.1 mm, the average value given is the arithmetic average of the four positions shown in Fig 4.7. Whereas for the 0.52 mm tube the average is calculated over the short sample across circumference as shown in Figure 4.10 (a). Although the average roughness for this tube seems to be lower than the larger tubes, the single phase friction factor (which will be reported later) is much higher than the conventional correlations. This indicates the roughness average along the axes is relevant, which could be larger than the tubes with diameter 4.26 mm to 1.1 mm. Note

that the four tubes were supplied by a different company named Coopers Needle Works Ltd. (CNW) than 0.52 mm tube.

Table 4.3 Summary of the measured roughness of the tubes.

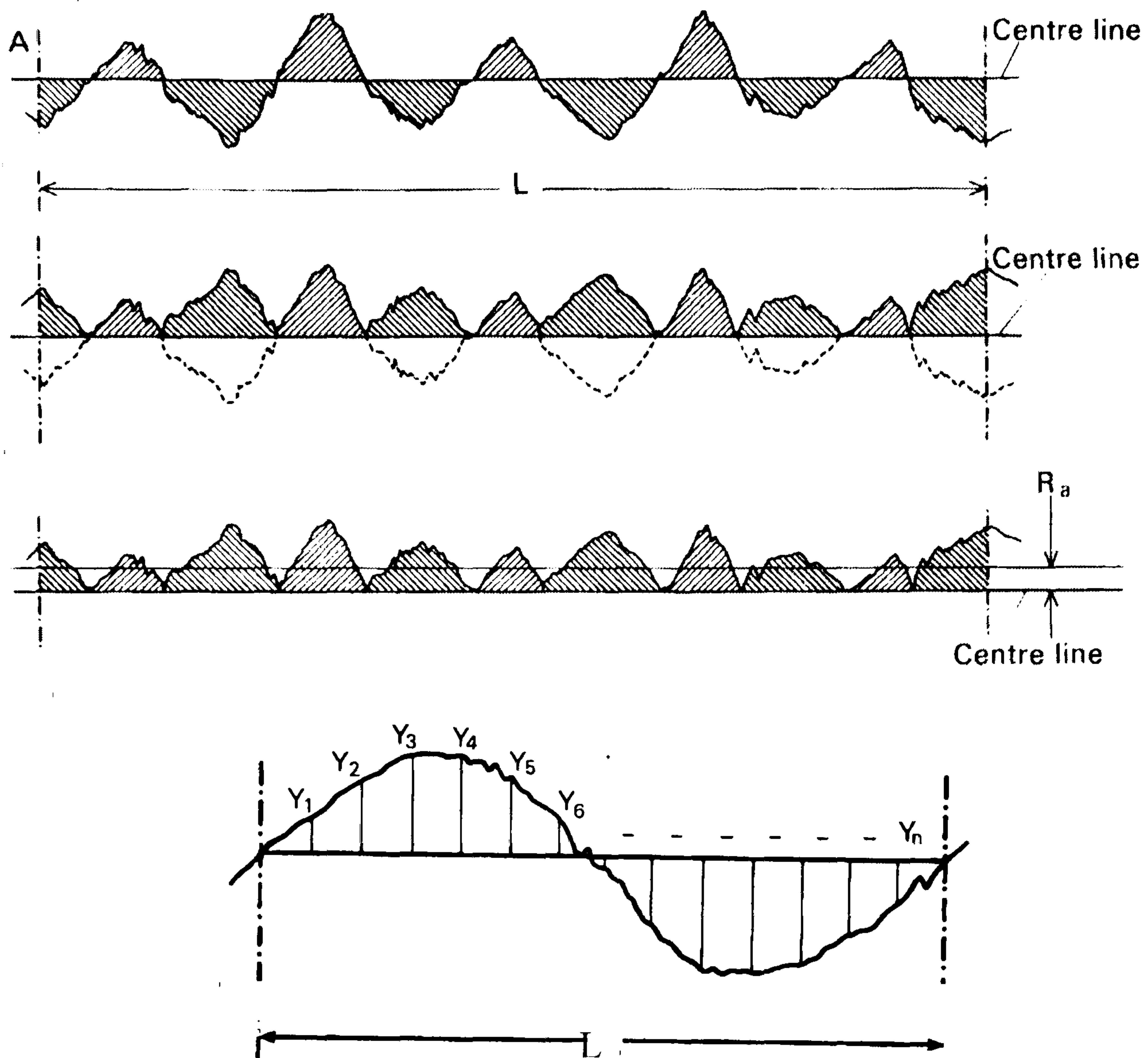
Parameters	R_a	R_q	R_p	R_t
4.26 mm				
Min	1.64	2.03	5.06	12.54
Max	1.93	2.51	8.16	14.65
Average	1.74	2.25	6.78	13.14
2.88 mm				
Min	1.54	1.83	4.18	9.35
Max	1.59	1.96	6.33	12.17
Average	1.54	1.89	5.26	10.70
2.01 mm				
Min	1.74	2.24	6.23	16.89
Max	1.88	2.49	14.09	20.91
Average	1.82	2.36	9.01	18.40
1.10 mm				
Min	1.18	1.51	4.59	10.00
Max	1.34	1.86	16.57	20.94
Average	1.27	1.68	8.18	12.94
0.52 mm				
Min	0.80	0.96	1.66	4.17
Max	1.90	2.35	6.05	11.46
Average	1.16	1.47	3.47	7.47

Different parameters are used to represent roughness. ISO definitions of the various roughness parameters used in the Table 4.3 are briefly provided below to help understand the measured values listed in the table.

Average roughness (R_a)

R_a is most commonly used roughness parameter in surface texture analysis, but does not give any information regarding the irregularities. The equation for evaluating R_a is

given in Eq. (4.3). The sampling length (L) should also be provided to make the parameter meaningful. Figure 4.11 describes how the R_a is evaluated.



$$R_a = \frac{|y_1| + |y_2| + \dots + |y_n|}{n} \quad (4.3)$$

Figure 4.11 Sketch showing how average roughness is calculated

Root Mean Square (RMS) value (R_q),

It is usually referred to as R_q and is obtained by squaring each value and taking the square root of the mean, Eq. (4.4).

$$RMS = \sqrt{\frac{y_1^2 + y_2^2 + \dots + y_n^2}{n}} \quad (4.4)$$

Peak to valley heights (R_t)

It is the vertical height between the highest and lowest points of the profile within the evaluation length.

R_p is the height of the highest point of the profile above the centre line within the sampling length, see Fig. 4.12.

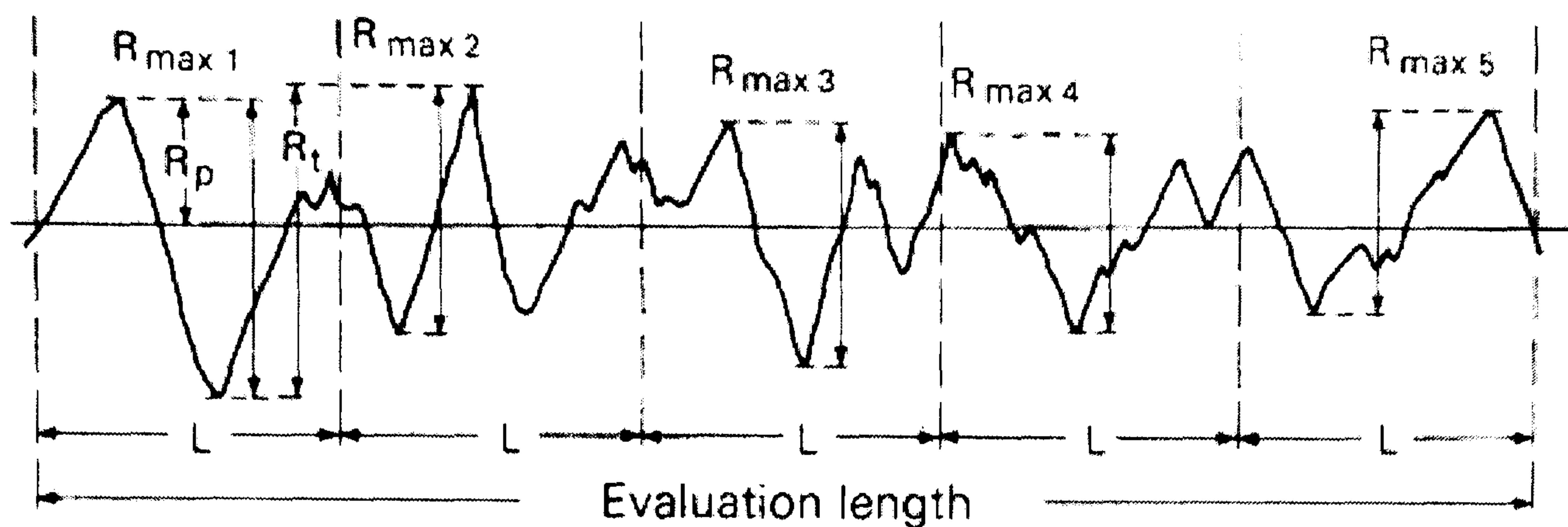


Figure 4.12 Sketch describing how peak to valley parameters are evaluated

4.2.2 Flow visualization test section

At the exit to the heating section, a borosilicate glass tube with an internal diameter matched to the test section is installed for flow pattern observation. The purpose of the visualization experiments in this study is to support the understanding of the heat transfer characteristics by relating the flow regimes with the heat transfer results. This is the reason that the flow visualization was performed immediately after the exit of the heated section, although strictly direct relation could not be made due to the fact that flow pattern developments may occur inside the heat transfer section. The pressures and temperatures at the inlet and outlet of the glass tube were measured using pressure transducers (PDCR 910-0826) and T-type needle probes (grounded thermocouples). A digital high-speed camera (Phantom V4 B/W, 256 x 512 pixels resolution, 1900 pictures/sec or 526 μ s interval between images, 80 μ s exposure time) was used to observe the flow patterns. However, at much reduced resolution (128 x 32 pixels) the frame rate can reach up to 32000 pictures/sec. The high frame rate per second means it is possible to capture image details that happen fast such as phenomena related to boiling. Figure 4.13 shows a photograph image of the visualization section with the high speed camera positioned to take pictures with two halogen light lamps standing on both sides.

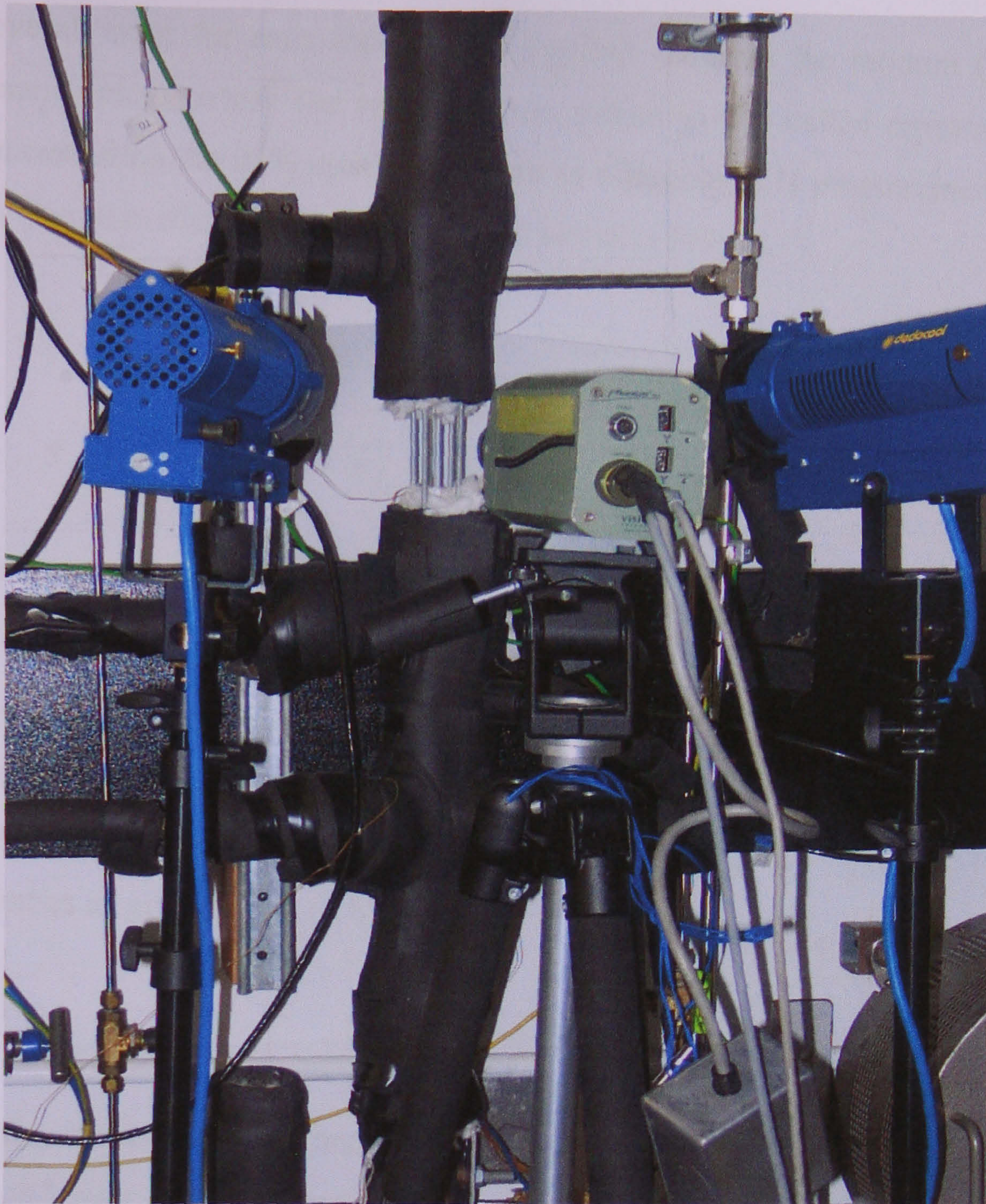


Figure 4.13 Photograph of the high-speed camera positioned to take pictures.

The dimensions of the visualization section, i.e. length and external diameter for the five glass tubes are included in Table 4.4.

Table 4.4 Glass tube dimensions

Internal diameter (mm)	4.26	2.88	2.01	1.10	0.52
Outside diameter	9.4	7.8	7.6	7.8	7.8
Length	450	450	300	200	80
Length recoded on video	30	30	20	20	20

4.3 Measurement accuracy

All the measuring sensors and instruments were carefully calibrated. A thorough error analysis were also carried out to quantify the accuracy of the measuring probes as well as the calculated data based on the method given in Coleman and Steele (1999).

The overall error for each independent variable contains the random (precision) and systematic (bias) errors. The random error, which is also called repeatability error, is determined using the 95% confidence limit of a sample of N measurements of X drawn from a Gaussian distribution Coleman and Steele (1999) as,

$$U_{ra} = t_{95} S_x \quad (4.5)$$

where, $S_x = \left[\frac{1}{N-1} \sum_{i=1}^N (X_i - \bar{X})^2 \right]^{1/2}$ is the standard deviation of the sample population.

A table of values for t_{95} at different number of samples is included at the appendix of the book by Coleman and Steele (1999).

The systematic error incorporates calibration, data acquisition, data reduction and conceptual errors. For a measurement of X_j parameter, the overall systematic error is calculated as a root-sum-square (RSS) combination of elemental systematic uncertainties as given in Eq. (4.6)

$$U_{sys} = \left[\sum_{k=1}^M (B_j)_k^2 \right]^{1/2} \quad (4.6)$$

where, $(B_i)_k$ is the systematic uncertainty for each element and can be estimated for each variable X_i from manufacturer's specification or analytical estimates. However, this must be updated using the accuracy of the calibration standards and curve-fit procedures.

The total error for the independent variable X is therefore given by Coleman and Steele (1999) as

$$U_X = \sqrt{U_{ra}^2 + U_{sys}^2} \quad (4.7)$$

For the calculated parameters (dependent variable, r), the data reduction equation of the form, Eq. (4.8), was used to propagate the error and estimate for the uncertainty of a general variable r ,

$$r = r(X_1, X_2, \dots, X_J) \quad (4.8)$$

The uncertainty for variable r is therefore given by Coleman and Steele (1999) as,

$$U_r = \left[\left(\frac{\partial r}{\partial X_1} U_{x_1} \right)^2 + \left(\frac{\partial r}{\partial X_2} U_{x_2} \right)^2 + \dots + \left(\frac{\partial r}{\partial X_J} U_{x_J} \right)^2 \right]^{1/2} \quad (4.9)$$

The experimental ranges of these parameters need to be defined, in order to be able to estimate the experimental errors for various measured and calculated parameters. Table 4.5 summarizes the experimental range for the boiling experiments.

Table 4.5 Range of experimental parameters

Parameters	Range
Internal Diameter (D_i)	4.26 - 0.52 mm
Heated length (L)	500 - 100 mm
Mass flux (G)	100 – 700 kg/m ² s
Heat flux (q)	1.6 – 150 kW/m ²
Pressure (P)	6, 8, 10, 12, and 14 bar
Degree of inlet subcooling (ΔT_{sub})	1-5 K
Vapour quality (x)	0-0.9

The uncertainty results of the various parameters are discussed below.

Internal tube diameter

The uncertainty results for the larger tubes ($D_i > 1.1$ mm) were reported in Chen (2006). The internal diameter of the tubes has been calculated by measuring the external diameter (D_o), length (L) and weight (W) of a sample from each tube. The same method was followed for the 0.52 mm tube. The external diameter and the length of the samples were measured using a Vernier Caliper with minimum scale of (1/100 mm) while a digital-weigher with microgram scale was used for weighing the sample. The uncertainty of the internal diameter was calculated following the above uncertainty analysis and is given in Eq. (4.11), as:

$$D_i = D_o - \sqrt{\frac{4W}{\pi \rho L}} \quad (4.10)$$

$$U_D = \sqrt{\frac{\left(2D_o U_{D_o}\right)^2 + \left(\frac{4W U_L}{\pi \rho L^2}\right)^2 + \left(\frac{4U_W}{\pi \rho L}\right)^2}{4 \left(D_o^2 - \frac{4W}{\pi \rho L}\right)}} \quad (4.11)$$

This method assumes that the density of the material provided by the manufacturer is accurate value. The measurements were repeated several times at different locations. The uncertainty results of the stainless steel tubes are given in Table 4.6.

Table 4.6 Uncertainty results for the internal diameter of the stainless steel tubes (4.26 – 1.1 mm, Chen 2006)

Calculated internal diameter (mm)	Uncertainty (%)
4.26	0.26
2.88	0.38
2.01	0.59
1.10	1.31
0.52	2.8

For 4.26 mm to 1.1 mm glass tubes, the internal diameter was estimated by deducting the weight of the empty tube from water-filled glass tube and calculating the internal diameter from the weight of the water, Chen (2006). However, for the 0.52 mm the same method as that of the steel tubes was used and later re-checked using optical microscope.

Table 4.7 Uncertainty results of the internal diameter of the borosilicate glass tubes (4.26 – 1.1 mm, Chen 2006)

Calculated internal diameter (mm)	Uncertainty (%)
4.26	0.11
2.88	0.06
2.01	0.17
1.10	0.36
0.52	0.19

Heated length

The heated length of the test section is the vertical length between the electrode connections. It was measured using Vernier caliper with accuracy of $\pm 100 \mu\text{m}$. Therefore, the uncertainty of the heated length for each tube as a result of the measuring device is given in Table 4.8.

Table 4.8 Uncertainty results of the heated length measurements

Internal diameter (mm)	Measured heated length (mm)	Uncertainty (%)
4.26	500	0.02
2.88	300	0.033
2.01	211	0.047
1.10	150	0.67
0.52	100	0.1

Temperature

The wall temperatures measuring thermocouples are K-type (Chromel – Alumel) wires, while the fluid temperature at the test section inlet and outlet was measured using T-type (Copper–Constantan), grounded needle probes. These crucial temperature sensors for the experiments, i.e. test section wall and inlet and outlet fluid measuring thermocouples, used an external reference temperature for improved accuracy. This was obtained by means of water triple point (mixture of water and ice in an external box, ~0.01 °C accuracy). All the other thermocouples used an internal reference point (cold junction compensation), which was regulated by the data logger. The thermocouples were calibrated using standard calibrating equipment. A calibrating bath with refrigerator unit (RCTB 3050) was supplied by Omega and works in a range of temperature -20 to 80 °C. Platinum (Pt 100) resistance probe supplied by Automatic Systems Laboratories (ASL) (a division of Hartest Precision Instruments) was used as standard thermometer. This has maximum error of 0.01K and is capable of measuring a maximum temperature of 250 °C. The uncertainty analysis of each temperature sensor consists of the errors from the data logger, calibrator and curve fitting equations. The results are summarised in Table 4.9.

Table 4.9 Uncertainty values for temperature sensors.

Thermocouple location		Type	Absolute Error (K)
Flow meter inlet	T1	K type ungrounded probe	0.79
Preheater inlet	T2	K type ungrounded probe	0.11
Test section inlet	T3	T type grounded needle probe	0.16
Test section exit	T4	T type grounded needle probe	0.16
Glass section exit	T0	T type grounded needle probe	0.16
Condenser exit	T5	K type ungrounded probe	0.79
R134a Tank	T6	K type ungrounded probe	0.79
Test section wall * (4.26 – 1.1 mm)	T_{w1-15}	K type thermocouple wires	0.16
Test section wall (0.52 mm)	T_{w1-10}	K type thermocouple wires	0.15

* Huo (2005)

Pressure

Five pressure transducers were installed at different locations as described in section 4.2. They used a 12 V DC power supply and provide analog output signal to the data logger (SI 3535F). The digital voltage from the data logger is then converted to pressure (bar) by the respective calibration equations. These pressure sensors were calibrated using a dead weight tester (Barnet Instrument Ltd, accuracy 0.1%). The calibration was made for the whole experimental range (6.0-14.0 bar), see Huo (2005) and Chen (2006). The error for each pressure sensors was calculated considering the systematic error of the sensors (manufacturers' data), systematic error of the data logger, the accuracy of the calibrator and the accuracy of the curve-fit. The sensor specifications and overall error from each pressure transducer are summarized in Table 4.10.

Table 4.10 Uncertainty values for pressure transducers, (Chen, 2006)

Pressure transducer location	Model (Supplier)	Measuring range	Error (%)
Flow meter inlet (P1)	GP series (RS)	0-40 bar gauge	0.25
Preheater inlet (P2)	PDCR 4010 (Druck)	0-10 bar abs.	0.24
Test section inlet (P3)	PDCR 4010 (Druck)	0-20 bar abs.	0.27
Test section exit (P4)	PDCR 910-0826 (Druck)	0-10 bar abs.	0.26
Glass section exit (P0)	PDCR 910-0826 (Druck)	0-10 bar abs.	0.26
Condenser exit (P5)	GP series (RS)	0-40 bar gauge	0.31

Flow meters

As discussed above, the flow rate to the test section was measured using two Coriolis flow meters working in different ranges supplied by Micro Motion Ltd. It is claimed that they offer the most accurate measuring technique. Therefore, they did not need to be calibrated against any other standard device at the laboratory. Instead calibration was carried out at the manufacturer's site and the calibration results were provided by the manufacturer. The results were then combined with the error introduced by the data logger to determine the overall accuracy. Although these flow meters are known to be most accurate, the measuring error increases as the flow rate decreases, i.e. near zero flow rate the error becomes significantly high. Therefore, the largest error from these devices occurs at the lowest mass flux condition, i.e. for the case of the smallest tube (0.52 mm) experiments. In the present study, the minimum flow rate is 0.23 kg/hr, and the corresponding accuracy is 1.05 %. For the rest of the tubes, with relatively larger flow rates, the accuracy ranges from 0.15 to 0.54 %.

Differential Pressure transducer

Although pressure transducers are installed at the inlet and outlet of the test section, the pressure drop across the test section was measured directly using a differential pressure transducer (PX771-100WDI of Omega). Deducting the two absolute pressures could not give accurate result, due to measuring time lags or leads introduced by the data logger scanning speed. The differential pressure transducer was calibrated by measuring the hydrostatic pressure drop and the liquid level height, Chen (2006). Therefore, the

uncertainty of the pressure drop includes the errors from measuring the liquid level (± 0.001 m), the resistor that converts the milli-Amp output to milli-Volt, the data logger, and curve-fit equation. The maximum absolute combined error was ± 70 Pa.

Power meter

The power input to the preheater and test section was measured using a digital power meter. The AC power supply to the test section was connected through a transformer with ranges of voltage (0 – 28 V) and current (0-200A) to step up the current, since the heating requires high current and low voltage. However, the measuring range of the power meter is up to 20 A. Therefore, another current transformer that steps down the current to a measurable range was necessary. The uncertainty of the measured power consists of the errors from the current transformer and the power meter itself, both are provided by the manufacturer. The overall uncertainty ranges from 0.10 to 0.49 %.

Fluid properties

Thermodynamic properties for R134a were obtained using the fundamental equation of state developed by Tillner-Roth and Baehr (1994). Transport properties are taken from correlations developed by Huber et al. (2003) for viscosity, by Assael et al. (1999) for thermal conductivity and McLinden et al. (1995) for surface tension. These equations are functions of pressure and temperature. In the uncertainty analysis of calculated results that involve property data, the errors from determining the fluid properties were also included.

Propagated errors

So far the error analysis results for the directly measured parameters are discussed. Data reduction equations will be required, in order to examine the uncertainty analysis of the calculated parameters. The uncertainties of the main calculated parameters such as mass flux, heat flux and quality will be given below, while the overall error associated with determining the local heat transfer coefficient will be addressed in the experimental data reduction section.

Mass flux

Mass flux is determined from the mass flow rate and tube internal diameter measurements as,

$$G = \frac{4\dot{m}}{\pi D_i^2} \quad (4.12)$$

The uncertainty of the mass flux (U_G) is therefore,

$$U_G = G \left[\left(\frac{U_{\dot{m}}}{\dot{m}} \right)^2 + \left(2 \frac{U_D}{D_i} \right)^2 \right]^{1/2} \quad (4.13)$$

Since the uncertainty of each internal tube diameter and the corresponding experimental range of mass flow rate are different, the uncertainty of the mass flux will be different for each tube and range of flow rate. Table 4.11 summarizes the results.

Table 4.11 Uncertainty results of mass flux

Tube internal diameter (mm)	Mass flux range (kg/m ² s)	Mass flow rate range (Kg/hr)	Mass flux Uncertainty (%)
4.26	100 – 500	5.13 – 25.65	0.54
2.88	100 – 500	2.4 – 11.73	0.78
2.01	100 – 500	1.14 – 5.71	1.2
1.1	200 – 600	0.68 – 2.05	2.5
0.52	300 – 700	0.23 – 0.535	3.1

Heat flux

The heat flux is the ratio of the net heat supplied to the internal surface area of the tube. Therefore, the convection and radiation heat loss to the ambient across the insulation and conduction heat loss at the electrode connections is considered in the net heat input calculation.

$$q = \frac{Q_{net}}{\pi D_i L} \quad (4.14)$$

where, $Q_{net} = Q_{tot} - Q_{loss}$

Q_{tot} , is the total electric heat input, which is equal to the product of the voltage and the current applied directly to the test section.

During the flow boiling experiments, the heat loss (Q_{loss}) is predicted using a loss coefficient obtained from single phase experiment conducted at the same mass flux and pressure just before the heating is applied and the average temperature across the insulation, see also Huo (2005)

$$Q_{loss} = C(\overline{T_w} - T_o) \quad (4.15)$$

$\overline{T_w}$, is the average outer tube wall temperature and T_o is the outer wall temperature of the insulation. C is determined from the single phase energy loss along the tube from the inlet to the exit of the heated section given as.

$$C = \frac{\dot{m}(h_{in} - h_{ex})}{\overline{T_w} - T_o} \quad (4.16)$$

The uncertainty of the heat flux value can then be determined from the uncertainty analysis of net heat input, which incorporates the heat loss and the total heat input as follows.

$$U_{Q_{net}} = [U_{Q_{loss}}^2 + U_{Q_{tot}}^2]^{1/2} \quad (4.17)$$

Where the error from the heat loss calculation is obtained as

$$U_{Q_{loss}} = \left[(\overline{T_w} - T_o)^2 U_C^2 + C^2 (U_{T_w}^2 + U_{T_o}^2) \right]^{1/2} \quad (4.18)$$

Therefore, the uncertainty of the heat flux is given as

$$U_q = q \left[\left(\frac{U_{Q_{net}}}{Q_{net}} \right)^2 + \left(\frac{U_D}{D_i} \right)^2 + \left(\frac{U_L}{L} \right)^2 \right]^{1/2} \quad (4.19)$$

Again, this value depends on the internal diameter of each tube, heated length, wall temperature measurement accuracy and accuracy of loss coefficient. As some of these are different for each tube, the results will be summarised in tabular form in Table 4.12.

Table 4.12 Uncertainty values of heat flux for the different tubes

Internal Diameter	Heat flux range (kW/m ²)	Uncertainty range (%)
4.26	13.5 – 148	0.5 – 0.75
2.88	11 – 140	0.4 – 0.92
2.01	13 – 150	0.7 – 1.1
1.1	14 – 135	0.9 – 1.4
0.52	1.6 – 130	1.57 – 2.7

Local quality

The local quality is calculated from the local specific enthalpy at each thermocouple position, which was determined from the energy balance in each heated section considering the losses. It is given by:

$$h_i = h_{i-1} + \frac{q\pi D L_i}{\dot{m}} \quad (4.20)$$

where, i is the thermocouple location index and L_i is the uniform distance between each thermocouple positions. The local vapour quality is given as:

$$x_i = \frac{h_i - h_l}{h_{lg}} \quad (4.21)$$

where, h_l is specific enthalpy of saturated liquid and h_{lg} is the latent heat. These are evaluated using the local saturation pressure, which was obtained assuming a linear pressure drop across the test tube heated length.

The uncertainty associated with determining the local quality is therefore

$$U_{x_i} = \frac{1}{h_{lg}} \left(U_{h_i}^2 + U_{h_l}^2 + \left(\frac{h_i - h_l}{h_{lg}} \right)^2 U_{h_{lg}}^2 \right)^{1/2} \quad (4.22)$$

where, U_{h_i} is the uncertainty in determining the local enthalpy and can be evaluated using Eq. (4.23) as

$$U_{h_i} = \left\{ \left(U_{h_{i-1}} \right)^2 + \left(\frac{q \pi D_i L_i}{\dot{m}} \right)^2 \left[\left(\frac{U_q}{q} \right)^2 + \left(\frac{U_D}{D_i} \right)^2 + \left(\frac{U_L}{L_i} \right)^2 + \left(\frac{U_m}{\dot{m}} \right)^2 \right] \right\}^{1/2} \quad (4.23)$$

The uncertainty will vary depending on each tube internal diameter, length and range of other parameters involved in the equations, the uncertainty will vary. Table 4.13 summarizes the results for each tube.

Table 4.13 Uncertainty results of vapour quality determination

Internal Diameter (mm)	Uncertainty (%)
4.26	0.87
2.88	1.082
2.01	1.31
1.1	1.93
0.52	3.3

4.4 Experimental data reduction

The overall experimental results provide data for three major subjects: heat transfer, pressure drop and flow regime. The heat transfer measurements among other parameters are mainly aimed to determine the local flow boiling heat transfer coefficient. The simultaneously measured total pressure drop along the test section, in addition to supplying values required for calculating the local heat transfer coefficient, i.e. local saturation pressure, it provides boiling two phase pressure drop data. This section describes the equations used to determine the experimental local heat transfer coefficient. The pressure drop data reduction equations that are employed for deducting friction pressure drop component from the total measured pressure drop are also discussed.

4.4.1 Local heat transfer coefficient

As previously discussed, the heat transfer and pressure drop data are the average of 20 consecutive measurements. Therefore, the local heat transfer coefficient at each

measuring station is time-averaged over 120 sec after steady state is attained. The local heat transfer coefficient $\alpha(z)$ at each thermocouple position is calculated by using the local values of the inside wall temperature and the saturation temperature. It is given as:

$$\alpha(z) = \frac{q}{(T_{wi})_z - (T_{sat})_z} \quad (4.24)$$

where, q is the inner wall heat flux, T_{wi} is the local inner wall temperature and T_{sat} is the local saturation temperature. The inside wall temperature, T_{wi} , was determined using one-dimensional radial heat conduction across the tube wall with internal heat generation and is given by:

$$T_{wi} = T_{wo} - \frac{q \cdot D_i}{4k} \left[\frac{(D_i/D_o)^2 - 2 \ln(D_i/D_o) - 1}{1 - (D_i/D_o)^2} \right] \quad (4.25)$$

T_{sat} was deduced from the local saturation pressure assuming a linear pressure drop across the test section.

The corresponding uncertainty of the local heat transfer coefficient is obtained from the above data reduction equations and measured results as,

$$\frac{U_\alpha}{\alpha} = \left[\left(\frac{U_q}{q} \right)^2 + \left(\frac{U_{T_{wi}}}{T_{wi} - T_{sat}} \right)^2 + \left(\frac{U_{T_s}}{T_{wi} - T_s} \right)^2 \right]^{1/2} \quad (4.26)$$

The uncertainty related to the heat flux is already addressed in page 156. The uncertainty of the inner wall temperature is determined from the outer wall temperature measurement accuracy and error propagation using Eq. (4.25). The uncertainty in determining the saturation temperature consists of the errors from the local saturation pressure and fluid property equation. Finally, the overall uncertainty range in determining the local heat transfer coefficient for each tube is summarised in table 4.14.

Table 4.14 Overall uncertainty results for determining local heat transfer coefficient

Internal Diameter (mm)	Uncertainty range (%)
4.26	5 – 9
2.88	5 – 9
2.01	6 – 10
1.1	6 – 11.3
0.52	7 – 12.5

4.4.2 Boiling two phase pressure drop

As described in Chapter two, the total boiling two phase pressure drop is the sum of the friction, acceleration and gravity contributions. In this experiment, the inlet temperature was controlled at a subcooling of 1 – 5 K. Therefore, the boiling two phase pressure drop is calculated after deducting the single phase pressure drop (before saturation is achieved) from the measured value. In case of using separated flow model, there are several void fraction correlations proposed to calculate the acceleration and gravity pressure drop contributions. In the present pressure drop analysis, the void fraction relations that were used in the original pressure drop model or correlation to which the current measured results are compared were used. Therefore, when the friction or total measure pressure drop is compared with other correlations, the comparison will not be biased on the selection of the acceleration and gravity pressure drop equations as these were taken from the particular model or correlation selected for comparison. Data reduction equations for the three pressure drop components of the two well known models, homogeneous and separated flow are presented below, since these equations will be used later in Chapter six. The pressure drop is calculated from the gradient considering a uniform heat flux condition over length L with inlet and exit qualities of zero and x_e respectively. The derivations as well as the equations (4.27)-(4.33) are found in most two phase flow books, Tong and Tang (1997), Collier and Thome (1994), Whalley (1987). The symbols are defined in the nomenclature.

Homogeneous

Gravity component

$$\Delta P_g = \rho_l g L \frac{1}{x_e \left(\frac{\rho_l - \rho_g}{\rho_l} \right)} \ln \left[1 + x_e \left(\frac{\rho_l - \rho_g}{\rho_l} \right) \right] \quad (4.27)$$

Acceleration

$$\Delta P_a = G^2 \frac{1}{\rho_l} \left(\frac{\rho_l - \rho_g}{\rho_l} \right) x_e \quad (4.28)$$

Separated (Lockhart-Martinelli)

Gravity

$$\Delta P_g = g L \frac{1}{x_e} \int_0^{x_e} [\rho_g \alpha_{LM} + \rho_l (1 - \alpha_{LM})] dx \quad (4.29)$$

Acceleration

$$\Delta P_a = G^2 \frac{1}{\rho_l} \left[\frac{x_e^2}{\alpha_{LM}} \frac{\rho_l}{\rho_g} + \frac{(1 - x_e)^2}{1 - \alpha_{LM}} - 1 \right] \quad (4.30)$$

The Lockhart-Martinelli void fraction (α_{LM}) is given in terms of the Martinelli parameter (X_M) as:

$$\alpha_{LM} = \frac{1}{1 + X_M} \quad (4.31)$$

where,

$$X_M = 0.28 \left(\frac{\rho_g}{\rho_l} \right)^{0.36} \left(\frac{1 - x_e}{x_e} \right)^{0.64} \left(\frac{\mu_l}{\mu_g} \right)^{0.07} \quad (4.32)$$

The experimental friction two phase pressure drop component is therefore given as

$$\Delta P_f = \Delta P_{tot} - \Delta P_{sp} - \Delta P_g - \Delta P_a \quad (4.33)$$

where, ΔP_{sp} is the single phase pressure drop in the front part of the test section before saturation achieved and ΔP_{tot} is the measured total pressure drop. When the

homogeneous model is considered, it uses the homogeneous equations for gravity and accelerations to compare with homogeneous friction pressure drop. The same is true for the separated flow model and other correlations.

4.5 Experimental validation

Further to the calibration tests and error analysis carried out to verify the overall measurement accuracy, single phase experiments (both heat transfer and pressure drop) are conducted and compared with well-known theories to validate the general suitability and to method of the experiment. The validation was made using the largest tube (4.26 mm) for which established classical correlations are believed to work satisfactorily. Although the small diameter effect on single phase heat transfer and pressure drop is not clearly understood and thus applicability of conventional correlations for small diameter tubes is not resolved yet, as the tube diameter becomes very small, there is an extreme challenge to conduct an accurate experiment. Therefore, it was necessary to conduct the single phase experiments for the very small tube (0.52 mm) to verify any difference with the classical single phase pressure drop and heat transfer correlations. This also confirms any measurement bias in this tube. Therefore, the single phase friction factor and Nusselt number for the 0.52 mm tube were also compared with the conventional correlations and those that are based on small tube data.

4.5.1 Single phase pressure drop

The results of the single phase friction factor was compared with two well-known correlations of Blasius (1913) and Haaland (1983), both cited in Massey and Ward-Smith (1998). The Blasius friction factor is given as,

$$f_f = 0.079 Re^{-1/4} \quad (4.34)$$

The Haaland friction factor is given as a function of roughness as,

$$\frac{1}{\sqrt{f}} = -3.6 \log_{10} \left[\frac{6.9}{Re} + \left(\frac{e}{3.71D} \right)^{1.11} \right] \quad (4.35)$$

The experimental friction factor was derived from the measured pressure drop using the following equations.

$$f_f = \frac{\rho_l D \Delta P_f}{2 G^2 L} \quad (4.36)$$

where $\Delta P_f = \Delta P - \Delta P_{db}$,

ΔP_{db} is used to compensate the measured pressure drop due to the density difference in the pipe leading to the differential transducer compared with that in the test section. The error associated with determining the measured friction factor is given as,

$$\frac{U_f}{f_f} = \left[\left(\frac{U_\rho}{\rho_l} \right)^2 + \left(\frac{U_{\Delta p_f}}{\Delta p_f} \right)^2 + \left(\frac{U_D}{D} \right)^2 + \left(\frac{U_L}{L} \right)^2 + 4 \left(\frac{U_G}{G} \right)^2 \right]^{1/2} \quad (4.37)$$

Single phase pressure drop experiment was conducted for the 4.26 mm tube at 7.8 bar. The results of the comparison are presented in Figure 4.14. The single phase friction factor results agree well with the Blasius correlation, i.e. within the uncertainty of the experiment, which is indicated by the error bars. However, the Haaland correlation over-predicted the results by about 5 % at high Reynolds number ($Re > 50000$). The comparison was made in the turbulent region, since the inlet condition to the larger tubes was mostly turbulent.

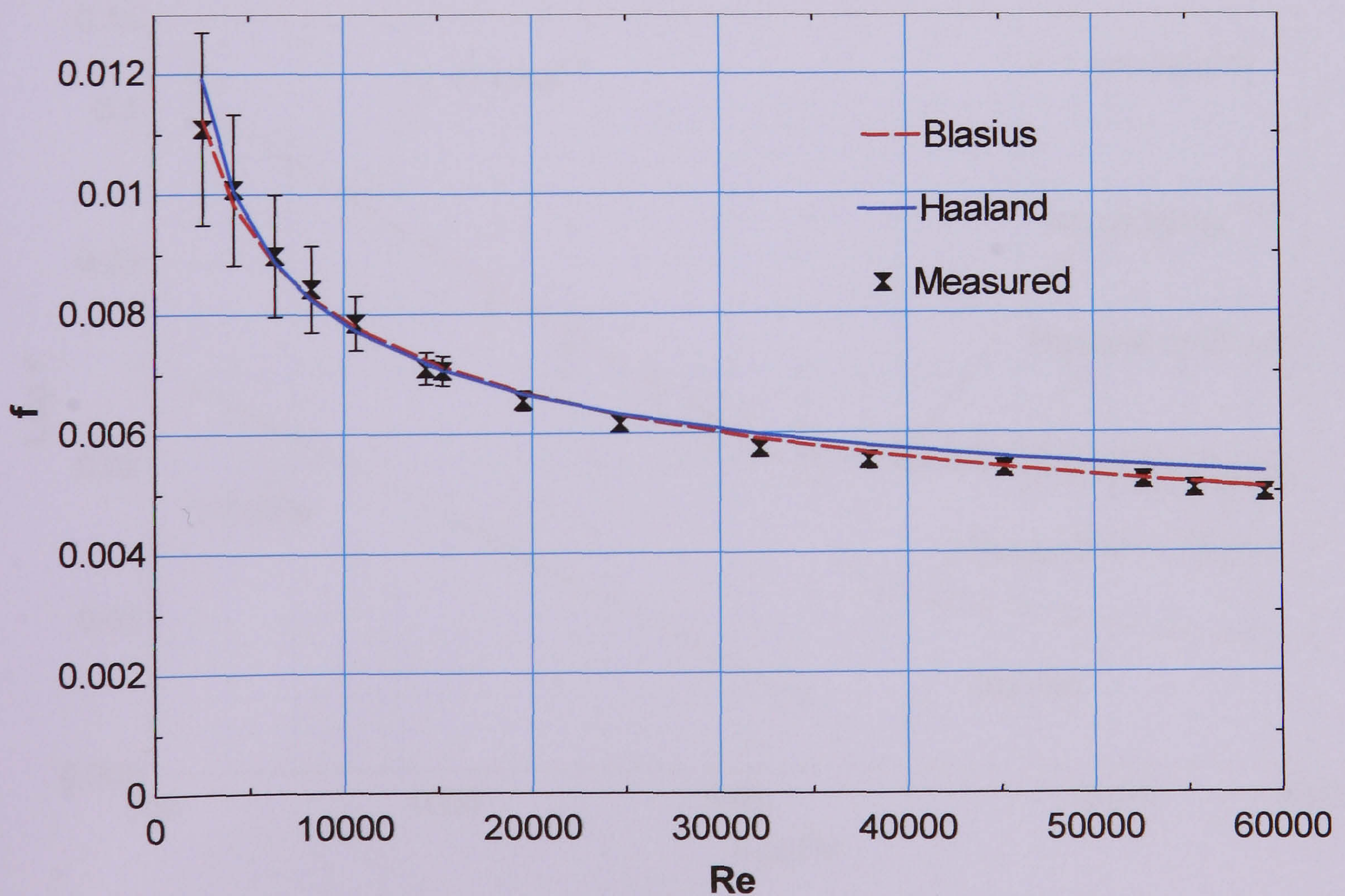


Figure 4.14 Comparison of the measured friction factor with well-known correlations for $D = 4.26$ mm and $P = 7.9$ bar.

The measured friction factor for the 0.52 mm tube is plotted as a function of Re in Figure 4.15. As seen in the figure, the friction factor in this tube is much higher than the conventional correlations developed for large tubes although a similar trend is obtained. Also, the transition from laminar to turbulent regime seems to occur at Reynolds number of about 2400, which is very close to the conventional threshold value (~ 2300). In the laminar regions, the measured friction factor is almost 3.4 times the theoretical value, while in the turbulent region it is roughly twice the theoretical values. Therefore, the “jump” at the transition is much smaller than the conventional tubes. In addition, in the turbulent regime, comparison with the Halaand correlation using roughness value from Table 4.3 showed highly under-prediction of the measured data. However, one has to increase the roughness value in the correlation (Eq. 4.35) to unreasonably high value ($\sim 23 \mu\text{m}$), to obtain a better prediction of the results by Halaand correlation. This could be related to the possible combined effects of surface roughness and large wavelength, large amplitude disturbances; in which sharp change in flow direction may also cause local flow separation. Later, this issue will be raised again when the boiling two phase pressure drop and heat transfer results are discussed in the coming chapters.

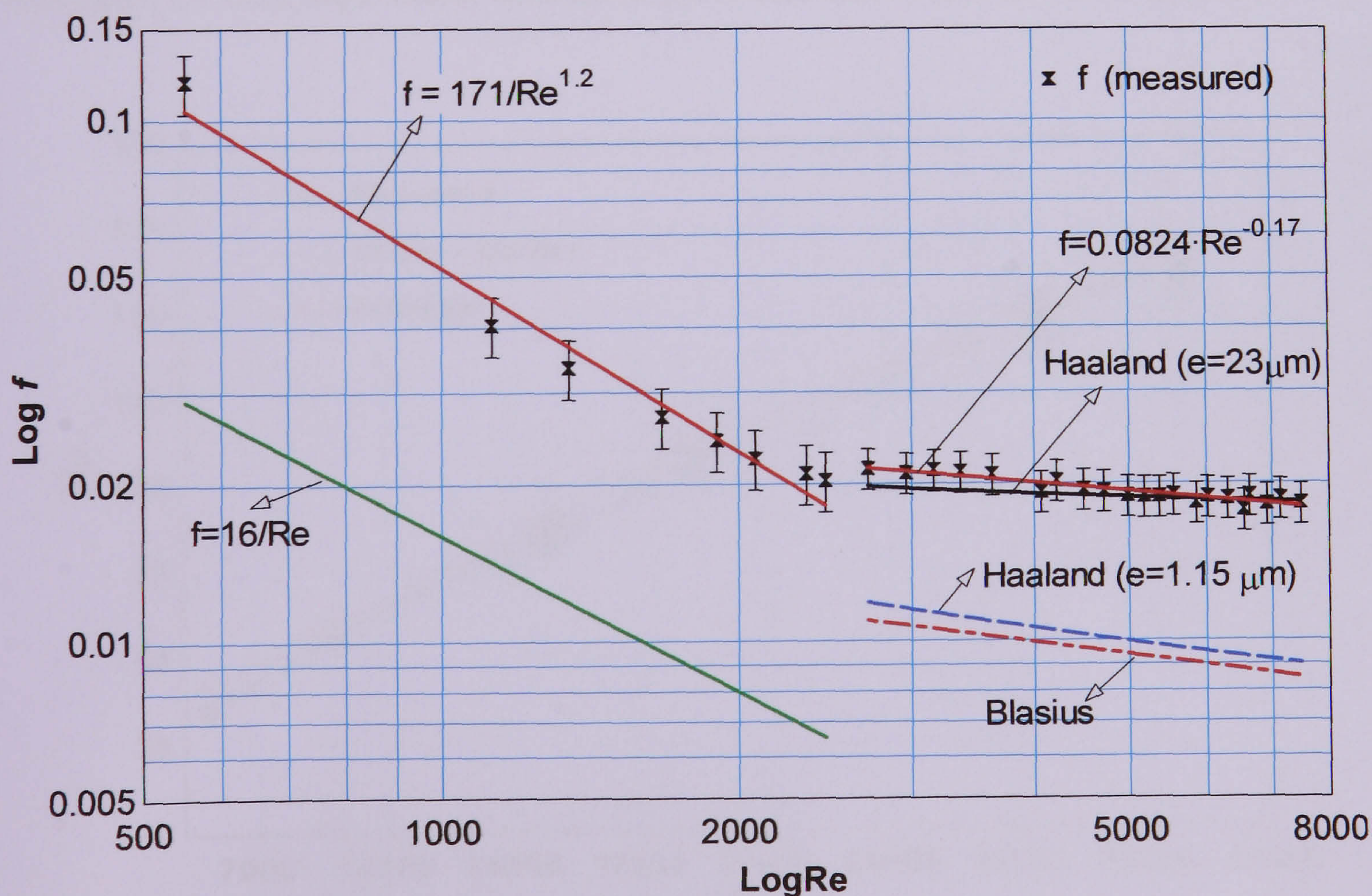


Figure 4.15 Measured friction factor as a function of Re for the 0.52 mm tube at 8 bar pressure.

4.5.2 Single phase heat transfer

In addition to the pressure drop experiments, single phase heat transfer tests were also conducted for the larger diameter tube at a pressure of 7.5 bar. The results are compared with the two well-known large tube correlations, Dittus-Boelter (1930) and Petukhov (1970). Their equations are given below,

Correlation for turbulent flow

Dittus-Boelter

$$Nu = 0.023 Re^{0.8} Pr^{0.4} \quad (4.37)$$

Petukhov

$$Nu = \frac{(f/8) Re Pr}{1.07 + 12.7 (f/8)^{0.5} (Pr^{2/3} - 1)} \quad (4.38)$$

The comparison results are depicted in Fig. 4.16. As seen in the figure, the single phase experimental Nusselt number agrees very well with both correlations. The above results verified the overall accuracy of the experimental system and validated the experimental technique, i.e. data acquisition, calibration procedure and overall instrumentation.

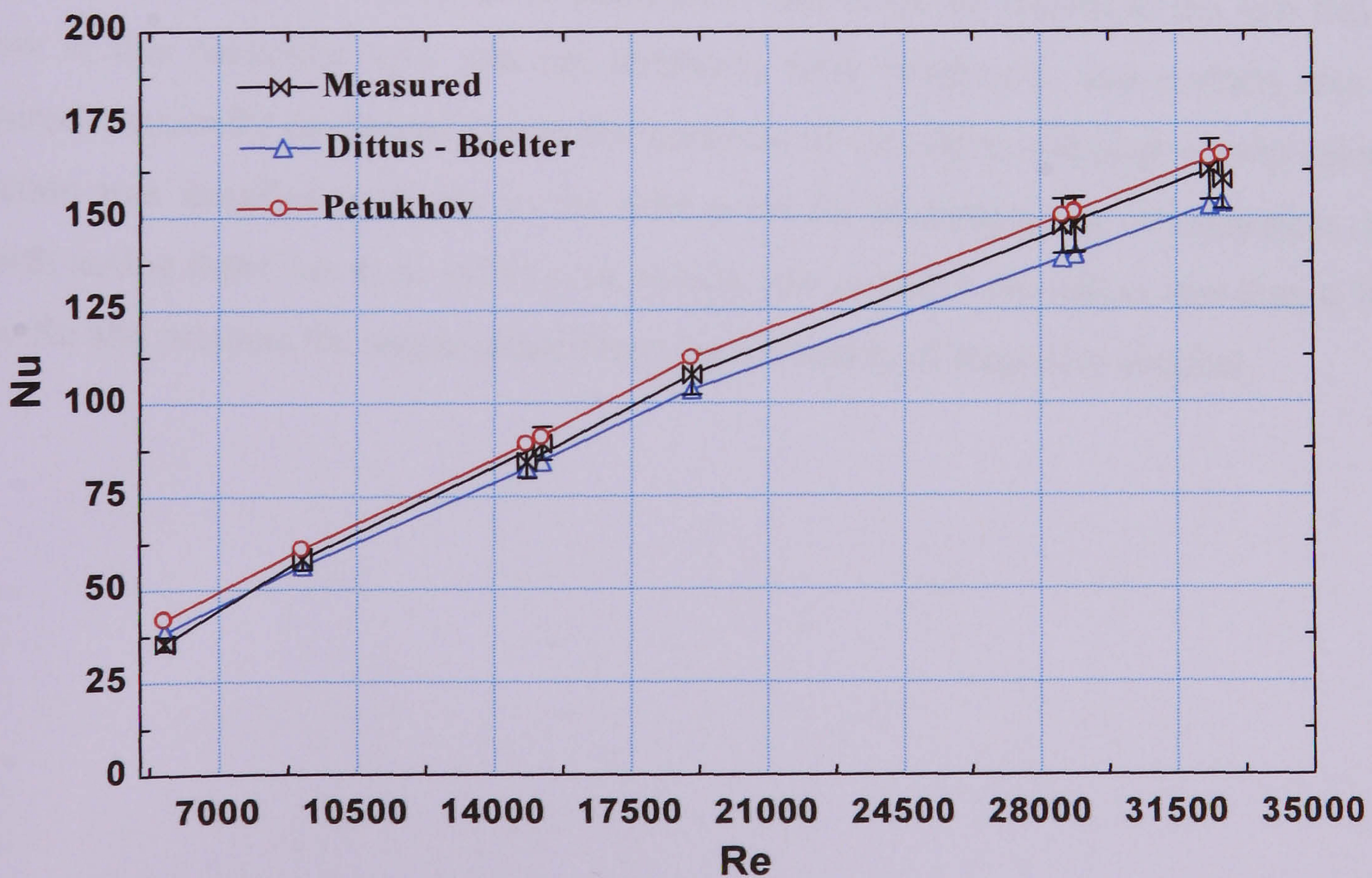


Figure 4.16 Comparison of single phase heat transfer results with well-known large tube correlations for $D = 4.26$ mm at $P = 7.5$ bar.

Comparisons of the single phase Nusselt number for the 0.52 mm tube with various well-known correlations both for turbulent and laminar flows are shown in Figures 4.17 and 4.18, respectively. The modified Gnielinski (VDI-1997) correlation accounts for both transition region and developing effects; the Adams et al. (1998) correlation is a modification of the Gnielinski correlation to accommodate the small diameter effect. In the laminar regime the experimental results were compared with the Peng and Peterson (1996) correlation for rectangular microchannels and the Choi et al. (1991) correlation for microtubes. The correlation equations used in the comparison figures 4.17 and 4.18 are included in Appendix B. The results agree quite well with modified Gnielinski (VDI-1997) and Adams et al. (1998) for the turbulent regime and Choi et al. (1991) in the laminar regime. This validates the experimental methodology and provides reasonable confidence towards the two-phase experiments. In the turbulent region Dittus-Boelter and Petukhov did not match the experimental data probably because of the fact that both were developed for $Re > 10^4$ and large tubes, while the other correlations can work down to the transition region. In the laminar region, the Peng and Peterson correlation is a function of channel aspect ratio. Consequently, the large deviation from the experimental data may be attributed to the effect of geometry. The measured Nusselt number becomes less than the theoretical constant value for a fully developed flow ($Nu = 4.36$) as Re decreases. This could be related to the fact that the flow in this particular tube was not thermally fully developed, and perhaps also not hydrodynamically developed due to the presence of curvature, although a long calming section was installed upstream to the inlet point for hydrodynamic development. It is worth noting that Choi et al. (1991) correlation also provides Nu values less than 4.36 at low Re and predicts the single phase Nu to be a function of Reynolds number.

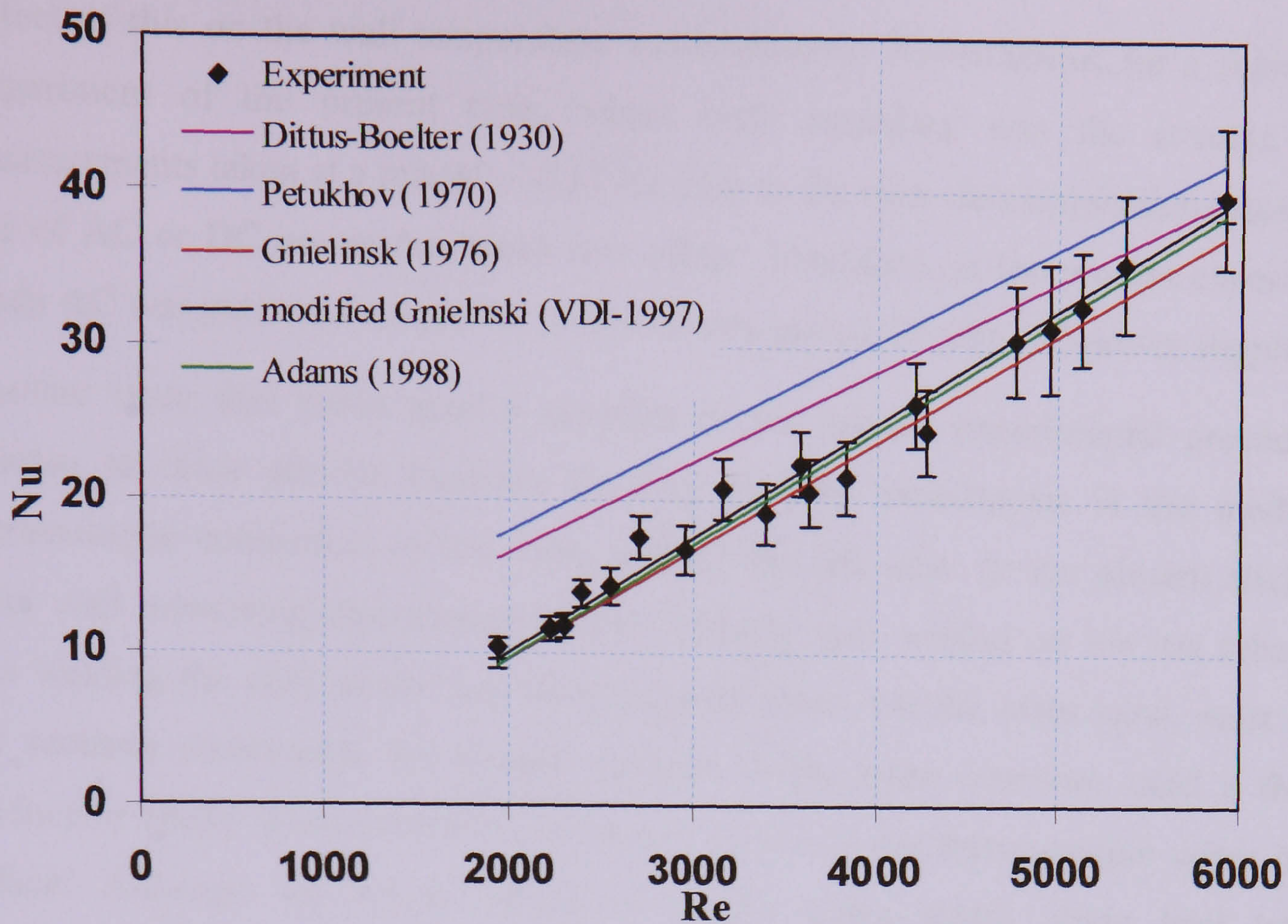


Figure 4.17 Single phase heat transfer results for $D = 0.52$ mm in the turbulent region.

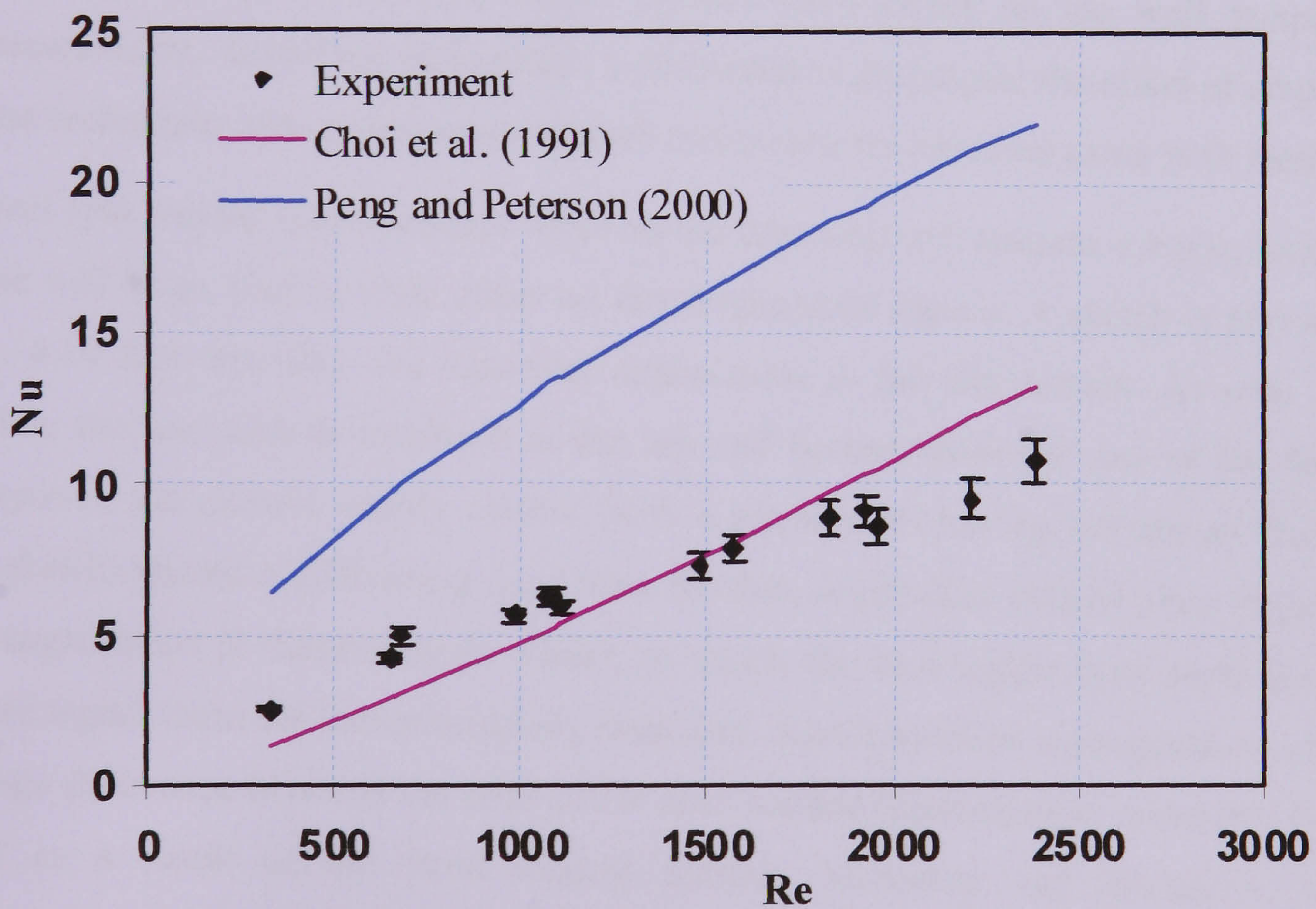


Figure 4.18 Single phase heat transfer for $D = 0.52$ mm in the laminar region.

4.5.3 Thermocouple connection method

As mentioned before, the test sections are heated by passing an alternating electric current (AC). However, most similar facilities employed direct electric current (DC). The significance of using AC over DC is the 100 Hz fluctuation it will produce and the

effect of this on the wall temperature measurements. Nevertheless, for a steady state experiment of the present type, where each recording was the average of 20 measurements taken at a rate of ~ 0.17 Hz (due to the slow data acquisition system), the use of AC or DC power has much less effect. Therefore, in the present experimental study AC was preferred simply for its lower cost compared with DC power supplies.

Another issue that could pose a question in the present experimental procedure in relation to other similar facilities for heat transfer experiments is the method of thermocouple connection to the outer wall of the test tube. In the present study, the outer wall measuring thermocouples were directly spot welded on the test tube, after spot welding the ends of the two thermocouple wires. On the other hand, most of the test sections constructed for similar purpose in the open literature used a thermal conductive epoxy paste (electrical insulator) to attach the thermocouple wires on the surface. Although the above validation results using single phase heat transfer experiments did not show any discrepancy, this may not be extended to boiling tests to generalise that there will not be an electric field effect on the wall temperature measurements. Therefore, this section is dedicated to investigate the effect of employing these techniques and presents temperature measurements obtained using both methods.

Direct spot welded thermocouple wires on the tube wall will become a major concern if there will be an electric field effect on the temperature signals. A sketch is provided in Fig. 4.19 that describes the electrical connections to the test section. As seen in the sketch, the test tube is insulated at the top and bottom from the rest of the facility. Moreover, the electric supply system (with a transformer having isolator as shown in the sketch) shared a different ground than the data acquisition system (data logger and the ungrounded K thermocouple wires), in which the data logger type itself does not accept inputs from the thermocouples. Therefore, there cannot be a complete circuit and voltage difference between the ends of the spot welded thermocouple wires that has no bead as a result of the input electric current. Moreover, the resistance of the thermocouple wires is big enough to ignore any current passing through the wire. In principle, it is very unlikely that an electric field will be generated in the thermocouple wires. In fact this method of connection was also used by other researchers like Hu et al. (1998), when they experimentally investigated the heat transfer enhancement during flow boiling using the longitudinal microchannels etched on the inside of a tube wall.

The tube wall temperature at different locations and the distributions along flow direction were measured by thermocouples embedded inside the wall.

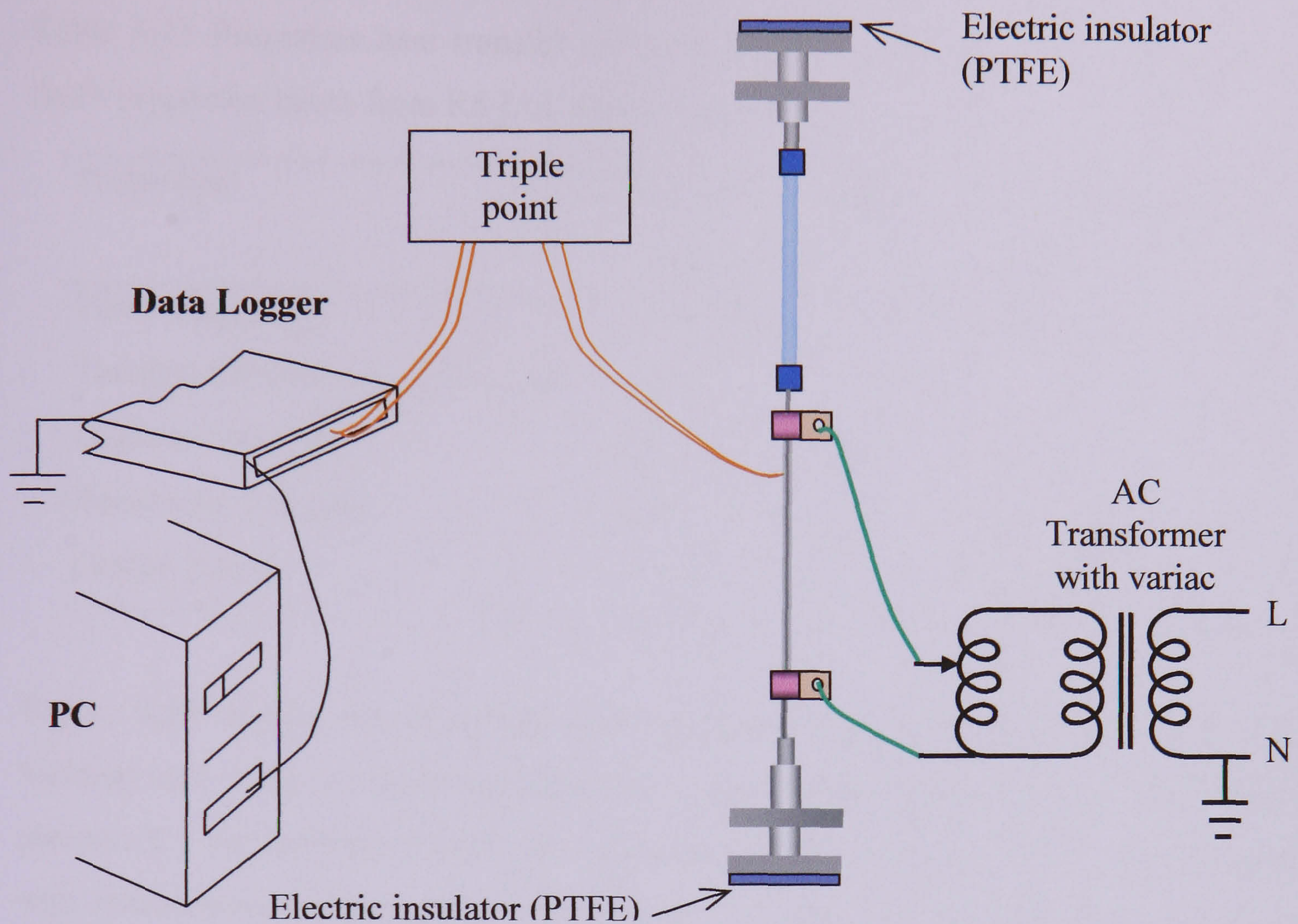


Figure 4.19 Rough sketch showing electric and thermocouple wire connections.

Although the above explanation sounds reasonable, it may not be adequate unless one performs tests with both methods and compare the results. Consequently, boiling experiments were conducted employing both ways of connection at the same axial location to prove whether the technique used in the present studies are reliable and resolve the presumption that one method is better than the other. A thin film of silicon heat transfer compound was used to attach one extra thermocouple wire next to the spot welded one, along the same circumference line. The properties of the compound used in the comparison are given in Table 4.15. Also, in the table properties of thermal bonding epoxy, a paste used by many researchers to attach thermocouple wires is included. Although thermal bonding epoxy is most often used with measuring thermocouples, its properties were not usually reported. Table 4.15 also provides a comparison on the main important properties of these two pastes. The electric insulating capability is implied by its dielectric strength. The useful properties are therefore the thermal conductivity and the dielectric strength. It is also worth considering the aging factor in the properties of

these compounds. Most experimental investigations did not report how often they had to re-apply these compounds (if indeed they did check and re-applied the paste).

Table 4.15 Properties heat transfer compounds used in attaching thermocouple wires (both properties taken from RS Ltd. online catalogue)

Properties	Silicon heat transfer compound	Thermal bonding epoxy
Temp range [$^{\circ}\text{C}$]	-50 to 200	~ 100
Thermal Conductivity [W/m K]	3.0	1.1
Dielectric strength	18	11 - 12
Resistivity [Ω cm]	10^{15}	$10^{14} - 10^{15}$
Usable [hour]	-	3- 4 hrs

Figure 4.20 depicts results of the wall temperature measurements from direct spot welding and using a silicon heat transfer compound for a mass flux of $200 \text{ kg/m}^2\text{s}$, pressure 6.5 bar at different heat flux values (shown in the figure). As it can be seen, the wall temperature measured by spot welding is slightly higher than that obtained by using silicon compound. The average temperature differences between the two methods are 0.25, 0.3 and 0.55 K for exit qualities of 0.15, 0.3 and 0.5 respectively. These variations, which showed an increase with heat flux, could be related to the increase in heat loss and temperature drop due to conduction resistance of the silicon heat transfer compound as heat flux increases. For instance, assuming approximately the thickness of the compound film applied is 0.05 mm, a temperature drop of about 0.08 K is expected for a heat flux of 29.2 kW/m^2 and an average heat loss of 5 %. However, the assumption of the thickness of the film can be quite rough, since there was no standard technique used. The uncertainty of the temperature measurement was reported to be $\sim 0.16 \text{ K}$. At low heat flux where the conductivity effect is very low, the deviation is below the uncertainty of the thermocouples. However, at high heat flux there is a slight difference above the uncertainty of the temperature measurement, which could be attributed to the increase in heat loss and corresponding temperature drop due to low thermal conductive paste. This in addition to the electrical connection sketch ensures that the direct spot welding technique is acceptable as far as the test section is electrically insulated from the rest of the system.

There is another important issue to consider for those experiments that use thermal bonding epoxy between the thermocouple tip and the wall. In conditions where there are no ways to determine the thickness of the paste applied, the thickness applied sometimes can be large to increase the electrical insulation capacity. Depending on how well the test tube is insulated, there will be a drop in the heat transfer coefficient caused by the additional temperature drop associated with the existence of conductive compounds. Also, the temperature deviations observed above could have been larger, if thermal bonding epoxy was instead used, since its thermal conductivity is almost three times lower than silicon compound, as shown in Table 4.15. Again, mostly experimental studies did not clearly mention, if they have considered the temperature drop due to the thermal conductivity of the bonding agent (which also depends on the heat loss) or whether a standard method has been used to control the thickness of the paste used. If they do not allow for this and correct the wall temperatures accordingly, their heat transfer coefficient will be at least slightly lower depending on the heat flux and heat loss.

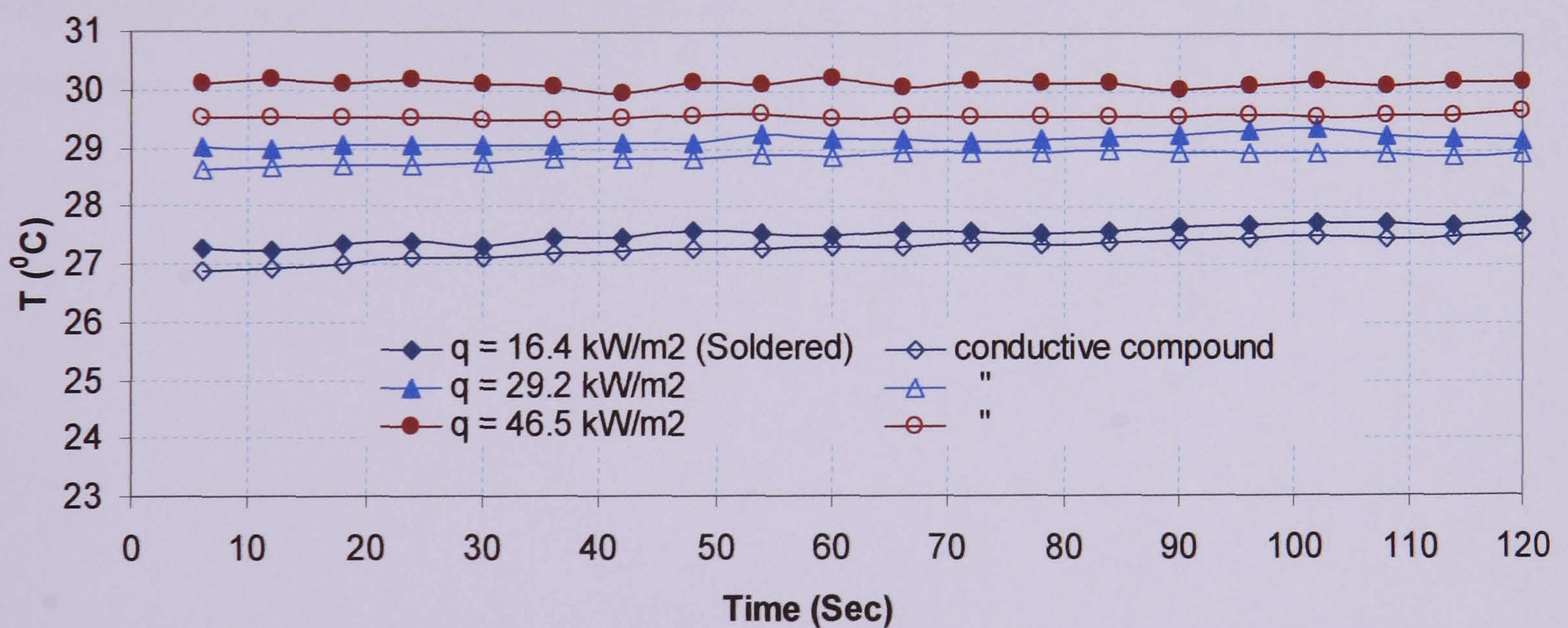
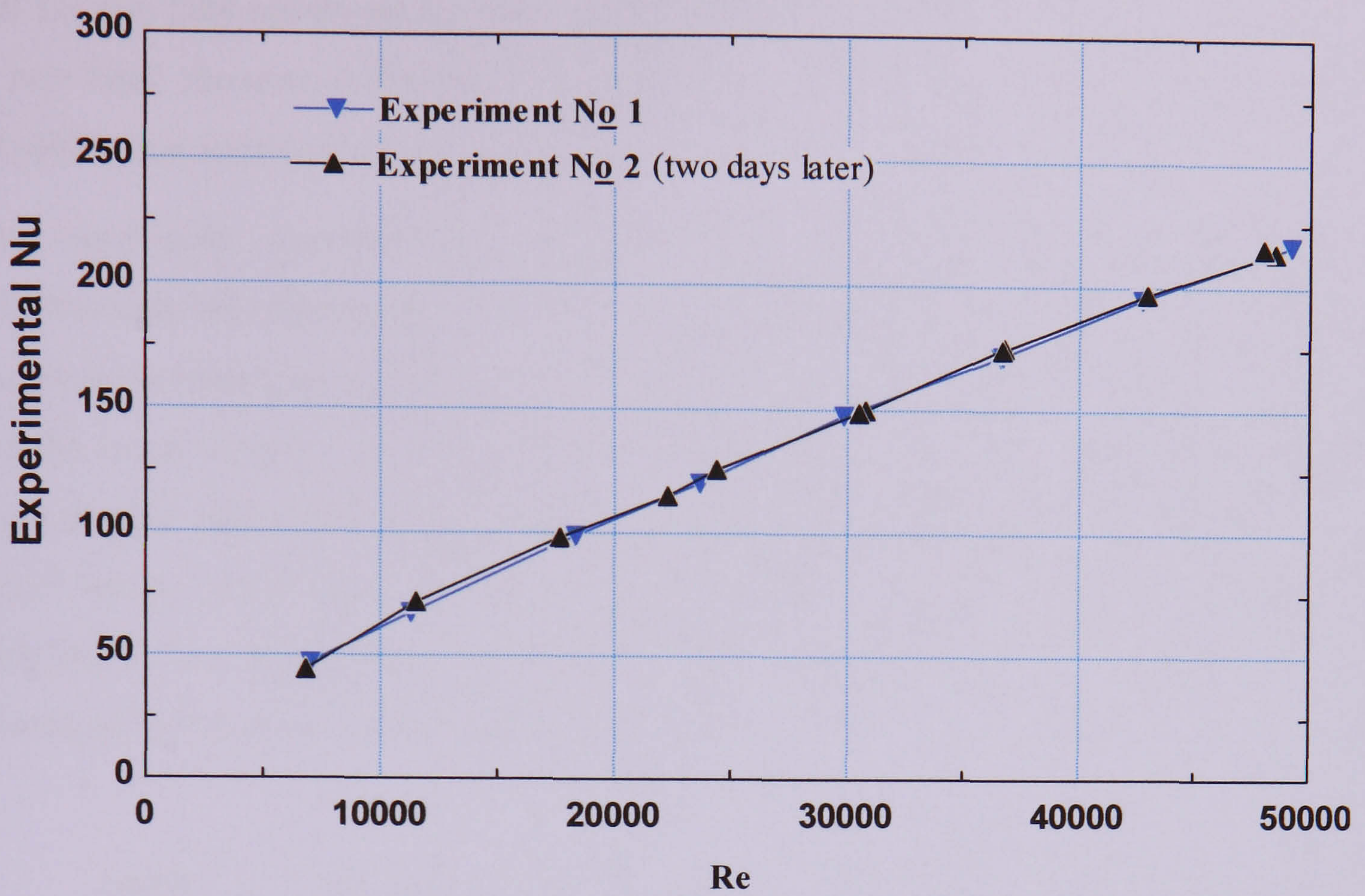


Figure 4.20 The measured wall temperature difference between different ways of thermocouple attachment, at different vapour quality.

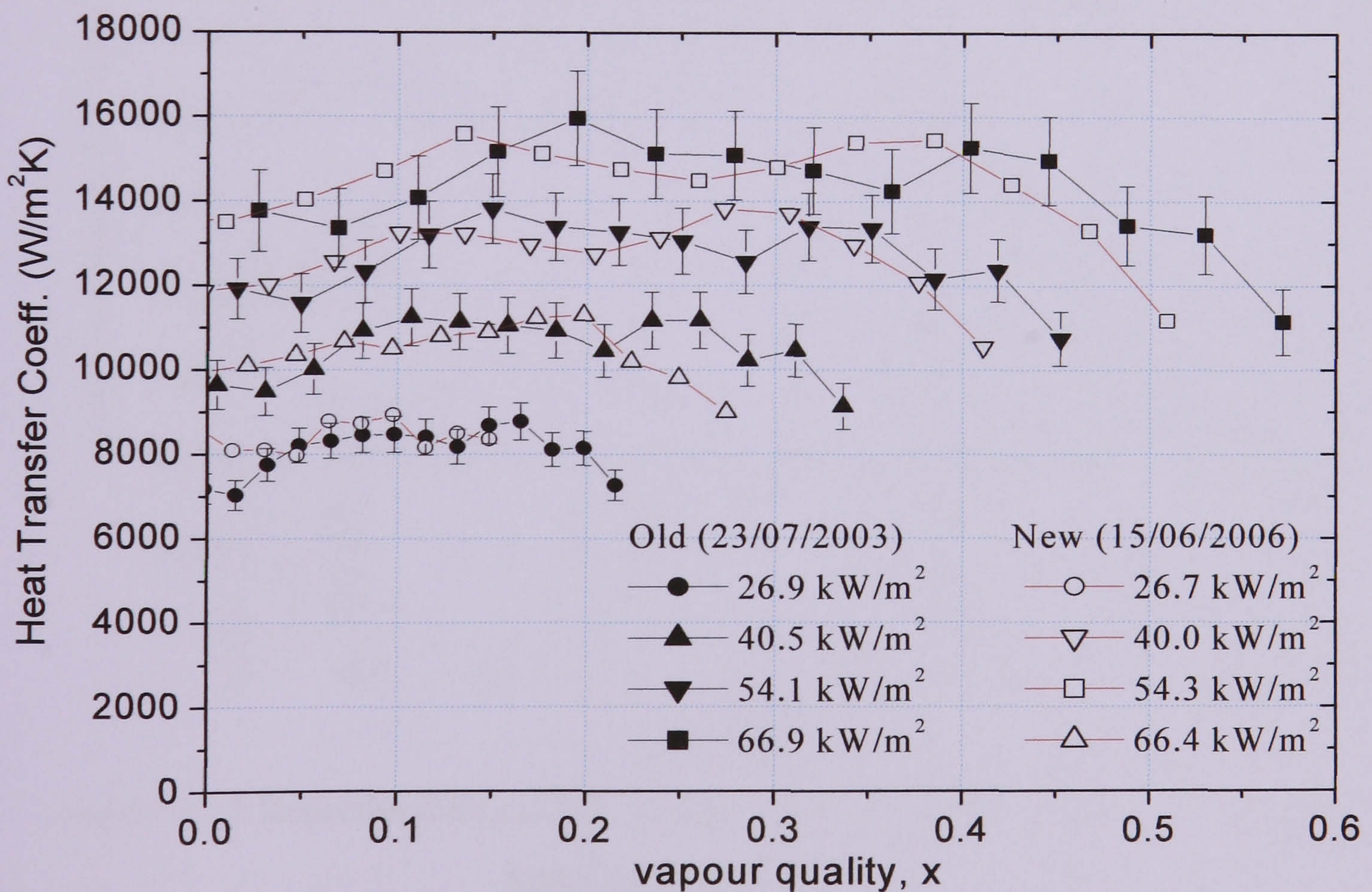
4.6 Repeatability of the experiments

Although calibration of measuring instruments plus single phase validation tests provides an acceptable degree of confidence over the experimental results, we could not conclude on the accuracy and validation of our data unless repeatability of the measured data is checked frequently. However, it is important to note that repeatability results can be affected by factors, other than measuring instrument, such as fouling, surface conditions and environmental conditions. This is more probable in boiling tests, which

is affected by a large number of factors in contrast with single phase tests. In the current experiment, the long and short term reproducibility of the data was tested frequently at different conditions. Typical examples are presented for the 4.26 and 1.1 mm tube. The single phase heat transfer and boiling repeatability tests for the larger tube (4.26 mm) are shown in Figures 4.21 (a) and (b). The results of Figure 4.21 indicate that the single phase results can be repeated in very much higher accuracy than boiling experiments. For this tube, the old results were measured by X. Huo in 2003, (Huo, 2005). This implies the results are repeatable even after a longer period of time. As indicated above, the boiling tests can be influenced by different parameters. Moreover, maintaining exactly the same inlet degree of subcooling, flow rate and system pressure can also be difficult. With all this in mind, Figure 4.21 (b) shows that the boiling results are repeatable within the uncertainty limit. Nevertheless, data in the decreasing heat transfer coefficient region showed some deviation above the uncertainty. This region, as discussed later, is associated with dryout and high temperature fluctuations, which could be a reason to for the deviation observed. Overall, the patterns of the heat transfer dependence and the magnitude of the coefficient are repeatable with an acceptable accuracy.



(a)



(b)

Figure 4.21 Repeatability results of 4.26 mm tube: (a) single phase experiments at pressure of 11 bar; (b) two phase boiling results at a mass flux of 300 kg/m²s and pressure of 8 bar.

The same conclusions were reached when we performed boiling reproducibility tests for the 1.1 mm tube are shown in Figure 4.22. These were performed a few days and almost a year later. As seen in the figure, the differences in the results were mostly within the experimental error and hence reproducible.

The short-term reproducibility of the 0.52 mm tube experiments was worse at intermediate heat flux range (11-18 kW/m²), but it is improved significantly as heat flux increases beyond this range. Because the same experimental methods were employed as for the larger tubes, it will be argued in chapter 5 that this irreproducibility, particularly for a certain intermediate heat fluxes may be inherent in the physics of boiling in very small tubes, where the number of nucleation sites could be significantly small and stability of few sites matter. The reproducibility plots of this tube will be presented and discussed in Chapter 5 along with the results.

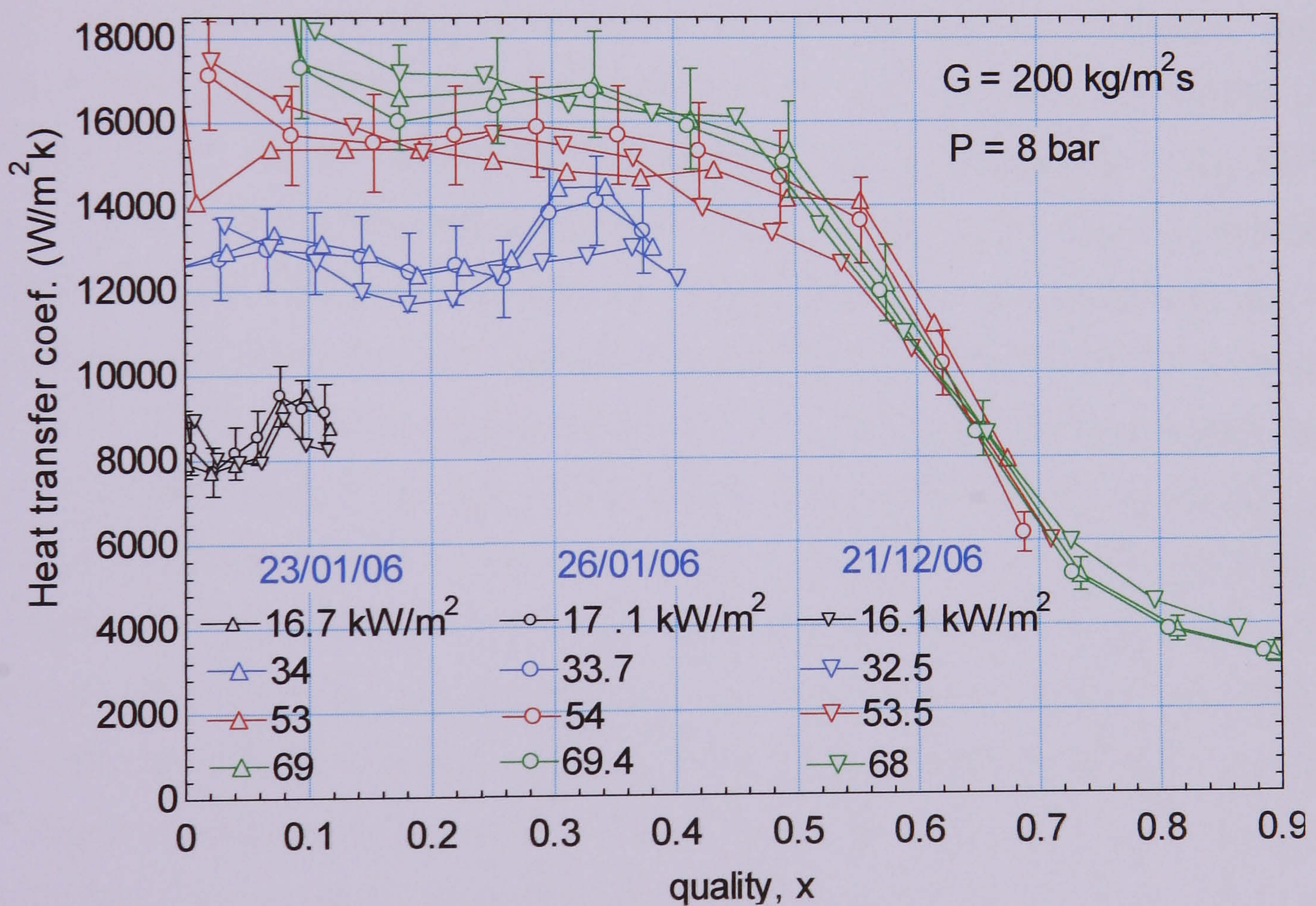


Figure 4.22 Reproducibility of the 1.1 mm tube experiments at a mass flux of 300 kg/m²s and 8 bar pressure.

4.7 Summary

An experimental facility designed first by Huo (2005) and Chen (2006), to investigate flow patterns, heat transfer and pressure drop during flow boiling in small diameter tubes has been described. The facility was then transferred to Brunel University by the present author and the tube diameter range was extended to include microtubes in a way that will provide important data to help resolve some of the important challenges raised during two phase flow boiling in small passages. Also, simultaneous visualisation of flow regimes with heat transfer measurements was carried out in this study. The measuring instruments were carefully calibrated and associated measurement errors thoroughly analysed. Moreover, validation experiments (both pressure drop and heat transfer) were conducted using single phase tests and compared with well known correlations. The single phase friction factor and heat transfer results agreed very well with the empirical correlations developed for larger tubes. Experimental accuracy becomes a difficult challenge as the size of the passages decreases. Therefore, further single phase experiments were performed for the 0.52 mm tube and results were compared with various correlations for large tube and microchannels. The friction factor in the 0.52 mm tube was observed to be significantly higher than the theoretical values. This was attributed to the internal surface condition of this particular tube. The single phase heat transfer results agreed with modified Gnielinski (1997) and Adams et al. (1998) for the turbulent regime and Choi et al. (1991) in the laminar regime. Also, reproducibility of the single phase and boiling heat transfer data were checked and satisfactory results were obtained for the larger tubes (1.1 – 4.26 mm) showing the repeatability of the data over long and short periods. However, the results of the smallest tube were not reproducible over the whole range of heat flux. This is hypothesised to lie in the nature of boiling in the smallest tube, discussed in more detail in Chapter 5, and not in the experimental methods, which were the small for all the tubes. Therefore, it can be concluded that the data that will be presented in this study meet the standards of reasonably accurate information. Hence, the present facility can be capitalised to provide important data necessary to understand two phase flow thermal hydraulic phenomena in small tubes.

Chapter 5

Boiling Heat Transfer Results and Discussion

5.1 Introduction

This chapter presents the flow boiling experimental results and the study of the heat transfer characteristics in the five different diameter tubes (4.26, 2.88, 2.01, 1.10 and 0.52 mm). A discussion of the results of the flow patterns observed directly at a transparent tube located immediately after the heated section is also included. The experimental results of the two tubes (4.26 and 2.01 mm) have been reported in Huo (2006). They are included here for the sake of providing a complete picture of the heat transfer characteristics as the range of tube diameter is varied covering small to micro scale. The chapter is organised as follows: section 5.2 presents the time-averaged local heat transfer coefficient and its dependence on various parameters such as heat flux, quality, mass flux, pressure and tube diameter. The dryout phenomenon is also discussed in this section. The relation of the heat transfer results with the flow patterns observed by the digital high-speed camera in a borosilicate glass tube with an internal diameter matched to the test section and installed at its exit is presented in section 5.3. A global comparison of the local heat transfer coefficient with several existing correlation was made and the results are presented in section 5.4. A new correlation capable of predicting the present results is proposed in section 5.5. Finally a summary of the chapter is provided in Section 5.6.

5.2 Experimental time-averaged local heat transfer coefficient

The heat transfer coefficient, which is an indicator of the heat transfer performance of the various tubes, is the main parameter sought in each experiment. In this study, the local values are prominently used to describe the heat transfer features. Therefore, the

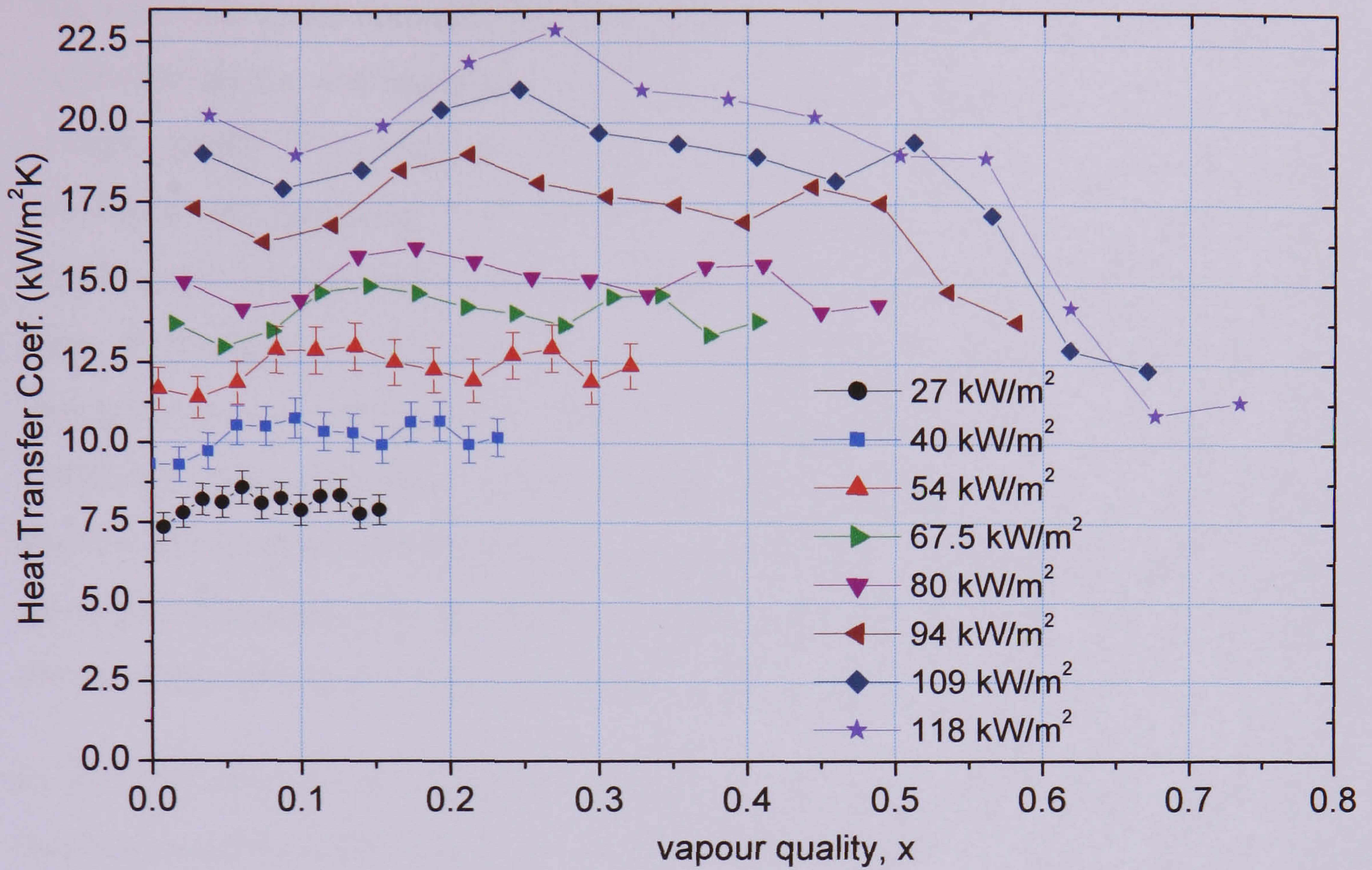
influence of various parameters such as heat flux, mass flux and pressure are discussed using local values of the heat transfer coefficient versus local quality or relative axial position.

5.2.1 Effect of heat flux

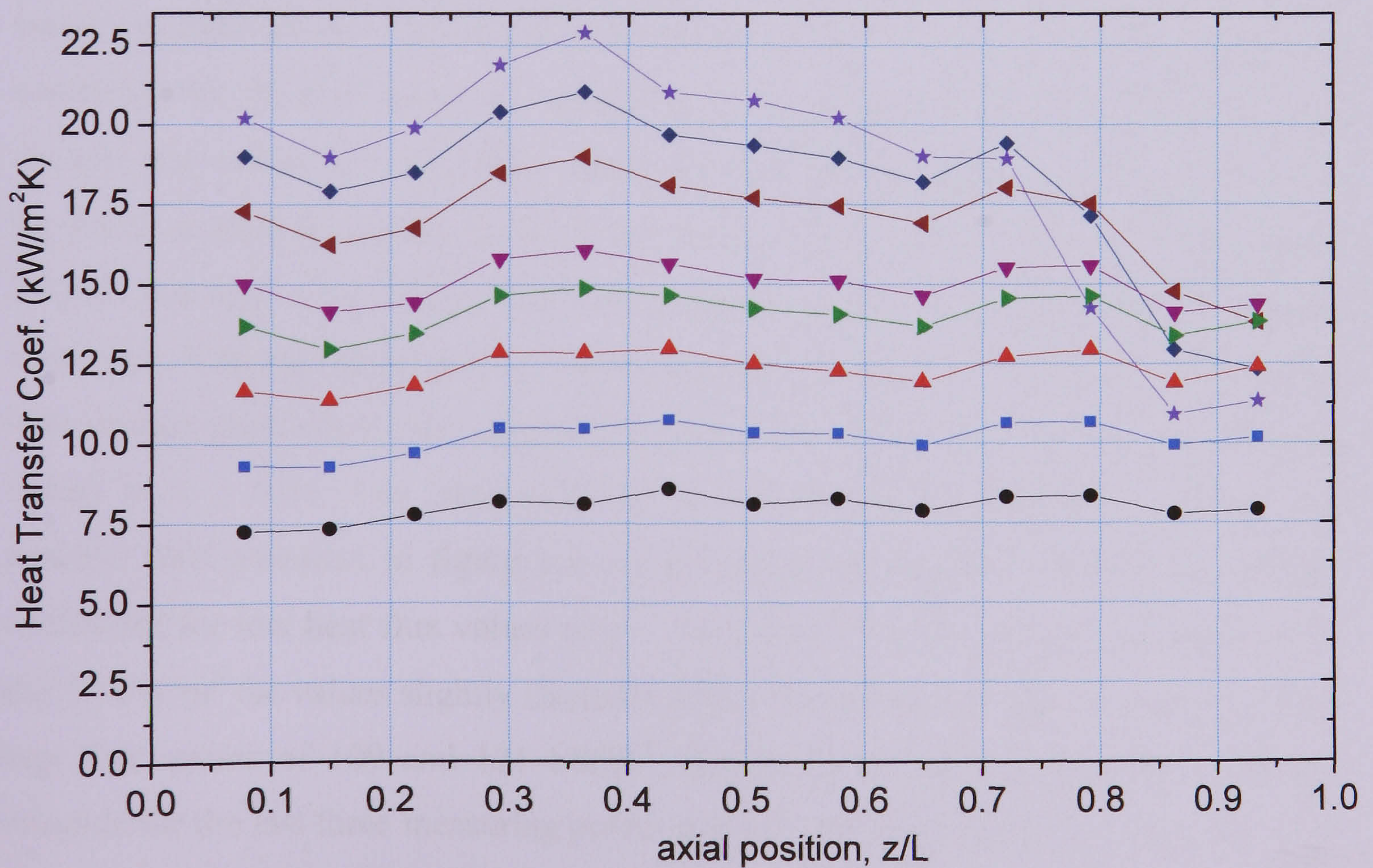
Heat flux was one of the main parameters varied during the boiling experiments using the direct electric heating. The data can be interpreted in two ways, one based on the heat transfer coefficient versus quality plot, the other on the heat transfer coefficient versus axial distance plot. Therefore, typical experimental data for the local time-averaged heat transfer coefficients are plotted as a function of quality and axial position at different heat flux for the five tubes at constant mass flux and pressure. The various heat transfer characteristics obtained, as the heat flux gradually increased in small steps, are discussed below for each tube.

Figure 5.1 depicts the local heat transfer coefficient in the 4.26 mm tube at a constant mass flux of 400 kg/m²s and 8 bar pressure. As mentioned earlier these data are available in Huo (2006). However, plotting them versus axial distance was first done for the purpose of this thesis. As shown in figure 5.1 (a) for the local heat transfer coefficient versus local quality plot, at qualities $x \leq 0.5$ approximately the heat transfer coefficient is constant within $\pm 10\%$ at a value that increases with increasing heat flux. Within this region, with increasing heat flux, it becomes obvious that there is a small decrease from the first to the second measuring point, then an increase to a maximum value at the fifth measuring point, followed by a gradual decrease. This pattern of small changes becomes more pronounced with increasing heat flux. Also, they occur at higher values of x as the heat flux increases. They exceed the experimental uncertainty and do not occur in the single-phase tests, so they are thought to be genuine and not the consequence of systematic errors at individual thermocouples. At the three highest heat fluxes $q \geq 94 \text{ kW/m}^2$, $x > 0.5$, the heat transfer coefficient decreases rapidly with increasing quality and the data for the three high heat fluxes converge on a single line. Figure 5.1 (b) shows the same plot but as a function of axial position. This plot reveals the axial heat transfer development as the heat flux increases. An almost constant local heat transfer coefficient with slight consistent pattern of variations that depends on axial position is obtained throughout the test tube for the lower heat fluxes ($q \leq 67 \text{ kW/m}^2$). For the highest heat fluxes ($q > 80 \text{ kW/m}^2$), the heat transfer coefficient values near the

inlet showed a uniform pattern of changes. However, near the exit of the tube, the heat transfer coefficient rapidly falls crossing the lower constant heat flux curves, especially for the two highest heat fluxes 109 and 118 kW/m².



(a)

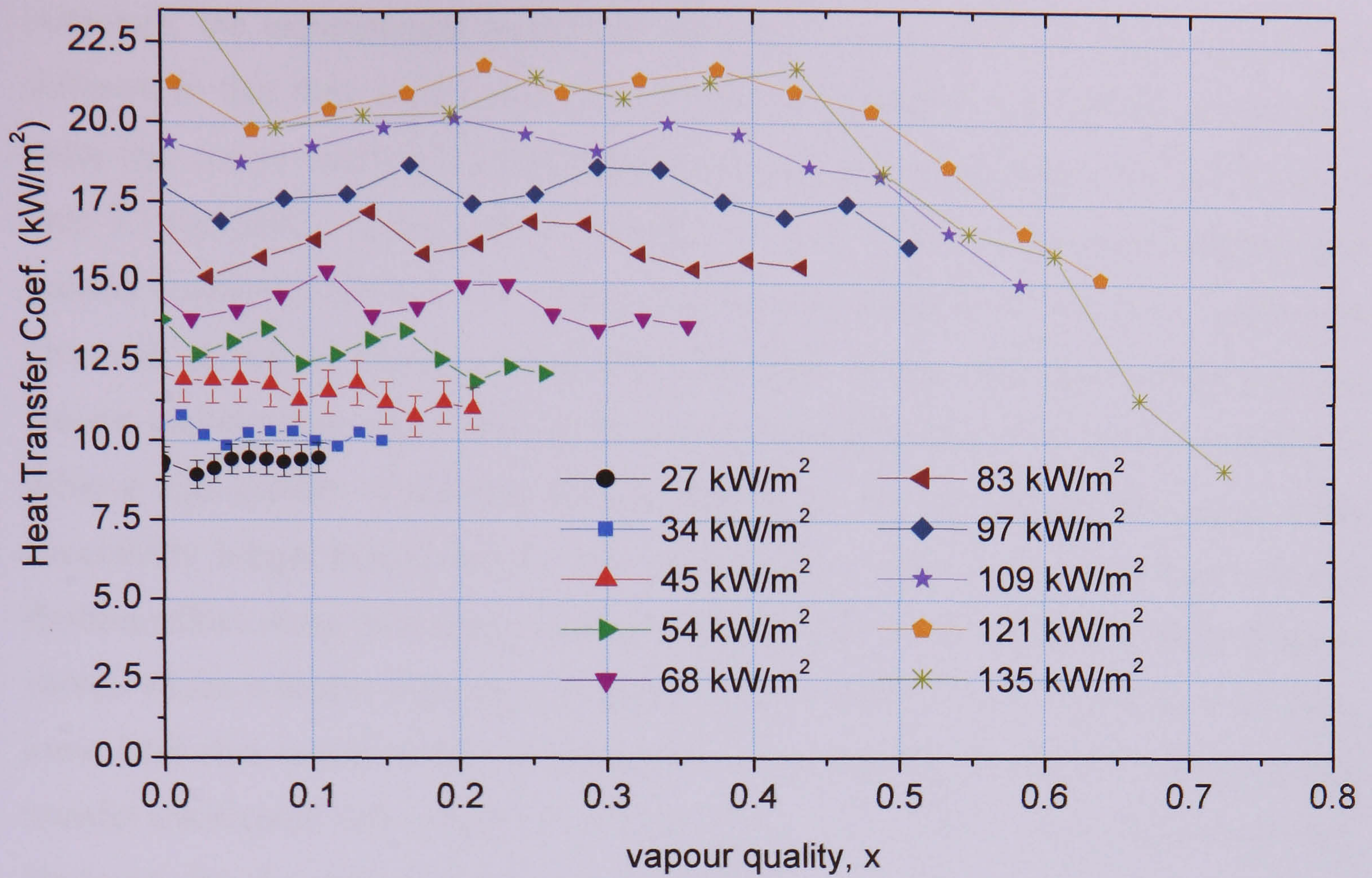


(b)

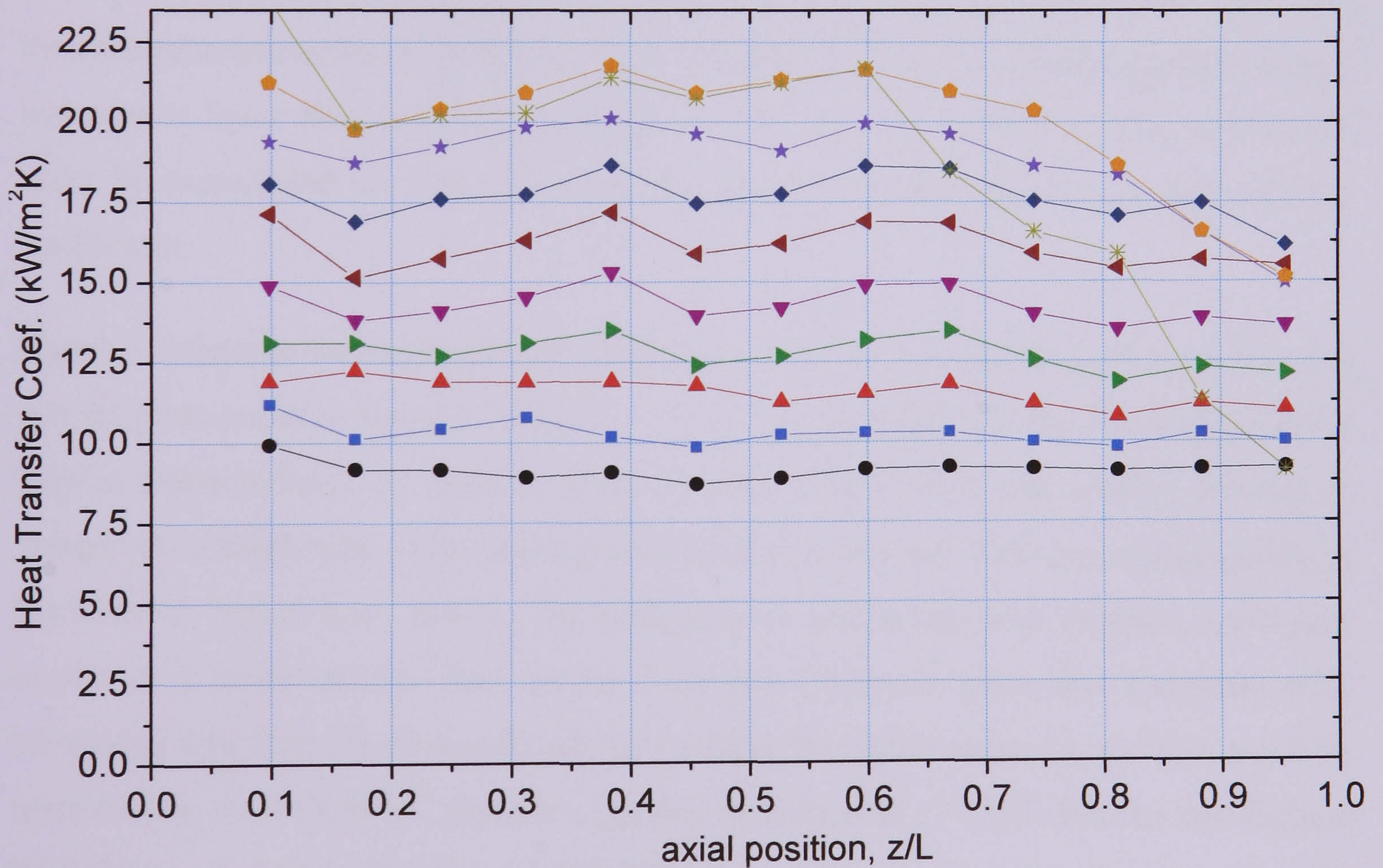
Figure 5.1 Local time-averaged heat transfer coefficient, for $D = 4.26$ mm, $G = 400$ kg/m²s and $P = 8$ bar, as a function of: (a) local quality, (b) axial position.

The pattern of separate lines of nearly constant heat transfer coefficient at low quality merging with a single line of *increasing* heat transfer coefficient at higher quality is familiar in flow boiling experiments in large tubes performed with axially uniform heat flux and leads to the conventional interpretation of nucleate boiling at low quality being suppressed as the wall superheat is depressed by the increase in convective heat transfer at high quality. This interpretation is inconsistent with the *decreasing* heat transfer coefficient and increasing wall superheat in the present experiments. In this particular region only, the tube wall temperature was observed to be highly unstable, leading to large fluctuations so that the experiment had to be stopped occasionally to avoid damaging the test section. It is therefore likely that the decrease in the heat transfer coefficient with increasing vapour quality may be attributable to the occurrence of partial (intermittent) dryout with a long timescale. The data logging system was not set up to record accurately rapid changes in wall temperature in these experiments and the nature of the variations will require further investigation.

In the 2.88 mm tube at a mass flux of $400 \text{ kg/m}^2\text{s}$ and 8 bar pressure, Figure 5.2, the local heat transfer coefficient increases with increasing heat flux and at low heat flux the value is approximately uniform within the uncertainty limit. In Figure 5.2 (a) (local heat transfer coefficient as a function of local quality), there is a decrease in the heat transfer coefficient for the first one or two measuring points at the inlet to the test section. Then, for heat flux values $q \geq 54 \text{ kW/m}^2$, the coefficient slightly increases with quality up to the fourth or fifth data point and fluctuates within the uncertainty range. At 109 and 121 kW/m^2 , the lines of constant heat flux gradually shift to a decrease in heat transfer coefficient with increasing quality, which occurs at $x > 0.4$. At 135 kW/m^2 , the constant heat transfer coefficient line merges with that of the 121 kW/m^2 and a sharp transition occurs at $x = 0.44$. The corresponding local heat transfer coefficient versus axial position plot presented in figure 5.2 (b) also shows a roughly constant heat transfer coefficient for low heat flux values of $q \leq 54 \text{ kW/m}^2$. For heat flux values between 54 and 97 kW/m^2 the values slightly fluctuate within the uncertainty limit. For the two high heat flux values of 109 and 121 kW/m^2 , the values of the heat transfer coefficient coincide for the last three measuring points and fall with axial distance towards the exit. On the other hand, at 135 kW/m^2 , the heat transfer coefficient drops sharply after the eighth measuring point crossing the constant heat flux curves.



(a)



(b)

Figure 5.2 Local time-averaged heat transfer coefficient, for $D = 2.88$ mm, $G = 400$ kg/m²s and $P = 8$ bar, as a function of: (a) local quality, (b) axial position.

Although, the experimental method of Saitoh et al. (reviewed in section 3.4.2) was different in that they used typical compression refrigeration cycle (with an expansion valve and compressor), it is interesting to make a quick comparison with the results of their 3.1 mm tube. As discussed in chapter 3, Figure 3.14(a), a region of constant heat transfer coefficient up to $x=0.6$ followed by an increasing coefficient with quality was observed. It will be worth noticing their heat flux values were much lower than the present experiments and consequently a long heated length (3.24 m) is employed to achieve high quality. A pressure drop as high as 4.9 bar was measured because of the excessively longer heated length. The corresponding saturation temperature drop and flashing effect along their tubes, their inlet quality (0.2 to 0.25 created by the expansion valve), which is higher than the exit quality (~ 0.11) of the current experiments at nearly same heat flux could be one of the reasons for having a region of increasing heat transfer coefficient with quality in cases of Saitoh et al. (2005), unlike the present data. However, for the uniform heat transfer coefficient region ($x < 0.6$), the magnitude of their coefficients are only slightly lower (by $\sim 8\%$, which is within the uncertainty limit) than the present results of 2.88 mm at $q = 27 \text{ kW/m}^2$. Since the system pressure in their test tube is lower than the current values, i.e. the effect of pressure on the coefficients must be considered in order to compare correctly magnitudes of the heat transfer coefficient.

Figure 5.3 depicts the experimental data for the 2.01 mm tube at the same mass flux and system pressure as in figures 5.1 and 5.2. As shown in figure 5.3 (a), the results exhibit similar characteristics of separate lines for each heat flux at low quality, tending to merge into a single line of decreasing heat transfer coefficient with increasing quality in the tests at higher heat fluxes. The transition to decreasing heat transfer coefficient occurs at a lower quality than in the 4.26 and 2.88 mm tubes that decreases with increasing heat flux. At 67 and 81 kW/m^2 , a sharp transition occurs at $x = 0.31$ and 0.38 respectively. At 95 kW/m^2 , there is a gradual transition at $x = 0.27$. For the two highest heat fluxes of 122.6 kW/m^2 and 134 kW/m^2 , the region of decreasing heat transfer coefficient commences very close to the start of the heated length. The lines for the two heat fluxes initially coincide (as far as $x=0.05$), but then there is a relative increase in the heat transfer coefficient for 122.6 kW/m^2 that persists until the lines for all heat fluxes merge.

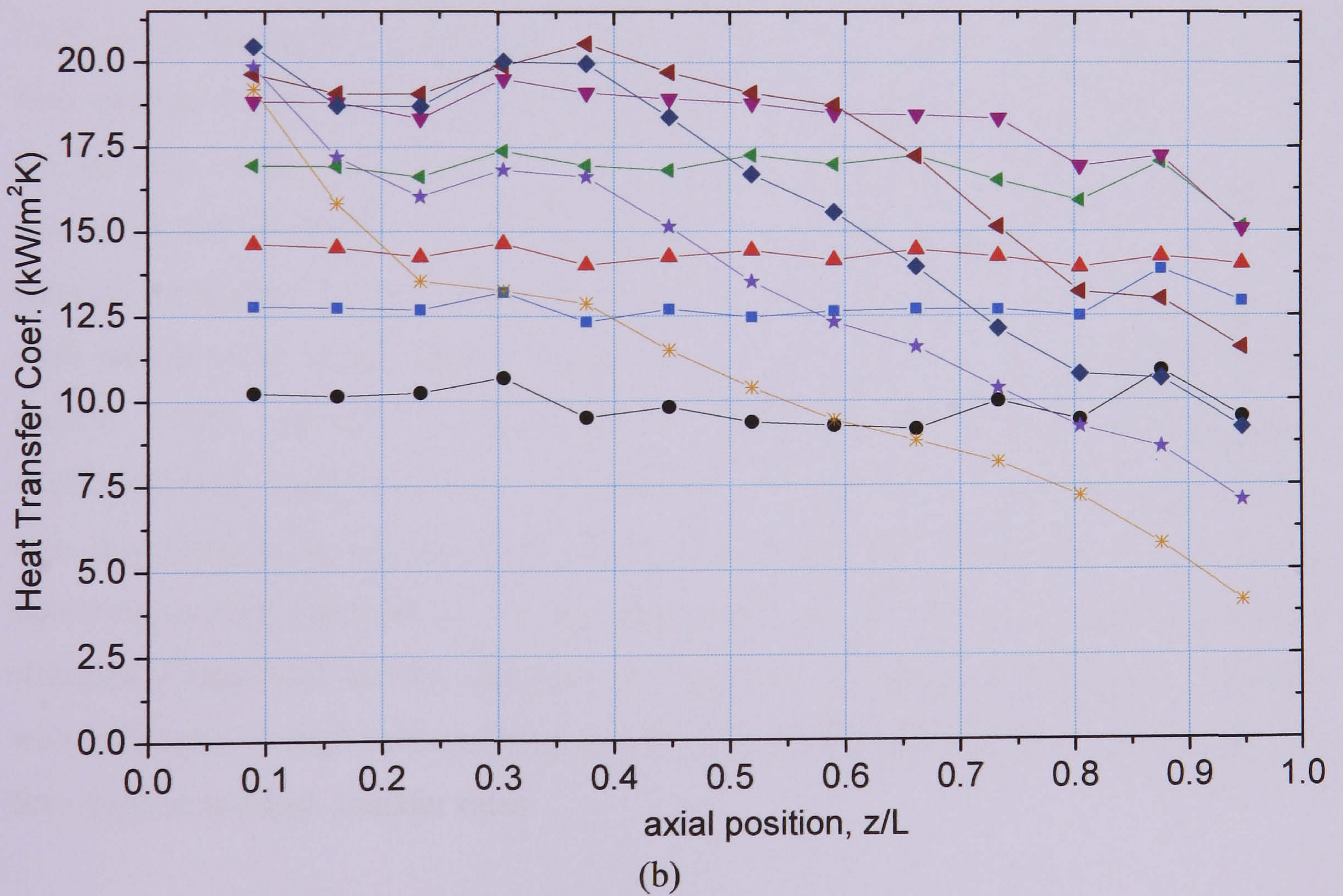
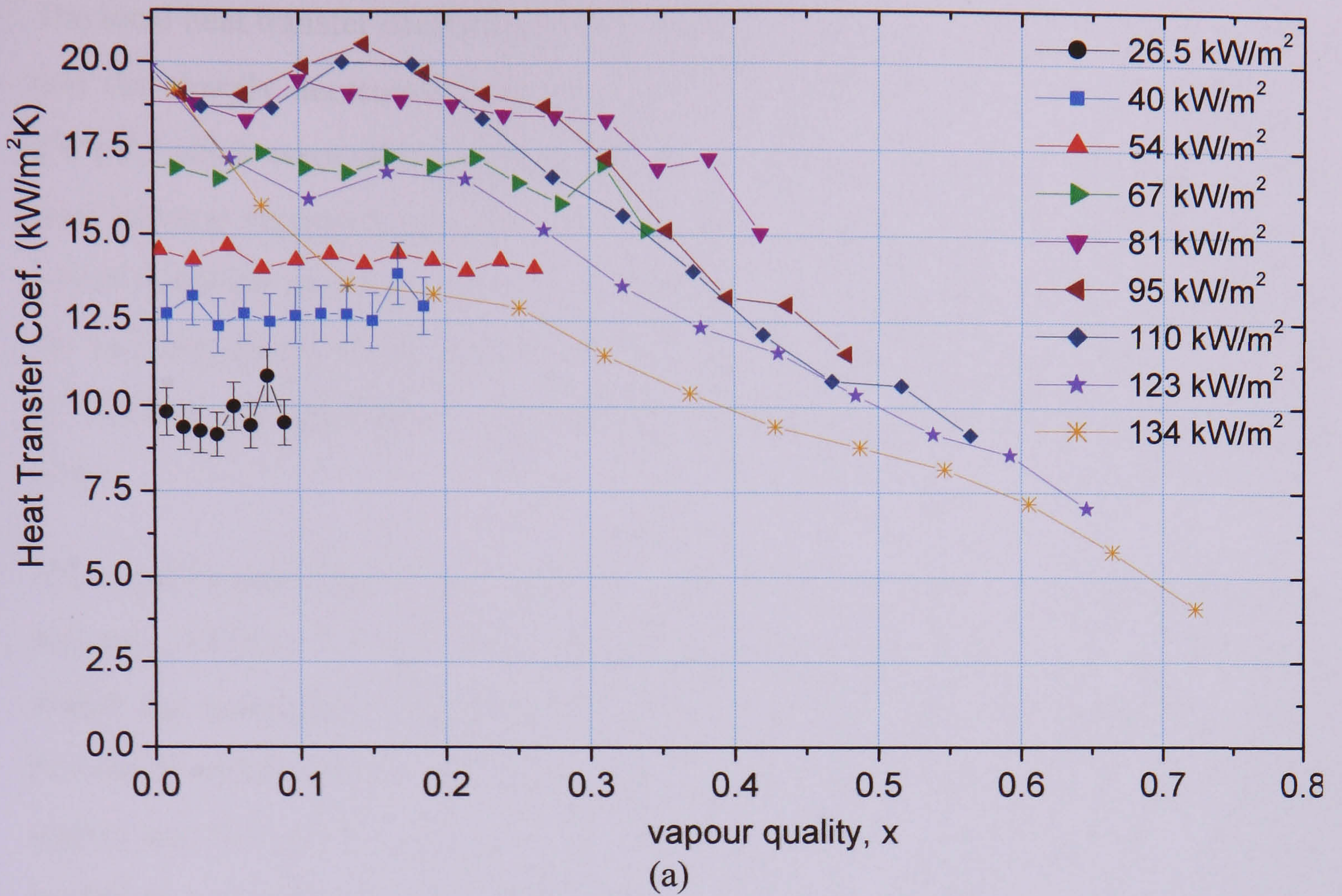


Figure 5.3 Local time-averaged heat transfer coefficient, for $D = 2.01$ mm, $G = 400$ $\text{kg/m}^2\text{s}$ and $P = 8$ bar, as a function of: (a) local quality, (b) axial position.

The local heat transfer coefficient versus axial distance shown in Figure 5.3 (b) revealed that the sharply decreasing heat transfer coefficient curves for heat flux values ≥ 95 kW/m², which were observed to approximately merge to single lines at high quality, now become separated and the value decreases with heat flux. The axial position at which transition to the rapidly decreasing heat transfer coefficient occurs coincides for the two heat fluxes of 95 and 110 kW/m². For the lowest heat flux value of 26.5 kW/m², there is a slight gradual increase in heat transfer coefficient towards the exit of the tube.

The experimental data for the 1.10 mm tube at the same mass flux and pressure are depicted in Figure 5.4. As shown in the figures, the heat transfer coefficient is constant within the uncertainty limit and increases with increasing heat flux, up to 69 kW/m². For the 89 and 96 kW/m², the lines of constant heat flux coincide for the entire quality region and shift to the region of decreasing heat transfer coefficient with increasing quality at $x = 0.23$. The 126 kW/m² follows the same line until $x=0.23$, and gradually shifts to the decreasing heat transfer coefficient region at $x = 0.26$. However, the actual heat transfer coefficient value is higher than the rest until about $x=0.6$, Figure 5.4 (a). On the other hand, looking at Figure 5.4 (b), the values for the 126 kW/m² merge with that of 89 and 96 kW/m² up to the position ($z/L = 0.65$). Beyond this point, the heat transfer coefficient for the 126 kW/m² falls sharply with axial distance. This contrasts with Saitoh et al., at the same diameter shown in Figure 3.14 (b), in which the heat transfer results showed a very significant region of an increasing heat transfer coefficient with quality up to $x= 0.85$ followed by a sharper decreasing region. There was very small or no constant heat transfer coefficient region. These variations in the local heat transfer dependence could be again attributed to the fact that their results were obtained at high inlet quality, relatively low heat flux and longer heated length and they were subjected to high pressure drop and flashing effect, which may have influence on flow regime and heat transfer rates.

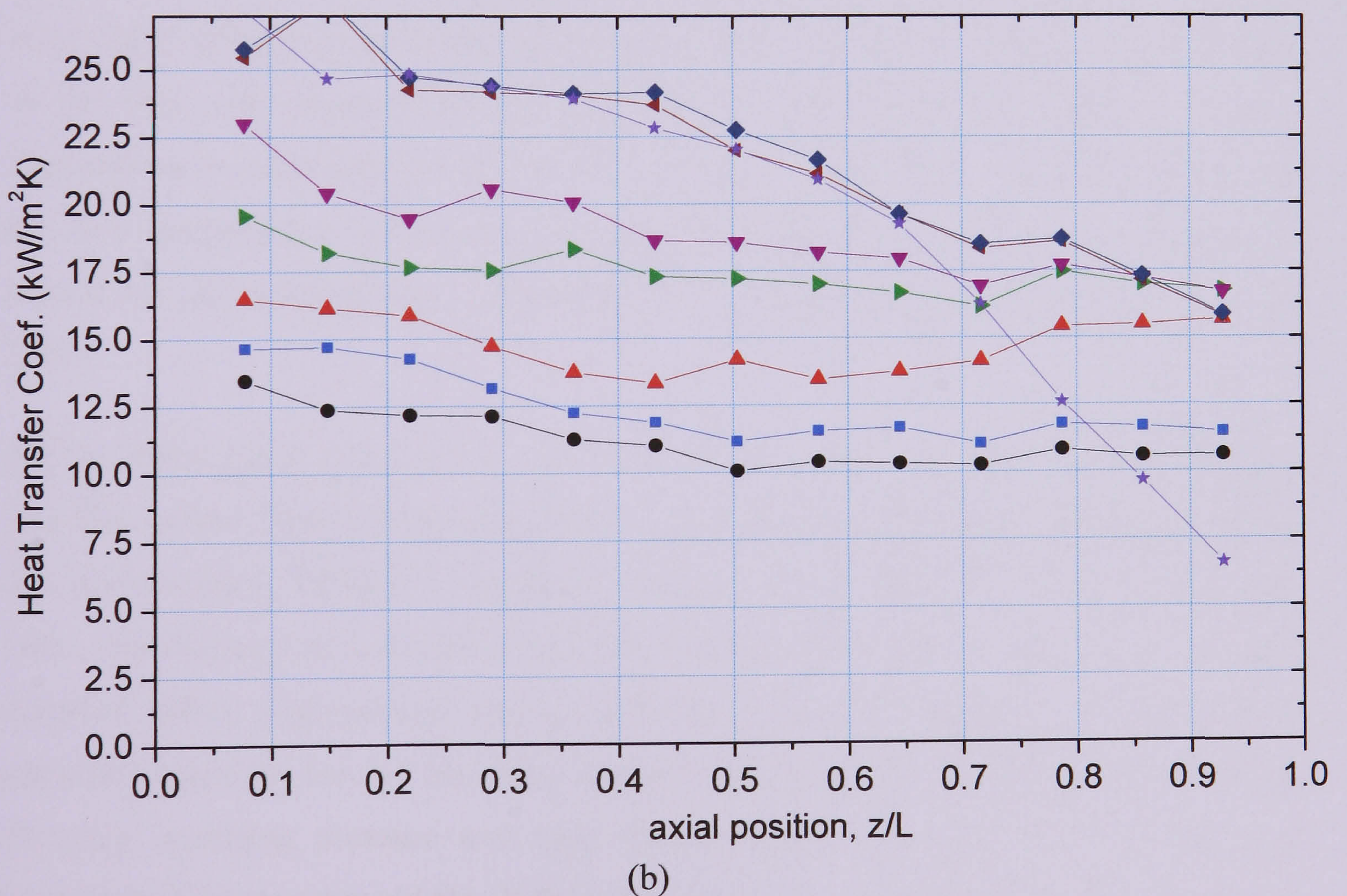
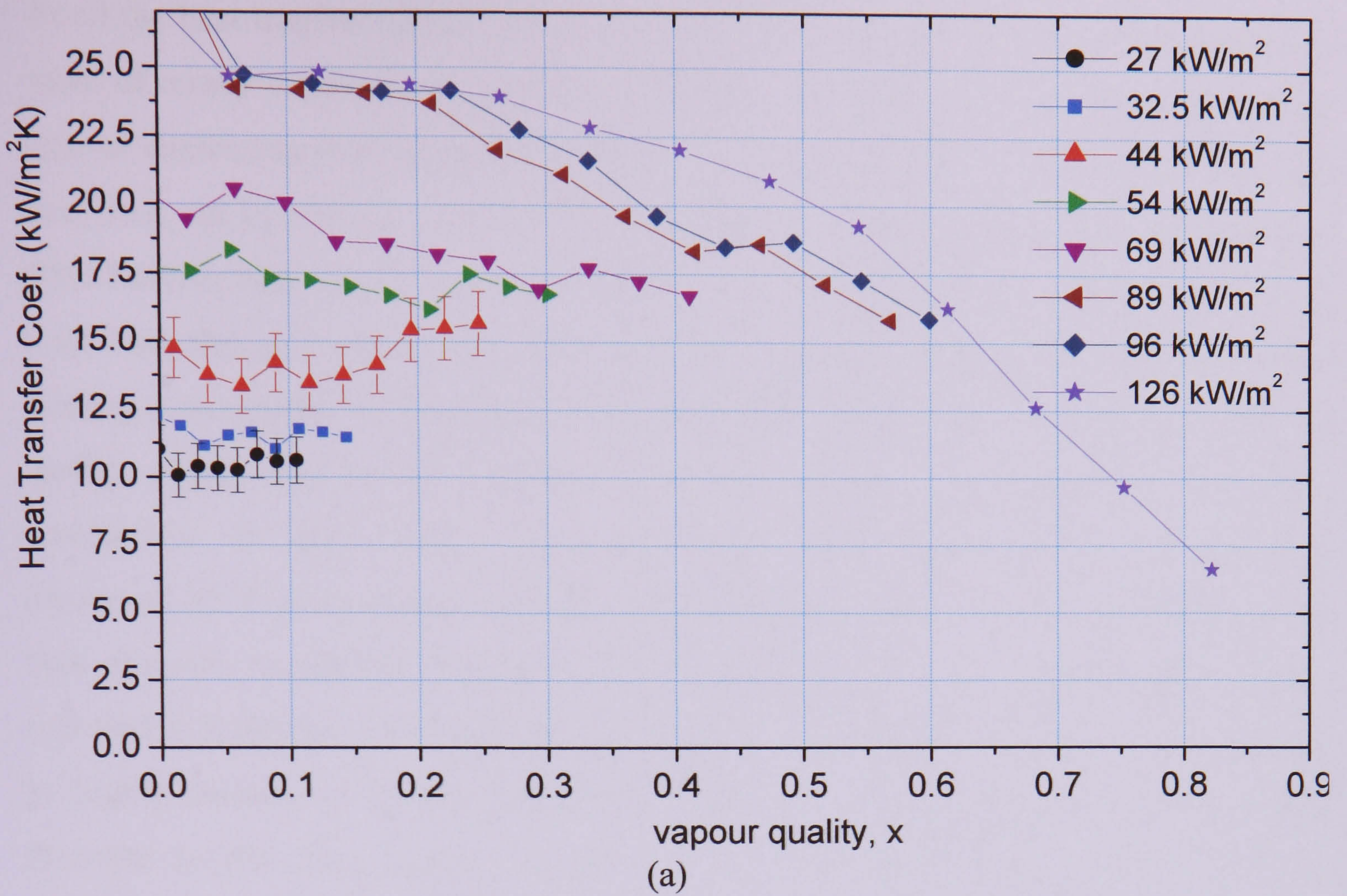


Figure 5.4 Local time-averaged heat transfer coefficient, for $D = 1.10$ mm, $G = 400$ $\text{kg/m}^2\text{s}$ and $P = 8$ bar, as a function of: (a) local quality, (b) axial position.

In all the heat transfer results in the 4.26 to 1.1 mm tubes, a similar pattern of separate lines of nearly constant heat transfer coefficient at low quality merging with a single line of decreasing heat transfer coefficient at higher quality is observed. At very high heat flux, the results also showed the heat transfer coefficient decreases with heat flux. This limiting heat flux for a reverse in the trend of heat transfer coefficient increasing with heat flux is found to decrease with decreasing tube diameter. Referring to flow boiling experiments in large tubes performed with axially uniform heat flux, the low quality results lead to the conventional interpretation of nucleate boiling dominant mechanism. At high quality, the typical large tube phenomena of wall superheat depressed by the increase in convective heat transfer is not observed here, instead the heat transfer coefficient decreases (wall superheat increases) with quality. It was reported in Shiferaw et al. (2007) that Huo (2006) observed the tube wall temperature to be highly unstable in this particular region. This could be an indication that the data of decrease in the heat transfer coefficient with increasing vapour quality may be attributable to the occurrence of partial (intermittent) dryout with a long timescale, Huo et al. (2007), Shiferaw et al. (2007). Similar phenomena of partial dryout and rewetting of the wall were assumed by Lin et al. (2001) and Sumith et al. (2003) to cause fluctuations in wall temperature. Lin et al. (2001) and Sumith et al. (2003) found that the wall temperature fluctuations increased with heat flux. This was assumed to be related to time varying local heat transfer coefficient and local pressure, Lin et al. (2001).

All the above plots show typical results at a fixed mass flux and pressure for different heat flux values. However, the experiments in all the tubes cover a wider range of mass flux and pressure. Therefore, the effect of mass flux and pressure will be investigated later. Nevertheless, because of its size and the possible benefits to the study of small diameter tubes, experimental data at different values of mass flux and pressure is presented again for the 1.1 mm tube to verify that similar behaviour is observed with changing operating pressure and mass flux, although the effect of mass flux and pressure will be investigated for all the tubes in the coming sections. Figure 5.5 presents similar plot as figure 5.4 (a), but decreasing the mass flux to the lowest value of 200 kg/m²s, while keeping the pressure the same. This is shown in figure 5.5 (a). On the other hand, figure 5.5 (b) depicts similar result but decreasing the system pressure to the lowest value of 6 bar, which maintaining same mass flux as the base case (figure 5.4 a).

As seen in figure 5.5 (a) for the lowest mass flux case, it is interesting to see that the heat transfer coefficient tends to increase with quality towards the test section exit at relatively low and moderate values of heat flux, $q \leq 34 \text{ kW/m}^2$ (also seen at $q = 44 \text{ kW/m}^2$ in figure 5.4). This tendency of increasing heat transfer coefficient with quality for low heat flux conditions could be related to the fact that the heat flux is not so intense to cause dryout, so that a smooth transition to flow boiling regime occurs, i.e. nucleate boiling at relatively low quality becomes suppressed as the wall superheat is depressed by the increase in convective heat transfer at relatively high quality. It is also worth to note that the all-liquid Reynolds number has decreased from 2500 to 1250 falling more into the laminar regime. However, for the higher heat flux values of $q \geq 53 \text{ kW/m}^2$, the heat transfer coefficient becomes independent of heat flux and sharply decreases with quality when the vapour quality is greater than 50 %. This could be due to the fact that, at the higher heat flux values dryout and/or departure from nucleate boiling (DNB) occurs before convective boiling commences. Moreover, the highest heat flux value, at which the heat transfer coefficient does not increase with heat flux anymore, decreases from 96 to 69 kW/m^2 as the mass flux decreases from 400 to 200 $\text{kg/m}^2\text{s}$. On the other hand, in figure 5.5 (b) at 400 $\text{kg/m}^2\text{s}$, the effect of decreasing the saturation pressure from 8 to 6 bar is not significant, i.e. when $x < 0.3$, the heat transfer coefficient depends on the heat flux and is almost independent of quality. At high values of heat flux (69 and 85 kW/m^2), the heat transfer coefficient decreases with quality for vapour quality greater than 20 %. At the highest heat flux value of 107 kW/m^2 , the region of decreasing heat transfer coefficient commences very close to the start of the heated length followed by a short constant region for the intermediate quality range (0.12 to 0.3). Beyond this range, it monotonically drops with quality.

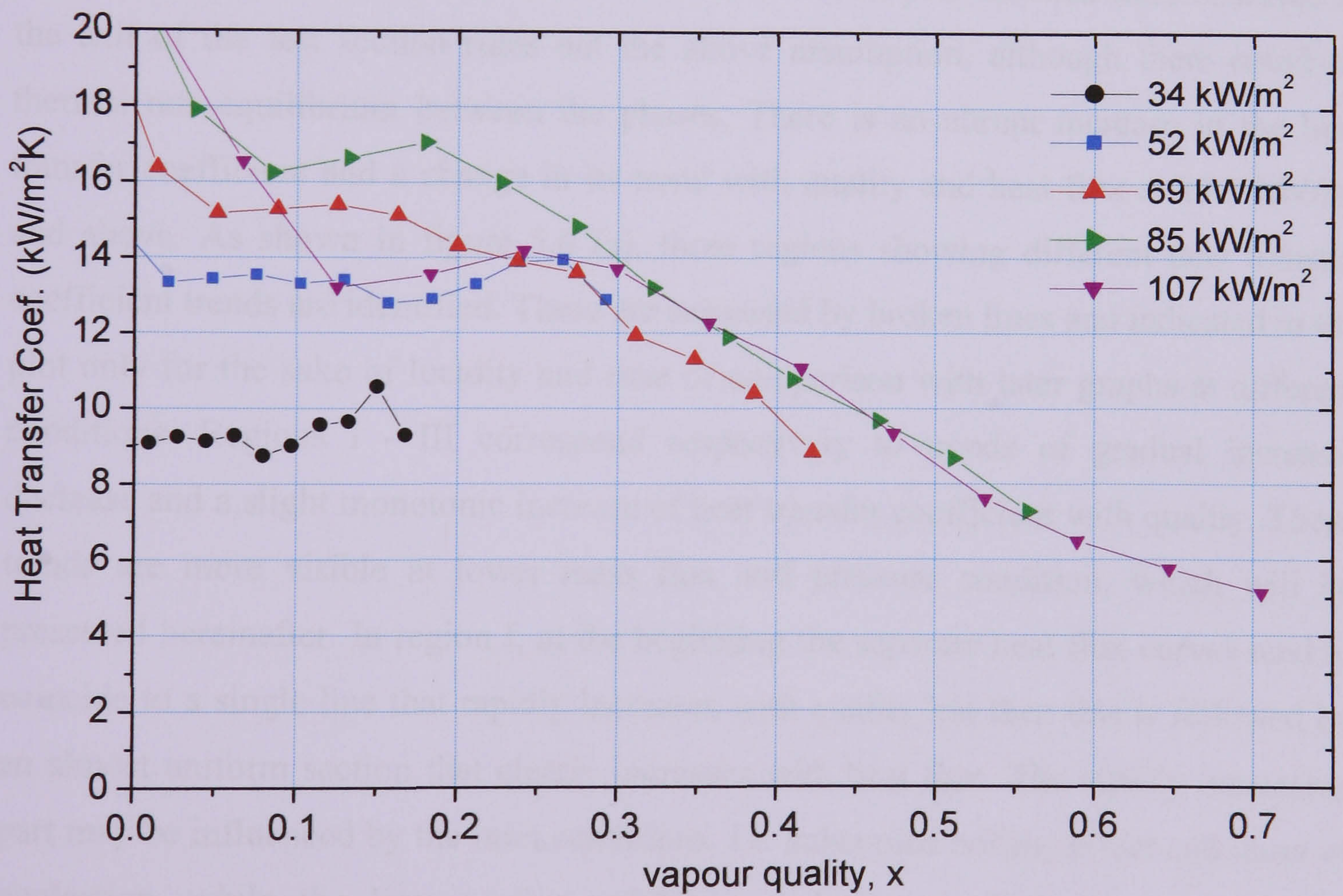
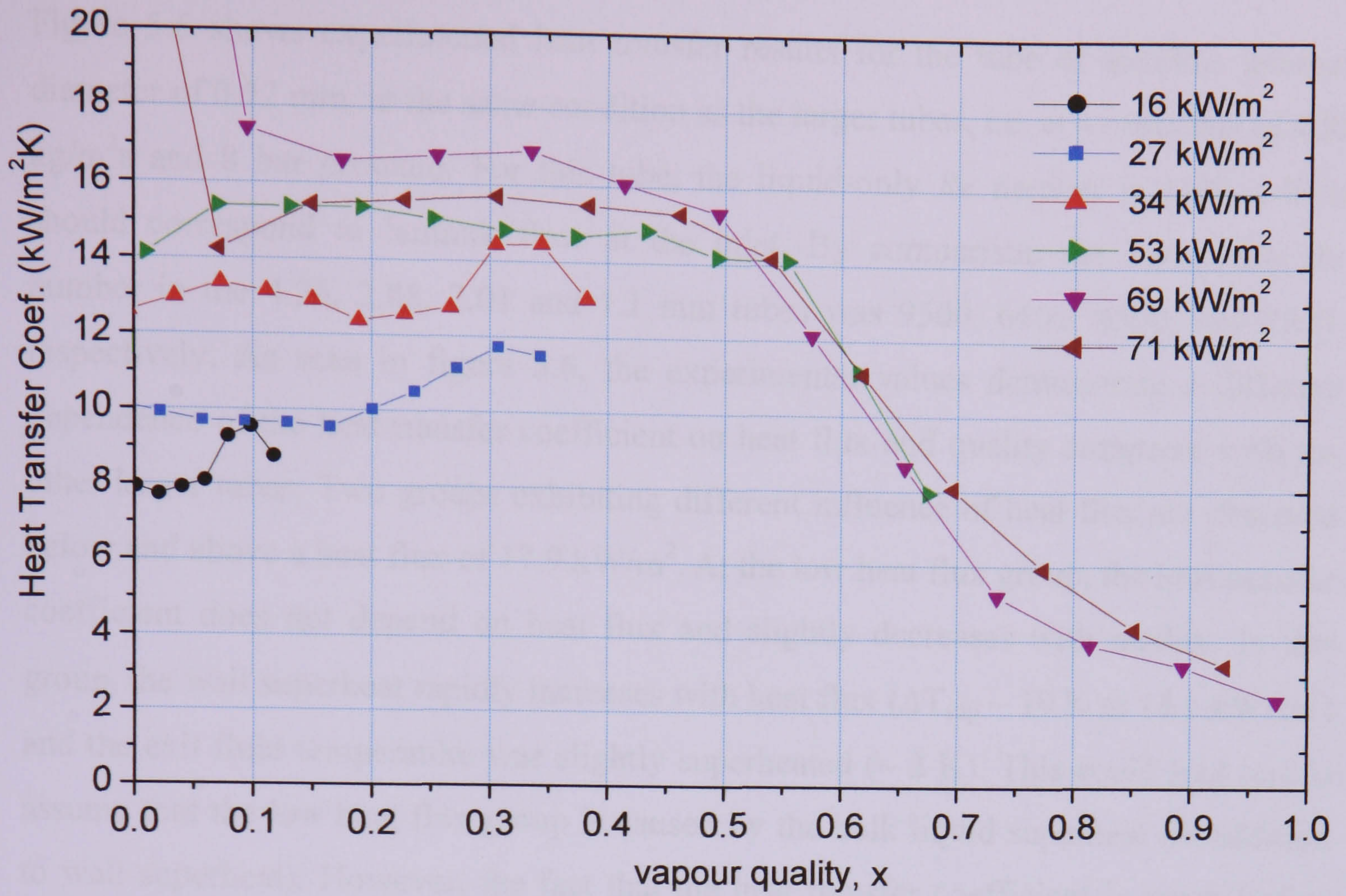
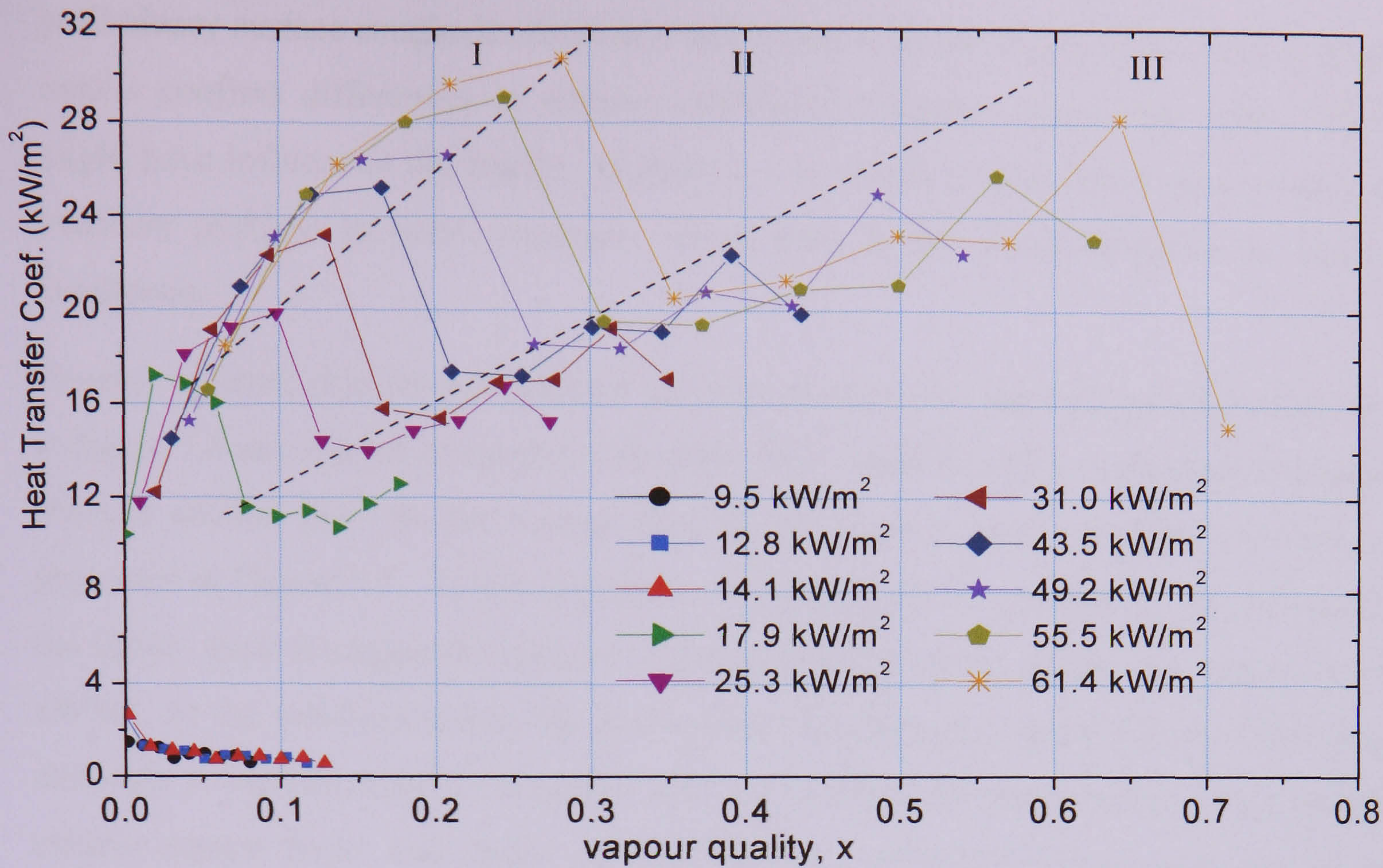


Figure 5.5 Local time-averaged heat transfer coefficient as a function of local quality for $D = 1.10 \text{ mm}$: (a) $G = 200 \text{ kg/m}^2\text{s}$, $P = 8 \text{ bar}$ (b) $G = 400 \text{ kg/m}^2\text{s}$, $P = 6 \text{ bar}$

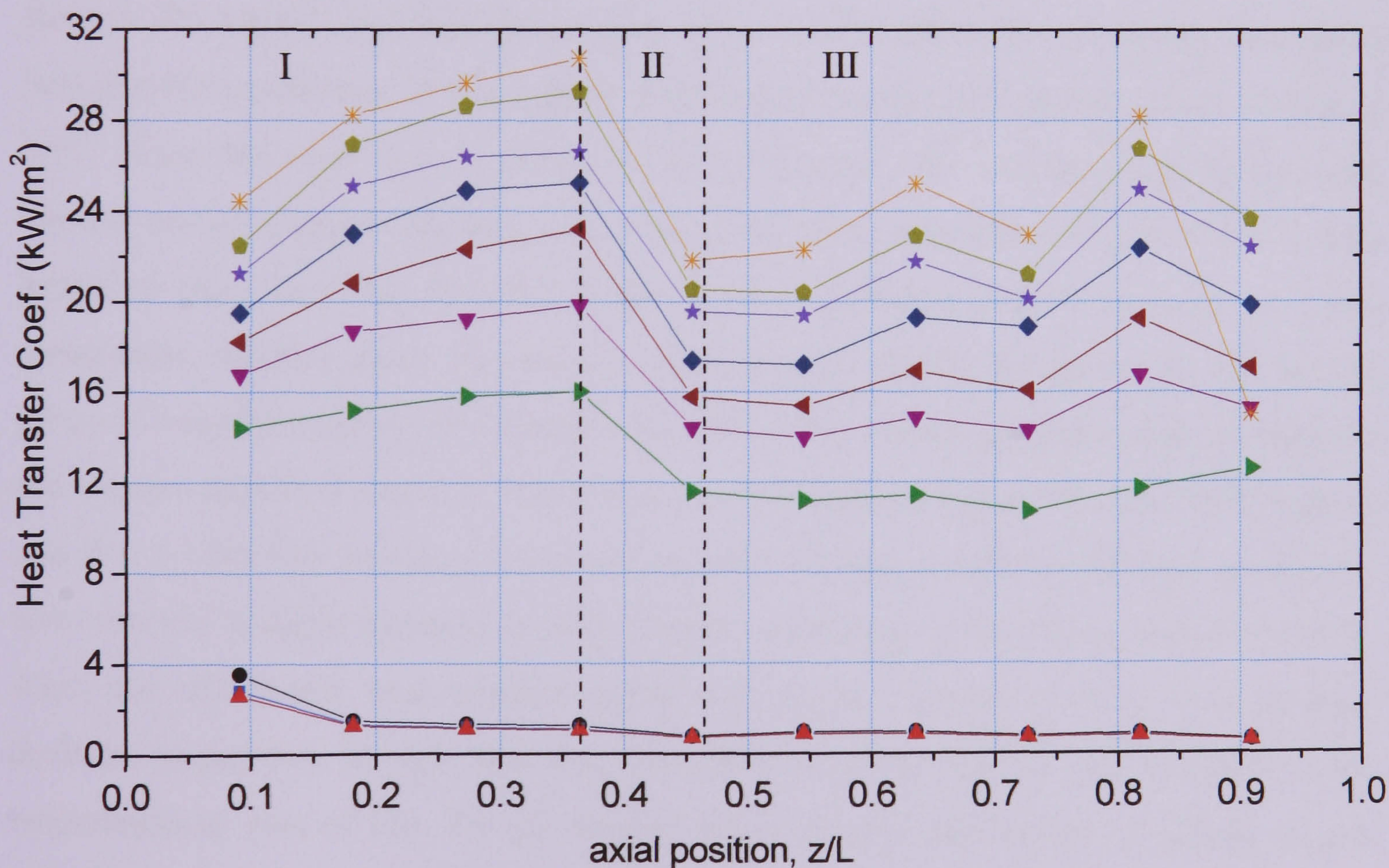
Figure 5.6 shows experimental heat transfer results for the tube of smallest internal diameter of 0.52 mm, at the same condition as the larger tubes, i.e. at a mass flux of 400 kg/m²s and 8 bar pressure. For this tube, the liquid-only *Re* number is 1100, which should correspond to laminar flow at the inlet. By comparison the liquid-only *Re* number in the 4.26, 2.88, 2.01 and 1.1 mm tubes was 9500, 6400, 4500, and 2500, respectively. As seen in figure 5.6, the experimental values demonstrate a different dependence of the heat transfer coefficient on heat flux and quality compared with the other larger tubes. Two groups exhibiting different influence of heat flux are observed below and above a heat flux of 17.9 kW/m². At the low heat flux group, the heat transfer coefficient does not depend on heat flux and slightly decreases with quality. In this group, the wall superheat rapidly increases with heat flux ($\Delta T_{\text{sup}} \sim 19 \text{ K}$ at 14.1 kW/m²) and the exit fluid temperature was slightly superheated ($\sim 2 \text{ K}$). This could lead one to assume that the low heat flux group is caused by the bulk liquid superheat (in addition to wall superheat). However, the fact that the heat transfer coefficient is much higher than the expected single phase value of $\sim 0.62 \text{ kW/m}^2\text{K}$, plus bubbles were observed at the exit of the test section rules out the above assumption, although there could be thermal non-equilibrium between the phases. There is an abrupt increase in the heat transfer coefficient and a change in its trend with quality and heat flux at 17.9 kW/m² and above. As shown in figure 5.6 (a), three regions showing different heat transfer coefficient trends are identified. These are separated by broken lines and indicated in the plot only for the sake of lucidity and ease of comparison with later graphs at different conditions. Regions I - III correspond respectively to trends of gradual increase, decrease and a slight monotonic increase of heat transfer coefficient with quality. These trends are more visible at lower mass flux and pressure condition, which will be presented hereinafter. In region I, at the beginning the separate heat flux curves tend to coincide to a single line that rapidly increases with quality but then this is followed by an almost uniform section that clearly increases with heat flux. The rapidly increasing part may be influenced by the inlet conditions, i.e. subcooled boiling effect and onset of nucleation, while the later section exhibits a behaviour, which is conventionally interpreted as evidence for a nucleate boiling dominant region. This region changes suddenly to region II, in which the heat transfer coefficient decreases sharply with increasing quality. The decrease in heat transfer observed in the present results is different from that of a continuous decrease, observed towards the test section exit in the larger tubes of this study. This could occur due to intermittent dryout, at nucleation

sites or might be related to flow regimes of large disturbances in laminar film. This is a speculation that requires further investigation. After region II (region of sharp drop in heat transfer coefficient with quality), the heat transfer coefficient increases with quality. The heat transfer results of the smallest diameter tube (0.52 mm) demonstrated different characteristic than the rest of the tubes, particularly at the high quality region (region III). In this region, the effect of heat flux is lessened at high quality. Unlike the larger tubes that were examined in this study, which exhibit phenomena indicative of dryout as the high heat flux increases, i.e. continuous decrease of heat transfer coefficient with quality towards the test section exit seen in Figures 5.1 to 5.5, a monotonic increase in heat transfer coefficient was observed near the exit for the smallest diameter tube. This could be related to laminar flow and domination of surface tension force over momentum, providing more uniform liquid film thickness along the circumference or small scale disturbances, which improve wetting of the wall, Shiferaw et al. (2008). For the larger tubes, the dryout was associated with highly unstable wall temperature variations. Moreover, Saitoh et al. (2005) found oscillating flows and unstable conditions for the 3.1 and 1.12 mm diameter tubes. However, they did not observe similar fluctuation for their 0.51 mm tube. Although they did not mention any reason for this, their finding agrees with the present case of the fact that the 0.52 mm diameter tube did not exhibit dryout behaviour. Nevertheless, as seen in figure 5.6, the heat transfer coefficient does drop sharply at the highest quality and heat flux values. This could indicate complete dryout of the liquid film during annular flow at relatively high quality.

On the other hand, looking at the heat transfer coefficient versus axial distance plot, Figure 5.6 (b), the heat transfer coefficient increases almost uniformly with heat flux all along the tube, especially for the second group of heat flux curves ($q \geq 17.9 \text{ kW/m}^2$). The region corresponding to the monotonic increase of heat transfer coefficient with quality (region III), now showed a relatively very weak dependence on axial distance. For the highest heat flux value of 61.4 kW/m^2 , the heat transfer coefficient sharply drops for the last measuring point. Although the variations in the local heat transfer coefficient happened to match with particular thermocouple positions, temperature measurement errors at particular measuring stations are ruled out by the disappearance of unexpected temperature readings in single phase flow.



(a)



(b)

Figure 5.6 Local time-averaged heat transfer coefficient, for $D = 0.52$ mm, $G = 400$ kg/m²s and $P = 8$ bar, as a function of: (a) local quality, (b) axial position

The above behaviour observed in this very small tube could be attributable to the axial variation in surface roughness, which has a large influence on local nucleation. The

preliminary surface roughness measurements along with the single phase friction factor results confirm differences in surface conditions compared with other tubes, which might have influenced the results. Moreover, it is worth to note that fouling is another common problem in small passages, which adds to the local variations in surface conditions.

In order to verify that most of the new features observed for the 0.52 mm diameter tube in figure 5.6 are indeed consistent with other flow conditions (lower pressure and mass flux), a similar plot but for a mass flux of 300 kg/m²s and a pressure of 6 bar is presented in Figure 5.7. At this condition, the liquid-only *Re* number is 720. As seen in the figure, there are again two groups of data below and above a heat flux value of 14.8 kW/m². At the low heat fluxes, the heat transfer coefficient is independent of heat flux although, it initially drops with quality and then exhibits a weak increase. These results exhibit similar trend and range of heat transfer coefficient values with the R123 experimental results conducted by Yen et al. (2003) for 0.51 mm diameter and mass flux of 295 kg/m²s and heat flux values of ($q \leq 12.3$ kW/m²), i.e. sharply decreasing heat transfer coefficient at low quality followed by an almost constant value, see figure 3.17. When the heat flux is increased to 14.8 kW/m², the second group that exhibit varying trends is again observed. Lin et al. (2001) for 1 mm tube using R141b (for their heat flux value less than 60 kW/m²) and Di'az and Shmidt (2007) for 0.3 x 12.7 mm rectangular channel using ethanol observed loosely similar behaviour to this second group of heat flux curves. In contrast with Figure 5.6, a more gradual transition between the regions specified above is obtained at low pressure and mass flux ($G = 300$ kg/m²s and $P = 6$ bar). For instance, the sharp increase of heat transfer coefficient in region I now showed a slight increase in heat transfer coefficient within the uncertainty limit. Also, the decreasing heat transfer coefficient portion (region II) is a more gradual decrease (especially at high heat flux) compared with the sharper fall observed in the corresponding plot of Fig. 5.6 (a). Region III is almost independent of quality at low heat flux values and gradually increases with quality as the heat flux increases. The sharp drop toward the exit of the test section, seen in figure 5.6 for $q = 61.4$ kW/m², is not shown in Fig. 5.5 (at least for the slightly lower value of 58.4 kW/m²).

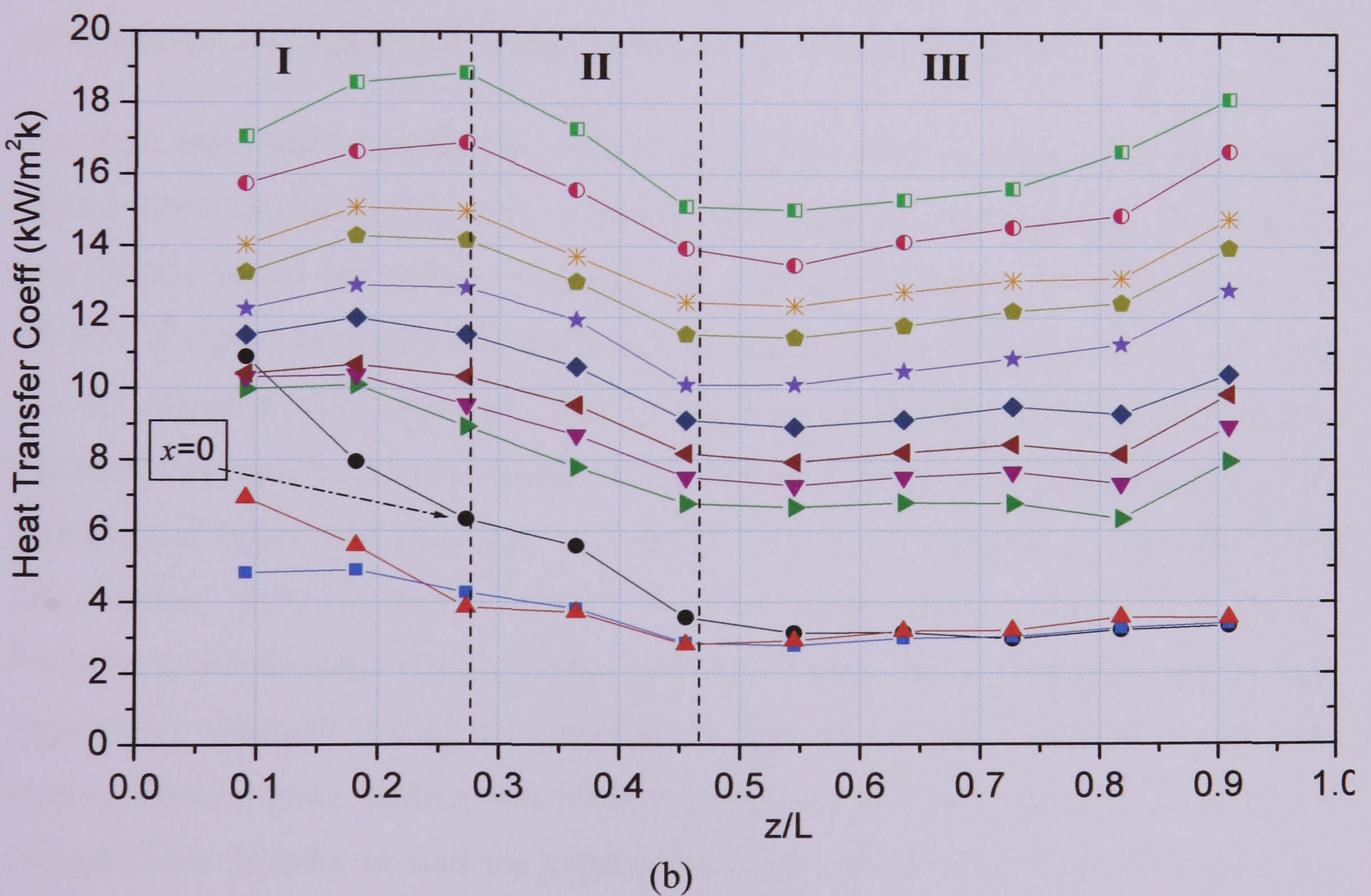
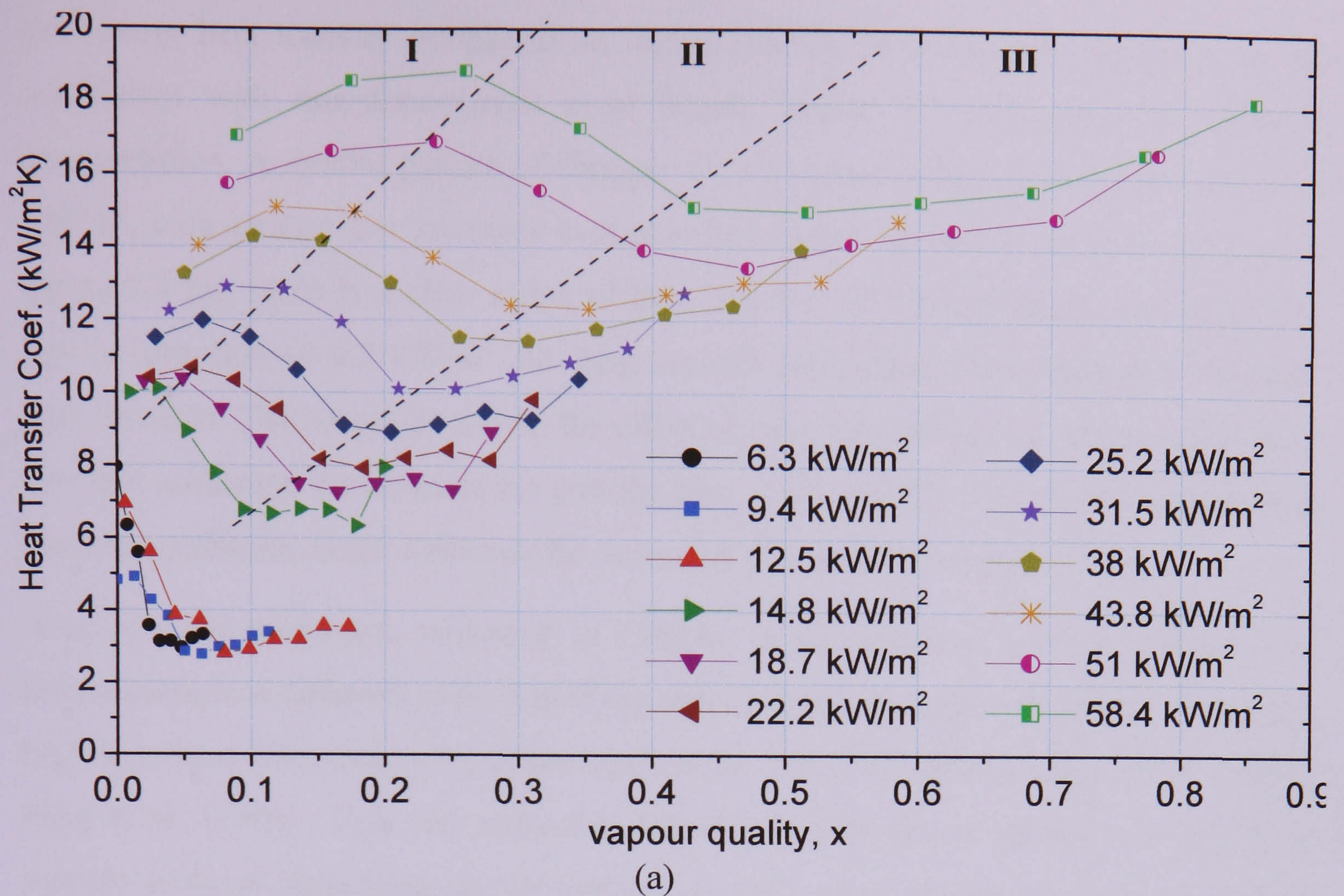


Figure 5.7 Local time-averaged heat transfer coefficient, for $D = 0.52$ mm, $G = 300$ $\text{kg/m}^2\text{s}$ and $P = 6$ bar, as a function of: (a) local quality, (b) axial position.

Looking only at heat transfer coefficient versus quality plot, one could suggest that the results are more similar with the large-tube patterns: the pattern of separate lines of nearly constant heat transfer coefficient at low quality merging with a single line of

increasing heat transfer coefficient at higher quality. However, the variations in the coefficient with non-dimensional axial length, Figure 5.7 (b), suggest a different interpretation. A similar pattern of changes for all values of heat flux greater than 14.8 kW/m^2 , with a value that increases with heat flux almost uniformly, is observed. Unlike figure 5.7 (a), there is a clear effect of heat flux for all the regions. However, for the lowest heat flux of 6.3 kW/m^2 , the heat transfer coefficient drops with axial distance near the inlet. This could be due to the effect of inlet subcooling, i.e. the heat flux is so low that saturation commences far into the tube at $z/L \sim 0.27$. Therefore, the large heat transfer coefficient at the inlet may be caused by the onset of subcooled boiling.

A number of researches reviewed in Chapter 3 reported that boiling incipience in microchannels is different from that of the conventional channels and requires unusually high superheat temperature to initiate nucleation, Yen et al. (2003), Hapke et al. (2000), Peng et al. (1998). This was related to the fact that firstly microchannels may have smooth surfaces depending on the fabrication and manufacturing process, i.e. lack of enough active nucleation sites and secondly due to laminar liquid flow.

The wall superheat is plotted as a function of heat flux in Figure 5.8 for different thermocouple positions (numbers in increasing order from inlet side) at a mass flux of $300 \text{ kg/m}^2\text{s}$ and 6 bar system pressure. As seen in the figure, for heat flux $q < \sim 13 \text{ kW/m}^2$, which corresponds to the first set of relatively low heat flux curves of figure 5.7, the degree of wall superheat increases rapidly with heat flux. This may be linked to the high wall superheat that was required to initiate boiling, indicating hysteresis in the activation of nucleation sites as a consequence of the smoothness or small size of the tube surface (more probable for this case), Brereton (1998), Zhang et al (2002), Piasecka and Poniewski (2004). Boiling was initiated by increasing the heat flux until vapour was observed through the visualization glass tube located immediately after the heating section. Once boiling was observed, the heat flux was reduced to the lowest desired value in order to start the experiment from a lower exit quality. However, the boiling was still sustained during the decrease of the heat flux, i.e. bubbles were still observed at the glass tube. This could be due to the fact that the surrounding liquid is superheated and provided energy to sustain the bubbles. This indicated the single-phase liquid can absorb considerable thermal energy, suppressing nucleation at the wall during boiling in very small tubes, as reported by a number of studies in very small size channels. This may cause non-equilibrium in the local temperature distribution of the

phases in the early stage of boiling. The result is a lower heat transfer coefficient and fast increase of wall superheat with heat flux. After the heat flux is increased above a certain value, which is enough to disturb the temperature difference across the bubble interface, the wall superheat suddenly decreases associated with a slight increase of system pressure and pressure drop. This could also cause a rapid vapour generation, resulting in a sudden increase of heat transfer coefficient, in which case the local phase temperature could be back in equilibrium. Again, this is deduced due to the fact that the superheating of the fluid at the exit from the test section gradually decreases as the heat flux increases. Beyond a heat flux of $\sim 13 \text{ kW/m}^2$, the exit superheating disappears and there is a sudden decrease in the wall superheat. This is associated with a slight increase of system pressure and pressure drop. This was not observed in the tests with the larger tubes.

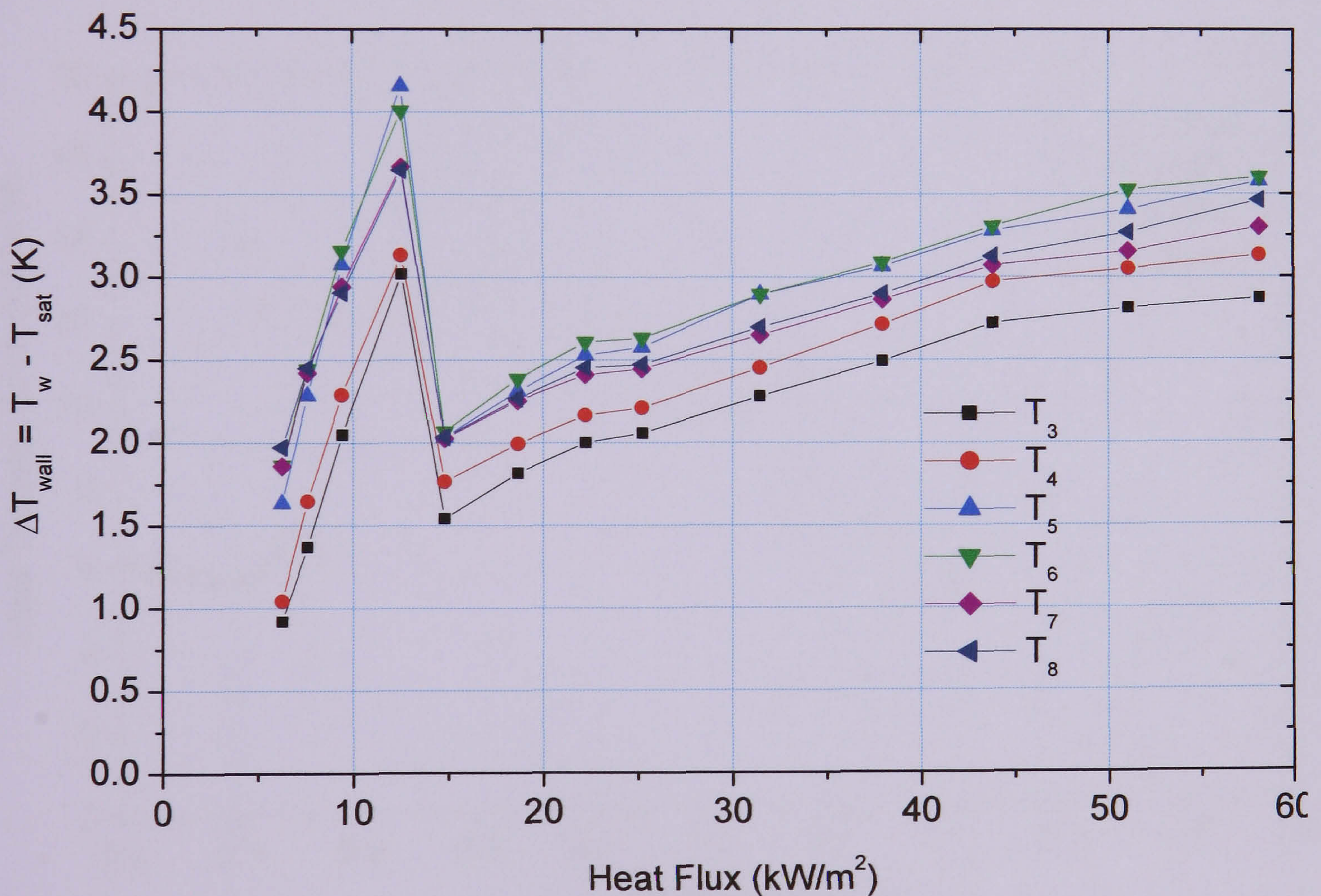


Figure 5.8. Degree of wall superheat as a function of heat flux for the $D = 0.52 \text{ mm}$ tube $G = 300 \text{ kg/m}^2\text{s}$, $P = 6 \text{ bar}$.

The existence of groups of data with different heat flux dependent regions was also observed in the experiments of Wambsganss et al. (1993) at very low mass flux ($Re \sim 360$), see Fig. 3.11. This indicates some of the features observed in the smallest tube could also be related to the flow being laminar in addition to high confinement and

surface tension effects. This can also be checked by looking at the results of 1.1 mm tube results, but at the lowest mass flux of $200 \text{ kg/m}^2\text{s}$. In order to keep the pressure the same with that of 0.52 mm diameter tube (Figure 5.7), experimental results of 1.1 mm tube at a pressure of 6 bar are shown in Figure 5.9. As seen in the figure, at low heat flux there is a tendency that the heat transfer coefficient increases with quality. It is also worth to note the effect of low heat flux over a relatively longer length in contrast with the high heat flux over a short length both providing the same exit quality, which could influence the transition regime from nucleation to convection boiling and/or dryout. In the present experiment, the length-to-diameter ratio of the 1.1 and 0.52 mm tubes are 136.4 and 192, respectively. Further experiments are required to resolve the issue, using longer heated lengths to achieve larger exit qualities at low heat flux, subject to any limitations imposed by pressure drop.

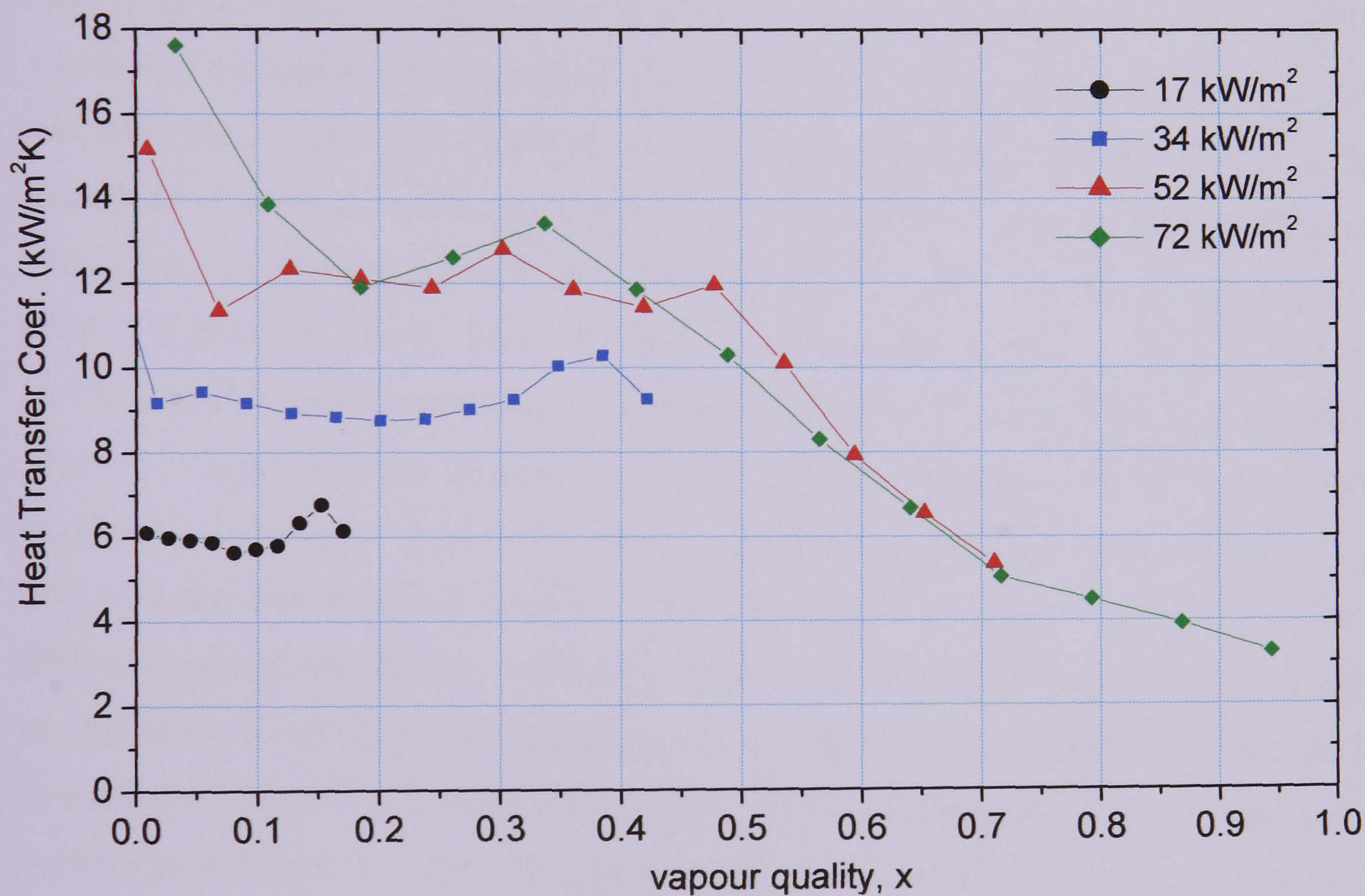


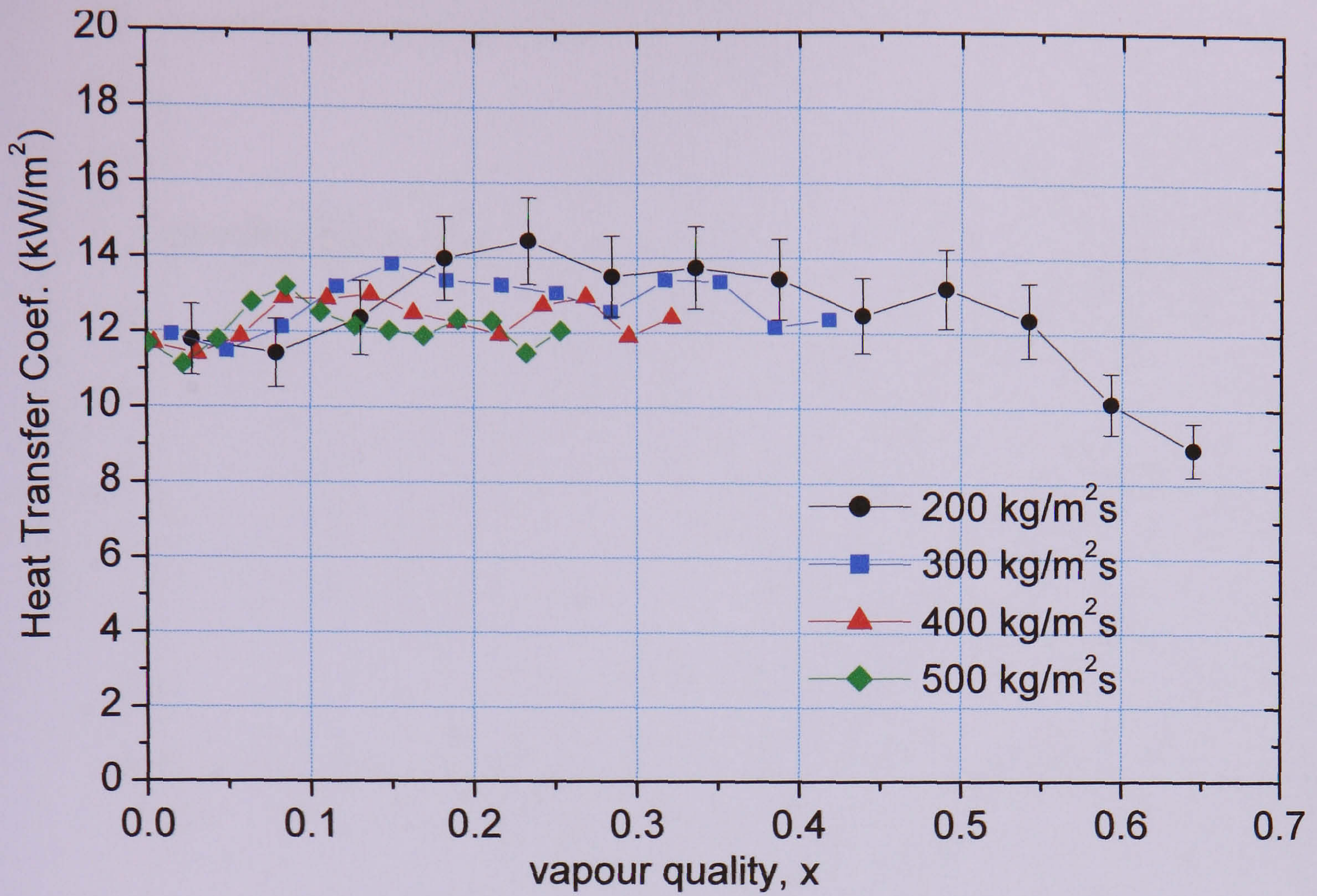
Figure 5.9 Local time-averaged heat transfer coefficient as a function of local quality for $D = 1.10 \text{ mm}$, $G = 200 \text{ kg/m}^2\text{s}$ and $P = 6 \text{ bar}$.

5.2.2 Effect of mass flux

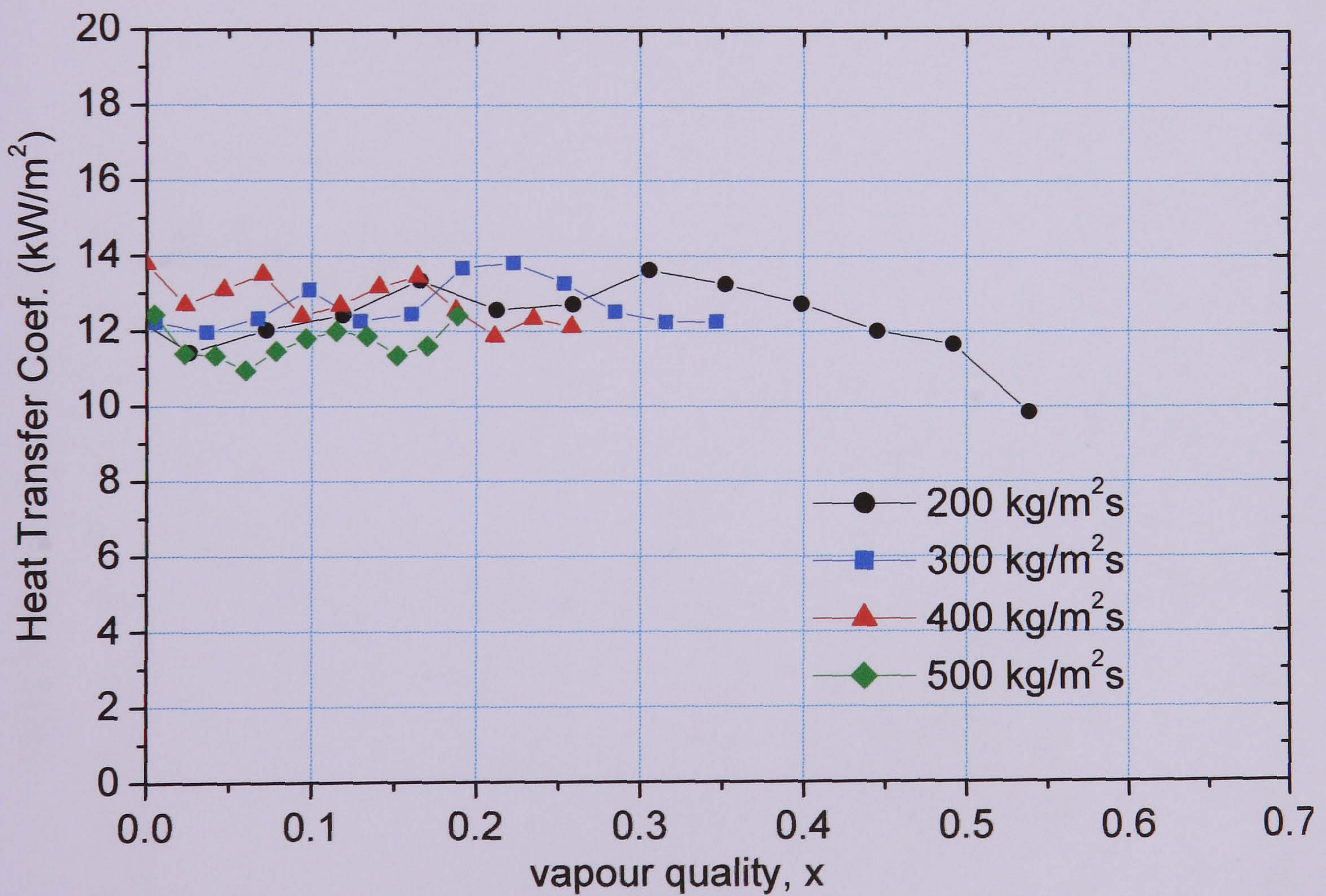
The dependence of the heat transfer coefficient on mass flux is depicted in Figure 5.10 for a heat flux of 54 kW/m^2 (4.26-1.1 mm tubes) and 58 kW/m^2 (0.52 mm tube) and 8 bar pressure. As seen in the figure, there is no mass effect on the heat transfer coefficient

versus quality curves for the tubes of diameter down to 1.1 mm. At low qualities, the approximately constant values of the heat transfer coefficient are almost independent of the mass flux within experimental uncertainty for the four larger diameter tubes. It is worth noting here that for the 4.26 mm tube, after $x = 0.15$, a slight effect of mass flux is visible, where the heat transfer coefficient decreases with mass flux. This could just be a coincidence, as it is not observed at other heat flux values. Moreover, the effect is not repeated in the other tubes (2.88 – 1.1 mm diameter). The use of longer heated lengths to achieve higher exit qualities at lower heat flux (subject to any limitations imposed by pressure drop) can help confirm the consistency of the mass flux effect at higher qualities.

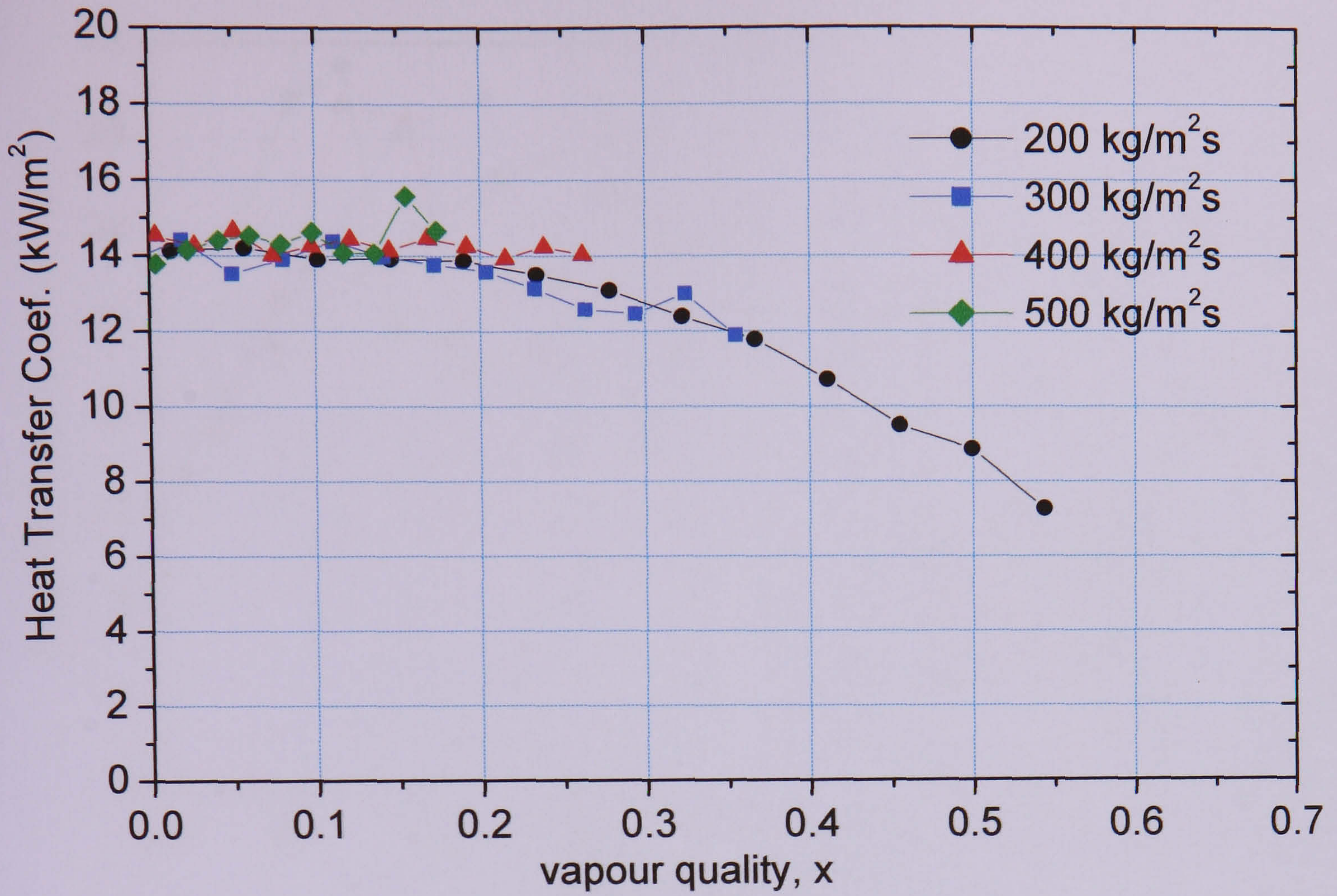
The results for the smallest diameter tube are clearly different. There is a significant effect of mass flux in the region identified as increasing trend of heat transfer coefficient with quality (region III according to Figure 5.6). In this region, the heat transfer coefficient increases with increasing mass flux and as seen in figure 5.6, there is no obvious effect of heat flux especially at high quality. This plus the observations at the visualization section support the previous speculation that at high quality convective evaporation of the annular flow dominates the heat transfer mechanism, Sumith et al (2003), Saitoh et al. (2005), Lin et al. (2001). Also, the quality beyond, which the region of heat transfer coefficient increases with quality begins, is lower at higher mass flux. There is a smaller effect of mass flux in region I (gradual increase of heat transfer coefficient with quality followed a slightly uniform trend). However the length of the uniform trend decreases with increasing mass flux. (Refer to figures 5.6 and 5.7, for the different regions). For further understanding the influence of changing mass flux, it will be interesting to see how these plots behave in a heat transfer coefficient versus axial distance plot. Figure 5.11 presents the results in a heat transfer coefficient versus axial position plot for the 1.1 and 0.52 mm diameter tubes. Since the four larger diameter tubes exhibit similar mass flux effect, the results of the 1.1 mm diameter tube will be enough to note any differences.



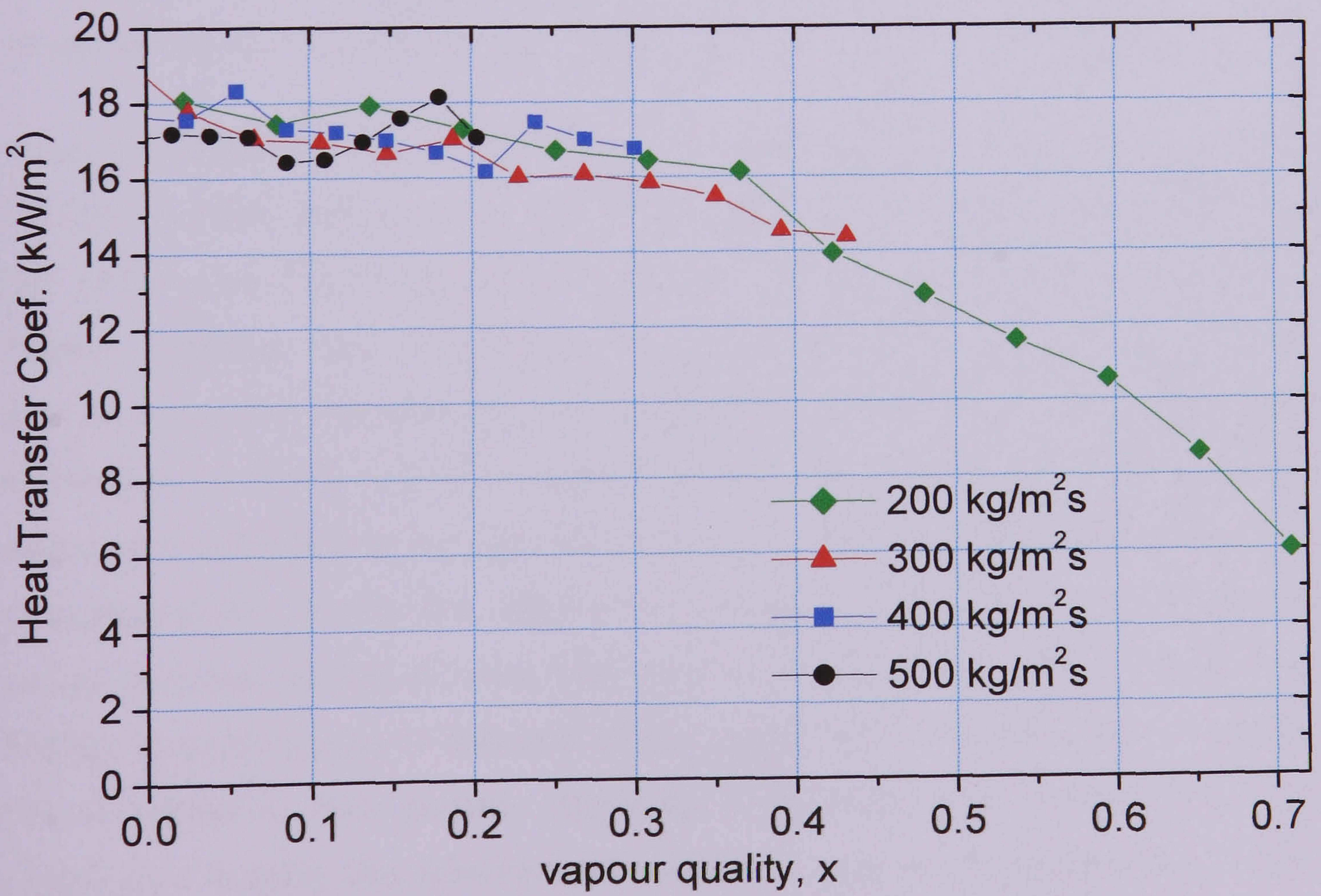
(a) $D = 4.26 \text{ mm}$



(b) $D = 2.88 \text{ mm}$



(c) $D = 2.01 \text{ mm}$



(d) $D = 1.1 \text{ mm}$

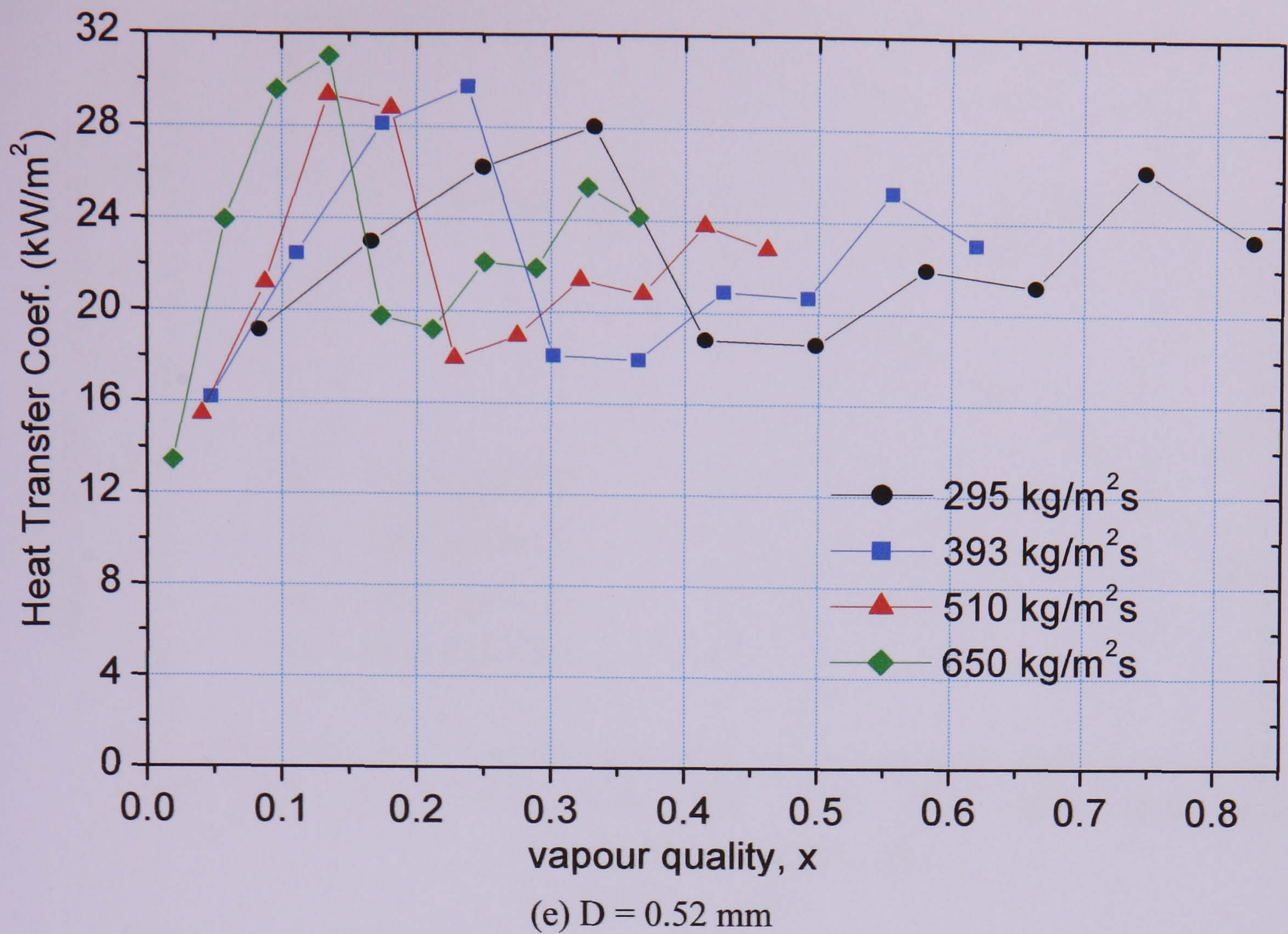


Figure 5.10 Effect of mass flux on heat transfer coefficient versus quality at $P = 8 \text{ bar}$: (a) $D = 4.26 \text{ mm}$, $q = 54 \text{ kW/m}^2$; (b) $D = 2.88 \text{ mm}$, $q = 54 \text{ kW/m}^2$; (c) $D = 2.01 \text{ mm}$, $q = 54 \text{ kW/m}^2$; (d) $D = 1.1 \text{ mm}$, $q = 54 \text{ kW/m}^2$; (e) $D = 0.52 \text{ mm}$, $q = 58 \text{ kW/m}^2$.

As seen in Figure 5.11(a), the data that was considered to show no effect of mass flux in a quality plot now indicated some variations towards the test section exit. After roughly half of the tube, the $200 \text{ kg/m}^2\text{s}$ curve drops rapidly with axial distance and the heat transfer coefficient tends to decrease with decreasing mass flux towards the test section exit. However, it seems there is a small but noticeable opposite effect at the inlet to the test section. In Figure 5.11 (b), on the other hand, the different mass flux curves in the quality plot collapse into a single line in the axial distance plot, indicating there is no significant effect of mass flux. These observations raise the question of whether using quality as a base to plot different heat transfer curves could introduce another effect, bearing in mind, quality is indicator of the vapour fraction or void fraction, which in turn is related to flow pattern. Intuitively, it is tempting to generalise that using independent variable like relative axial position in heat transfer comparisons could be better than quality (in some cases) to avoid the additional bias the quality effect would cause.

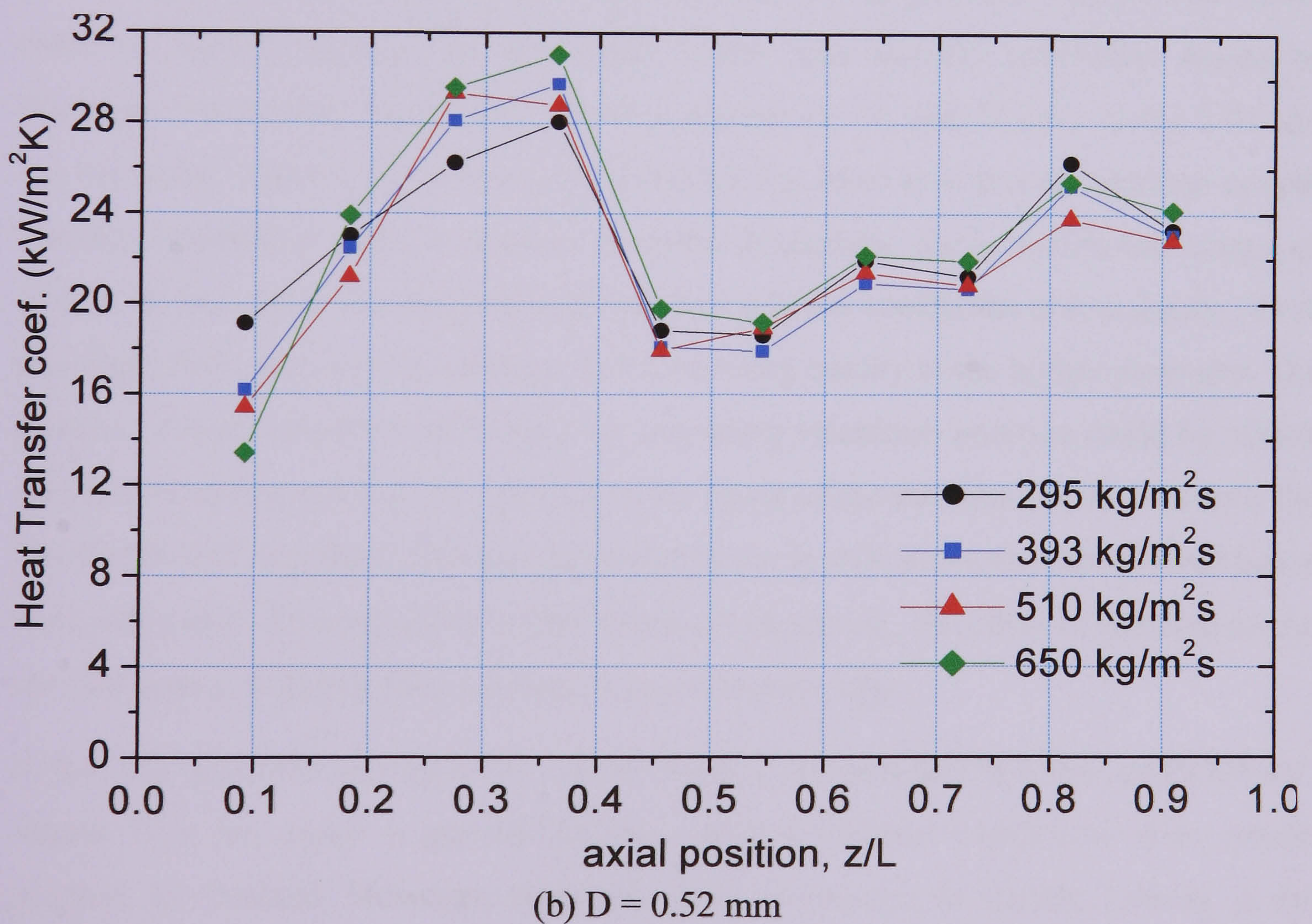
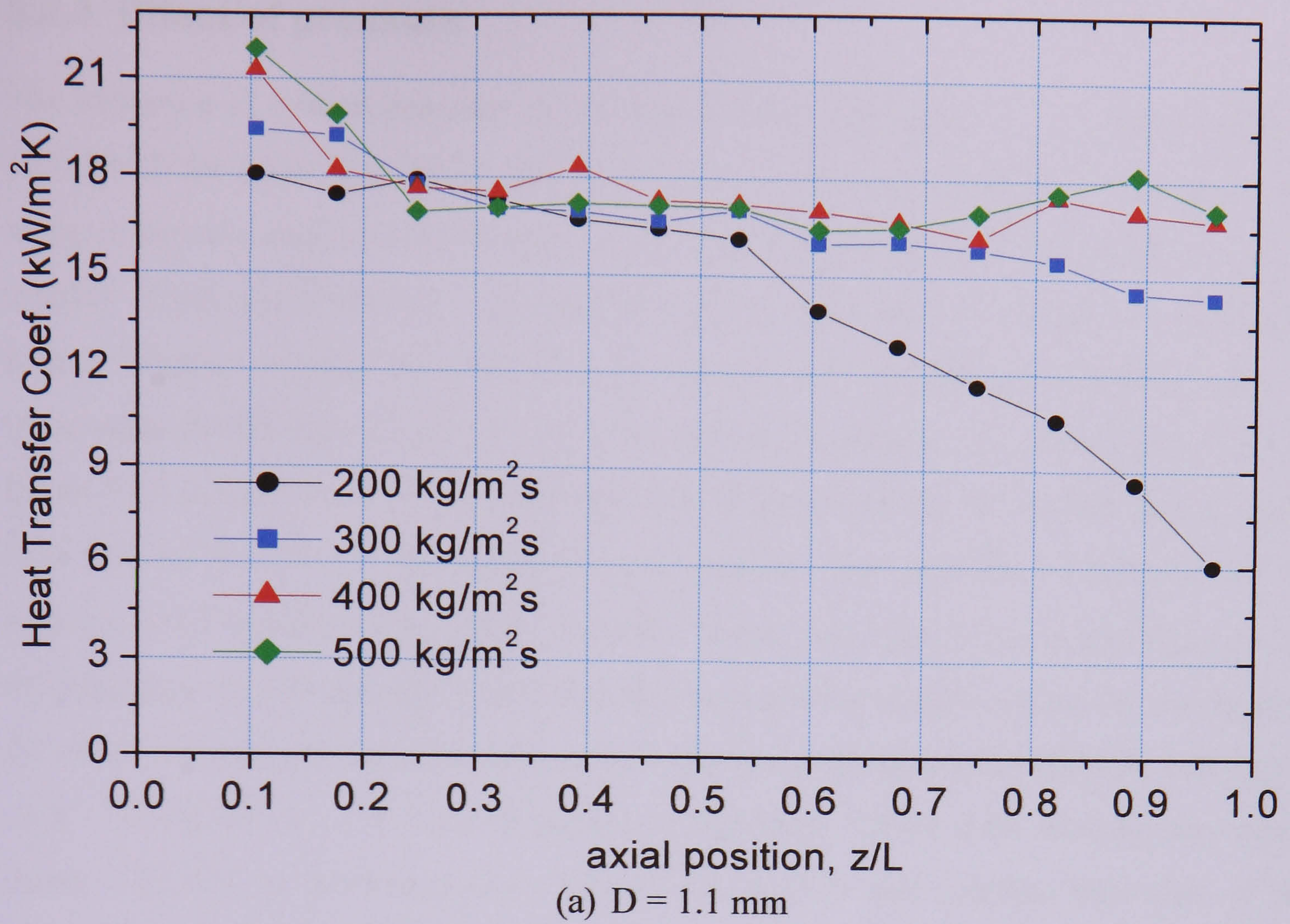


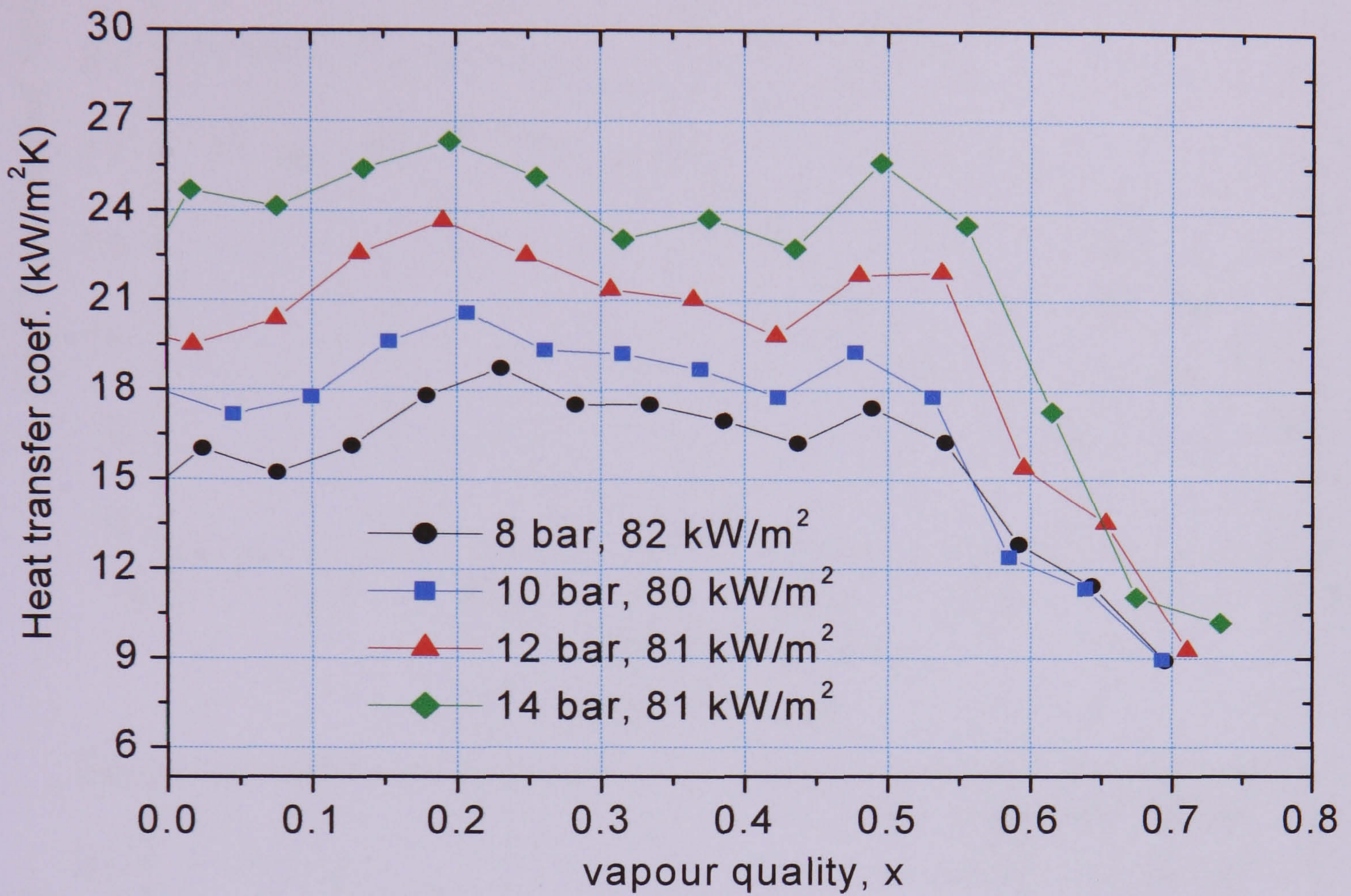
Figure 5.11 Effect of mass flux on heat transfer coefficient versus axial position at $P = 8$ bar: (a) $D = 1.10 \text{ mm}$, $q = 54 \text{ kW/m}^2$; (b) $D = 0.52 \text{ mm}$, $q = 58 \text{ kW/m}^2$.

5.2.3 Effect of pressure

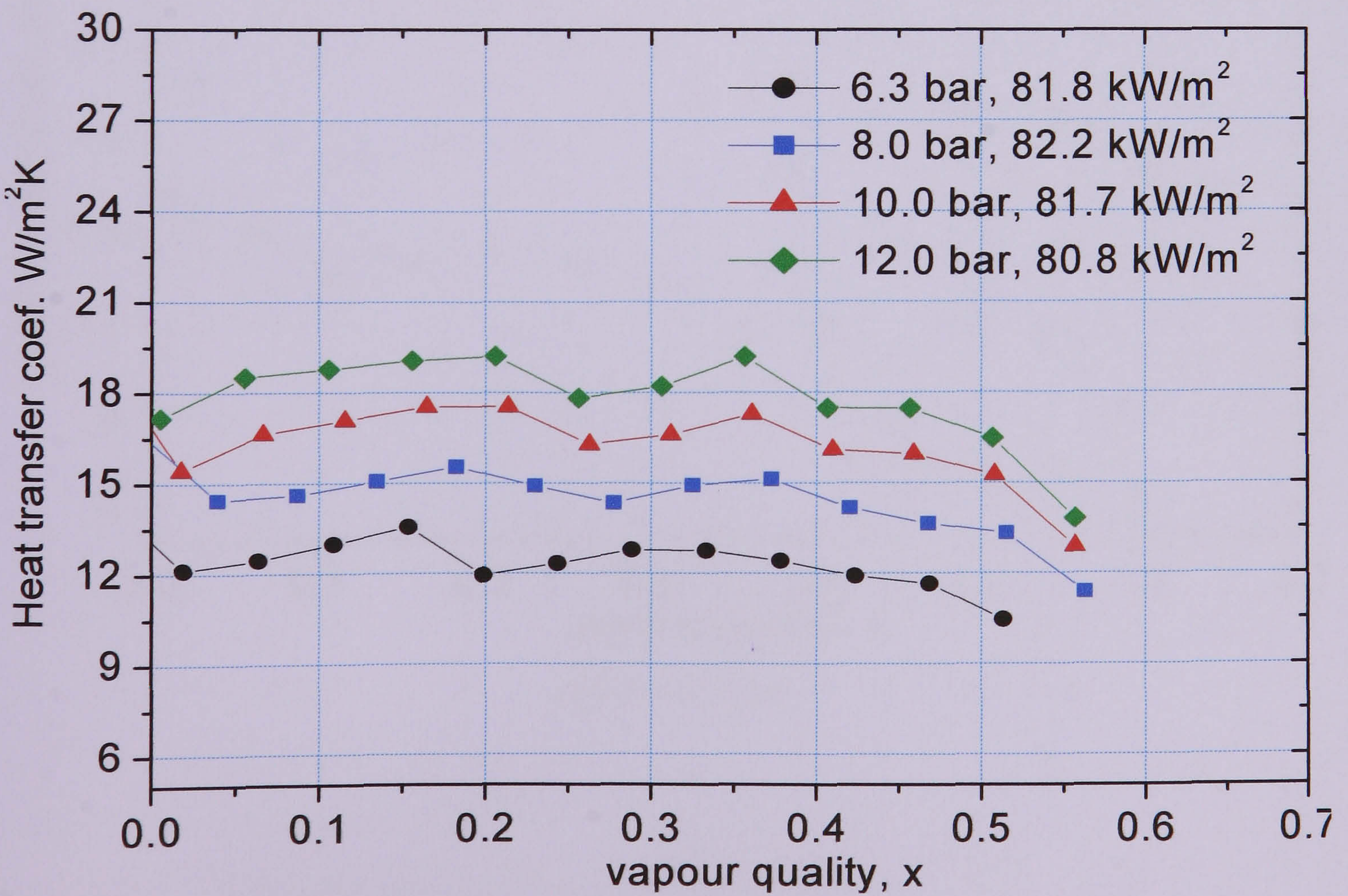
The influence of system pressure on the heat transfer coefficient is illustrated in Figure 5.12 for all the tubes at different heat flux shown in the respective plots. The reason for using different conditions is because of the fact that the experiments aimed to cover roughly equal and relatively high quality regions and since the tubes have different heated lengths, varying the heat flux to achieve this is needed. However, plots at approximately the same conditions are also included in section 5.3.1. It is clearly seen in figure 5.12 (a), for the 4.26 mm diameter tube at mass flux of $300 \text{ kg/m}^2\text{s}$ and nominal heat flux of 80 kW/m^2 , the approximately uniform heat transfer coefficients in the region $x \leq 0.5$ increase with system pressure. There is no change in the quality at which the transition to heat transfer coefficient decreasing with quality occurs. In this region, the effect of pressure becomes less regular and the heat transfer coefficient converges on $8 - 10 \text{ kW/m}^2$ at $x = 0.7$ for all pressures. Similarly, for the 2.88 mm diameter tube, figure 5.12 (b), at the same mass flux of $300 \text{ kg/m}^2\text{s}$ and nominal heat flux of 80 kW/m^2 , the heat transfer coefficient increases with system pressure. The pressure effect tends to slightly decrease in the region where heat transfer coefficient begins to decrease with quality for the three higher pressures (8, 10, and 12 bar). In the 2.01 and 1.1 mm tube, Figures 5.12 (c) and (d) respectively, there is a general increase in heat transfer coefficient with increasing pressure throughout the experimental range of quality. In the region of nominally constant heat transfer coefficient at low quality, there is a slight decrease in the coefficient with increasing quality at the higher pressures. The increase in heat transfer coefficient with increasing saturation pressure could be related to different causes such as the decrease in the slope of the saturation pressure curve, the fact that bubble departure diameter decreases as the system pressure increases and hence high probability for increase in bubble departure frequency, the effect of pressure on the specific heat of vaporization and liquid-vapour density ratio.

In the 0.52 mm tube at a mass flux of $400 \text{ kg/m}^2\text{s}$ and nominal heat flux of 58 kW/m^2 , Figure 5.12 (e), again a general increase in heat transfer coefficient with system pressure is obtained. However, there are some differences in closely looking at the trends. For the lowest pressure (6 bar), region II (the decreasing heat transfer coefficient with quality) showed a gradual decrease with an approximate drop of $3 \text{ kW/m}^2\text{K}$ over a quality range of $0.2 < x < 0.28$. Moreover, it has a more flat uniform coefficient region (Region I, $x < 0.2$). In contrast, the 8 and 10 bar pressure curves showed a sudden drop

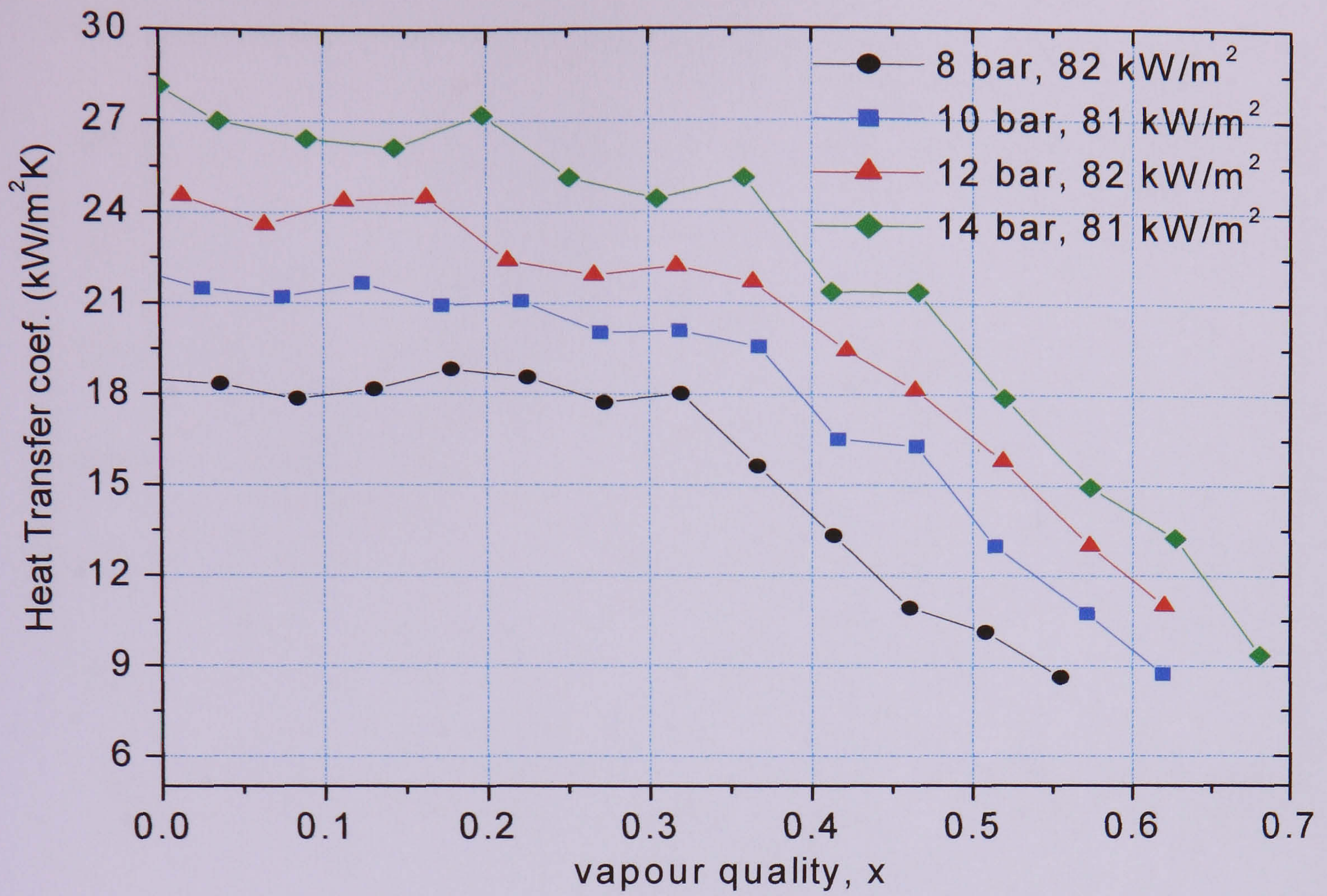
from the 4th to the 5th measuring point ($x = 0.23 - 0.3$). There is also a drop in heat transfer coefficient at the last measuring point after the second maximum for 8 and 10 bar pressure, which might be caused by thin film dryout during the annular flow.



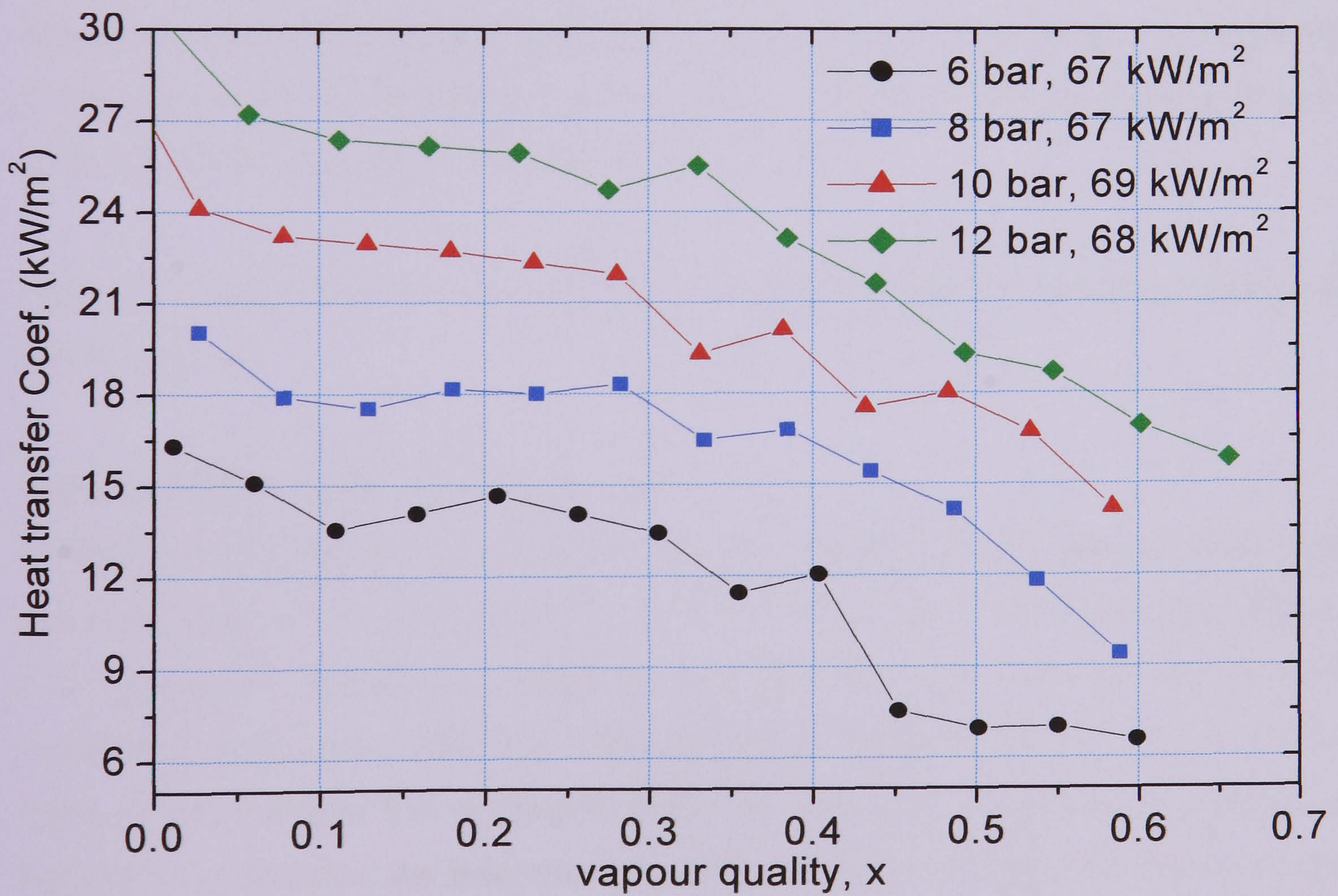
(a) $D = 4.26$ mm



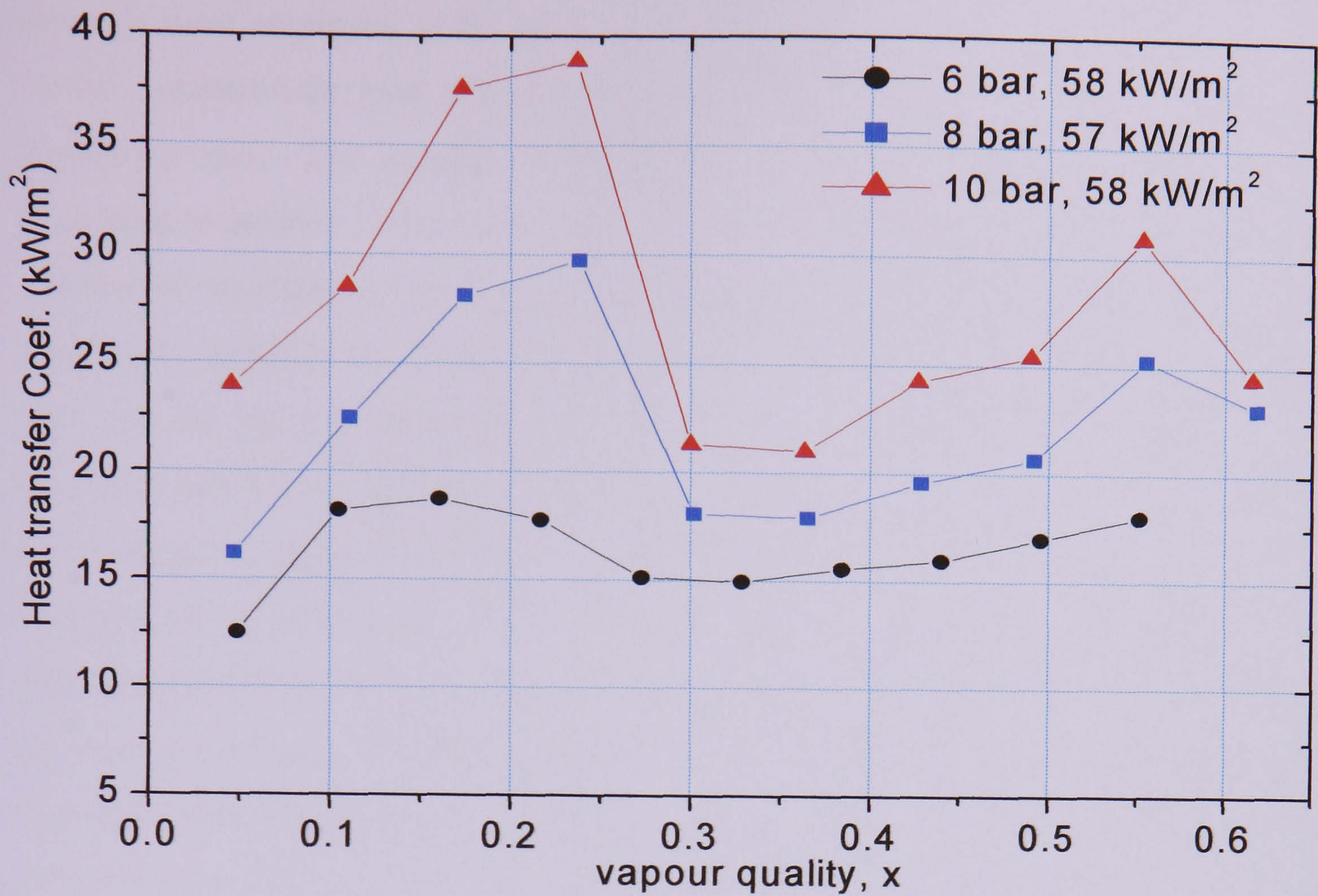
(b) $D = 2.88$ mm



(c) $D = 2.01 \text{ mm}$



(d) $D = 1.1 \text{ mm}$



(e) $D = 0.52$ mm

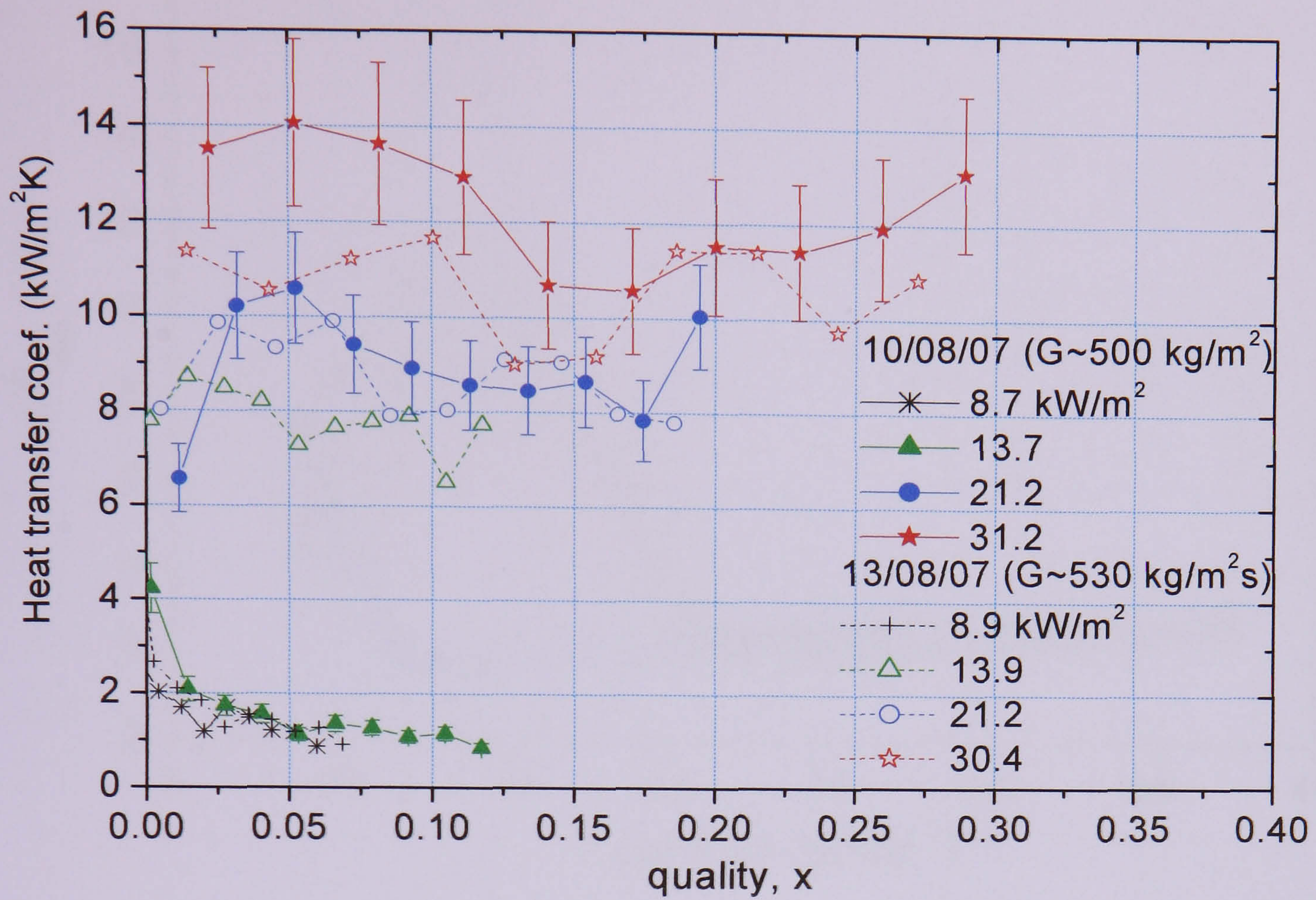
Figure 5.12 Local heat transfer coefficient as a function of vapour quality for different system pressure, $G = 300$ kg/m²s: (a) $D = 4.26$ mm, (b) $D = 2.88$ mm, (c) $D = 2.01$ mm, (d) $D = 1.10$ mm, and (e) $G = 400$ kg/m²s, $D = 0.52$ mm.

Figure 5.12 (e) for the 0.52 mm tube indicates that the effect becomes more marked at higher pressure.

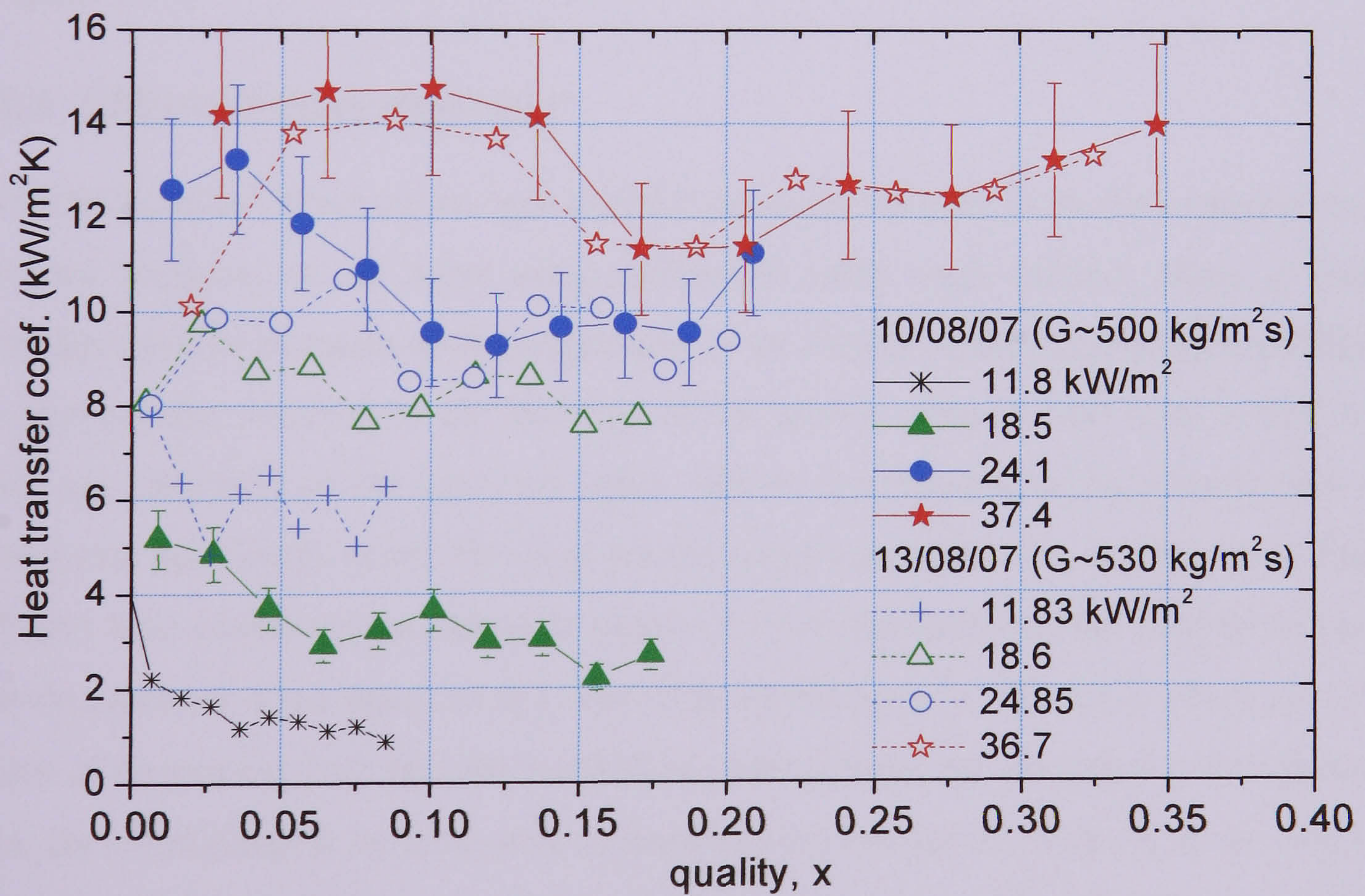
Reproducibility of the 0.52 mm tube results

In chapter 4, the repeatability results of the larger tubes (4.26 mm and 1.1 mm) were presented. Here, the repeatability of the 0.52 mm tube data will be discussed. Figure 5.13 depicts the repeatability results in two different plots (only for the sake of readability) at the same mass flux ~ 500 kg/m²s and pressure ~ 6 bar. As seen in the figure, at very low heat flux of about 9 kW/m², the results are reproducible. However, as the heat flux increases, the heat transfer coefficient values on date 13/07/08 increased with heat flux, while those obtained on 10/07/08 became independent of the heat flux until about 14 kW/m². In the intermediate heat flux range (11-18 kW/m²), the reproducibility is significantly worse. At relatively higher heat flux, $q > 21$ kW/m², the reproducibility is improved, in which at the highest heat flux value of ~ 37 kW/m², the results were reproducible within the uncertainty limit. Because the same experimental

methods were employed as for the larger tubes, this irreproducibility, particularly for a certain intermediate heat fluxes may be caused by the effects of sparse or unstable nucleation sites. The number of nucleation sites could be significantly small and activation or stability of few sites may have a significant effect on the local heat transfer coefficient. Nucleation has to occur before confined bubbles can affect heat transfer coefficient downstream. Figure 5.14 shows the corresponding wall superheat versus heat flux for the experiments on the two different dates presented in figure 5.13. As discussed before, the wall superheat value increases rapidly with increasing heat flux up to a certain threshold heat flux. In this region, the heat transfer coefficient was independent of heat flux, and the fluid at the outlet was slightly superheated. This threshold heat flux value was observed to randomly vary with mass flux and pressure. As seen in the figure, after this heat flux limit, the superheat value dropped sharply with heat flux. The reproducibility of the values was worse in the heat flux range (10 – 20 kW/m²), where the wall superheat values were still higher for the condition on 10/08/07. Beyond, this range the values are reasonably reproducible, in which the number of active sites could have increased. Also, at the lowest heat flux value of $q \sim 9 \text{ kW/m}^2$, the results were repeatable, where activation of very few relatively big cavities is expected. Therefore, it can be argued that the discrepancy in reproducibility with heat flux could be related to the variation in the activation of small population of nucleation sites and hysteresis on the effect of heat flux. In the present experiment, there was no any valve installed before the evaporator to stabilise high wall superheat that was required to initiate boiling, indicating hysteresis in the activation of nucleation sites as a consequence of small size of the tube surface. Preliminary experiments by the new PhD researcher in the same tube indicated evidence of hysteresis effects. It is also worth mentioning that the different date experiments were not conducted at exactly same mass flux and inlet subcooling (varies 1 – 5 K). Since, the flow rate was very small in the smallest tube for a same mass flux as the larger tubes, hence there was a relative difficulty in maintaining a constant mass flux between different tests, but the difference may not be big to cause reproducibility problem. Further study is required to clarify the effect of surface roughness, i.e. nucleation sites and understand the new features observed in the very small tube. This will be considered as one of the recommendations for future work. A collaborative study is under way between Brunel University and Prof. Andrea Luke at the Institute for Thermodynamic in Hannover University to characterise internal surface conditions.



(a)



(b)

Figure 5.13 Reproducibility of the 0.52 mm tube experiments at a mass flux of about 500 kg/m²s and pressure ~6 bar.

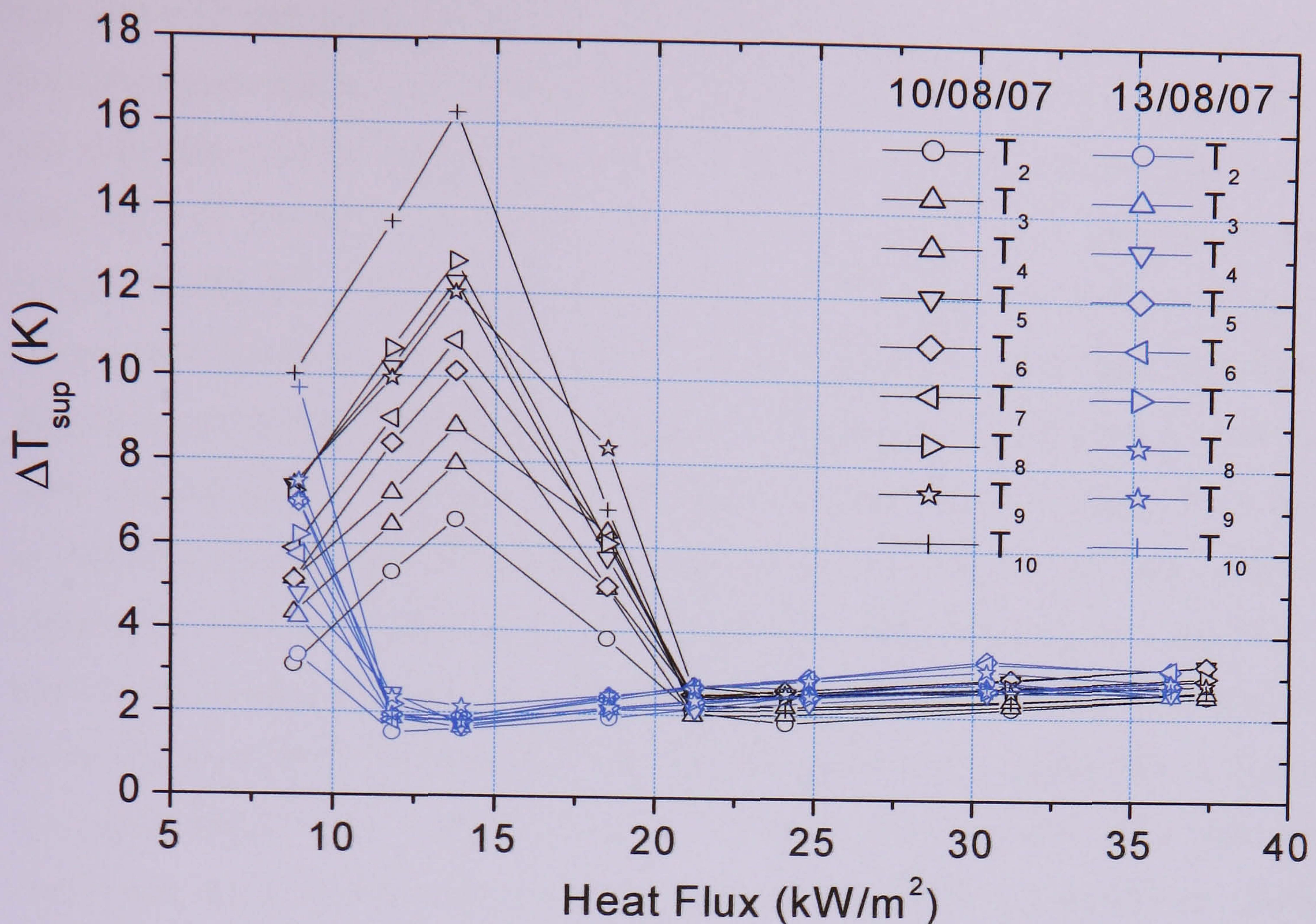


Figure 5.14 The degree of wall superheat versus heat flux at conditions corresponding to figure 5.13.

5.2.4 Effect of tube diameter

The tube diameter effect on the heat transfer characteristics has been demonstrated in the previous sections, as all tubes were addressed under each subject. Here, a further investigation will be made on the magnitude of the change of the heat transfer coefficient or enhancement obtained as the diameter of the tube is reduced from 4.26 to 0.52 mm. Also, any threshold of the tube size effect will be investigated using a single plot that incorporate the results of all the tubes for the same condition. The experimental data at different tube diameters are shown in Figure 5.15 on the heat transfer coefficient versus heat flux plot for 8 bar pressure at a mass flux of $400 \text{ kg/m}^2\text{s}$. The data, which are in the region of decreasing heat transfer coefficient with quality, are excluded in this figure as these are considered to be indicative of transient dryout and the purpose of the figure is to compare tubes at the same condition. Such representation of data is likely to be useful because it may be more desirable to design compact heat exchangers that operate at low exit quality to avoid dryout and the consequent drop in the heat transfer performance. Curve fitting was applied to the data using a relation in the form $\alpha = C \cdot q^n$. The exponent n was kept constant at 0.62. The values of constant C for the 4.26, 2.88, 2.01,

1.10 and 0.52 mm tubes are 14.3, 14.5, 16.6, 19.5 and 33.7 respectively. It can be seen from the figure that the values of 4.26 and 2.88 mm diameter tubes are almost the same and also exhibit similar dependence of heat transfer coefficient on heat flux. However, with the 2.01 mm diameter tube an average increase of 14 % is obtained in the heat transfer coefficient. When the tube diameter is reduced to 1.10 mm, a further 17 % increase is obtained in the heat transfer coefficient. There is a very large increase in the magnitude of the heat transfer coefficient as the diameter decreases from 1.1 to 0.52 mm tube; this increase is as large as 70 %. Based on the results of figure 5.15, without considering decreasing heat transfer coefficient region (observed at high quality), the progressive increase in magnitude of heat transfer coefficient suggest a tube size of 2 mm could be considered as a critical threshold to distinguish small and large tubes. However, considering plots of heat transfer coefficient versus quality, the 2.01 and 1.1 mm tubes have similar behaviour as the 4.6 and 2.88 mm tubes on a heat transfer coefficient versus quality plot. Moreover, the 4.26 and 2.88 mm tubes do not exhibit the characteristics of conventional tubes with axially uniform heat flux, which is *the pattern of separate lines of nearly constant heat transfer coefficient at low quality merging with a single line of increasing heat transfer coefficient at higher quality*. Instead, both tubes showed a region of *decreasing* heat transfer coefficient with quality and *increasing* wall superheat at high quality. This is different behaviour from large tubes, although an eventual decrease is seen in some big-tube data. Nevertheless, Chen et al. (2006) indicated that the flow patterns in the 2.88 and 4.26 mm tubes do not exhibit any common characteristics of the flow patterns in small tubes. In contrast, they observed confined flow, slimmer vapour slug, thinner liquid film, smoother vapour-liquid interface in the 2.01 and 1.10 mm, which is considered to be the effect of a significant surface tension force. If this is confirmed to be indicative of “small tube characteristic”, as reported in Chen et al. (2006), the present heat transfer results are consistent with their observation, since the effect of smallness of tube diameter on heat transfer begins to be noticeable when the diameter is reduced to 2.01 mm. At a tube diameter of 1.10 mm, the “small tube characteristics”, are also reported in the previous studies of Damianides and Westwater (1988) and Mishima and Hibiki (1996). According to the criterion proposed by Cornwell and Kew (1993) for small tube characteristic, confinement effect should be observed at diameters of 1.4 to 1.7 mm at 6 -14 bar pressure. This is again roughly consistent with the present heat transfer results and flow visualization observations of Chen et al. (2006). The heat transfer characteristics in the smallest tube (0.52 mm) were

different than those described above for the larger tubes. Two groups of data were obvious, exhibiting different influences of heat flux, below and above a heat flux threshold. There is also relatively a very large enhancement in the magnitude of heat transfer coefficient when the tube size is reduced from 1.1 to 0.52 mm. These differences indicate a possible gradual second change from what could be referred to as small to micro behaviour at diameters less than 1 mm for R134a. This of course remains to be verified by subsequent research and is one of our main recommendations for further work in this area.

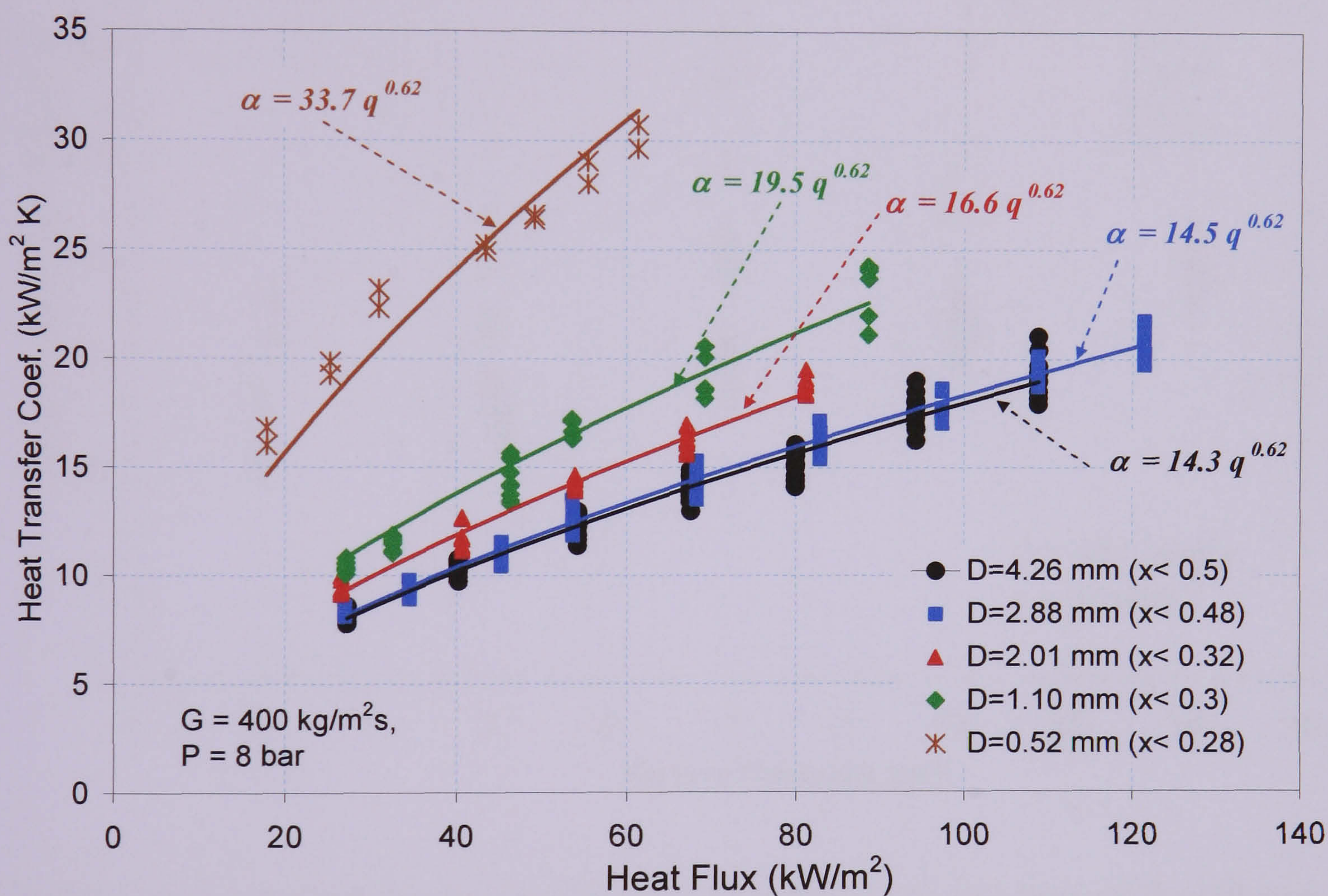


Figure 5.15 Local heat transfer coefficient as a function of heat flux for different tube diameters at a mass flux of 400 kg/m²s and 8 bar pressure.

Since the above heat transfer comparison plot (figure 5.15) was made at a single pressure, it seems appropriate to see the effect of pressure for all tubes in a single plot. These results are plotted in the heat transfer coefficient versus pressure plot in Figure 5.16 for different tube diameters. It can be seen in the figure that a linear increase in heat transfer is observed with increasing pressure in all the tubes. For the 0.52 mm diameter tube, the local heat transfer coefficient varies with quality almost for the whole range of quality especially at high pressure. As a result, the influence of pressure is different at different values of vapour quality as seen in the figure. On the other hand,

tubes with diameter larger than 1.1 mm have a constant heat transfer coefficient region at relatively low quality, i.e. in the front part of the test section. Hence, data in this region are plotted altogether shown grouped as indicated in the figure. In general, there is again a linear increase in heat transfer coefficient with system pressure for all tubes at different quality.

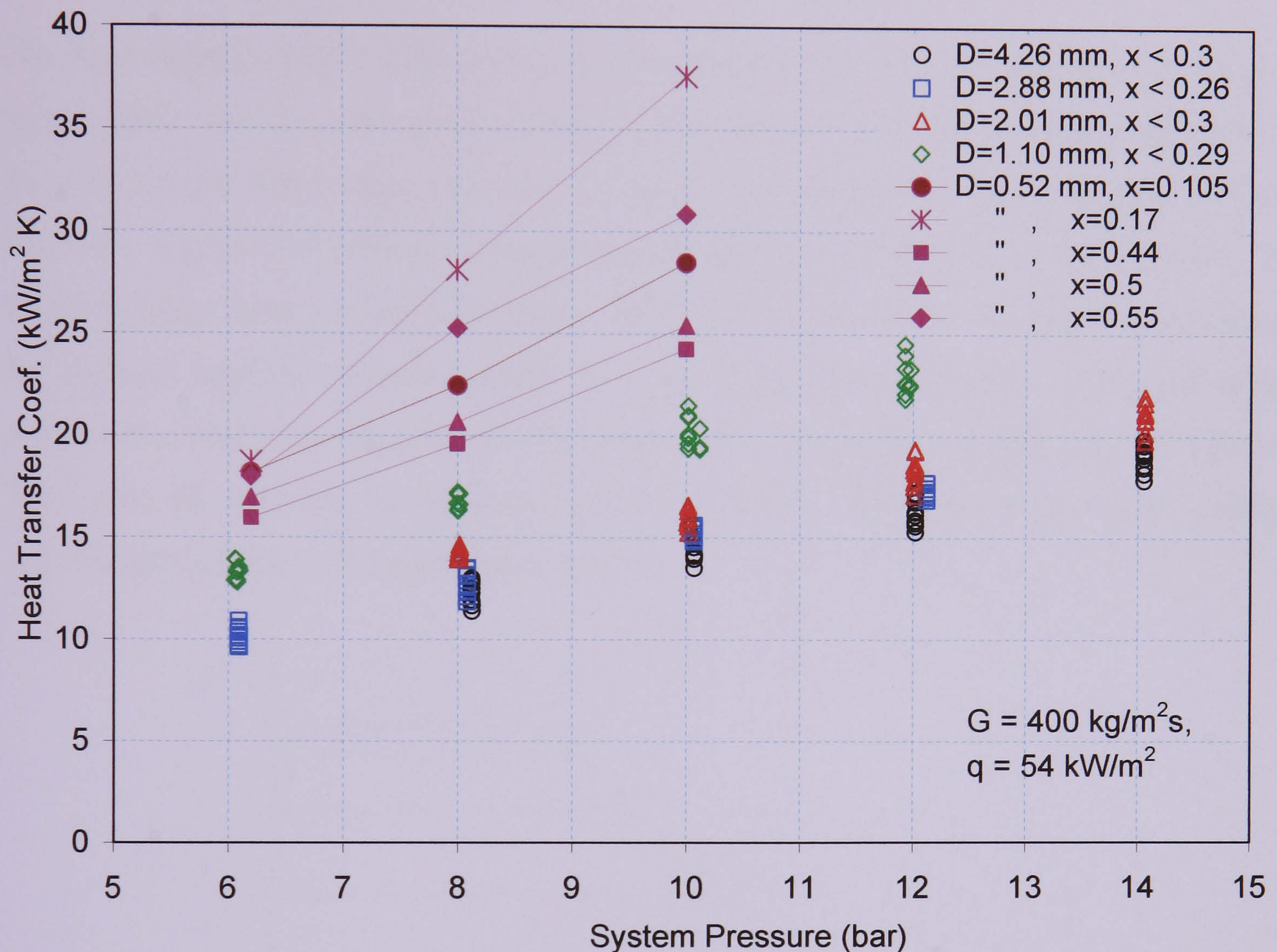


Figure 5.16. Local heat transfer coefficient as a function of system pressure for different tube diameters at a mass flux of $400 \text{ kg/m}^2\text{s}$ and heat flux 54 kW/m^2 .

In general considering the effect of the various parameters (discussed above) such as heat flux, mass flux and pressure on the heat transfer coefficient, for the larger tubes, the observed characteristics at low quality are similar to those conventionally interpreted as evidence that flow boiling in large tubes is dominated by nucleate boiling: the coefficients increase with increasing heat flux and pressure but are insensitive to quality and mass flux. However, there are claims that suggest that, for small passages, the same behaviour can be explained if transient evaporation of the thin liquid film surrounding elongated bubbles, without nucleate boiling contribution, is the dominant heat transfer mechanism, Thome et al. (2004). The similarity is not altogether surprising, as the

results of Figure 5.15 also indicate that the heat transfer coefficient dependence on heat flux suggest that similar phenomena with that of pool boiling. This could be due to the fact that both mechanisms (pool and transient film evaporation) involve the cyclic creation and evaporation of thin liquid films which may involve small-scale dryout.

5.2.5 Dryout heat transfer

The heat transfer results presented in the previous sections clearly indicated that for the larger tubes with diameter greater than 1.1 mm, towards the exit of the heated section, there is a rapid fall in heat transfer coefficient with increasing vapour quality at high heat flux. Figure 5.17 presents a sketch that shows typical heat transfer characteristics in the four larger tubes to clarify the point. As seen in the sketch, as the heat flux increases the separate heat flux curves collapse to a single line at high quality. In this particular region, the tube wall temperature was observed to be highly unstable. It is therefore likely that the decrease in the heat transfer coefficient with increasing vapour quality may be attributable to the occurrence dryout.

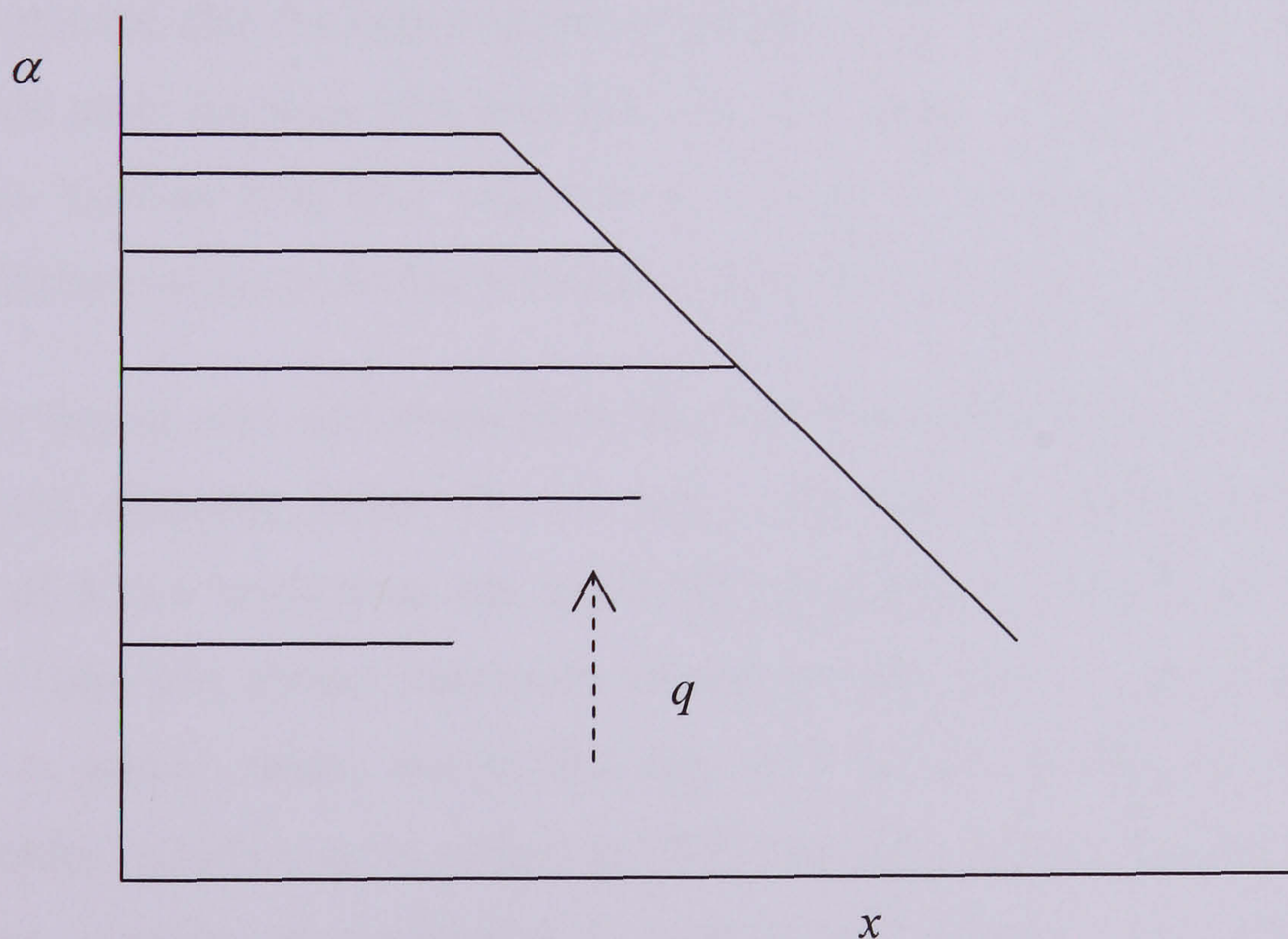


Figure 5.17 Sketch showing typical heat transfer characteristics for tubes of 1.1 mm internal diameter and larger.

There may be different kinds of dryout. One is the intermittent or partial dryout, which is mostly obtained in the slug flow regime in small tubes. This is a cyclical process caused by regular dryout of the liquid film near the rear of each confined bubble, similar

to dryout of the microlayer under individual bubbles in pool nucleate boiling, which can happen at relatively low quality. The other is a complete dryout of the liquid film in annular flow, which occurs at relatively high vapour quality. There is also a dryout that may involve several bubbles or the expulsion of liquid from the tube, so that it has a longer timescale and is analogous to transition boiling preceding film boiling in pool boiling, Kenning et al. (2006). The dryout obtained in the present experiments occurred at high heat flux and high quality towards the exit of the tube and it seems it has a longer timescale, which is deduced from the fact that the decrease in heat transfer coefficient with quality is continuous. This could also be related to the phenomena of departure of nucleate boiling (DNB), which may be caused by the bubble crowding phenomena as a result of intense heat over a relatively short length.

The heat transfer results for the 4.26 to 1.1 mm diameter tubes also showed that the quality at which the dryout commences depends on heat flux, i.e. the critical quality to dryout decreases with increasing heat flux. Also, as the tube size decreases, the heat flux and the quality, which dryout begins, decrease. In these tubes, at very high heat flux, the results also showed that the heat transfer coefficient can become independent of heat flux or in most cases decrease with heat flux, see for example, Figure 5.3 for $q = 95\text{-}134 \text{ kW/m}^2$. The limiting heat flux value for a reversal in the dependence of the heat transfer coefficient on the heat flux is found to decrease with decreasing tube diameter.

The fact that dryout was not observed in the 0.52 mm tube, while it was commonly found in small diameter tubes ($D > 1 \text{ mm}$), can also be related to number and distribution of active nucleation site and DNB phenomena. The dryout condition in small tubes (1mm and above) was more related to high heat flux (high quality) than intermittent or partial nature dryout that can exist at low quality and heat flux in confined bubbles, which is more related to DNB than film dryout. This could be caused by the bubble crowding phenomena as a result of intense heat over a relatively short length and small inside tube diameter, especially at high heat flux. The length-to-diameter ratio of the 1.1 and 0.52 mm tubes are 136.4 and 192 respectively. Therefore, relatively low and moderate heat flux is required to reach high exit quality in the case of 0.52 mm tube, thereby relatively reducing the intensity of the heat flux. Besides, in the smallest tube (0.52 mm), the number of active nucleation sites is expected to be very scarce and sparsely distributed, which indicates that the crowding effect of DNB is very unlikely in this tube. As mentioned previously, Saitoh et al. (2005) found oscillating

flows and unstable conditions for the 3.1 and 1.12 mm diameter tubes. However, they did not observe similar fluctuation for the 0.51 mm tube. If unstable conditions are related to dryout, the fact that the 0.52 mm diameter tube did not exhibit dryout behaviour agrees with their observation.

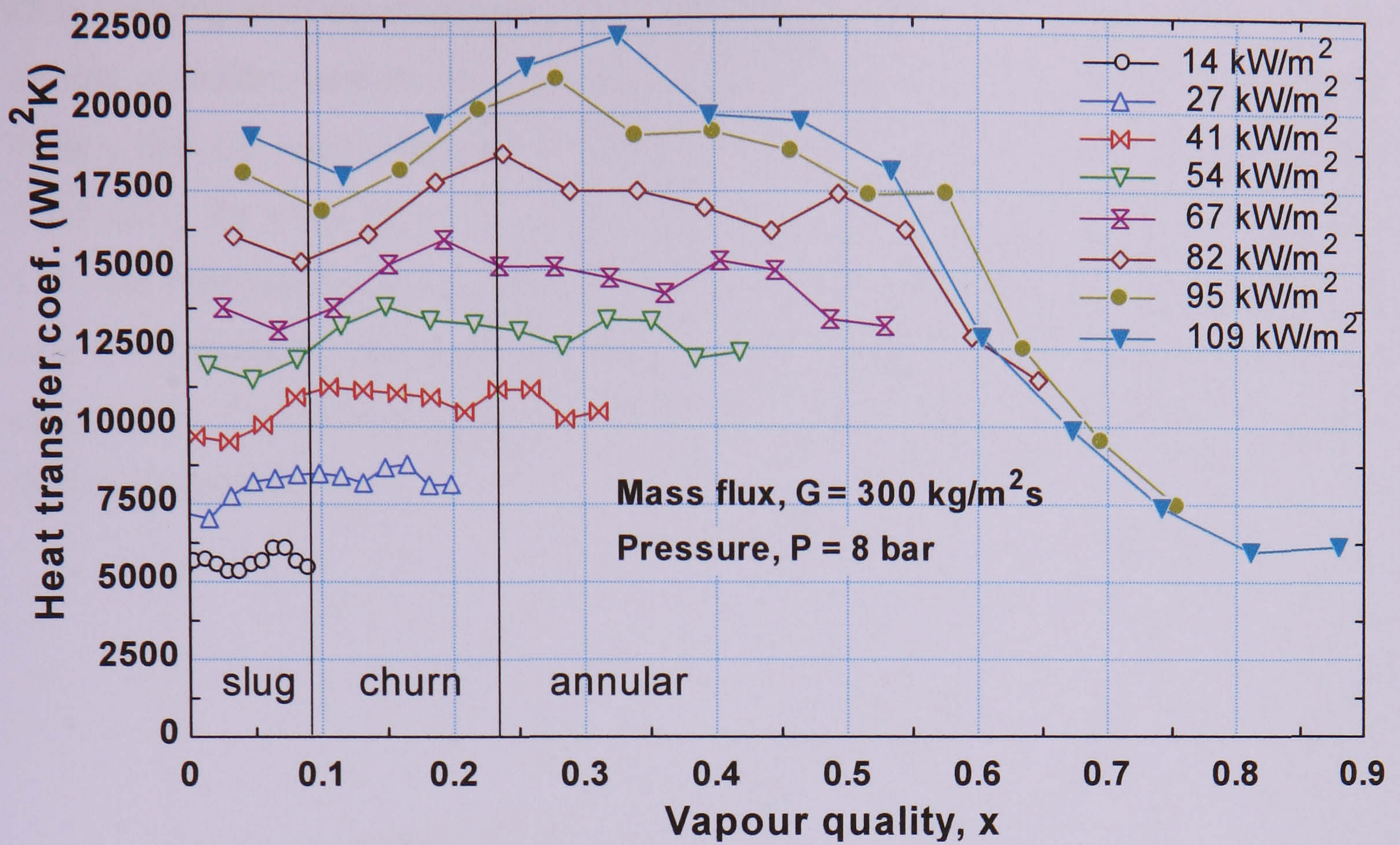
5.3 Discussion of results using flow pattern transitions

Simultaneous flow visualization experiments have also been carried out in order to further investigate the heat transfer characteristics in the various tubes and better understand the heat transfer mechanisms. The flow patterns were observed by the digital high-speed camera directly at a borosilicate glass tube with an internal diameter matched to the test section and installed immediately after the heated section. It was not the objective of this study to make a detail examination of the flow patterns for the purpose of producing flow pattern maps at different conditions. That part of the study has been addressed by Chen (2006) for the same tubes ranging in diameter from 4.26 mm down to 1.1 mm using R134a over a pressure range of 6-14 bar. The flow pattern transition maps of the Chen study will be used to discuss the heat transfer results further. Moreover, flow visualization experiments were also conducted during this study in parallel with the heat transfer tests for some of the tubes (2.88, 1.1 and 0.52 mm). Although the flow patterns were taken at the same condition with the heat transfer experiments in an effort to relate the flow regimes with the heat transfer characteristics, they are observed at the exit of the heated section, i.e. in the adiabatic section, and are liable to any flow regime development that might exist. Therefore, it is worth to note the difficulties of directly relating the flow visualization results with the local heat transfer measurements. This is a general problem of heat transfer experiments using circular tubes and trying to visualize the local flow regime at the same time. Experiments using glass tubes with electric conductive coatings has been proposed as an alternative (Owhaib et al. 2006), but it has a different surface condition and thermal wall properties than metal tubes. Most often flow boiling experiments were also carried out with rectangular channels that have a direct observation window installed on one side. These are easier to manufacture in small cross-sections and are related in many ways to real applications. However, they do not provide a uniform heat flux condition, which is a more desired boundary condition for heat transfer modelling. Also, controlling the nucleation from unwanted locations such as corners and connections with the transparent window is another drawback.

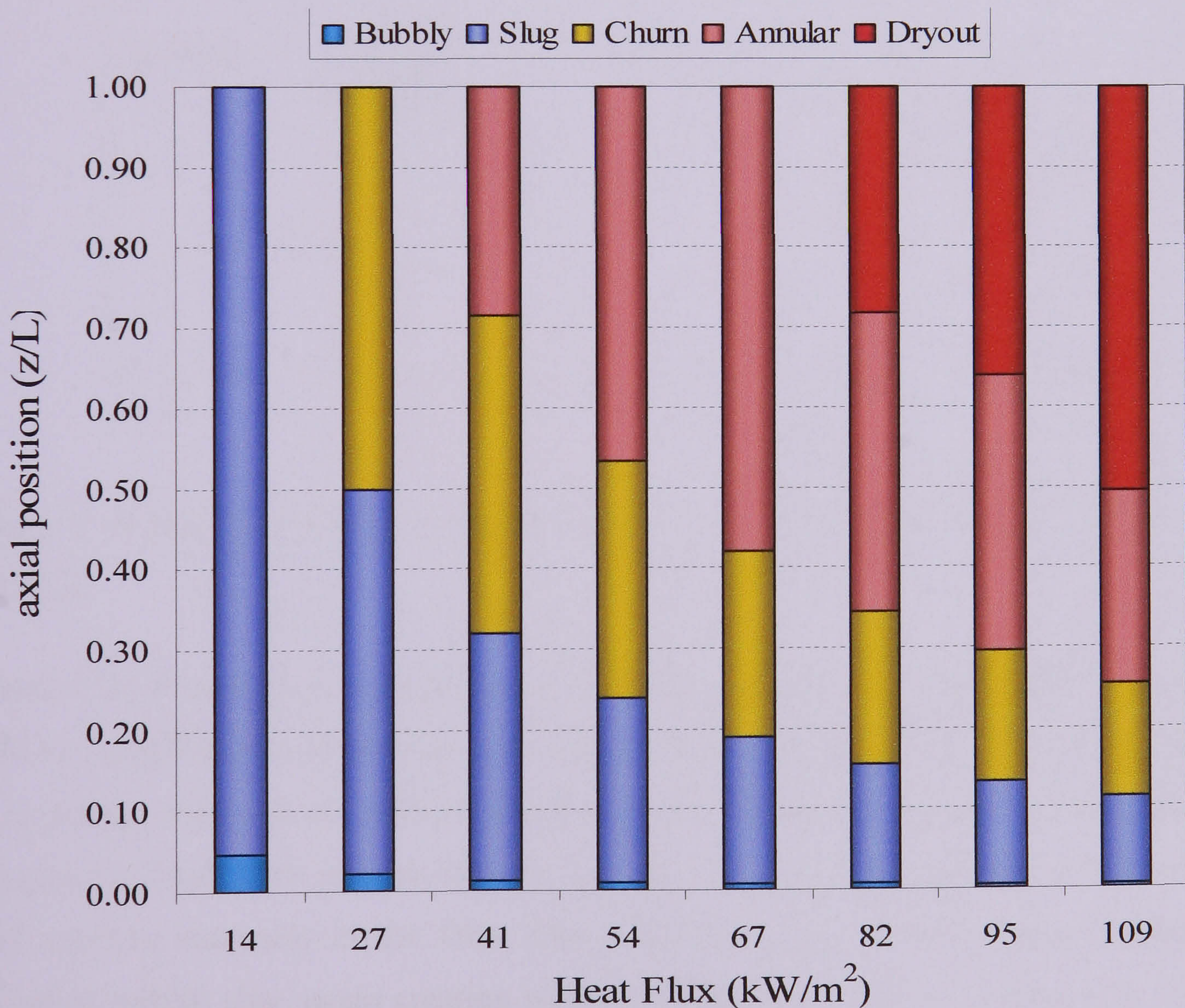
5.3.1 Small diameter tube results (4.26 - 1.1 mm)

In this section, further discussion of the small tube heat transfer results is made using the flow patterns observed at the test section exit. For this purpose, the flow pattern transition boundaries predicted by Chen et al. (2006) regime maps are superimposed with the local heat transfer coefficient versus quality plots.

In Figure 5.18 (a) for the 4.26 mm tube at a mass flux of $300 \text{ kg/m}^2\text{s}$ and pressure of 8 bar, the flow regime boundaries do not seem to coincide with the patterns of small changes visible at higher heat flux. The transition point to the region of rapidly decreasing heat transfer coefficient, achievable only at the three higher heat fluxes $\geq 80 \text{ kW/m}^2$, lie well in the annular regime. Translating the flow pattern transitions qualities to the relative axial position, the flow pattern development inside the heated section at different heat flux can roughly be deduced and is shown in Figure 5.18 (b). The dryout region in this figure is deduced from the heat transfer coefficient versus quality plots; this is the region where the heat transfer coefficient decreases sharply with quality, while the other flow pattern transition boundaries are from Chen et al. (2006) flow maps. This is again extrapolation of the flow pattern map taken at the exit of the test section towards the heated section, which may not be exactly the same as the prevailing conditions along the tube. However, it provides an insight needed to understand the effect of heat flux on axial flow regime development and provides qualitative information for mechanistic modelling. As seen in the figure, as the heat flux increases, the transition lines shift towards the front part of the tube providing a significant portion for annular flow regime. Flow pattern images from Chen (2006) showing bubbly, slug, churn and annular flow types as defined by the Chen are included in Figure 3.1. Dispersed bubble and mist flows, which were observed in the study of Chen (2006), are not found here. This is because in his study dispersed flow was observed at the high mass flux condition ($\sim 2200 \text{ kg/m}^2\text{s}$) and mist flow was obtained only at 10 bar pressure for high heat flux condition (162 kW/m^2). However, the range of experimental parameters, especially mass flux, are different in the current study and do not allow us to observe these two flow patterns.



(a)



(b)

Figure 5.18 Flow regime transition lines of Chen et al. (2006) for $D = 4.26 \text{ mm}$, $G = 300 \text{ kg/m}^2\text{s}$ and $P = 8 \text{ bar}$ pressure superimposed: (a) on a local heat transfer coefficient versus vapour quality plot, (b) relative axial position versus heat flux plot.

Plots showing axial development of flow regimes provide valuable information for heat transfer modelling and are also necessary to define the range of validity of mechanistic models that are regime-specific. One could also roughly anticipate of a heat transfer trend using the axial flow regime development graph as shown in the sketch, figure 5.19, and speculate the actual heat transfer coefficient trend. However, it is important to bear in mind that the flow patterns are not obtained by direct observation at the heated opaque tube. They are extrapolated from the adiabatic section located immediately after the heat transfer section.

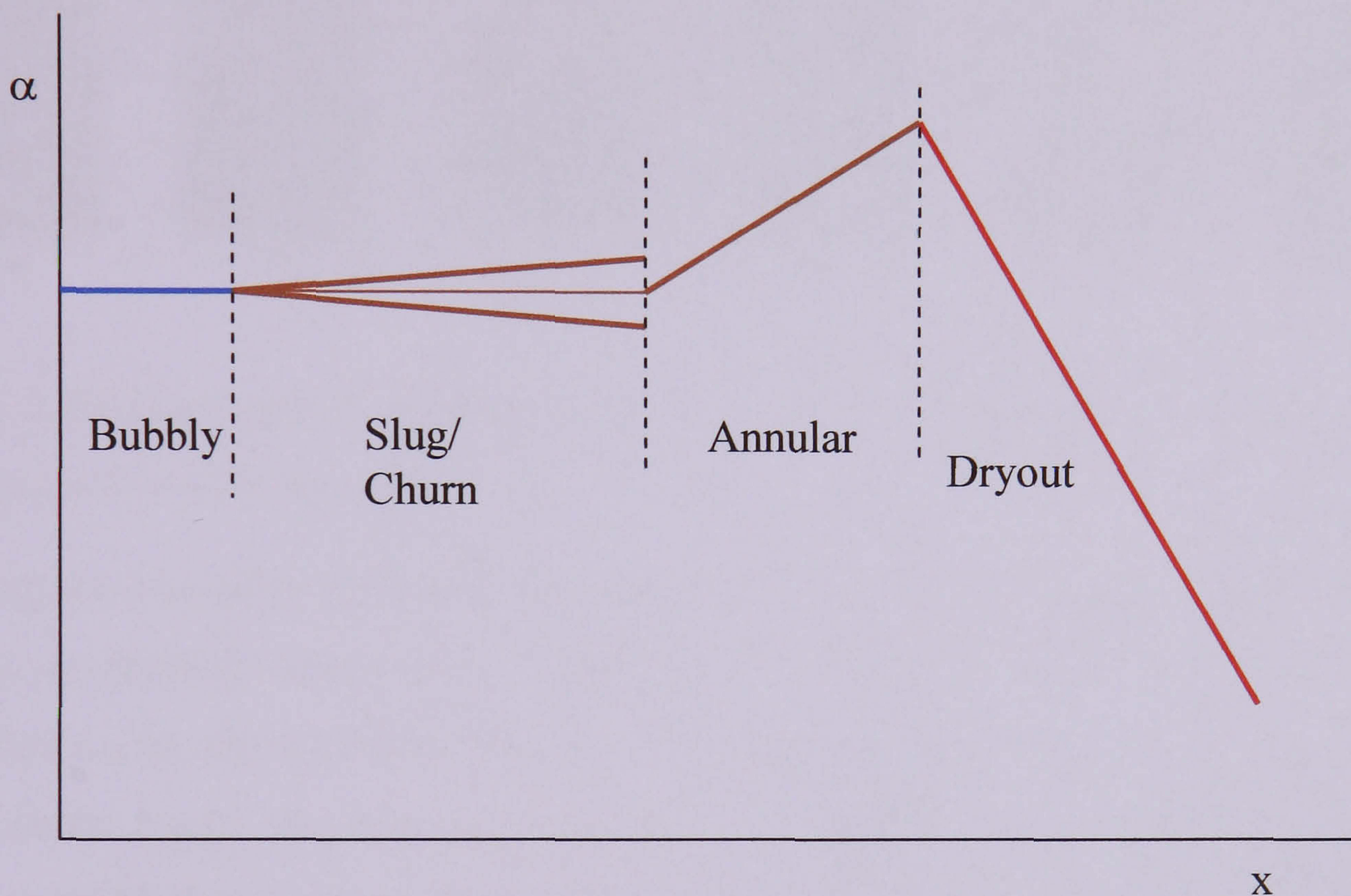


Figure 5.19 Sketch showing anticipated heat transfer coefficient trend in various flow regimes.

Figure 5.20 shows flow patterns during slug flow that describe instability caused by trails of small bubbles in the 4.26 mm diameter tube. The tail of the bubble slug (image a) is usually followed by trails of small bubbles. The small enough bubbles descend through the liquid film and can become a wedge between the long bubble slug and the wall creating waviness in the film. The relatively larger bubbles coalesce with the incoming bubble slug, again creating wave and instability of the slug (image b). As the number of small bubbles at the tail of the long bubble slug is considerably large, in many cases they may affect the film instability (image c), although this is not exclusively caused by coalescence of small bubbles. Then a chaotic interface or some kind of circulating motion (image e) is created as the bubble slug velocity increases

breaking the long bubble in to relatively short pieces and forming other fine trails of bubbles that disturb the coming bubble slug (image f).

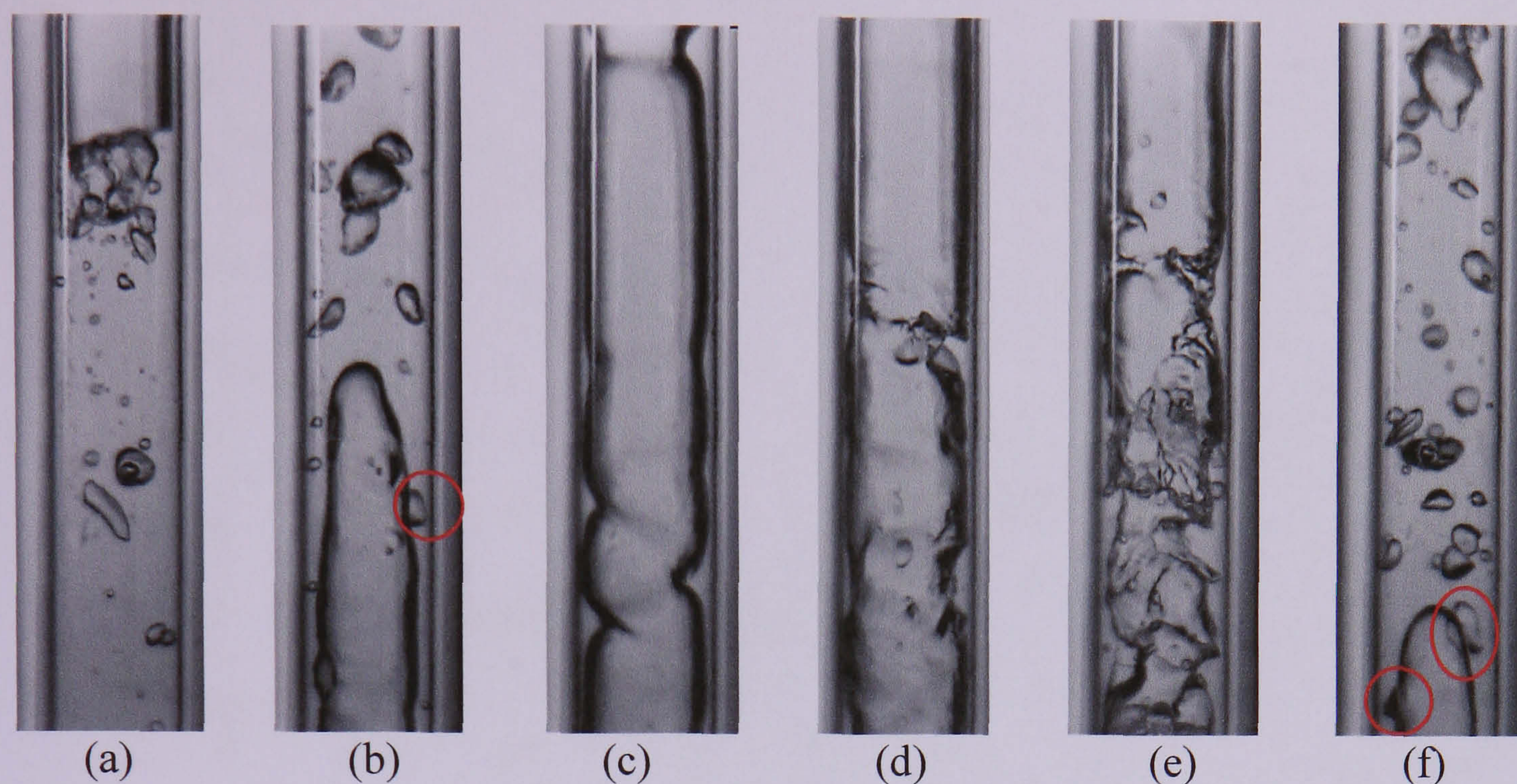


Figure 5.20 Flow pattern photos showing interface instability due to trails of small bubbles for $D = 4.26$ mm tube.

Flow regime transition lines from Chen et al. (2006) were also superimposed in the heat transfer coefficient versus quality of figure 5.21 for the 2.88 mm tube at the same condition as for the 4.26 mm tube, i.e. $300 \text{ kg/m}^2\text{s}$ mass flux and 8 bar pressure. As shown in the figure, the decreasing heat transfer coefficient with quality region again lie in the annular flow regime. This could indicate that dryout deduced from the current results is most probably attributed to continuous dryout of the film in annular flow than the partial or intermittent dryout at the rear of confined/slug flows. For the two highest heat fluxes of 98.3 and 115.3 kW/m^2 , a sharp transition to the continuous fast decreasing heat transfer coefficient region occurred approximately at 0.4 and 0.28 respectively. Therefore, as the heat flux increases, the dryout region shifts towards the churn/annular boundary, which takes place at $x \sim 0.24$. The transition boundary lines were again translated into an axial position versus heat flux graph in Figure 5.21 (b). As seen in the figure, at low heat flux a considerable portion of the heated pipe was occupied by slug flow. This tends to be taken over by the annular flow regime as the heat flux increases. Bubbly flow is expected to exist only in a small portion near the inlet at low heat flux conditions

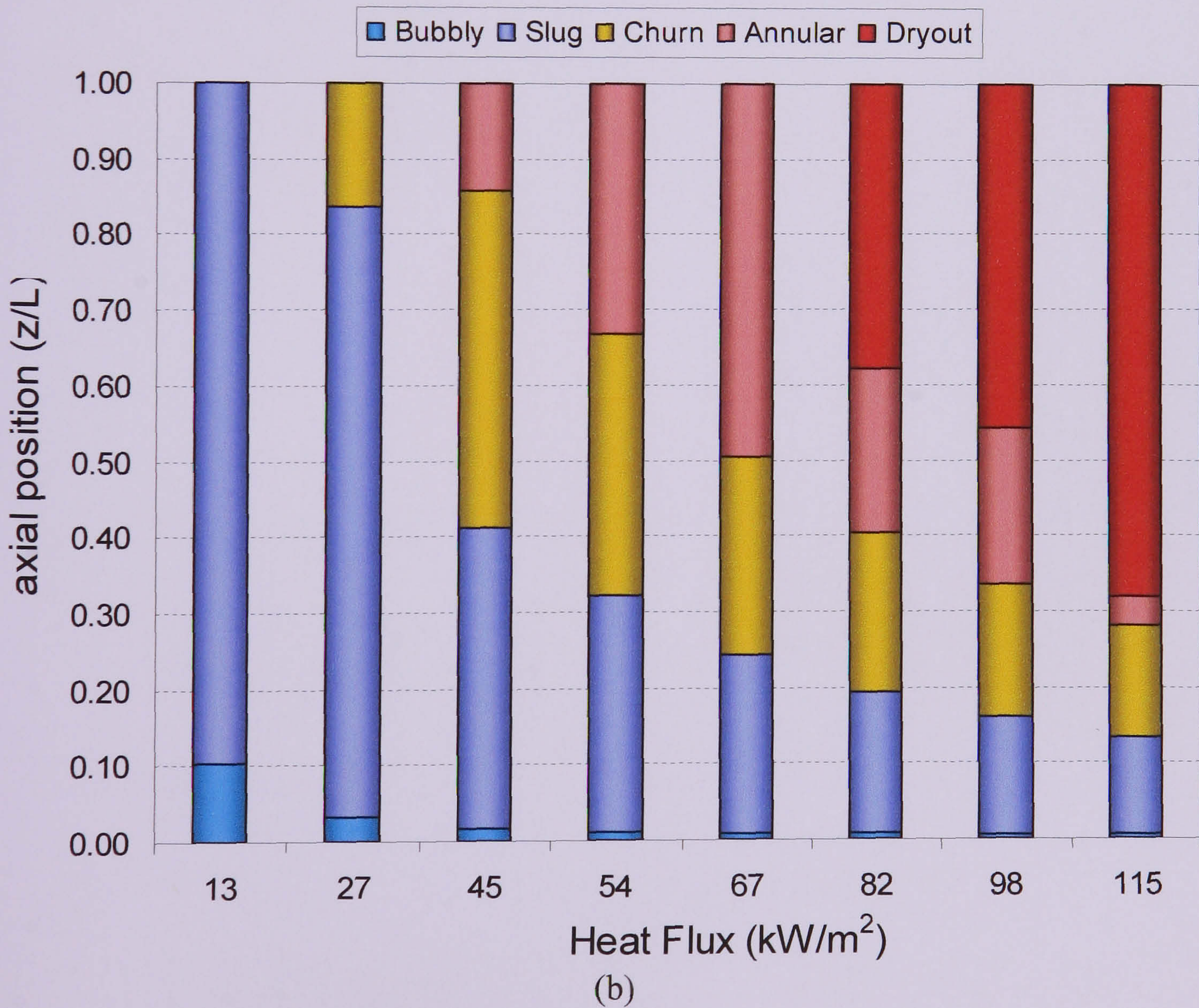
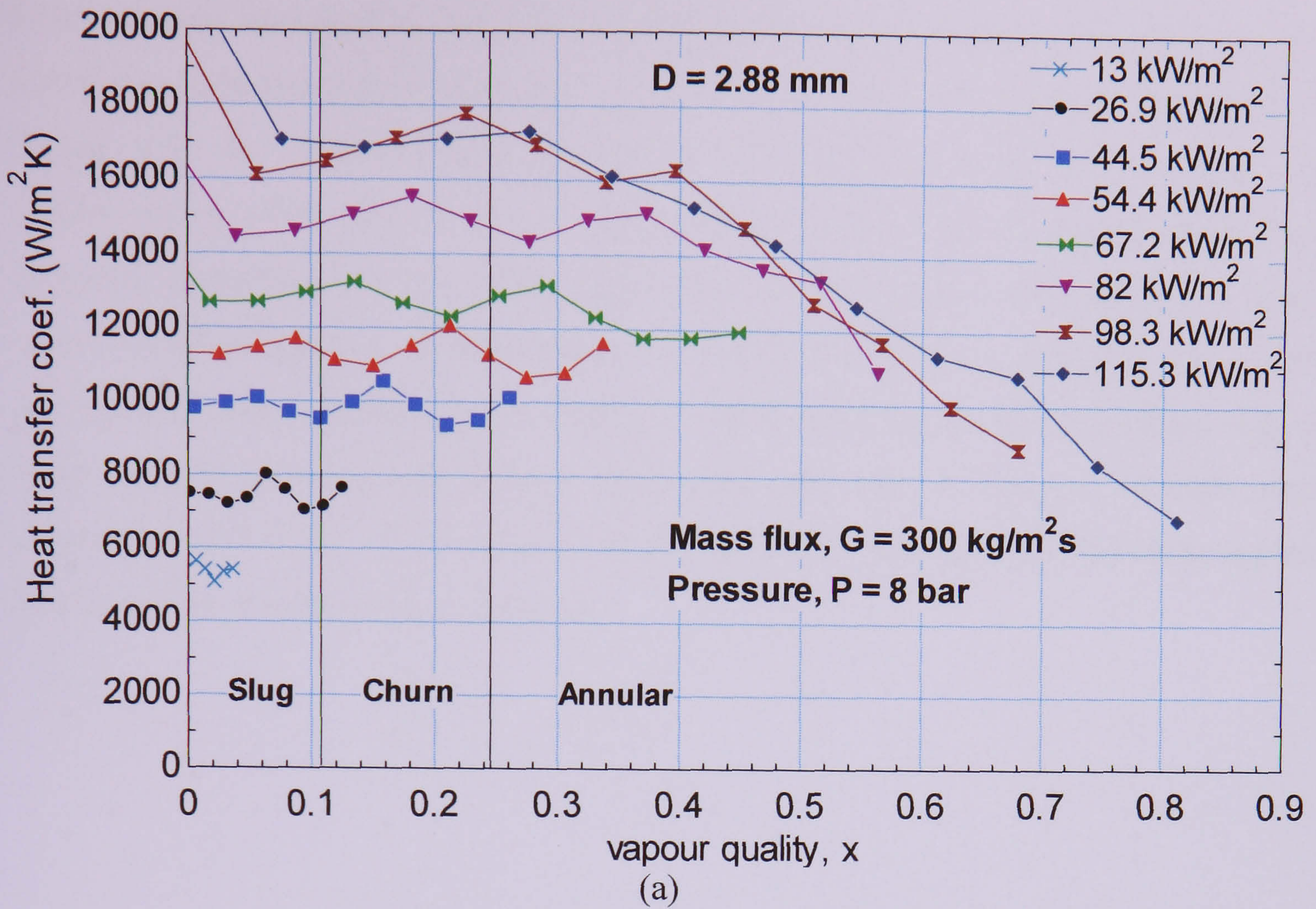


Figure 5.21 Flow regime transition lines of Chen et al. (2006) for $D = 2.88$ mm, $G = 300$ kg/m²s and $P = 8$ bar pressure superimposed: (a) on a local heat transfer coefficient versus vapour quality plot, (b) relative axial position versus heat flux plot.

Flow patterns observed in the 2.88 mm diameter tube, simultaneously with the heat transfer measurement at a mass flux of $300 \text{ kg/m}^2\text{s}$ and 8 bar pressure are shown in Figure 5.22 for different heat flux values. The photos shown in the figure are representatives of the more frequently observed flow pattern for the particular heat flux. However, more than one type of flow patterns could be obtained intermittently in some cases. The flow patterns indicate the conventional flow regimes (bubbly, slug, churn and annular) with transition flow regimes. As seen in the figure, transition from slug to churn, which shows a continuous vapour slug with narrow rings in between, was observed at 26 kW/m^2 . At a heat flux value of 54 kW/m^2 , another transition flow regime from churn to annular flow is obtained.

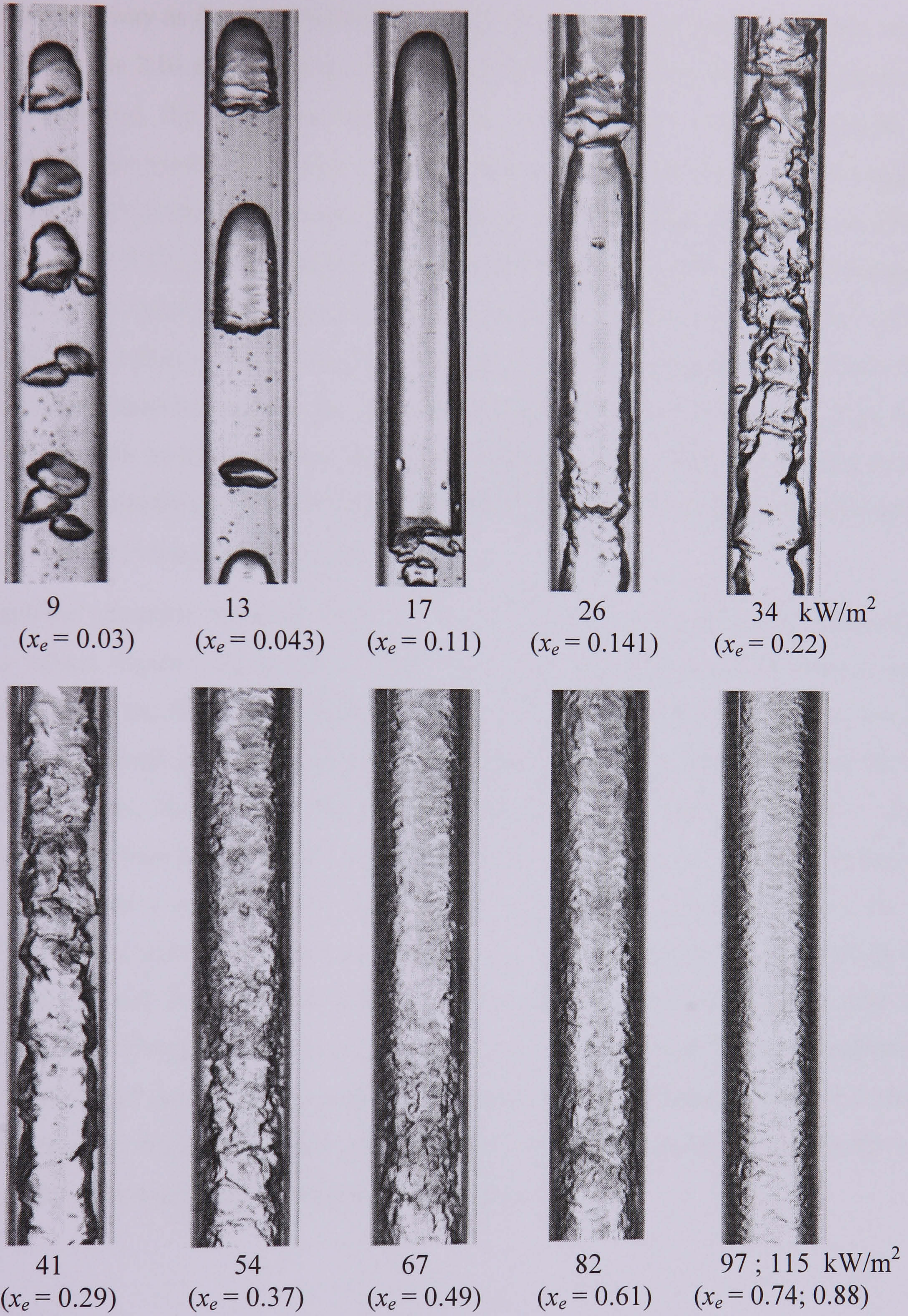
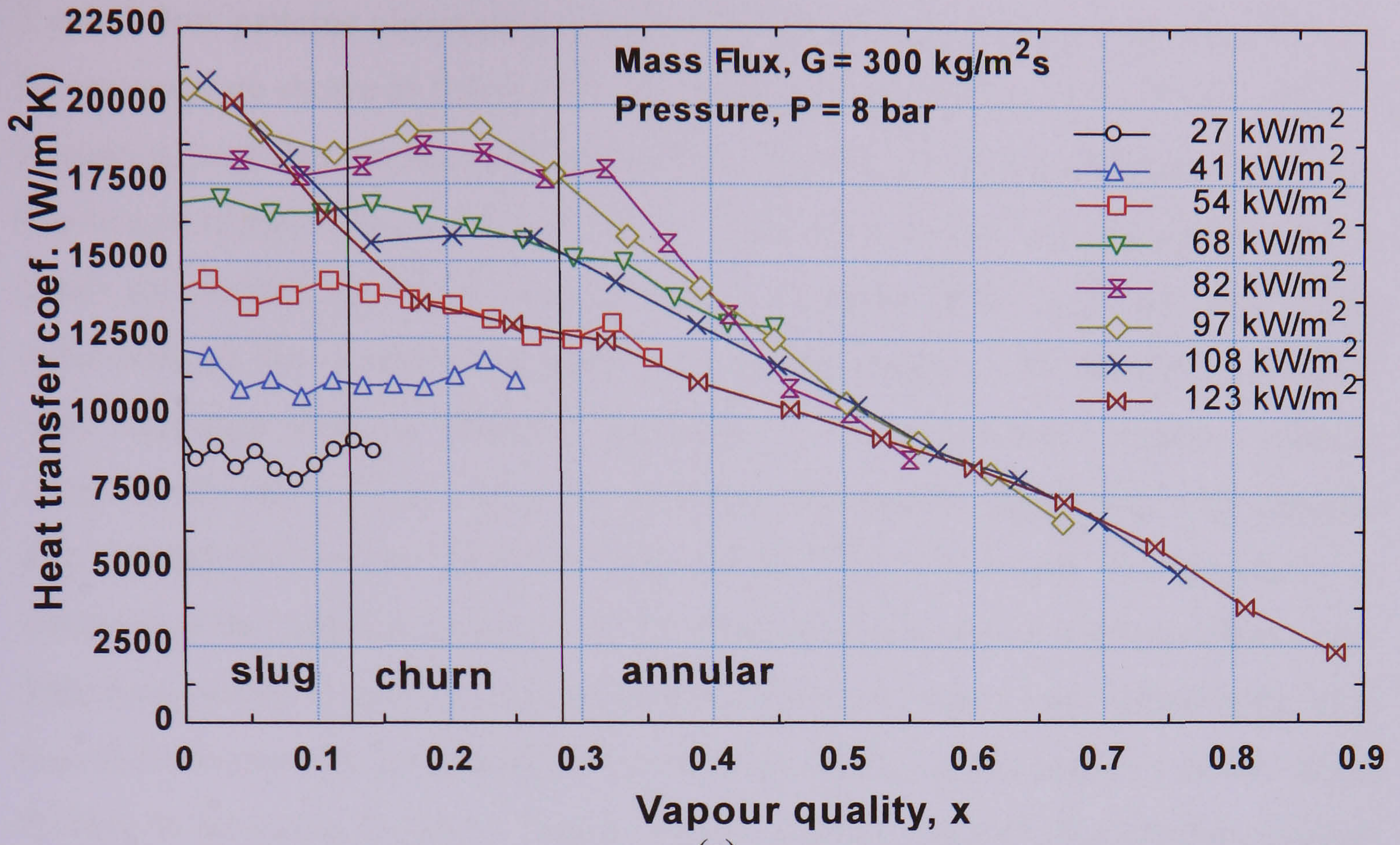


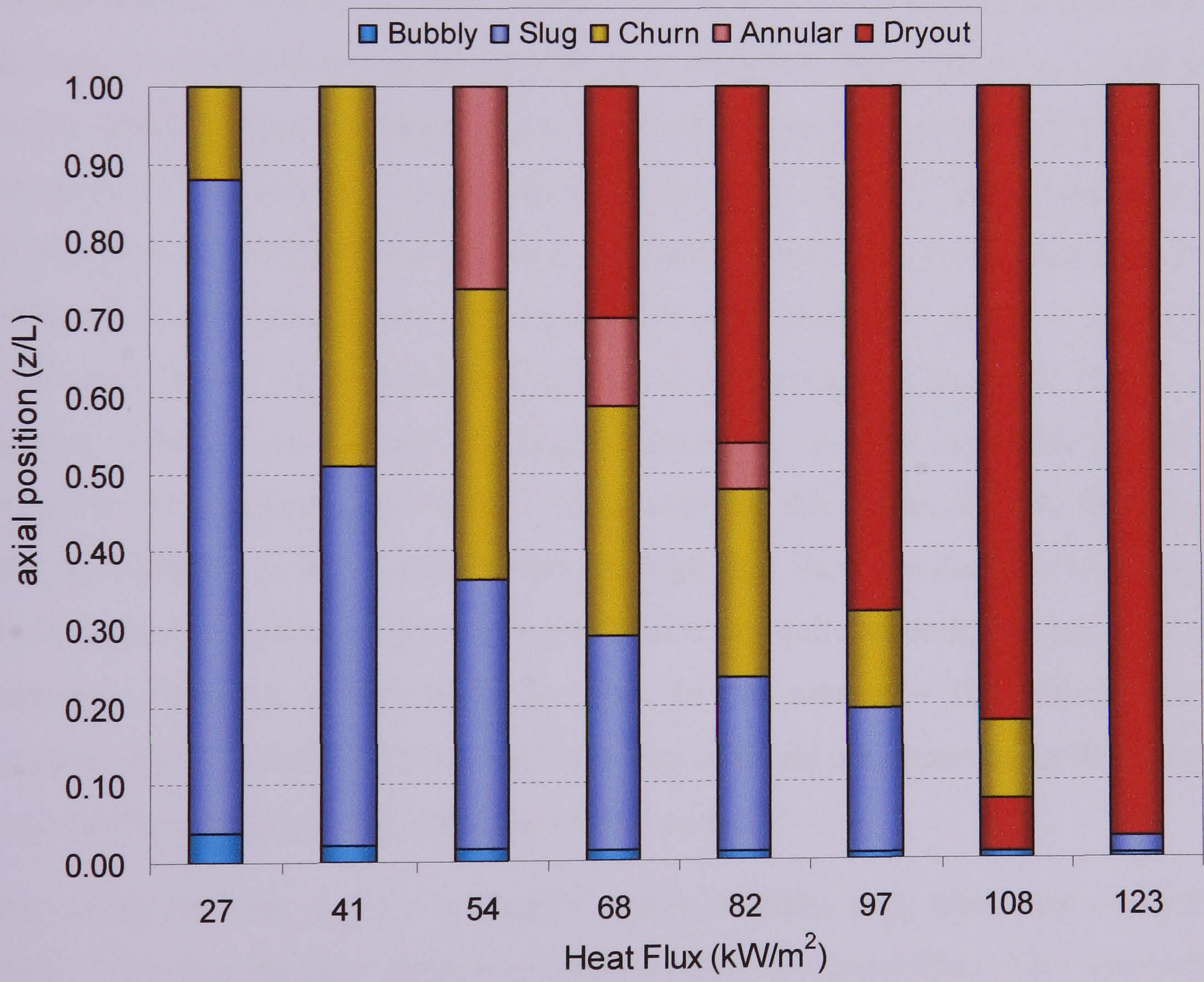
Figure 5.22 Flow patterns for the 2.88 mm tube at $G = 300 \text{ kg/m}^2\text{s}$ and 8 bar pressure.

In the same way as the above tubes, the transition boundaries from Chen (2006) are also shown for the 2.01 mm diameter tube in Figure 5.23. At a mass flux of $300 \text{ kg/m}^2\text{s}$ and 8 bar pressure, the transition boundary lines for slug/churn and churn/annular shift towards higher quality providing a larger quality range for the slug and churn regimes. At 82 kW/m^2 , a sharper transition to the region of decreasing heat transfer coefficient occurs at $x = 0.32$, just beyond the churn-annular boundary. At 97 kW/m^2 , it occurs at $x = 0.22$ in the churn flow region. For the two highest heat fluxes of 108 kW/m^2 and 123 kW/m^2 , the region of decreasing heat transfer coefficient commences very close to the start of the heated length in the slug flow regime. The lines for the two heat fluxes coincide as far as the estimated slug/churn boundary, where there is a relative increase in the heat transfer coefficient for the 108 kW/m^2 that persists until the lines for all heat fluxes merge in the annular regime.

Again the transition boundary lines were mapped onto axial positions for different heat flux values. Figure 5.23 (b) shows flow regime developments inside the heated section derived from the flow regime maps of Chen (2006). As shown in the figure, at low heat flux a significant portion of the tube is covered by slug and churn flows. As the heat flux increases, the annular flow regime begins to be observed. However, dryout commences close to the test section inlet as the heat flux increases. The two highest heat fluxes showed a continuous decrease in the heat transfer coefficient, except for 108 kW/m^2 , where there was a short constant region, which happens to lie in the churn flow regime. Typical flow patterns observed by Chen (2006) for the 2.01 mm tube were discussed in Chapter 3. However, since the mass flux and heat flux were adjusted to vary the liquid and vapour superficial velocities (main parameters in Chen's study), conditions are different to match and post flow pattern photographs at exactly the same mass flux and heat fluxes corresponding to Figure 5.23.



(a)



(b)

Figure 5.23 Flow regime transition lines of Chen et al. (2006) for $D = 2.01 \text{ mm}$, $G = 300 \text{ kg/m}^2\text{s}$ and $P = 8 \text{ bar}$ pressure superimposed: (a) on a local heat transfer coefficient versus vapour quality plot, (b) relative axial position versus heat flux plot.

Typical flow patterns observed in the 1.1 mm tube at a mass flux of $300 \text{ kg/m}^2\text{s}$ and 6 bar pressure are shown in figure 5.24. The flow patterns images are arranged in order of increasing heat flux. Image 1 shows confined bubble, which was obtained at low heat flux or exit quality. Chen (2006) also observed this flow pattern at a combination of low liquid and vapour superficial velocities at all pressures in the 1.10 mm tube. These indications of the increasing importance of surface tension with decreasing diameter were consistent with the diameters predicted by the confinement number criterion, which for R134a is 1.7 mm at 6 bar pressure. Continuous vapour slug with irregular film interface is observed (image 2), when the heat flux is increased. The irregularity or waviness of the interface seems to emerge from the coalescing of relatively short slugs. This flow pattern is more of a transition flow regime, in which case further increase in heat flux increases the irregularity of the interface leading to discontinuity of the vapour flowing in the centre (image 3). Image 4 shows that the vapour/liquid interface tends to become relatively regular, with the vapour flow in the core increasing in radial size, i.e. transition to annular flow regime. For the same diameter tube, Chen et al. (2006) found that the liquid–vapour interfaces in slug and churn flow that occurred at higher liquid and vapour velocities were better defined. In this experiment the flow parameters were not adjusted to obtain particular flow regimes, instead the flow visualization was performed at the conditions of the heat transfer tests. Therefore, the flow patterns may not directly fit with the conventional distinction. For instance, Chen et al. (2006) found dispersed bubble flow at about $1820 \text{ kg/m}^2\text{s}$ mass flux, but this is outside the range of the current heat transfer parameters, which could be the reason for not observing the same flow pattern in the present studies. At high heat flux, annular flow was observed which is shown in photograph 5. The interface is not quite smooth, but has small-scale roughness. However, at very high heat flux, in this case at $\sim 104 \text{ kW/m}^2$, the film becomes very thin and sometimes small droplets of liquid are observed on the surface of the glass tube perhaps ejected from the vapour core.

Most commonly four or more descriptive names (bubbly, slug, churn and annular) are used to categorize the flow regimes exhibited during two phase flow. This conventional way of sorting flow patterns into specified categories often leads researchers to round off important flow features towards these main flow regimes. However, in some cases flow patterns that do not exactly fit to one of the conventional names might appear. Also, more than one type of flow patterns can be obtained intermittently in some cases especially during flow regime transition. In fact, there is no particular reason why there

should be an abrupt transition boundary from one flow pattern to another instead of a gradual transform. In this study the main purpose of the flow visualization is not to produce flow pattern transition maps, but to support the understanding of the heat transfer process in small tubes. Therefore, relating the respective flow structure with heat transfer result and understanding the distinguished features is more useful than segregating the flow regimes into conventional categories.

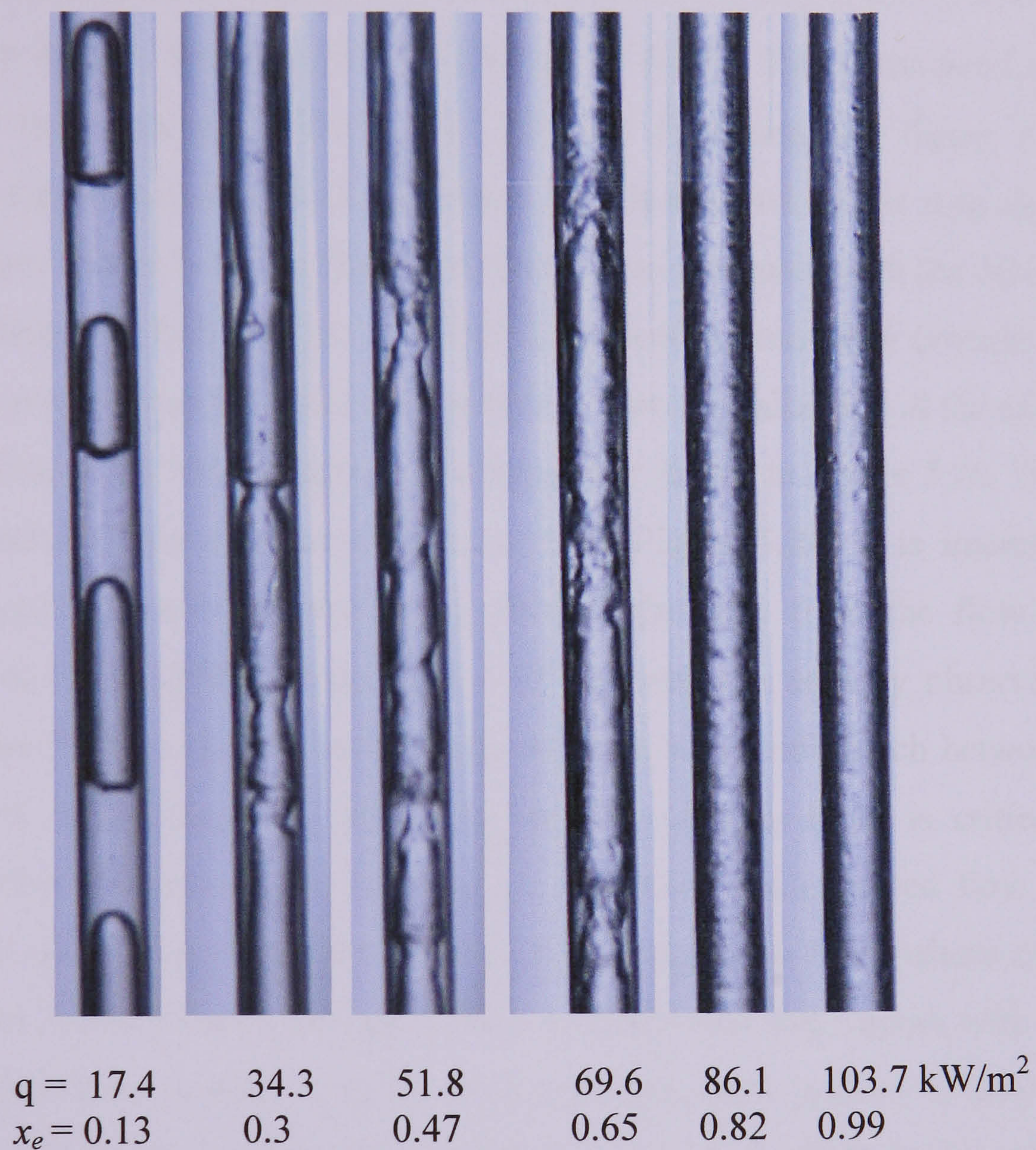
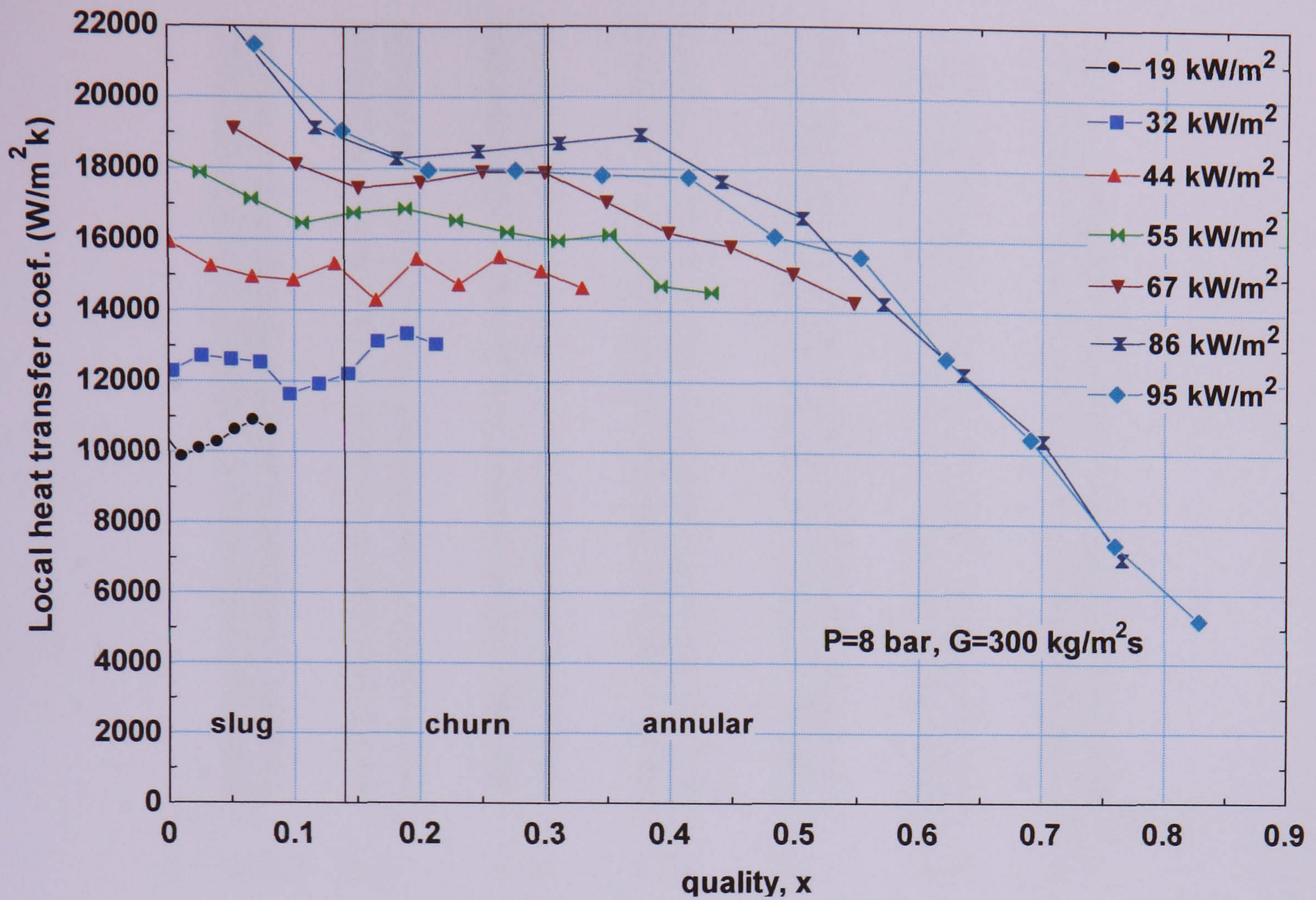


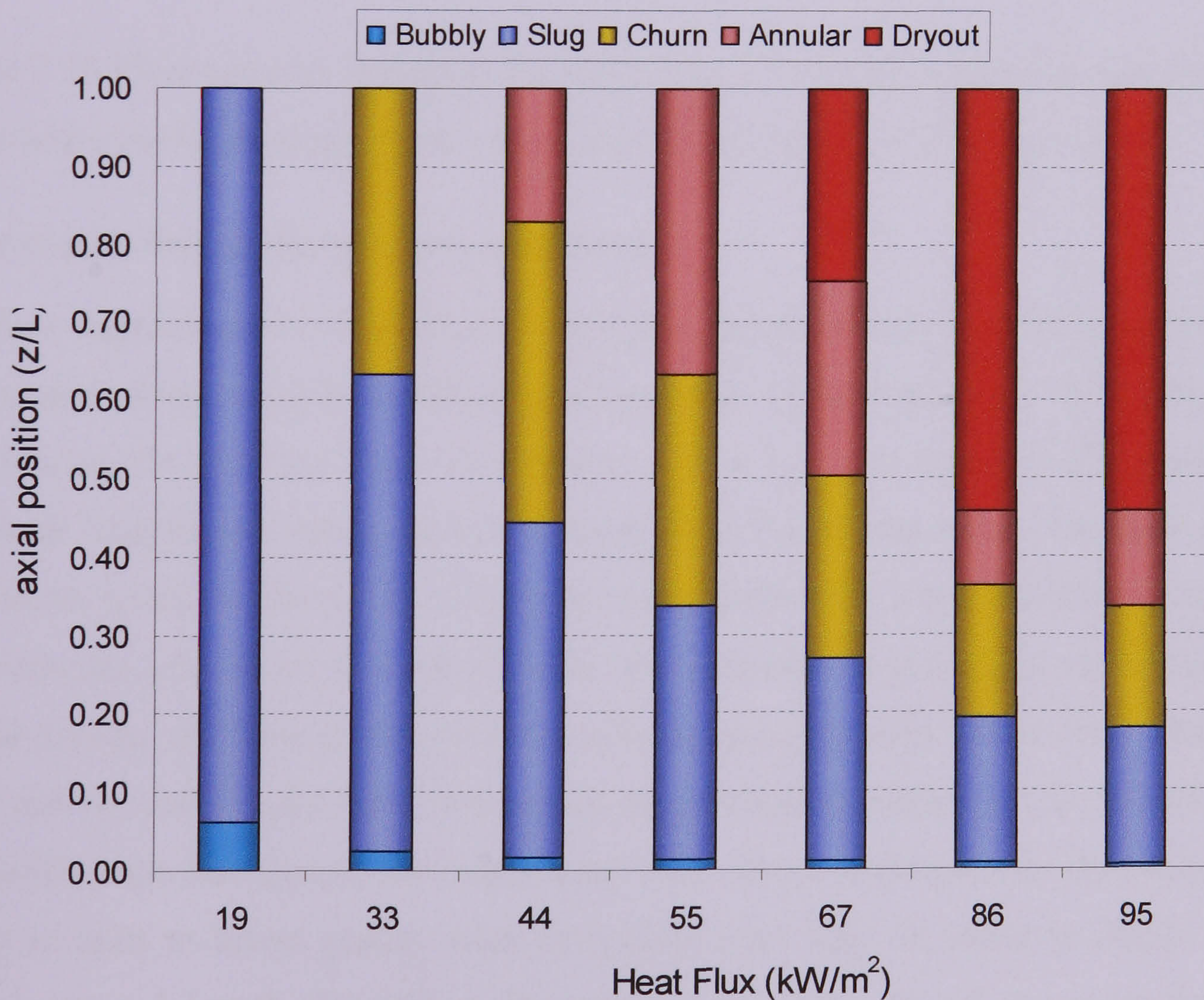
Figure 5.24 Flow patterns observed for the 1.1 mm tube at a mass flux of $300 \text{ kg/m}^2\text{s}$ and 6 bar pressure.

Figure 5.25 also presents the heat transfer coefficient as a function of quality for the 1.1 mm diameter tube with flow regime boundary lines shown at the same mass flux of $300 \text{ kg/m}^2\text{s}$ and 8 bar pressure with the other tubes. As shown in the figure, at low heat flux values (19 and 33 kW/m^2), the heat transfer coefficient tends to increase with quality towards the test section exit and lies mostly in the slug flow regime. At heat flux values $q \geq 44 \text{ kW/m}^2$, the heat transfer coefficient decreases with quality at low quality region below the slug-churn boundary. Beyond this region, the heat transfer coefficient was

nearly independent of quality, which mostly lies in the slug and churn flow regimes. The sharply decreasing heat transfer coefficient region is in the annular flow regime and the quality at which the transition to this region shifts towards the churn-annular boundary as the heat flux increase. However, in the constant heat transfer coefficient region, the heat transfer coefficient value for the highest heat flux ($q = 97 \text{ kW/m}^2$) is lower than that for the 86 kW/m^2 . Beyond this region the two curves merge. Also, the transition quality towards decreasing heat transfer coefficient region for 97 kW/m^2 ($x \sim 0.42$) is slightly higher than that for 86 kW/m^2 ($x \sim 0.38$). The corresponding axial position versus heat flux plot showing the different flow regimes, figure 5.25 (b), indicates that a significant portion of the heated tube is covered by the slug and churn flow regime, especially at low heat flux. This is also true compared with the other tubes, i.e. as the tube diameter decreases the slug and churn flow regimes shift towards the test section exit and prevail over the other flow patterns. Flow visualization at the exit of the tube corresponding to the heat transfer experiments are shown in Figure 5.26. The flow patterns are similar to the ones described above in Figure 5.24. It is interesting to compare the expected flow patterns at the exit of the tube from the flow pattern transition map of Chen (2006) using figure 5.25 (b) with the actually observed flow patterns of Figure 5.26. As can be seen clearly, there is an overall match between both figures. However, identifying and describing the flow pattern types is critical as it involves subjective judgement. For instance, at 33 kW/m^2 the expected flow pattern using figure 5.25 should be churn flow. However, looking at the flow pattern observed at the exit (figure 5.26), it seems that the flow is a continuous slug vapour with narrow liquid rings in between, perhaps it could be a transition flow pattern to churn (if it exists) or annular. If the flow pattern observed in Figure 5.26 at 33 kW/m^2 is considered as churn flow as considered by flow map of Chen (2006) then the two matches. Most often flow regimes maps present a sense of abrupt transition between the conventional flow patterns and do not show the existence of transition flow regimes.



(a)



(b)

Figure 5.25 Flow regime transition lines of Chen et al. (2006) for $D = 1.1$ mm, $G = 300$ kg/m²s and $P = 8$ bar pressure superimposed: (a) on a local heat transfer coefficient versus vapour quality plot, (b) relative axial position versus heat flux plot.

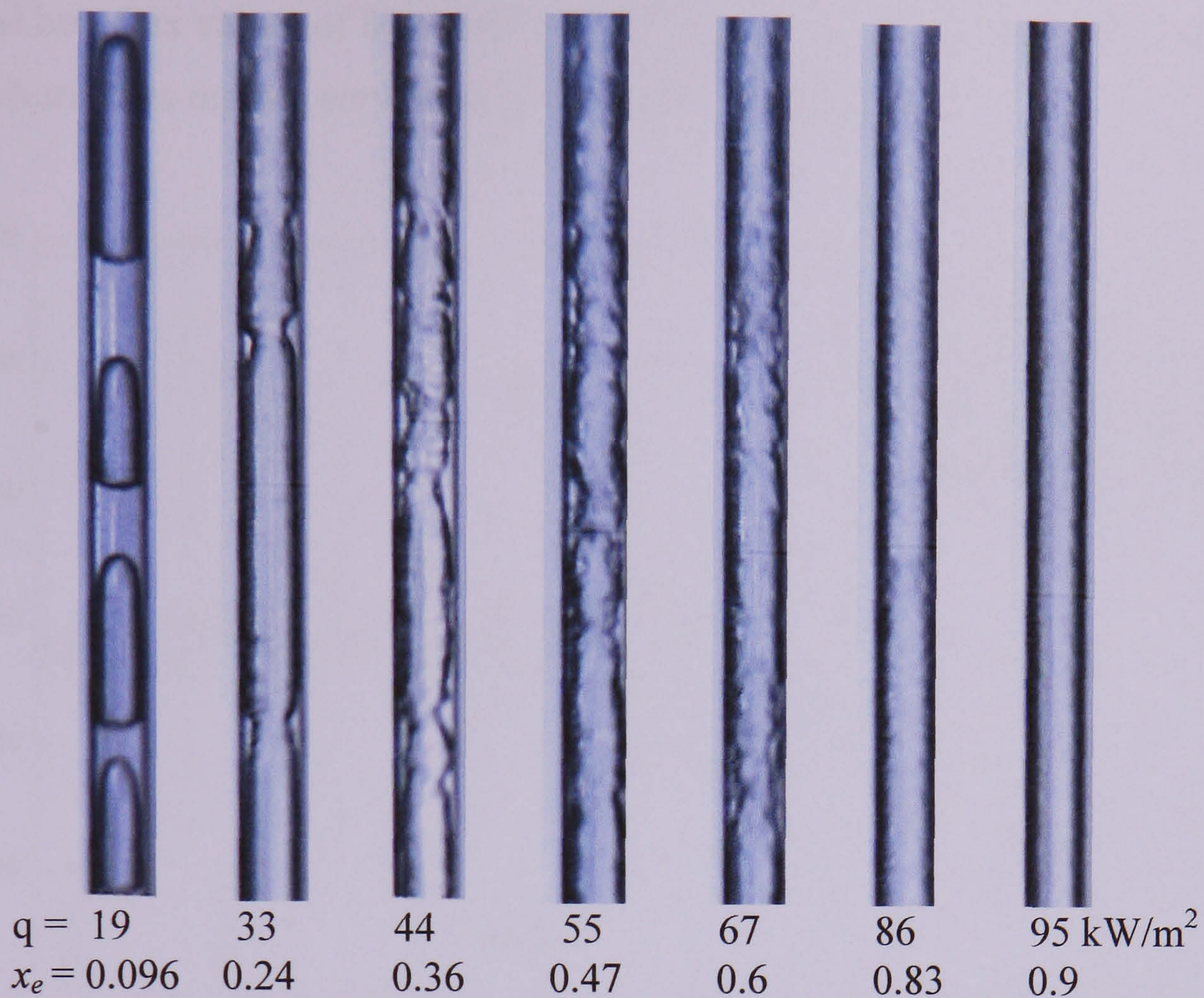
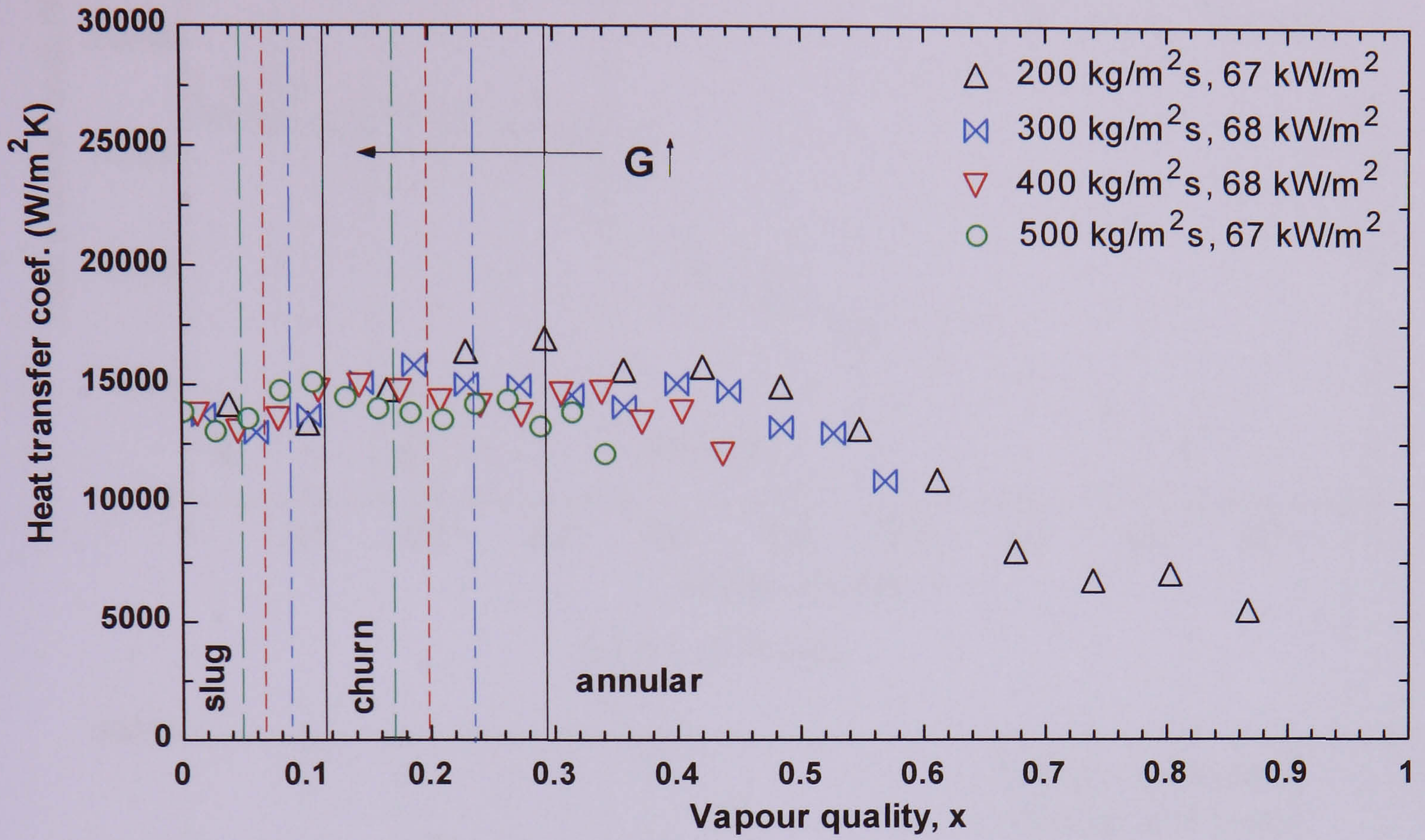


Figure 5.26 Flow patterns images at the exit of the 1.1 mm diameter tube corresponding to the heat transfer experiments at a mass flux of $300 \text{ kg/m}^2\text{s}$ and 8 bar pressure.

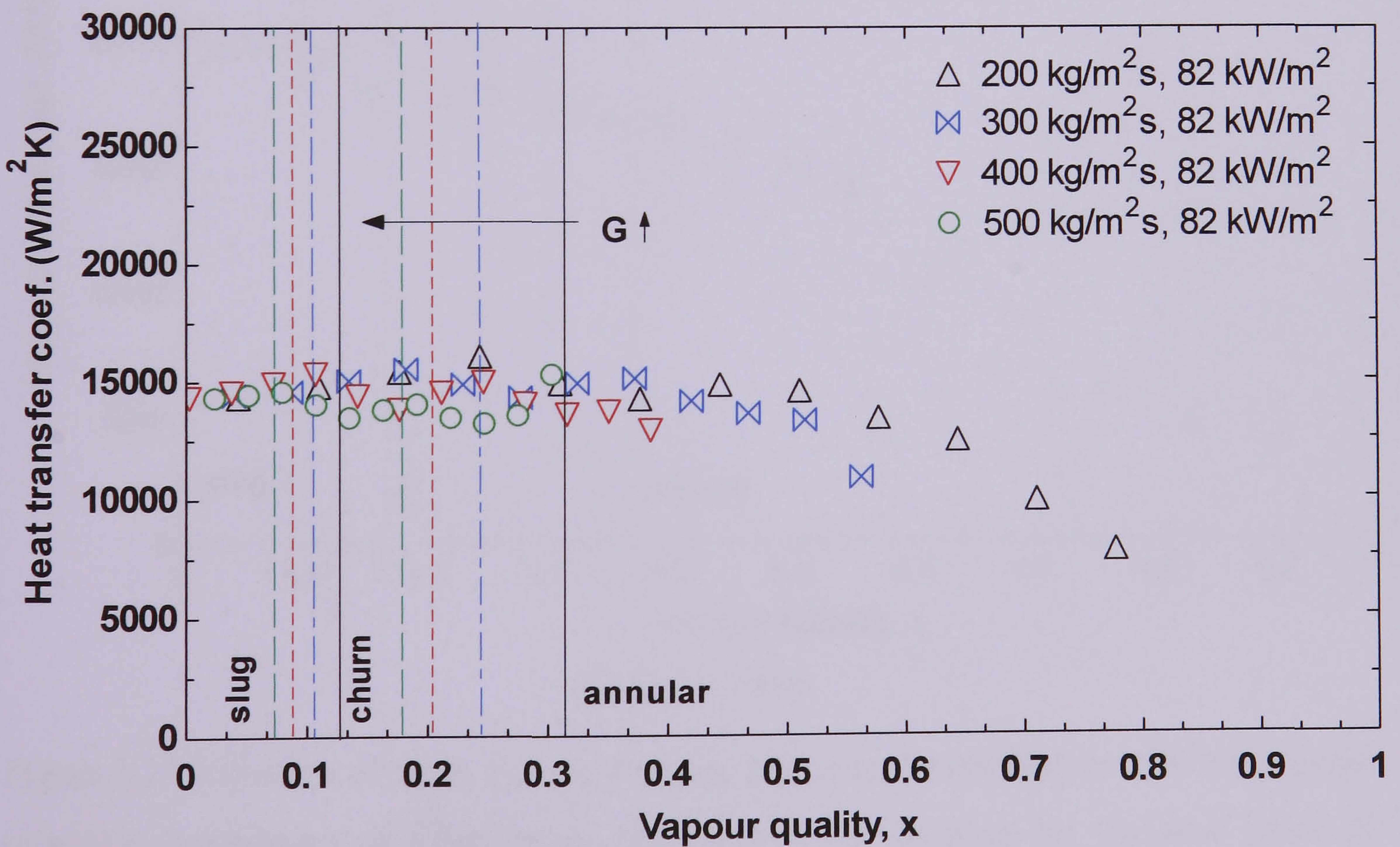
Effect of mass flux on the transition boundaries

The flow regime transition boundaries were also superimposed on the plots showing the dependence of heat transfer coefficient on mass flux in the range $200 - 600 \text{ kg/m}^2\text{s}$ at 8 bar pressure for the four tubes of diameter 4.26 - 1.1 mm. Figure 5.27 presents the results at heat fluxes values shown in each plot. For all the tubes, the flow regime boundaries based on Chen et al. (2006) move to significantly lower qualities as the mass flux increases (shown by the dotted lines). The influence of mass flux on the transition to heat transfer coefficients that decrease with increasing quality is less clear. This point could not be investigated fully, because of the physical limitation on the heated length to provide high exit quality for larger mass flux values. However, the transition point seems to shift to lower quality with increasing mass flux. In order to clarify this, a variable heated length that allows the same exit quality for all the mass fluxes at constant heat flux is required. For the 4.26 mm and 2.88 mm tubes at nominal heat flux of 68 and 82 kW/m^2 respectively, the transition to the decreasing heat transfer coefficient region occurs in the annular flow regime. For the 2.01mm and 1.1 mm tubes

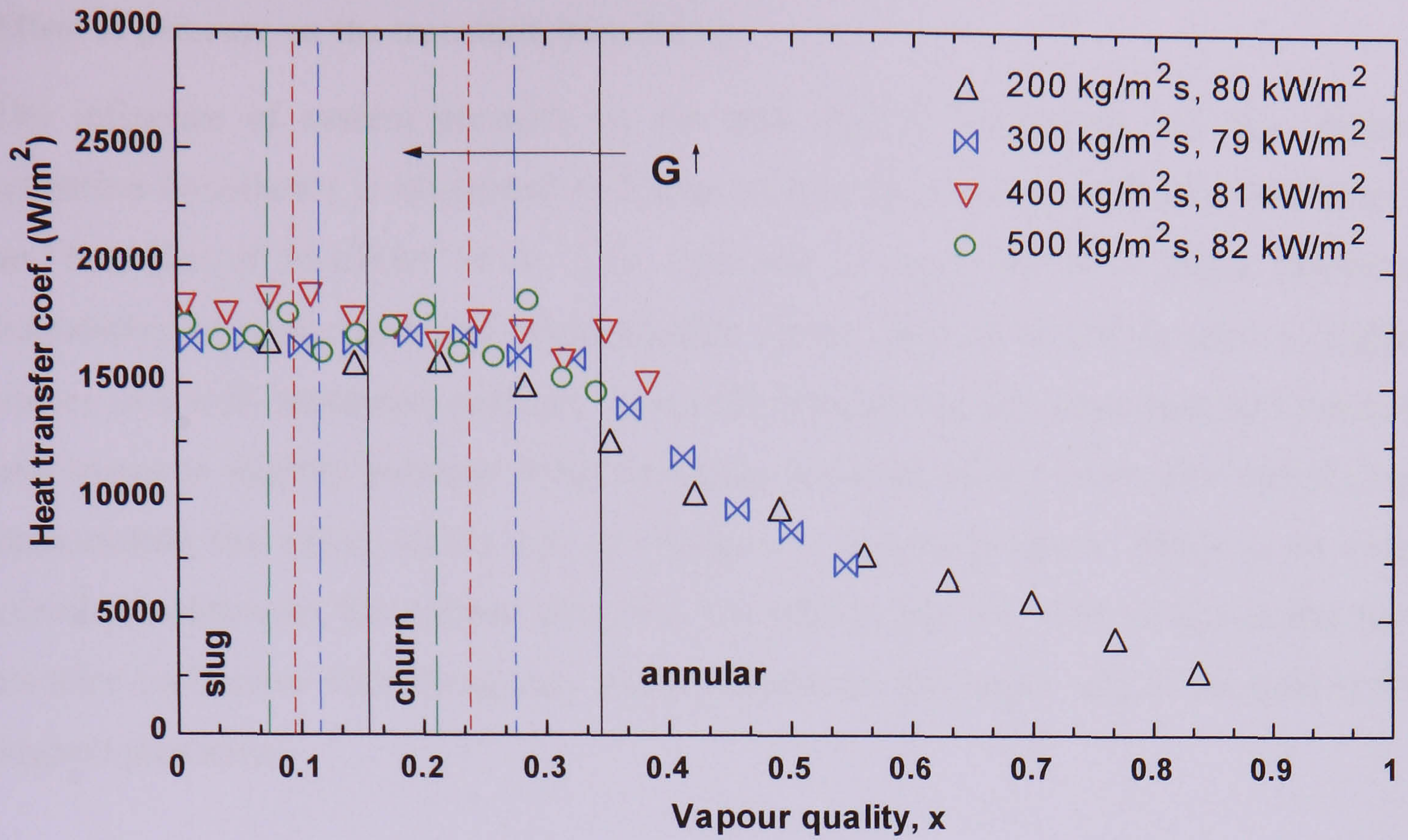
at nominal heat flux values of 80 and 68 kW/m² respectively, the transition occurs in the nominal churn flow regime very close to churn-annular boundary.



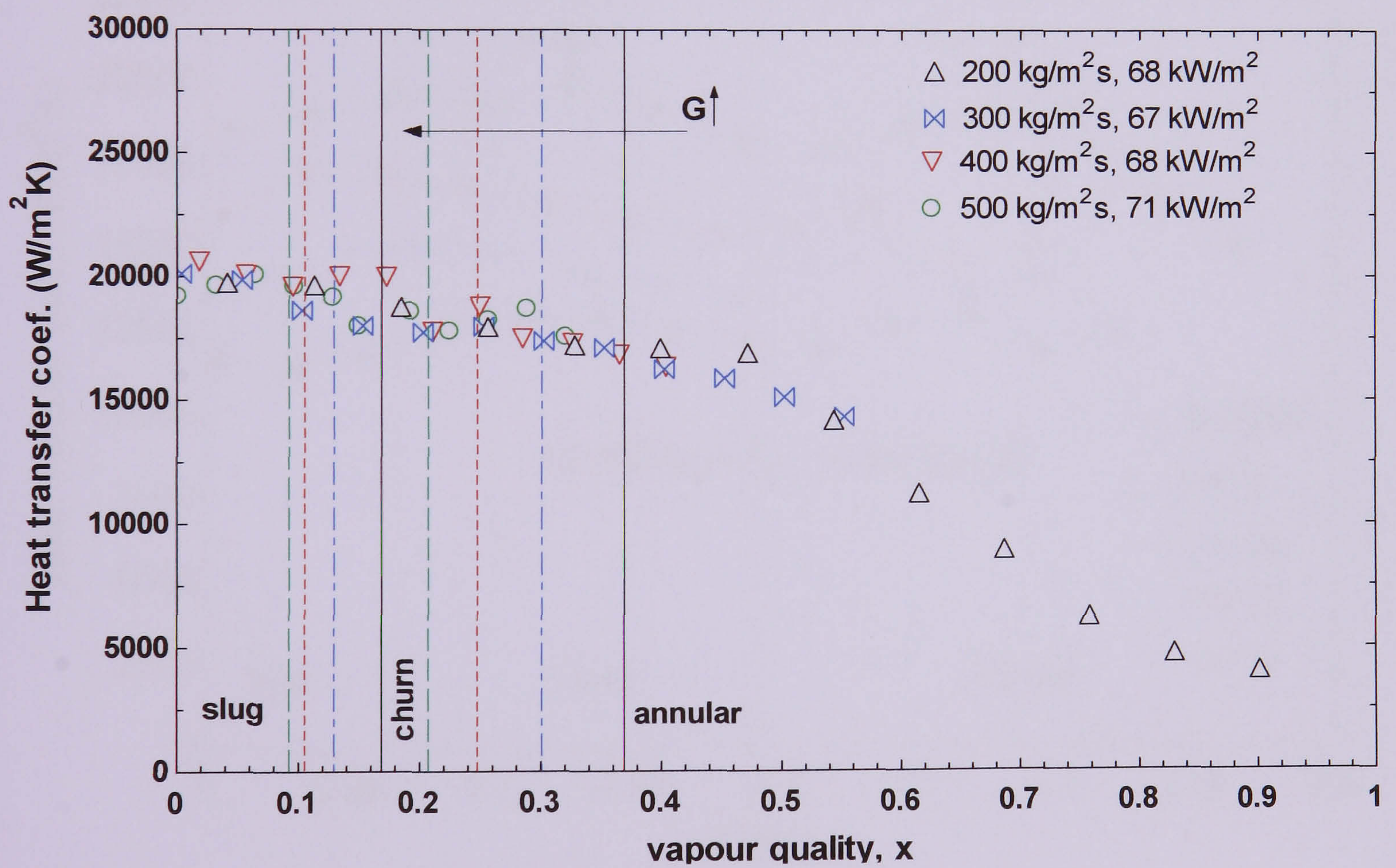
(a) D = 4.26 mm



(b) D = 2.88 mm



(c) $D = 2.01 \text{ mm}$

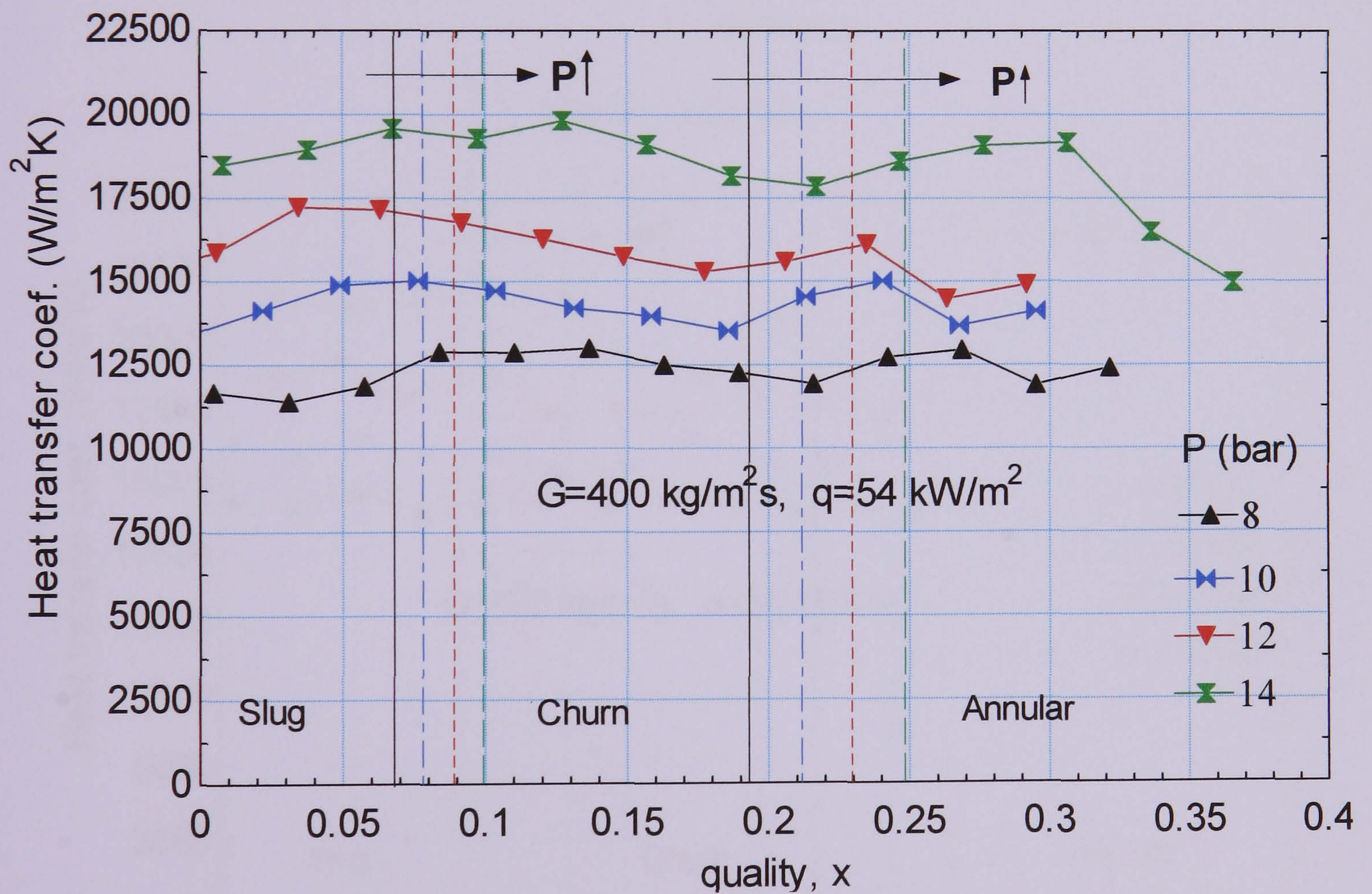


(d) $D = 1.1 \text{ mm}$

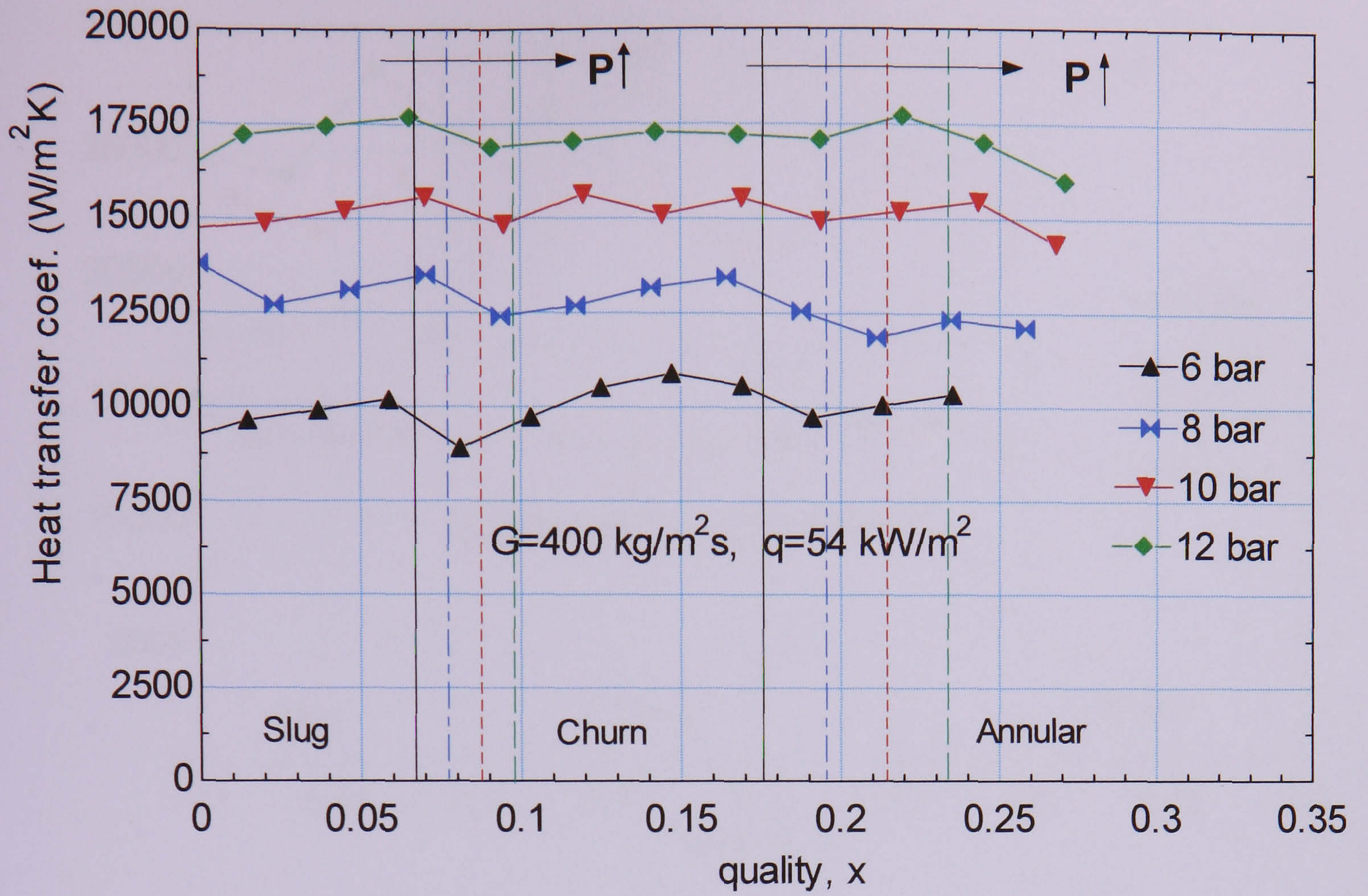
Figure 5.27 Influence of mass flux on the local heat transfer coefficient and flow regime transition boundaries of Chen et al. (2006) at 8 bar pressure for the four tubes of diameter: (a) 4.26 mm, (b) 2.88 mm, (c) 2.01 mm and (d) 1.1 mm.

Effect of pressure on the transition boundaries

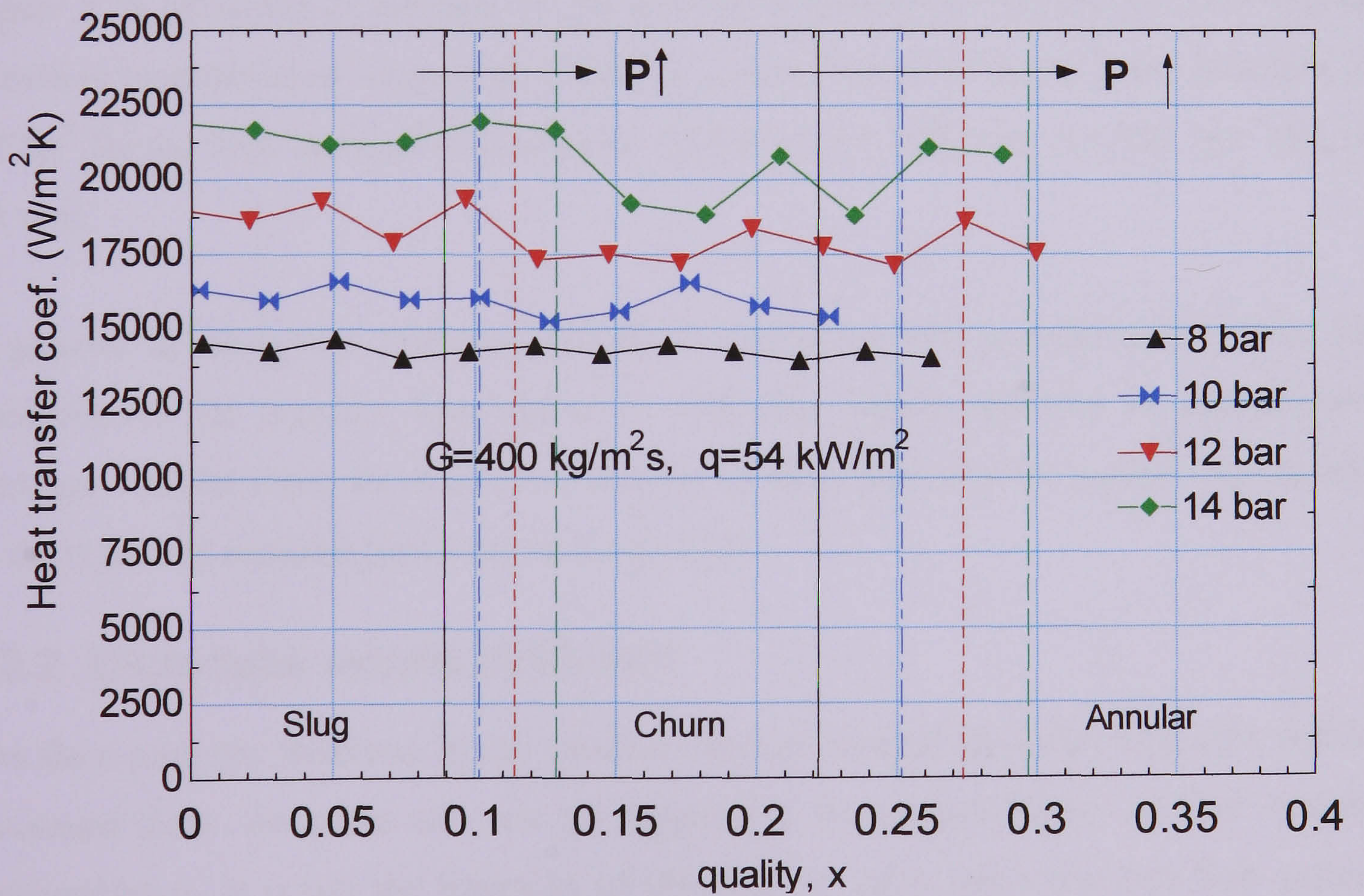
The influence of system pressure on the heat transfer coefficient and flow regime transition boundaries is illustrated in Figure 5.28 at the same mass flux of $400 \text{ kg/m}^2\text{s}$ and heat flux of 54 kW/m^2 (4.26, 2.88, 2.01 and 1.1 mm). The flow pattern transition boundaries of slug-churn and churn-annular (from Chen et al. 2006) shift to higher values of x with increasing pressure. The shift is larger for the churn-annular boundary and seems to slightly increase with decreasing diameter of the tubes. The dotted lines demonstrate the effect (shift) due to changes in system pressure. There is no clear correlation between the regime transition boundaries and the start of decreasing heat transfer coefficient with the quality region shown for the larger tube (4.26 mm) at the highest pressures.



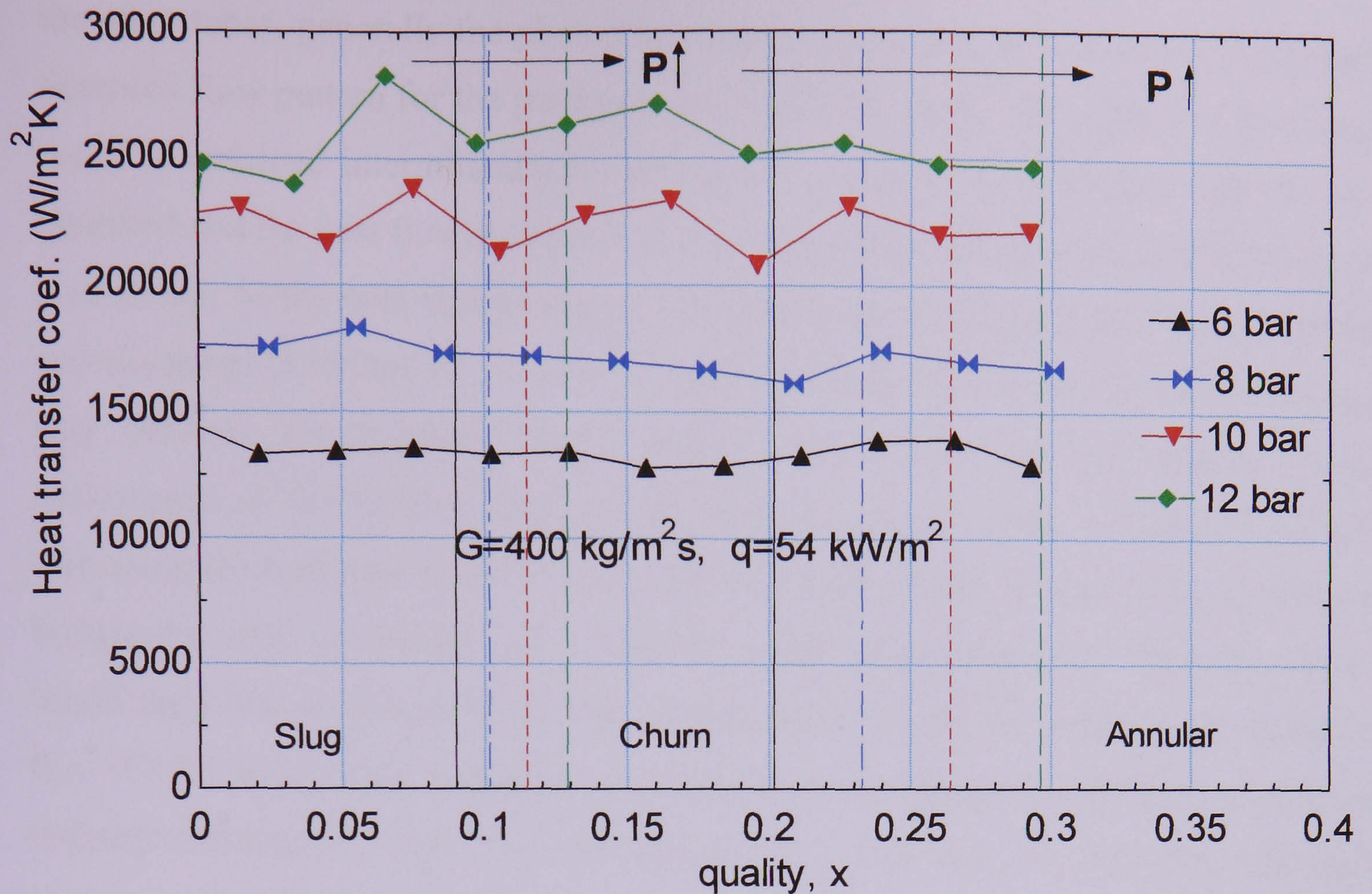
(a) $D = 4.26 \text{ mm}$



(b) $D = 2.88 \text{ mm}$



(c) $D = 2.01 \text{ mm}$



(d) $D = 1.1 \text{ mm}$

Figure 5.28 Influence of pressure on the local heat transfer coefficient and flow regime transition boundaries of Chen et al. (2006) at a mass flux of $400 \text{ kg/m}^2\text{s}$ and heat flux 54 kW/m^2 for the four tubes of diameter: (a) 4.26 mm , (b) 2.88 mm , (c) 2.01 mm and (d) 1.1 mm .

In general, at the typical low mass fluxes covered in the present heat transfer tests, the transition to the annular flow shifts to relatively higher qualities as the pressure increases. As the diameter decreases, slug-churn flow becomes the typical flow pattern in the region of constant heat transfer coefficient.

5.3.2 Micro-tube results (0.52 mm)

The flow patterns observed in the smallest tube of internal diameter 0.52 mm will be discussed from the point of view of supporting the understanding of heat transfer characteristics. It is not the intention of this PhD to carry out a detailed flow pattern study. The flow patterns in this tube exhibit somewhat different characteristics compared with the other tubes ($4.26 - 1.1 \text{ mm}$). Figure 5.29 presents typical flow patterns observed during the boiling test at a mass flux of $400 \text{ kg/m}^2\text{s}$ and 8 bar pressure. These flow patterns were taken simultaneously with the heat transfer tests presented earlier in Figure 5.6 at each value of heat flux. As mentioned previously for

the other tubes, generally the photographs show a representative of the more frequently observed flow pattern for the particular heat flux. However, more than one flow pattern could be obtained intermittently in some cases. At very low heat flux, bubbly flow is observed and the heat flux increased in small steps until an exit quality of about 80-90% is obtained. As the heat flux increased, the bubbles grew in length and become confined and elongated (12.8 and 14.1 kW/m²). Further increase in heat flux resulted in the liquid slug between the bubbles being “pushed” on to the upstream bubble creating coalescence of the bubbles and a wavy film. As shown again in figure 5.29, when increasing the heat flux even further, liquid ring flow (a flow where the liquid no longer bridges the tube) is obtained for a relatively wider range of quality. The appearance of liquid rings that no longer bridge the tube happens to coincide with the threshold heat flux (17.9 kW/m²) that separates the two groups of heat transfer curves exhibiting different influences of heat flux, see figure 5.6. In this case, the film interface shows narrow necks (high amplitude waves with relatively shorter wave length) in certain intervals equivalent to the length of short bubble (17.9 and 25.3 kW/m²). This seems a transition regime to the flow with highly non-uniform and wavy film interface (31 kW/m²). This could lead a transition to annular flow (43.5 kW/m²), since further increase in heat flux reduces the wave irregularity and distributes the waves almost uniformly - annular flow (49.2 and 55.2 kW/m²). At high heat flux, the annular flow patterns have small-scale roughness of very short amplitude and wavelength (61.4 kW/m²). Overall, the flow patterns observed in the smaller tube, of internal diameter 0.52 mm were different than those observed in the larger tubes by Chen et al. (2006). In general, they defined the conventional regimes of dispersed bubble, bubbly, slug, churn, annular and annular-mist flow. However, in the current flow patterns for the 0.52 mm diameter tube; dispersed bubble flow was not observed, the liquid–vapour interfaces in conventionally referred as churn flow were less disturbed and became diminished as heat flux increases. Also, continuous vapour slug with narrow liquid rings turn out to be more visible. This particular flow pattern could also be transition regime from slug to annular flow. In general, the flow patterns observed in the smallest tube of internal diameter 0.52 mm were distinctively different than the smaller tubes (4.26 – 1.1 mm) and could be represented as bubbly, elongated bubble (slug), liquid-ring, wavy annular and annular flow regimes. It was not the intention of this PhD to carry out a detailed flow pattern study. This will be further investigated and regarded as one of the recommendations for future work.

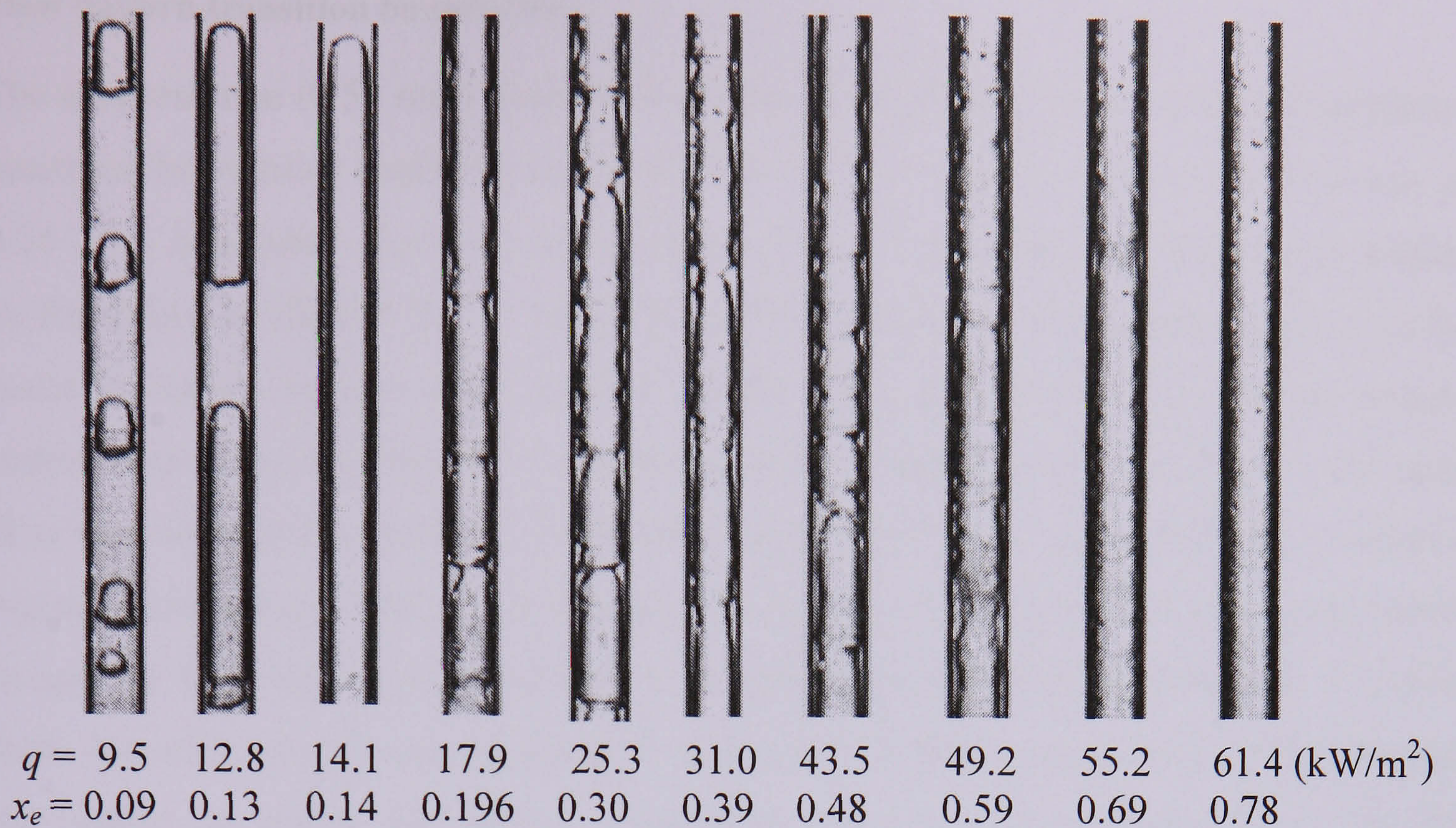


Figure 5.29 Flow pattern in the smaller tube of 0.52 mm internal diameter at different heat flux, for mass flux, $G = 400 \text{ kg/m}^2\text{s}$ and pressure, $P=8 \text{ bar}$.

In the 0.52 mm diameter tube, it was also observed that the elongated bubbles with wavy film interface were created as a result of coalescence of relatively shorter bubbles, especially at low pressure. A similar phenomenon was observed by Revellin et al. (2006). Figure 5.30 shows for low mass flux, how three relatively short bubbles coalesce together to form an elongated bubble leaving the film interface wavy.

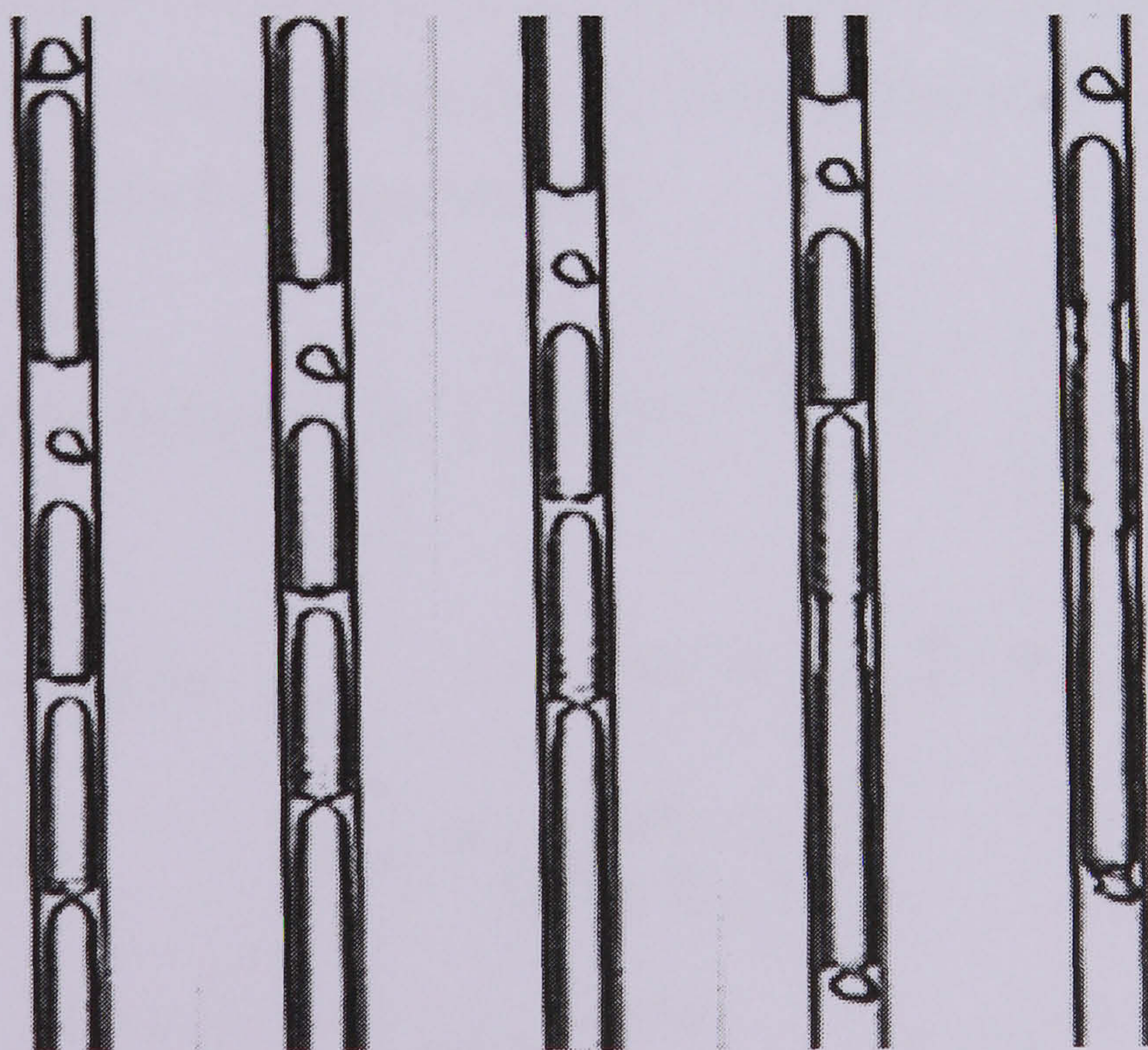


Figure 5.30 Sequence of flow patterns showing coalescence, $G=300 \text{ kg/m}^2\text{s}$, $P=6 \text{ bar}$ and $q = 3.7 \text{ kW/m}^2$

Flow pattern transition boundaries

The smallest tube (0.52 mm) was not studied by Chen (2006), hence similar flow pattern transition boundaries could not be found from his flow regime maps in the same way as 4.26 – 1.1 mm tubes. However, flow patterns in a 0.5 mm tube were extensively studied by Revellin and Thome (2007). They identified three main flow patterns named as: a) the *isolated bubble* regime that includes bubbly flow and short slugs; in this regime coalescence is not significant, b) *coalescing bubble* regime, where slug flow is the main flow with some of the bubbles coalescence together to form a longer slug and c) *annular regime*. According to their observation churn flow is a transition from coalescing bubble to annular flow and it is considered as indication for the end of coalescing of bubble flow. Revellin and Thome proposed flow pattern transition correlations, which provide the quality at which the regime transitions occur in non-adiabatic flows. For the transition from isolated bubble to coalescing bubble regime their correlation contained Reynolds number, Boiling number and Weber number, Eq. (5.1). A similar correlation for the transition from the coalescing bubble to the annular regime contained only the Reynolds and Weber numbers, Eq. (5.2). Both equations predict the respective flow pattern transition boundaries within a $\pm 20\%$ uncertainty limit. The critical quality for the occurrence of the dryout phenomenon was also proposed after modifying the Katto-Ohno critical heat flux correlation, Eq. (5.3) ($\pm 15\%$). These equations will now be used to superimpose flow pattern boundaries in the current heat transfer plots for the 0.52 mm diameter tube at a mass flux of $300 \text{ kg/m}^2\text{s}$ and 6 bar pressure in order to relate the heat transfer behaviour with the flow visualizations.

$$\text{Isolated bubble – Coalescing bubble } x = 0.763 \left(\frac{Re_{lo} Bo}{We_{go}} \right)^{0.41} \quad (5.1)$$

$$\text{Coalescing bubble - annular } x = 0.00014 (Re_{lo})^{1.47} We_{lo}^{-1.23} \quad (5.2)$$

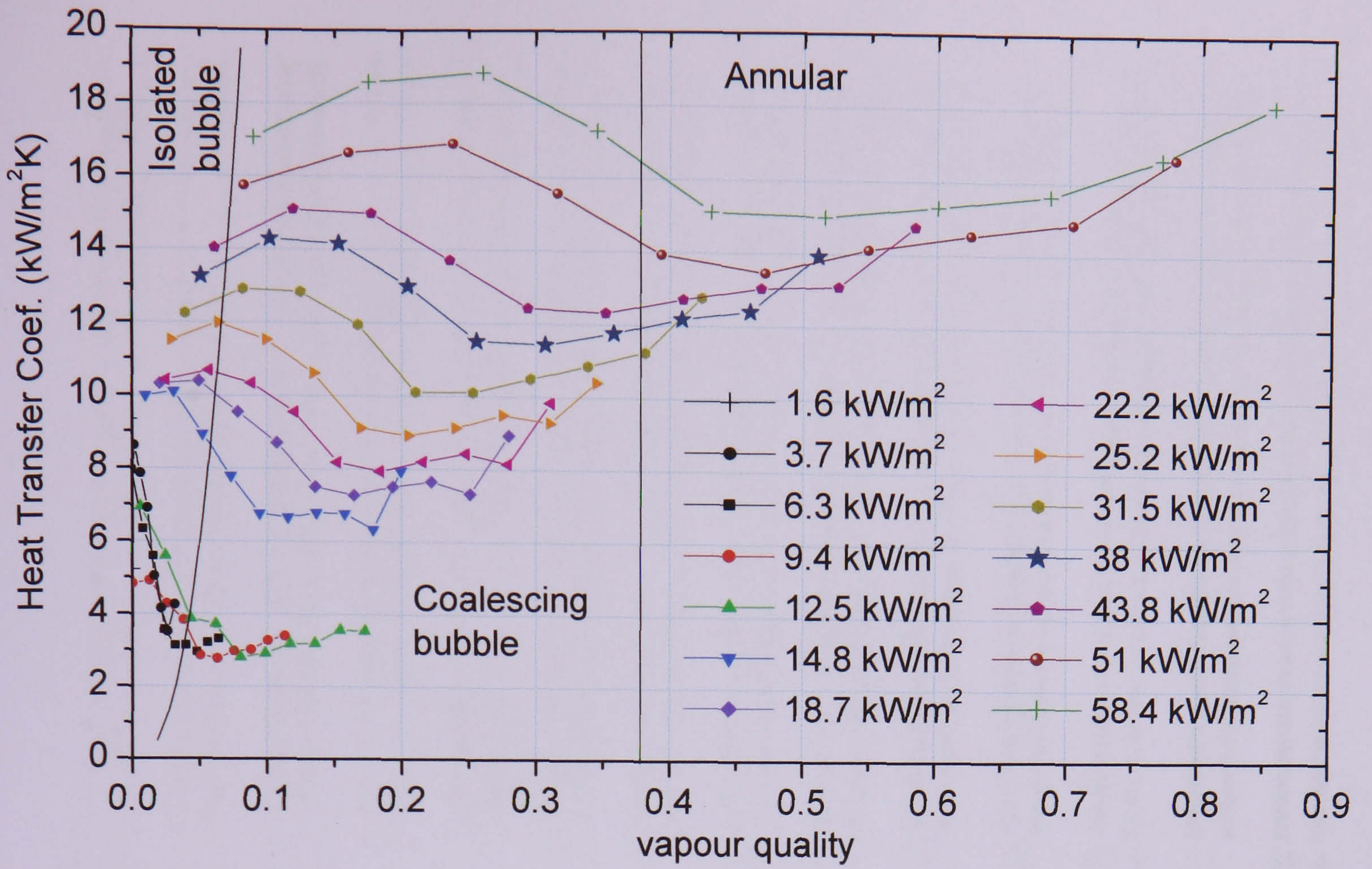
$$\text{Occurrence of dryout } x_{dryout} = \frac{q_{CHF}}{G(\lambda + h_{sub})} \frac{4L}{D} \quad (5.4)$$

$$\text{where, } q_{CHF} = 0.437 \left(\frac{\rho_g}{\rho_l} \right)^{0.073} We_{lo}^{-0.24} \left(\frac{L}{D} \right)^{-0.72} G h_{lg} \quad (5.5)$$

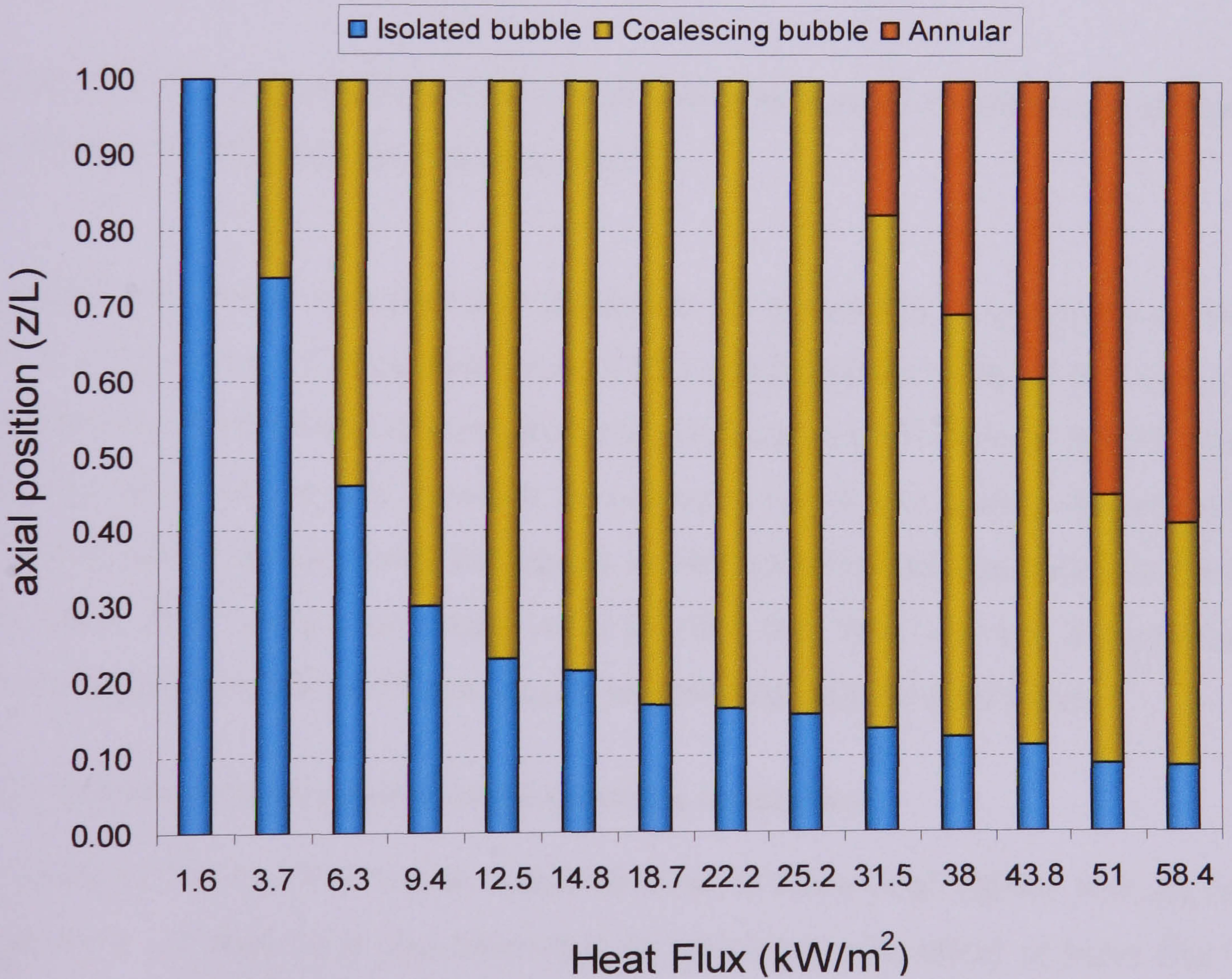
Figure 5.31 presents the local heat transfer coefficient as a function of quality with transition boundaries predicted by the Revellin and Thome correlation shown on the

plot for a mass flux of $300 \text{ kg/m}^2\text{s}$ and pressure of 6 bar. The isolated bubble-coalescing bubble boundary depends on the Boiling number, as a result the transition quality increases with heat flux. For the lowest heat flux group ($q \leq 12.5 \text{ kW/m}^2$), the isolated bubble-coalescing bubble boundary intersects the constant heat flux curves very close to the threshold quality at which a characteristic change in heat transfer coefficient (from fast decreasing to gradual increase with quality) occurs. For groups of heat flux values, $q \geq 14.8 \text{ kW/m}^2$, the isolated-coalescing bubble and coalescing bubble-annular flow boundaries do not exactly match with any of the possible boundaries that separate the different heat transfer dependence on quality, i.e. regions discussed in figure 5.7. The coalescing bubble-annular flow boundary predicted by Revellin and Thome is constant with heat flux, while in the heat transfer results the critical qualities that separate the high quality region (gradually increasing heat transfer coefficient with quality) is highly dependent on heat flux. For the highest heat flux curves ($q > 38 \text{ kW/m}^2$), the gradually increasing heat transfer coefficient region lies in the annular flow regime.

For the sake of completeness, this transition quality lines are also translated into axial distance versus heat flux plot in the same way as the other larger tubes. This is shown in figure 5.31 (b). This plot also indicates what should be expected at the exit of the tube according to the flow map of Revellin and Thome. Since parallel flow visualizations were carried out at the exit of the tube for each heat flux simultaneously with the heat transfer measurements, they can be compared with Figure 5.31 (b). Figure 5.32 shows the flow patterns observed at the exit for each heat flux corresponding to the heat transfer results presented in figure 5.31. At the lowest heat flux of 1.6 kW/m^2 , bubbly flow or isolated bubbles are observed, as also predicted by the correlation. In the current flow visualization results, coalescing of relatively shorter bubbles forming elongated bubbles (shown in Fig. 5.30) commence at a heat flux value of 3.7 kW/m^2 . This is consistent with the Revellin and Thome prediction as shown in Fig. 5.31 (b). If the flow types with liquid ring and highly non-uniform film interface are assumed either transition or coalescing bubble flows then annular flow begins at 31.5 to 38 kW/m^2 , which is again roughly predicted by the correlations. This assumption is taken based on the fact that Revellin and Thome considered churn flow or flow with irregular vapour-liquid interface as a transition to annular flow. Therefore, they categorised the whole flow regimes observed in small tubes into only three main regimes.



(a)



(b)

Figure 5.31 Flow regime transition boundaries using Revellin and Thome (2007) correlation superimposed on heat transfer results at a mass flux of 300 kg/m²s and 6 bar pressure: (a) heat transfer coefficient versus quality, (b) axial distance versus heat flux.

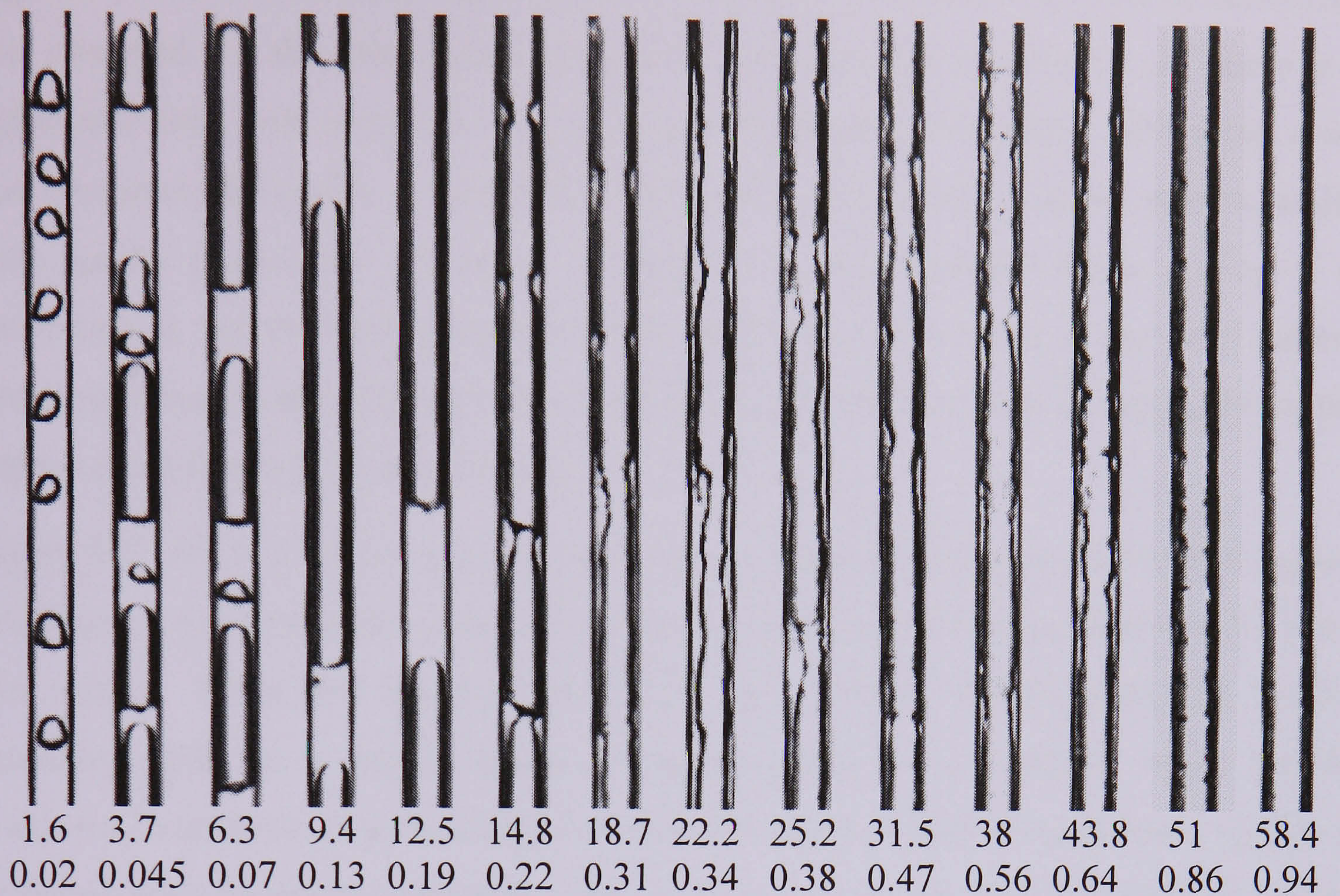


Figure 5.32 flow patterns for a mass flux of $300 \text{ kg/m}^2\text{s}$ and 6 bar pressure at different heat flux in kW/m^2 and exit evaporator quality.

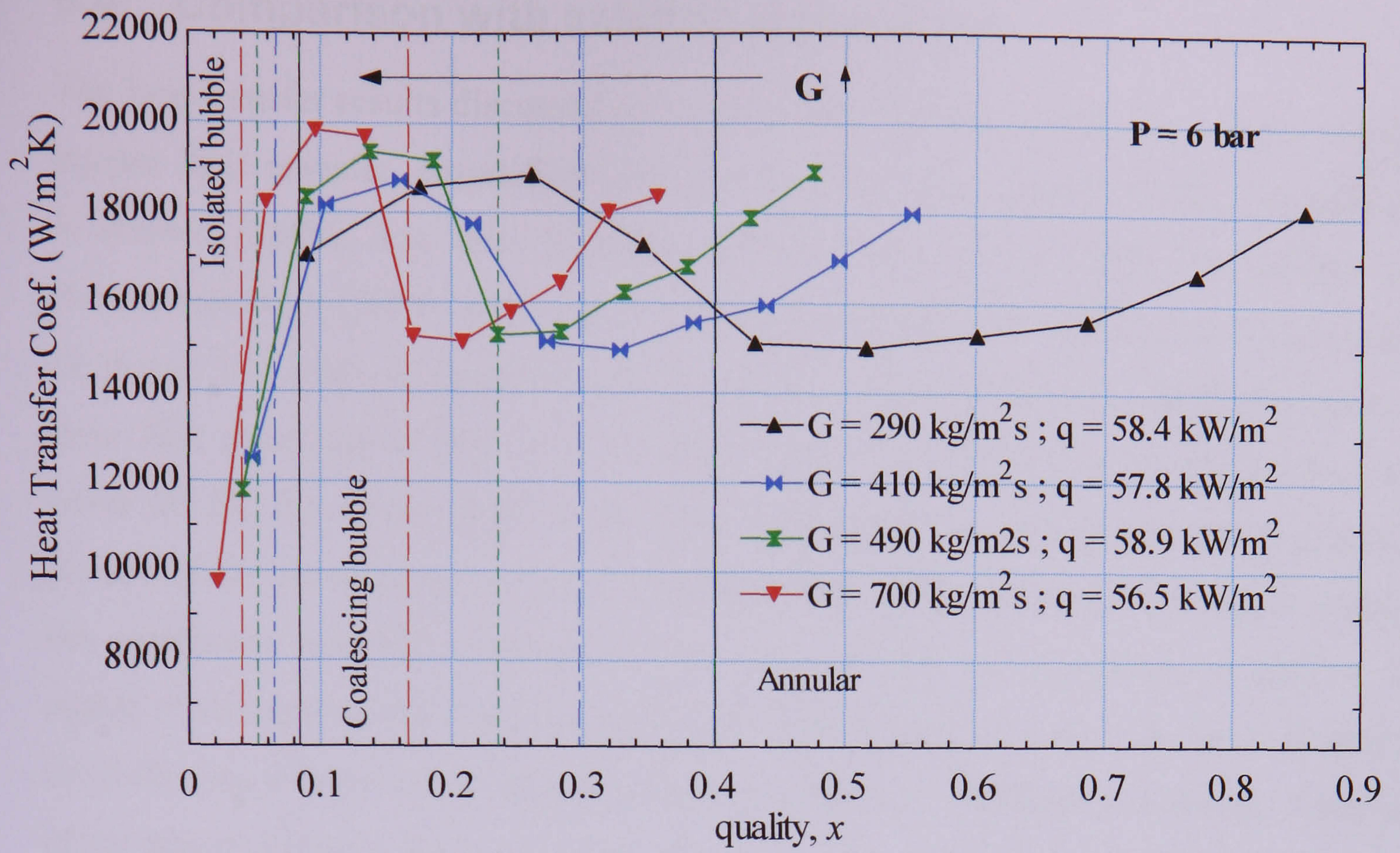
Revellin and Thome also provided correlation for the quality at which dryout occurs (Eq. 5.4) based on a Critical Heat Flux (CHF) relation given in Eq. (5.5). Using these equations for the 0.52 mm tube experimental condition, a CHF value of 285.5 kW/m^2 is obtained for the above case, in which the corresponding dryout quality was greater than 1. This indicates dryout should not happen at these experimental conditions for the 0.52 mm tube. These results also agree with the fact that there was not a continuously decreasing heat transfer coefficient region as observed with the other tubes.

Effect of mass flux and pressure on the transition boundaries

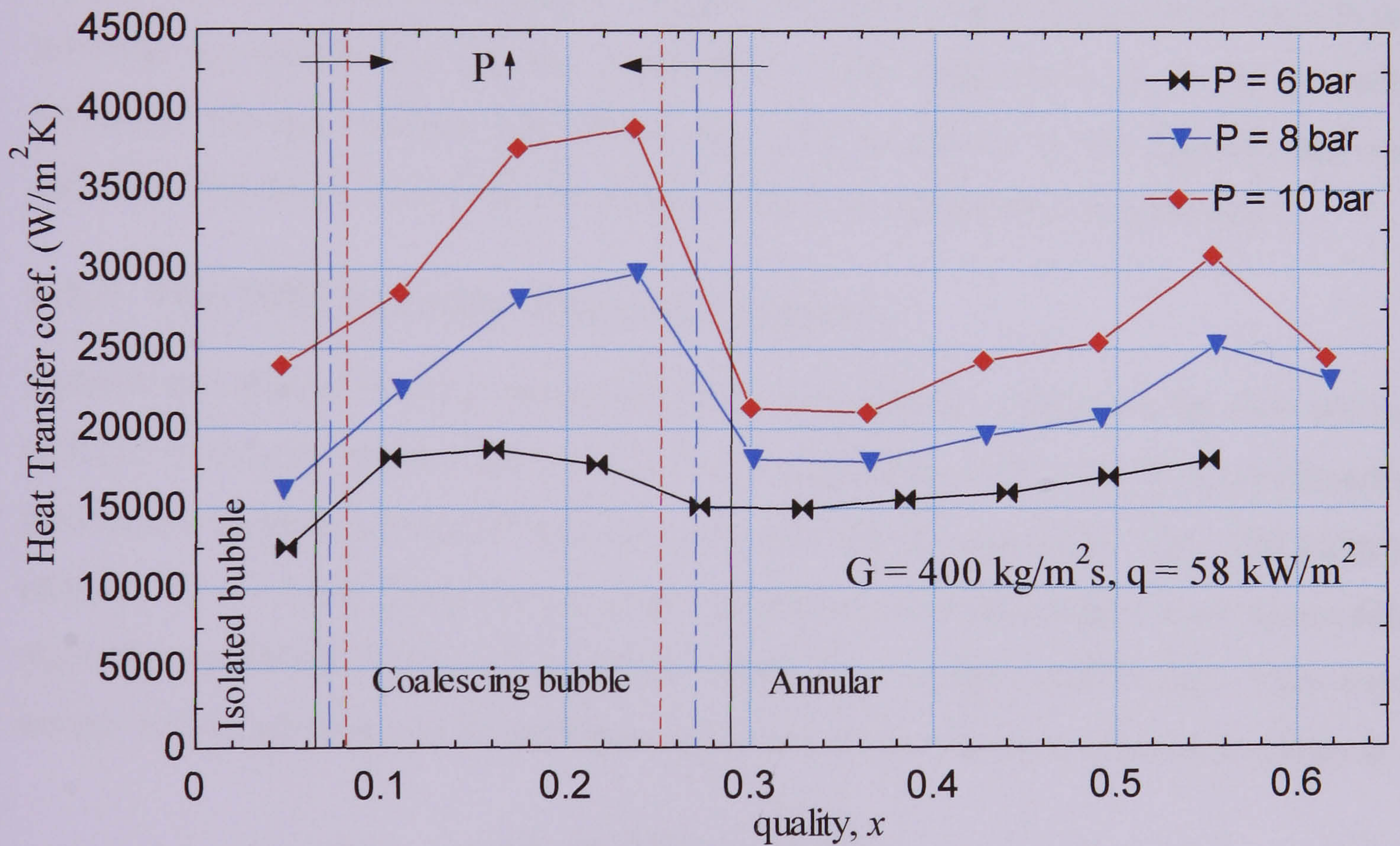
As observed for the flow regime transition maps of Chen et al. (2006) with the tubes larger than 1.1 mm, it is also interesting to investigate the effect of mass flux and pressure on the superimposed transition boundary lines of Revellin and Thome (2007). The results are presented in Figure 5.33. As shown in Fig. 5.33 (a) both boundaries, isolated-coalescing bubble and coalescing bubble-annular moved towards lower quality when the mass flux increases. The transition qualities for both boundaries showed a

negative power-law relation with mass flux. As discussed previously, similar behaviour was observed for the other tubes using flow regime maps of Chen et al. There is a significant shift with mass flux for the coalescing/annular boundary. When the mass flux increases, the quality at which the heat transfer coefficient increases monotonically with quality (region IV according to figure 5.7) shifts towards lower quality. It is interesting to see the coalescing/annular boundary line also shifts in the same pattern and almost exactly matches with this threshold quality (end of zone II) especially for the highest mass fluxes (490 and 700 kg/m²s).

Figure 5.33 (b) is a similar plot but showing the effect of pressure on the flow regime boundaries. As seen in the figure, the effect is not as significant as observed for mass flux effect. When the pressure increases, the isolated bubble/coalescing bubble boundary shifts to a higher quality. However, there is an opposite effect for the coalescing bubble/annular boundary, i.e. almost a uniform shift towards lower quality is observed with increasing pressure. This is also in contrary with the relatively larger tubes using the flow regime transition map of Chen et al. (2006). The agreement between the critical quality at which heat transfer coefficient increases with quality and the coalescing bubble/annular boundary becomes better when the pressure decreases. A relatively best match is obtained for the lowest pressure of 6 bar.



(a)



(b)

Figure 5.33 Transition boundaries using correlation of Revellin and Thome (2007) superimposed on the plot showing influence of: (a) mass flux at $P = 6$ bar, (b) pressure at $G = 400$ kg/m²s, both for a nominal heat flux of 58 kW/m².

5.4 Comparison with existing correlations

The heat transfer results discussed above were also compared with some of the existing known heat transfer correlations such as Lazarek and Black (1982), Gungor and Winterton (1986), Liu and Winterton (1994), Tran et al. (1996), Kandlikar and Balasubramanian (2004), Zhang et al. (2004) and Saitoh et al. (2007). For the two tubes (4.26 and 2.01 mm), comparison with the all the above correlations, except the last two, were first presented in Huo et al. (2007). Again, the comparison in this section will cover all the five tubes (4.26, 2.88, 2.01, 1.10 and 0.52 mm) to provide a complete picture of the performance of these correlations for different tubes, and help to identify the correlation that have considered tube size effects. The experimental data in the region of decreasing heat transfer coefficient with increasing quality are not included in the following comparisons. This is because the region is attributed to dryout, while all of the above correlations, except the last one by Saitoh et al.(2007), did not consider dryout and post dryout heat transfer. This section presents global comparison results and relevant discussions for all the correlations mentioned above at 8 bar pressure. However, for the smallest tube (0.52 mm), the results for 6 bar pressure are also included. The detail form of the correlation equations is included in Appendix C.

5.4.1 The 1982 Lazarek- Black correlation

Lazarek and Black (1982) measured the local heat transfer coefficient for flow boiling of R113 in a round vertical tube with an internal diameter of 3.1 mm. The experimental parameters covered a range of heat flux 14 - 380 kW/m², mass flux 125 - 750 kg/m²s, pressure 1.3 - 4.1 bar. They correlated the experimental results using a least square data algorithm to fit the 728 local saturated boiling heat transfer coefficients. They tried several functional forms to fit their data and proposed an empirical correlation given as:

$$Nu_{tp} = 30 Re_{lo}^{0.857} Bo^{0.714} \quad (5.6)$$

As can be seen from the equation, a slight effect of mass flux is considered due to the introduction of Re number in the correlation ($G^{0.143}$). The present experimental results for the different tubes are compared with the Lazarek–Black correlation in Figure 5.34. As seen in the figure 5.34 (a), the correlation under-predicts the larger diameter result consistently by about 30 %. In Figure 5.34 (b) for the 2.88 mm tube, the prediction is better especially for the higher heat transfer coefficient values. This could be due to the

fact that the correlation was developed based on data from 3.1 mm diameter tube, which is close to 2.88 mm tube. The correlation under-predicts the experimental results for 2.01 and 1.1 mm tubes, Figures 5.34 (c) and (d), especially for the lower heat transfer coefficients by more than 30%. However, for the 1.1 mm tube, the prediction gets better near high heat transfer coefficient values. The reason could be that the predicted coefficient increases with heat flux consistently while the experimental heat transfer coefficient becomes independent of heat flux at high heat flux values. As seen in figure 5.34 (e), there is a significant scatter in the comparison with the data for the 0.52 mm tube and the values are mostly under-predicted, especially for the larger heat transfer coefficient values. This suggests that there is a systematic difference with these experimental results. For instance, unlike the experimental data, the correlation assumes heat transfer coefficient is constant with vapour quality. The prediction is relatively better at low pressure for the smallest diameter tube.

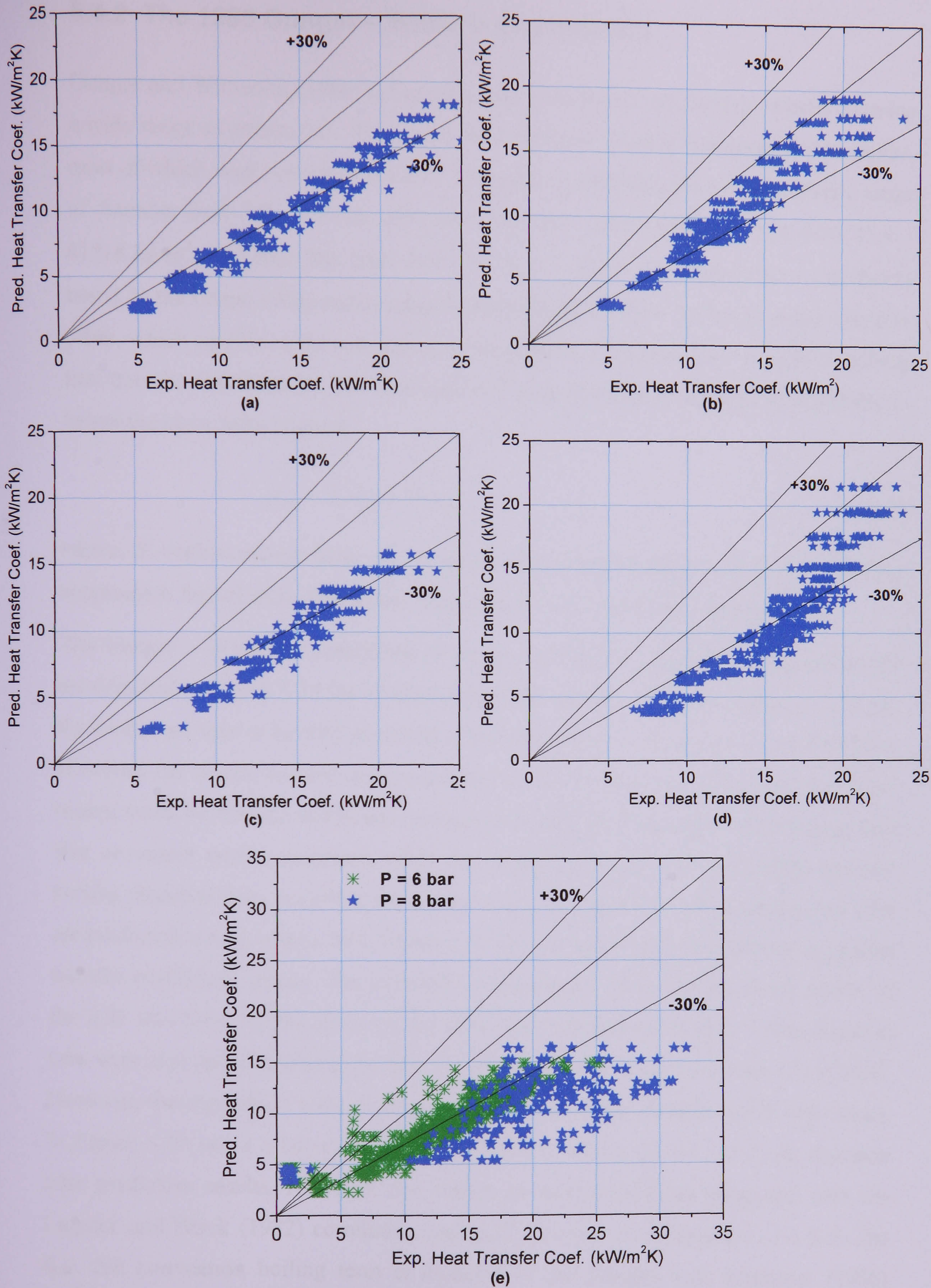


Figure 5.34 Comparison with Lazarek and Black (1982) correlation for tubes of diameter: (a) 4.26 mm, (b) 2.88 mm, (c) 2.01 mm, (d) 1.10 mm and (e) 0.52 mm.

5.4.2 The 1986 Gungor – Winterton correlation

Gungor and Winterton (1986) collected a huge data bank from various sources covering a wide range of parameters. They used 3693 saturated boiling heat transfer data points, most of which were for water and R11. The collected experimental results cover a range of diameter from 3.0 – 32 mm; pressure from 0.08 – 202.6 bar; mass flux from 12.4 – 61518 kg/m²s and heat flux from 350 – 9.1 × 10⁷ W/m². They proposed a correlation based on the Chen (1966) method that was developed for flow boiling in larger diameter tubes, which employed the concept of superposition of nucleate and convective boiling heat transfer contributions. The detail form of the correlation is included in Appendix C, below the basic form is given:

$$\alpha_{tp} = E_c \alpha_{sp} + S_c \alpha_{pool} \quad (5.7)$$

where, E_c (enhancement factor to the single phase heat transfer) and S_c (pool boiling suppression factor) were determined using iteration to match the large data bank.

The Gungor – Winterton correlation is compared with the present data and the results are depicted in Figure 5.35 for all diameters at the pressure of 8 bar. In Figure 5.34 (a), the results are seen to be well predicted at low heat transfer coefficient (<~10 kW/m²K). However, the results become under-predicted as heat transfer coefficient increases. One reason could be that the additional convective boiling term becomes significant as heat flux or vapour quality increases, while the experimental data showed mostly nucleate boiling characteristics excluding the dryout zone. The results of 2.88 mm diameter tube are predicted mostly within 30%, Figure 5.35 (b), but again under-predicted at high heat transfer coefficient values. The correlation consistently under-predicted the results of the 2.01 mm tube, within 30 %. In the same way, the results of the 1.1 mm diameter tube were also under-predicted for heat transfer coefficient values less than 15 kW/m²K. However, the correlation tends to over-predict the large heat transfer coefficient values. In Figure 5.35 (e), a relatively significant scatter is shown for the 0.52 mm diameter tube prediction results. However, the values are better predicted compared with the Lazarek and Black (1982) correlation, especially for the lower pressure of 6 bar. The fact that convection boiling term is included in the Gungor and Winterton (1986) correlation could be the reason for this, bearing in mind that the experimental results for the smallest tube showed dependence on vapour quality.

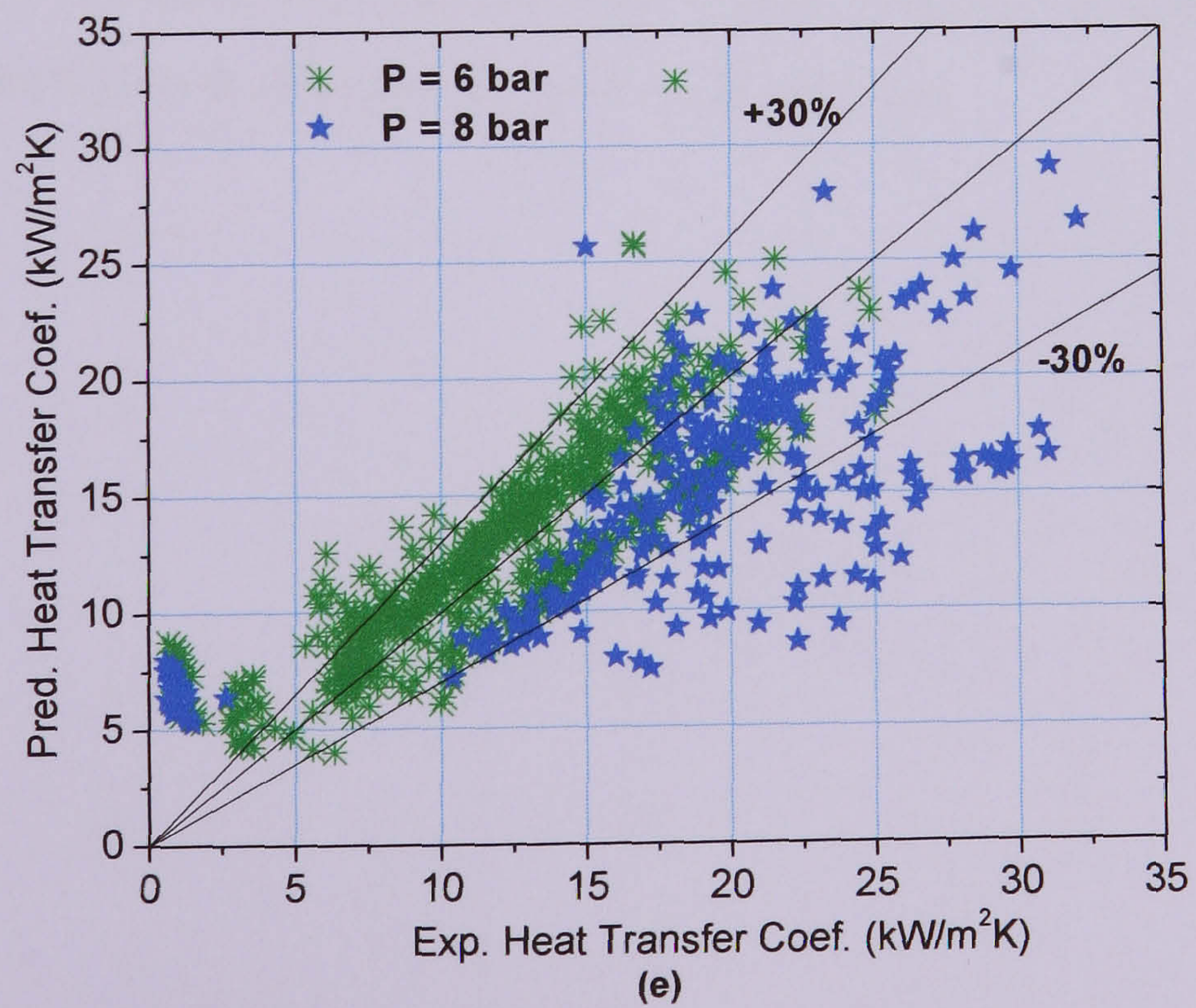
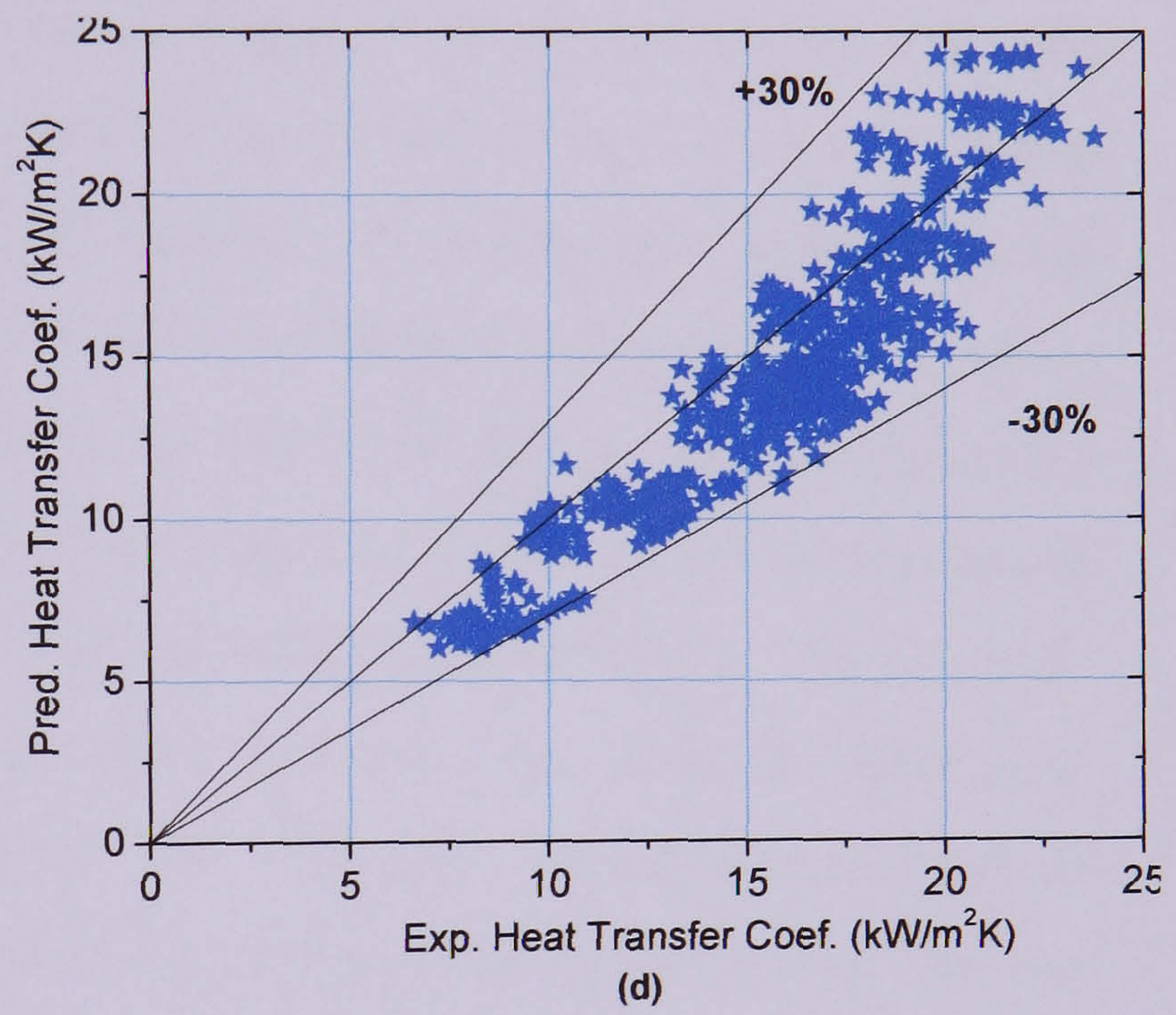
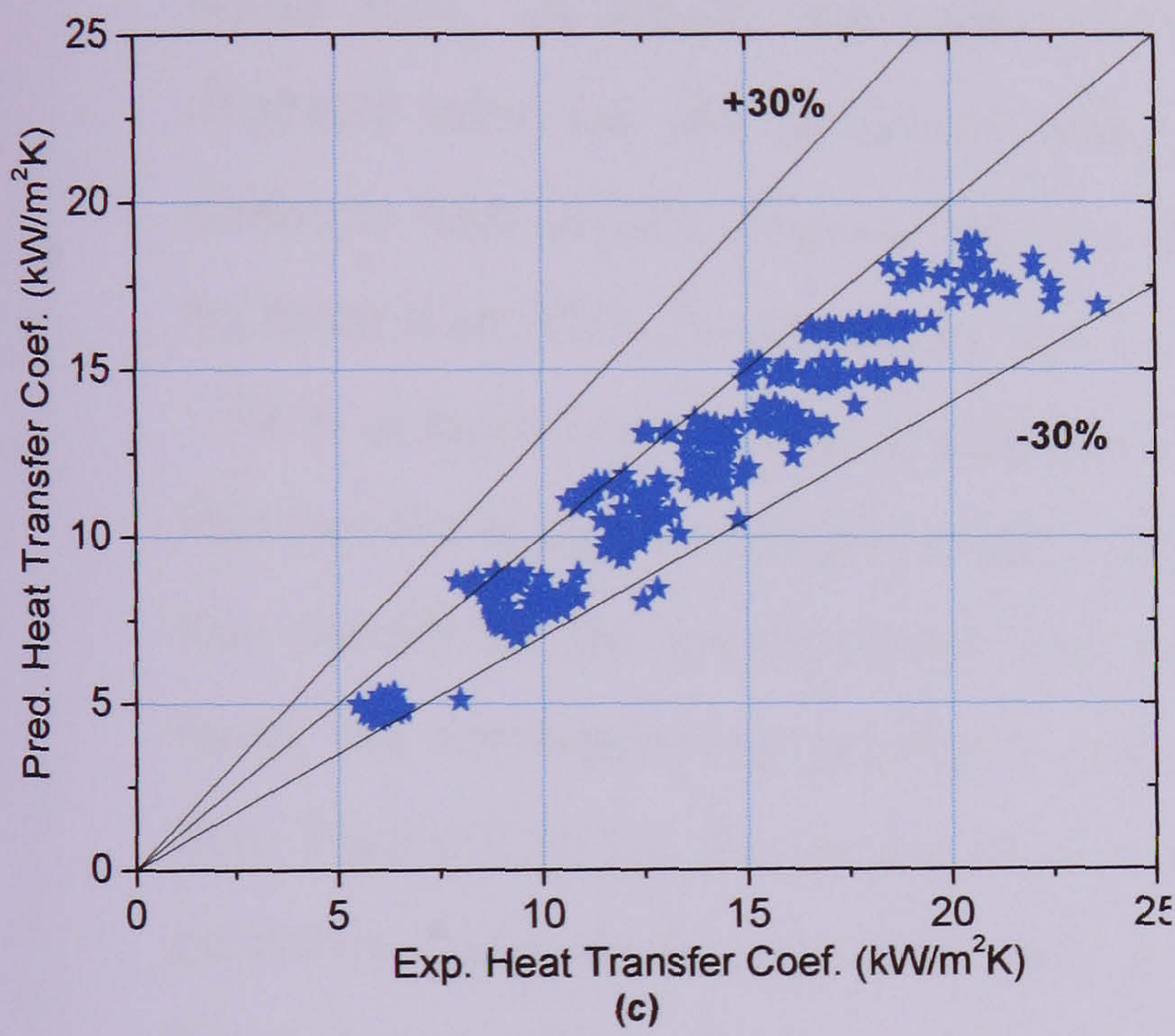
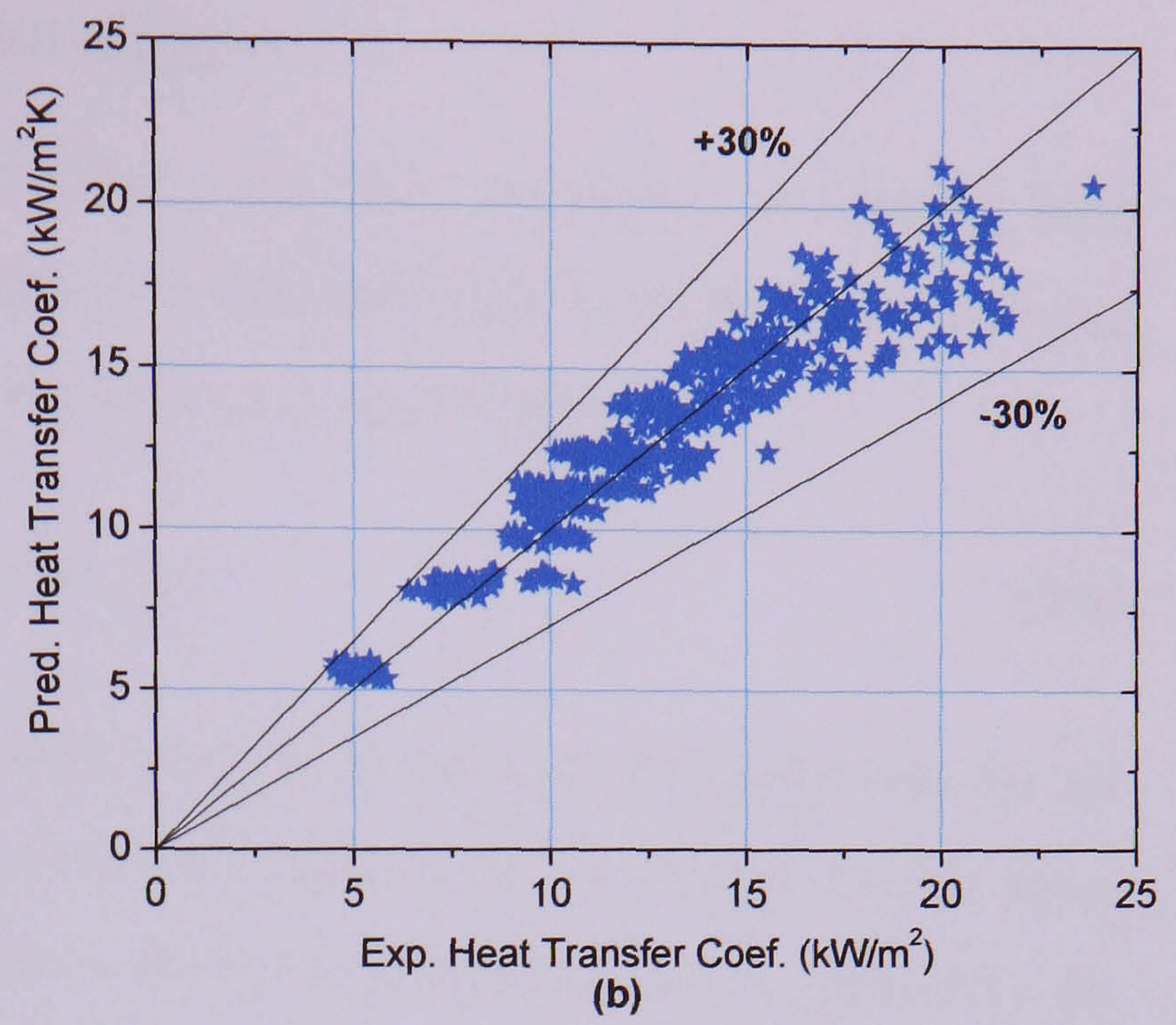
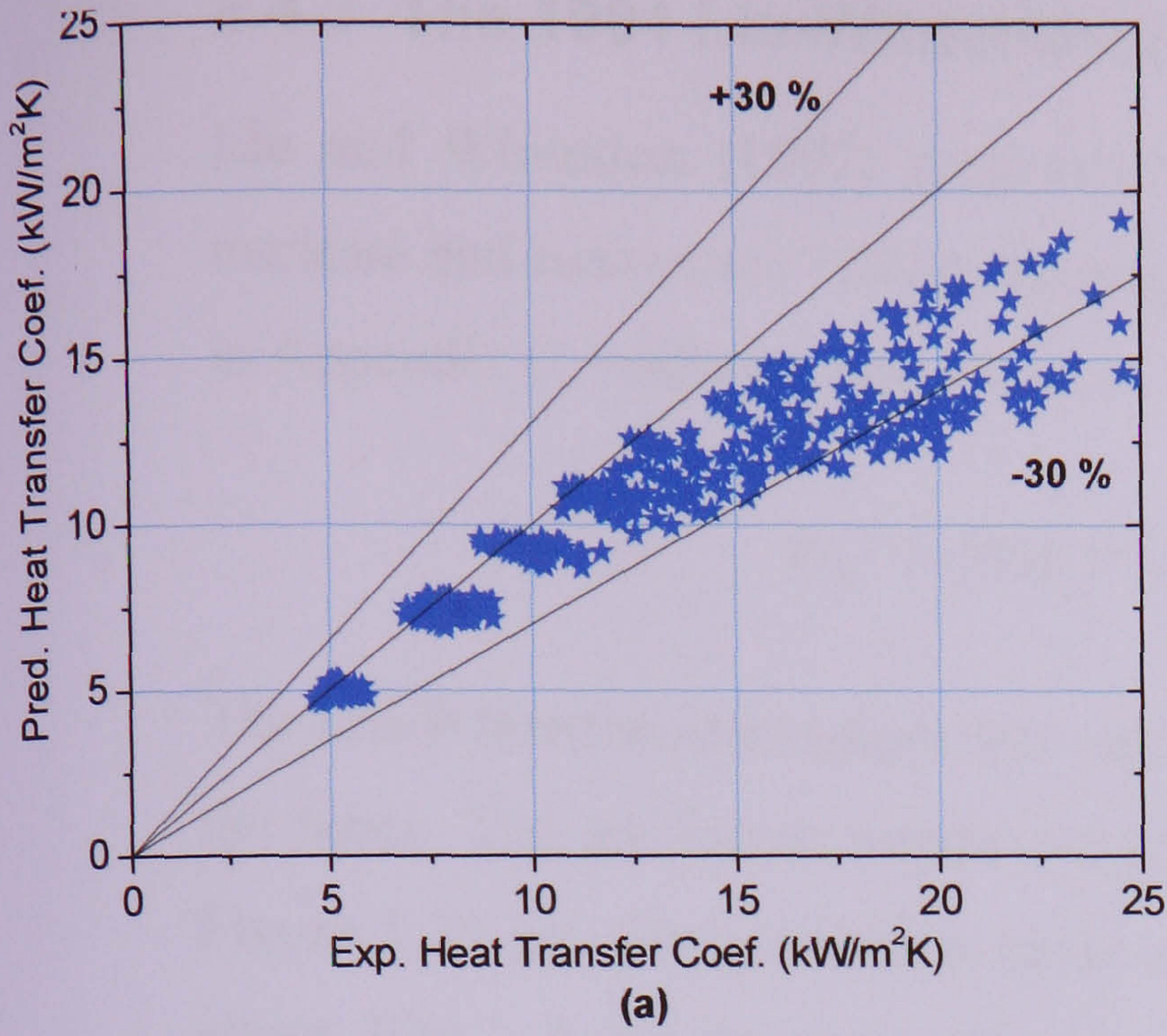


Figure 5.35 Comparison with Gungor and Winterton (1986) correlation for tubes of diameter: (a) 4.26 mm, (b) 2.88 mm, (c) 2.01 mm, (d) 1.1 mm and (e) 0.52 mm.

5.4.3 The 1991 Liu-Winterton correlation

Liu and Winterton (1991) proposed an asymptotic type correlation combining both nucleate and convective boiling components. The details of their correlation are included in Appendix C, while the basic form of the equation is given below.

$$\alpha_{tp}^2 = (E\alpha_l)^2 + (S\alpha_{pool})^2 \quad (5.8)$$

The Liu-Winterton correlation was compared with the present experimental data for all the tubes. The prediction results are presented in Figure 5.36. For the 4.26 mm tube, Figure 5.36 (a), the correlation under-estimates the experimental data consistently by about 30%. A similar but relatively better prediction is observed for the 2.88 mm diameter tube, i.e. the data were under-predicted up to 30%. The 2.01 and 1.10 mm diameter tube results, Figure 5.36 (c) and (d) respectively, were again under-predicted by more than 30%. However, for the 1.1 mm tube, the data tends to be predicted within - 30 % at large heat transfer coefficient values. As explained above, this is related to the fact that the high heat transfer coefficient data correspond to high heat flux values and at this conditions the experimental data become independent of heat flux. On the other hand, the corresponding predicted value increases with heat flux even at higher heat flux. Figure 5.36 (e), for the smallest diameter tube (0.52 mm), the experimental data is generally under-predicted within 30% for the 6 bar pressure and by more than 30% for the 8 bar pressure. Besides, the data for the higher pressure is scattered while a consistent under prediction is obtained for the lowest pressure.

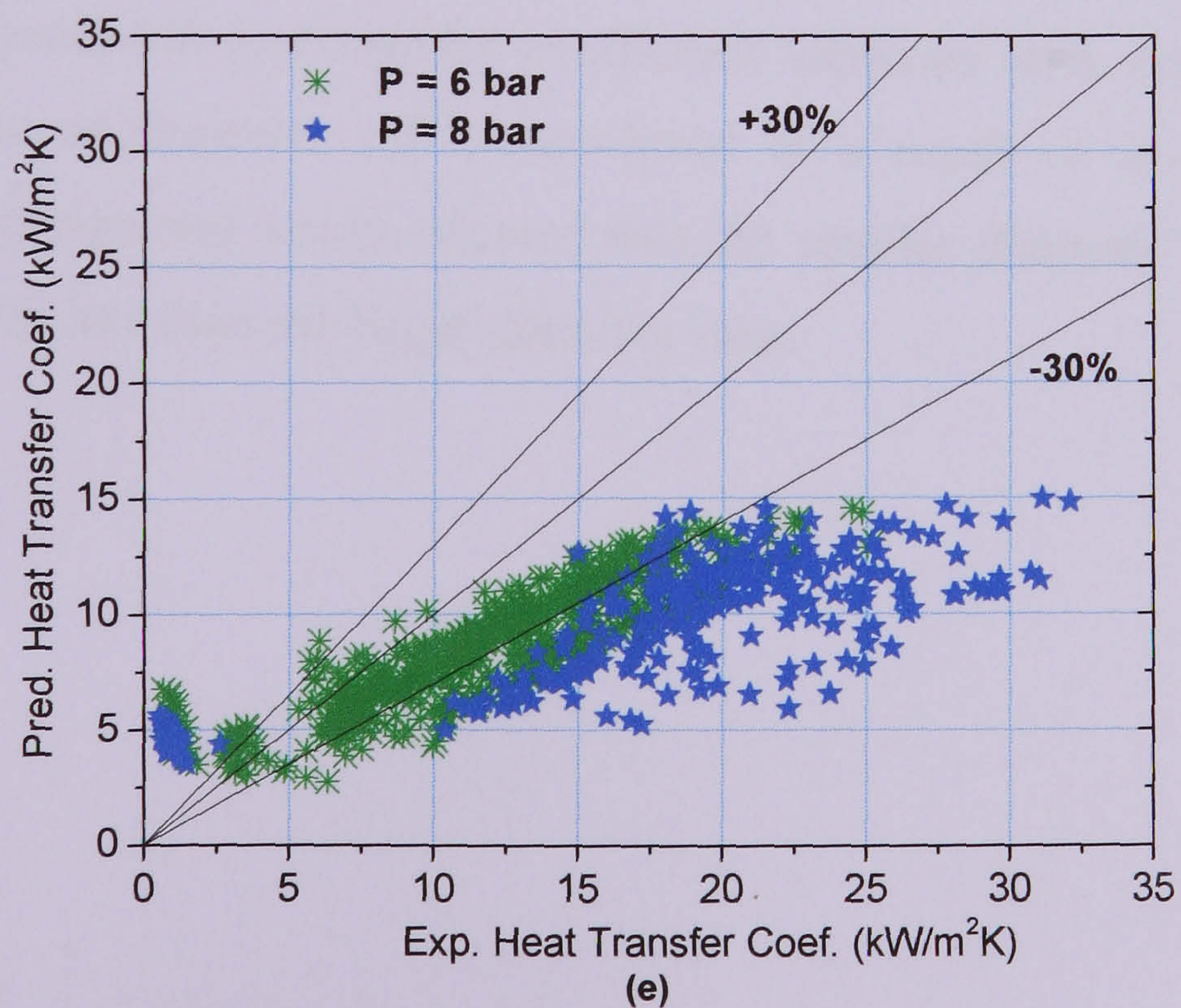
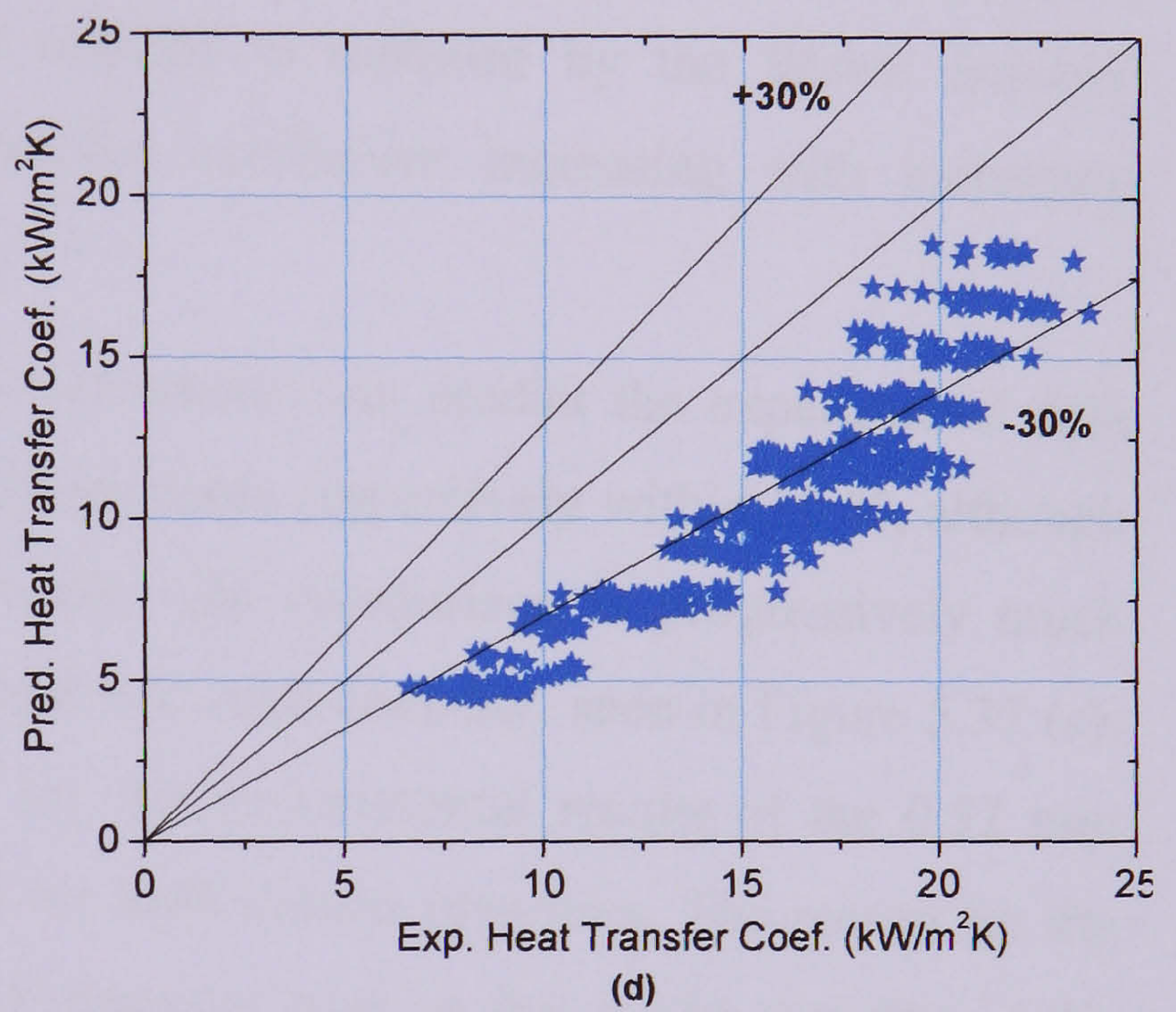
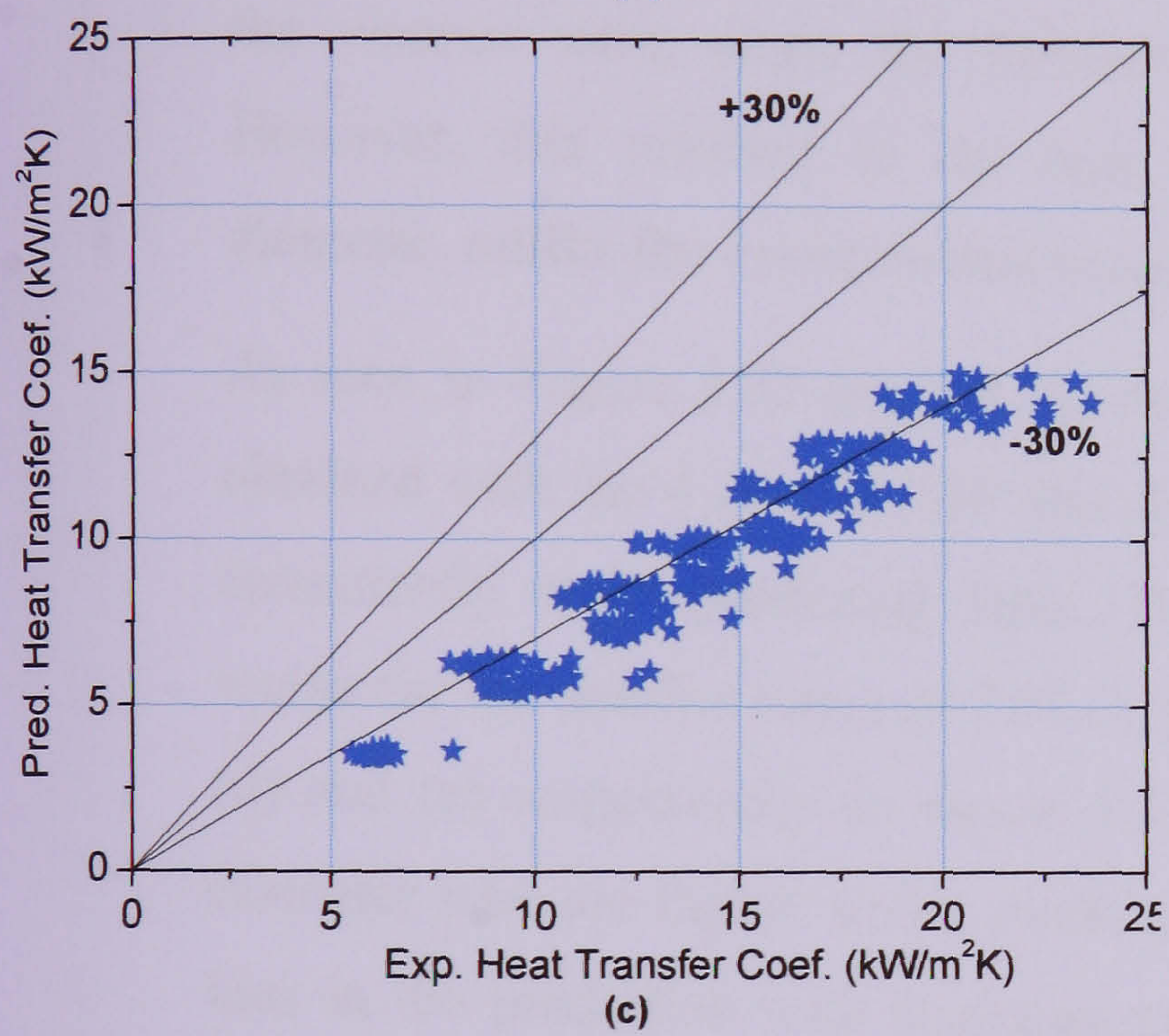
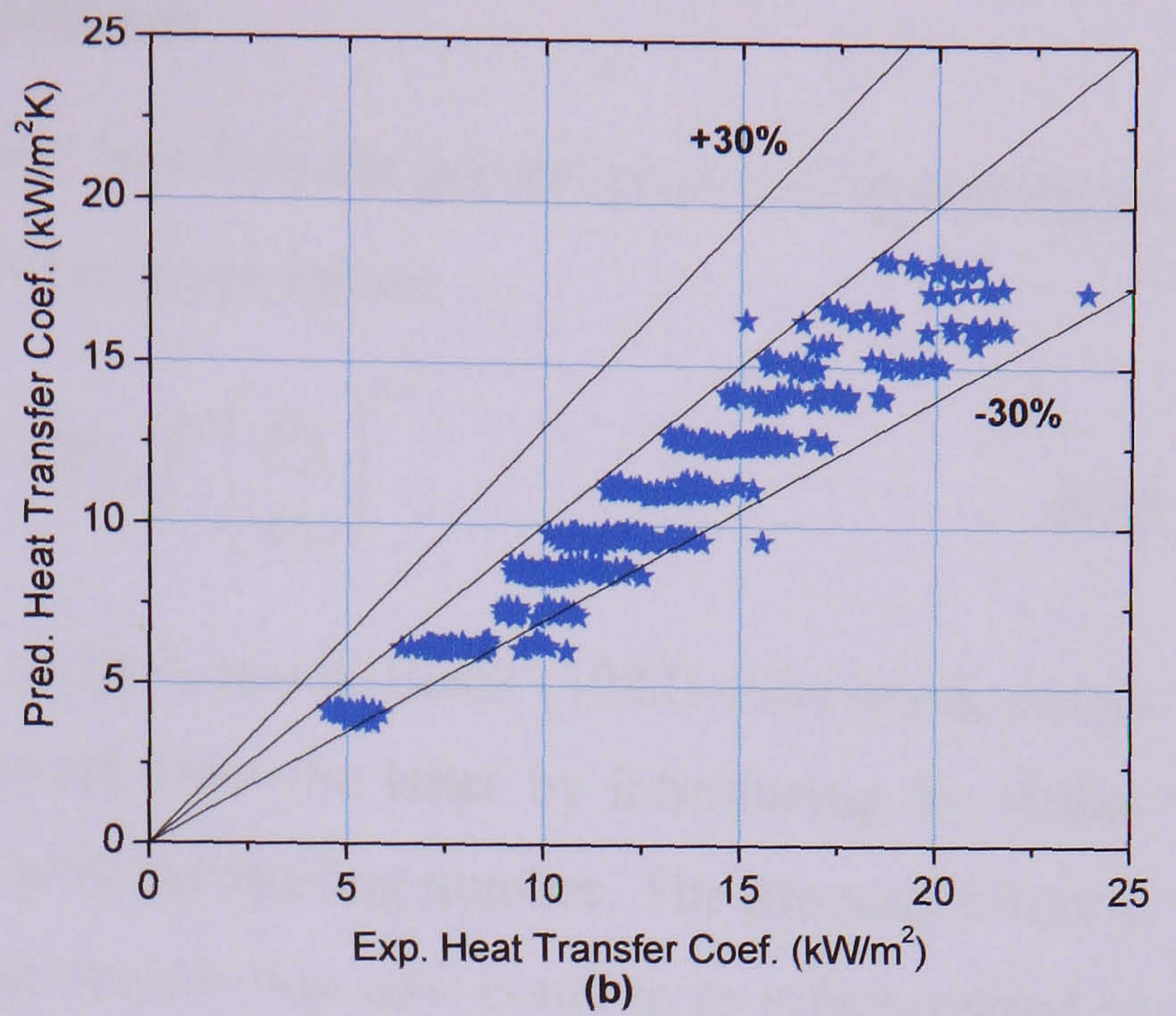
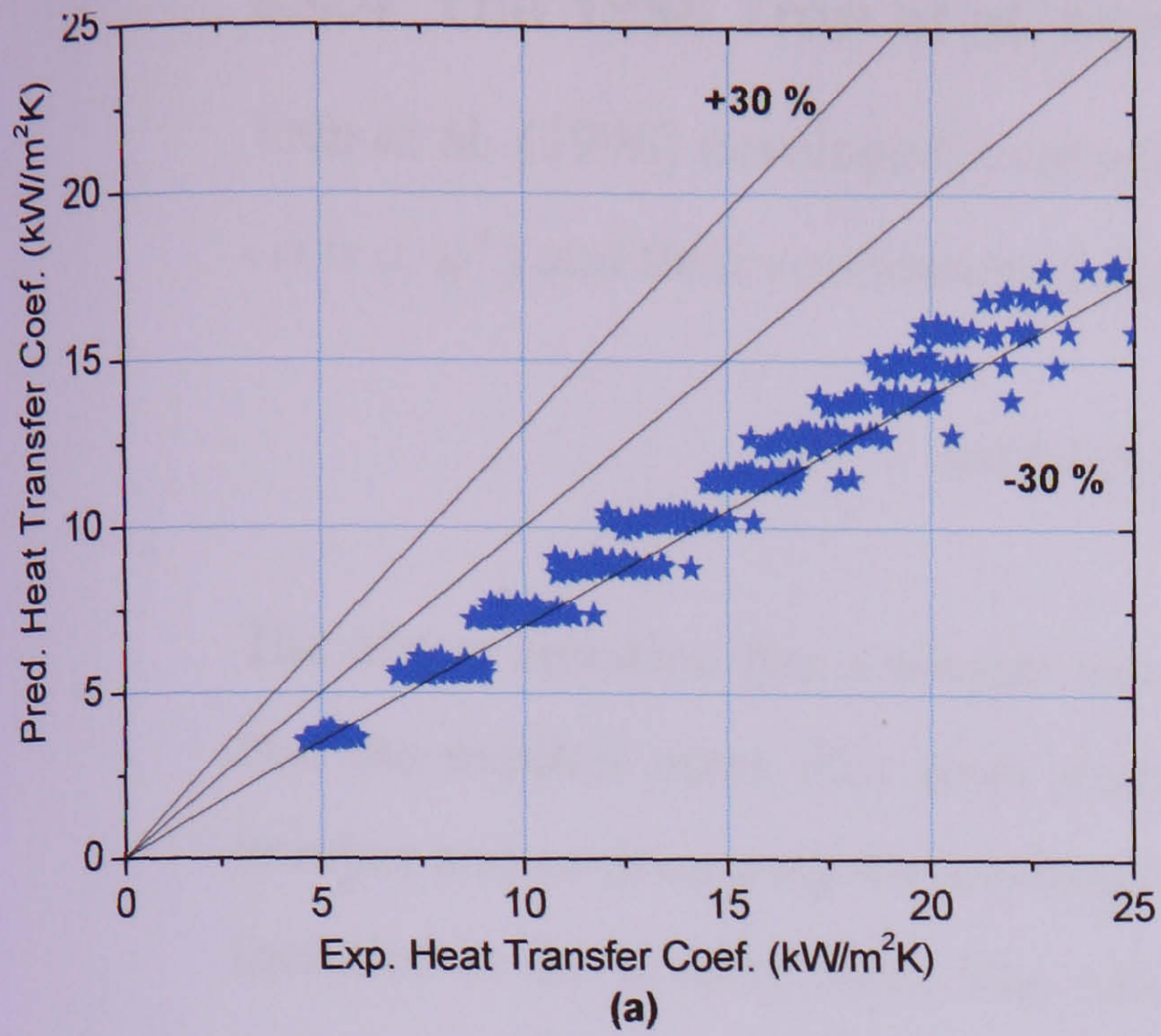


Figure 5.36 Comparison with Liu and Winterton (1994) correlation for tubes of diameter: (a) 4.26 mm, (b) 2.88 mm, (c) 2.01 mm, (d) 1.1 mm and (e) 0.52 mm.

5.4.4 The 1996 Tran et al. correlation

Tran et al. (1996) developed a correlation based on the general pool boiling correlation ($\alpha = c \cdot q^n$) and their experimental results as given below.

$$\alpha_{tp} = 840000 (Bo^2 We_l)^{0.3} \left(\frac{\rho_l}{\rho_v} \right)^{0.4} \quad (5.9)$$

The above equation has a similar form to the Lazarek-Black (1982) correlation, except that the explicit mass flux term is removed from the latter by introducing the Weber number and re-arranging the exponents with the Boiling number. The property effect is included in the density ratio. The surface tension has now come in to effect instead of the viscous term, since the Reynolds number is replaced by the Weber number. However, this resulted in the heat transfer coefficient increasing with increasing diameter, unlike the experimental results.

As seen in Figure 5.37 (a) and (b) the correlations can predict the experimental data obtained with the 4.26 and 2.88 mm diameter tubes respectively within 30 %, although consistently under-predicting these. However, the comparison is progressively much worse for the smaller tubes of 2.01, 1.1 and 0.52 mm diameter, seen in Figure 5.37 (c), (d) and (e) respectively. In figure 5.37 (e), the experimental results of the 0.52 mm diameter tube are highly under predicted for both system pressures. The reason for the bias in the prediction with changing tube diameter may be due to the fact that in the correlation, the predicted heat transfer coefficient increases with diameter due to the positive exponent of diameter ($D^{0.3}$) introduced as a result of the Weber number. However, the experimental results showed that the smaller diameter tube has a better heat transfer coefficient than the larger diameter tube.

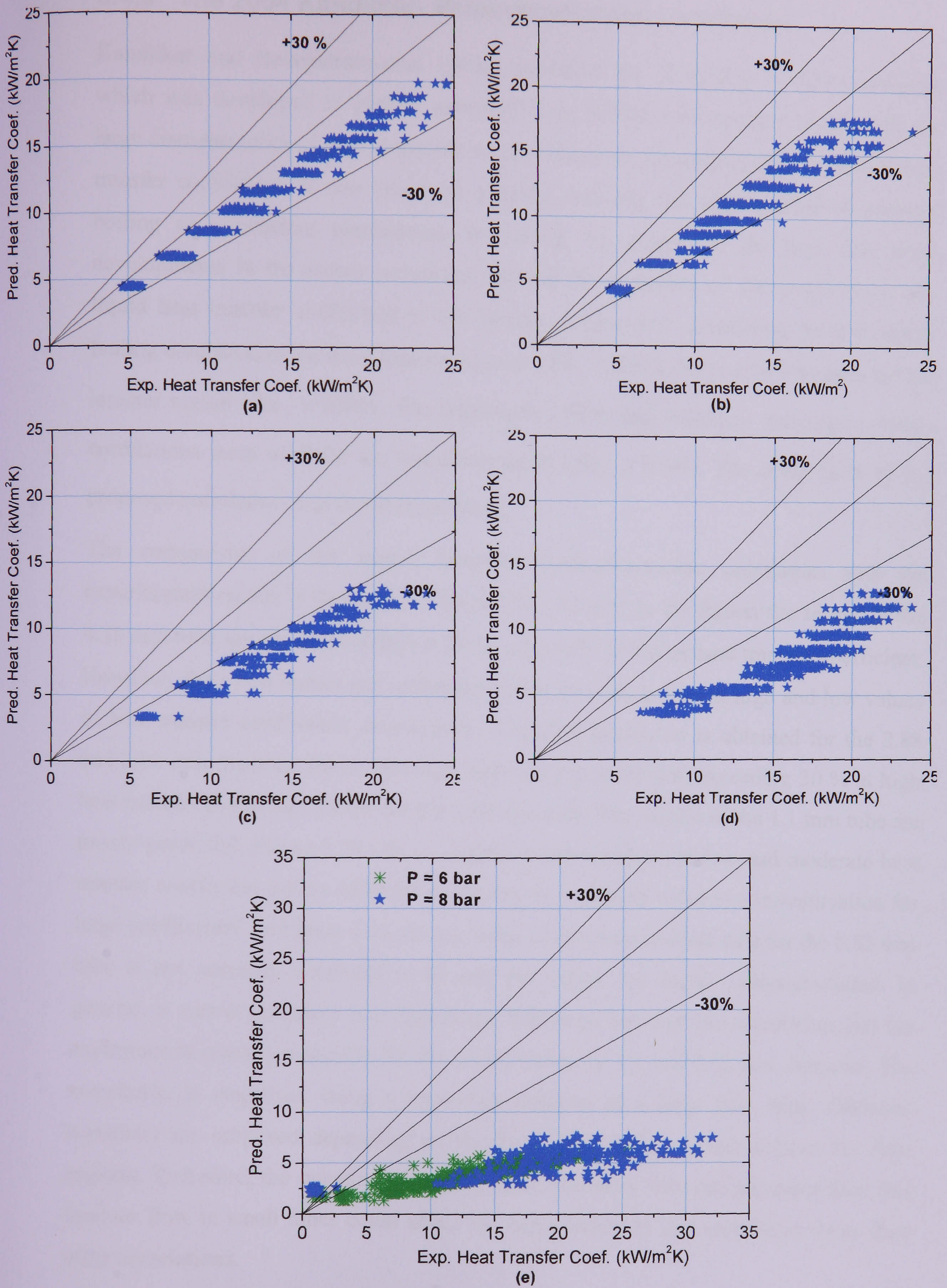


Figure 5.37 Comparison with the Tran (1996) correlation for tubes of diameter: (a) 4.26 mm, (b) 2.88 mm, (c) 2.01 mm, (d) 1.1 mm and (e) 0.52 mm.

5.4.5 The 2004 Kandlikar- Balasubramanian correlation

Kandlikar and Balasubramanian (2004) modified the Kandlikar (1990) correlation which was developed to predict saturated flow boiling heat transfer coefficients for large diameter tubes of high Reynolds number based on the single-phase, all-liquid, heat transfer coefficient. It was based on a model utilizing the contributions of nucleate boiling or convective mechanisms by taking the greater of the two. The main developments in the recent correlation include the extension of the single phase all-liquid heat transfer coefficient to the laminar region and considering no convective boiling contribution for deep laminar regions ($Re_{lo} \leq 100$). $Nu = 4.36$ was used for the laminar region ($Re_{lo} < 1600$). The Gnielenski (1976) and Petukhov and Popov (1963) correlations were used for the turbulent region ($Re_{lo} \geq 3000$). The detail form of the proposed correlation is given in Appendix C.

The comparison of the recent Kandlikar–Balasubramanian correlation with the experimental results is depicted in Figure 5.38. As seen in the figure, the results of the 4.26 mm tube are predicted within $\pm 30\%$, especially at higher heat transfer coefficient. However, there is a scatter and under-prediction exceeding 30% at high and low values of heat transfer coefficient, respectively. A similar prediction is obtained for the 2.88 and 2.01 mm diameter tubes; although there is over-prediction exceeding 30% at high heat transfer coefficient values for the 2.88 mm tube. The results of the 1.1 mm tube are poorly predicted, Figure 5.38 (d), i.e. highly under-predicted at low and moderate heat transfer coefficient values followed by a jump in predicted value to over-estimation for large coefficients. In Figure 5.38 (e), the trend of the experimental data for the 0.52 mm tube is not correctly predicted at all and the values are highly under-predicted. In general, it seems that there is a significant difference between the correlation and the experimental results, especially for the smaller tubes of 1.1 and 0.52 mm diameter. The correlation is empirical, using a regression analysis of a large data bank. Different equations are proposed depending on the Reynolds number, which defines the flow regions. Therefore, the question of the uncertain boundary between turbulent flow and laminar flow in small tubes could affect the applicability of this correlation more than other correlations.

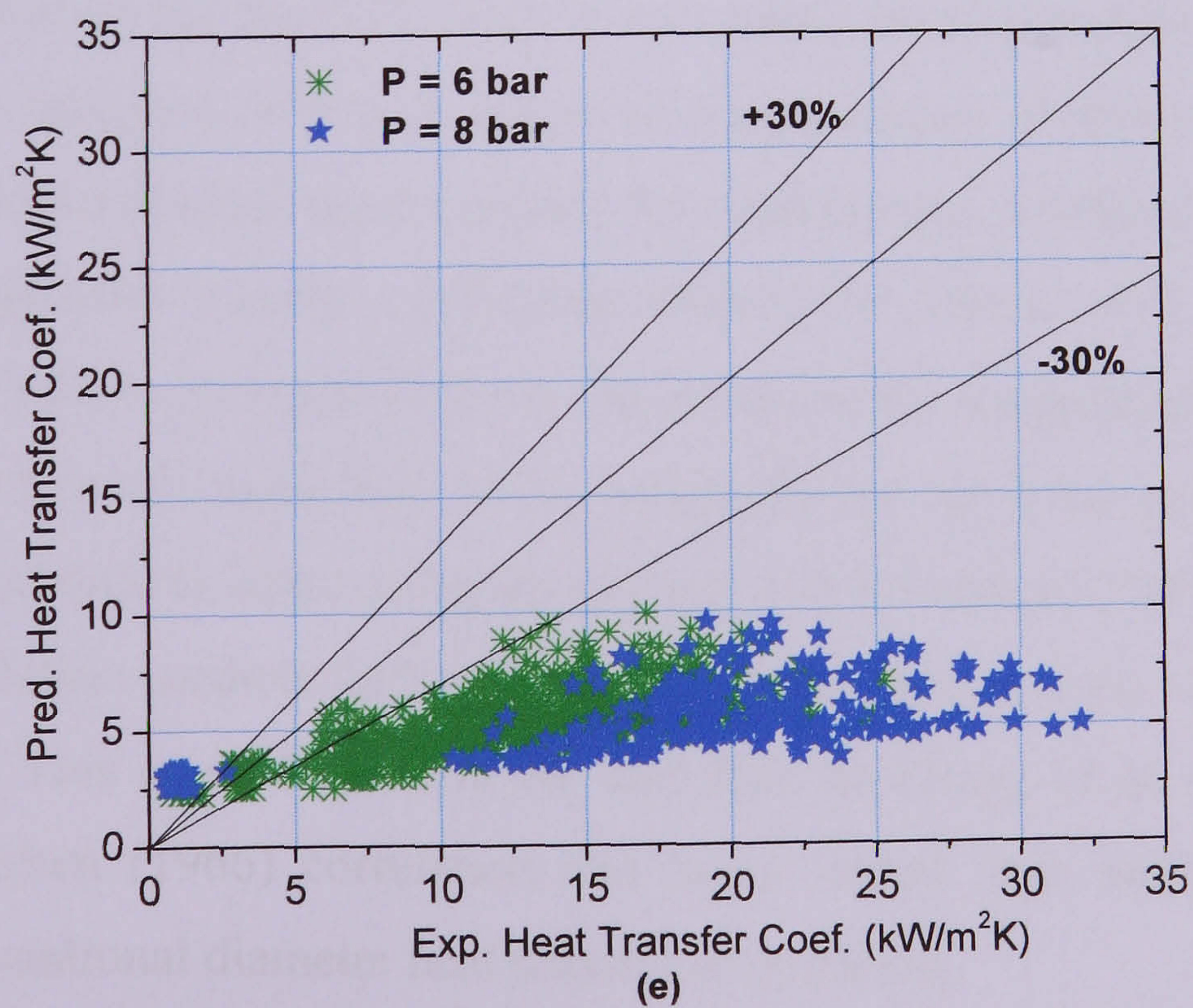
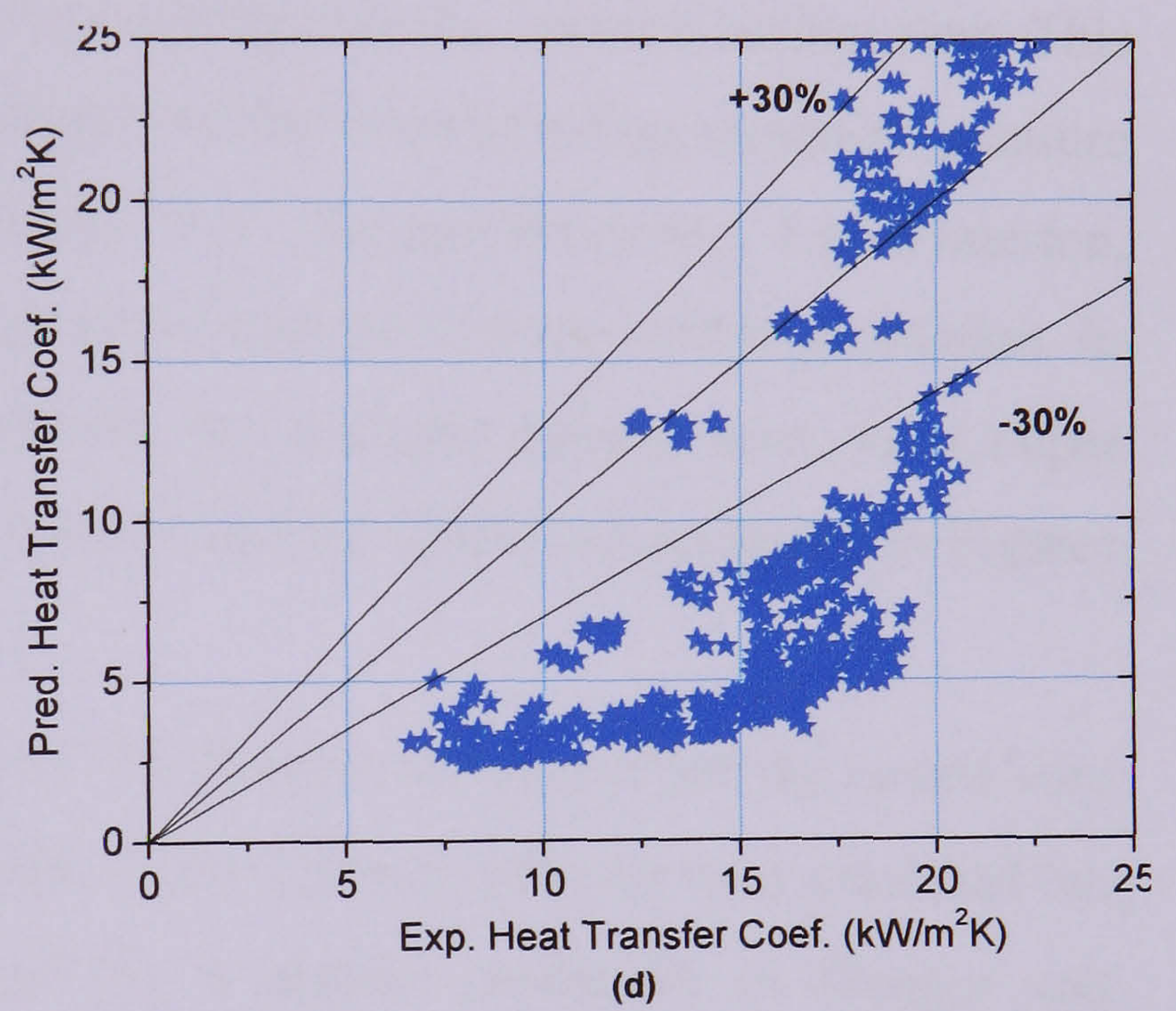
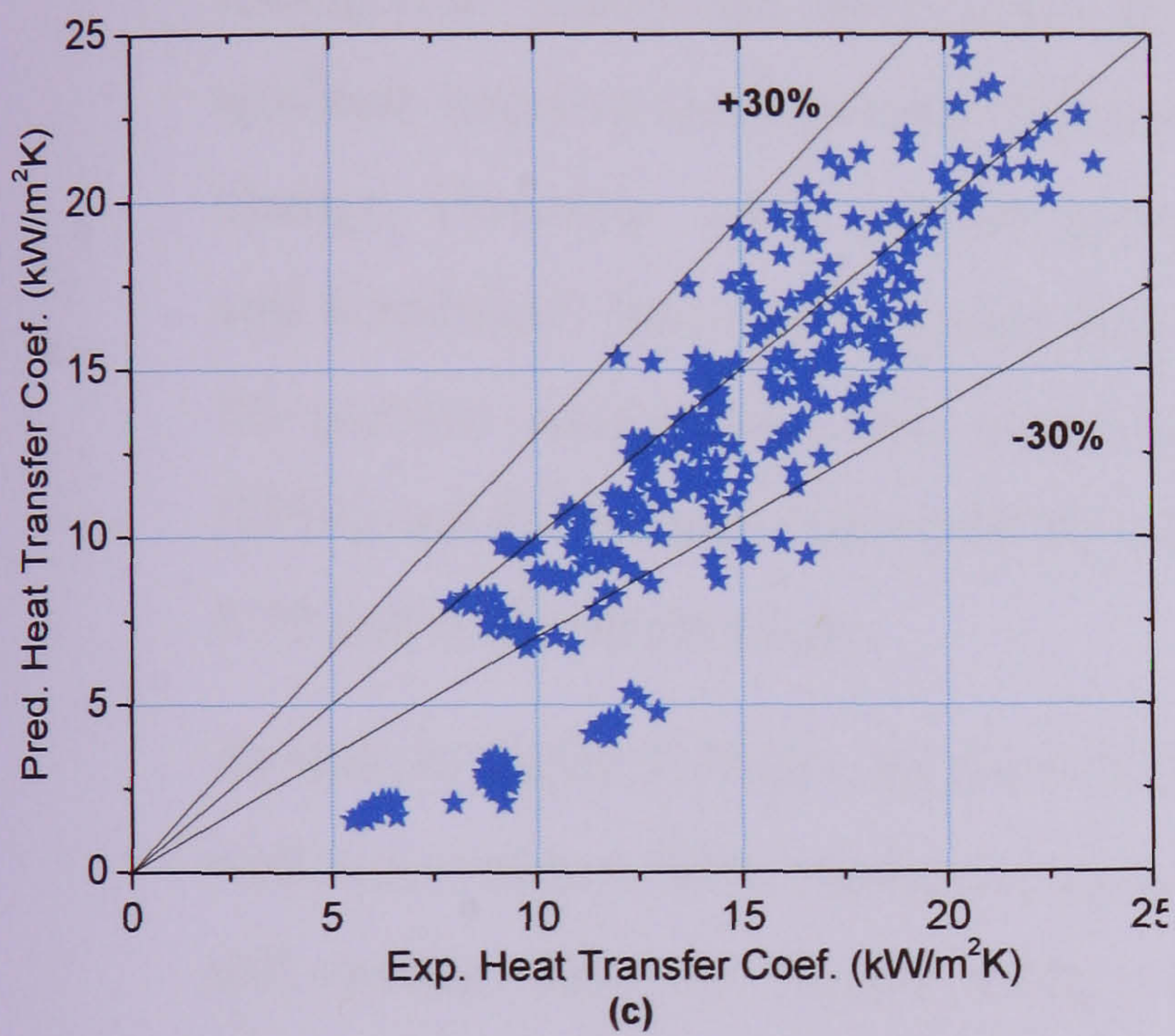
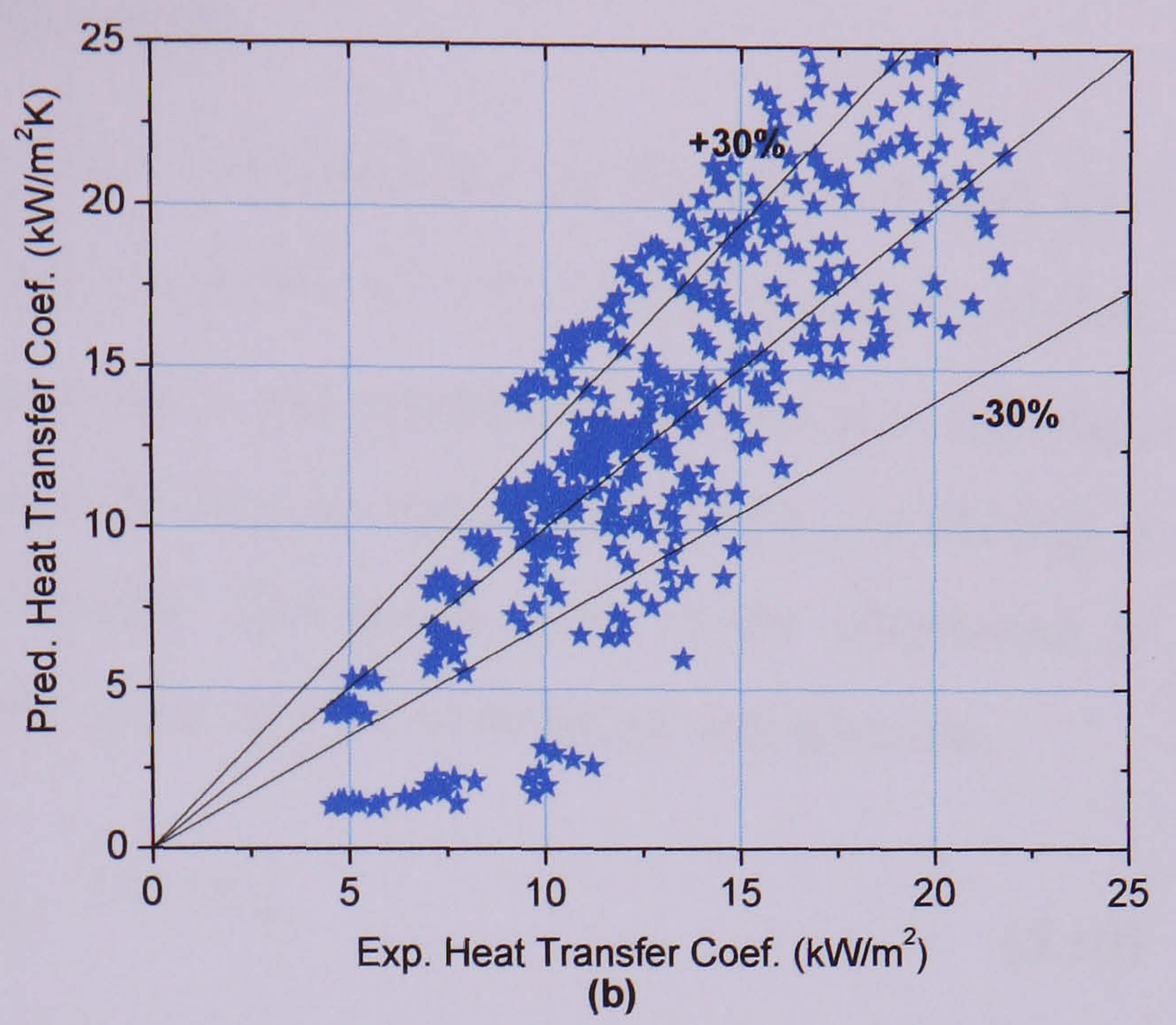
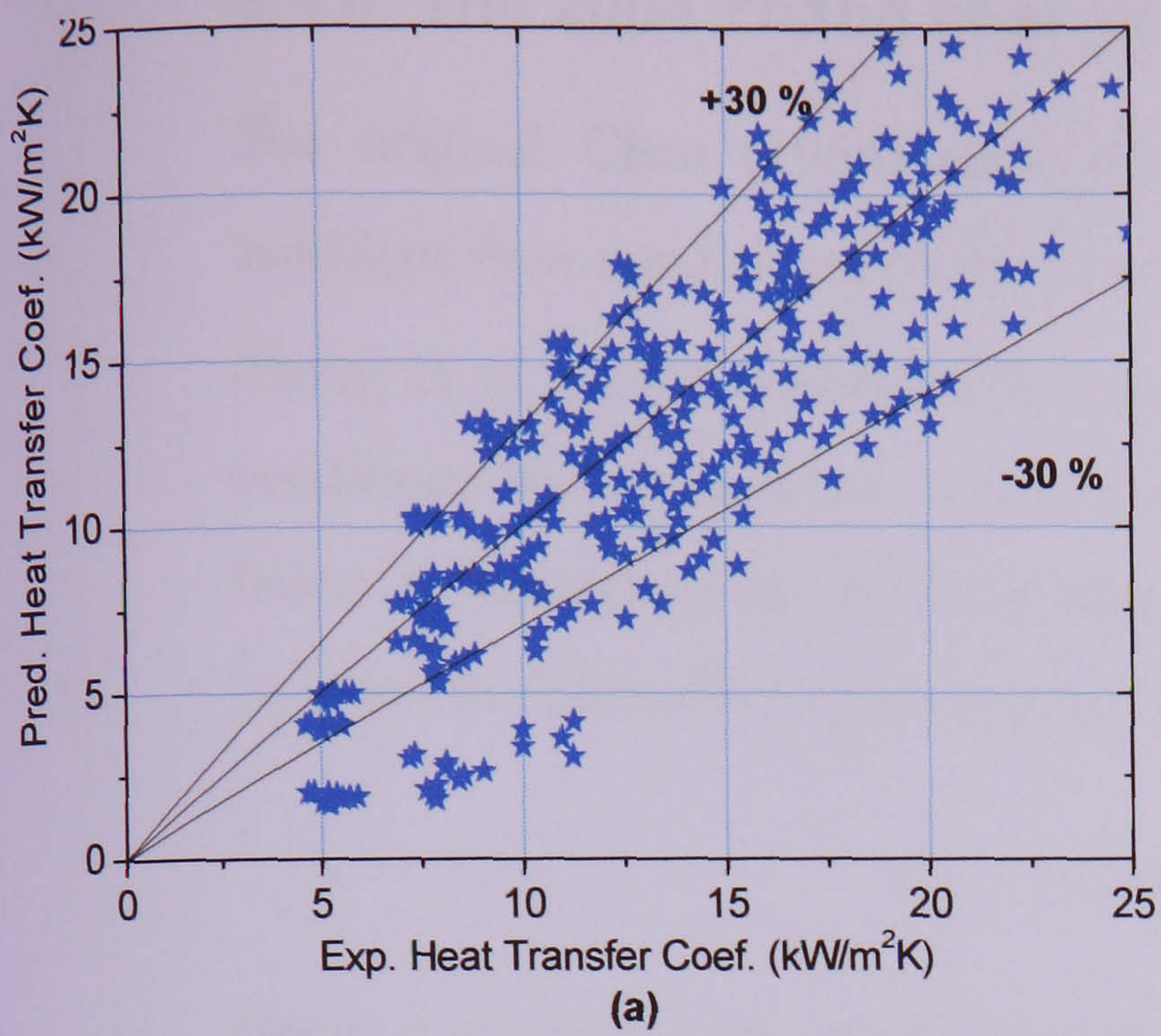


Figure 5.38 Comparison with Kandlikar (2004) correlation for tubes of diameter: (a) 4.26 mm, (b) 2.88 mm, (c) 2.01 mm, (d) 1.1 mm and (e) 0.52 mm.

5.4.6 The 2004 Zhang et al. correlation

The original Chen (1966) correlation was developed for liquid-turbulent and gas-turbulent flow conditions, so the Martinelli parameter $X = X_{tt}$. Following on from that, Zhang et al. (2004) extended the correlation to the liquid-laminar and gas-turbulent conditions and considered to characterize boiling in mini-channels by introducing a factor E dependent on the Reynolds number. The detail form of the correlation is included in Appendix C, however the basic form of their correlation was given as:

$$\alpha_{tp} = S \cdot \alpha_{pool} + E \cdot \alpha_{sp} \quad (5.10)$$

Zhang et al. used Foster and Zuber (1955) correlation for the nucleate boiling term. This equation requires the degree of wall superheat and the corresponding saturation pressure change. However, other similar correlations (e.g. Gungor-Winterton, Liu-Winterton, and Kandlikar) that used nucleate boiling terms used the Cooper (1984) correlation. In the present comparison, both correlations for the nucleate boiling term, i.e. Cooper (1984) and Foster and Zuber (1955) were tested and the results are presented in Figures 5.39 and 5.40, respectively.

As seen in figure 5.39 (a), for the 4.26 mm tube, the correlation predicts the results very well, i.e. within $\pm 20\%$. However, the results of the 2.88 mm tube are over-predicted but still within 30%. In Figure 3.39(c) and (d), a similar prediction as Gungor and Winterton is observed for the 2.01 and 1.1 mm tubes. Both correlations modified the Chen's (1966) correlation, which is based on superposition of the two main boiling mechanisms. The correlation under-predicts the experimental results of both tubes up to 30%, but at large heat transfer coefficient values, the results of 1.1 mm tube are predicted within $\pm 20\%$. In figure 5.39 (e), the results of the smallest tube are seen to be under-predicted by much more than 30 %, especially for the 8 bar pressure data. The comparison for this tube is better using the Gungor and Winterton (1986) correlation. In general, the correlation predicts the larger diameter tube experimental results better than the smaller tube. This could be due to the fact that the Zhang et al. (2004) basically generalised the Chen (1966) correlation and hence based their work on the model proposed for conventional diameter heat transfer correlations.

In Figure 5.40, the comparison results using the Foster and Zuber (1955) correlation, which Zhang et al. (2004) originally used for the nucleate boiling term, indicates that the data is under-predicted by more than 30% for all the tubes.

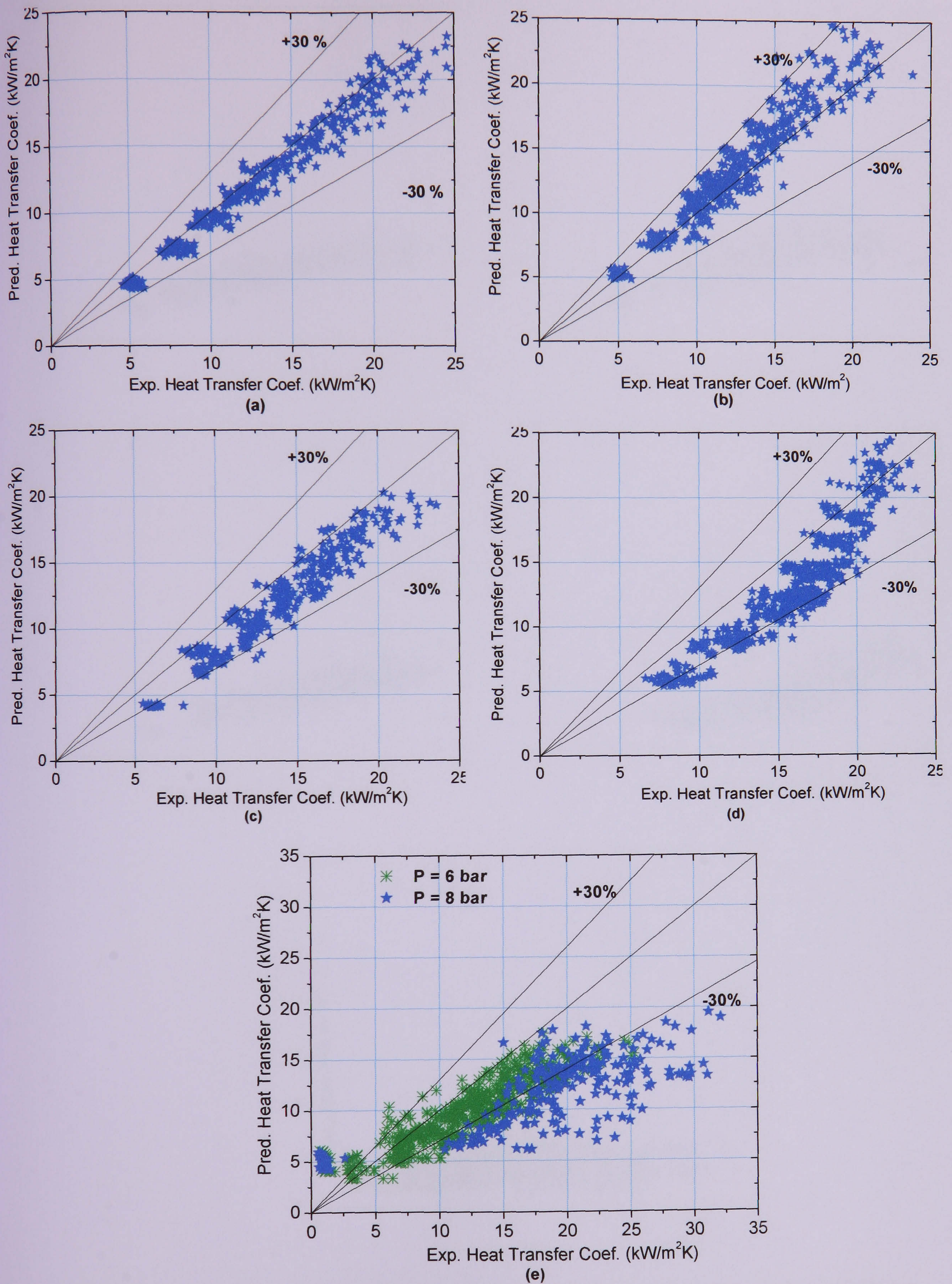


Figure 5.39 Comparison with Zhang et al. (2004) correlation using Cooper (1984) for nucleate boiling term at different tubes of diameter: (a) 4.26 mm, (b) 2.88 mm, (c) 2.01 mm, (d) 1.1 mm and (e) 0.52 mm.

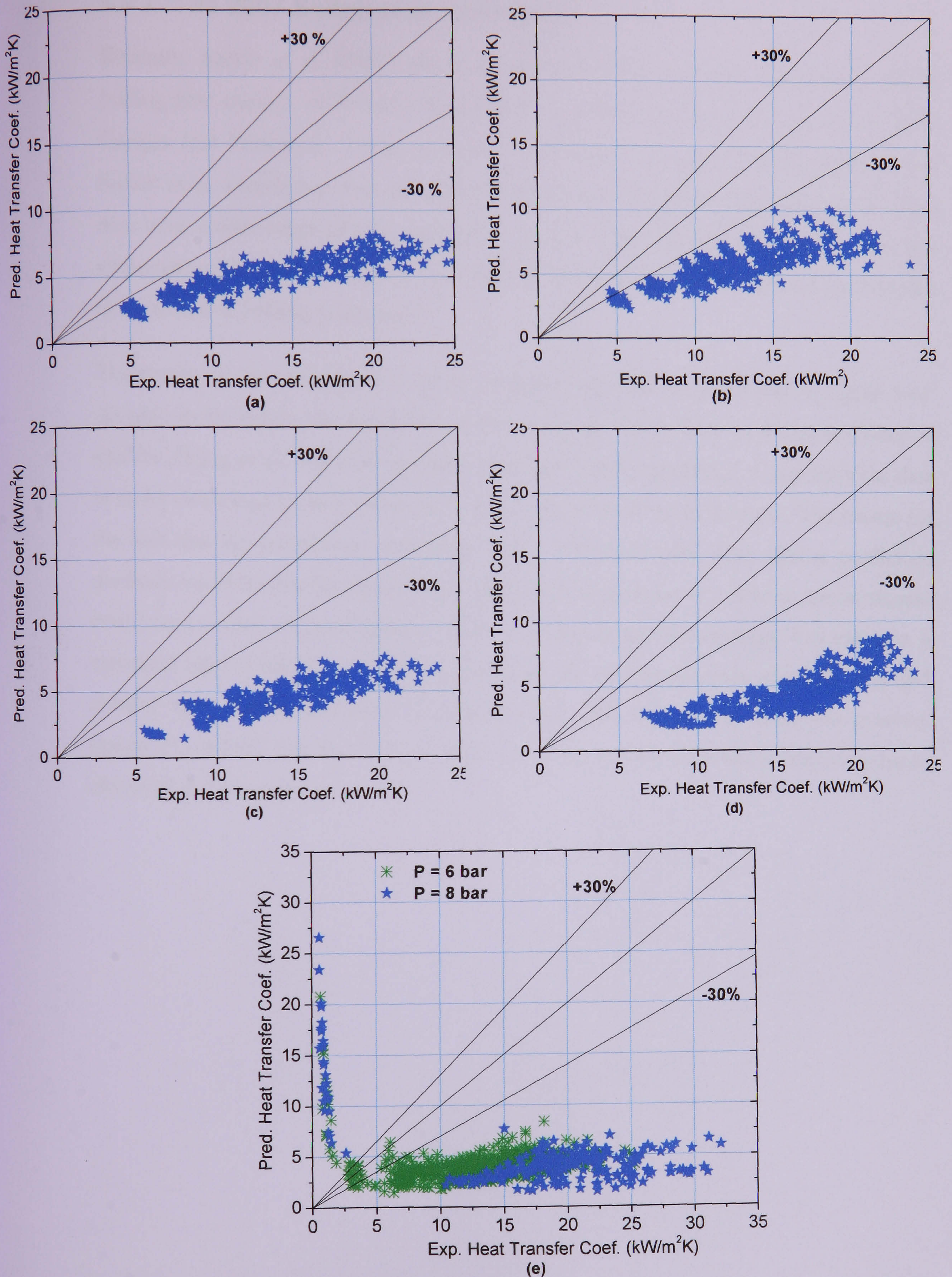


Figure 5.40 Comparison with Zhang et al. (2004) correlation using Foster and Zuber (1955) correlation for the nucleate boiling contribution at different diameter of tubes: (a) 4.26 mm, (b) 2.88 mm, (c) 2.01 mm, (d) 1.1 mm and (e) 0.52 mm.

5.4.7 The 2007 Saitoh et al. correlation

Recently, Saitoh et al. (2007) proposed a modified Chen (1966) correlation for flow boiling heat transfer of R134a. The basic form of the equation is similar to that of the Gungor and Winterton (1986) correlation and details are given in Appendix C. The Saitoh et al. correlation was developed to consider the influence of tube size by using data from a wide range of tube sizes (0.5 – 11 mm). The effect of the tube diameter was characterised by introducing the gas phase Weber number in the factor that multiplies the convective boiling component.

The results of the comparison with the experimental data are presented in Figure 5.41. As seen in the figure, the prediction of the results are worse than the Gungor-Winterton and the Zhang et al. who also modified the Chen (1966) equation, i.e. generally the data is under-estimated by more than 30 % for all the tubes at 8 bar pressure. The reason for the fact that the correlation performed poorly compared with other similar prediction methods could be that the data, used to empirically determine the various exponents and coefficients, were obtained using a different experimental methodology. For instance, a saturated inlet condition with flow patterns at the test section inlet showing slug and annular flow regime was used. In addition, their data was mainly from low pressure system (~ 4 bar). For the 0.52 mm tube data, Figure 5.41 (e), a slight improvement is observed at 6 bar pressure.

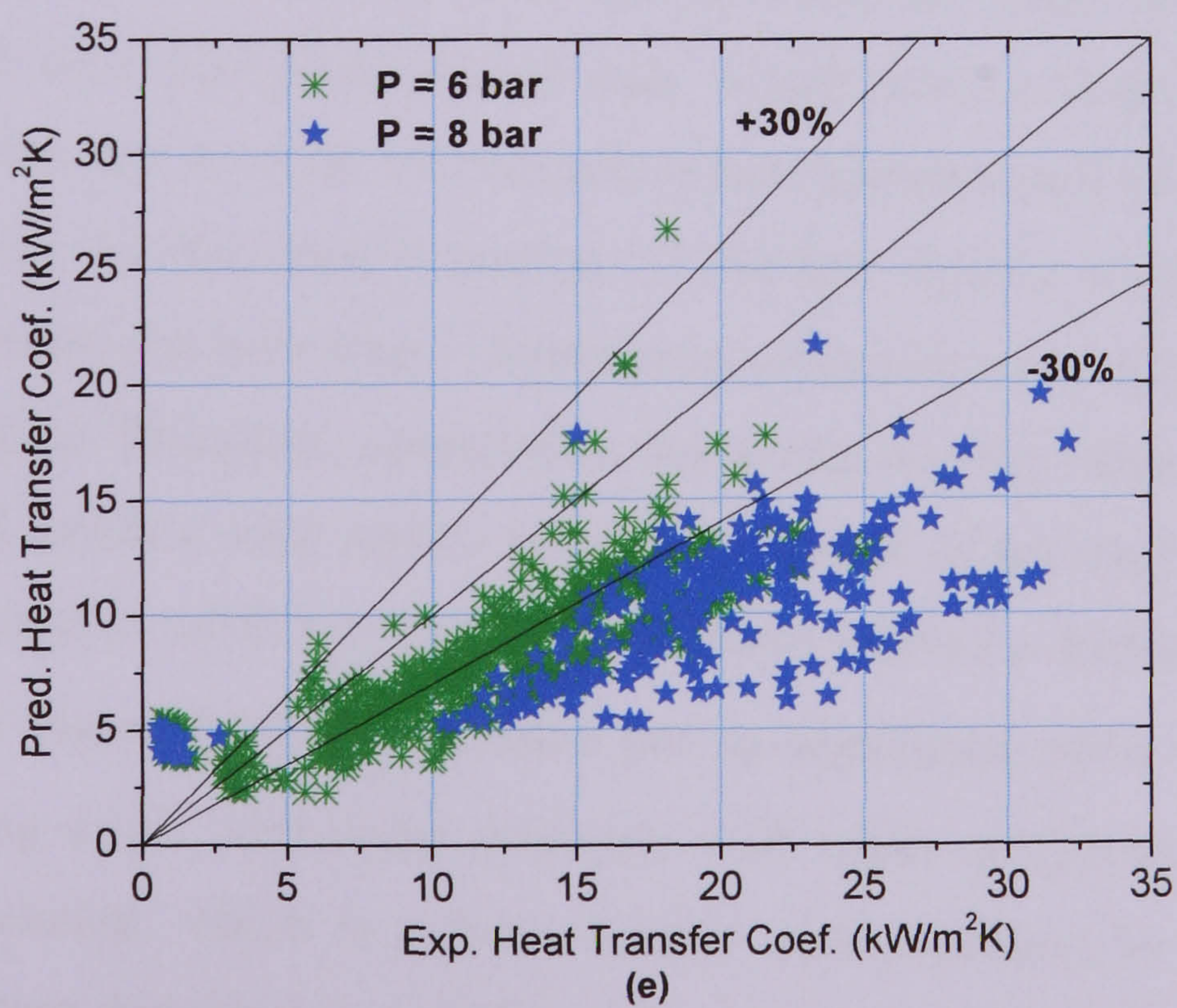
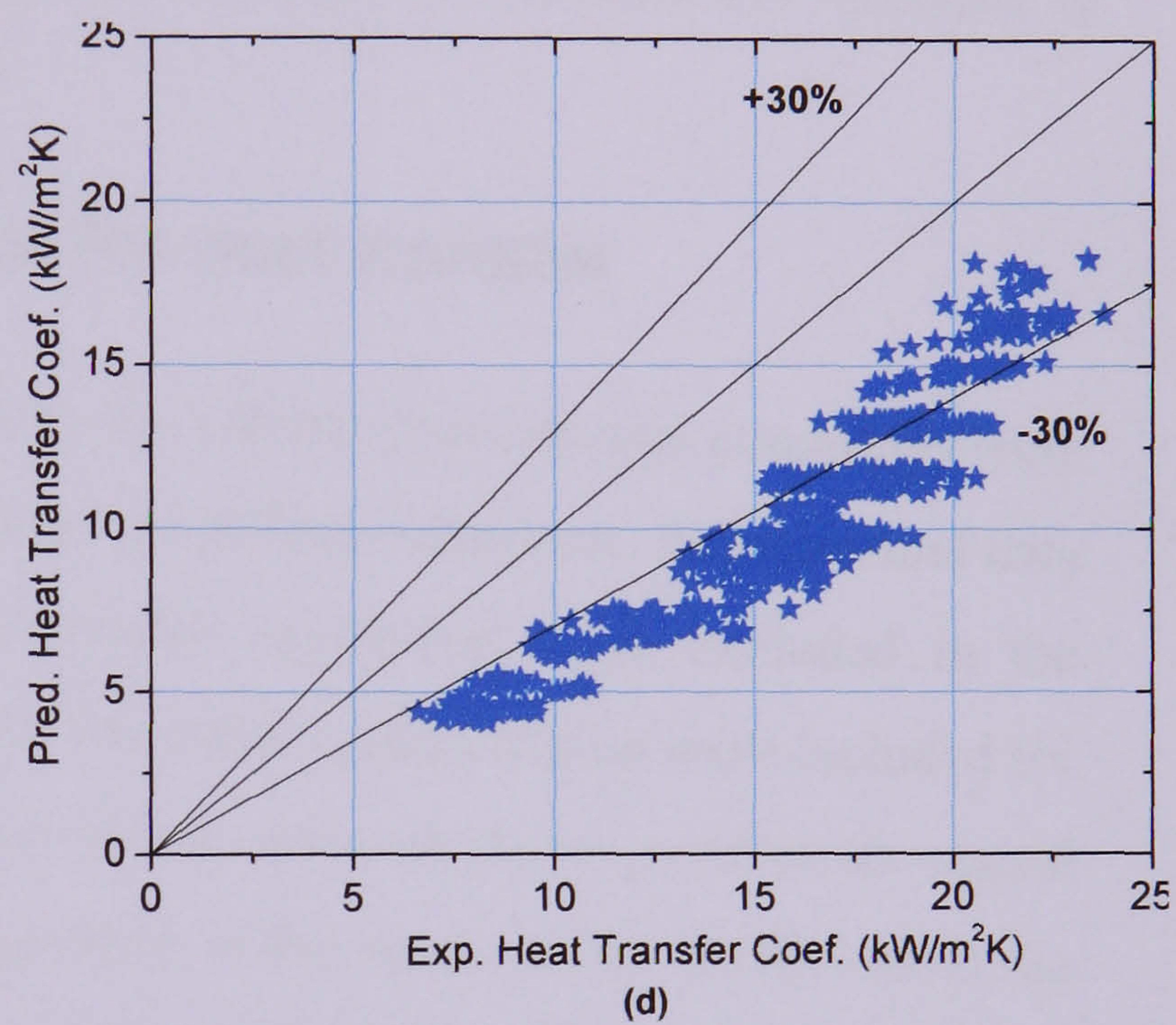
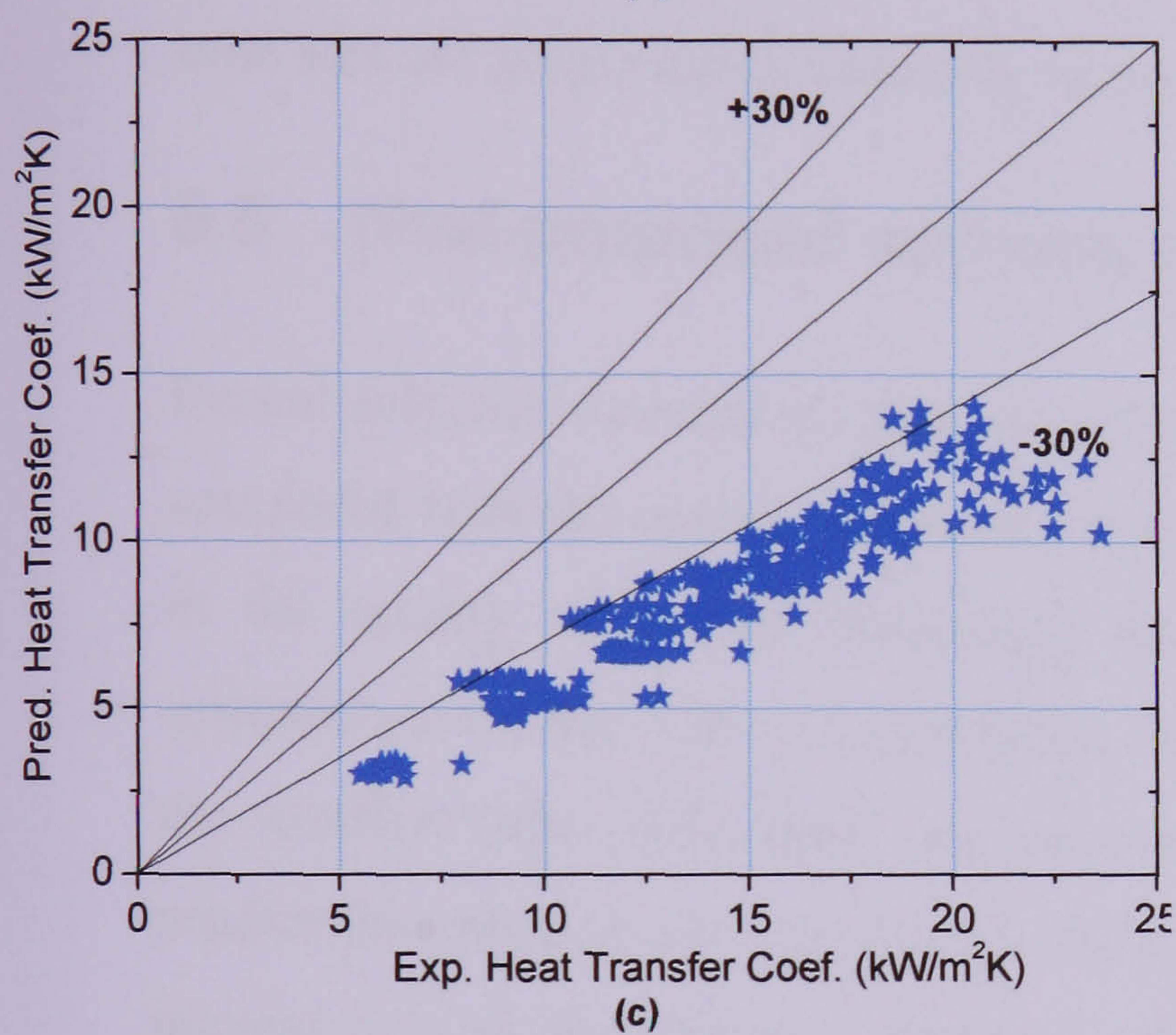
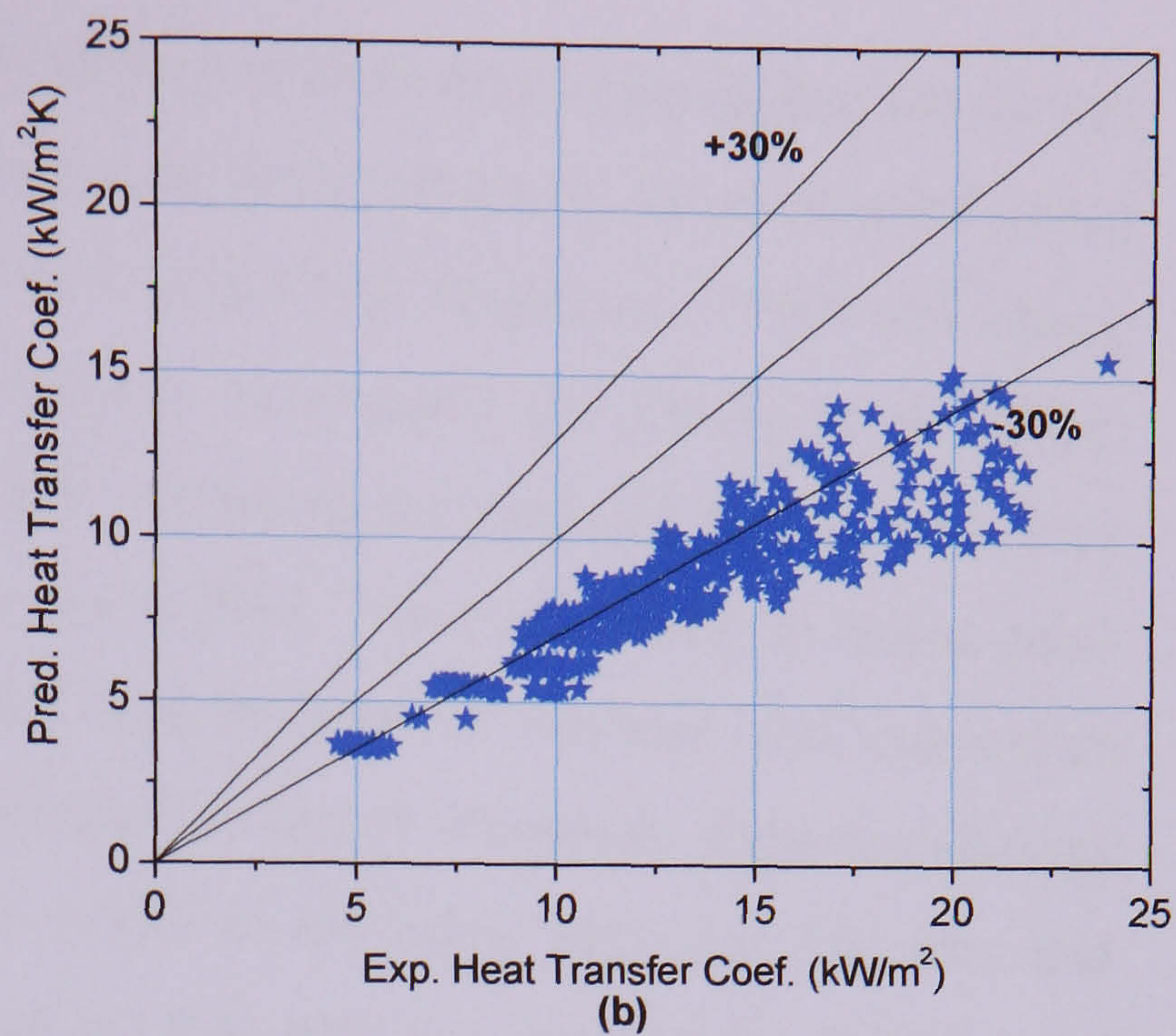
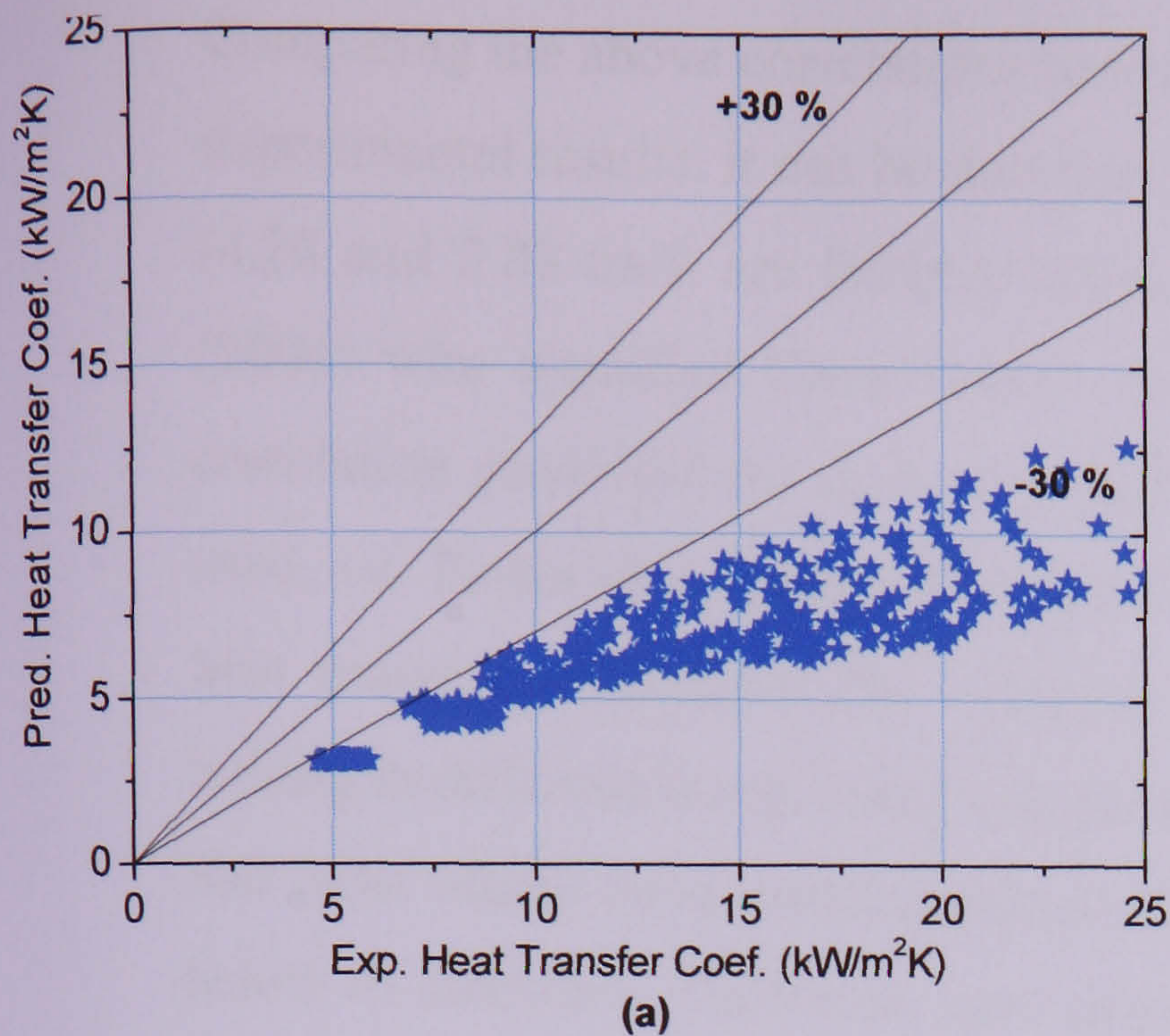


Figure 5.41 Comparison with Saitoh et al. (2007) for different tubes of diameter: (a) 4.26 mm, (b) 2.88 mm, (c) 2.01 mm, (d) 1.1 mm and (e) 0.52 mm.

Comparing the above correlations in terms of their performance in predicting the current experimental results, it can be said that the results of the relatively larger diameter tubes (4.26 and 2.88 mm) are fairly predicted by Gungor and Winterton (1986) and Zhang (2004) who modified Chen (1966) correlation, particularly the Zhang et al. (2004) correlation predicted the data very well after replacing the nucleate boiling term they used, i.e. Foster and Zuber (1955) by Cooper (1984). These are based on macro-scale heat transfer predictions that combine the contributions of nucleate and convective boiling in different forms using various multiplying factors. However, these correlations and most others have under-predicted the results of the tubes with size 2.01 mm and below in diameter. Therefore, new correlations that take into account the influence of tube size are proposed in following section.

5.5 New proposed correlations for heat transfer

Recent selected correlations that are related to the current experimental conditions were compared with the present results for five tubes of different diameter. Experimental data in the quality region of decreasing heat transfer coefficient were excluded in the comparison for the 4.26 -1.1 mm tubes, while the entire quality region were included for the smallest tube (0.52 mm). As mentioned above, most of these correlations cannot predict the enhancement obtained in the magnitude of the heat transfer coefficient of the present data as the diameter decreases. This indicates that the effect of tube diameter was not considered well. Using the present data, which cover a wide range of tube diameter, a correlation that accounts the increase in heat transfer coefficient as diameter decreases is proposed. As discussed in section 5.2 the heat transfer results of the 0.52 mm tube show different characteristics – dependence on quality and position – than the rest of the tubes studied. Therefore, a correlation that works well for the rest of the tubes may not predict the smallest tube results in terms of trends or accuracy. The present experimental heat transfer coefficient for (4.26 - 1.1 mm) showed a dependence on heat flux ($\alpha = c \cdot q^n$, see Figure 5.15) and pressure but no significant effect of mass flux. Moreover, the Zhang et al. correlation performs well when modified by using the Cooper (1984) correlation, which is a ‘pool boiling’ type equation for the nucleate boiling term, suggesting that the new correlation for this range of tubes should consider this fact and the increase in heat transfer coefficient with decreasing diameter. Therefore, in the new correlation, a modified Cooper (1984) correlation is proposed by

making the exponent of the heat flux to depend on the ratio of tube diameter to bubble departure diameter. The nucleate boiling suppression factor of Chen (1966) is also modified after introducing the diameter effect in this relation. The Cooper (1984) is also preferred for the fact that it considers the roughness of the tube as one parameter, added to the various property effects incorporated in the correlation. A correlation that works well for the larger tubes (4.26 -1.1 mm) tube cannot predict the smallest tube data, because of the basic difference in the dependence of the heat transfer coefficient on the various parameters. Therefore, a new correlation that takes the effect of mass flux, surface tension, and quality or axial distance is proposed. The detail forms of the equations are given below.

For tubes with diameter 1 mm and larger,

$$\alpha_{tp} = S_m \cdot C_{Cooper} q^n \quad (5.11)$$

where, the coefficients and exponent are given as follows.

C_{Cooper} is the coefficient given by Cooper (1984) and expressed as,

$$C_{Cooper} = 55 P_R^{(0.12 - \log e)} (-\log P_R)^{-0.55} M^{-0.5} \quad (5.12)$$

e is the roughness of the tube in μm .

S_m is the new suppression factor modified by introducing the tube diameter effect in the Chen (1966) suppression factor ($S = 1/(1 + 2.53 \times 10^{-6} Re_i^{1.17})$) and is given as,

$$S_m = \frac{24.7 \left(\frac{D}{D_b} \right)^{-1.32}}{1 + 2.53 \times 10^{-6} Re_i^{1.17}} \quad (5.13)$$

n is the new exponent obtained based on the current data, which depends on the ratio of tube to bubble departure diameter.

$$n = 0.4243 \left(\frac{D}{D_b} \right)^{0.19}, \quad (5.14)$$

D_b is the bubble departure diameter given by the Stephan and Abdelsalam (1980) correlation. For refrigerants, a contact angle of $\theta = 35^\circ$ was recommended.

$$D_b = 0.0146 \theta \left(\frac{2\sigma}{g(\rho_l - \rho_g)} \right)^{0.5} \quad (5.15)$$

As stated above the results of the smallest tube demonstrated different heat transfer characteristics, which showed two groups of heat flux with different heat flux effect. Moreover, the heat transfer coefficient trend also changes with heat flux and axial distance. Therefore, another correlation is proposed for very small tubes of size below 1 mm. The correlation combines the effect of heat flux and mass flux by incorporating Boiling and Reynolds non-dimensional numbers. The fact that these tube exhibited a different flow patterns was related to the effect of surface tension force, hence Weber number is also introduced in the correlation to take account the effect of surface tension. The correlation equations are given below.

$$\alpha_{tp} = C_a \left(\frac{We_l \times 10^5}{Re_l} \right)^{0.7} Bo^{0.49} + F \alpha_{lam} \quad (5.16)$$

C_a [W/m²K] is coefficient that depends on a new non-dimensional axial parameter (Z_c). This parameter is introduced because of the fact that the heat transfer coefficient showed patterns of changes with axial measuring position. It is calculated using the local quality as,

$$Z_c = \left(\frac{x}{Bo} \right) \left(\frac{D}{L} \right) \quad (5.17)$$

For $Z_c < 2$, $C_a = 5073$ otherwise use $C_a = 3800$

An additional single-phase term with enhancement factor is included in equation (5.16), because of the fact that the heat transfer coefficient was relatively very low and independent of heat flux below a certain heat flux threshold. The single phase heat transfer factor (F) is a similar form as that of Chen (1966) modified later by Saitoh et al. (2007) based on small tube data using R134a. In the present correlation, the second term in Eq. (5.16) is added to consider the first group of heat flux independent curves observed at low heat flux; F is zero except when $Bo < 0.00021$ and $P_R > 0.17$, in which case it is given by,

$$F = 1 + \left(\frac{(1/X)^{1.05}}{1 + We_g^{-0.4}} \right) \quad (5.18)$$

where X is the Martinelli Parameter

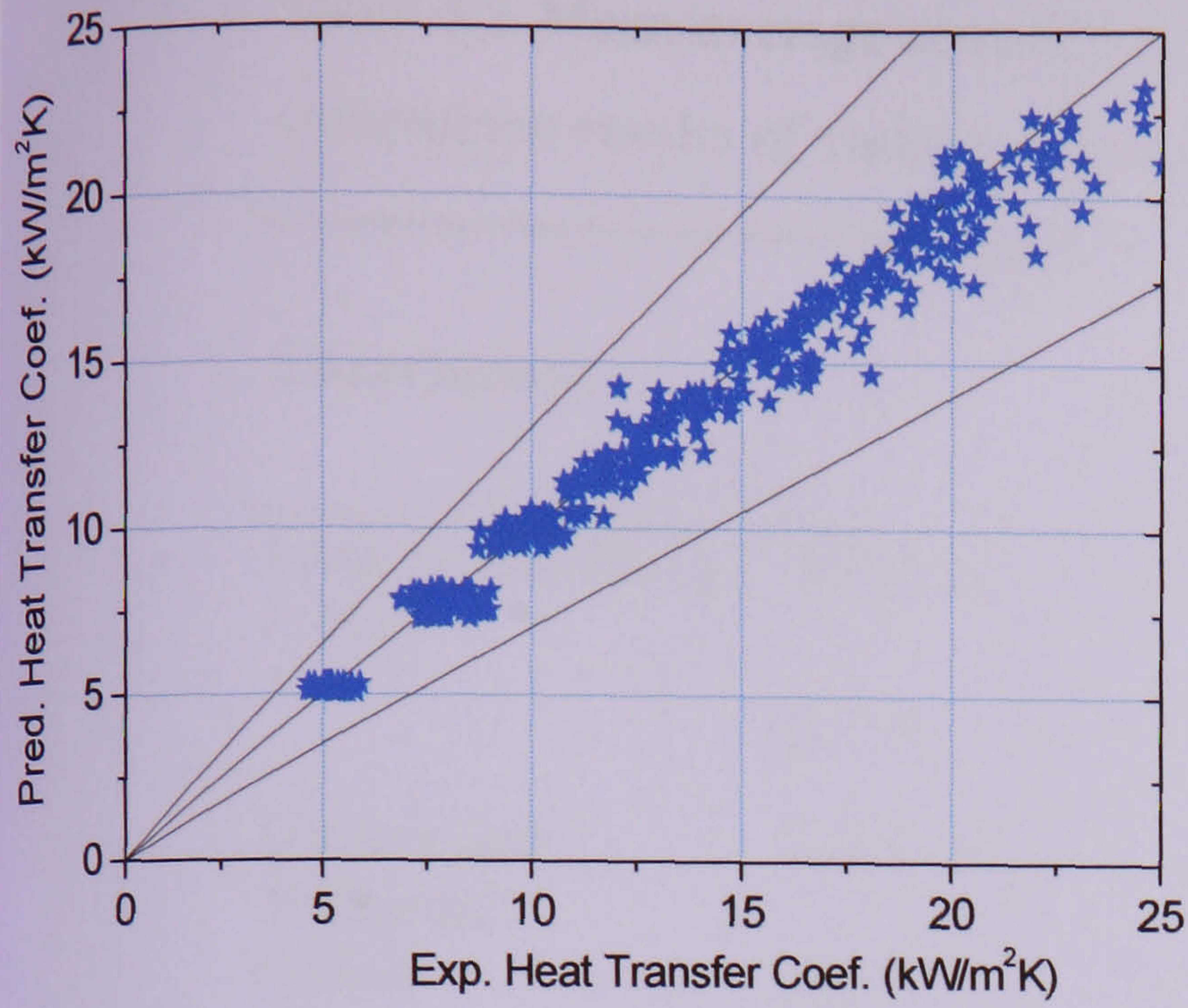
$$X^2 = \frac{(dP/dz)_l}{(dP/dz)_g} \quad (5.19)$$

The laminar single phase heat transfer coefficient was obtained from the constant Nusselt number for constant heat flux condition ($Nu = 4.36$).

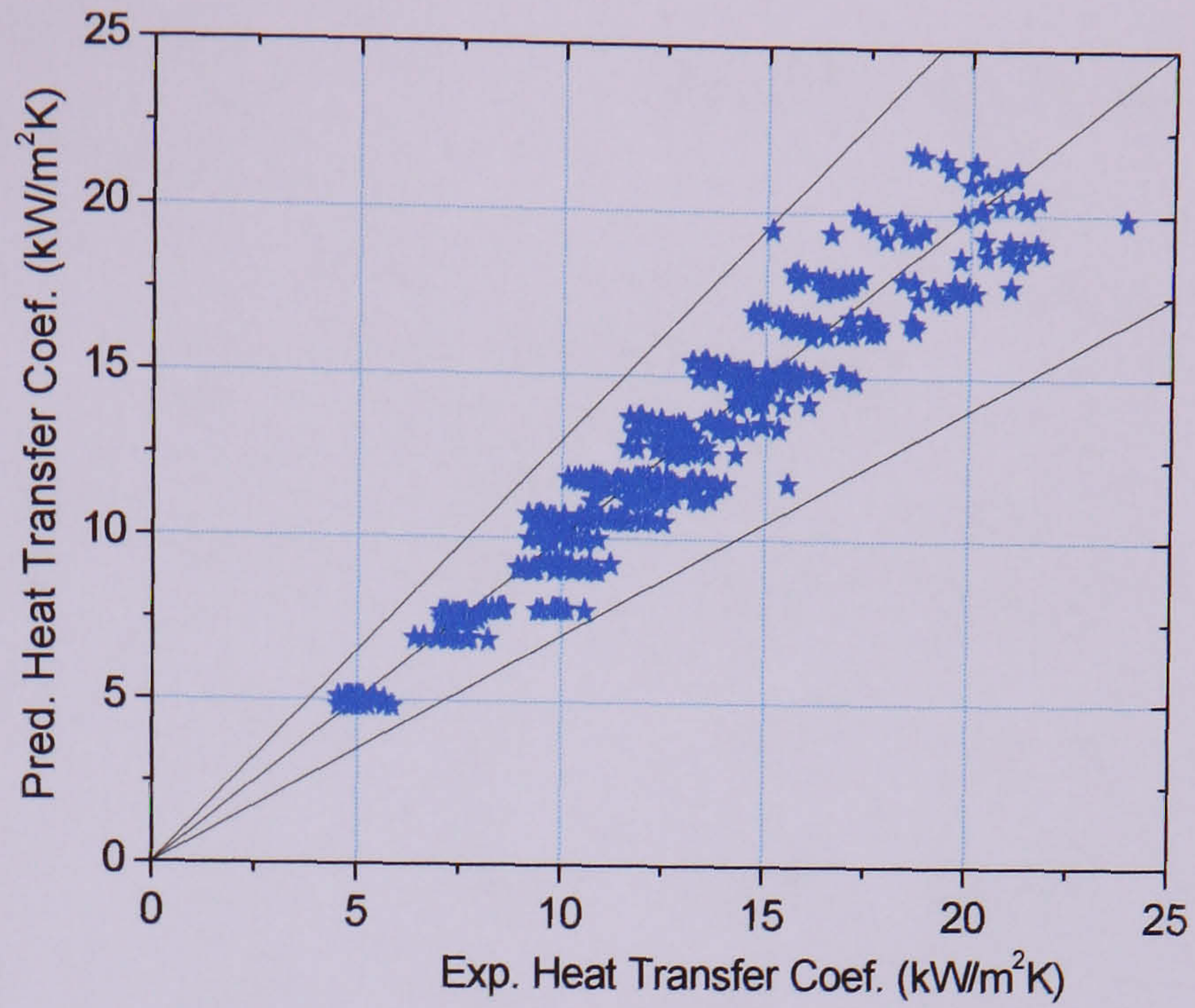
Comparison of the new correlation results with the current data is depicted in Figure 5.42. As seen in the figure, the new correlations predicted very well the experimental data and account for the effect of diameter on the heat transfer coefficient, while other correlations showed a bias with varying tube diameter. Mean Absolute Error (MAE) and percentage of data within $\pm 30\%$ (β) is given for each correlations in Table 5.1 to clearly see the performance of the various correlations in comparison with the new proposed here.

$$MAE = \frac{1}{N} \sum^N \frac{|\alpha_{exp} - \alpha_{pred}|}{\alpha_{exp}} \times 100\% \quad (5.20)$$

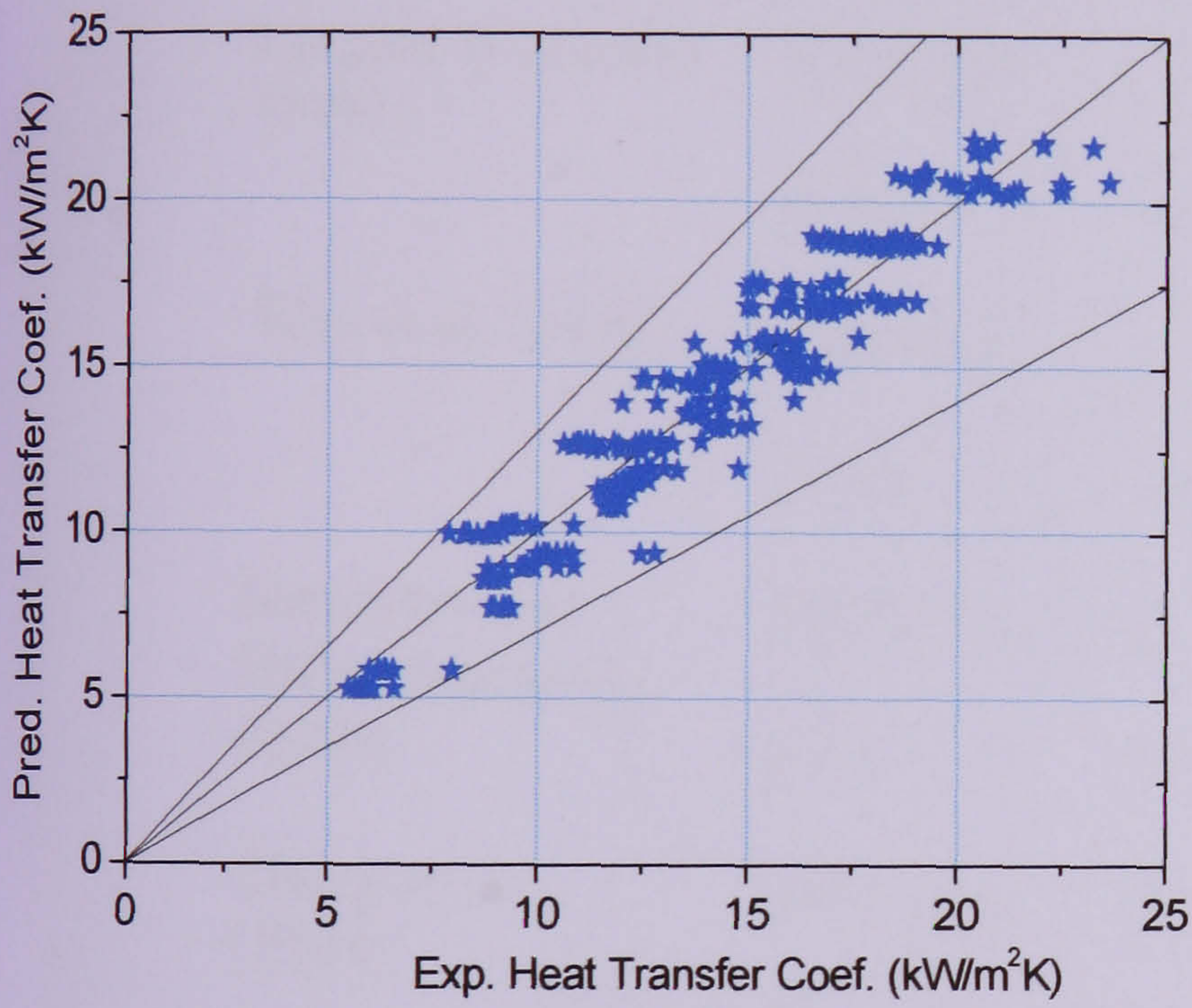
As can be seen from the table, the new correlation has a mean deviation of only 4.6, 7.2, 6.7, 8.5 and 15.5 for the 4.26, 2.88, 2.01, 1.1 and 0.52 mm tubes respectively. In contrast, most correlations have under-estimated the data as the tube diameter decreases. For instance, all correlations predicted the 0.52 mm data by an absolute error that is higher than 50 %, while the new correlation predicted the data by a mean deviation, which is almost the same as the experimental error. The Zhang et al. (2004) correlation predicted the larger tubes data very well, but this is after replacing their original Foster and Zuber (1955) nucleate boiling correlation by that proposed Cooper (1984). For the 4.26 - 1.1 mm and 0.52 mm tubes, 100 and 85.5 % of the data are predicted within $\pm 30\%$ respectively, by the new proposed correlations.



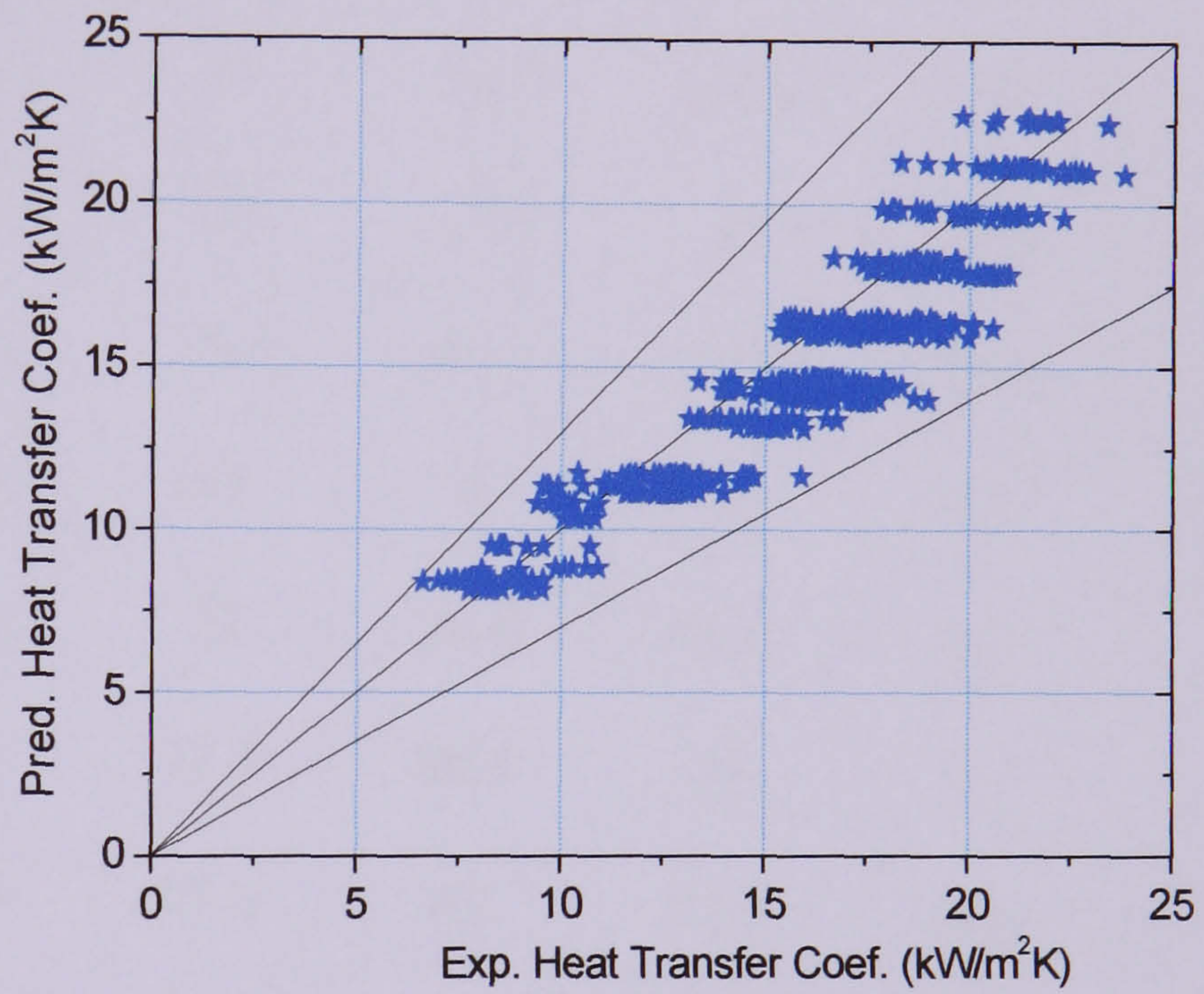
(a)



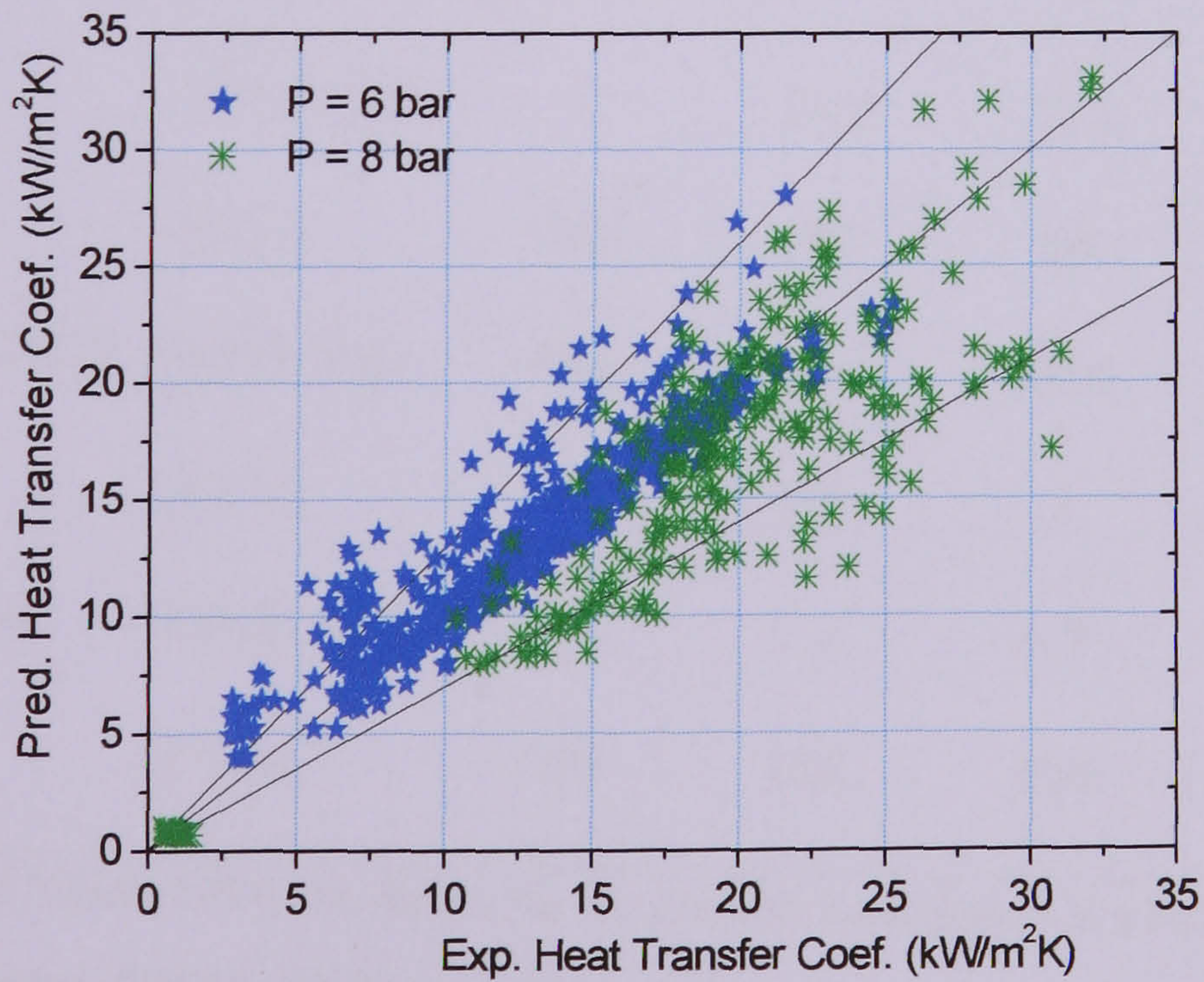
(b)



(c)



(d)



(e)

Figure 5.42 Comparison with the new proposed correlation for different tubes of diameter: (a) 4.26 mm, (b) 2.88 mm, (c) 2.01 mm, (d) 1.1 mm and (e) 0.52 mm.

Table 5.1 Mean average error (MAE) and percentage of data within $\pm 30\%$ (β) for the comparison results of various correlations shown above.

Correlations		Tube internal diameter (mm)				
		4.26	2.88	2.01	1.1	0.52
Lazarek and Black (1982)	MAE (%)	33.8	21.8	37	32.7	52.5
	β (%)	40	75	23	35	37
Gungor and Winterton (1986)	MAE (%)	15.3	8.5	13.2	12.15	51.15
	β (%)	88	100	99	99	62.5
Liu and Winterton (1991)	MAE (%)	26.3	17	34.5	34.5	57
	β (%)	79.5	96	25.1	30	40.5
Tran et al. (1996)	MAE (%)	15	16.3	41.3	52.5	73.5
	β (%)	100	97	2	0	1.5
Kandlikar and Balasubramanian (2004)	MAE (%)	21.1	23	20.4	48.7	67
	β (%)	79.5	73.5	80.5	25	5
Zhang et. al (2004) ¹	MAE (%)	60.5	53.5	67	72.5	144
	β (%)	0	1	0	0	3
Zhang et al. (2004) ²	MAE (%)	7	10.5	15.1	19.6	50
	β (%)	100	99	94	86.5	56
Saitoh et al. (2007)	MAE (%)	48.6	33	41.4	37.2	57.3
	β (%)	0	35	3	20	30
New correlation	MAE (%)	4.6	7.2	6.7	8.5	15.5
	β (%)	100	100	100	100	85.5

¹ Using Foster and Zuber (1952) correlation for the nucleate boiling term as given in Zhang et al. (2004)

² Modified Zhang et al. (2004) correlation using Cooper (1984) for the nucleate boiling contribution.

5.6 Summary

Flow boiling experimental results for five tubes of diameter 4.26, 2.88, 2.01, 1.10 and 0.52 mm over a range of pressures and mass fluxes were presented and discussed. The range of diameters was first chosen based on an initial assessment using the confinement number proposed by Cornwell and Kew (1993) and aimed to investigate thresholds for macro, small or micro tube characteristics by systematic measurements of flow boiling of R134a over wide ranges of pressures, flow rates and heat fluxes. Flow visualization experiments were conducted by direct observation at a borosilicate glass tube located at the exit of the heated test section. The heat transfer results were also discussed by relating with the flow regimes observed simultaneously.

The heat transfer coefficients in tubes ranging from 4.26 mm down to 1.1 mm increased with heat flux and system pressure, but did not change with vapour quality when the quality was less than about 40% to 50%, for low heat flux values. At higher quality, the heat transfer coefficients decreased with quality, indicating local dryout. For tube diameter 4.26 to 1.1 mm, the observed characteristics of the heat transfer coefficients at low quality are similar to those conventionally interpreted as evidence that flow boiling in large tubes is dominated by nucleate boiling: the coefficients increase with increasing heat flux and pressure but are insensitive to quality and mass flux. There are however, claims that suggest, for small passages, the same behaviour can be explained if transient evaporation of the thin liquid film surrounding elongated bubbles, without nucleate boiling contribution, is the dominant mechanism, Thome et al. (2004). The observed heat transfer coefficient versus heat flux curves suggest a nucleate pool boiling phenomena. The similarity could be related to the fact that both mechanisms involve evaporation of thin liquid films which may involve small-scale dryout.

The heat transfer results of the smallest diameter tube (0.52 mm) demonstrated different characteristic than the rest of the tubes. The data fell into two groups that exhibited different influences of heat flux below and above a heat flux threshold. In addition, the dependence of the heat transfer coefficient on axial position is much stronger in the 0.52 mm tube extending to high quality in the annular flow regime. In the low heat flux region, there is no significant effect of heat flux but the heat transfer coefficient decreases (at low mass flux and pressure) or remains constant (at higher mass flux and pressure), then increases slightly with thermodynamic quality. At moderate and high heat flux, in the front part of the channel, the heat transfer coefficient increases with

increasing heat flux and reaches a maximum at an intermediate quality, which could be caused by local variations in surface conditions. At higher quality, towards the test section exit, the heat transfer coefficient gradually increases again with quality but there is no clear effect of heat flux. The heat transfer coefficient increases with mass flux in this region. According to the conventional interpretation, this is evidence for a convective boiling dominant heat transfer mechanism in the annular flow region. This unexpected behaviour observed in the smallest tube could be attributable to the axial variations in surface roughness, which may have large influence on local bubble nucleation. The single phase friction factor in this tube is much higher than the other tubes. Preliminary surface roughness measurements were reported in Chapter four. It is the only tube for which the incoming liquid flow is laminar and this may also influence the initiation of confined bubble (slug) flow. Unlike the larger tubes that were examined in this study, which exhibit dryout phenomena at high quality as the heat flux increases with a drop of the heat transfer coefficient with quality, a monotonic increase in heat transfer coefficient was observed towards the exit for the smallest diameter tube. This could be related to laminar flow and domination of surface tension force over momentum, providing more uniform liquid film thickness along the circumference, with less interfacial waves and disturbances, which improve wetting of the wall. In general, the complex dependence of the heat transfer rate on various parameters suggest, the difficulty of interpreting the heat transfer mechanisms using general conventional terms.

There was no significant difference between the characteristics and magnitude of the heat transfer coefficients in the 4.26 mm and 2.88 mm tubes but the coefficients in the 2.01 were 15 % higher, with further increase in the 1.1 mm tube by 35%. The heat transfer results suggested that a tube size of about 2 mm might be considered as a critical diameter to distinguish small and conventional tubes. This is consistent with the study of Chen et al. (2006) who observed differences between the flow patterns leaving the 2.88 and 4.26 mm diameter tubes and those from the 2.01 and 1.1 mm tubes, which exhibited confined flow, slimmer vapour slugs, thinner liquid films, and smoother vapour-liquid interfaces. Generally, they identified dispersed bubble, bubbly, confined bubble, slug, churn, annular and mist flows in the same tubes (4.26 -1.1 mm). Further differences have been observed in the 0.52 mm tube: ring flow appeared over a significant range of quality/heat flux, while dispersed and churn flows were absent and diminished respectively. These differences, both in flow patterns and heat transfer,

indicate a possible second change from small to micro behaviour at diameters less than 1 mm for R134a.

The results of the five tubes were also compared with the existing correlations. Most of the correlations did not correctly predict the tube diameter effect, i.e. the data were underestimated as the tube diameter decreases. Therefore, the new correlations that take into account both magnitude and characteristic effect of tube diameter are proposed covering the 4.26 mm-1.1 mm and the smallest 0.52 mm tube. The new correlation is capable of predicting the present data for the 4.26, 2.88, 2.01, 1.1 and 0.52 mm tubes with a mean absolute error of 4.6, 7.2, 6.7, 8.5 and 15.5 % respectively.

Chapter 6

Boiling Two Phase Pressure Drop Results and Discussion

6.1 Introduction

The two phase pressure drop measured during the boiling experiments for the five tubes of diameter: 4.26, 2.88, 2.01, 1.1 and 0.52 mm will be presented in this chapter. Again, the results of the two tubes 4.26 and 2.01 mm tubes have been reported in Huo et al. (2006). These are included here to provide a better understanding on the influence of tube diameter using a wide range of data. The chapter is organised as follows: Section 6.2 presents examination of the dependence of the total two phase pressure drop on the various parameters such as heat flux or exit quality, mass flux, system pressure and tube internal diameter. The contributions of the various boiling two phase pressure drop components, i.e. acceleration, gravitational and friction pressure drop, to the experimentally measured total value are also discussed. The current experiment data are compared with the various existing pressure drop models and correlations in section 6.3. A summary of the chapter is provided in Section 6.4.

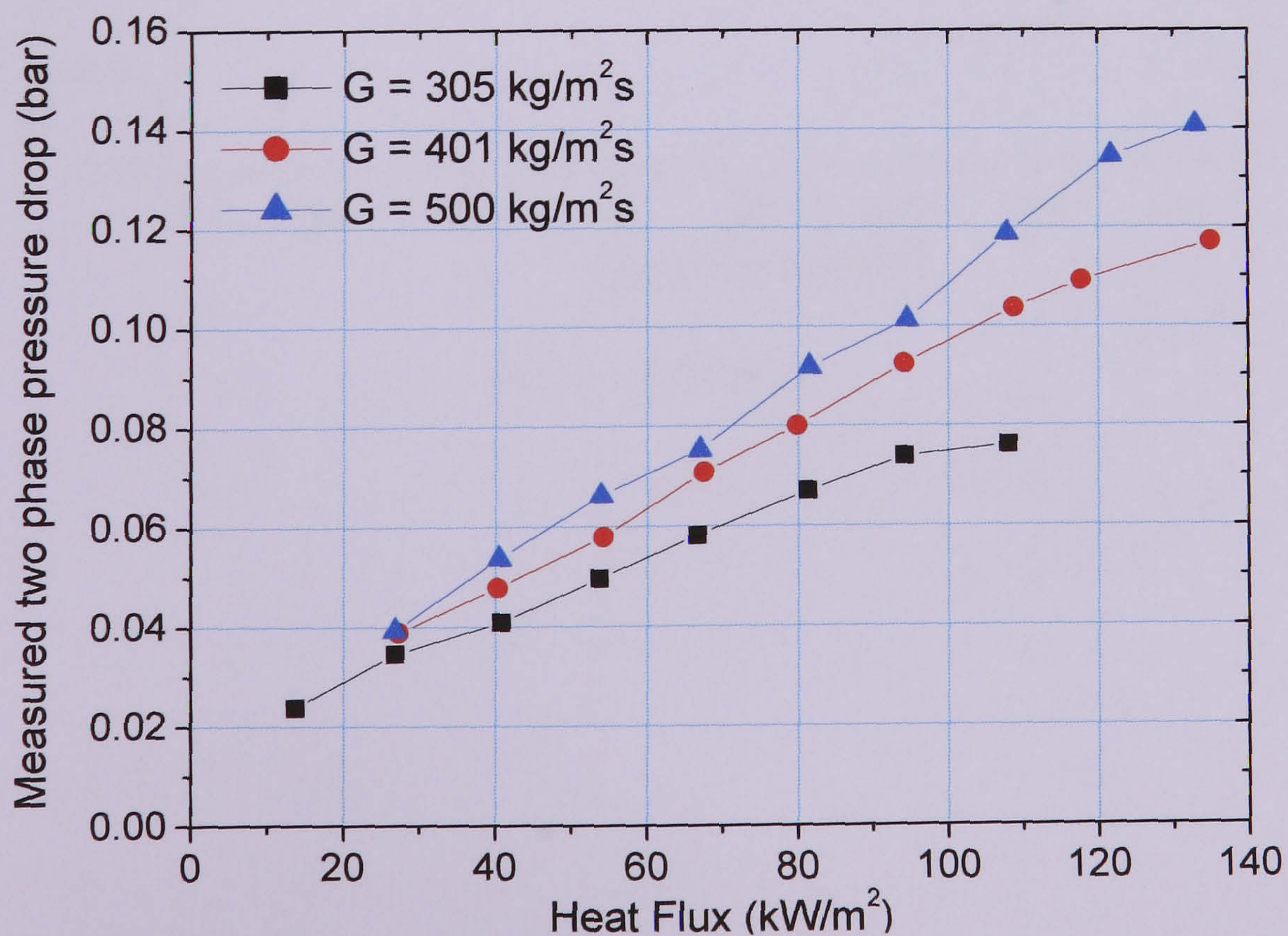
6.2 Total pressure drop

In this section the influence of the various parameters, such as: heat flux, mass flux, system pressure and tube internal diameter, on the total measured pressure drop is investigated. Only saturated two phase pressure drop is taken into account, i.e. the single phase pressure drop at the front part of the test section because of subcooled

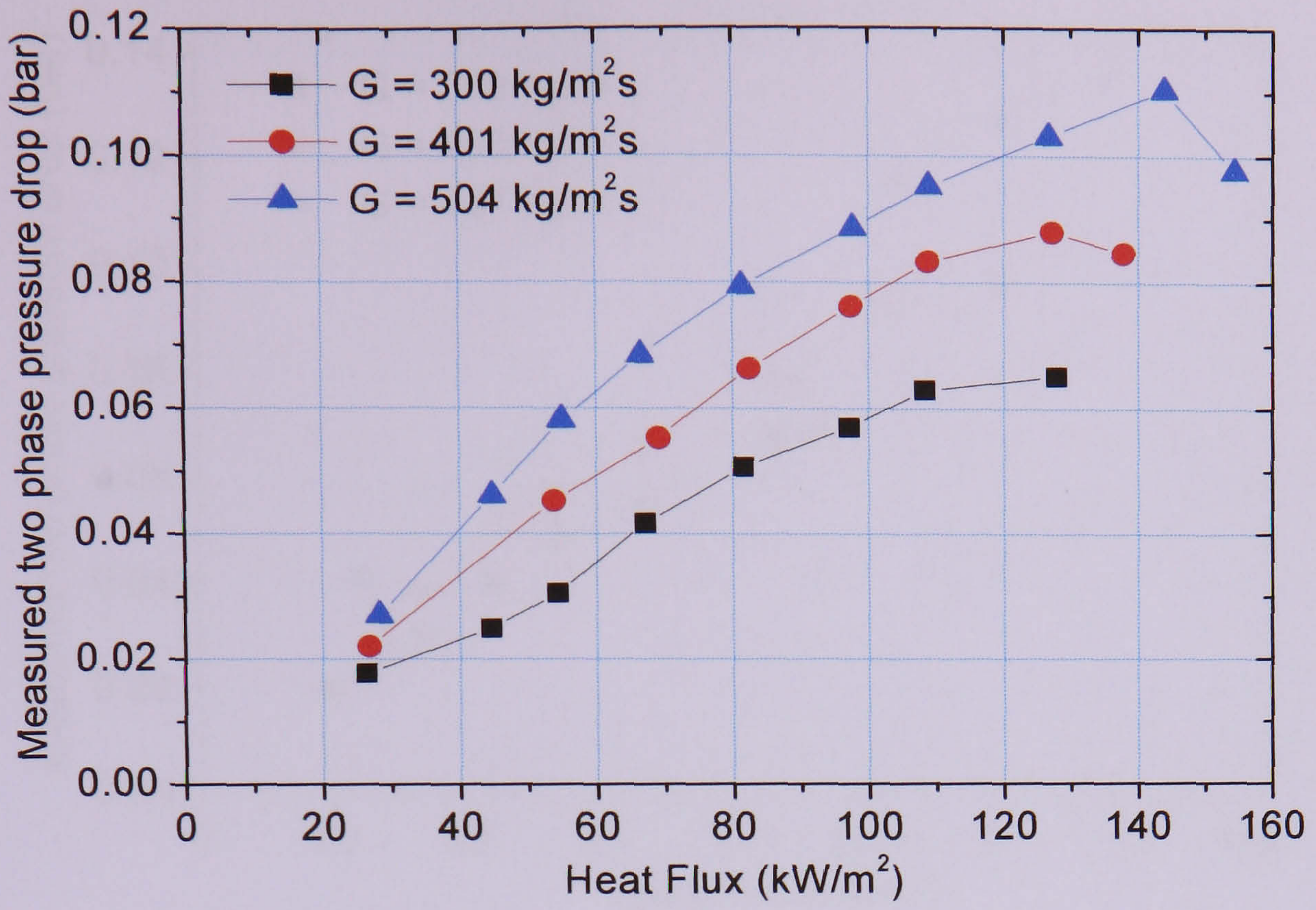
liquid inlet (1-5 K), is deducted from the total measured value. The single phase pressure drop for ($x < 0$) is calculated by adding the gravitational component and frictional pressure drop using the Halaand's correlation for friction factor, see Eq. (4.35). Also, no allowance is made for pressure drop at inlet and outlet because there is a smooth continuation of the internal diameter, unlike experiments in which a channel connects to large inlet and outlet plena.

6.2.1 Effect of heat flux

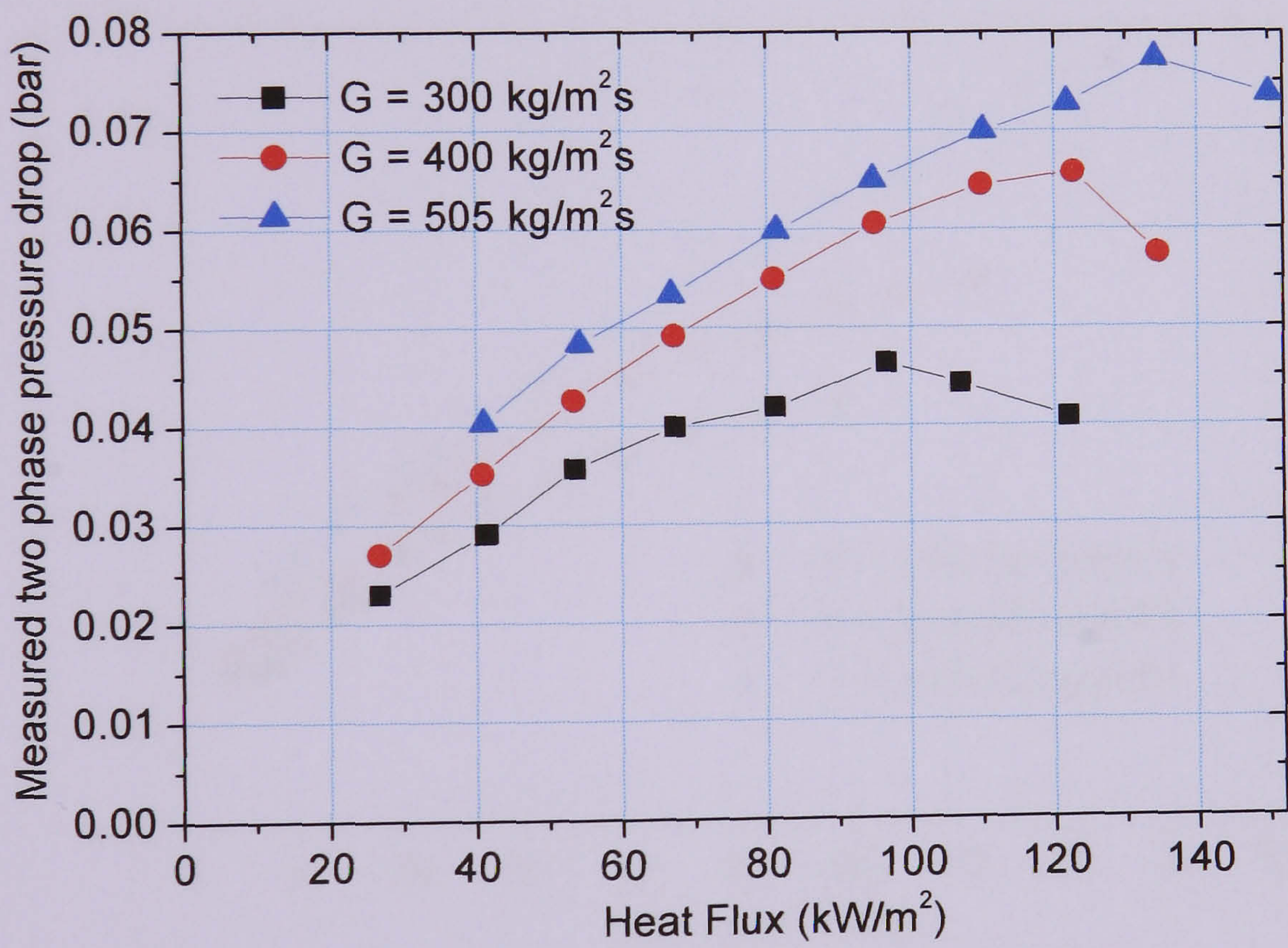
The total measured two phase pressure drop in the five tubes (4.26 – 0.52 mm internal diameter) is plotted in Figure 6.1, as a function of heat flux at 8 bar system pressure and various mass fluxes. As seen in the figure, the pressure drop increases almost linearly with heat flux. If we were to extend the lines in Figure 6.1 to the abscissa (quality, $x=0$), the total pressure drop value is expected to be approximately equal to the single-phase pressure drop, e.g. for the 4.26 mm tube the single phase values range from 0.015 – 0.025 bar. In figures 6.1 (b) and (c), for tubes with internal diameter (2.88 and 2.01 mm), the two phase pressure drop decreases at the highest heat fluxes. This is because of the fact that at high heat flux there was early dryout that begins at low quality as deduced from the heat transfer coefficient plots. Therefore, a significant time-share of the single phase vapour flow could be the reason for the decrease in two phase pressure drop at high heat flux. In the 0.52 mm tube, Figure 6.1 (e), a mass flux rang is given due to difficulties of maintaining a constant mass flux.



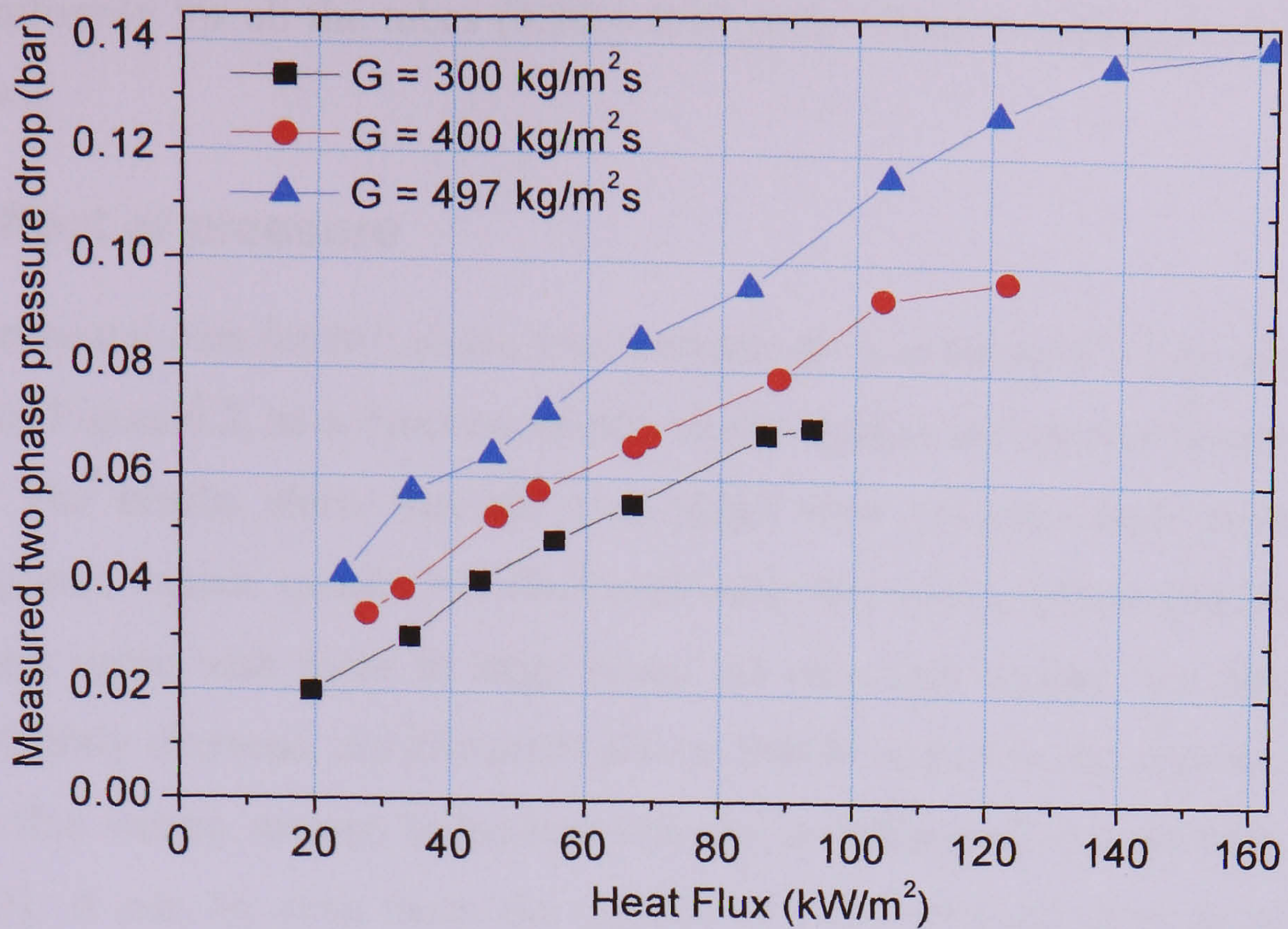
(a) $D = 4.26$ mm



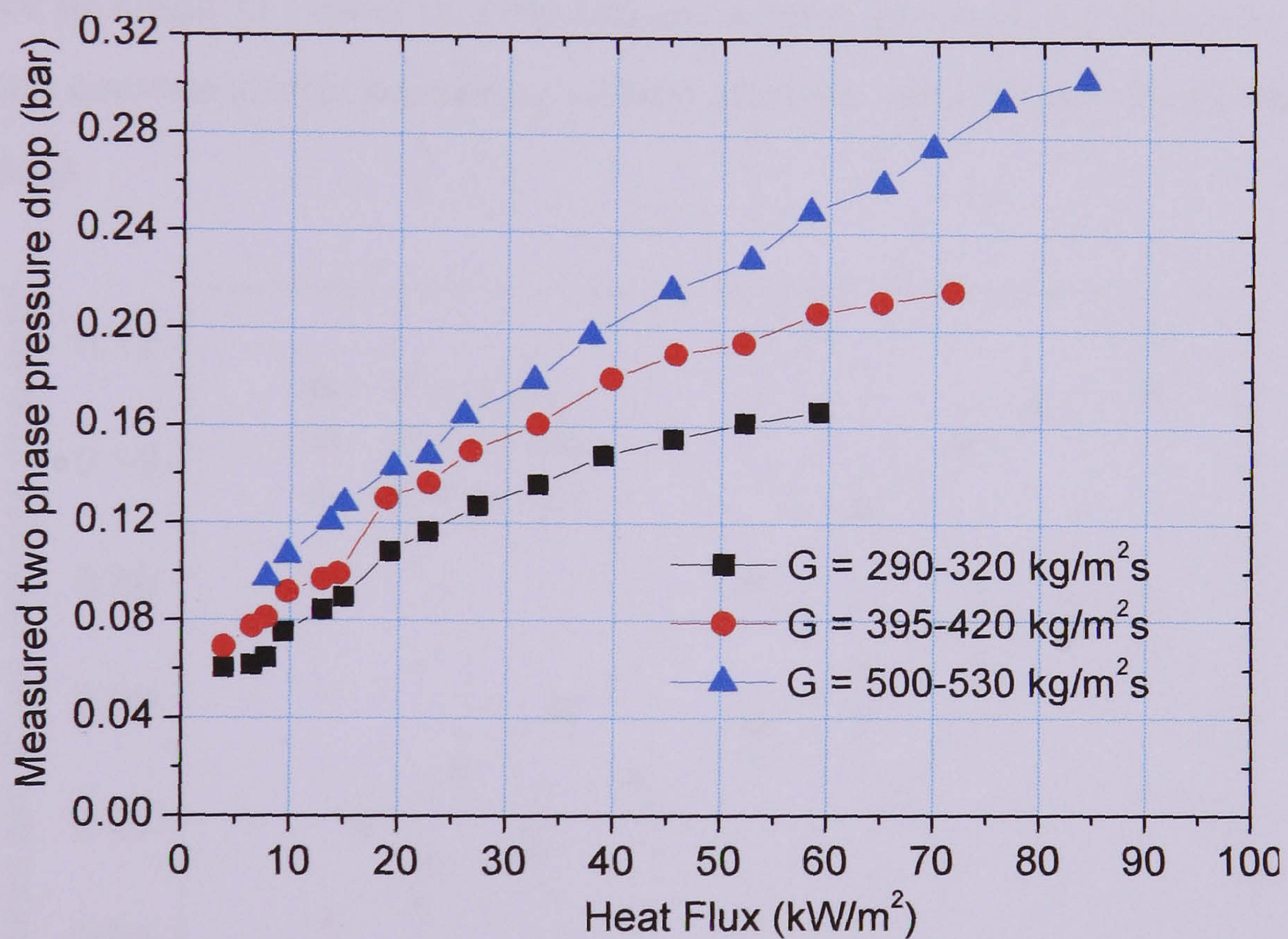
(b) D = 2.88 mm



(c) D = 2.01 mm



(d) $D = 1.1$ mm



(e) $D = 0.52$ mm

Figure 6.1 Effect of heat flux on the total measured two phase pressure drop at a system pressure of 8 bar and various mass fluxes for different internal tube diameters: (a) 4.26 mm, (b) 2.88 mm, (c), 2.01 mm, (d) 1.1 mm and (e) 0.52 mm

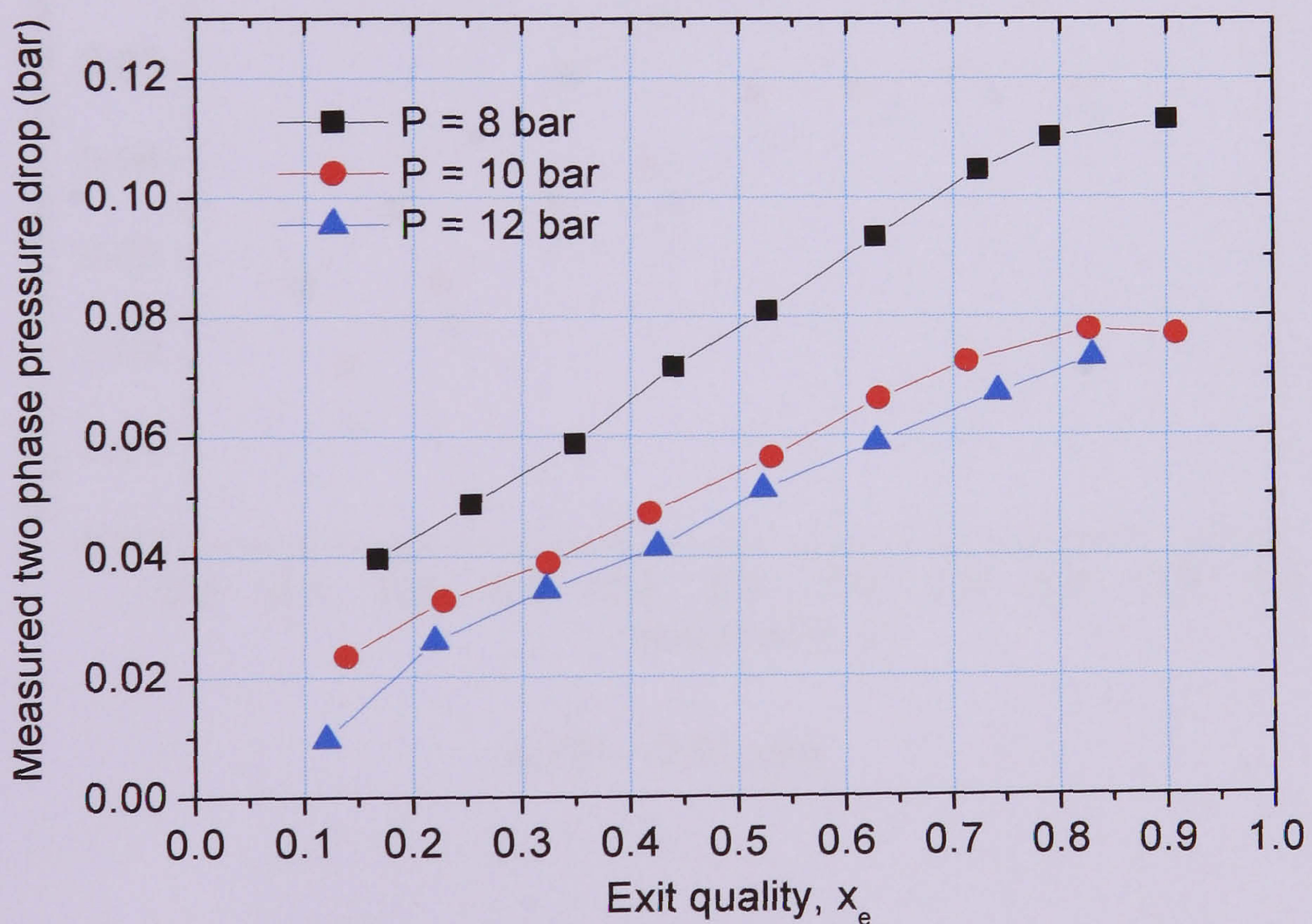
6.2.2 Effect of mass flux

The influence of changing the mass flux is also depicted in Figure 6.1 above. The results show that the two-phase flow pressure drop increases with increasing mass flux

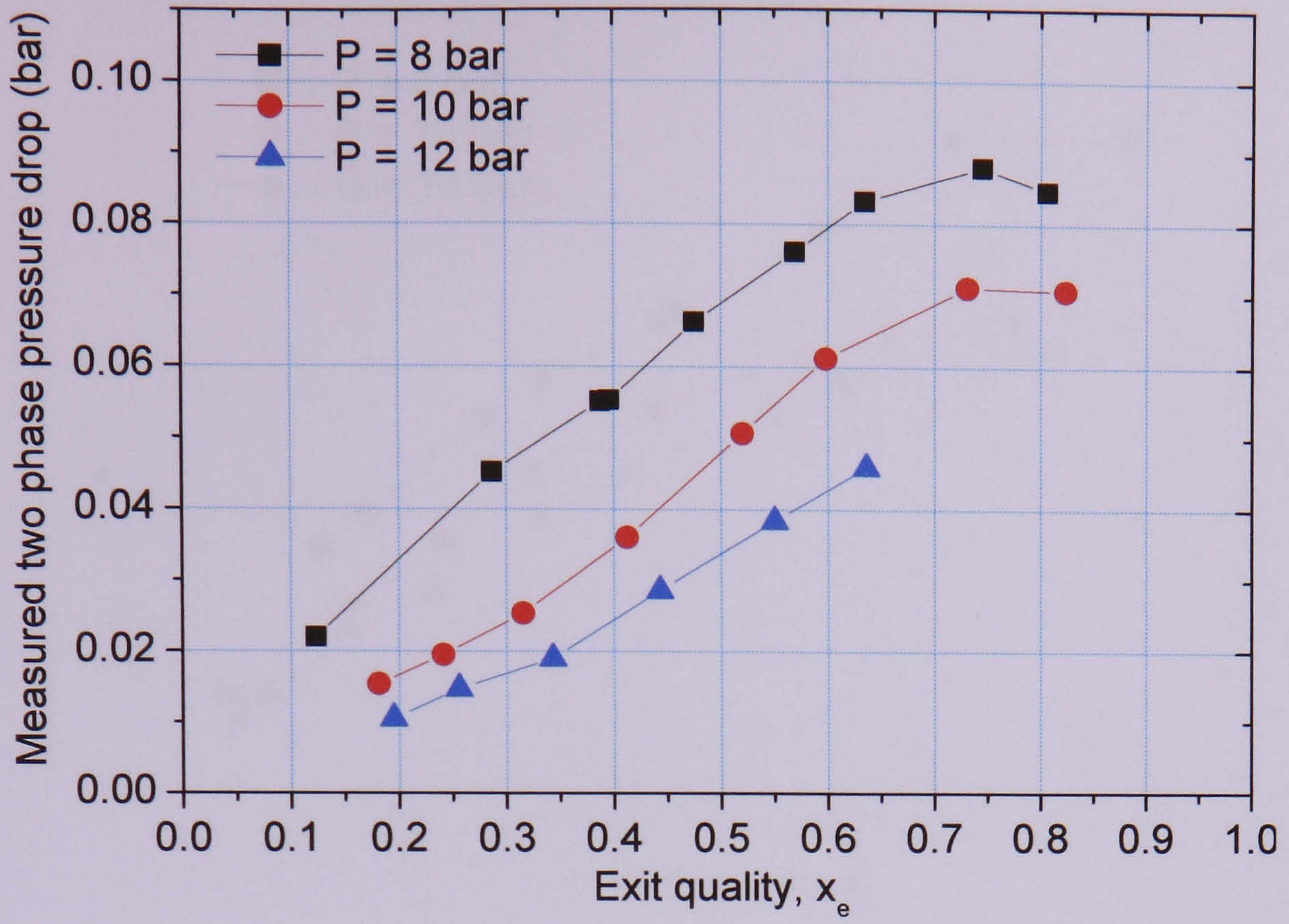
almost uniformly for all the tubes (4.26 – 0.52 mm). These trends agree with those in large tubes.

6.2.3 Effect of pressure

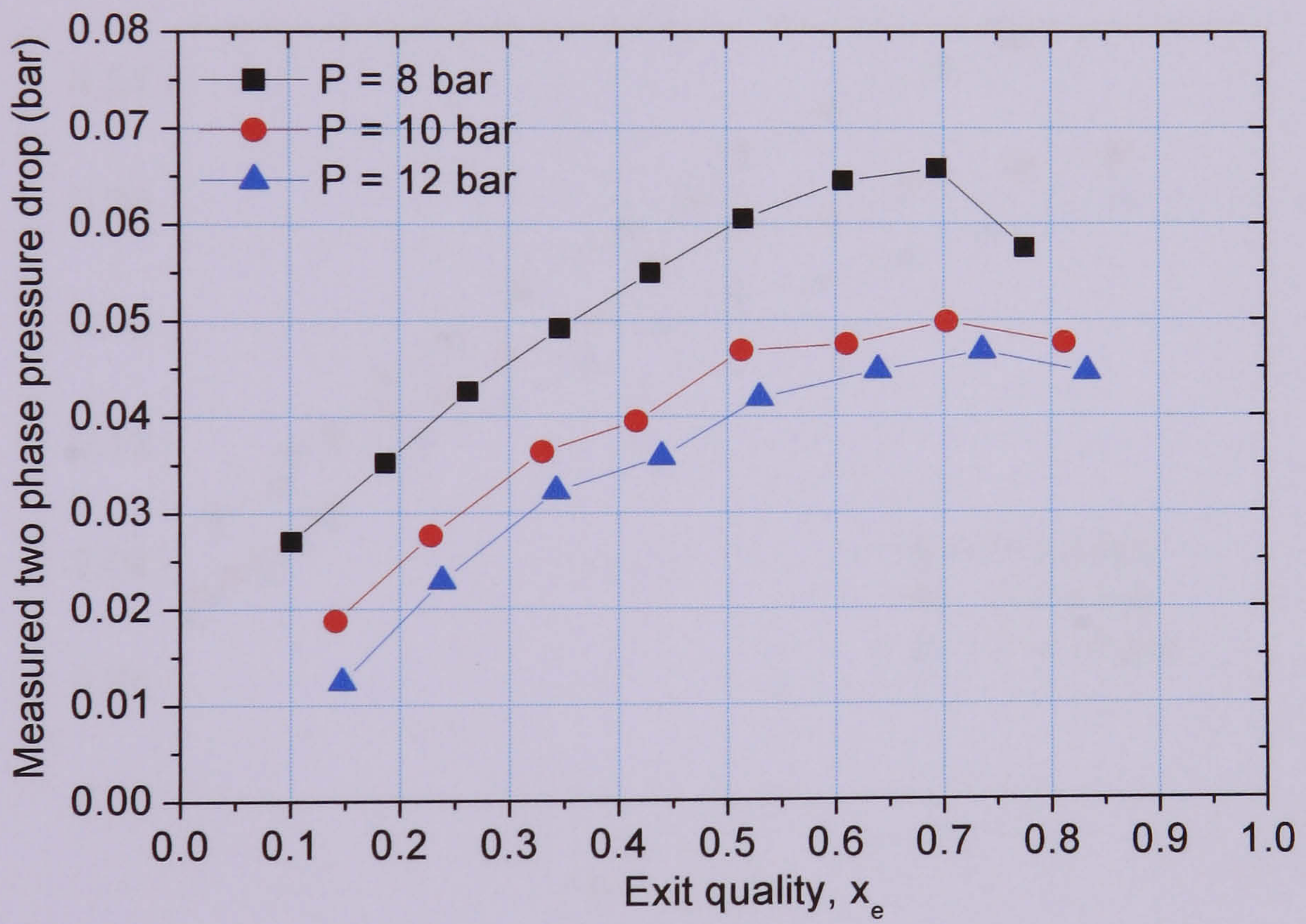
The experimental data for two phase total pressure drop in the 4.26 – 0.52 mm tubes are depicted in Figure 6.2, as a function of exit vapour quality for various values of system pressure. The results show that the two phase flow pressure drop increases with increasing exit vapour quality but decreases with increasing system pressure. Again, these trends agree with those in large tubes. At very high quality, the pressure drop tends to slightly decrease. As discussed above, this is related to the dryout obtained at high heat flux values, as seen in the heat transfer coefficient plots in section 5.2.1 (e.g. figure 5.3). It can be seen from the figures that the pressure drop is not linearly decreasing with increasing system pressure. This could be due to the non-linear dependence of liquid to vapour density ratio on system pressure. As shown in figure 6.3 density ratio decreases with increasing system pressure, which has a direct effect on the pressure drop.



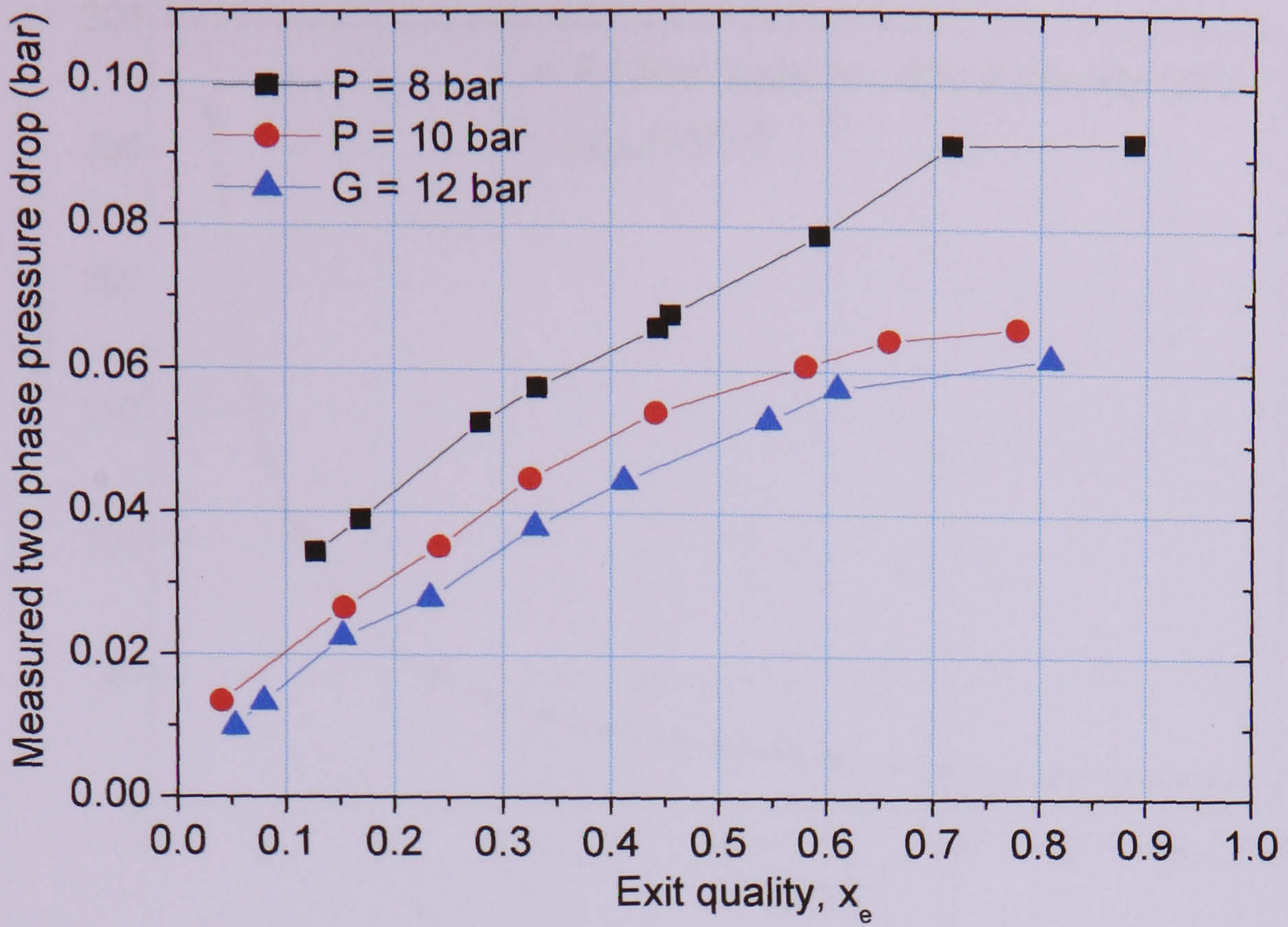
(a) $D = 4.26$ mm



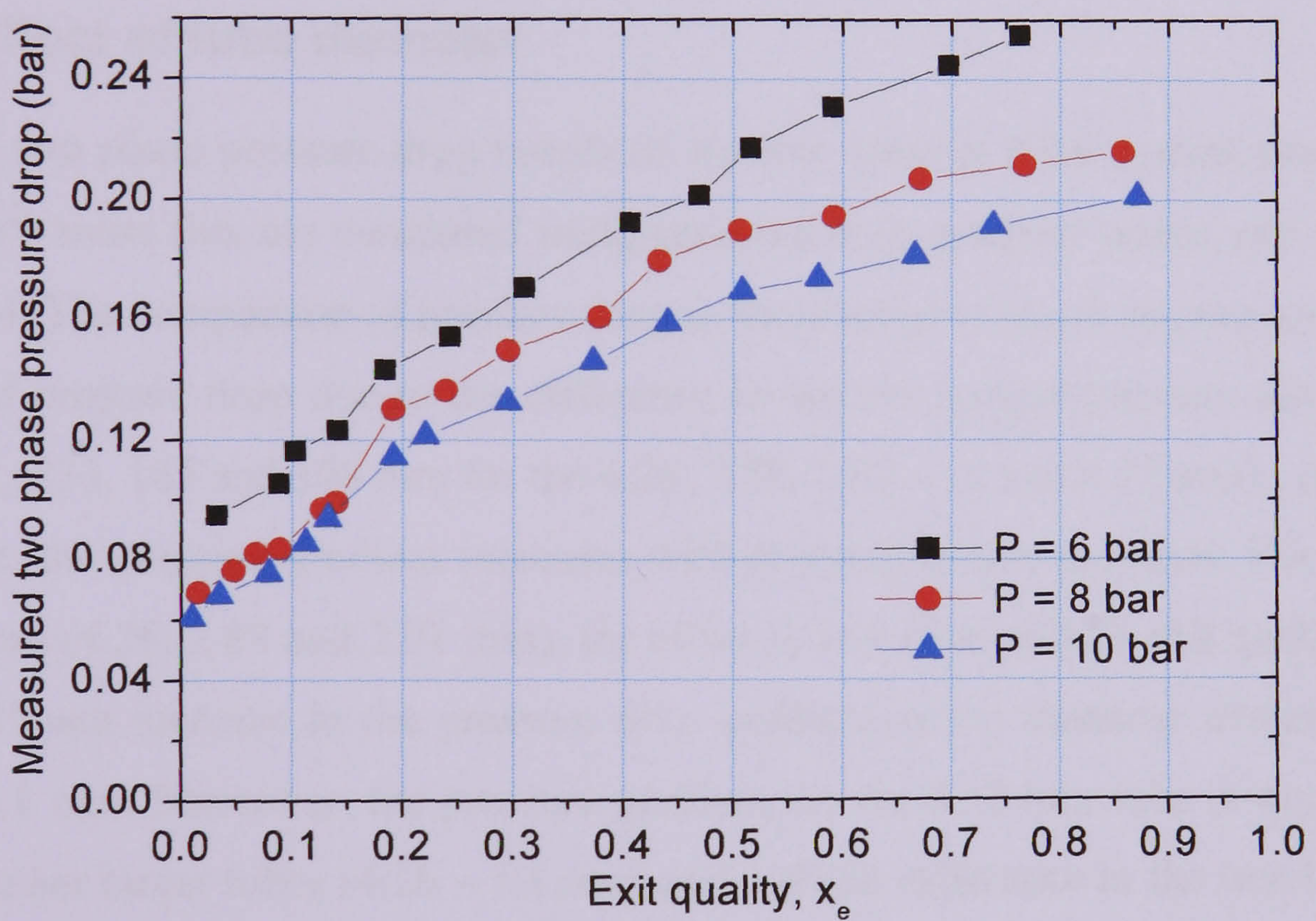
(b) $D = 2.88$ mm



(c) $D = 2.01$ mm



(d) $D = 1.1$ mm



(e) $D = 0.52$ mm

Figure 6.2 Effect of system pressure on the measured two phase total pressure drop at various system pressures and a mass flux value of $400 \text{ kg/m}^2\text{s}$ for different tube internal diameter: (a) 4.26 mm, (b) 2.88 mm, (c) 2.01 mm, (d) 1.1 mm and (e) 0.52 mm.

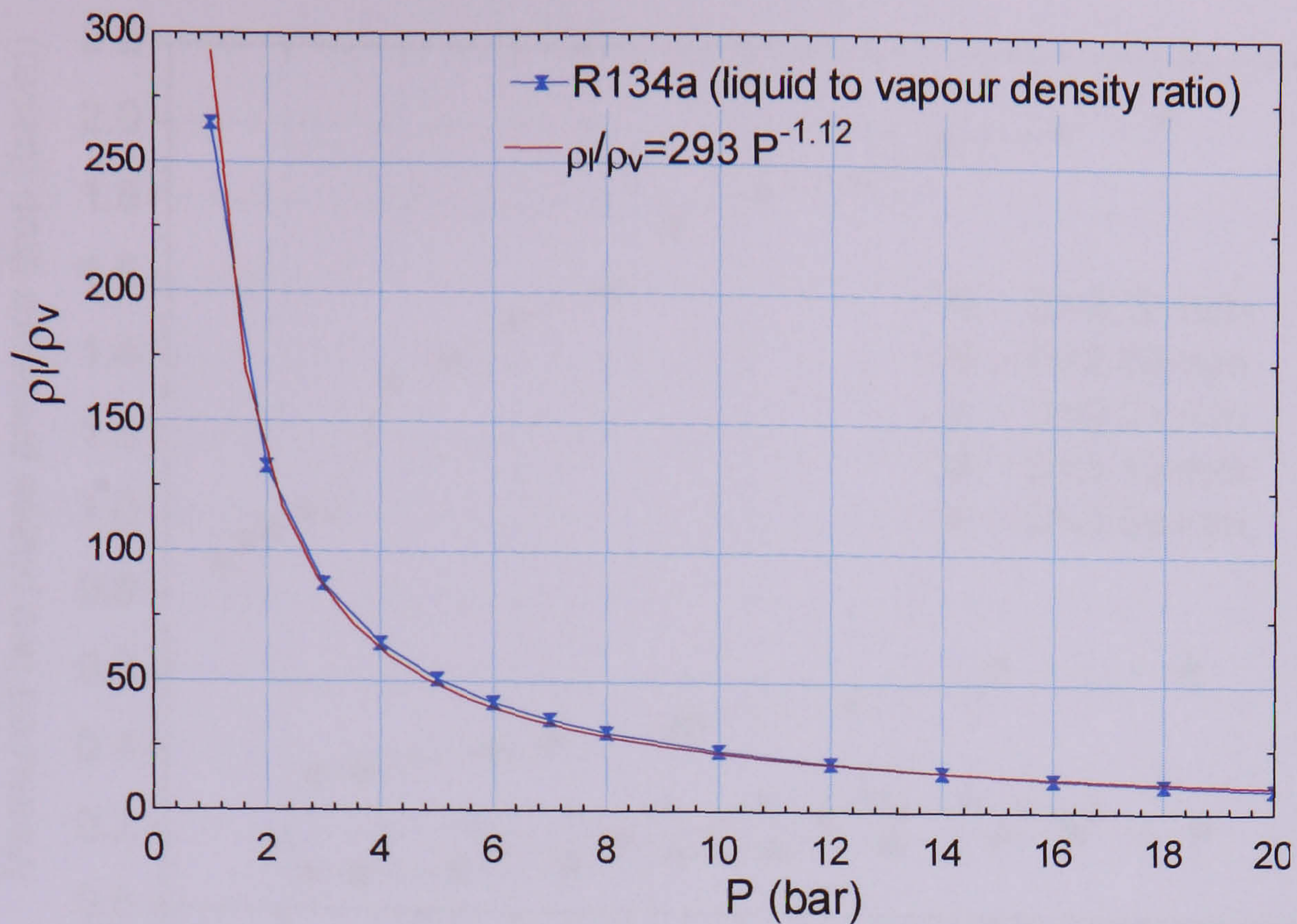


Figure 6.3 Effect of system pressure on liquid to vapour density ratio for R134a

6.2.4 Effect of tube diameter

The total two phase pressure drop results of the five tubes at 8 bar system pressure and $400 \text{ kg/m}^2\text{s}$ mass flux are compared using pressure drop gradient versus exit quality in Figure 6.4. The comparison of pressure drop in these tubes is based on pressure gradient instead of pressure drop due to the difference in the test section pressure drop lengths (521, 321, 233, 165 and 108 mm for the 4.26, 2.88, 2.01, 1.1, and 0.52 mm). As seen in the figure, the pressure gradient increases with decreasing tube diameter. For the three larger tubes (4.26, 2.88 and 2.01 mm), the effect is less clear at high exit quality. There is a significant increase in the pressure drop gradient as the diameter decreases from 2.01 to 1.1 mm. Moreover, the pressure gradient for the 0.52 mm tube is much higher than the other larger tubes (4.26 – 1.1 mm) and a slight difference in the trend with exit quality is also shown, i.e. it indicated two distinct trends below and above exit quality of about 0.18. These two groups of different behaviour were also observed in the heat transfer plots and were discussed in chapter 5. It is worth to reminding that the single phase friction factor for the 0.52 mm tube presented in Chapter 4 (figure 4.15) was much higher than the commonly used correlations (Blasius, 1913 and Haaland, 1983) in the turbulent region and $(16/Re)$ in the laminar region. Also, the preliminary results of surface roughness measurement from Hannover University indicated non-uniformity in the channel cross-section.

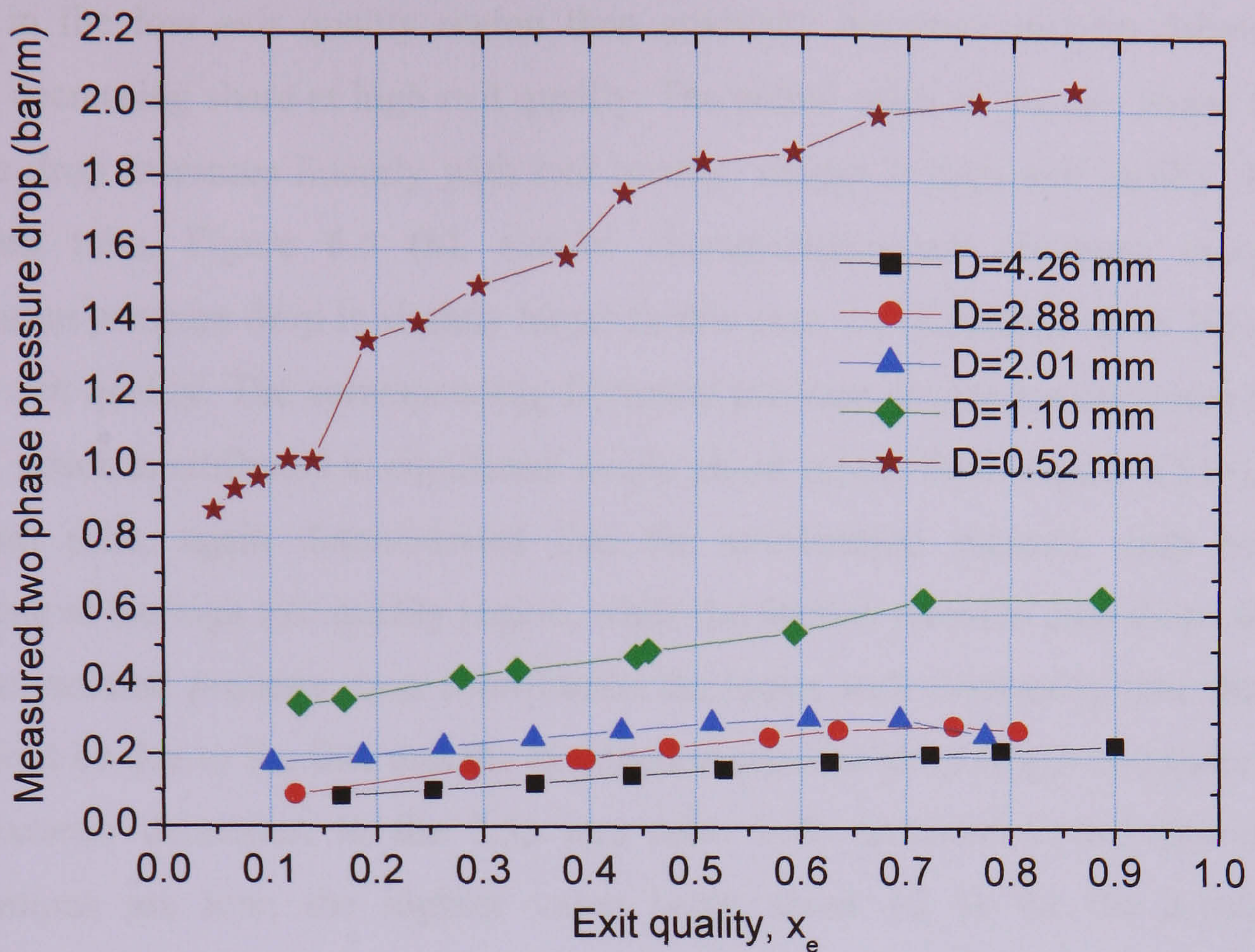


Figure 6.4 Effect of tube internal diameter on two phase total pressure drop gradient as a function of exit quality at 8 bar system pressure and $400 \text{ kg/m}^2\text{s}$ mass flux.

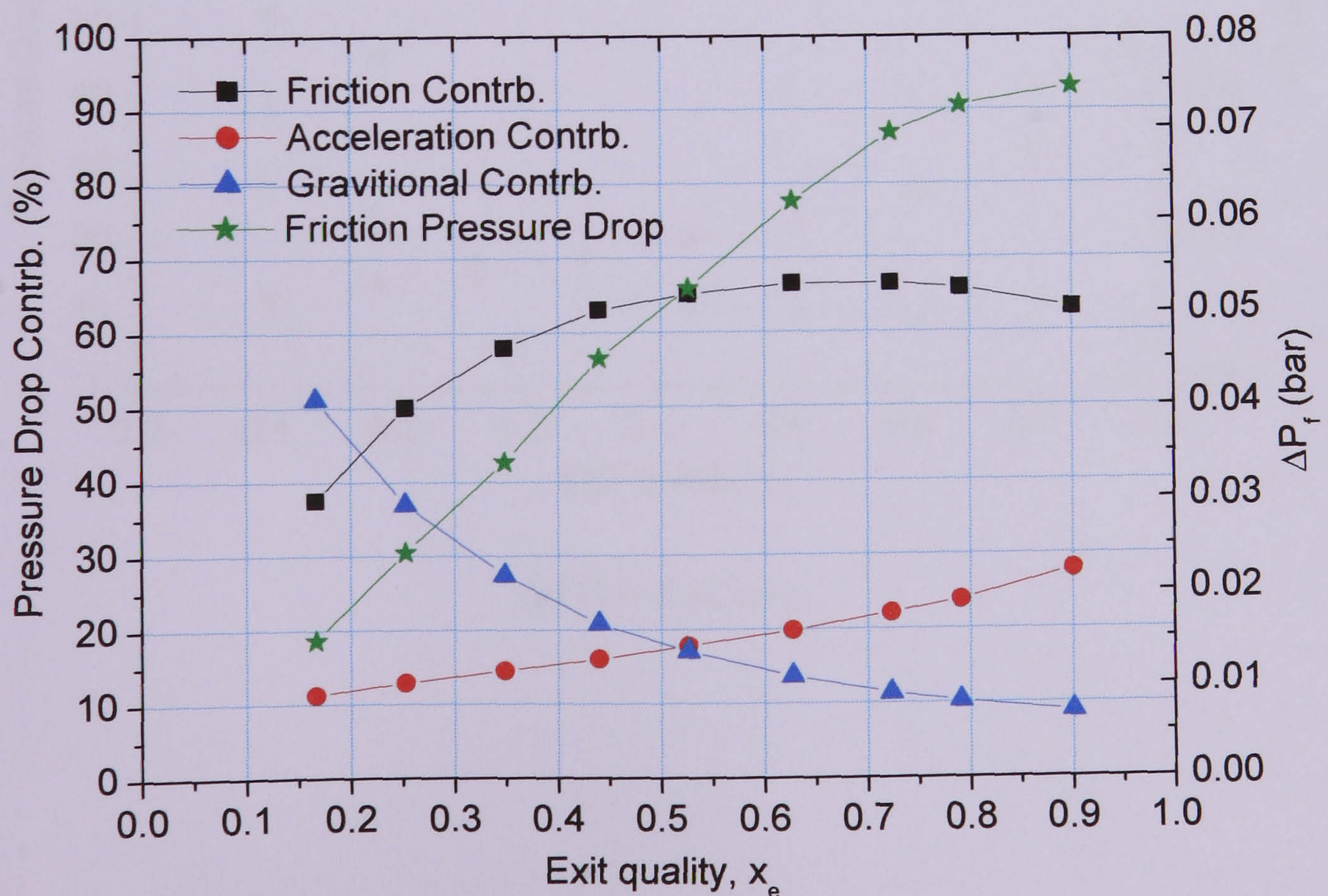
6.2.5 Contributions of the three pressure drop components

As discussed in section 4.5.2, the two phase total pressure drop is comprised of three main components: acceleration, gravity and friction pressure drops. The contributions from these components to the total measured two phase pressure drop in the five tubes are depicted in Figure 6.6, for a mass of $400 \text{ kg/m}^2\text{s}$ and 8 bar system pressure. The separated flow model was employed to calculate the acceleration and gravitational pressure drops (see equations 4.29 and 4.30), while the friction contribution is subtracted from the total measured value. The void fraction used to evaluate the acceleration and gravitational pressure drops is given in Eq. (6.1), which was obtained by applying the Lockhart-Martinelli two phase multiplier relation to the annular flow, see Collier and Thome (1994).

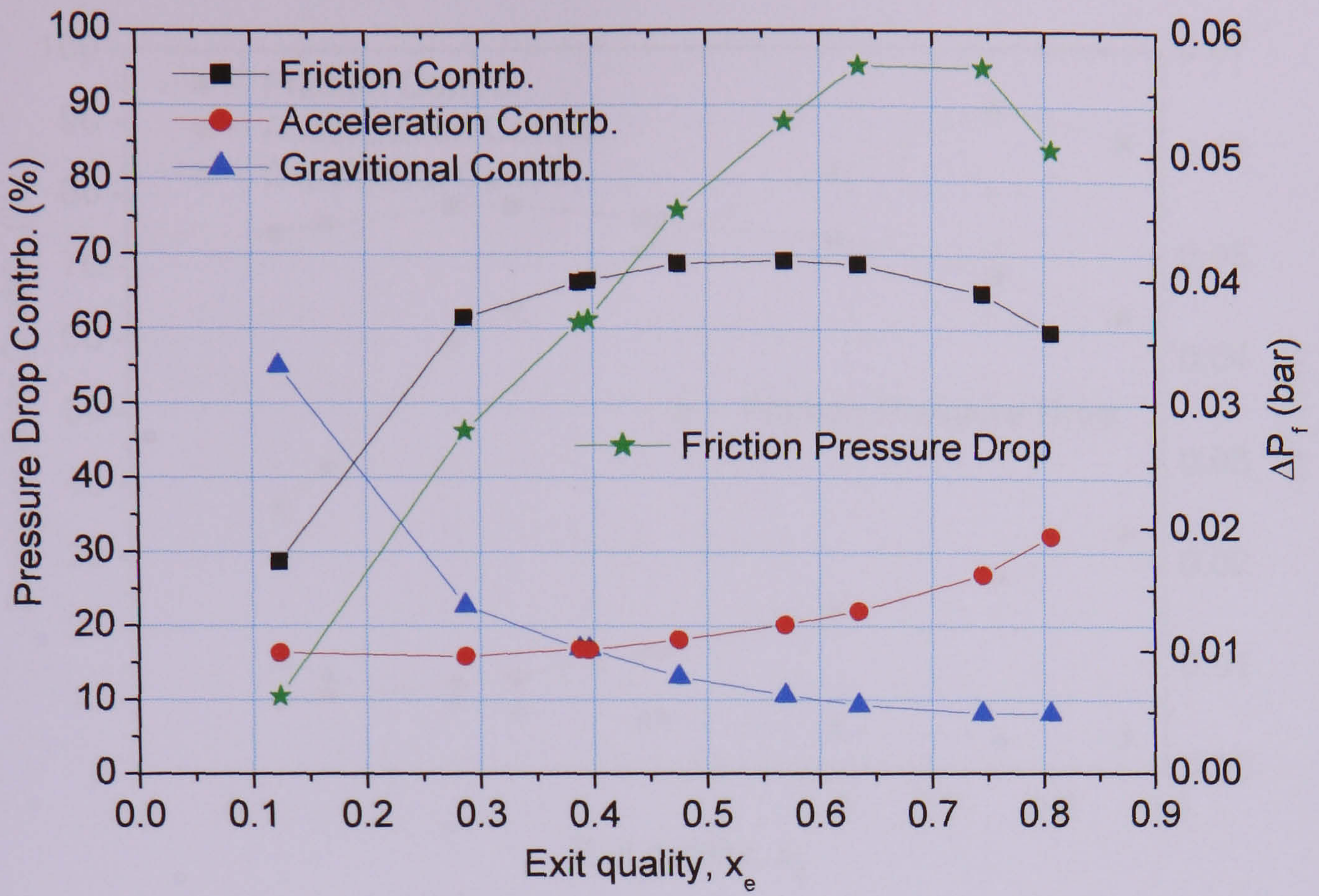
$$\varepsilon = 1 - \frac{1}{\phi_l} \quad (6.1)$$

In Figure 6.7 (a), for the 4.26 mm, there is non-linear decrease in the share of the gravitational contribution from 50 % to about 10 % of the total value, while the corresponding acceleration contribution increased from 10 to 20 % with increasing quality. On the other hand, the frictional pressure drop contribution increases with

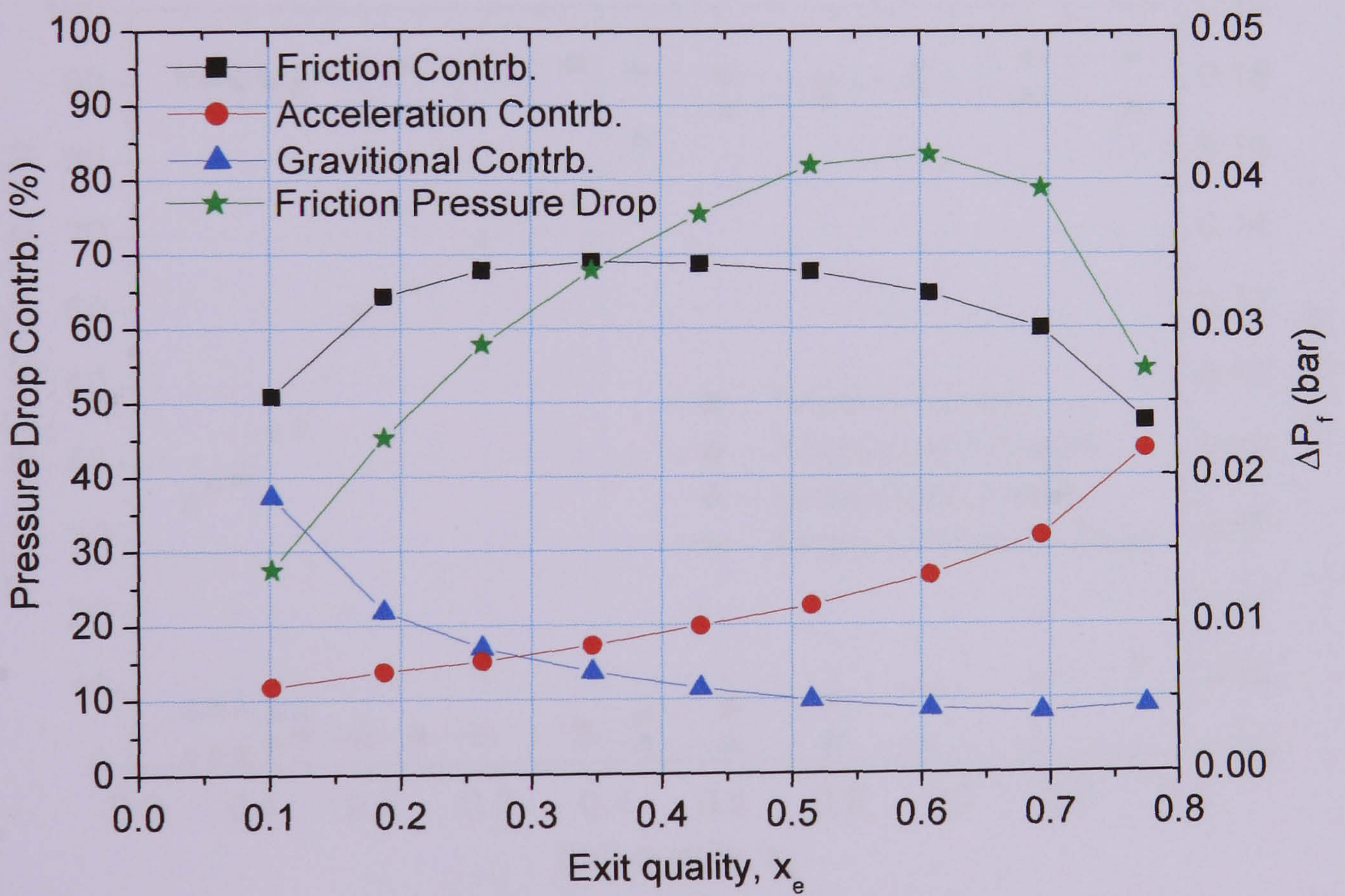
quality in the low exit quality region then gradually becomes uniform followed by slightly decreasing share at high exit quality. The actual value of the two phase friction pressure drop increases linearly with exit quality, except at high exit quality. For the 2.88 mm tube, Figure 6.5 (b), similar characteristics are observed except the acceleration pressure drop is slightly larger in this case, i.e. it reaches up to 30% at the highest exit quality. The corresponding frictional pressure drop value decreases at high quality, which is attributed to significant single phase vapour flow. Figure 6.5 (c), in the 2.01 mm tube, again demonstrated that the acceleration pressure drop becomes significant at the high exit quality region, while the friction pressure drop drops sharply. The gravitational pressure drop contribution decreases with decreasing tube diameter. This could be due to the fact that the test section pressure drop length is smaller as the tube diameter decreases. In the 0.52 mm tube, both acceleration and gravitational contributions are low, the highest value being about 12 % for the acceleration contribution. The fact that the single phase friction factor of this tube was much higher than larger tubes makes its frictional pressure drop contribution highly significant. Besides, there was no similar dryout phenomena observed in the smallest tube as that of the larger tubes. This could also be another reason for lower acceleration contribution compared with the other tubes (4.26 – 1.1 mm).



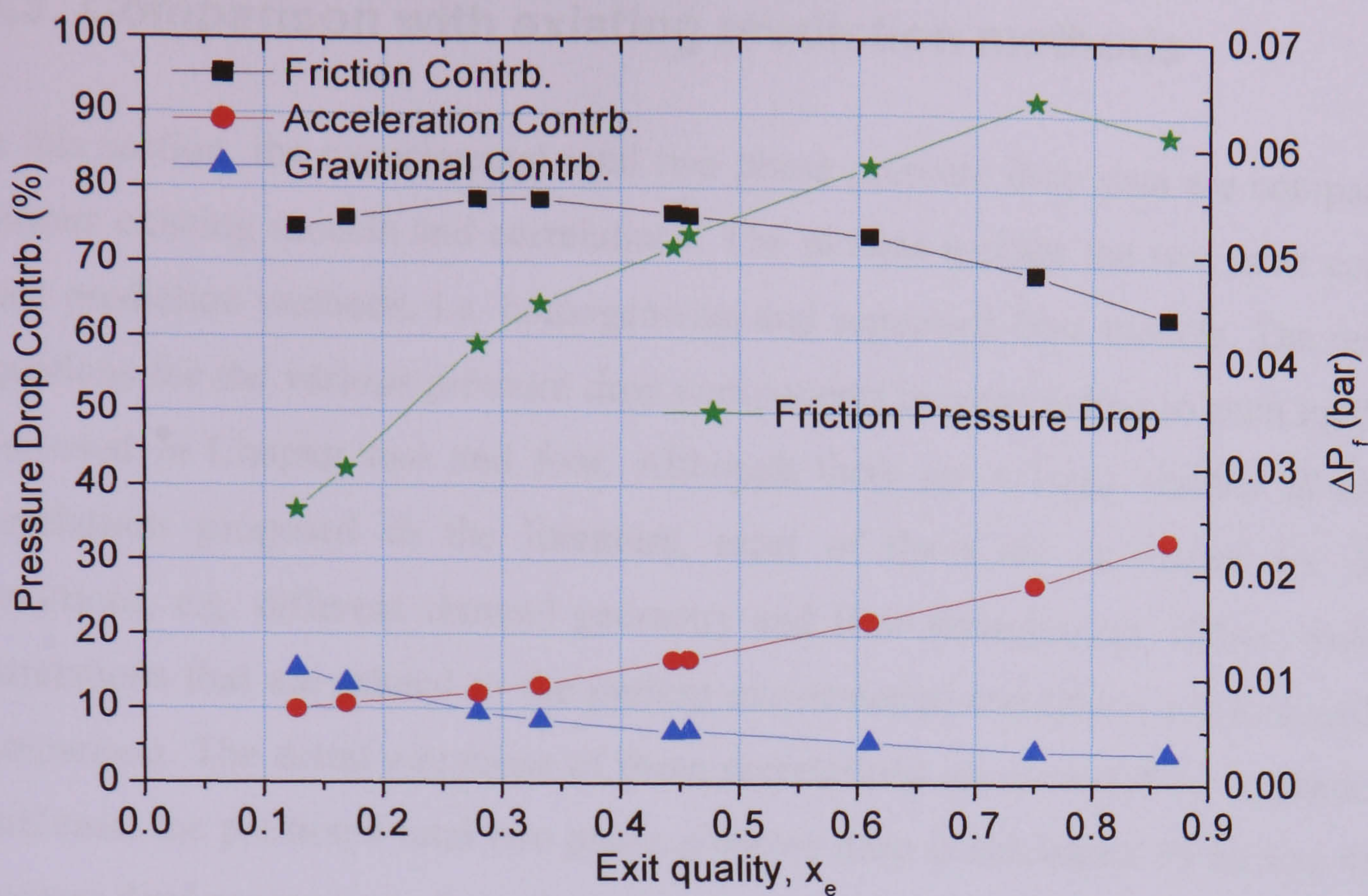
(a) $D = 4.26$ mm



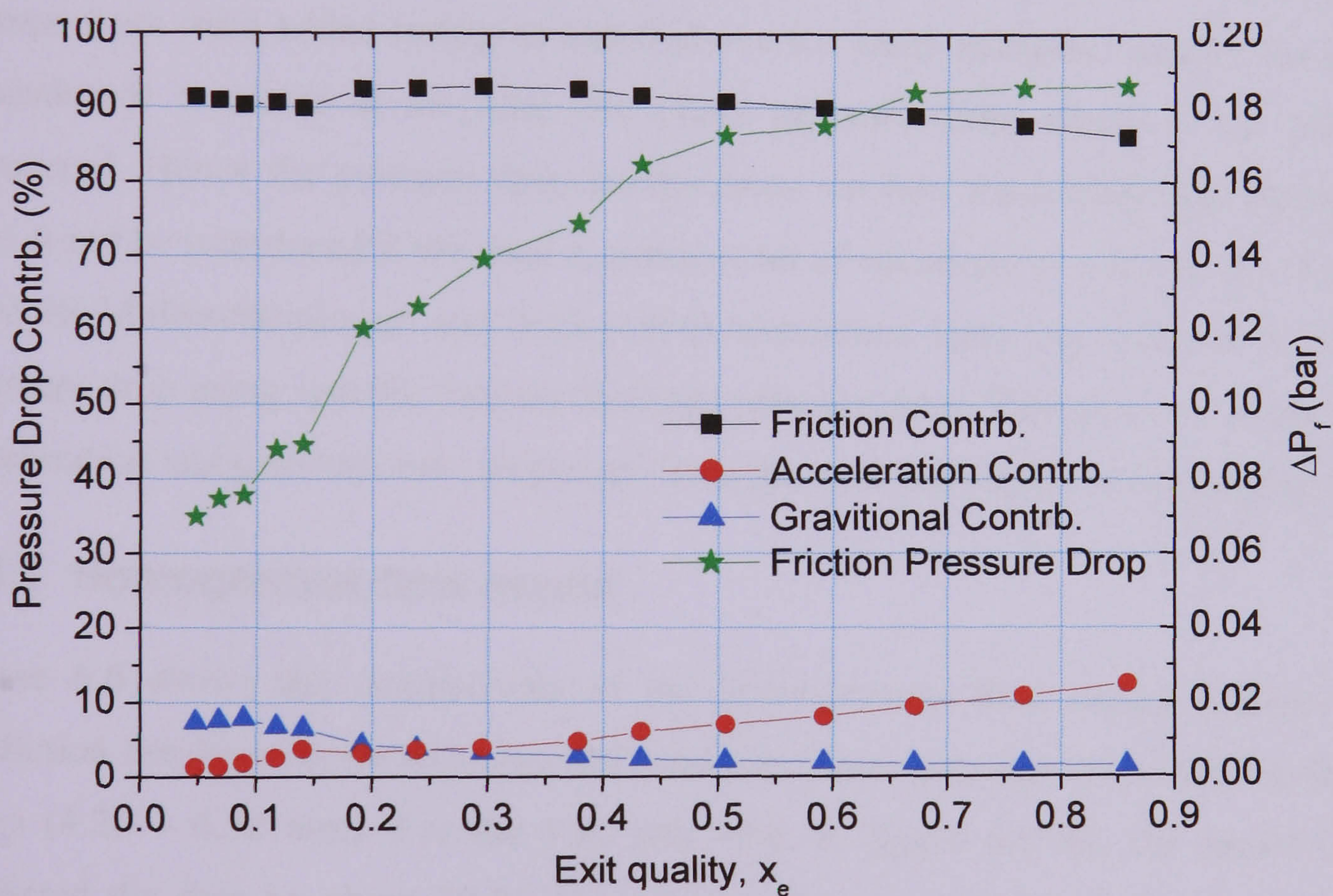
(b) $D = 2.88$ mm



(c) $D = 2.01$ mm



(d) $D = 1.1$ mm



(e) $D = 0.52$ mm

Figure 6.5 Contribution percentages from the three pressure drop components to the total measured value and the deducted friction pressure drop component at a mass flux of $400 \text{ kg/m}^2\text{s}$ and 8 bar system pressure for different tube diameters: (a) 4.26 mm, (b) 2.88 mm, (c) 2.01 mm, (d) 1.1 mm and (e) 0.52 mm.

6.3 Comparison with existing prediction methods

In this section, the experimental total two phase pressure drop data are compared with various existing models and correlations. The models include the two most commonly used prediction methods, i.e. homogeneous and separated flow models. The respective equations for the various pressure drop components corresponding to each model were discussed in Chapter two and four. Although there are a large number of empirical correlations proposed in the literature, most of them are developed for different conditions, e.g. different channel geometry and flow arrangement. Hence, only a few correlations that are related to the present experimental conditions are included in the comparison. The detail equations of these correlations are included in Appendix D. In each case, the predicted total two phase pressure drop is calculated by adding the three pressure drop components from the respective model or correlations. In other words, for the correlation that predict the frictional pressure drop, the acceleration and gravitational components were added (using as stated above the same relations used by the authors considered) to arrive at the total two phase pressure drop, which is the value we measured. Hence the pressure drop comparisons are free from additional discrepancy that could be introduced if we used a common set of equations to convert. An exception is to the Muller-Steinhagen and Heck (1986) correlation. Here they reported the friction pressure drop using specific data on frictional pressure drop. Therefore, we deducted the acceleration and gravitational component from the total measured for this comparison.

6.3.1 Homogenous flow model

Figure 6.6 shows the comparisons of the homogeneous flow model pressure drop prediction results with the experimental total two phase pressure drop data for the five tubes (4.26 – 0.52 mm). For the 4.26 mm tube, in figure 6.6 (a), the model under-predicted the data by about 30 %. However, it also over-predicted the data when the pressure drop is less than about 0.03 bar. Similarly and as seen in Figures 6.6 (b) – (d), for the three tubes (2.88 – 1.1 mm), the experimental data are mostly under-predicted within 30%, although better prediction is obtained for the lower pressure drop values. In general, when the tube diameter decreases, the homogeneous model predicts the experimental data slightly better. However, as seen in figure 6.6 (e), the 0.52 mm tube results are under-predicted by much more than 30%.

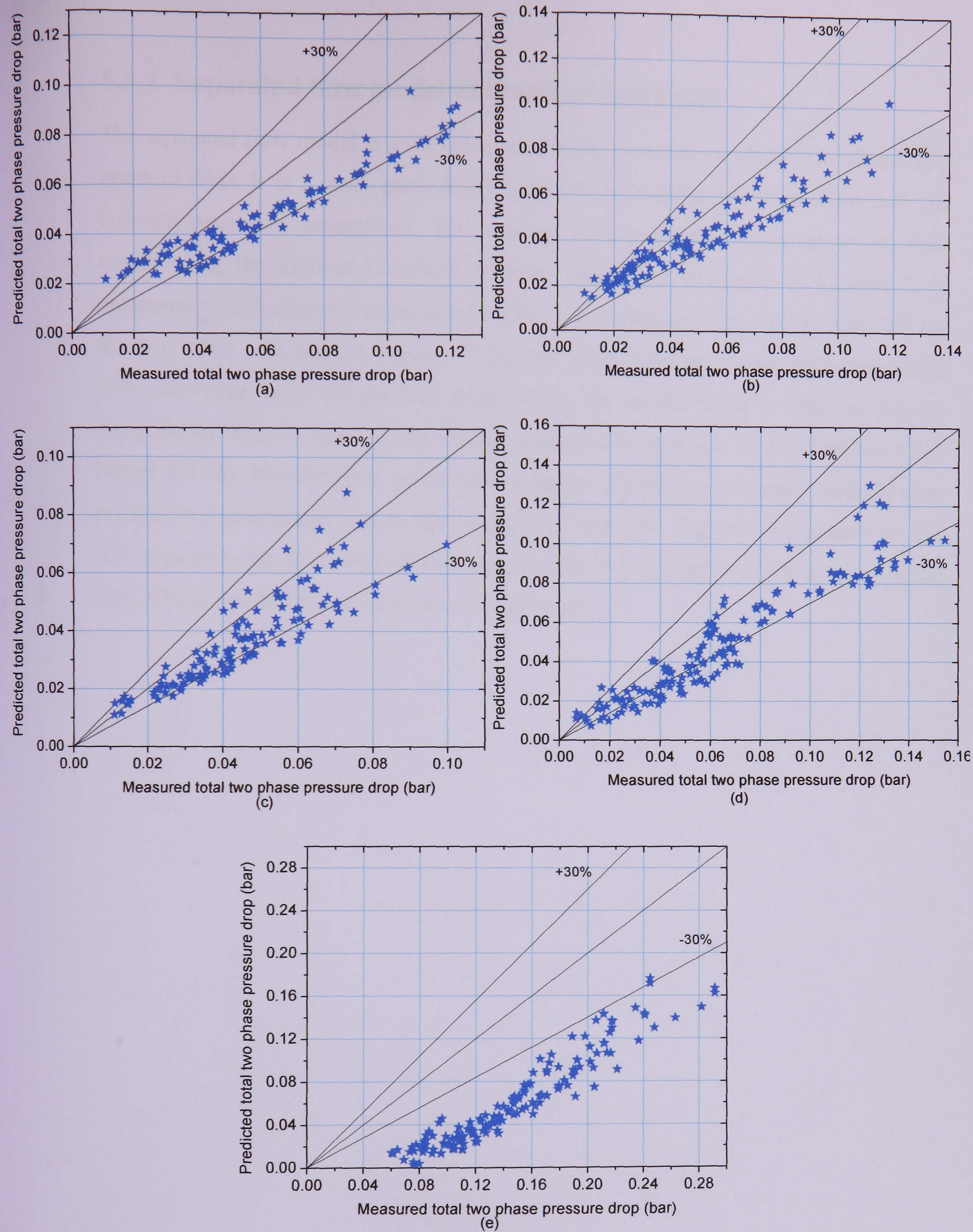


Figure 6.6 Comparison with the homogeneous flow model pressure drop for different tube diameters: (a) 4.26 mm, (b) 2.88 mm, (c) 2.01 mm, (d) 1.1 mm and (e) 0.52 mm

6.3.2 Separated flow model of Lockhart-Martinelli

The separated flow model is quite often used in the literature to predict two phase flow pressure drop. It is a more generalised approach of treating two phase flow than the homogeneous flow assumption. The pressure drop predicted by the separated flow model using the Lockert-Martinelli relation, which was discussed in Chapter 2, is compared with the present experimental data. The results are depicted in Figure 6.7 for the five tubes. As seen in Figure 6.7 (a), the larger tube results are predicted within 30%. However, at lower pressure drop values, the model tends to over predict the experimental data. A more or less similar prediction is observed for the 2.88 mm tube, Figure 6.7 (b). Nevertheless, as the tube diameter decreases, the model tends to over predict the experimental data except for the 0.52 mm tube. Figure 6.7 (e), again for the 0.52 mm tube, the experimental data is under-predicted in some cases by much more than 30% at low and moderate pressure drop values.

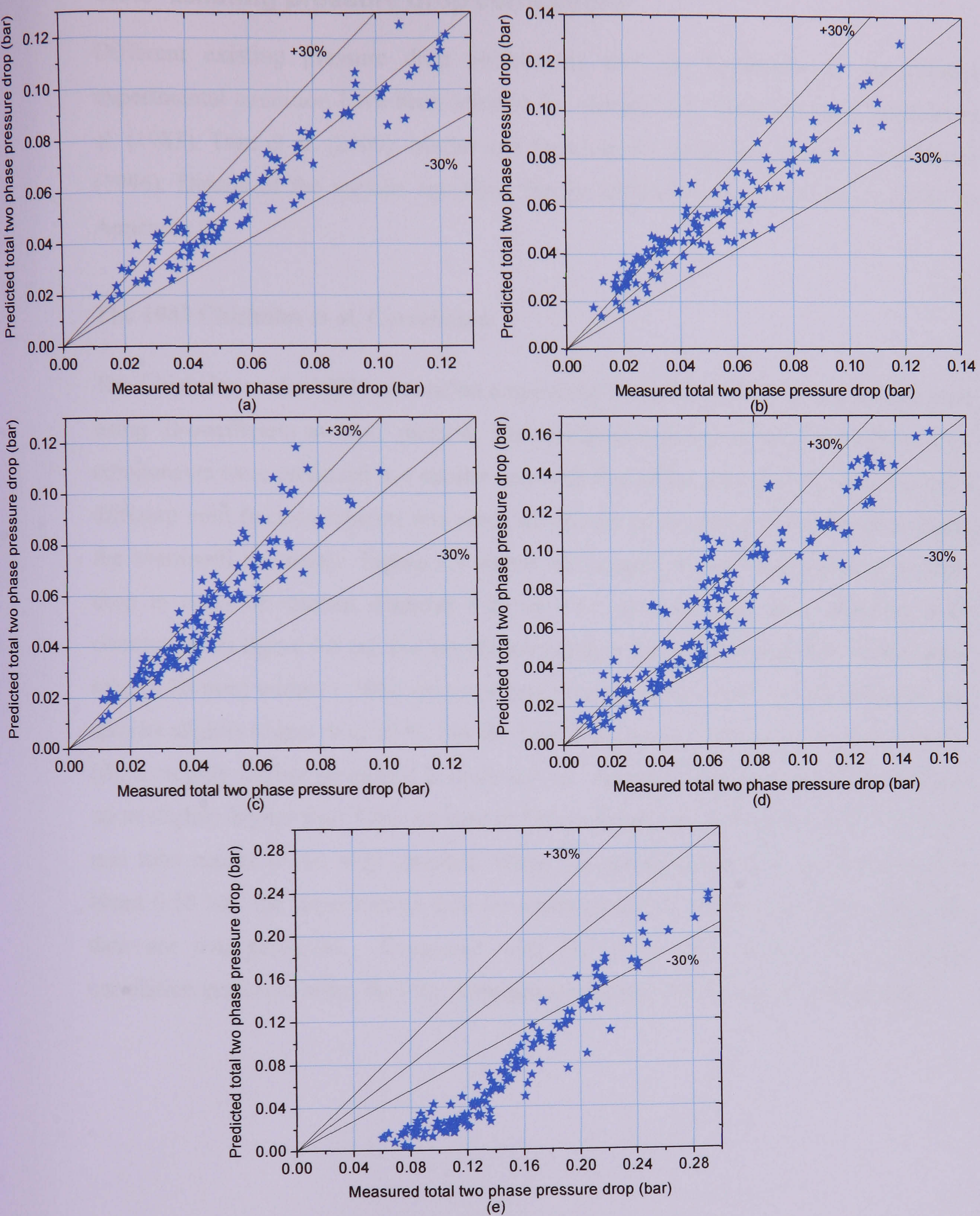


Figure 6.7 Comparison with the separated flow model pressure drop for different tube diameters: (a) 4.26 mm, (b) 2.88 mm, (c) 2.01 mm, (d) 1.1 mm and (e) 0.52 mm

6.3.3 Existing pressure drop correlations

Different existing pressure drop correlations that are applicable to the present experimental condition have been selected for comparison. These include Chisholm et al. (1983), Tran et al. (2000), Muller and Steinhagen (1986), and Mishima and Hibiki (1996). Details of the various equations for the different correlations are included in Appendix D.

The 1983 Chisholm et al. Correlation

The Chisholm et al. (1983) correlation empirically formulated the friction pressure drop using 'B-coefficient method' method. The acceleration and gravitational pressure drop components were predicted in a similar way with that of the separated flow model, but a different void fraction relation was used, which was proposed by Chisholm et al. using the Martinelli parameter. Figure 6.8 shows the comparisons of experimental pressure drop in tubes of internal diameter 4.26 to 0.52 mm tube with the Chisholm et al. correlation. In figure 6.8 (a), the correlation predicts the experimental data of the larger tube (4.26 mm) within $\pm 30\%$, except at low pressure drop, where it over predicted the data by slightly higher than 30 %. For the 2.88, 2.01, and 1.1 mm tubes, Figures 6.8 (b)-(d), a roughly similar prediction is observed, i.e. the correlation over-predicted the data up to slightly higher than 30%. As seen in Figure 6.6(e), the prediction trend of the 0.52 mm tube results is not well matched. When the measured pressure drop is less than about 0.18 bar, the experimental data are under-predicted, while beyond this value the data are over-predicted. Compared with the above two models, the Chisholm correlation performs better than the homogeneous model for the larger tubes studied.

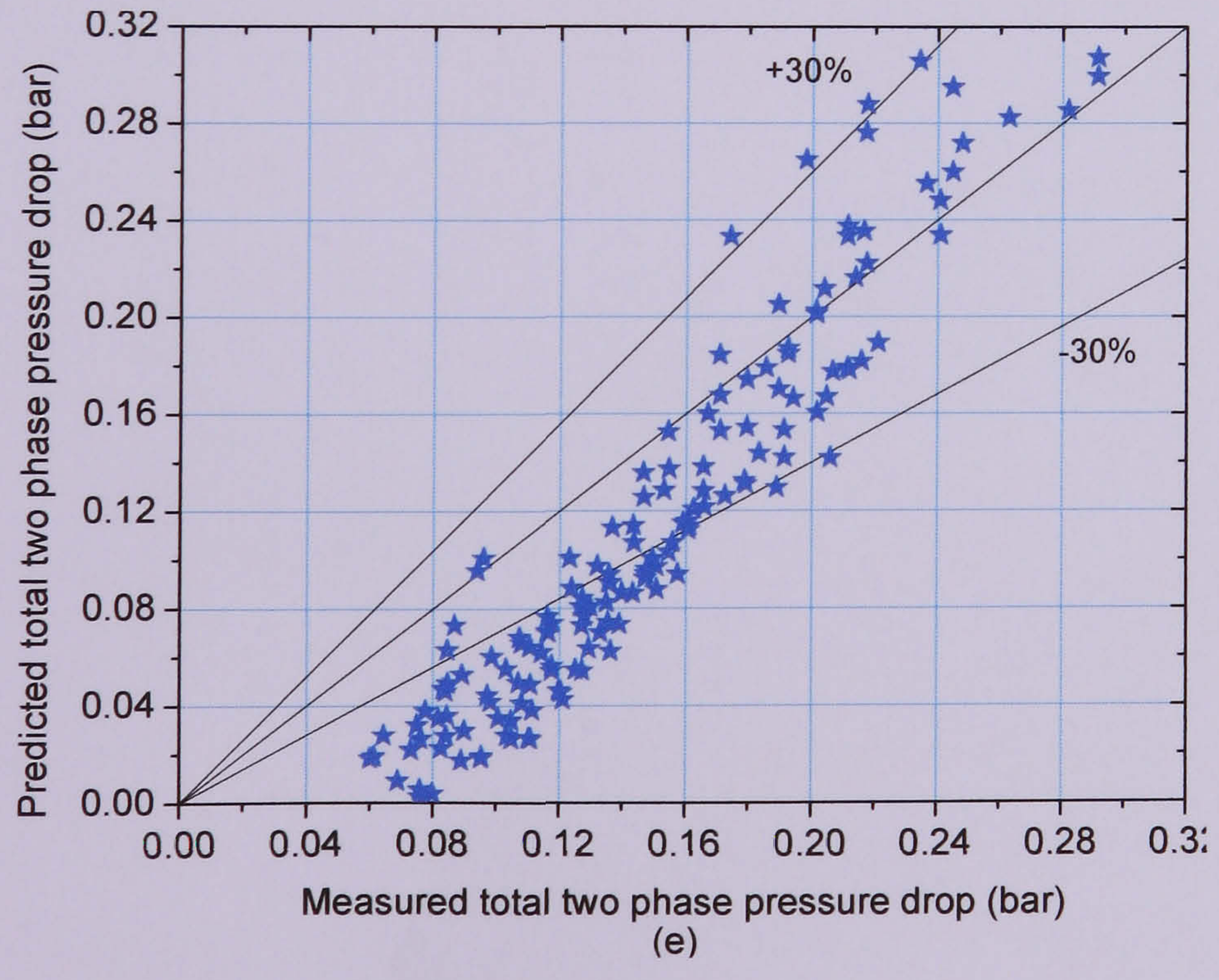
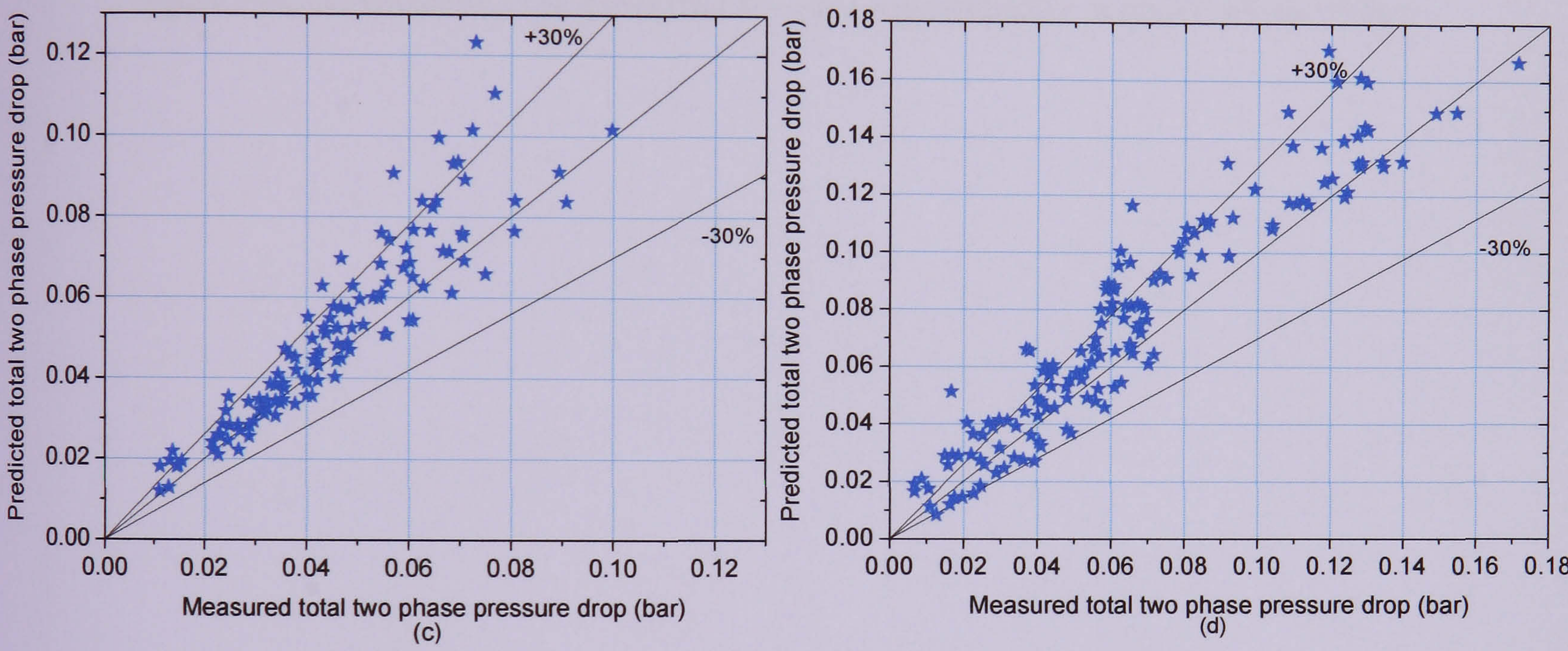
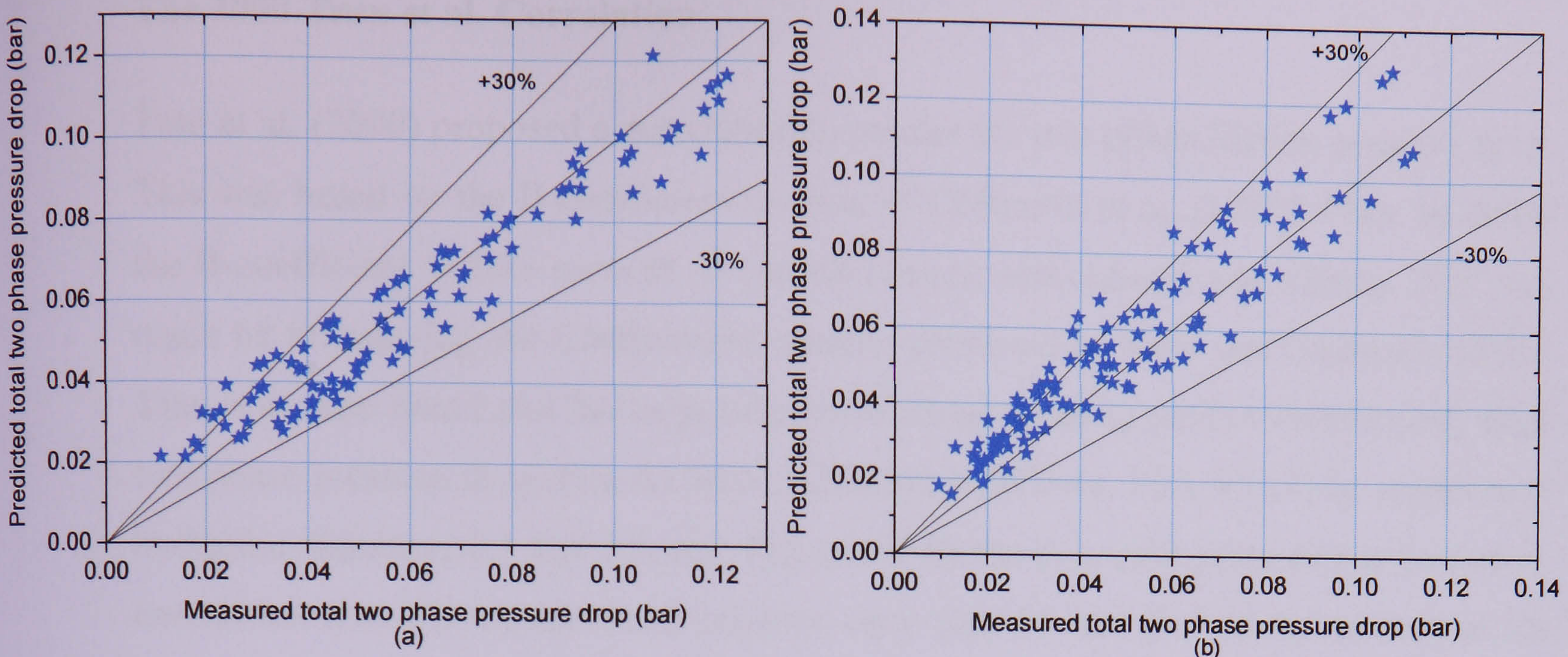


Figure 6.8 Comparison with the Chisholm et al. (1983) pressure drop correlation for different tube diameters: (a) 4.26 mm, (b) 2.88 mm, (c) 2.01 mm, (d) 1.1 mm and (e) 0.52 mm.

The 2000 Tran et al. Correlation

Tran et al. (2000) proposed a correlation to predict the two phase friction pressure drop. This was based on the B-coefficient method of Chisholm et al. (1983). They modified the B-coefficient to take account of surface tension and channel size effects. This was made by introducing the Confinement number proposed by Kew and Cornwell (1995). Tran et al. also found that the large tube correlations failed to predict satisfactorily their two-phase pressure drop data for three refrigerants (R134a, R12, R113) in channels of hydraulic diameters 2.5 and 2.9 mm. Figure 6.9 shows the comparison of the Tran et al. correlation with the experimental pressure drop data for the five tubes. As seen in the figure, the correlation over predicted the data significantly high for all the tubes.

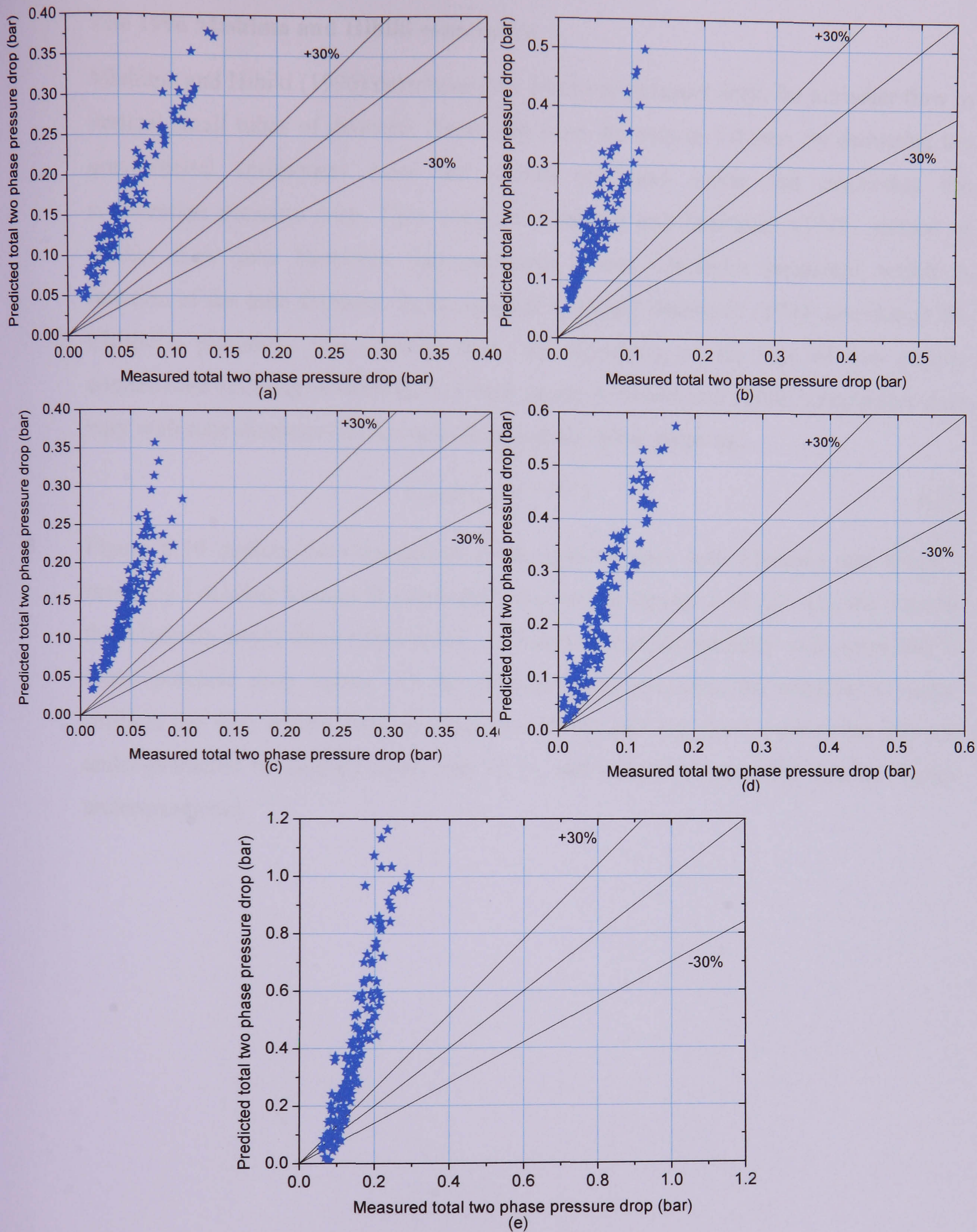


Figure 6.9 Comparison with the Tran et al. (2000) pressure drop correlation for different tube diameters: (a) 4.26 mm, (b) 2.88 mm, (c) 2.01 mm, (d) 1.1 mm and (e) 0.52 mm.

The 1996 Mishima and Hibiki correlation

Mishima and Hibiki (1996) determined the frictional pressure drop, for air/water flow in vertical small tubes of diameter decreasing from 4.9 mm to 1.0 mm, by deducting the gravitational component from the overall measured value and neglecting the acceleration pressure drop. They used the Lockhart and Martinelli (1949) method to predict their data. However, they proposed a new Chisholm parameter, which is function of the tube diameter. In the original Lockhart-Martinelli (1994) correlation the Chisholm parameter was constant that vary depending on the type of flow regime combination (laminar or turbulent) of each phase. Mishima and Hibiki's parameter does vary with tube diameter but not with flow regime and is given as,

$$C = 21(1 - e^{-0.316D}) \quad (6.2)$$

Figure 6.10 depicts the comparison of the present data with Mishima and Hibiki's modified Lockhart-Martinelli correlation. As seen in figures 6.10 (a) –(c), the data for the relatively larger three tubes (4.26 - 2.01 mm) are predicted fairly well, especially at lower pressure drop values. As the pressure drop increases, the correlation under-predicts the data within 30%. In Figures 6.10 (d) and (e), the 1.1 mm tube data are under-predicted by slightly more than 30 %, while the 0.52 mm tube data are highly under-predicted.

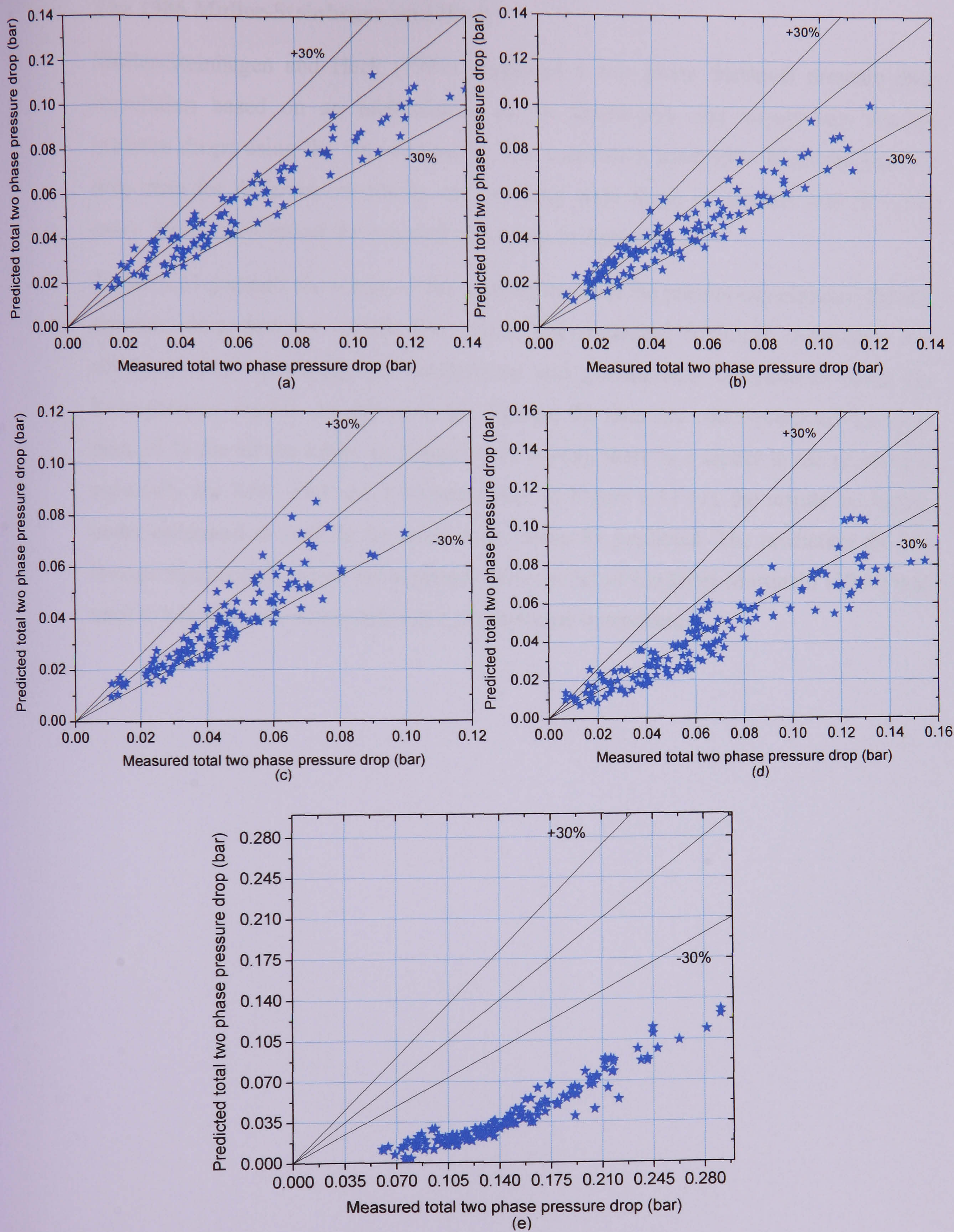


Figure 6.10 Comparison with the Mishima and Hibiki (1996) pressure drop correlation for different tube diameters: (a) 4.26 mm, (b) 2.88 mm, (c) 2.01 mm, (d) 1.1 mm and (e) 0.52 mm.

The 1986 Muller-Steinhagen and Heck

Muller-Steinhagen and Heck (1986) suggested a two phase frictional pressure drop correlation based on an interpolation of the liquid-only and vapour-only friction pressure drops using the vapour quality. The correlation used 9300 frictional pressure drop data for different conditions and covering wide range of channel size (4 – 392 mm). The detail form of the correlation is given in Appendix D.

Figure 6.11 presents the results of the comparison with the present experimental friction pressure drop data for all the five tubes. The measured frictional component was obtained after calculating the acceleration and gravitational components using the homogeneous model. As shown in the figures, the data are under-predicted by more than 30 % for all the tubes. In Figures 6.11 (b)-(d), there is a scatter in the prediction, especially for 2.88, 2.01 and 1.10 mm tubes. In Figure 6.11 (e), the results are highly under-estimated as well as the trend is not correctly predicted. The prediction did not change significantly when the separated flow model of Lockhart-Martinelli (1949) was used to calculate the acceleration and gravitational components.

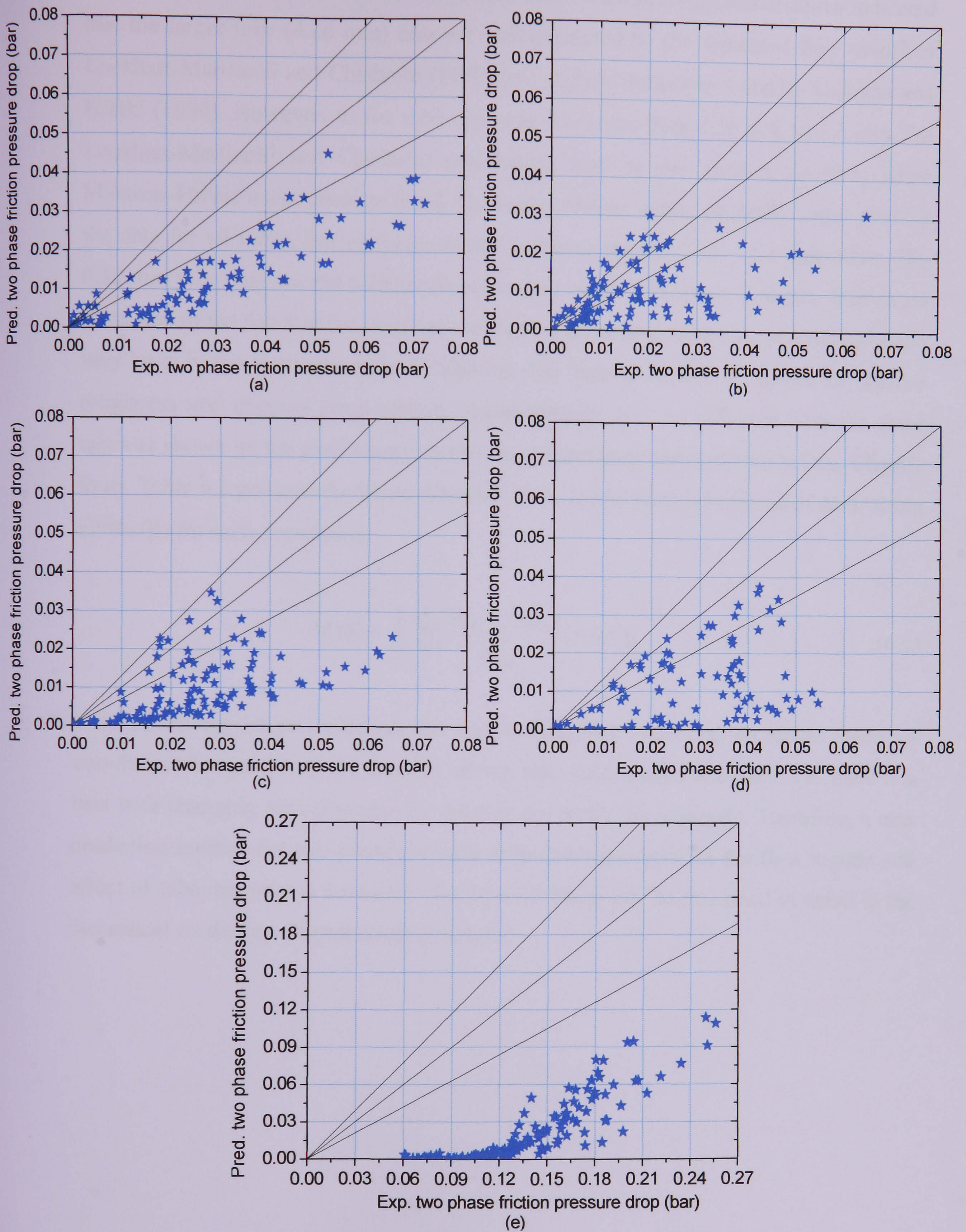


Figure 6.11 Comparison with the Muller-Steinhagen and Heck (1986) pressure drop correlation for different tube diameters: (a) 4.26 mm, (b) 2.88 mm, (c) 2.01 mm, (d) 1.1 mm and (e) 0.52 mm.

The comparison results with various models and correlations presented above indicated that the larger tube (4.26 mm) data are well predicted by the separated flow model of Lockhart-Martinelli and Chisholm (1983) and slightly under-predicted by Mishima and Hibiki (1996). However, as the tube diameter decreases from 4.26 mm to 1.1 mm, the Lockhart-Martinelli and Chisholm correlations tend to over-predict the data, while Mishima-Hibiki under-predicts them. The homogeneous model generally under-predicts the data for all tubes, but performs relatively better for the 2.88 – 1.1 mm tubes. The 0.52 mm tube data are not well predicted by any of the prediction methods. This could be related to the fact that the single phase friction factor and two phase pressure drop are very large in this particular tube. In addition, the internal surface condition, i.e. surface roughness and channel cross-section non-uniformity may be different than the other tubes as shown by the preliminary surface roughness measurement results (see, Chapter four). Table 6.1 presents the Mean Absolute Error (MAE) and percentage of data within $\pm 30\%$ (β) for each correlation.

$$MAE = \frac{1}{N} \sum \frac{|\alpha_{exp} - \alpha_{pred}|}{\alpha_{exp}} \times 100\% \quad (6.3)$$

Overall, among the presented models and correlations, there was no single model or correlation that predicted the data for all the tube with similar accuracy, i.e. there is a bias with changing tube diameter for most of the prediction methods. Therefore, a new prediction method for two phase pressure drop that takes account the flow regime and effect of tube diameter is necessary. Such possibilities will be discussed in detail in the theoretical modelling chapter (chapter seven).

Table 6.1 Mean average error (MAE) and percentage of data within $\pm 30\%$ (β) for the comparison results of various correlations shown above.

Models and Correlations		Tube internal diameter (mm)				
		4.26	2.88	2.01	1.1	0.52
Homogeneous Model	MAE (%)	24.5	19.8	20.5	27	62
	β (%)	75	83	70	65	0
Separated Model of L-M	MAE (%)	14	23.4	21	25	56
	β (%)	90	81	82	75	12
Chisholm (1983)	MAE (%)	15.1	23.5	16.3	27	35
	β (%)	91	80	88	74	40
Tran et al. (2000)	MAE (%)	197	285	221	260	152
	β (%)	0	0	0	0	16.5
Mishima and Hibiki (1996)	MAE (%)	16	19.7	19.7	35.6	75
	β (%)	92	82	70	40	0
Muller-Steinhagen and Heck (1986)	MAE (%)	45	77	62	59	88
	β (%)	5	28	16	23	0

6.4 Summary

Flow boiling pressure drop results for five tubes of diameter 4.26, 2.88, 2.01, 1.10 and 0.52 mm over a range of pressure and mass flux were presented and discussed. The two phase pressure drop increases with increasing mass flux, while it decreases with increasing system pressure. The boiling two phase pressure drop is observed to increase with heat flux. However, at very high heat flux, it tends to decrease with heat flux. This is related to the fact that dryout occurs at high exit quality, in which a significant portion of the tube experiences single phase vapour flow. The acceleration pressure drop contribution becomes significant as the heat flux increases, while the corresponding gravitational pressure drop contributions decrease with increasing heat flux. A similar conclusion was made by Kureta et al. (1998), who found that the acceleration loss is

comparable to the friction loss under certain conditions in small diameter tubes. This is unlike most studies, in which the contribution of friction loss was dominant and the contribution of acceleration and hydraulic loss were very small and neglected (Saitoh et al. 2005, Coleman and Krause 2004, Mishima and Hibiki 1996, Ould Didi et al. 2002). The reason why most studies neglected the acceleration and gravitational component could be related to the fact that most of the studies were conducted for adiabatic flows in horizontal tubes and also used correlations developed for such conditions.

In general, the pressure drop gradient increases with decreasing tube diameter. The pressure drop results of the smallest diameter tube (0.52 mm) were much higher than the rest of the tubes and demonstrated a slightly different characteristic. This could be due to the fact that the single phase friction factor in this tube was very large, which may indicate that the internal surface roughness value could be unusually high. This needs to be further investigated later, since spot measurement seems to indicate the contrary. Moreover, the flow pattern in the smallest tube is different compared with the larger tubes as discussed in Chapter five, i.e. dominant flows with fluctuating liquid film interface.

The results of the five tubes were also compared with the existing pressure drop models and correlations. The 4.26 and 2.88 mm tube results were predicted by the Lockhart-Martinelli (1949) separated flow model and Chisholm (1983) correlations reasonably well. However, these correlations did not predict well the smaller tube (2.01 and 1.1 mm) results. The Homogeneous model predicted the results of these two tubes better than the others. In general, there was a bias in the prediction results with changing tube diameter, i.e. there was no single correlation that works for all tubes. Therefore, a model based on the slug flow regime is proposed and will be presented in Chapter seven. The model follows a similar approach as three-zone model proposed by Thome et al. (2004). Therefore, the model calculates the total pressure drop by time averaging of the three zones. In the film boiling region, momentum equations in the liquid film and bubble slug are solved to determine the pressure gradient.

Chapter 7

Models for Two Phase Flow Boiling Heat transfer and Pressure Drop

7.1 Introduction

In general there is a limited number of modelling works compared with the large number of experimental based empirical correlations. This could be due to the extreme difficulties in completely understanding all features of the boiling processes, which are non-linear and stochastic in nature. From this point of view, the conventional way of developing correlations from a regression analysis of data covering a wide range of parameters seems to be feasible and easy to implement. However, when new phenomena or application emerge, the limitations of the later method begin to show up. One example is the fact that many researchers reported that the heat transfer correlations developed for large diameter tubes failed to predict well the data from small diameter tubes, i.e. the fact that the macroscale theory is not able to represent and include the new features of microscale heat transfer processes, although some principles could still be “borrowed”. Some of the attributes of flow boiling that pose difficulties in modelling phase change heat transfer or producing a comprehensive correlation is the fact that the heat transfer process in both modes of heat transfer mechanisms in different channel size scale is distinctively affected by various parameters such as heat flux, mass flux, system pressure, surface finishing, vapour quality, channel size, channel geometry and inlet conditions. Complete numerical

simulation of boiling processes can be challenging and requires a huge computation time and resource (super computers), while industry may favour low cost and fast solutions/decisions. Therefore, the usual approach is to reduce the dimensionality and complexity of the process by introducing several viable assumptions. Hence, it is now highly desirable to develop relatively simple mechanistic models for flow boiling in small to micro-channels that are well validated by experiments.

In this chapter, the state-of-the-art existing one-dimensional mechanistic models are presented and compared with the current experimental data. Also, features of the models that may require considerations are pointed out. The chapter is organised as follows: section 7.2 presents the three-zone evaporation model developed by Thome et al. (2004) and investigates various features of the model by detailed comparison with the current experimental data. The three-zone model is a flow regime-specific model, which was originally based on the confined bubble or slug flow regime. Section 7.3 presents a flow-regime based mechanistic model developed for the annular two phase flow regime. This model has been used quite extensively for large diameter tubes. However, it has now been used for small diameter tubes especially for flow boiling of water by Qu and Mudawar (2003b) and Boye et al. (2007). The possibilities of improving some features of the three zone model are investigated and the results of some of the new improvements made to the three-zone evaporation model are presented in section 7.4. A new pressure drop prediction method is also proposed based on the newly emerging heat transfer modelling approach, existing correlations and past theoretical pressure drop studies. Section 7.5 presents the new proposed two phase pressure drop prediction method and the comparative results with the current data. Finally, the chapter is summarised in section 7.6.

7.2 Three-zone evaporation heat transfer model

In the past, mechanistic models have been partly used to support semi-analytical models. Ishibashi and Nishikawa (1969) was among the first who proposed a heat transfer model for saturated flow boiling in narrow gaps, assuming that 70% of the heat when a confined bubble passes is carried away by transient conduction, while the remaining portion is by the latent heat. Later, they developed a model based on evaporation of the film, taking the time duration of bubble passing to be $\tau_b = 0.0255$ sec and thickness of the film to the 28-47 μm .

However, the effect of heat flux on the frequency of the bubble was not considered. Later, Kew and Cornwell (1997) formulated a heat transfer model that utilises one or more of the different mechanisms suggested as nucleate boiling, confined bubble boiling, convective boiling and partial dryout. As discussed before in the literature review section, the main heat transfer mechanism in the confined/slug bubble regime (which is considered as the prevailing flow pattern in small diameter passage) is conduction across the liquid film surrounding the bubble and evaporation at the interface. Based on this assumption, Jacobi and Thome (2002) proposed a mechanistic heat transfer model that was based on thin film evaporation during elongated bubble flow. Later, Thome et al. (2004) extended this model in to a three-zone evaporation model by incorporating the single phase heat transfers during liquid slug flow and single phase vapour flow, i.e. allowing a mechanism of periodic dryout at the rear of confined bubbles. In this section, the results of the three-zone model in predicting the current experimental data and its various features are discussed.

7.2.1 Presentation of the model

For the purpose of the present comparisons, it is necessary to briefly summarise the model in order to highlight important and relevant parameters that will be discussed later. The model predicts the local dynamic and the local time-averaged heat transfer coefficient at fixed locations along the channel based on the evaporation of elongated bubbles. As shown in Figure 7.1, following the passage of a liquid slug, a bubble is modelled to pass as a confined elongated bubble trapping a thin liquid film against the inner wall. If the liquid film dries out before the arrival of the next liquid slug, then a vapour slug follows (triplet). If not, then the model assumes the existence of a pair consisting of the liquid slug and the elongated bubble. Therefore, a novel feature of the model is that it considers a dryout zone and exploits the transient evaporation of the film. The model does not include a contribution from nucleate boiling.

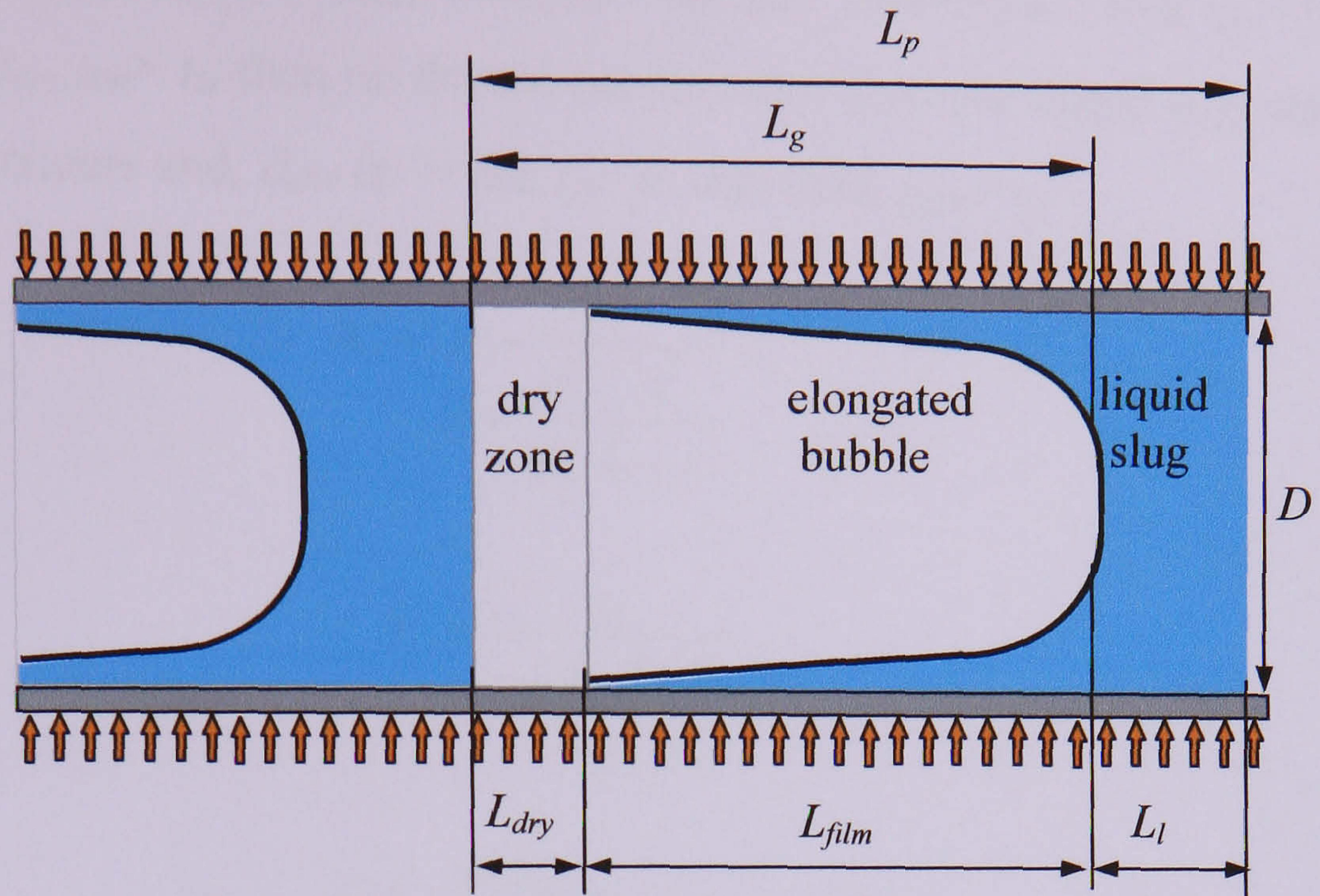


Figure 7.1 Diagram illustrating the three zones: a liquid slug, an elongated bubble and a vapour slug, redrawn from original, Thome et al. (2004).

The local heat transfer coefficient is given as the time averaged of the three zones namely liquid slug, elongated bubble and dryout zone as follows.

$$\alpha_{ip}(z) = \frac{t_l}{\tau_b} \alpha_l(z) + \frac{t_{film}}{\tau_b} \alpha_{film}(z) + \frac{t_{dry}}{\tau_b} \alpha_v(z) \quad (7.1)$$

where, the period for the pair or triplet (if dryout occurs) is the reciprocal of the bubble generation frequency.

$$\tau_b = \frac{1}{f_b} \quad (7.2)$$

The time periods given below in Equations (7.3) – (7.5) are used in the model as follows: t_l corresponds to the time it takes for the liquid slug to pass a fixed location z through the cross section; t_{film} is the residence time of the film; t_{dry} represents the duration of the local wall dryout; t_v corresponds to the presence of vapour (dryout and film zone) passing location z ; $t_{dry\ film}$ is the maximum duration of the existence of the film at position z till dryout occurs at the minimum feasible film thickness (δ_{min}). According to Thome et al. (2004), if $t_{dry\ film} < t_v$, local dryout occurs, i.e. the liquid film thickness reaches the minimum

feasible film thickness, $\delta_{end}(z) = \delta_{min}$, and $t_{film} = t_{dry\ film}$. This implies that $t_{dry} = t_v - t_{film}$. On the other hand, if $t_{dry\ film} > t_v$, then no dryout occurs since the next liquid slug arrives before dryout of the film occurs and, $\delta_{end}(z) = \delta(z, t_v)$, In this case, $t_{film} = t_v$.

$$t_l = \frac{\tau_b}{1 + \frac{\rho_l}{\rho_v} \frac{x}{1-x}} \quad (7.3)$$

$$t_v = \frac{\tau_b}{1 + \frac{\rho_v}{\rho_l} \frac{1-x}{x}} \quad (7.4)$$

$$t_{dry\ film}(z) = \frac{\rho_l h_{lg}}{q} [\delta_0(z) - \delta_{min}] \quad (7.5)$$

In equation (7.1) above, $\alpha_l(z)$ and $\alpha_v(z)$ are heat transfer coefficients of the liquid and vapour slugs. They are calculated from their local Nusselt numbers using the respective equivalent lengths of the liquid slug, L_l and dry wall zone L_{dry} , see Figure 7.1. The London and Shah correlation for laminar developing flow and the Gnielinski correlation for transition and turbulent developing flow (both given in VDI-GVC, 1997) were used by Thome et al. (2004). The Churchill and Usagi (1972) asymptotic method was used to obtain a continuous expression of the mean single phase heat transfer coefficient as a function of Reynolds number. The mean heat transfer coefficient through the evaporating thin liquid film surrounding the elongated bubble was obtained by assuming one-dimensional heat conduction in a stagnant thin liquid film and given as follows,

$$\alpha_{film}(z) = \frac{\lambda_l}{\delta_0 - \delta_{end}} \ln\left(\frac{\delta_0}{\delta_{end}}\right) \quad (7.6)$$

$$\delta(z, t) = \delta_0(z) - \frac{q}{\rho_l h_{lg}} t \quad (7.7)$$

The initial thickness of the liquid film was found by using the Moriyama and Inoue (1996) film thickness prediction and applying an empirical correction factor, C_{δ_0} as shown in equation (7.8).

$$\frac{\delta_0}{D} = C_{\delta_0} \left(3 \sqrt{\frac{U_l}{U_p D}} \right)^{0.84} \left[(0.07 Bo^{0.41})^{-8} + 0.1^{-8} \right]^{-1/8} \quad (7.8)$$

The pair velocity (U_p) was obtained assuming that the liquid and vapour travel at the same speed, where each phase velocity is determined using the total mass flow rate and vapour quality. The pair velocity is expressed as:

$$U_p = G \left[\frac{x}{\rho_v} + \frac{1-x}{\rho_l} \right] \quad (7.9)$$

Bo is the Bond number modified considering that the characteristic time is the ratio of tube diameter to the pair velocity and is given as:

$$Bo = \frac{\rho_l D}{\sigma} U_p^2 \quad (7.10)$$

The researchers did not define three parameters by fundamental analysis, namely the minimum thickness of the liquid film at dryout (δ_{min}), the pair frequency (f), which is the frequency of the bubble generation and the correction factor (C_{δ_0}) for the initial film thickness. These parameters had to be found by optimising the prediction of the model against an experimental database for the heat transfer coefficient. Dupont et al. (2004) compared the model predictions with a database (1591 test data for R11, R12, R113, R123, R134a, R141b and CO₂) and recommended general values of the parameters after optimising empirically each parameter with the whole range of the database. In the comparison, they used a constant average film thickness, although in the presentation of the model (Thome et al. 2004), the film thickness was governed by the evaporation of the liquid film. Equations (7.11)-(7.14) provide the empirical relations for the three optimised parameter, Dupont et al. (2004). These are given as follows,

The critical film thickness for dryout,

$$\delta_{min} = 0.3 \mu\text{m} \quad (7.11)$$

The optimum pair frequency of bubble formation,

$$f_{opt} = \left(\frac{q}{q_{ref}} \right)^{1.74} \text{ Hz} \quad (7.12)$$

The reference heat flux (q_{ref}) was given as a function of the reduced pressure based on the method employed by Cooper (1984) for the pool boiling correlation,

$$q_{ref} = 3328 \left(\frac{P_{sat}}{P_{crit}} \right)^{-0.5} \quad (7.13)$$

The constant value of 3328 W/m² as well as the values of the exponents of equation (7.12) and (7.13), i.e. 1.74 and -0.5, respectively were obtained from the complete experimental database (which included R134a). The constant in equation (7.8) was again obtained using the database as:

$$C_{\delta 0} = 0.29 \quad (7.14)$$

In the next section, which is a comparison of the model results with the current experimental data, the above recommended values of the three parameters were used. It is desirable, however, to obtain independent estimates of the three parameters from detailed observations.

7.2.2 Comparison with current results

The mechanistic three-zone evaporation model of Thome et al. (2004), briefly described above, was developed assuming that slug flow is the prevailing flow pattern in small diameter tubes. Consequently, the model should be compared with data in the slug flow regime. However, the model was compared with a database from different sources covering wide range of parameters and flow conditions, by Dupont et al. (2004). The model does not include a prediction of its own range of validity by modeling the extinction of the liquid bridge between confined bubbles. Nevertheless, the fact that the developers assumed intermittent flow (confined/elongated bubble, slug flow) as the dominant flow pattern in small diameter tubes is likely to predict a significant portion of the cases, especially refrigerant flows (where slug flow exists approximately for $x < 0.5$). In addition, the basic heat transfer mechanism in annular flow regime is also similar in many cases with slug flow, which is conduction through the thin liquid film and evaporation at the liquid/vapour

interface. Of course, the assumption of a smooth film by the model excludes convection heat transfer enhancement because of instabilities at the liquid-vapour interface (especially in churn flow regimes) during conduction through the liquid film.

In general, the comparisons cover the full range of experimental qualities, because it appears that the model can make satisfactory predictions at qualities expected to be in the annular flow regime, up to the onset of partial dryout. The model is examined by comparing with the current data on a more detailed local basis, i.e. comparisons of the axial development of the experimental and predicted coefficients are carried out by plotting heat transfer coefficient against quality.

Figure 7.2 shows the local heat transfer coefficient versus vapour quality for the 4.26 mm tube for various heat fluxes at a constant mass flux of $300 \text{ kg/m}^2\text{s}$ and at 8 bar pressure. As seen in the figure, the experimental values are always high at $x = 0$ and remain at approximately the same level up to the quality where partial dryout commences, with some fluctuations that are mostly within the bounds of experimental uncertainty. However, the examples in Thome et al. (2004) and Dupont et al. (2004) have a heat transfer coefficient that changes from a very low value at $x = 0$ to a large value at a small positive value of x , followed by a slight decrease with further increase in x . Hence, as seen in figure 7.2, the model greatly under-estimated the data in the region of very low vapour qualities ($x \cong 0$ to 0.13), i.e. near the inlet to the test section. This serious disagreement may be attributed to the onset of nucleate boiling, i.e. exclusion from the model of bubble formation in the unconfined bubbly flow region. The model assumes all-liquid flow up to the inception of the confined bubbles at $x = 0$ and employs a laminar fully developed single-phase heat transfer correlation that gives heat transfer coefficients much lower than for unconfined bubbly flow. The model over-predicts the data for the entire range, with the difference increasing with increasing heat flux. Heat transfer in the apparent conditions of partial dryout observed for $x > 0.55$ and $q \geq 97 \text{ kW/m}^2$ is highly over-predicted by the model. The model results do not follow the experimental data at all in this range. The effect of heat flux on the experimental heat transfer coefficient gets smaller as the heat flux is increased; this is not well predicted by the model. The churn/annular transition boundary from the flow pattern maps of Chen et al. (2006) is also shown in Figure 7.2 to indicate the extension of the model prediction in the annular regime. There may be some differences between the

highly transient flow conditions within the heated test section and those observed in Chen et al. (2004) in an adiabatic section following the test section, which require further investigation.

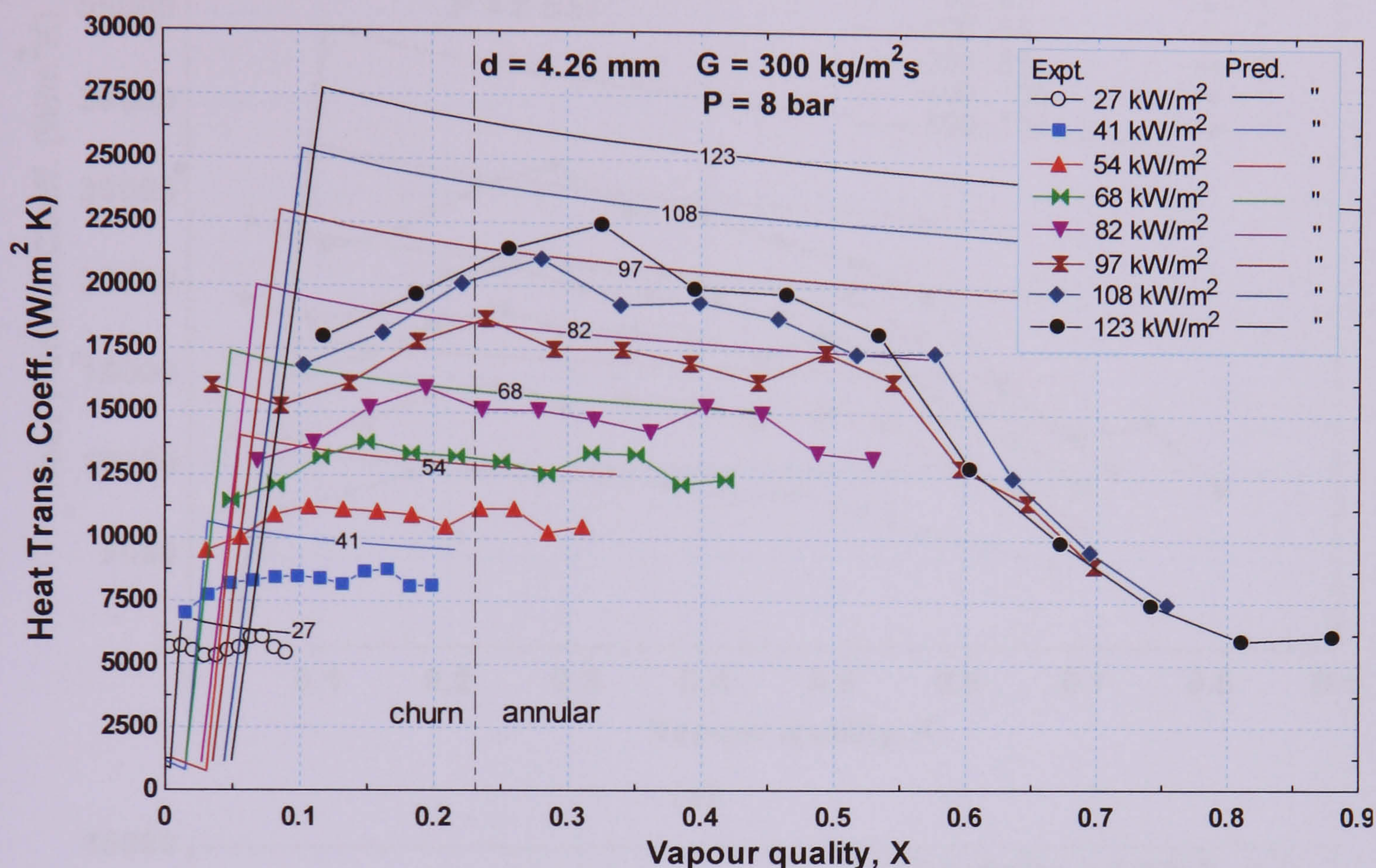
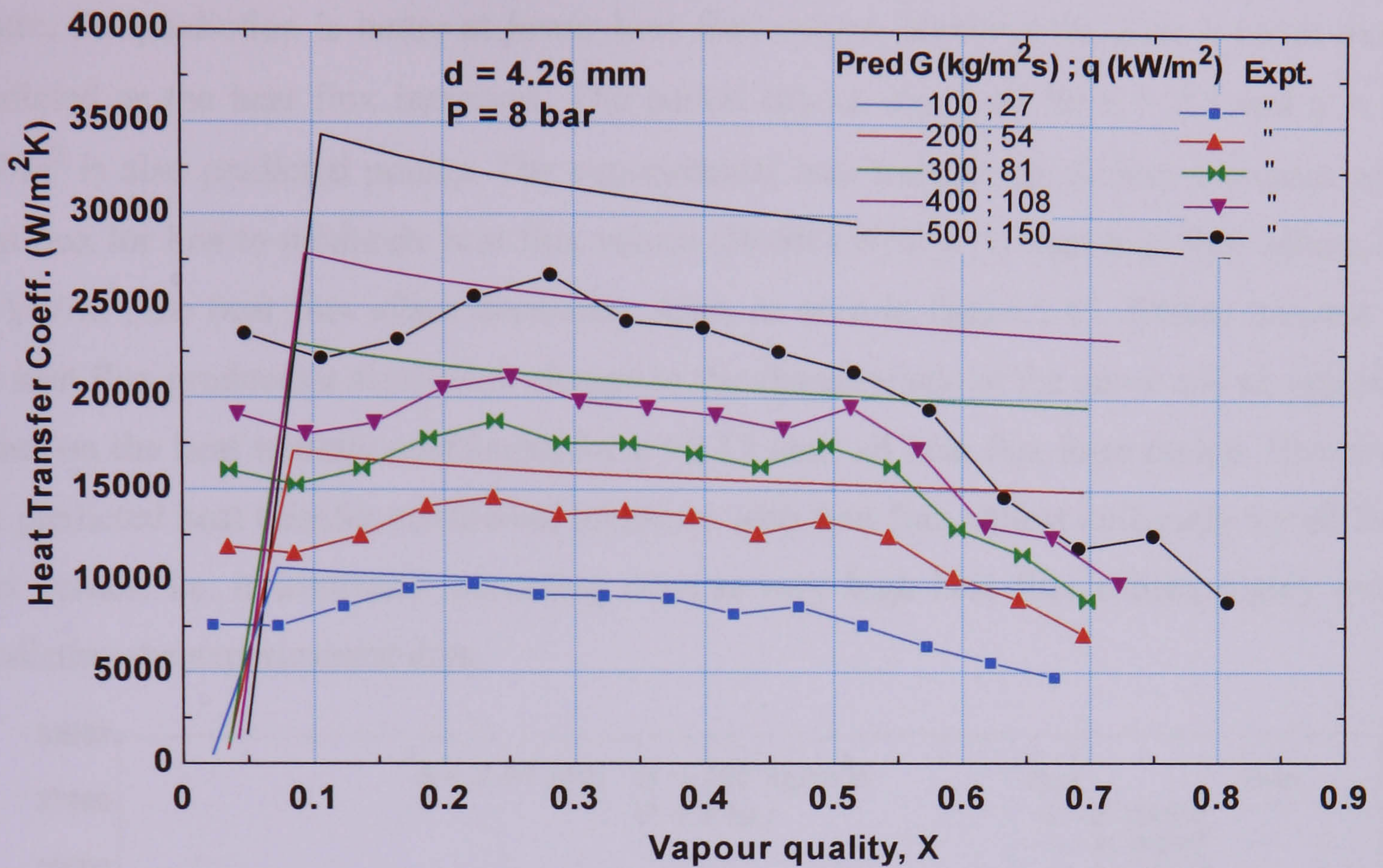


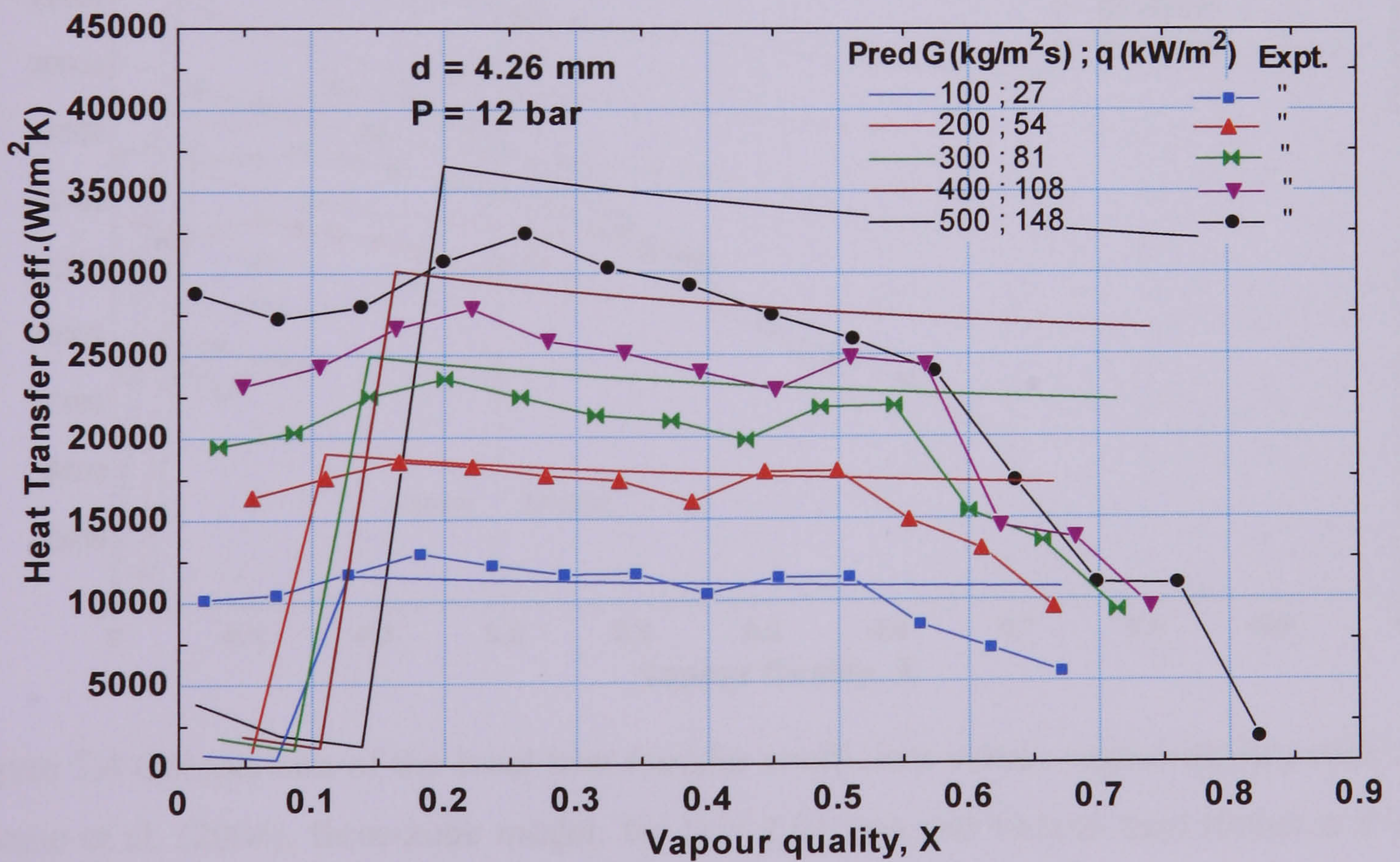
Figure 7.2 Comparison of the local heat transfer coefficient versus vapour quality with the Thome et al. (2004), three-zone model, for various heat fluxes at 8 bar pressure and $300 \text{ kg/m}^2\text{s}$ mass flux.

In figure 7.2, the exit quality varies, and the quality range considered in the comparison becomes quite low at the lower heat flux values. Therefore, various combinations of mass flux and heat flux that provide relatively high and approximately same exit qualities were selected and compared with the model in Figures 7.3 (a) and (b), for the 4.26 mm at a pressure of 8 bar and 12 bar respectively. These figures also demonstrate the effect of mass flux and pressure on the prediction. In Figure 7.3 (a), at 8 bar pressure, the model over-predicts the data with increasing mass flux and heat flux. However, in Figure 7.3 (b) at 12 bar, the experimental results are predicted very well for $q \leq 60 \text{ kW/m}^2$ and $G \leq 300 \text{ kg/m}^2\text{s}$. In general, at higher values of heat and mass flux the model over-predicts the experiment results. The model is developed for small diameter tubes and hence is not likely to work

very well for the larger tubes. Therefore, a similar comparison will be made for the 2.01 mm tube, while a slightly extensive examination is carried out for the 1.1 mm tube.



(a)



(b)

Figure 7.3 Comparison of the local heat transfer coefficient versus vapour quality with the Thome et al. (2004) three-zone model for D=4.26 mm tube: (a) P = 8 bar, (b) P = 12 bar.

Figure 7.4 shows the local heat transfer coefficient versus vapour quality for the 2.01 mm tube for various heat fluxes at constant mass flux and at 8 bar pressure. As shown in the figure, the prediction is better at lower heat flux values, however the data is again over-predicted as the heat flux increases. The partial dryout observed for $x > 0.3$ and $q \geq 80$ kW/m² is also predicted poorly. The experimental heat transfer coefficient increases with heat flux for low to moderate heat flux values (20-80 kW/m²). At high heat flux values, $q > 80$ kW/m², the heat flux effect decreases. Also, as seen in figure 5.13, further increase in the heat flux produces a significant change in the characteristic of the curve and an opposite effect on the heat transfer coefficient for $x > 0.15$ until all heat flux lines merge. However, the predicted heat transfer coefficient increases with heat flux almost uniformly for all heat flux values, i.e. it continues increasing even at very high heat flux values, highly over-predicting the experimental data.

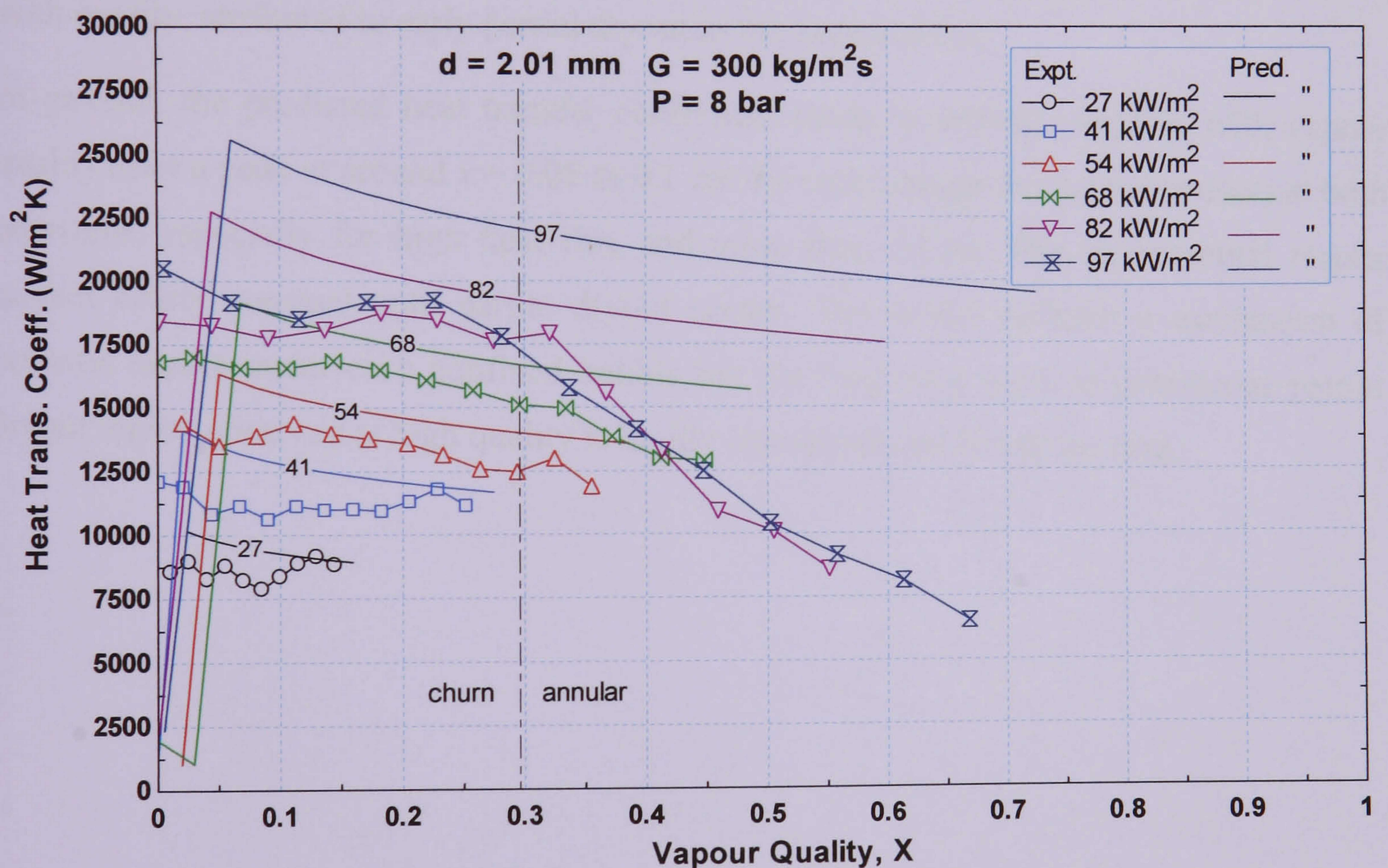
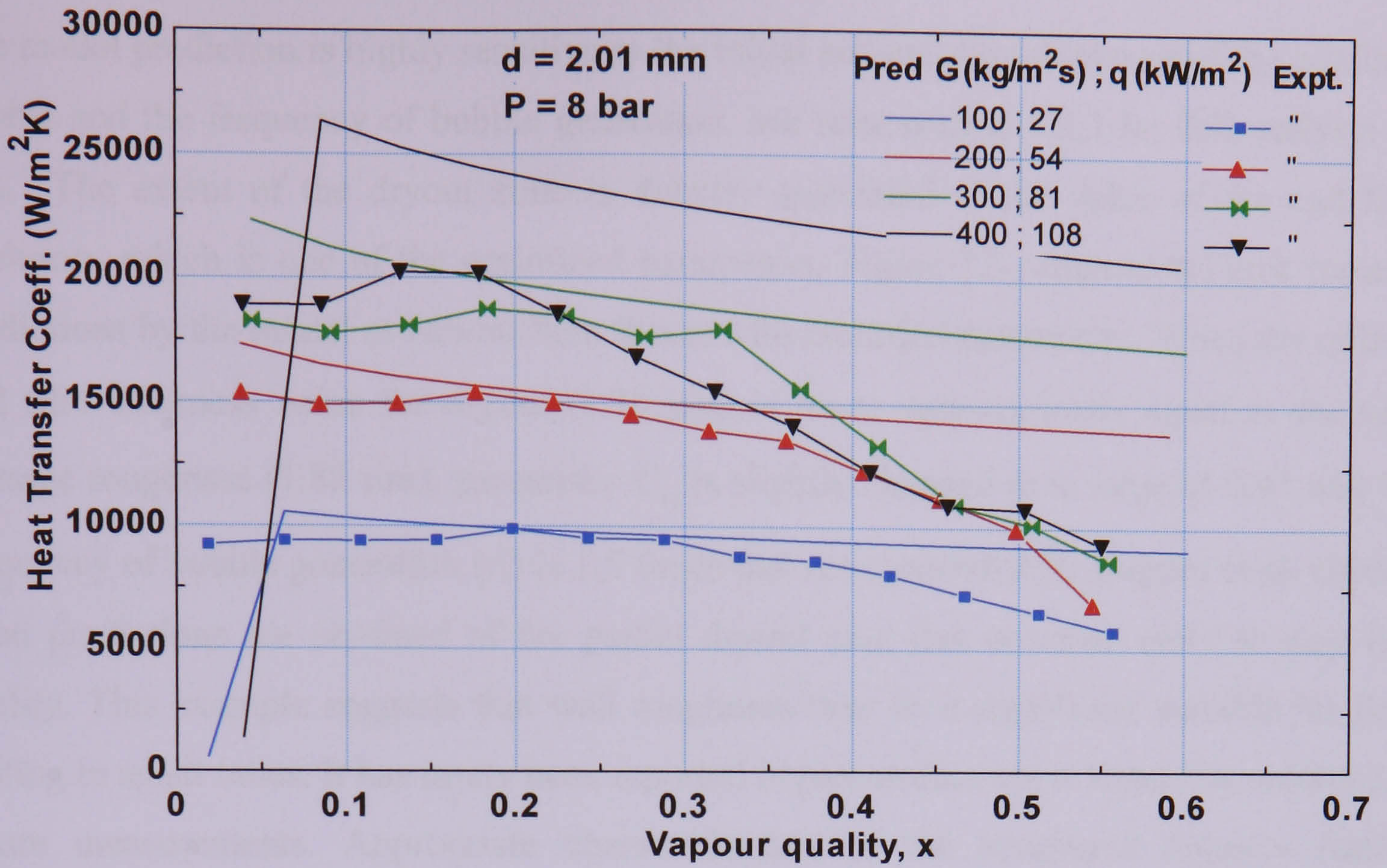


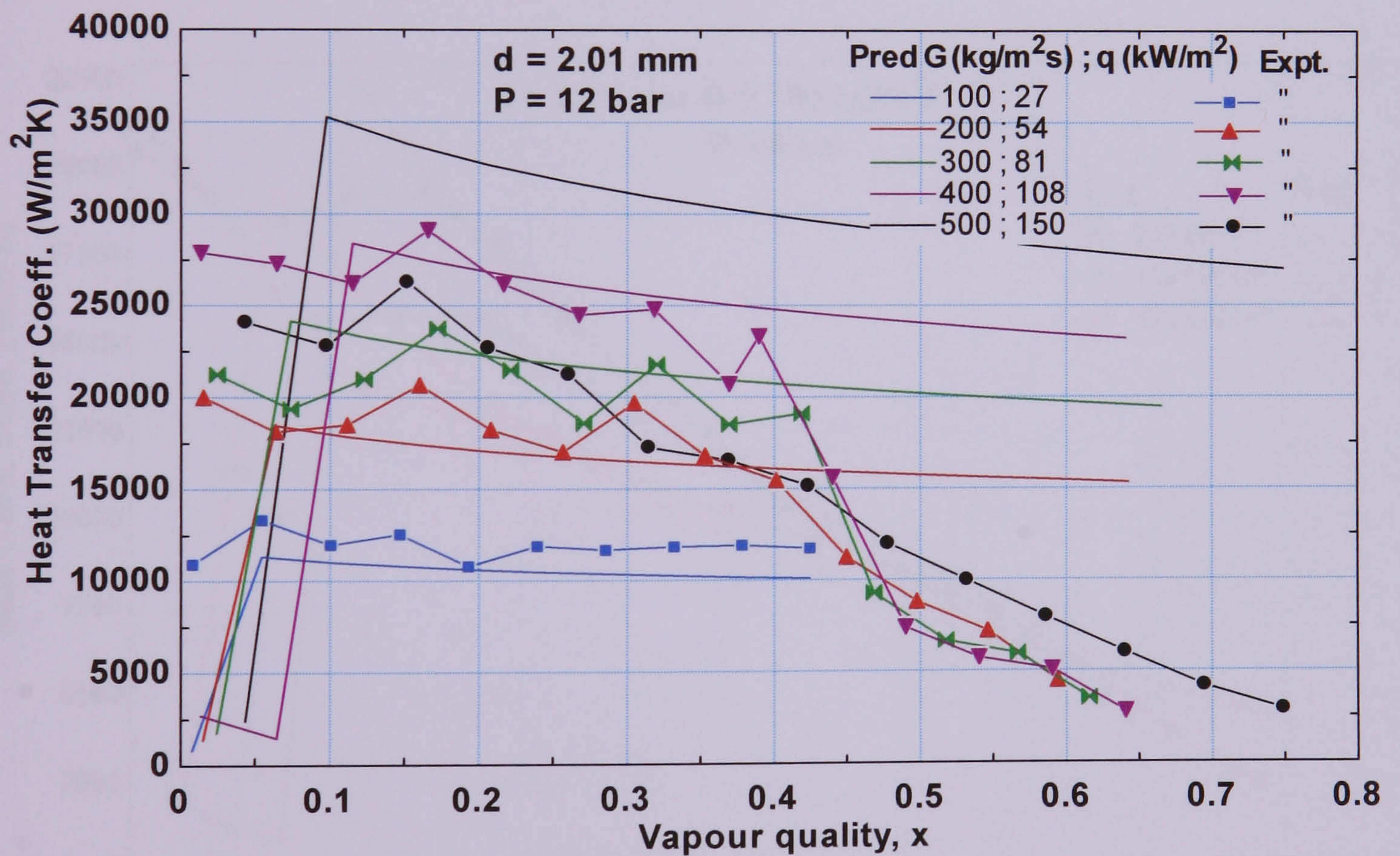
Figure 7.4 Comparison of the local heat transfer coefficient versus vapour quality with the Thome et al. (2004), three-zone model, for $D = 2.01$ mm and various heat fluxes at 8 bar pressure and $300 \text{ kg/m}^2\text{s}$ mass flux.

Similarly, in Figure 7.5 (a) and (b), the local heat transfer coefficient versus vapour quality for various combinations of mass flux and heat flux, selected to provide relatively high and approximately same exit qualities, is depicted for the 2.01 mm tube at 8 and 12 bar pressures, respectively. Examination of Figure 7.5 (a) indicates a very good agreement with the experimental values in the range of quality $0.15 < x < 0.3$ for $G < 300 \text{ kg/m}^2\text{s}$ and $q < 80 \text{ kW/m}^2$. The experimental results are over-predicted outside the above quality range and the over-prediction increases as mass and heat flux values increase. Figure 7.5 (b) presents the same comparison for the same diameter but at a system pressure of 12 bar. The experimental data are slightly under-predicted at lower mass and heat flux ($G \leq 200 \text{ kg/m}^2\text{s}$, $q \leq 54 \text{ kW/m}^2$). Above these values, the model tends to slightly over-predict the data. A significant over-prediction is observed for the highest heat flux ($q = 147 \text{ kW/m}^2$), for which the corresponding experimental results show a monotonic drop in heat transfer coefficient with quality, attributed to early partial dryout in the experiments.

In general, the predicted heat transfer coefficient tends to decrease slightly with vapour quality after a peak at around $x \sim 0.05$ to 0.1 for the entire range, for both diameters at both pressures, especially for high heat flux and mass flux values. The experimental results remain nearly constant until partial dryout occurs. The model includes a mechanism of periodic dryout under each confined bubble but the long time scale or continuous partial dryout region observed at high quality is highly over-predicted for all the data.



(a)



(b)

Figure 7.5 Comparison of the local heat transfer coefficient versus vapour quality with the Thome et al. (2004) three-zone model for $D = 2.01$ mm tube at various mass and heat flux values: (a) $P = 8$ bar, (b) $P = 12$ bar.

The model prediction is highly sensitive to the initial and end film thickness of the confined bubble and the frequency of bubble generation, see later section 7.2.3 for full analysis on this. The extent of the dryout zone is directly associated to the value of the end film thickness, which is one of the optimized parameters. Figure 7.6 presents the heat transfer predictions by the model at various heat fluxes with modified parameters. When the critical end film thickness value for dryout ($1.75 \mu\text{m}$) is made approximately equal to the tube average roughness ($1.82 \mu\text{m}$), parameter C_{δ_0} is slightly changed to a value of 0.43 and the frequency of bubble generation (f_b) is 1.5 times that recommended by Dupont et al. (2004), good predictions are obtained of the partial dryout case that occurred early at very low quality. This example suggests that wall roughness may be a significant variable for flow boiling in small tubes. It has rarely been reported in past studies but it should be recorded in future measurements. Appropriate characterization of the roughness requires further investigation.

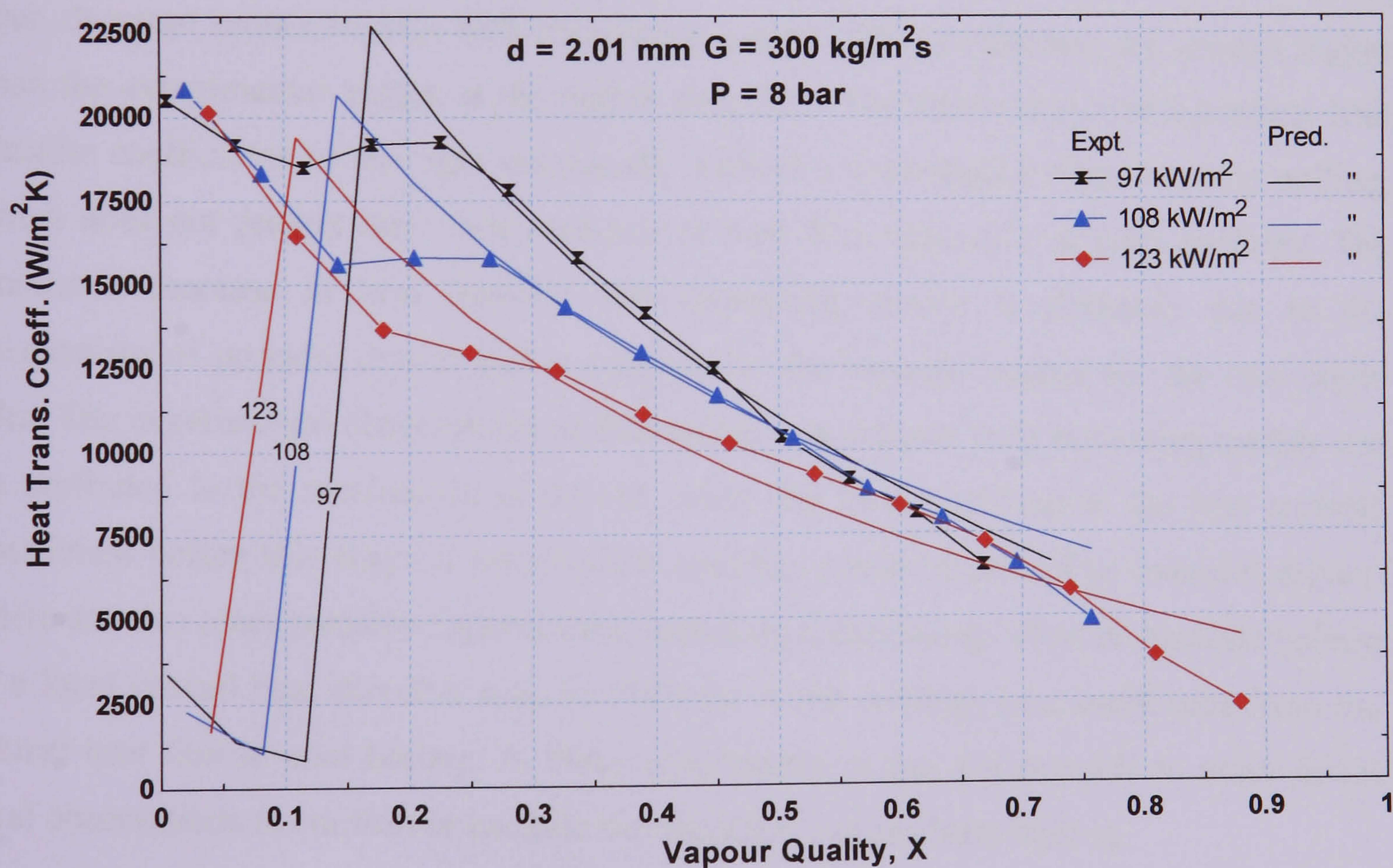
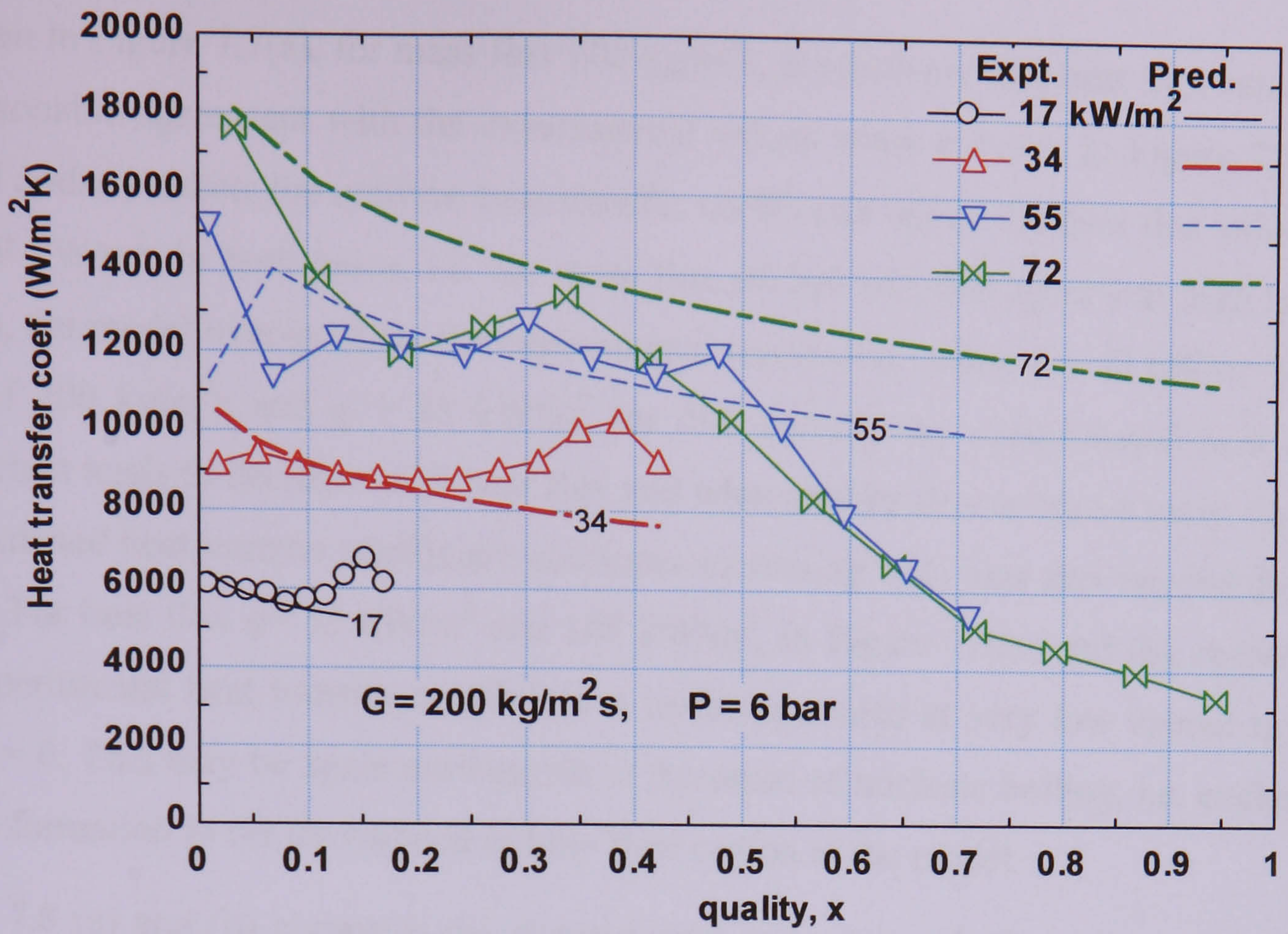
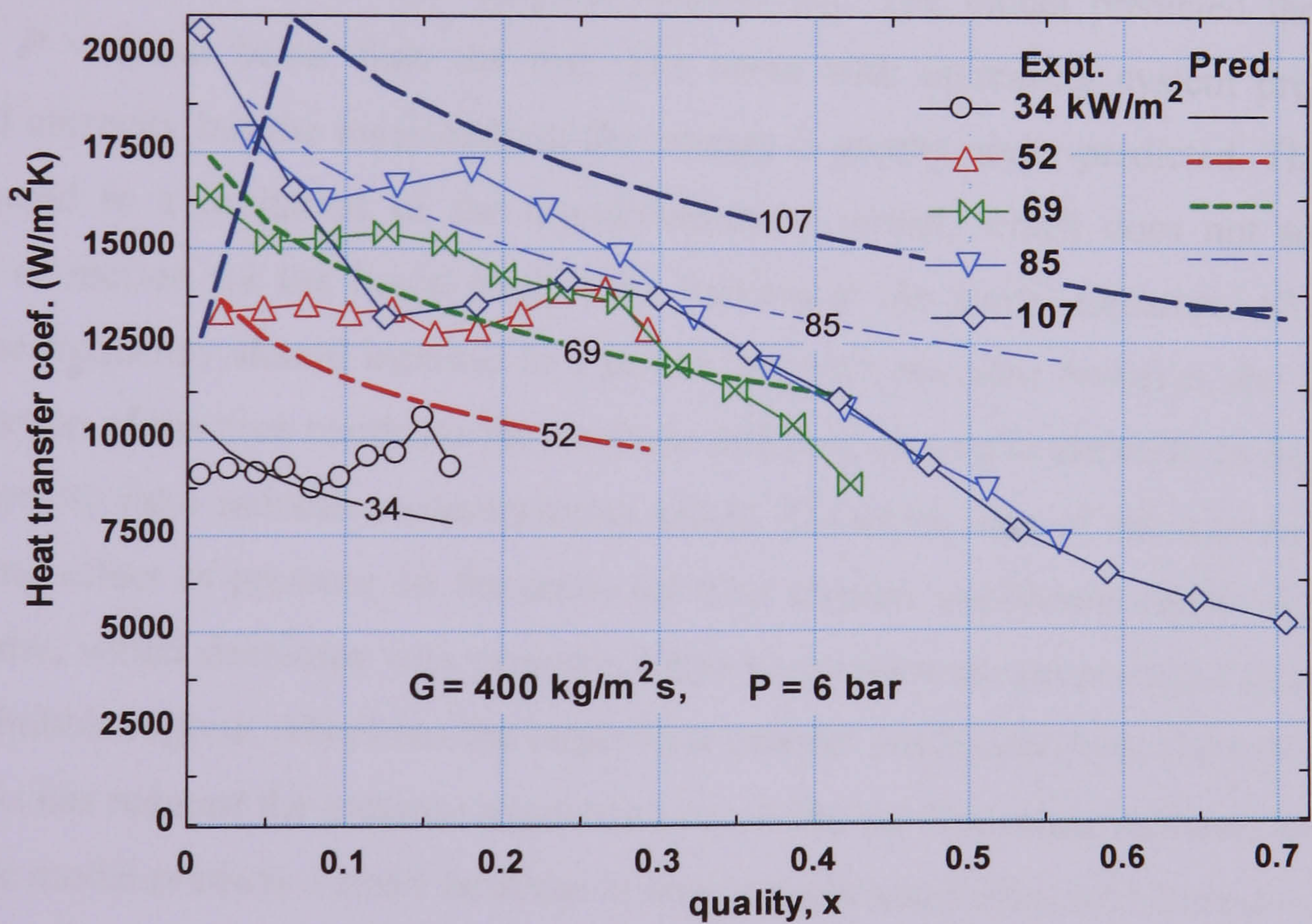


Figure 7.6 Experimental results and predictions for continuous dry out cases when the critical film thickness value $\delta_{min} = 1.75 \mu\text{m}$, $C_{\delta_0} = 0.43$ and the frequency of bubble generation, f equals 1.5 times that recommended by Dupont et al. (2004).

Comparisons of the three-zone model results with the experimental data of the 1.1 mm tube are given in Figures (7.7) and (7.8). Figures 7.7 (a) and (b) depict the effect of increasing heat flux at a pressure of 6 bar and mass fluxes of 200 and 400 kg/m²s respectively. At low heat fluxes, the experimental heat transfer coefficients increase with increasing heat flux; they are initially nearly independent of quality and then increase near the exit to the test section, e.g. $x > \sim 0.15$ at 34 kW/m². At higher heat fluxes, the coefficients have maximum values at the first measuring point that increase with increasing heat flux. Initially, they decrease with increasing quality, and then remain fairly constant within the uncertainty limit. In this intermediate quality range, the dependence on heat flux is not straightforward: in Figure 7.7 (b), the heat transfer coefficients at 107 kW/m² fall below those at 69 and 85 kW/m². Beyond the fairly constant heat transfer coefficient region, the experimental points at all heat fluxes converge on a single line that decreases monotonically towards the test section exit. On the other hand, the predicted heat transfer coefficients exhibit simpler behaviour. They increase to a maximum around $x \sim 0.05$ to 0.1 for both mass flux values, then decrease monotonically with increasing quality. The coefficients are always higher than the experimental values at the higher heat flux. The three-zone model predicts heat transfer coefficients of the right magnitude, without a contribution from nucleate boiling, but it does not predict their independence of heat flux especially at high qualities. The predicted decrease in heat transfer with increasing quality is primarily due to the mechanism of periodic dryout and is sensitive to the assumed values for the thin liquid film. The experimental observations of decreasing heat transfer with increasing quality can be attributed to the mechanism of dryout, while the local variation in the heat transfer coefficient before this stage at intermediate qualities could be related to transient dryout. There are also other possible explanations, including a decreasing effect of nucleate boiling or a local critical heat flux that may be different in the confines of a small tube from the critical heat flux in pool boiling. In these experiments, it was not possible to make direct local observations to confirm or exclude the occurrence of nucleate boiling.



(a)

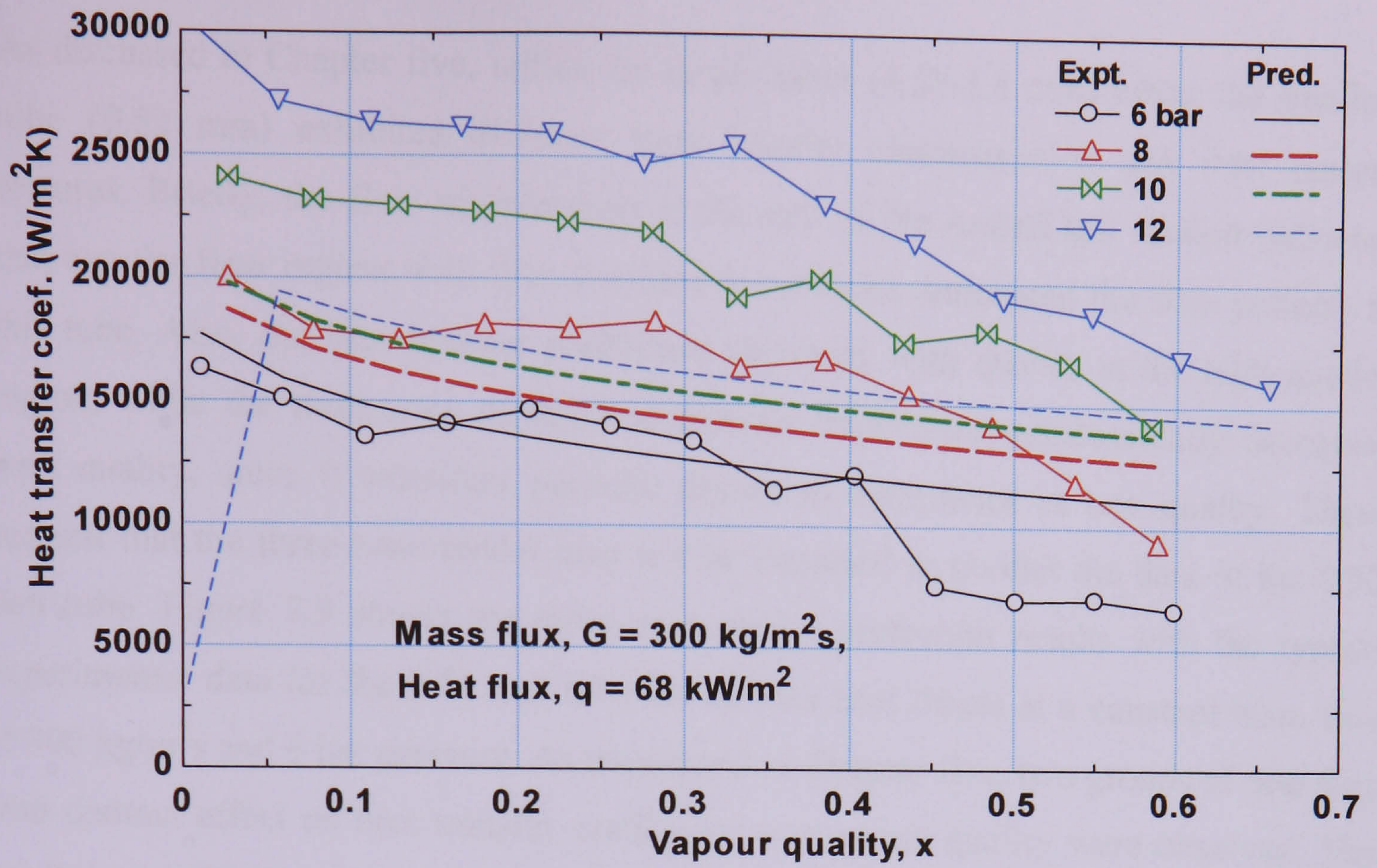


(b)

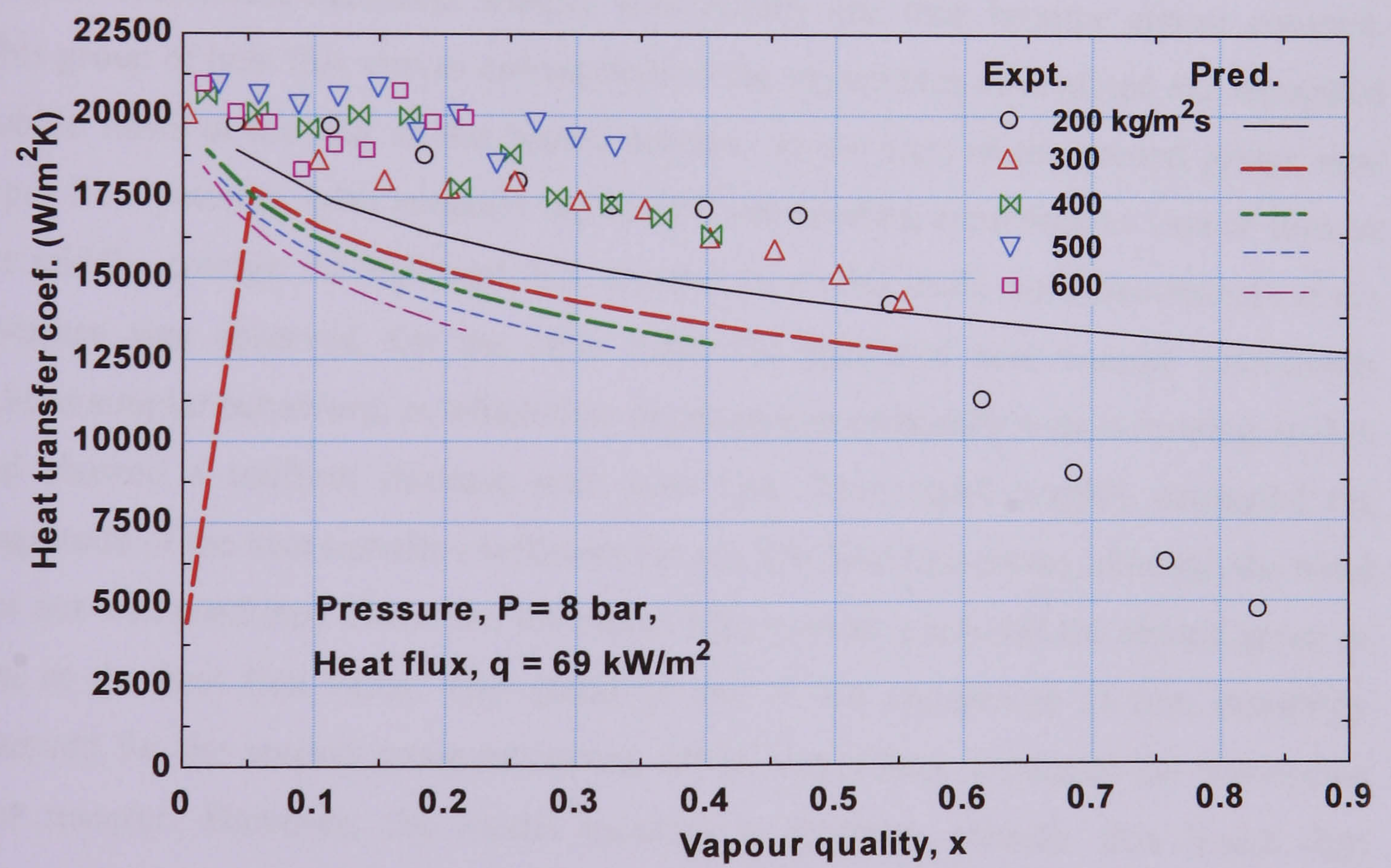
Figure 7.7 Comparison of the local heat transfer coefficient versus vapour quality with the Thome et al. (2004), three-zone model, $P = 6 \text{ bar}$: (a) $G = 200 \text{ kg/m}^2\text{s}$, (b) $400 \text{ kg/m}^2\text{s}$.

As seen in Figure 7.7(a), for mass flux $200 \text{ kg/m}^2\text{s}$, at relatively low heat flux values, there is reasonable agreement with the experimental values when $x < 0.5$. In Figure 7.7(b), the model under-predicts the uniform heat transfer coefficient region for heat flux values of 52 and 69 kW/m^2 . In both cases, i.e. for mass flux of 200 and $400 \text{ kg/m}^2\text{s}$ at high heat flux values, the model over-predicts the experimental results, i.e. when $q > 72 \text{ kW/m}^2$ for mass flux of $200 \text{ kg/m}^2\text{s}$ and $q > 85 \text{ kW/m}^2$ for $400 \text{ kg/m}^2\text{s}$, the experimental heat transfer coefficient tends to decrease with heat flux and what may be dryout begins early. However, the predicted heat transfer coefficient continues increasing with heat flux beyond the above limits. For heat flux $q = 55 \text{ kW/m}^2$ and 107 kW/m^2 , in Figure 7.7(a) and (b), respectively, the experimental heat transfer coefficient is under-estimated at very low vapour qualities, near $x = 0$. This may be again attributable to the onset of nucleate boiling, i.e. exclusion of bubble formation in the unconfined bubbly flow region in the model.

Figure 7.8 (a) and (b) compares the experimental and predicted effect of system pressure and mass flux on the local heat transfer, respectively. The model predicted the lowest pressure $P = 6$ bar better than the rest. The trend with increasing system pressure is predicted correctly but the magnitude of the change is greatly under-predicted. This could be attributed to a limitation of the one-dimensional model, which does not solve the equation of motion for the liquid slug. Also, looking at the model Equations (7.12) and (7.13), the frequency should increase in a power law with pressure; however, the fact that the proportion of the time residence for the three different zones also depends on the liquid-vapour density ratio induces a counteractive effect. Therefore, one of the reasons for the diminishing effect of pressure on the predicted heat transfer coefficient could be that the density ratio, which decreases with pressure, tends to decrease the proportional time of the confined bubble regime, which has the larger heat transfer coefficient from the three zones. Hence, this has reduced the increase in pressure caused by the frequency increase. In Figure 7.8 (b), the model predicts a small decrease in heat transfer coefficient with increasing mass flux, although it is noted that there is no significant effect of mass flux on the experimental heat transfer coefficient for the 4.26 to 1.1 mm tubes. The coefficients predicted by the convective model are only about 20% below the experimental values, which is a warning against interpreting independence of mass flux as an indication of the dominance of nucleate boiling.



(a)



(b)

Figures 7.8 Comparison of the 1.1 mm experimental data with the results of three-zone model: (a) effect of pressure at $300 \text{ kg/m}^2\text{s}$ and 68 kW/m^2 (b) effect of mass flux at a pressure of 8 bar and 69 kW/m^2 .

As discussed in Chapter five, unlike the larger tubes (4.26-1.1 mm) tubes, the smallest tube (0.52 mm) exhibited different heat transfer characteristics and flow pattern features. Briefly, the flow visualization at the exit of the heated test section indicated that annular flow regime with film interface instabilities dominated the flow patterns in this tube. Also, the heat transfer coefficient increases with quality at the high quality region, while the three-zone model heat transfer coefficient monotonically decreases with quality, since it considers periodic dryout to commence at low quality. These suggest that the three-zone model may not be expected to predict the data of the 0.52 mm tube. Figure 7.9 shows the three-zone model prediction results with the typical experimental data for the 0.52 mm tube for various heat fluxes at a constant mass flux of $300 \text{ kg/m}^2\text{s}$ and 6 bar pressure. As mentioned in Chapter five, two groups of heat flux with distinct effect on heat transfer coefficient and vapour quality were observed. The smaller heat flux group ($q < 14.8 \text{ kW/m}^2$) showed no effect of heat flux, while the heat transfer coefficient decreases sharply with quality and then become almost constant. This group of heat flux curves corresponds to the appearance of confined and elongated bubble flows at the exit of the heated section. At the start of the second group, new types flow patterns, with irregular liquid film surrounding a continuous vapour flow in the middle, emerge. At high heat flux, annular flow with small scale disturbances at the interface was observed. On the other hand, the predicted heat transfer coefficients exhibit simpler behaviour, in which they decrease monotonically with increasing quality and showed a uniform increase with heat flux. The model roughly estimated the magnitude of the heat transfer coefficient for the first heat flux group, although the trend was not well predicted. However, the model highly under-predicted the second group of data at the heat flux value. This could be due to the appearance of film instability observed for the second group of curves, which might have enhanced the convection heat transfer. However, the model assumes a stagnant, smooth, thin liquid film surrounding a confined bubble. Such flow regimes, i.e. confined bubbles with smooth liquid film were obtained for the first group of data for heat flux less than 14 kW/m^2 , i.e. low exit quality region. This suggests that for small diameter tubes, less than 1.1 mm diameter, the model may need to consider incorporating annular flow regimes with irregular film interface and adjust the one-dimensional steady state conduction because of the additional convection effect.

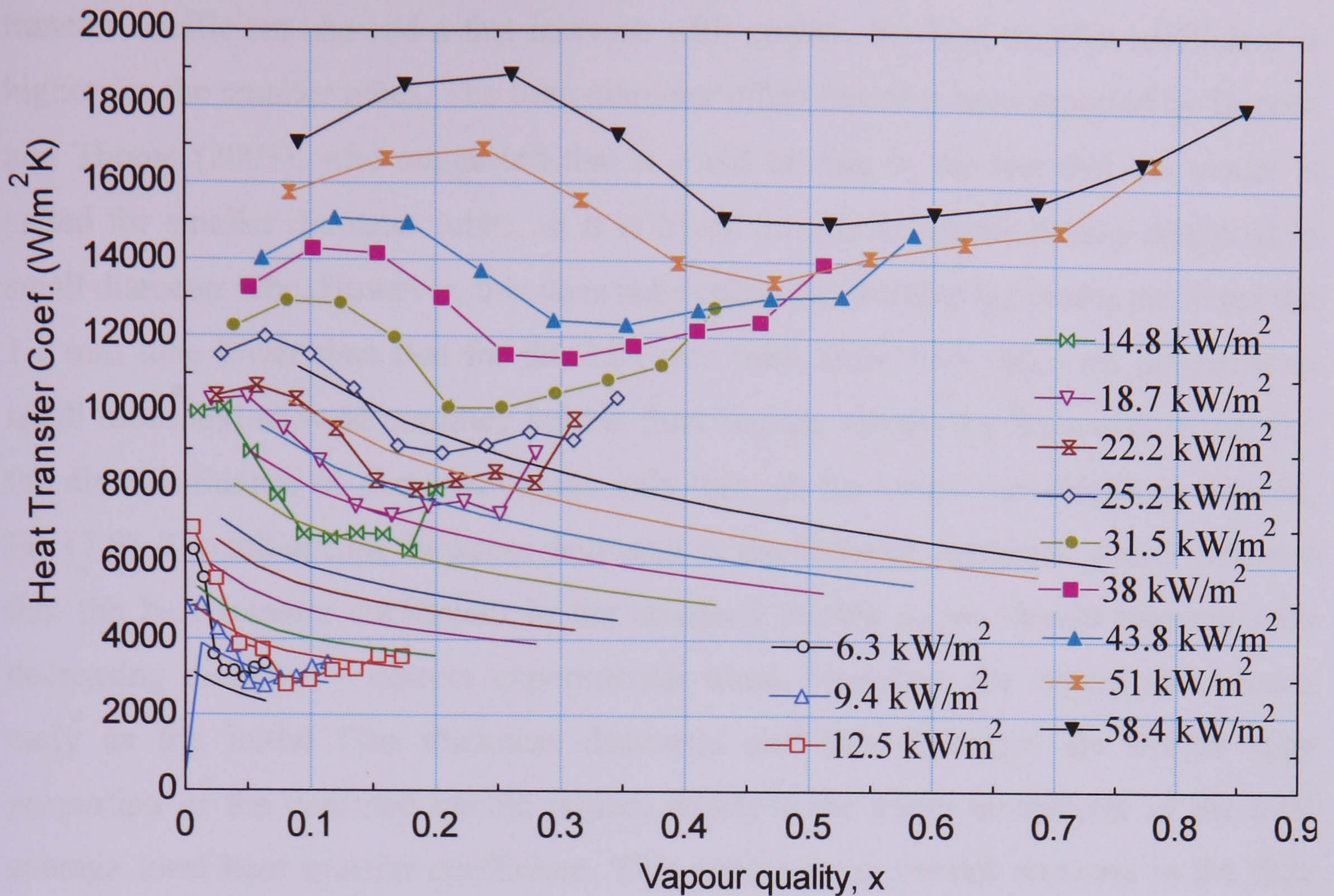


Figure 7.9 Comparison of the local heat transfer coefficient versus vapour quality of the 0.52 mm tube with the Thome et al. (2004), three-zone model, for various heat fluxes at 6 bar pressure and $300 \text{ kg/m}^2\text{s}$ mass flux.

Figure 7.10 presents the diameter effect as predicted by the model in comparison with the corresponding experimental result, at a system pressure of 8 bar and a mass flux of $300 \text{ kg/m}^2\text{s}$. The experimental results show that the heat transfer coefficient for the 4.26 and 2.88 mm tubes are almost the same, while it increases with decreasing diameter beyond 2.88 mm tube, indicating some sort of transition between 2.88 to 2.01 mm diameter. However, the model predicted nearly uniform decrease in heat transfer coefficient as the tube diameter decreases from 4.26 to 2.01 mm and slightly larger step of decrease when the diameter decreases from 2.01 to 1.1 mm. This is most likely because of the fact the difference in diameter between each tube is not uniform added to the slight variation in heat flux. As seen in Figure 7.9, the 0.52 mm results at high heat flux were under-predicted significantly. This was attributed to the fact that the prevailing flow regime was not confined bubble/slug, in which the model is based. Therefore, in figure 7.10, the 0.52 mm results are not included. In general, the model predicted opposite effect of diameter on the heat transfer coefficient, i.e. the heat transfer coefficient decreases with decreasing the tube diameter in the higher quality region ($x > \sim 0.08$). In the very low quality region ($x < 0.08$), where the predicted heat

transfer coefficient showed a fast increase with quality, the heat transfer coefficient is higher for the smaller tubes. The tube diameter effect has also been reported by Dupont and Thome (2005), who suggested that it could be due to the fact that the model is suited for smaller diameter tubes, as it is based on a flow pattern mostly observed in small diameter tube. However, this does not explain the fact that the model predicted the 1.1 mm tube lower than that for the 2.01 mm tube, since both tubes are classified as small tubes and showed confined bubble flow regime. Observing the model equations, the direct influence of diameter occurs only through the initial film thickness relation, Eq. (7.8). The initial film thickness decreases as the diameter decreases, which indicates that the heat transfer coefficient in the confined bubble region should increase with decreasing diameter – correct experimental trend. However, the dryout commences early as the initial film thickness decreases and this decreases the overall time proportion of the confined bubble region, which is the major contributor of the total average local heat transfer coefficient. This results in an overall decrease in the time average heat transfer coefficient.

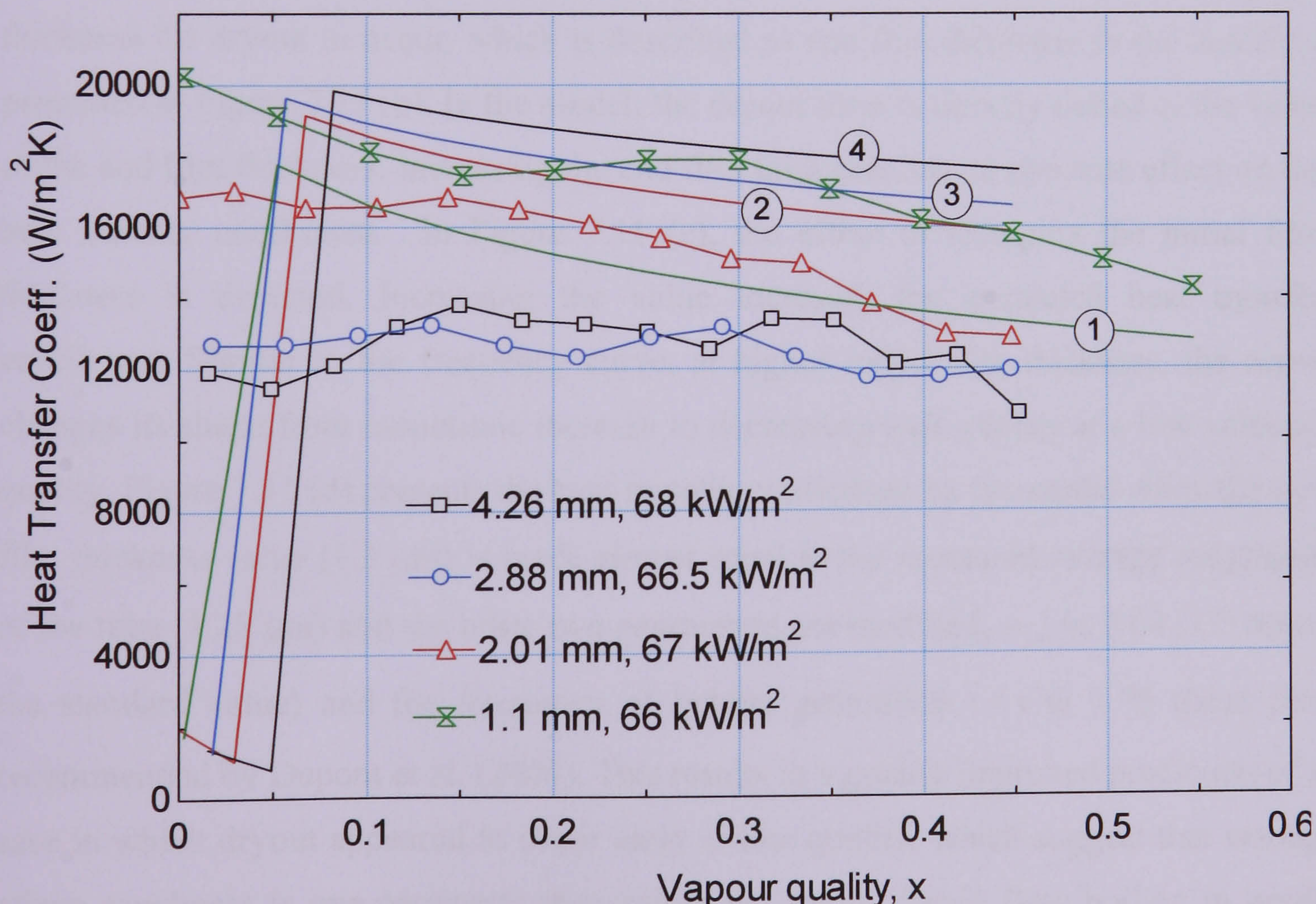


Figure 7.10. Effect of diameter on local heat transfer coefficient in comparison with that predicted by the three-zone model at 8 bar pressure and 300 kg/m² mass flux.

7.2.3 Parametric sensitivity of the three-zone model

The model prediction is highly sensitive to the three parameters, i.e. initial and end film thickness of the confined bubble and the frequency of bubble generation. As noted earlier, in all the above figures except Figure 7.6, the values used for these three parameters were those recommended by Dupont et al. (2004). Figure 7.11 shows the effect of varying each of these parameters, while keeping the others as given by their respective equations (7.11) to (7.14), on the predicted heat transfer coefficient for a sample case in which dryout appears to occur early at very low quality for the 1.1 mm tube. Increasing the bubble generation frequency increases the predicted heat transfer coefficient by an amount that decreases with quality, Figure 7.11 (a). At very low quality, (e.g. $x < 0.1$), a large increase in the frequency causes a sudden change in the character of the graph from a constant to a monotonic decrease. The frequency affects the relative contribution of the three zones using the respective residence times. This in turn affects the respective lengths of each zone (which also depend on local vapour quality), thereby changing the time-averaged heat transfer coefficient through the corresponding heat transfer coefficients of each zone. The sensitivity to the critical film thickness for dryout to occur, which is described as end film thickness in the model, is presented in Figure 7.11 (b). In the model, the dryout zone is directly linked to the value of the end film thickness. Increasing the end film thickness has an opposite effect on the heat transfer coefficient. In Figure 7.11 (c), the effect of changing the initial film thickness is depicted. Increasing the value increases the predicted heat transfer coefficient. Similar to the frequency curve, at higher initial film thickness, the curve changes its shape from monotonic increase to decreasing with quality at a low value of quality. Figure 7.11 (d) presents the heat transfer predictions by the model when the end film thickness value ($1.3 \mu\text{m}$) is made almost equal to the measured average roughness of the tube ($1.28 \mu\text{m}$) and the other two parameters are modified, C_{s0} to 0.64 (2.2 times the standard value) and the frequency of bubble generation (f) to 1.75 times that recommended by Dupont et al. (2004). This results in a greatly improved prediction of a case in which dryout appeared to occur early at low quality, which suggest that among others roughness is one parameter that influences dryout during flow boiling in small diameter tubes. Although, in the past roughness was not considered important factor for flow boiling, this study indicates that it should be measured and carefully characterised.

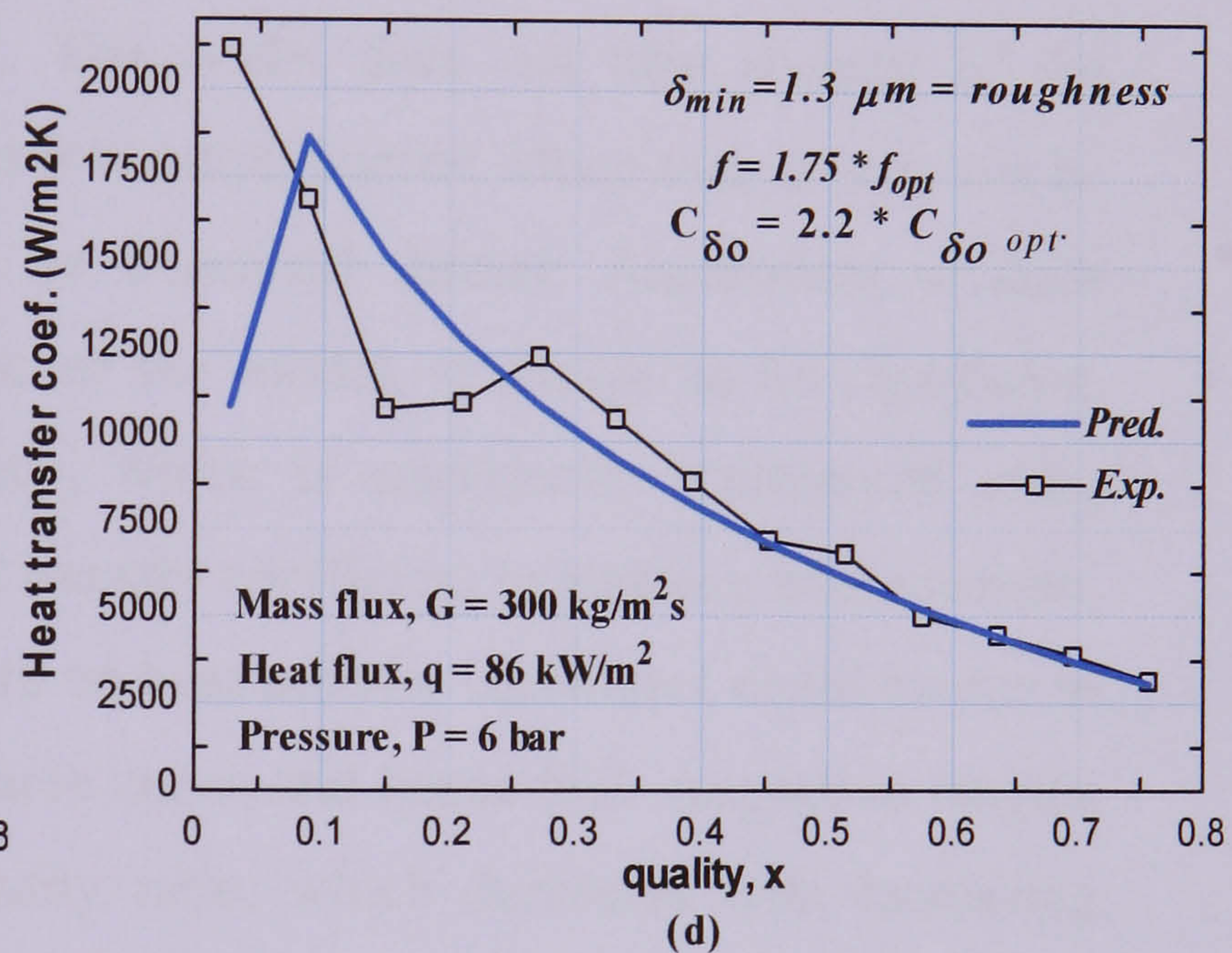
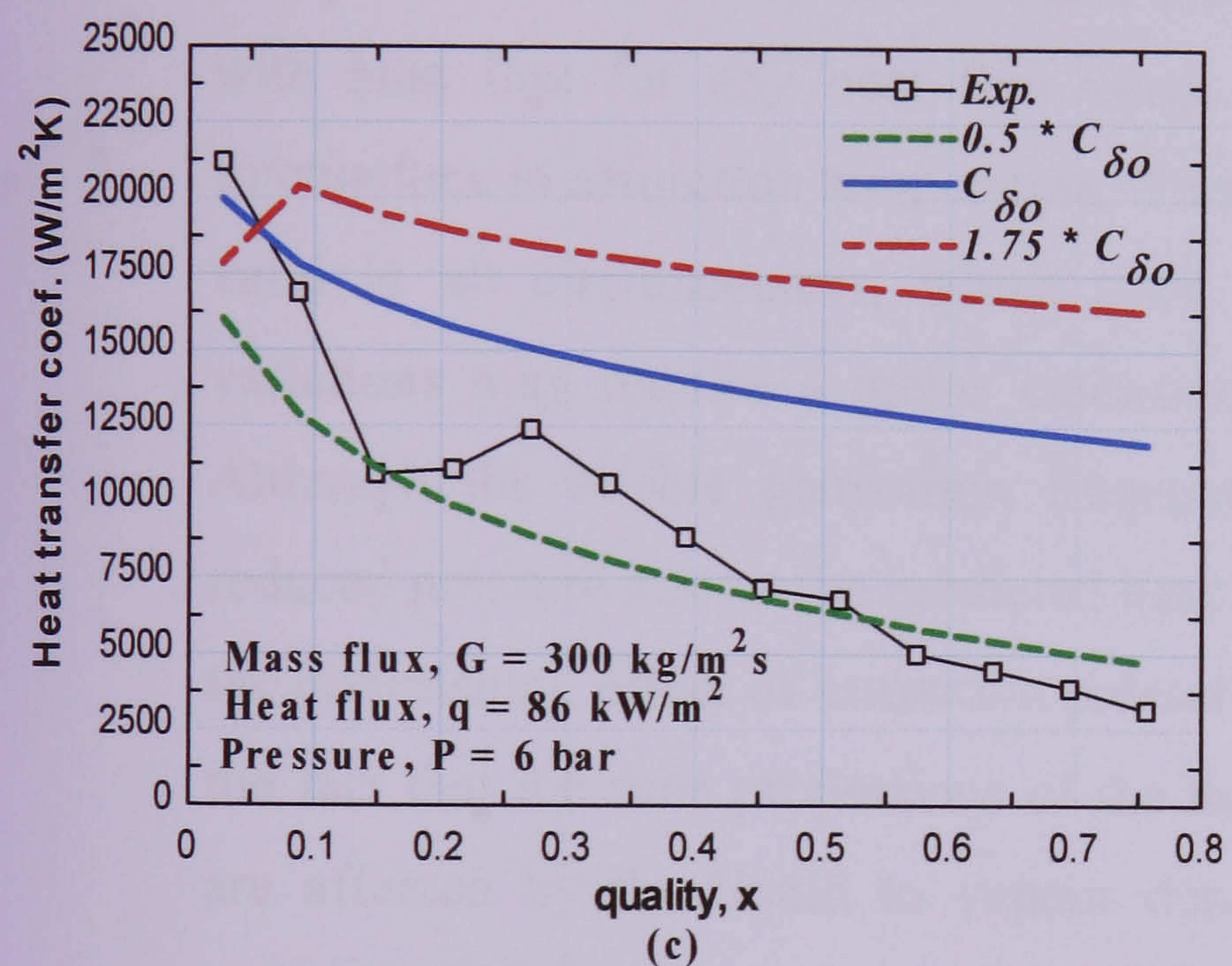
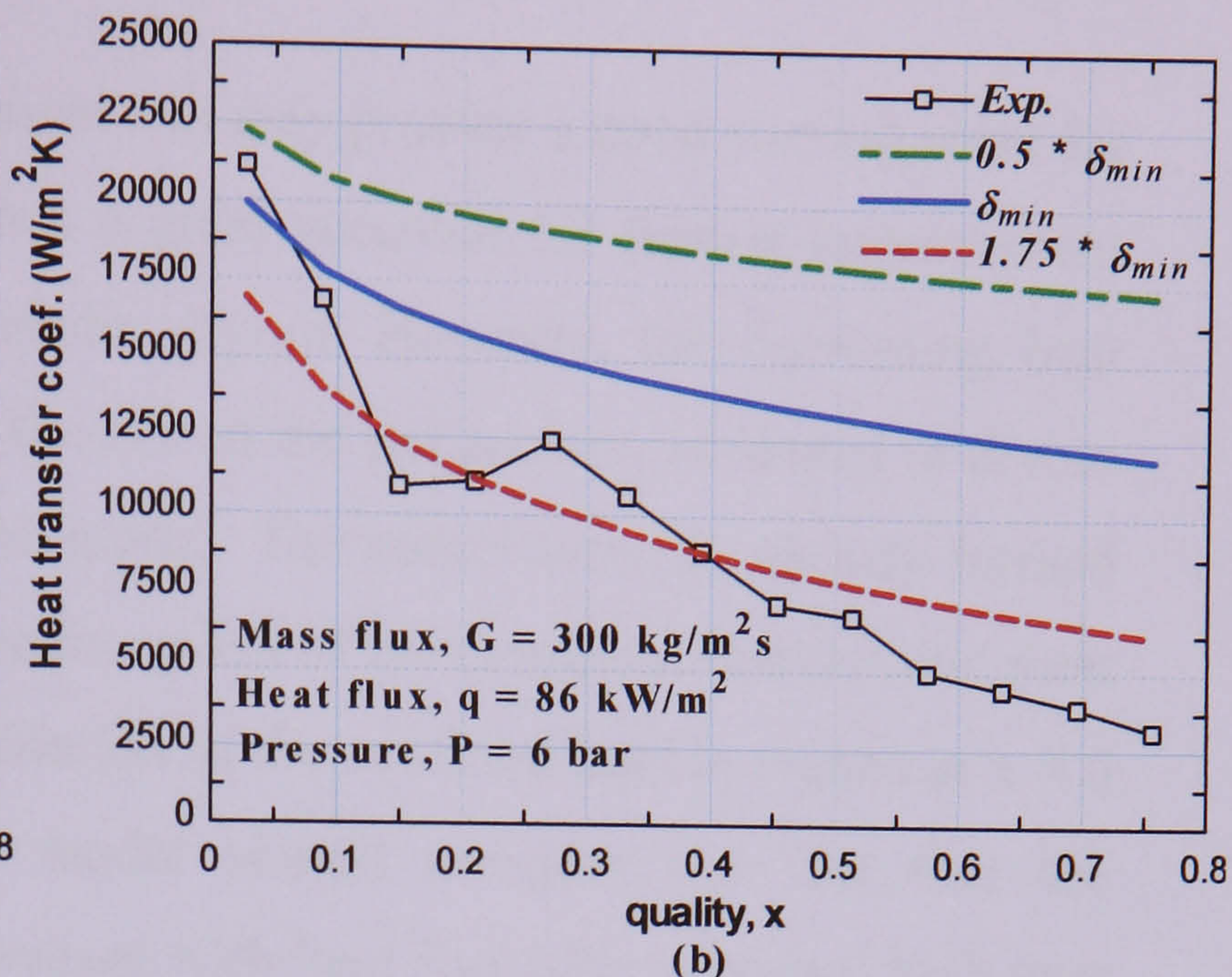
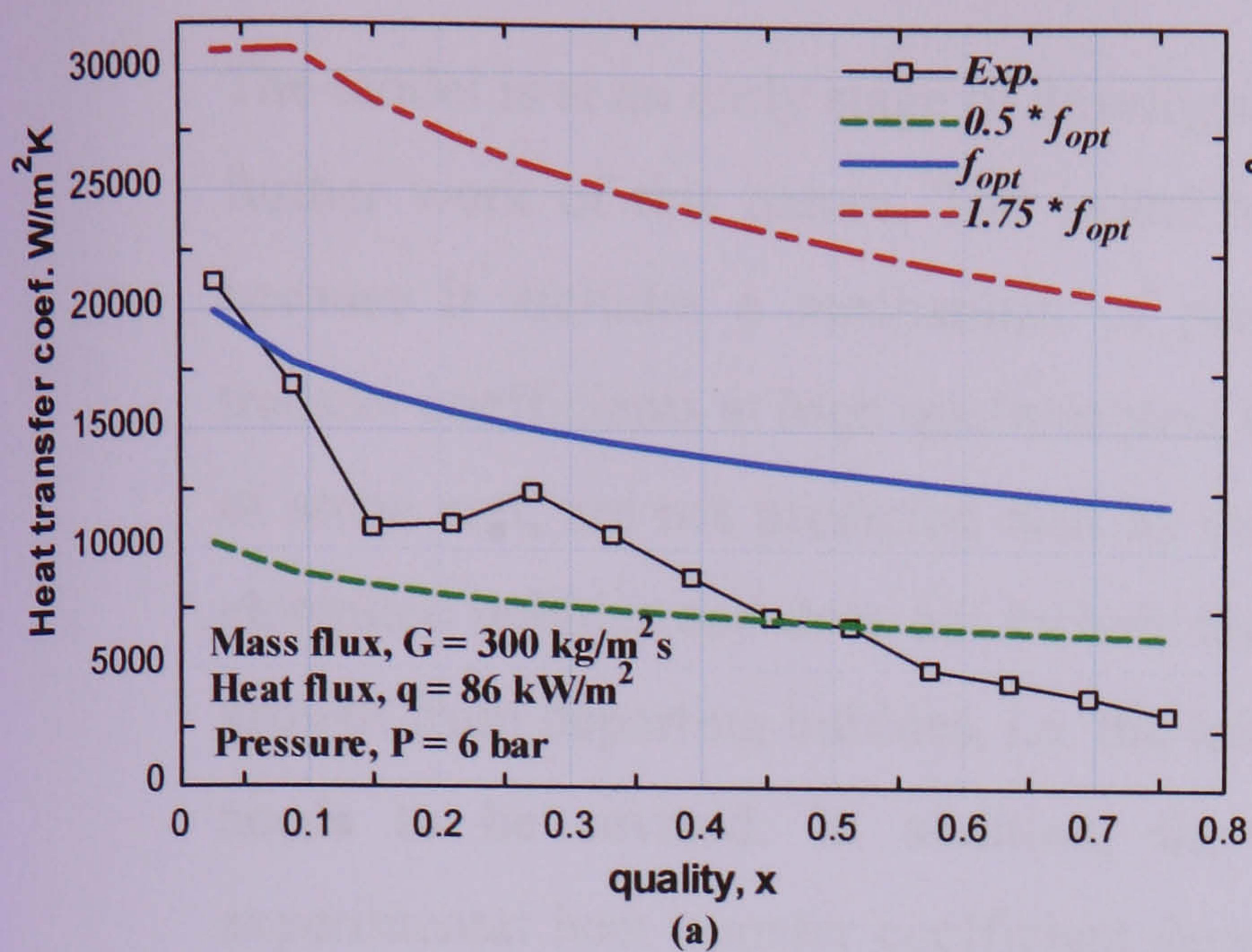


Figure 7.11. Sensitivity of the heat transfer coefficient to the three optimized parameters given by the model using the 1.1 mm tube results: (a) frequency of bubble generation (b) Correction factor to the initial film thickness, (c) critical film thickness to dryout, (d) prediction of dryout when the critical film thickness is same as roughness of the tube and the other two parameters are adjusted as shown.

7.2.4 Summary

The model is at an early stage of development and may provide a good starting point for further work of this nature. The model has a great potential for further improvement because it includes a mechanism of periodic dryout. However, the decreasing heat transfer coefficients at high qualities near the exit of the test section, attributed to dryout of some sort, are not predicted well by the model. The model assumes already formed elongated bubbles and does not include the inception of the elongated bubbles and their growth from departing bubbles, i.e. the initiation of the confined bubble regime at $x = 0$ needs to be revised. In addition, the model should consider the fact that the experimental heat transfer coefficient decreases with heat flux after a critical high heat flux value. At the moment the model provides heat transfer coefficient that increases with heat flux for any heat flux range. The model does not take account of the fluctuations in saturation temperature. This is a simplification which may or may not be valid in all circumstances, which must be examined further. Assessment of such variations may require a major extension of the model, if shown to be significant. Although the bubble generation frequency, which is empirically represented using reduced pressure allows the predicted heat transfer coefficient to increase with pressure, the diminishing effect of saturation pressure on heat transfer coefficient could be due to the fact that the time proportions of the three zones and hence their respective lengths are affected by the liquid to vapour density ratio, which decreases with increasing pressure. Solving the equation of motion for the liquid slug could also allow for the variations in pressure. Moreover, the fact that the three parameters, the bubble generation frequency, and the initial and end film thicknesses, in the model were optimised based on a large experimental database means that the model is not completely general and any genuine deviation in the prediction results could be compensated by the selection of these values. Therefore, further study leading to the independent evaluation of these parameters is necessary to make the model self-sufficient. Some of the modifications suggested will be considered in the improvement of the model in section 7.4.

7.3 Annular two phase flow model

The three-zone model predicts the local heat transfer coefficient for tubes with internal diameter greater than 1.1 mm reasonably well. However, when it comes to the 0.52 mm

tube, the model results are inconsistent with the experimental data both in magnitude and characteristics, especially for the second group of heat flux curves. This could be attributed to the new flow regimes observed in this tube, which were not commonly found in the larger tubes. After the threshold heat flux, a liquid-ring flow with symmetrical liquid rings that no more bridge the tube was observed followed by annular flow with highly irregular film interface as the heat flux increases. Such differences might have contributed to the enhancement of heat transfer coefficient observed in the 0.52 mm tube. Moreover, according to the flow regime map of Revellin and Thome (2007) for a 0.51 mm horizontal tube, the dominant flow patterns in the present 0.52 mm tube are annular flow at high vapour quality and coalescing bubble flow in moderate quality regions. The effect of coalescence of confined bubbles was not considered in the three-zone model. Therefore, it will be interesting to see how an annular two phase flow heat transfer model will perform with the results of the smallest tube. Flow maps of Chen et al. (2006) discussed in Chapter three, based on observations at the exit from the 4.26 – 1.10 mm tubes, show that the transition to annular flow shifts to higher qualities approaching $x \sim 0.5$, at the low mass fluxes covered in the present heat transfer tests. On the other hand, in this region ($x > 0.5$), these tubes exhibit a continuous decrease in heat transfer coefficient with quality, which are usually linked to dryout. This suggests that the use of annular two phase flow model for the 4.26 -1.10 mm tubes may not bring any sensible improvement unless it incorporates a mechanism of dryout. In the current study, it is likely that slug/churn flow is the typical flow pattern for the larger tubes in the region of near-uniform high heat transfer coefficient dependent primarily on heat flux. However, the relative importance of nucleate and convective boiling in this region is still unclear.

Qu and Mudawar (2003b) developed a steady-state, one-dimensional annular two phase flow model for flow boiling of water in microchannels. Such models have been intensively studied and proposed for large tubes, (Hewitt and Hall Taylor 1970, Wallis 1970, Whalley and Hewitt, 1978). In the Qu and Mudawar case, annular flow was observed at very low quality ($x \sim 0.0064$) with significant entrainment of liquid droplets. Therefore, their model considers the effect of droplet entrainment and deposition. Qu and Mudawar (2003b) also believed the decreasing heat transfer coefficient region to be caused by the increase in liquid film thickness as a result of droplet deposition. This may not be true for the present case, where droplet entrainment is not clearly observed

unlike flow boiling in very small channels using water. In general unlike water flow boiling, droplet entrainment and deposition are not commonly found phenomena for flow boiling of refrigerants. Boye et al. (2007) recently employed a one-dimensional simplified annular two phase flow model that does not consider droplet entrainment to predict their data. Consequently, the model of Boye et al. (2007) was chosen to predict the results of the smallest tube. In fact both studies assume laminar flow conditions with smooth liquid-vapour interface. As noted before, the present flow visualization for the smallest tube indicated that annular flow is the dominant flow regime, particularly for the second group of data with heat flux greater than 14 kW/m^2 . In addition, for this tube, the liquid-only Reynolds number is 769 at a mass flux of $300 \text{ kg/m}^2\text{s}$, which should correspond to laminar flow at the inlet, according to Kandlikar and Balasubramanian, 2004 ($Re < 1600$) and Zhang et al. 2004 ($Re < 1000$), unlike the liquid only Re numbers in the 4.26, 2.88, 2.01 and 1.1 mm tubes which were 7110, 4807, 3355 and 1850 respectively. However, the fact that the vapour flow was turbulent in the 0.52 mm tube at a mass flux of $300 \text{ kg/m}^2\text{s}$ (vapour-only Reynolds number of 13204) and given that significant film instability was observed for the smallest tube unlike the smooth film interface assumption, the use of the Boye et al. model for the 0.52 mm tube may not be appropriate. Nonetheless, the smallest tube data is compared with the model for the sake of completeness and curiosity. The following section presents comparison of the current 0.52 mm tube results with the Boye et al. (2007) annular two phase flow model.

Comparison with the current 0.52 mm tube results

The model developed by Boye et al. (2007) assumes steady-state laminar liquid film and vapour core flow. Short wave length ripples and long wave length disturbances, which are the main features of film interfacial instabilities, are neglected. The model also neglects capillary and gravitational forces. The model equations and various assumptions are briefly described in the literature review chapter. The heat transfer coefficient results of the model are compared with the current experimental data of the 0.52 mm tube in Figure 7.12 for a mass flux of $300 \text{ kg/m}^2\text{s}$ and 6 bar pressure. As seen in the figure, the annular two phase flow model has highly under-predicted the current results. As discussed in chapter 5, the 0.52 mm tube heat transfer results exhibited two groups of data with different influence of heat flux below and above a threshold heat flux. In the case of figure 7.12, the threshold heat flux is 14.8 kW/m^2 . There is no significant effect of heat flux on the heat transfer coefficient in the first group of data

($q < 14.8 \text{ kW/m}^2$), while the heat transfer coefficient in the second group increases with heat flux almost uniformly. On the other hand, the model showed no effect of heat flux and the predicted heat transfer coefficient increases monotonically with quality. This is somewhat expected from annular film flow model without droplet entrainment and deposition, where the film thickness continuously decreases with quality. The model analytically solves the momentum equation for a case of laminar vapour flow, while the vapour flow at $300 \text{ kg/m}^2\text{s}$ was turbulent. The fact that the predicted heat transfer coefficient is much lower than the corresponding experimental data is related to the oversimplification of the model assumptions. The model assumes a smooth film interface without interface shear stress, although the flow visualization results indicated wavy film and short wavelength disturbances. The film interface instabilities obtained in actual conditions could enhance the heat transfer rate, in which case the experimental heat transfer coefficient is much larger than the predicted value. In addition, the model neglects the acceleration in phases, interfacial shear stress and body forces. The experimental heat transfer coefficient increases with heat flux, while the annular flow model depends on quality. This indicates that there is a fundamental deviation in the model formulation and assumptions made with the actual condition, such as possibility of nucleation all along the tube including at high quality region, i.e. inside liquid film, which could also contribute to the significant disagreement. These variations have also not been discussed by Qu and Mudawar (2003b) with reference to their annular two phase model. Although acceleration of the vapour core flow and interfacial shear stress are considered, their model also assumes smooth film interface and droplet entrainment and deposition.

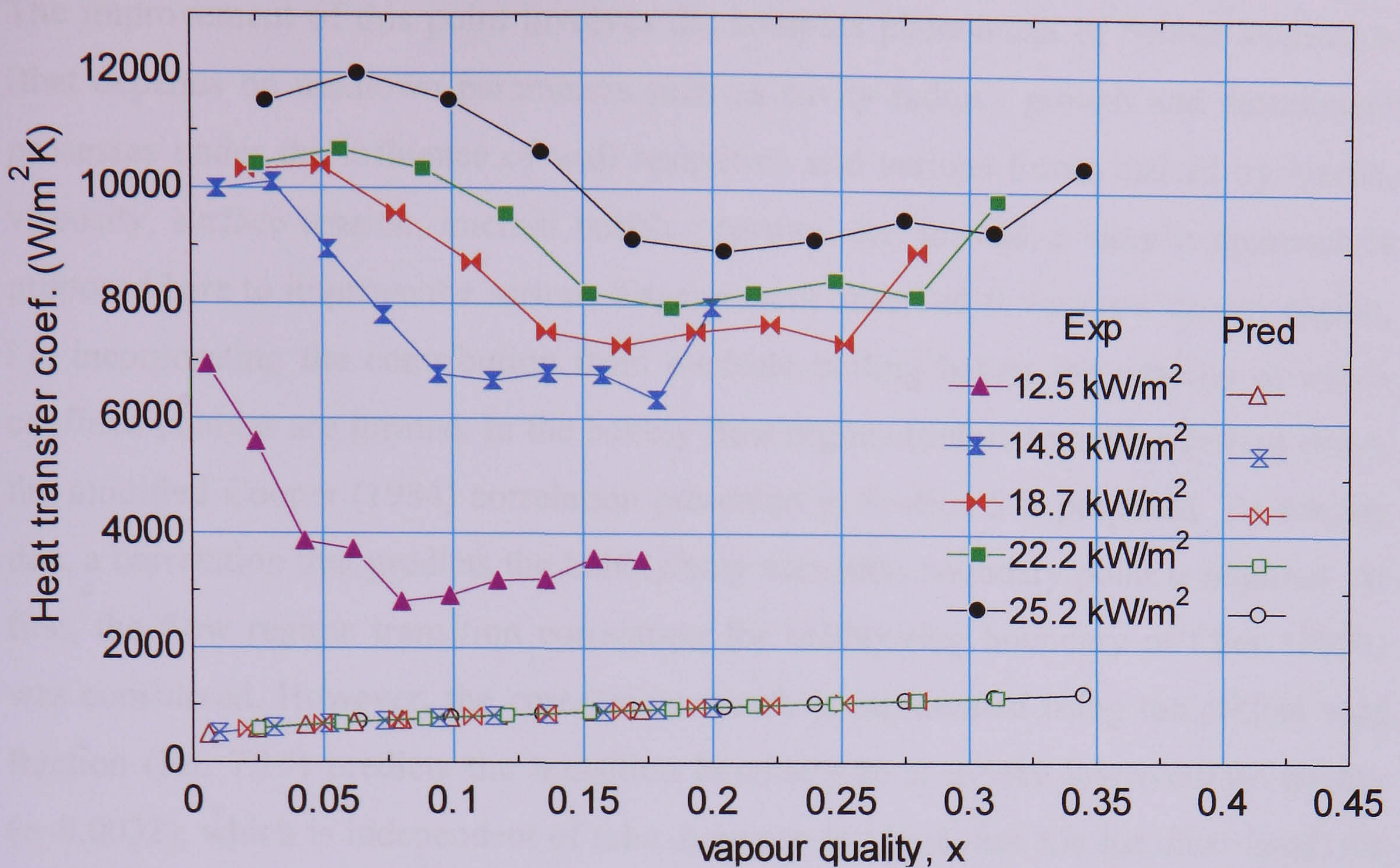


Figure 7.12 Comparison of the local heat transfer coefficient versus vapour quality of the 0.52 mm tube with the Boye et al. (2007), annular two phase model, for various heat fluxes at 6 bar pressure and $300 \text{ kg/m}^2\text{s}$ mass flux.

7.4 New improvements to the heat transfer models

As discussed before, the heat transfer data of the relatively larger tubes (4.26 – 1.1 mm tubes), before the occurrence of the sharply decreasing heat transfer region, lie mostly in the intermittent flow regimes (confined bubble, slug and churn flows). Therefore, a model, which is based on periodic flow and considers cyclic dryout, can be a good basis for further improvement. Consequently, the three-zone evaporation model of Thome et al. (2004) is selected for further development. Detail comparisons with the present heat transfer results and features of the model that require improvement have been addressed in section 7.2. This section discusses some possibilities of modifying or incorporating features that may improve the model performance based on the present heat transfer characteristics.

7.4.1 Incorporating nucleate boiling region

The model assumes already formed elongated bubbles and does not include the inception of the elongated bubbles and their growth from departing bubbles. In cases, where there is certain degree of subcooling, nucleation could start before $x=0$. Therefore, the experimental data is highly under-predicted at very low quality region.

The improvement of this point involves the complex phenomena of bubble nucleation (that depends on unknown parameters such as cavity radius), growth and detachment processes under the influence of wall restriction and various forces caused by inertia, viscosity, surface tension, internal bubble pressure, etc. Instead, a simpler approach is proposed here to improve the serious disagreement observed at very low quality region, i.e. incorporating the contribution from nucleate boiling before the position at which confined bubbles are formed. In the bubbly flow regime (before transition to slug flow), the modified Cooper (1984) correlation presented in Section 5 is proposed. To employ this, a correlation that predicts the bubbly/slug transition boundary point is required. At first, the flow regime transition correlation for bubbly/slug boundary of Chen (2006) was considered. However, the correlation, which is represented using the critical void fraction (Eq. 7.15) predicts the transition boundary to at a very low constant quality ($x \sim 0.0032$), which is independent of tube diameter and heat flux. On the other hand, the heat transfer coefficient of the three-zone model showed that the transition quality, at which the fast increasing heat transfer coefficient region shifts to the monotonically decreasing region, increases with heat flux. Consequently, the use of the Chen (2006) bubbly/slug transition correlation did not make any significant improvement.

$$\alpha_{crit} = 0.138(U_{gs} + U_{ls})^{0.344} \quad (7.15)$$

Recently, Revellin and Thome (2007b), proposed a correlation for flow regime transition boundary from their extensive flow visualization studies. Their correlation for the isolated bubble/coalescing bubble transition boundary varies with heat flux and tube diameter (Eq. 7.16). Therefore, the correlation was used to identify the nucleate boiling region, with no periodic dryout.

$$x_{IB/CB} = 0.763 \left(\frac{Re_{lo} Bo}{We_{go}} \right)^{0.41} \quad (7.16)$$

The results of this modification are shown for a sample case of 2.01 mm tube result in Figure 7.13 at a mass flux of 300 kg/m²s and 8 bar pressure. As seen in the figure, the highly under-predicted results at very low quality are improved although the sudden slight increase in the predicted heat transfer coefficient requires further investigation.

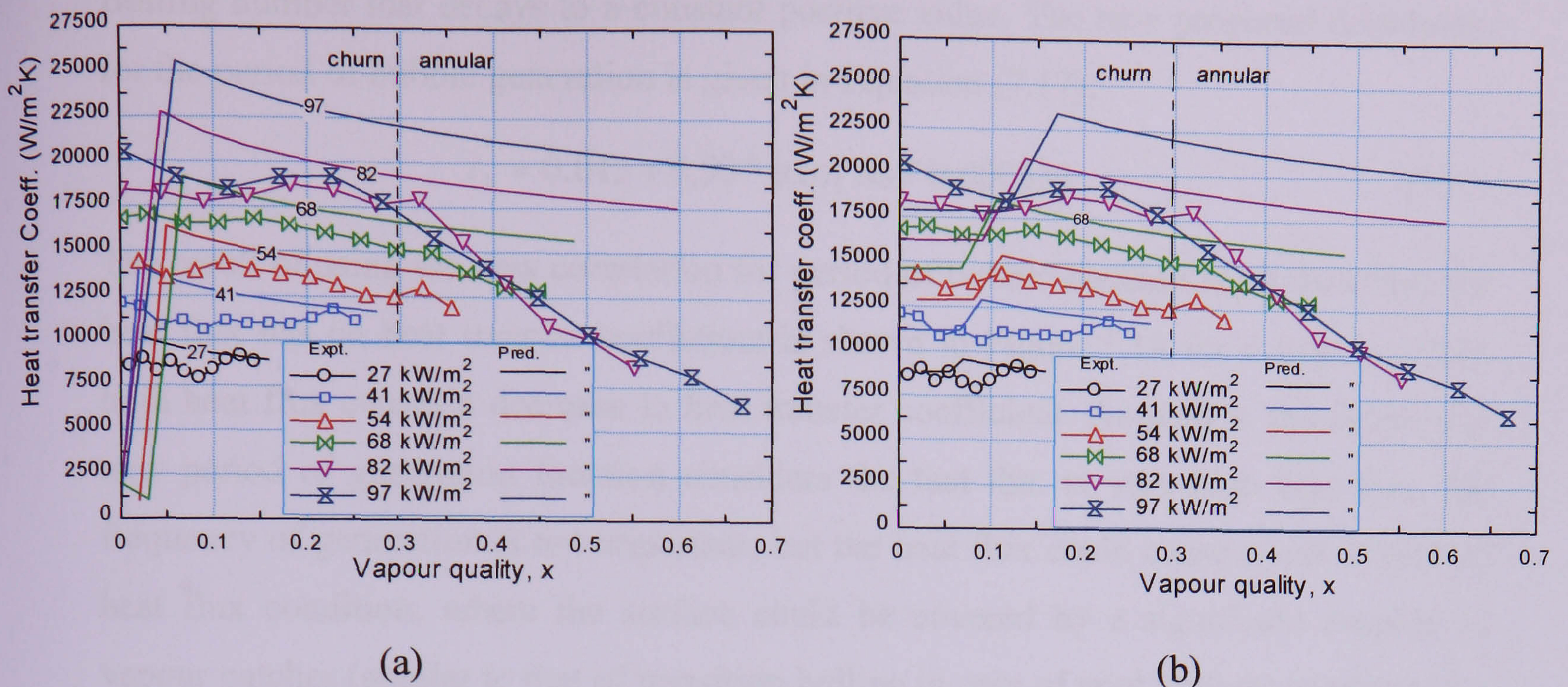


Figure 7.13 Comparison of local heat transfer coefficient for 2.01 mm tube at a mass flux of 300 kg/m²s and 8 bar pressure with: (a) original three-zone model, (b) modified by including nucleate boiling term in the bubbly flow regime.

7.4.2 Improving effect of heat flux on heat transfer coefficient

One of the features of the model that may require modification is the fact that the model does not have any limit for the effect of heat flux on heat transfer coefficient. The effect of heat flux on the experimental heat transfer coefficient gets smaller as the heat flux is increased; this is not well predicted by the model. As shown in the comparison results at different heat flux in Section 7.2.2, the experimental heat transfer coefficient increases with heat flux for low to moderate heat flux values (e.g. 20-80 kW/m² in case of Fig. 7.13a). At high heat flux values, the heat flux effect decreases and further increase in the heat flux produces an opposite effect on the heat transfer coefficient for $x > 0.15$ until all heat flux lines merge, see figure 5.3. However, the predicted heat transfer coefficient increases with heat flux almost uniformly for all heat flux values, i.e. it continues increasing even at very high heat flux values, highly over-predicting the experimental data. This could be due to the fact that the empirical correlation for the bubble generation frequency used in the model is a power function of the heat flux ($f_{opt} = C * q^{1.74}$), which gives a steep increase in frequency with heat flux; see also Eq. (7.12). However, in the actual case, after a certain high heat flux, the number of active nucleation sites should increase such that the frequency of bubble generation may not be important anymore. Therefore, this point is taken into account by modifying the period of bubble generation (reciprocal of the frequency) to be an exponential function of the

Boiling number that decays to a constant positive value. The new proposed correlation for the period of bubble generation is given in Equation (7.17).

$$\tau_b = 0.013 + 0.53 * \exp(Bo / 0.00033) \quad (7.17)$$

The result of using the new correlation for period of bubble generation on the effect the heat flux has on heat transfer coefficient is shown in Figure 7.14 for a case in which high heat flux causes a decrease in heat transfer coefficient. As seen in the figure, the new period of generation function considers the fact that at very high heat flux, the frequency of generation is not important, but the heat flux could cause a sort of critical heat flux condition, where the surface could be covered by a significant number of vapour patches (similar to that of transition boiling in case of pool boiling) resulting in a decrease in the heat transfer coefficient.

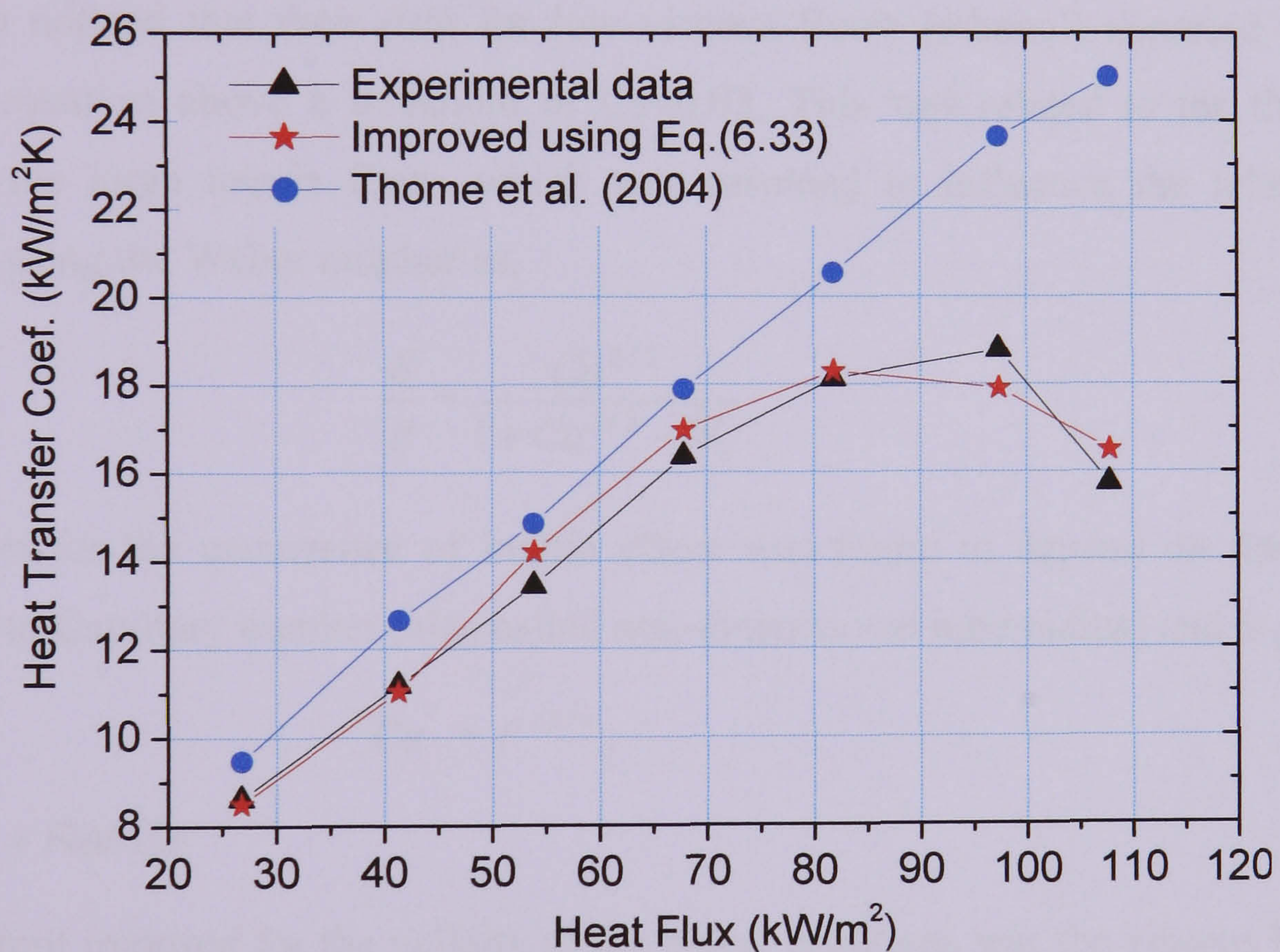


Figure 7.14 Comparison of the average heat transfer coefficient ($x \leq 0.25$) as a function of heat flux at a mass flux of $300 \text{ kg/m}^2\text{s}$, 8 bar pressure for the 2.01 mm tube data.

7.4.3 Film thickness predictions

As discussed before, the local heat transfer coefficient during the passage of a confined bubble is also highly sensitive to the local liquid film thickness. The local liquid film thickness is in turn influenced by the initial film thickness and evaporation rate, which also affects the final film thickness (dryout). The mechanism of the establishment of an initial film by a passing bubble is a complex phenomenon, which could involve several parameters as surface tension, inertia and viscous effects and in a microscale level to,

disjoining pressure, dynamic contact line. Most studies of film thickness have been focussed on steady adiabatic flows of highly viscous liquids with negligible inertia. In such cases, the film thickness is mostly given as function of the Capillary number (ratio of viscous to surface tension forces). For instance, Taylor (1961) obtained analytically a relative film thickness relation for $Ca \ll 1$.

$$\frac{\delta}{R} = 1.34Ca^{3/4} \quad (7.18)$$

Later, Aussillous and Quéré (2000) found precise curve fit to Taylor's data for viscous oils and their data for silicon oils using equation (7.35) for $Ca < 1.2$.

$$\frac{\delta}{R} = \frac{1.34Ca^{2/3}}{1 + 3.35Ca^{2/3}} \quad (7.19)$$

They also noticed that their data for low viscous fluids (ethanol) departed from the Taylor's equation above a threshold of $Ca \sim 0.03$. This was related to the thickening effect of the large inertia force, which was assumed to influence the relative film thickness using the Weber number as,

$$\frac{\delta}{R} \sim \frac{Ca^{2/3}}{1 + Ca^{2/3} - W_e} \quad (7.20)$$

A criterion for the occurrence of inertia effect was found to depend on the ratio of Reynolds to Capillary number (also called non-dimensional tube radius) and is given as

$$Ca^* \sim F^{-3/4}, \quad (7.21)$$

where, $F = Re/Ca$

Another limit imposed for the validity of the above equations was the viscous boundary layer limit obtained from Prandtl's law.

$$\delta \sim \left(\frac{\mu L}{\rho U_B} \right)^{1/2} \quad (7.22)$$

If the thickness obtained using equations (7.18) to (7.20) is larger than the viscous boundary layer, the deposition is controlled by the viscous boundary layer.

As mentioned before, the above relations are developed for adiabatic steady flows with negligible inertia effects. However, the phenomena of initial film thickness formation will be different when a nucleated bubble is passing inside a continuously heated liquid

field. There are no theoretical models developed for the later case. Thome et al. (2004) modified the film thickness relation of Moriyama and Inoue (1996), which is empirically obtained for unsteady growth of bubble in R113 between parallel transparent plates. The gap between the plates was varied from 0.1 to 0.4 mm. The film thickness was considered to be governed by two factors, i.e. viscous boundary layer and surface tension forces based on Bond number. Thome et al, (2004) used asymptotic expression between the above two effects and correlated it using a 1591 test data of various refrigerant flow boiling (Eq.7.8). A comparison of the modified Moriyama and Inoue (1996) relations with the various film thickness relations for adiabatic flows of negligible inertia is shown in Figure 7.15. The values calculated are for the 1.1 mm tube at a mass flux of $300 \text{ kg/m}^2\text{s}$ and 6 bar pressure for various Capillary numbers (of the present experimental range). The relative film thickness obtained using the modified Moriyama and Inoue (1996) equation has highly under-predicted the relations developed for viscous flows with negligible inertia. This indicates that the film thickness used in the three-zone model could be much lower than is expected for steady viscous flows. One could relate this to the inertia effect; however according to Aussillous and Quéré (2000) and de Ryck (2002), increasing inertia should have a thickening effect not a decrease in film thickness. Kenning et al. (2006) examined various film thickness relations and stated that the modifications applied by Thome et al. (2004) to the Moriyama and Inoue (1996) have eliminated the influence of bubble growth time. In addition, the behaviour of the film thickness with increasing bubble velocity, i.e. that the film thickness reaches a maximum value and then decreases, is inconsistent with the available experimental evidence for steady flow. They also pointed out the fact that there are no better guidelines to film thickness under boiling conditions except the correlation for steady, laminar flows.

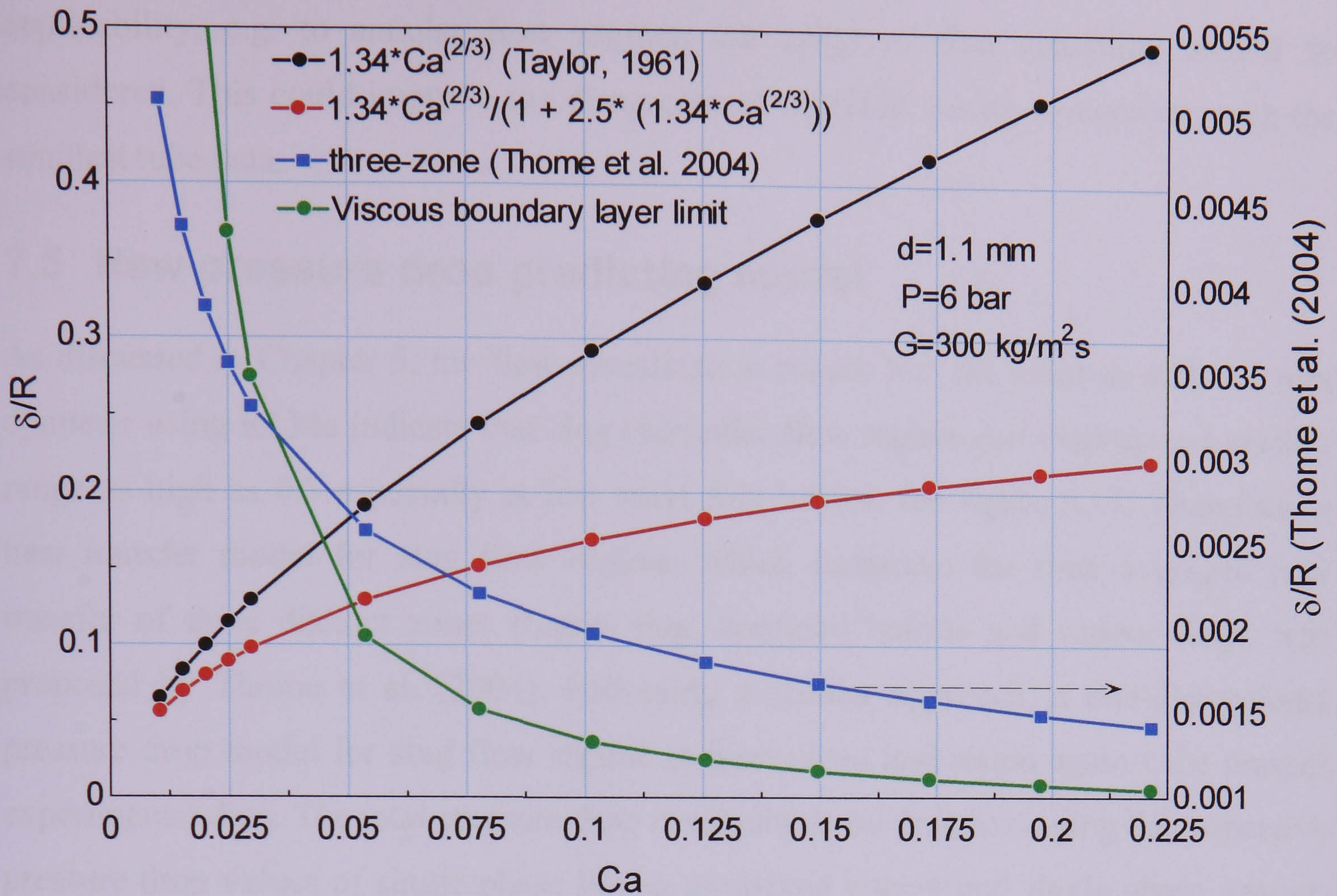


Figure 7.15 Comparison of various film thickness relations for 1.1 mm tube at a mass flux of 300 kg/m²s and 6 bar pressure.

7.4.4 Summary

After a detailed comparison of state-of-art-the-art, three-zone evaporation model of Thome et al. (2004) with the present experimental data, various features of the model that require improvement were pointed out and discussed. Some improvements that can be made to the model have been examined. Features that require further investigation include analytical evaluation of the currently optimised parameters (initial and end film thickness and frequency of bubble generation). Some modifications have been made to the model (e.g. incorporating nucleate boiling regime, new correlation for frequency of bubble generation and relating the end film thickness to the roughness of the tube). These changes resulted in an improvement of the model prediction capability. However, these and other features require further study. The additional features include a better theoretical model for predicting initial film thickness during slug flow, considering additional effect of coalescence and film waviness on heat transfer and determination of the model's validity range so that it can include annular flow regime once the liquid slug vanishes. The model is developed assuming a smooth film interface, a condition which can be achieved only at very low quality range. To extend the model's

applicability, e.g. to annular flow regime, the effect of film instability should be considered. This could improve the disagreement obtained during comparison with the smallest tube data.

7.5 New pressure drop predicting model

As discussed in Chapter 5, the flow visualization results for the tubes of 4.26-1.1 mm diameter using R134a indicate that slug (periodic) flow regime can exist up to a quality range as high as 0.5 especially at low mass flux values, see figure 3.15. Therefore, a heat transfer model for slug flow regime, which considers the time averaged heat transfer of three distinct zones (liquid slug, confined bubble and vapour slug), was proposed by Thome et al. (2004). Following a similar approach, a one-dimensional pressure drop model for slug flow regime is formulated and tested against the present experimental data. The total pressure drop is calculated by time-averaging the respective pressure drop values of single phase liquid, elongated bubble and single phase vapour. Total implies pressure drop from inlet to outlet; models are for local conditions and can also applies to local pressure gradients.

$$\Delta P = \frac{t_l}{\tau_b} \Delta P_l + \frac{t_{film}}{\tau_b} \Delta P_{film} + \frac{t_{dry}}{\tau_b} \Delta P_v \quad (7.23)$$

The pressure drop during the flow of liquid slug and vapour slug (if dryout occurs) can be obtained from well known correlations of single phase pressure drop gradients; multiplied by their respective lengths and assuming fully-developed flow.

$$\Delta P_l = \left(\rho_l g + \frac{G^2 f_{lo}}{\rho_l R} \right) L_{LS} \quad (7.24)$$

$$\Delta P_v = \left(\rho_g g + \frac{G^2 f_{go}}{\rho_g R} \right) L_{VS} \quad (7.25)$$

In the confined bubble zone, the axial pressure drop gradient is determined by solving the momentum equation both in the liquid film and vapour bubble regions as the bubble passes a fixed location and the additional assumptions discussed below.

$$\Delta P_{film} = \left(-\frac{dP}{dz} \right)_{CB} L_{CB} \quad (7.26)$$

The respective lengths of the three zones are determined by multiplying the residence time proportion of each zone by the total pressure drop length. The residence time proportions for the liquid slug (Eq. 7.27) and confined bubble flow (Eq. 7.28) are related to the period of bubble generation or frequency of bubble generation obtained from Thome et al.(2004) assuming homogeneous flow, i.e. the liquid slug and the confined bubble travel with the same velocity.

$$\frac{t_l}{\tau_b} = \frac{1}{1 + \frac{\rho_l}{\rho_v} \frac{x}{1-x}} \quad (7.27)$$

$$\frac{t_v}{\tau_b} = \frac{1}{1 + \frac{\rho_v}{\rho_l} \frac{1-x}{x}} \quad (7.28)$$

Again where, $\tau_b = \frac{1}{f_b}$

The explicit solution of the momentum equation requires an assumption of either shear stress or film thickness. The present analysis assumes a known average film thickness. The local film thickness is obtained by averaging the initial and end film thickness values as discussed for the three-zone heat transfer model, Dupont et al. (2004). Therefore, for each location a steady flow of constant film thickness was considered. The initial and end film thickness values are taken again from the expressions used in the three-zone heat transfer model (Eq. 7.8 for the initial film thickness and end film thickness value of $0.67 \mu\text{m}$ was taken). The selection of end film thickness has a significant effect on adjusting the dryout condition. If dryout does not occur, the end film thickness is obtained from the evaporation rate in the time elapsed as the confined bubble passes, i.e. the residence time of the confined bubble (Eq. 7.28).

The next step is to find an expression for the pressure drop gradient during the confined bubble flow. Figure 7.16 shows a sketch of the three zones and the control volumes in the confined bubble zone.

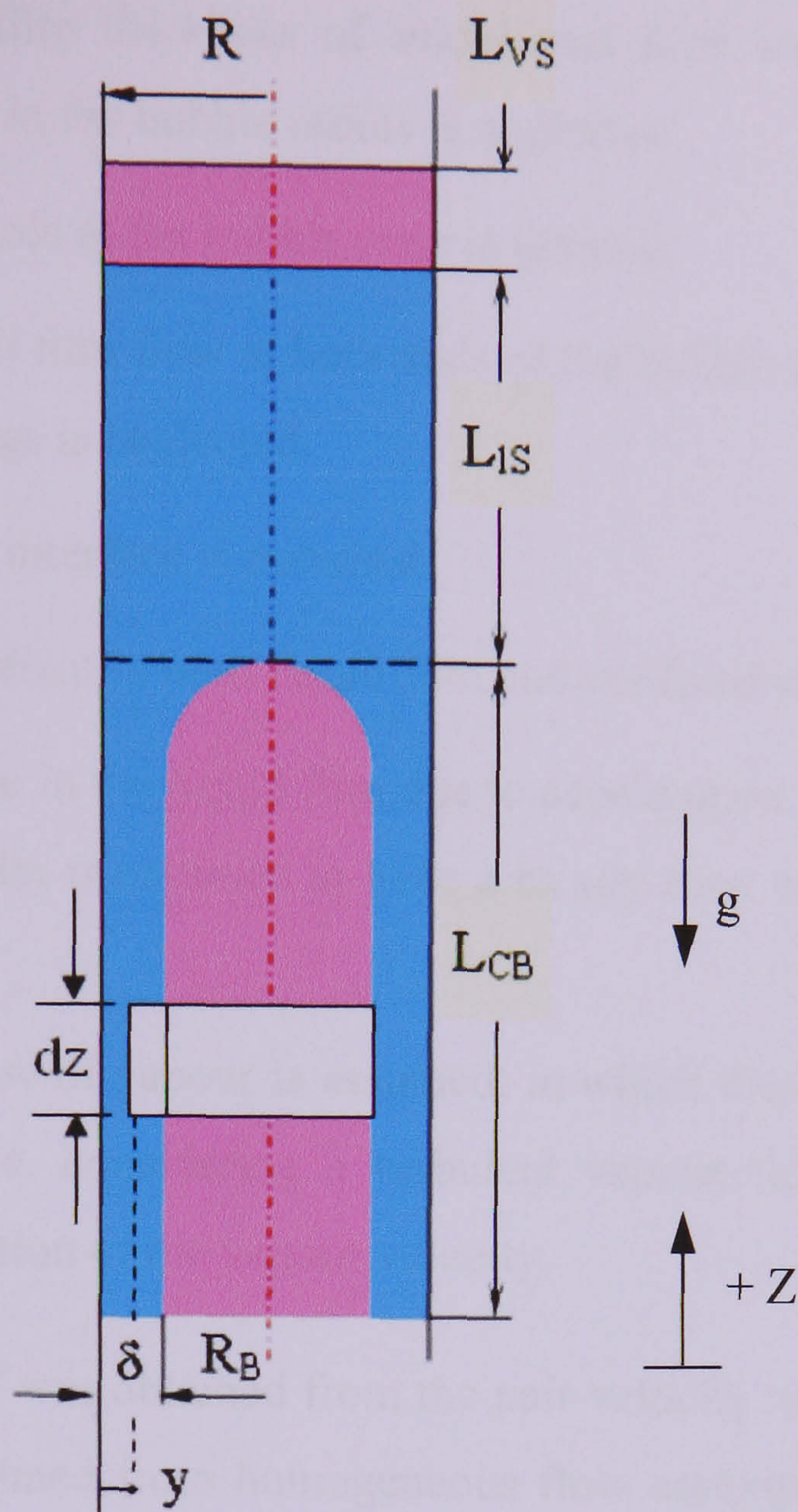


Figure 7.16 Sketch of the three zones and their respective length.

Momentum equations both in the liquid film and bubble region are solved simultaneously to obtain a pressure drop gradient expression in the confined bubble zone. Various assumptions are taken to simplify the physical condition in order to obtain a simple analytical expression. The flow in the liquid film is assumed laminar, while a turbulent vapour flow in the confined bubble regime is considered. This is due to the fact that the vapour-only Reynolds number for the larger tubes (1.1 – 4.26 mm) at the lowest inlet mass flux of $100 \text{ kg/m}^2\text{s}$ ranges from 8975 – 34759.

Other assumptions include:

1. The axial coordinate, Z , is fixed, while the respective lengths of the three zones change with time.
2. The film thickness is assumed to be much smaller than the tube diameter; hence the curvature effect is neglected.

3. A constant average film thickness of initial and final values is considered. Therefore, the change in the bubble radius is neglected.
4. The surface tension force at the bubble nose is ignored.
5. The effect of the liquid film flow at both ends of the bubble on the upstream and downstream liquid slugs is neglected.
6. Smooth liquid-vapour interface is assumed.
7. The axial pressure gradient in both liquid film and confined bubble is the same.
8. The momentum change in the liquid film due to acceleration of the liquid film is neglected, since the film is assumed to have a steady flow with relatively small velocity.
9. A one-dimensional flow of vapour is assumed, in which the bubble travels with the centre velocity, i.e. considering a turbulent vapour flow with an almost uniform radial distribution of the vapour velocity.

The velocity of the bubble was obtained from the pair velocity relation of Thome et al. (2004), which is calculated from homogeneous flow assumption, i.e. assuming the bubble travels at the same speed with the liquid slug,

$$U_P = U_h = G \left[\frac{x}{\rho_v} + \frac{1-x}{\rho_l} \right] \quad (7.29)$$

Since the quality in the above expression is obtained from the thermodynamic quality using the total mass flow rate and heat flux, it is time averaged over the whole flow patterns passing the fixed location. On the other hand the bubble rise velocity was also correlated using homogeneous velocity (U_h) and drift velocity (U_d) by Mishima and Hibiki (1996).

$$U_B = C * U_h + U_{df} \quad (7.30)$$

They recommended the coefficient, C and the drift velocity (U_d) from Ishii (1977) relation as,

$$C = 1.2 - 0.2 \left(\frac{\rho_g}{\rho_l} \right) \quad (7.31)$$

$$U_{df} = 0.35 \left(\frac{gD(\rho_l - \rho_g)}{\rho_l} \right) \quad (7.32)$$

The film velocity can be obtained from the mass balance and the area void fraction as,

$$\frac{U_{lf}}{U_B} = \frac{1-x}{x} \frac{\alpha}{1-\alpha} \frac{\rho_g}{\rho_l} \quad (7.33)$$

where,

$$\alpha = \left(1 - \frac{\delta}{R}\right)^2 \quad (7.34)$$

The two velocity expressions for the bubble velocity and the liquid film velocity calculated using equation 7.33 are compared in figure 7.17. As seen from the figure, the velocity correlation of Mishima and Hibik (1996) is higher than the homogeneous velocity of Equation (7.30), and the difference increases with heat flux. This is because of the additional terms of drift velocity and coefficient C (eq. 7.31). The film velocity is much lower than the bubble velocities and decreases at high heat flux.

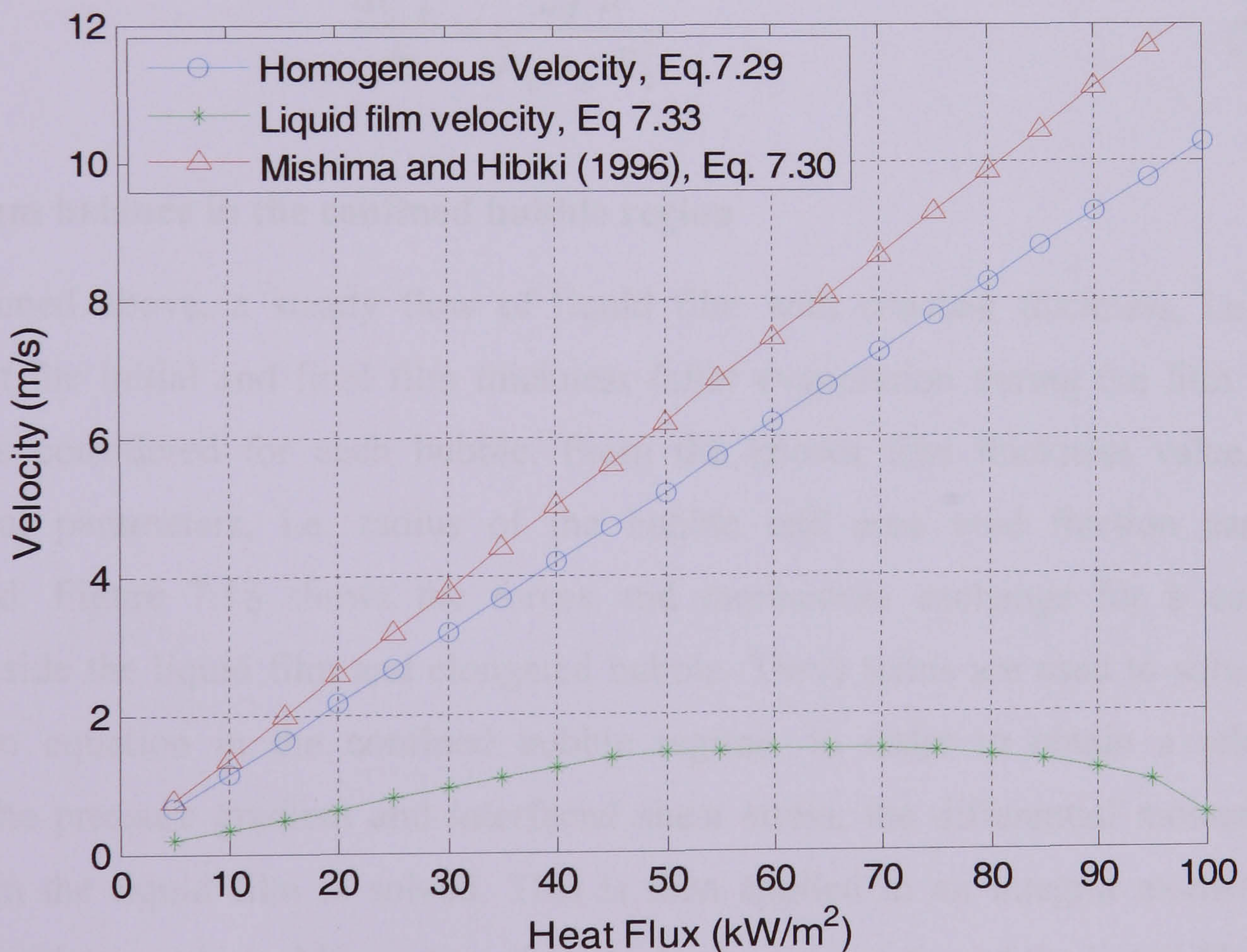


Figure 7.17 Comparison of the various velocity relations as function of heat flux for 1.1 mm tube at a mass flux of 300 kg/m²s and 6 bar pressure.

Mass conservation equations

The overall mass balance in the confined bubble region is given as

$$\frac{d\dot{m}_v}{dz} = -\frac{d\dot{m}_l}{dz} \quad (7.35)$$

An energy balance over the control volume length Δz , will be used to determine the rate of evaporation per unit length and the acceleration of the bubble.

$$-\frac{d\dot{m}_l}{dz} = \frac{d\dot{m}_v}{dz} = \frac{q(2\pi R)}{h_{lg}} \quad (7.36)$$

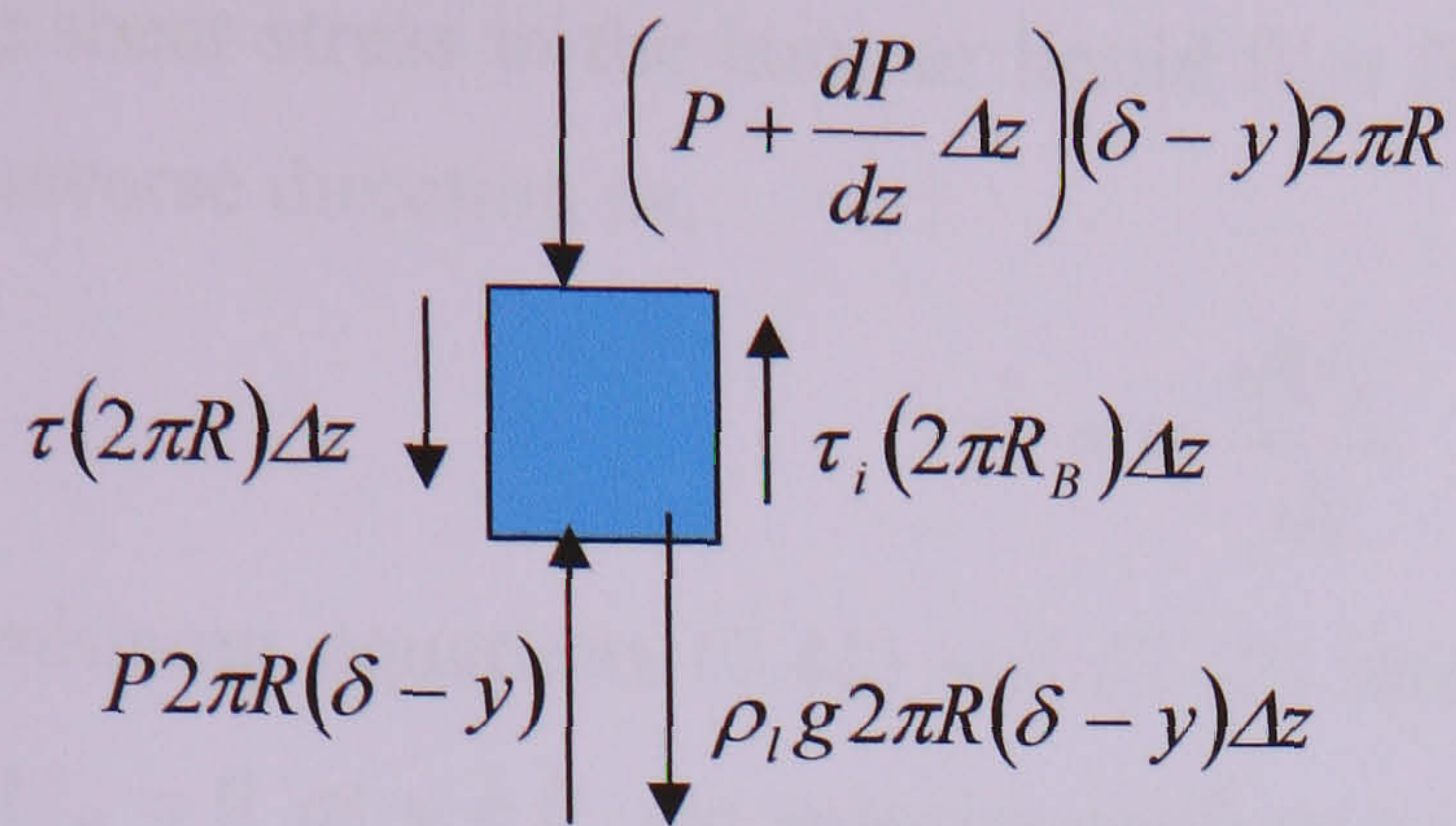
$$\dot{m}_v = \rho_g (\pi R_B^2) U_B \quad (7.37)$$

$$\frac{d\dot{m}_v}{dz} = \rho_g (\pi R_B^2) \frac{dU_B}{dz} = \frac{q 2\pi R}{h_{lg}} \quad (7.38)$$

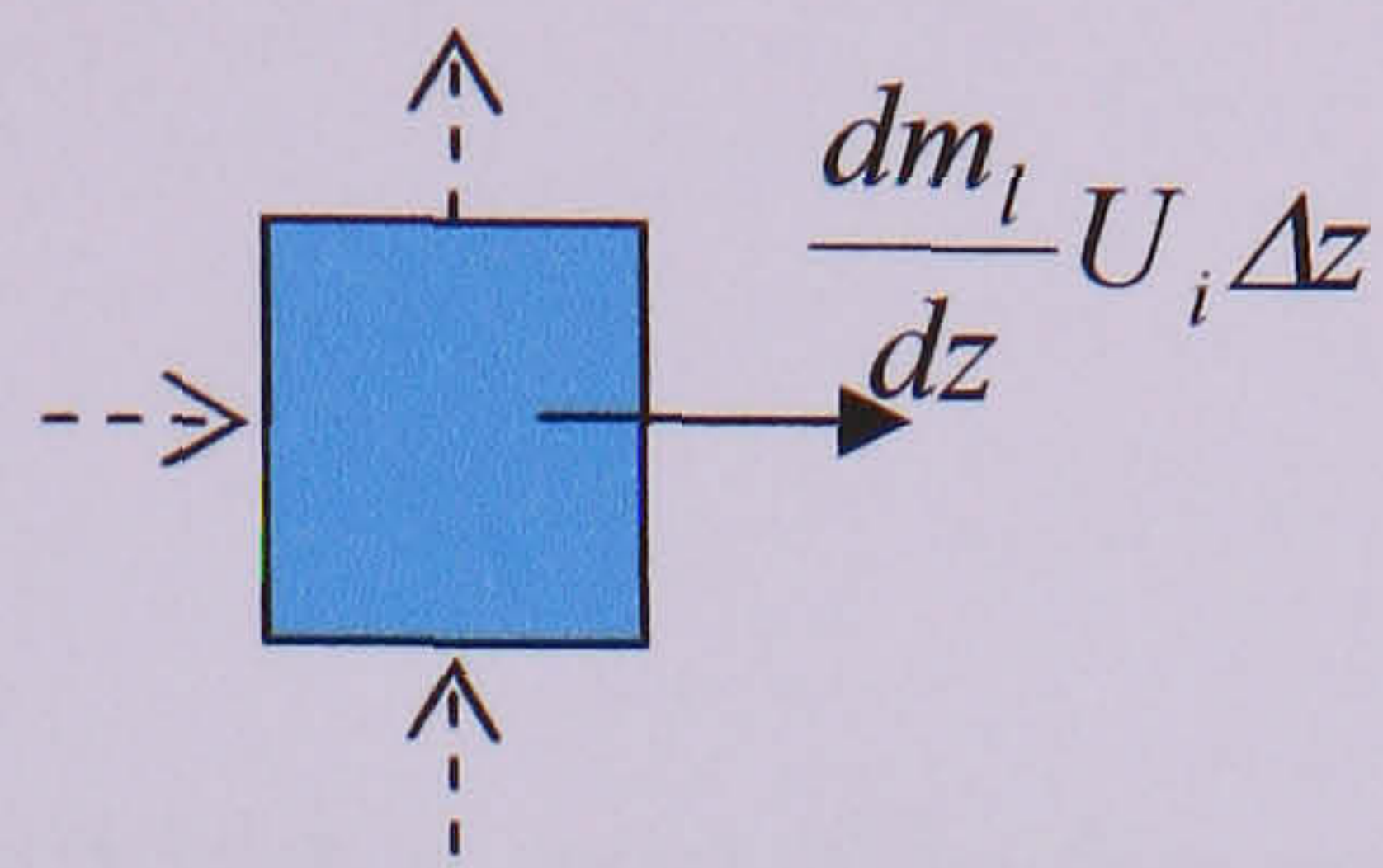
$$\frac{dU_B}{dz} = \frac{2q R}{h_{lg} \rho_g R_B^2} \quad (7.39)$$

Momentum balance in the confined bubble region

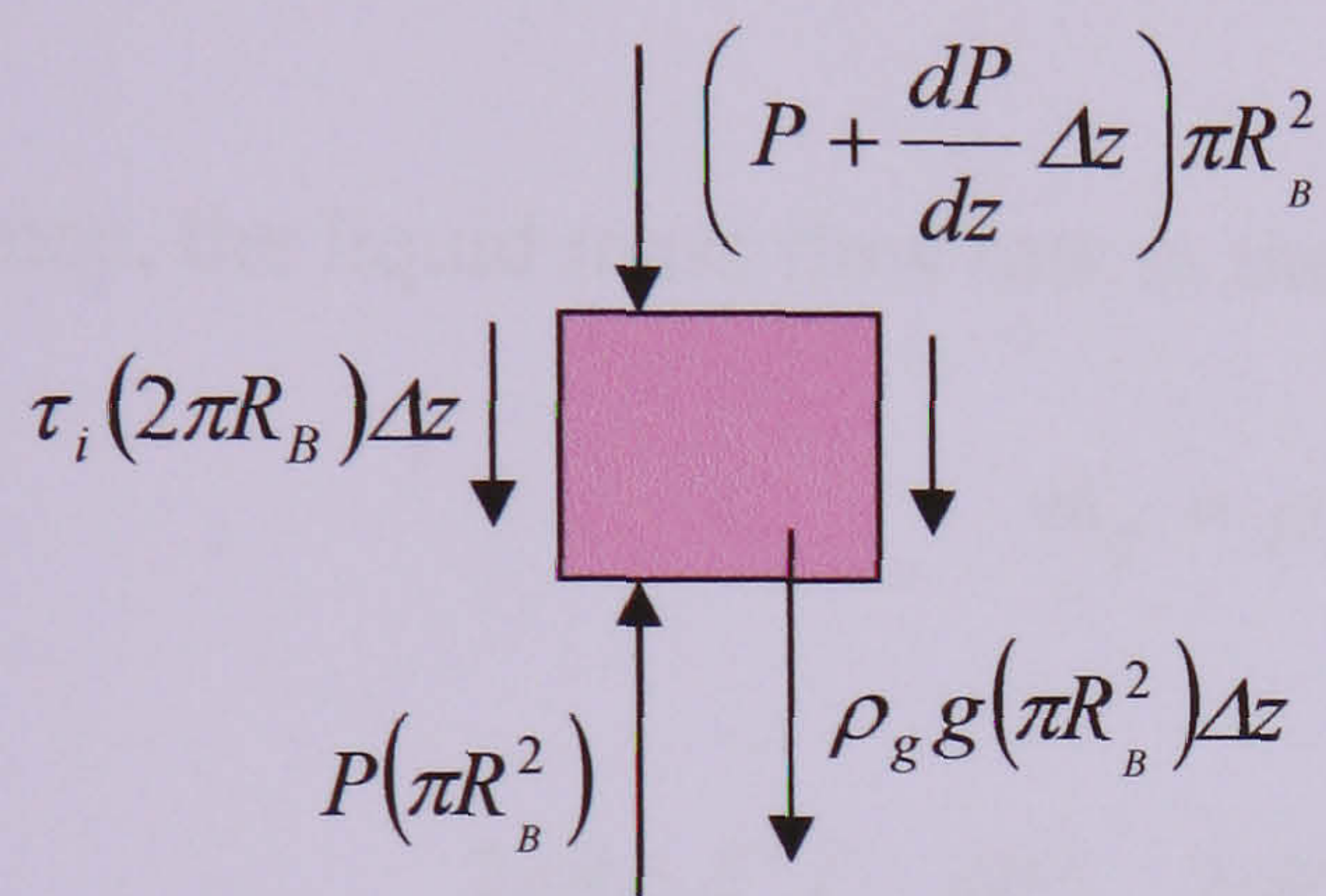
As mentioned above, a steady flow of liquid film with constant thickness, i.e. the average of the initial and final film thickness (after evaporation during the film flow period), is considered for each bubble. From the known film thickness value, the geometrical parameters, i.e. radius of the bubble and area void fraction can be determined. Figure 7.18 shows the forces and momentum exchange for a control volume inside the liquid film and elongated bubble. These terms are used to solve the momentum equation in the confined bubble regime. In order to obtain a relation between the pressure gradient and interfacial shear stress, the differential momentum equation in the liquid film is solved. This is then applied in an integral momentum equation for the gas phase. Momentum changes due to acceleration of the liquid film are neglected. However, for the sake of completeness of the equations in the gas phase, momentum change due to evaporation is considered.



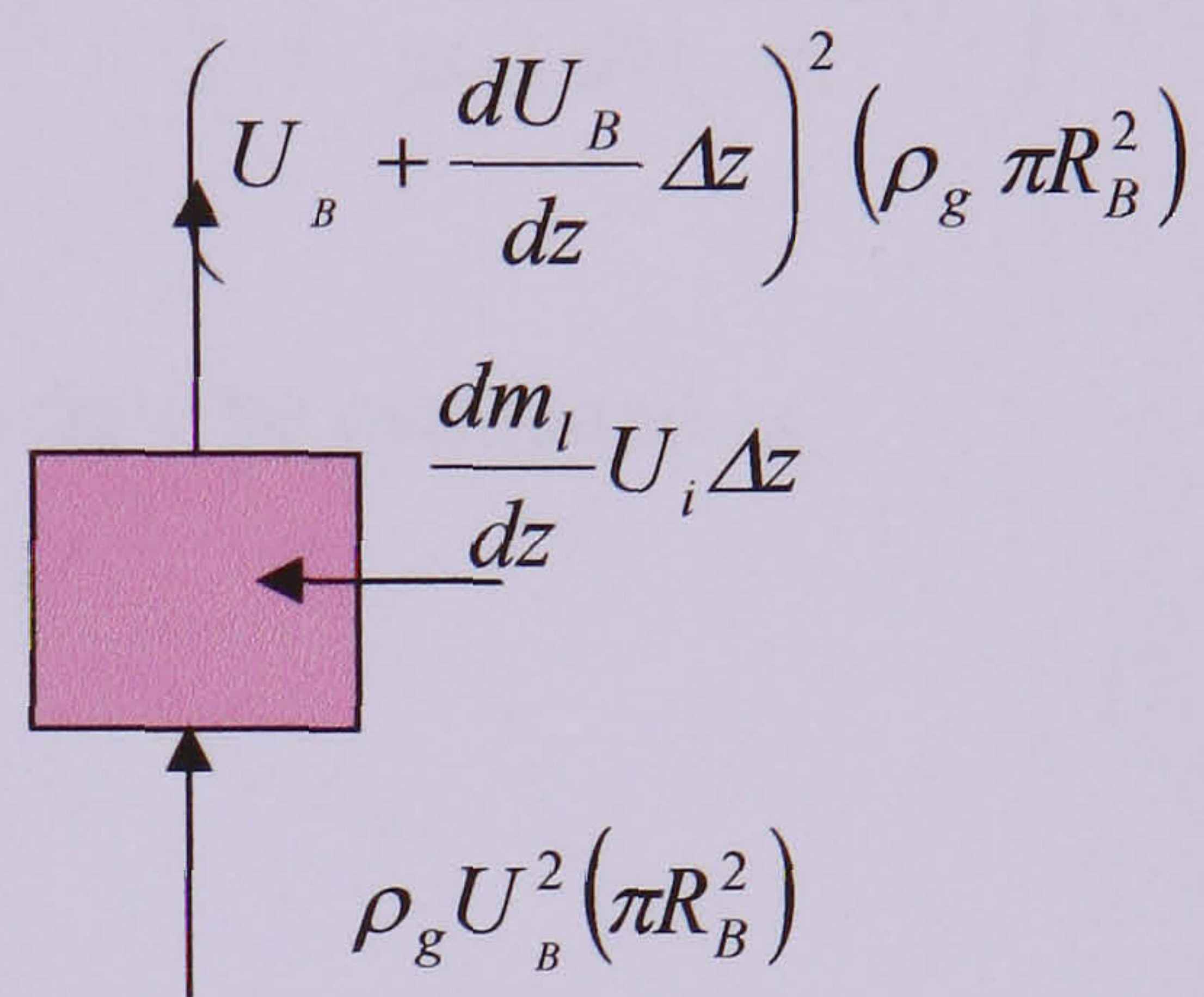
(a)



(b)



(c)



(d)

Figure 7.18 (a) forces in the liquid film control volume, (b) momentum exchanges in the liquid film control volume, (c) forces acting on the control volume in the elongated bubble, and (d) momentum exchanges for the control volume in the elongated bubble.

Liquid film

Considering a control volume of thin liquid film with axial length Δz , in figures 7.18 (a) and (b), the momentum equation for the liquid film is given by equating the sum of forces to the net momentum change as,

$$\frac{d\dot{m}_l}{dz} U_i = -\frac{dP}{dz} (\delta - y) 2\pi R - \tau 2\pi R + \tau_i 2\pi R_B - \rho_l g 2\pi R (\delta - y) \quad (7.40)$$

The shear stress in Eq. (7.40) is therefore expressed as,

$$\tau = (\delta - y) \left(-\frac{dP}{dz} \right) + \tau_i \left(\frac{R_B}{R} \right) - \rho_l g (\delta - y) - \frac{1}{2\pi R} \left(\frac{d\dot{m}_l}{dz} U_i \right) \quad (7.41)$$

The shear stress in the laminar liquid film flow is related to the velocity gradient in the transverse direction as,

$$\tau = \mu_l \frac{dU_{lf}}{dy} \quad (7.42)$$

Combining equations (7.41) and (7.42) and assuming a non-slip boundary condition, i.e. $U_{lf} = 0$ at $y = 0$, the velocity gradient equation is solved to give the local velocity in the liquid film as,

$$U_{lf}(y) = \frac{1}{\mu_l} \left(\delta y - \frac{y^2}{2} \right) \left(-\frac{dP}{dz} \right) + \frac{y}{\mu_l} \tau_i \left(\frac{R_B}{R} \right) - \frac{\rho_l g}{\mu_l} \left(\delta y - \frac{y^2}{2} \right) - \frac{y}{\mu_l 2\pi R} \left(\frac{d\dot{m}_l}{dz} U_i \right) \quad (7.43)$$

Hence, the liquid mass flow rate in the liquid film can now be evaluated as,

$$\dot{m}_{lf} = \rho_l 2\pi R \int_0^\delta U_{lf} dy \quad (7.44)$$

$$\dot{m}_l = \frac{2\pi R \rho_l \delta^3}{3\mu_l} \left(-\frac{dP}{dz} \right) + \frac{2\pi R_B \rho_l \delta^2}{2\mu_l} \tau_i - \frac{2\pi R \rho_l \delta^3}{3\mu_l} \rho_l g - \frac{\rho_l \delta^2}{2\mu_l} \left(\frac{d\dot{m}_l}{dz} U_i \right) \quad (7.45)$$

Therefore, the pressure gradient for the liquid film was obtained by re-arranging equation (7.45) and is given as

$$\left(-\frac{dP}{dz} \right) = \frac{3\mu_l}{2\pi R \rho_l \delta^3} \dot{m}_l - \frac{3}{2\delta} \left(\frac{R_B}{R} \right) \tau_i + \rho_l g + \frac{3}{4\delta \pi R} \left(\frac{d\dot{m}_l}{dz} U_i \right) \quad (7.46)$$

Elongated bubble

Balancing the sum of forces and net momentum change shown in figures 7.18 (c) and (d) respectively; the corresponding momentum equation in the elongated bubble is given as,

$$\left(\rho_g \pi R_B^2 \right) \frac{dU_B^2}{dz} - \frac{d\dot{m}_l}{dz} U_i = \left(-\frac{dP}{dz} \right) \left(\pi R_B^2 \right) - \tau_i 2\pi R_B - \rho_g g \pi R_B^2 \quad (7.47)$$

From Eq. (7.47), the interfacial shear stress can be rewritten as,

$$\tau_i = \frac{R_B}{2} \left(-\frac{dP}{dz} \right) - \frac{R_B}{2} \rho_g g + \frac{1}{2\pi R_B} \left(\frac{d\dot{m}_l}{dz} U_i \right) - \rho_g R_B U_B \frac{dU_B}{dz} \quad (7.48)$$

Inserting mass balance equations (7.36) and (7.39) into the interfacial shear stress equation (7.48), the interfacial shear stress can be expressed as,

$$\tau_i = \frac{R_B}{2} \left(-\frac{dP}{dz} \right) - \frac{R_B}{2} \rho_g g + \left(\frac{qR}{h_{lg} R_B} U_i \right) - U_B \left(\frac{2q R}{h_{lg} R_B} \right) \quad (7.49)$$

Substituting the interfacial shear stress expression (7.49) back in the pressure gradient equation (7.46), considering assumption 7 and re-arranging the terms, the final equation for the pressure gradient in the elongated bubble regime is given as,

$$\left(-\frac{dP}{dz} \right)_{CB} = \frac{\frac{3\mu_l}{2\pi R \rho_l \delta^3} \dot{m}_l + \frac{3q}{\delta h_{lg}} (U_B) + \left(\rho_l + \rho_g \frac{3R_B^2}{4\delta R} \right) g}{1 + \frac{3R_B^2}{4\delta R}} \quad (7.50)$$

The final form of the pressure gradient equation requires the liquid film mass flow rate. As mentioned before, the above analysis assumes a known film thickness. Once the film thickness is obtained from the average of initial and final film thickness (after evaporation for the time period of confined bubble), the geometry of the bubble, i.e. bubble radius and area void fraction can be determined. The bubble velocity can be obtained from Equation (7.29) or (7.30), which in turn can be used to calculate the average liquid film velocity using equation (7.33). Therefore, the average mass flow rate of liquid film is determined from the average velocity as,

$$\dot{m}_l = U_{lf} \rho_l \pi (R^2 - R_B^2) \quad (7.51)$$

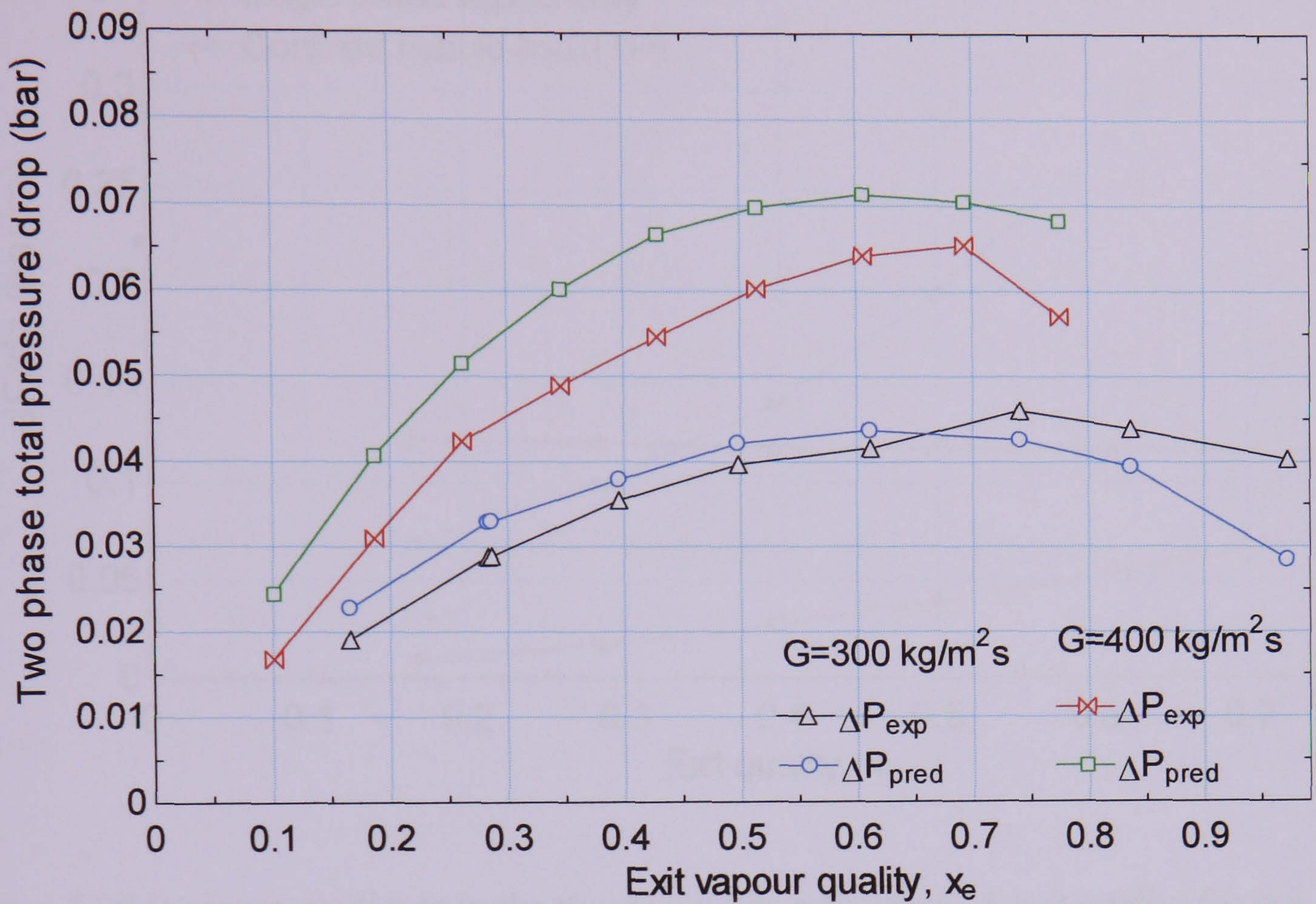
The model is based on the assumption that slug flow regime is the dominant flow pattern and considering smooth vapour-liquid interface. This is mostly true in case of the larger tubes (4.26 – 1.1 mm), in which flow pattern studies of Chen (2006) indicated the prevailing flow regime in these tubes to be slug flow up to a quality as high as 0.5. In addition, Chen (2006) also pointed out that the so called “small tube characteristics”, i.e. confined flow, slimmer vapour slug, thinner liquid film and smoother vapour-liquid interface, were observed when the tube diameter was reduced to 2.01 mm and further to 1.10 mm. Therefore, the model is recommended for such flow conditions, i.e. slug flow

with smooth vapour-liquid interface. Hence, an example case is presented for the 2.01 and 1.1 mm tubes. Figure 7.19 shows the predicted and experimental total pressure drop as a function of exit quality at 8 bar pressure and mass flux values of 300 and 400 kg/m², for the 2.01 and 1.1 mm tubes. The value is calculated by using the average film thickness of the three-zone heat transfer model as explained above. As discussed in section 7.4.3, the three-zone model predicts the average film thickness much lower than other correlations developed for steady viscous flows. On the other hand, the pressure gradient in the confined bubble, Eq. (7.50), is dependent on the film thickness value, in which the pressure gradient increases with decreasing film thickness. The value from the three-zone model is obtained using an optimization of the heat transfer database, Dupont et al. (2004), and may not be consistent with the physics. Therefore, a better theoretical film thickness predicting method that considers the physical mechanism in flow boiling is highly relevant for the present pressure drop model as well as it is also required for improving the three-zone heat transfer model. In general, the pressure model has correctly predicted the trend of the pressure drop with exit quality. However, the value is slightly over-predicted at high mass flux. The effect of dryout, which tends to decrease the pressure drop at high heat flux, is also captured by the model.

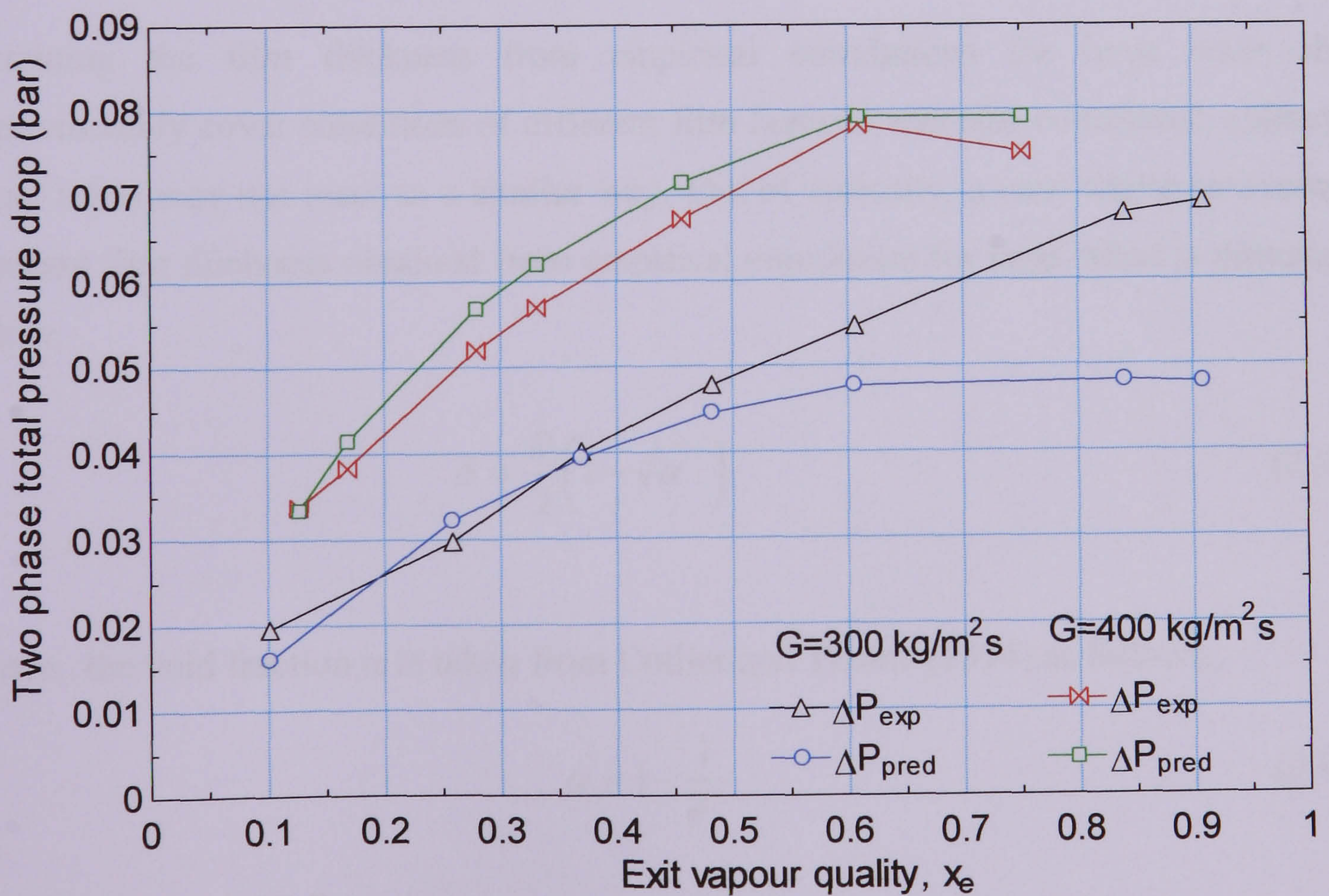
The pressure gradient in the three zones, i.e. liquid slug, confined bubble with liquid film and vapour-only flows, are also compared in Figure 7.20, for a mass flux of 300 kg/m²s and 8 bar pressure for the 2.01 mm tube. Below an exit quality of $x_e \sim 0.34$, the pressure gradient in the liquid slug is higher than the other zones. Beyond this exit quality limit, the pressure gradient in the confined bubble regime becomes higher than the rest two zones with the difference increasing with exit quality. As mentioned before, the pressure gradient in the film flow region is highly sensitive to the assumption of the average film thickness and increases with decreasing the film thickness. In general, the pressure gradient in the confined bubble flow regime increases rapidly with exit quality, while the value for the liquid-only flow remains almost constant. The vapour-only zone also increases moderately with exit quality.

The extinction of the intermediate liquid slugs between the bubbles is roughly considered as criterion for the end of the slug flow regime or validity range of the model. The model is not expected to work for annular flow conditions, particularly with liquid film instabilities typically observed for the smallest tube. However, it can be

further modified to incorporate such variations, because of its feature that it treats the liquid film and vapour flow separately and allows motion of liquid film.



(a)



(b)

Figure 7.19 Total pressure drop as a function of exit quality as predicted by the model, at 8 bar pressure: (a) 2.01 mm, (b) 1.1 mm

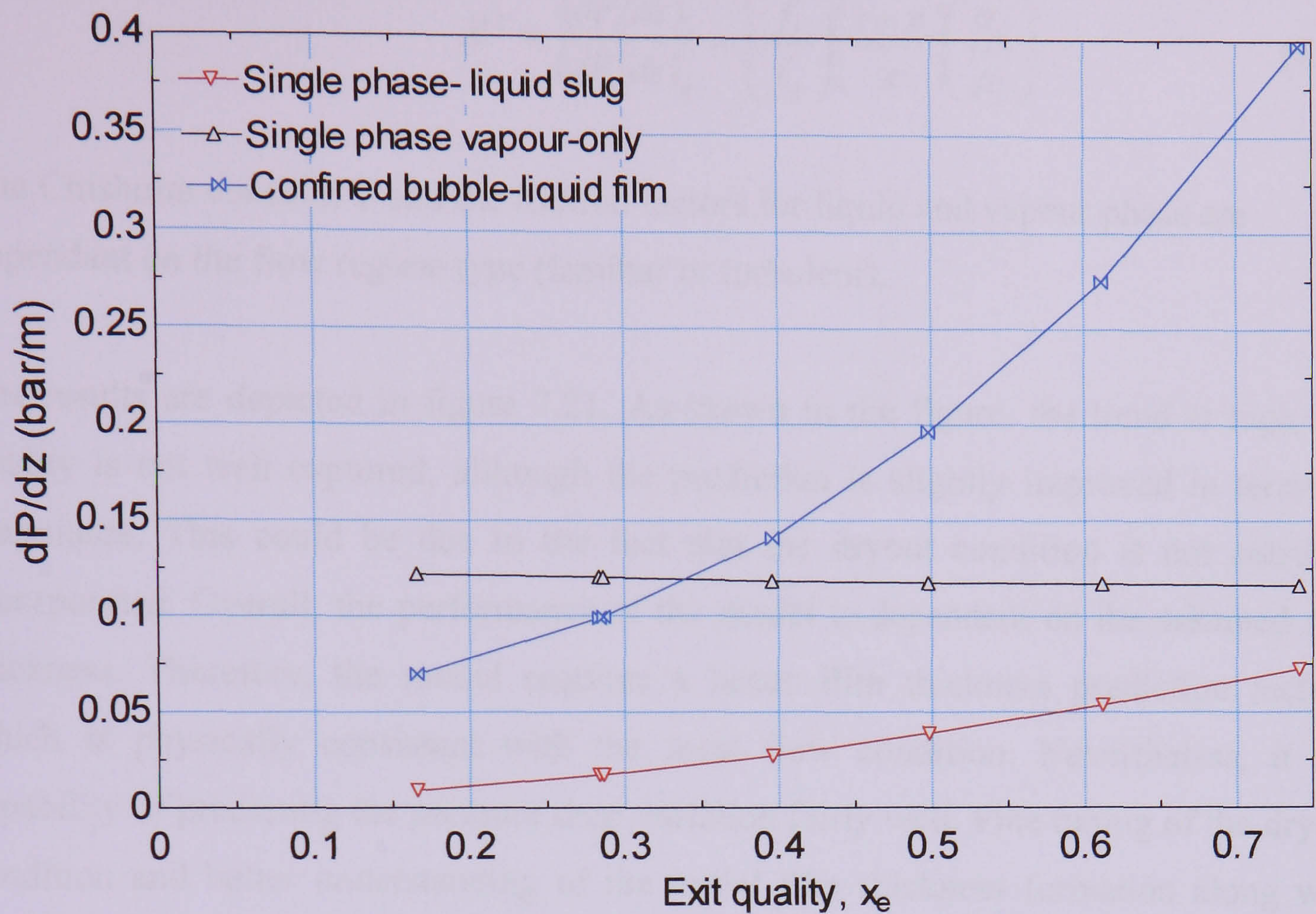


Figure 7.20 Pressure gradients in the three zones as a function of exit quality for the 2.01 mm tube at 8 bar pressure and mass flux of 300 kg/m²s.

Obtaining the film thickness from empirical correlations for large tubes that approximately cover conditions of different film features was also considered, although small tubes may not react in a similar way. Out of curiosity, a case where an average constant film thickness obtained from empirical correlation for large tubes is presented below.

$$\delta = \frac{D}{2} \left(1 - \sqrt{\alpha} \right) \quad (7.52)$$

where, the void fraction α is taken from Collier and Thome (1994) as follows,

$$\alpha = 1 - \frac{1}{\phi} \quad (7.53)$$

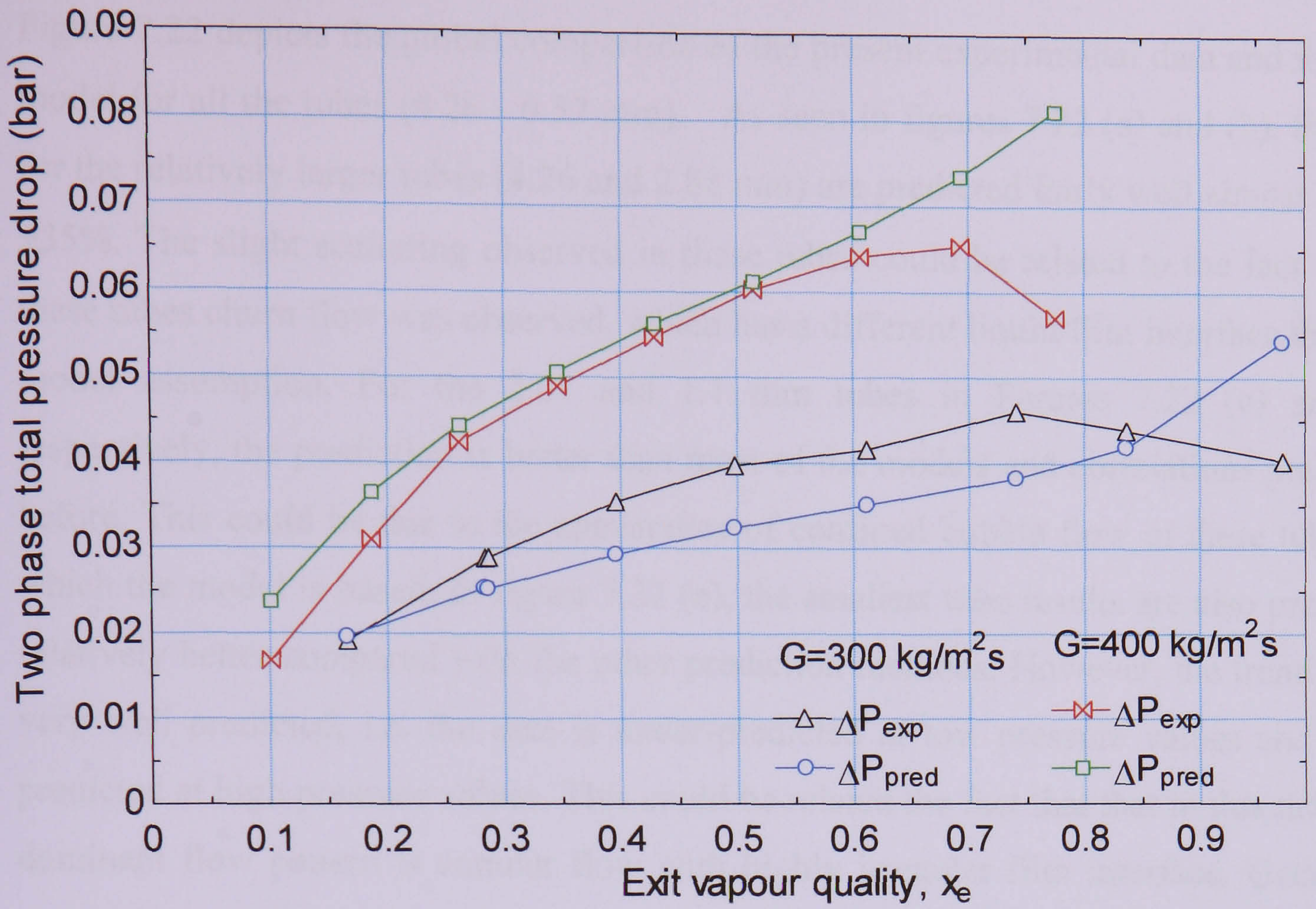
The two phase multiplier

$$\phi^2 = 1 + \frac{C}{X} + \frac{1}{X^2} \quad (7.54)$$

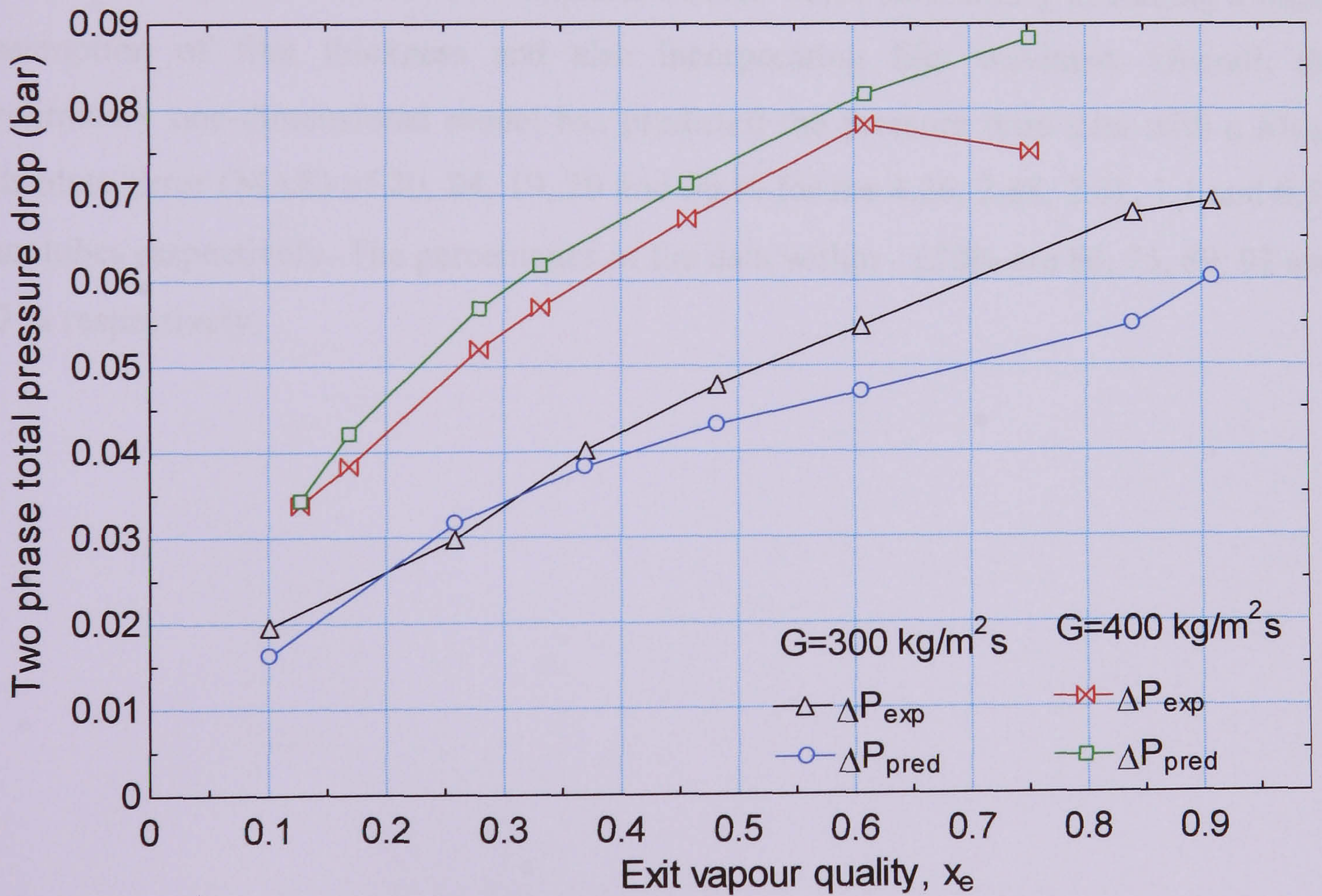
$$X^2 = \frac{(dP/dz)_l}{(dP/dz)_g} = \left(\frac{f_l}{f_g} \right) \left(\frac{1-x}{x} \right) \left(\frac{\rho_g}{\rho_l} \right) \quad (7.55)$$

The Chisholm constant C and the friction factors for liquid and vapour phase are dependant on the flow regime type (laminar or turbulent).

The results are depicted in figure 7.21. As shown in the figure, the trend at high exit quality is not well captured, although the prediction is slightly improved in terms of magnitude. This could be due to the fact that the dryout condition is not correctly incorporated. Overall, the performance of the model is dependent on the assumed film thickness. Therefore, the model requires a better film thickness prediction method which is physically consistent with the local flow condition. Nevertheless, it has capability of predicting the pressure drop variation fairly well. Fine tuning of the dryout condition and better understanding of the initial film thickness formation along with frequency of bubble generation could result in a significant improvement.



(a)



(b)

Figure 7.21 Total pressure drop as a function of exit quality as predicted by the model, at 8 bar pressure: (a) 2.01 mm, (b) 1.1 mm

Figure 7.22 depicts the global comparison of the present experimental data and the new model for all the tubes (4.26 - 0.52 mm). As seen in figures 7.22 (a) and (b), the data for the relatively larger tubes (4.26 and 2.88 mm) are predicted fairly well almost within $\pm 35\%$. The slight scattering observed in these tubes could be related to the fact that in these tubes churn flow was observed, which has a different liquid/film interface than the model assumption. For the 2.01 and 1.1 mm tubes in Figures 7.22 (c) and (d) respectively, the prediction is better than most of the models and correlations presented before. This could be due to the appearance of confined bubble flow in these tubes, in which the model is based. In figure 7.22 (e), the smallest tube results are also predicted relatively better compared with the other prediction methods. However, the trend is not very well predicted, i.e. the data is under-predicted at low pressure values and over-predicted at high pressure values. This could be related the fact that that in this tube, the dominant flow pattern is annular flow with highly irregular film interface. Generally, the model works reasonably well for cases, where slug flow with relatively smooth interface is expected. However, it requires further work, particularly in finding a better assumption of film thickness and also incorporating film waviness. Overall, the preliminary one-dimensional model has predicted the pressure drop data with a Mean Absolute Error (MAE) of 20, 24, 19, 20 and 30 % for the 4.26, 2.88, 2.01, 1.1 and 0.52 mm tubes respectively. The percentages of the data within $\pm 30\%$ are 80, 75, 89, 92 and 60 % respectively.

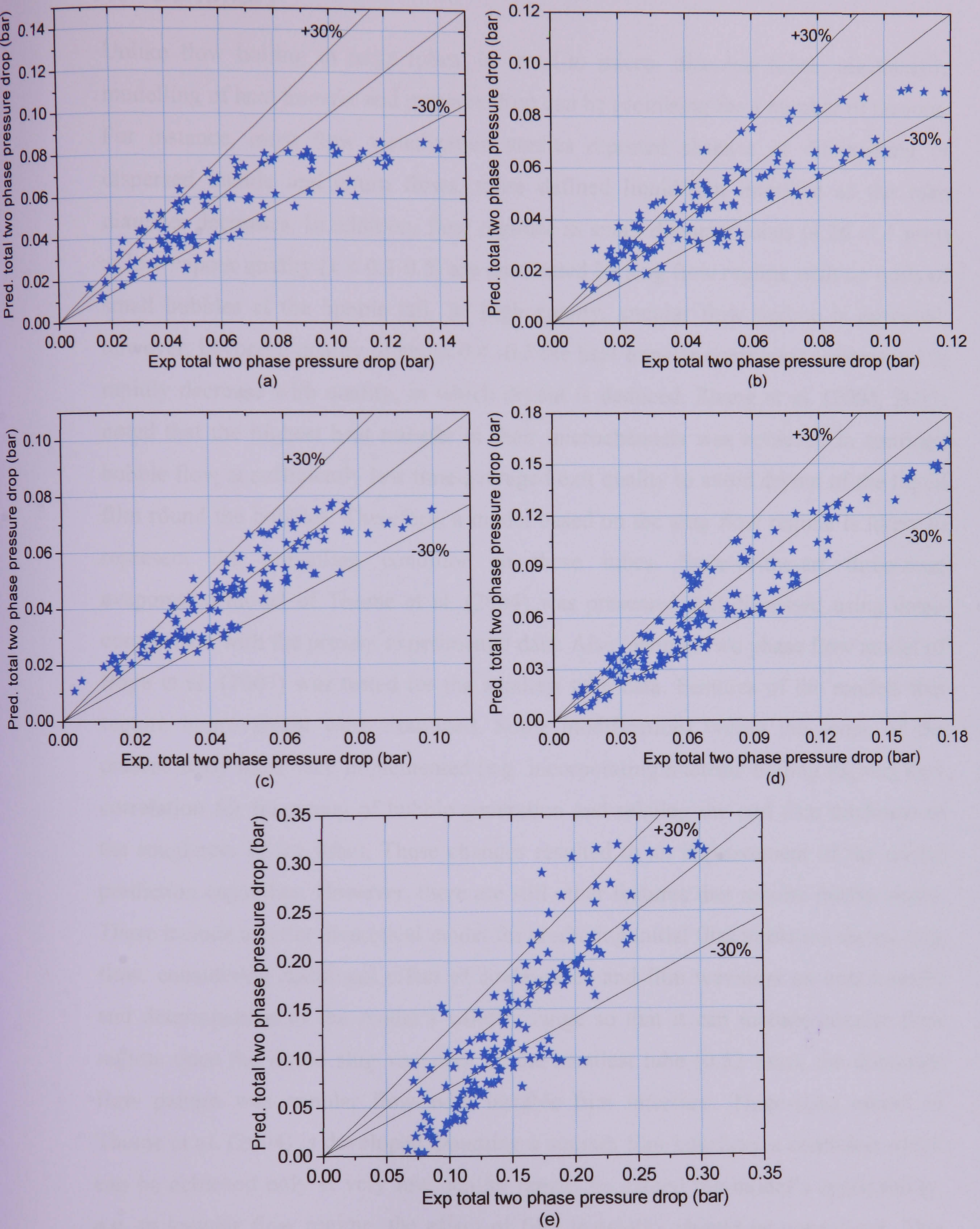


Figure 7.22 Comparison with the current pressure drop data for the different tube diameters: (a) 4.26 mm, (b) 2.88 mm, (c) 2.01 mm, (d) 1.1 mm and (e) 0.52 mm.

7.6 Summary

Unlike flow boiling in large tubes, in small-to micro- diameter tubes, mechanistic modelling of heat transfer and pressure drop can be promising for a number of reasons. For instance, most flow visualization studies reported absence or diminishing of dispersed bubble and churn flows, more defined liquid/film interface as the tube diameter decreases. In addition, flow regimes in small diameter tubes (4.26 -1.1 mm) at low vapour quality ($x < 0.3-0.5$) are dominated by slug flow regime with no trails of small bubbles at the bubble tail. At high quality, annular flow regime is expected, however, beyond a quality of about 0.4 -0.5 the heat transfer coefficient is observed to rapidly decrease with quality, in which dryout is deduced. Zhang et al. (2004, 2005) noted that the highest heat transfer in their microchannels was achieved in confined bubble flow at sufficiently low time-averaged exit quality to avoid dryout of the liquid film round the bubbles. Therefore, a model based on the slug flow regime is likely to represent the prevailing condition in these tubes. State-of-the-art three-zone evaporation model of Thome et al. (2004) was presented and discussed using detail comparison with the present experimental data. Also, annular two phase flow model of Boye et al. (2007) was tested for the smallest tube data. Features of the models that require improvement were examined. Some modifications within the scope of the present study have been implemented (e.g. incorporating nucleate boiling regime, new correlation for frequency of bubble generation and relating the end film thickness to the roughness of the tube). These changes resulted in an improvement of the model prediction capability. However, there are still other features that require further study. These include a better theoretical model for predicting initial film thickness during slug flow, considering additional effect of coalescence and film waviness on heat transfer and determination of the model's validity range so that it can include annular flow regime once the liquid slug vanishes. In the smallest tube (0.52 mm), the dominant flow pattern was annular flow with instable film interface. Three-zone model of Thome et al. (2004) is developed assuming a smooth film interface, a condition which can be achieved only at very low quality range. To extend the model's applicability, e.g. to annular flow regime, the effect of film instability should be considered. This could improve the disagreement obtained during comparison with the smallest tube data. A new three-zone pressure drop model for slug flow regime with an assumption of smooth liquid film interface was developed following a similar approach as the three-zone heat transfer model of Thome et al.(2004). During the confined bubble

flow, the pressure gradient was obtained using simplified one-dimensional momentum equation. The model correctly predicts the pressure drop trend with exit quality, However, it requires further improvement in the area of liquid film prediction and film waviness.

Chapter 8

Conclusions and Future work

8.1 Conclusions

Flow boiling experimental results (heat transfer, pressure drop and flow patterns) with five tubes of diameter 4.26, 2.88, 2.01, 1.10 and 0.52 mm using R134a over a range of pressures and mass fluxes were analysed. The heat transfer and pressure drop data in the 4.26 and 2.01 mm tubes were from X. Huo (2005). It was anticipated that the wide range of data at different diameters could be used to identify the threshold, where the effect of small or micro diameter effects become significant. The objective of the parallel flow visualization study of at the exit to the test section was to support the heat transfer study. The findings of L. Chen (2006) using the same facility for the 4.26 – 1.1 mm tubes were also used in the analysis. The major conclusions are summarised in this chapter:

8.1.1 Heat transfer and flow visualization

The flow boiling heat transfer experimental results in the five tubes are summarised below.

1. The experimental results for the 4.26 and 2.88 mm tubes demonstrate that the heat transfer coefficient increases with heat flux and system pressure, but does not change with vapour quality when the quality was less than about 40% to 50%, for low heat flux. The experimental results also indicate that there is no significant difference in the characteristic and magnitude of heat transfer between these two tubes.

2. For the 2.01 mm and 1.10 mm tubes, the uniform heat transfer coefficient boundary moves to 20% - 30% and 30% – 40% vapour quality, respectively. Moreover, the heat transfer coefficient of the 2.01 mm tube shows 14 % increase from the 2.88 mm tube. The enhancement in the coefficient increased further to 17 %, when the tube diameter was reduced from 2.01 to 1.10 mm.
3. The heat transfer coefficient behaviour of the tubes (4.26 -1.1 mm) at low quality was conventionally interpreted as evidence that nucleate boiling is the dominant heat transfer mechanism. For higher vapour qualities, the heat transfer coefficient becomes independent of heat flux and decreases with vapour quality. This could be caused by partial (intermittent) dryout.
4. The heat transfer results are consistent with the observation of Chen et al. (2006), who concluded that flow patterns for the 4.26 and 2. 88 mm exhibit strong flow pattern characteristics found in normal size tubes, whereas “small tube characteristics”, i.e. confined flow, slimmer vapour slug, thinner liquid film and smoother vapour-liquid interface, were observed when the tube diameter was reduced to 2.01 mm and further to 1.10 mm. According to the criterion proposed by Cornwell and Kew (1993) for small tube characteristics, confinement should be observed at diameters of 1.4 to 1.7 at 6 to 14 bar, which is roughly in agreement with the current observation.
5. In general, for 4.26 to 1.1 mm tubes, the results confirm that a tube size of roughly 2 mm can be considered as a critical diameter to distinguish small and conventional pipes in this study for R134a.
6. As the tube diameter decreased further down to 0.52 mm, different heat transfer characteristics were observed indicating another possible threshold between small and micro tube size. These include,
 - (a) The dependence of the heat transfer coefficient on thermodynamic quality, heat flux and mass flux change sharply in character at a threshold value of heat flux that varied randomly with different mass flux and pressure (showed hysteresis).
 - (b) In the low heat flux region, there is no significant effect of heat flux but the heat transfer coefficient decreases (at low mass flux and pressure) or remains constant (at higher mass flux and pressure), then increases slightly with thermodynamic quality.

- (c) At moderate and high heat flux, in the front part of the channel, the heat transfer coefficient increases with increasing heat flux and reaches a maximum at an intermediate quality which might be caused by transient partial dryout or dry patches in the confined bubble regime.
 - (d) At higher quality, towards the test section exit, the heat transfer coefficient gradually increases again with quality but there is no clear effect of heat flux. The heat transfer coefficient increases with mass flux in this region. According to the conventional interpretation, this is evidence for a convective boiling dominant heat transfer mechanism in the annular flow region.
 - (e) Unlike the larger tubes, which exhibited dryout phenomena at high quality as the heat flux increases and a decrease in heat transfer coefficient, a monotonic increase in heat transfer coefficient was observed towards the exit for the smallest tube, although at the higher pressures, there are indications of a second decrease in the heat transfer coefficient very close to the test section exit. In addition, the heat transfer coefficient in the 0.52 mm showed a significant dependence on the axial positions.
 - (f) The absence of dryout in this tube could be related to laminar flow and high surface tension force tending to coat the liquid along the circumference or small scale disturbances, which improve wetting of the wall.
 - (g) A flow regime with liquid-rings that no longer bridge the tube becomes more visible in a relatively wider range of exit quality. This flow regime could also be a transition flow regime.
7. The complex dependence of the heat transfer rate on various parameters suggest, the difficulty of interpreting the heat transfer mechanisms using simple conventional terms and the challenge of heat transfer modelling.

8.1.2 Boiling two phase pressure drop

Flow boiling pressure drop results for the five tubes over a range of pressure and mass fluxes were analysed and the results are summarised below.

- The pressure drop increases with increasing mass flux, while it decreases with increasing system pressure. It also increases with heat flux. However, at very high heat flux, it tends to decrease with heat flux. This is related to the fact that

dryout occurs at high exit quality, in which a significant portion of the tube experiences single phase vapour flow.

- The acceleration pressure drop contribution becomes significant as the heat flux increases, while the corresponding gravitational pressure drop contributions decrease with increasing heat flux. A similar conclusion was made by Kureta et al. (1998), who found that the acceleration loss is comparable to the friction loss under certain conditions in small diameter tubes.
- The pressure drop gradient increases with decreasing tube diameter. The pressure drop results of both single and two phase in the smallest diameter tube (0.52 mm) were much higher than the rest of the tubes. This could be due to the fact that the internal surface roughness value could be unusually high. Moreover, the flow pattern in the smallest tube is different compared with the larger tubes, i.e. dominant flows with fluctuating liquid film interface.
- The results of the five tubes were also compared with the existing pressure drop models and correlations. The 4.26 and 2.88 mm tube results were predicted well by the Lockhart-Martinelli separated flow model and the Chisholm (1983) correlation. However, these correlations and most others failed to predict the results of the 2.01, 1.1, and 0.52 mm tubes. In general, there was no single model or correlation that works for all tubes.

8.1.3 Correlations and modelling

Flow boiling heat transfer

- A global comparison of the present experimental data for the five tubes (4.26 mm to 0.52 mm) with existing correlations was carried out. The comparisons showed that the results of the relatively larger tubes (4.26 and 2.88 mm) are predicted fairly well by the Gungor and Winterton (1986) and the Zhang et al. (2004) correlations who modified the Chen (1966) correlation. The Zhang et al. (2004) correlation predicted the data well after replacing the nucleate boiling term they used, i.e. replacing the expression of Foster and Zuber (1955) by Cooper (1984). However, these correlations and most others failed to predict the results of the tubes with size 2.01 mm and below in diameter. Therefore, new correlations that take into account the influence of tube size were proposed. The new correlations predict the present data for the 4.26, 2.88, 2.01, 1.1 and 0.52

mm tubes with a mean absolute error of 4.6, 7.2, 6.7, 8.5 and 15.5% respectively.

- A detailed analysis of the state-of-the-art, three-zone evaporation model by Thome et al. (2004) was carried out, based on the present experimental data in the five tubes using R134a boiling over a range of pressures and mass fluxes. It is found that the model predicts experimental data of 4.26 – 1.1 mm tubes that would be conventionally interpreted as nucleate boiling at least as well as any correlation, confirming the claims of its authors that a model without a nucleate boiling contribution may provide a reasonably successful approximate prediction of the “apparently nucleate boiling” heat transfer regime. The model highly under-predicted the results of the 0.52 mm tube.
- The model requires further development. It predicts that the diameter of the tube has an opposite effect on the heat transfer coefficient as that indicated by the actual data. The pressure changes are correctly predicted but the magnitude of change was highly under-predicted. The model does not predict satisfactorily the conditions of decreasing heat transfer coefficient that occurred at high quality and which are attributed to dryout. However, a satisfactory prediction was achieved for some examples of partial dryout at high heat flux, by modifying the recommended values of the three parameters in the model, namely frequency of bubble generation, initial film thickness and critical film thickness for periodic dryout. In particular, assuming the end film thickness value to be equal to the average roughness of the tube produced significantly better result.
- Features of the model that may require modification include independent determination of the bubble generation frequency and the initial and end film thicknesses, the fluctuations in pressure and consequently in saturation temperature caused by the cyclic acceleration of the liquid slugs and the contribution from nucleate boiling before the position at which confined bubbles are formed.
- Some modifications have been made to the three-zone model. These include: incorporation of the nucleate boiling regime in the bubbly flow region and a new correlation for frequency of bubble generation that considers the effect of heat flux on the heat transfer coefficient. The results of these modifications showed improvements in the predicting capability of the model.

- The annular two phase flow model proposed by Boye et al. (2007) based on a laminar liquid film and vapour core flows and a smooth liquid-vapor interface did not show any effect of heat flux and highly under-predicted the results of the smallest tube (0.52 mm).

Boiling two phase Pressure drop

A two phase pressure drop model based on the slug flow regime is proposed. The model follows a similar approach as three-zone heat transfer model proposed by Thome et al. (2004). In the film boiling region, momentum equations in the liquid film and bubble slug are solved to determine the pressure gradient. The model predicted the effect of heat flux fairly well. In general, the model has the capability of predicting the pressure drop data with Mean Absolute Error (MAE) of 20, 24, 19, 20 and 30 % for the 4.26, 2.88, 2.01, 1.1 and 0.52 mm tubes respectively.

8.2 Future work

In this section, recommendations for future investigation on the study of flow boiling in small to micro passages are presented. The issues that require further investigation include:

1. Experiments by varying the heated length to clarify the effect this may have on the heat transfer characteristic and flow regime developments. The high pressure drop associated with increasing the heated length has to be considered as well.
2. Further experiments using different tubes with varying surface condition is required to confirm the importance of surface roughness, which is pointed out in this study as a major parameter.
3. The preliminary results of the smallest 0.52 mm tube brought a number of new interesting issues, which require further investigation. These include the number, distribution and stability of nucleation sites, and study of new flow patterns emerging in this tube. Therefore, studying the importance of nucleation sites and onset of nucleate boiling by conducting experiments in the 0.52 mm tube with different surface conditions can provide an insight on the various heat transfer characteristics at this size and probably smaller.
4. A better understanding of how the initial film is formed around a slug bubble, the critical film thickness for dryout and the effect of irregular film interface

will bring a significant improvement to the heat transfer and pressure drop modeling. Although there is a large number of experimental studies, heat transfer and pressure drop models for small to micro passages are still scarce.

5. Most models in flow boiling heat transfer are based on one dimensional analysis. However, the present preliminary results for the 0.52 mm tube indicated that the heat transfer coefficient varies with axial distance. This may suggest that local conditions could have downstream and upstream effects. Therefore, increasing the number of dimensions may be required in modeling to fully understand the various phenomena.

Bibliography

- [1]. T.M. Adams, S.I. Abdel-khalik, S.M. Jeter, and Z.H. Qureshi. An experimental investigation of single phase forced convection in microchannels. *International Journal Heat Mass Transfer*, 41(6-7):851-857, 1998.
- [2]. B. Agostini and A. Bontemps. Vertical flow boiling of refrigerant R134a in small channels. *International Journal Heat Fluid Flow*, 26(2):296-306, 2005.
- [3]. B. Agostini, M. Fabbri, J.E. Park, L. Wojtan, J.R. Thome, and B. Michel. State of the art high heat flux cooling technologies. *Heat Transfer Engineering*, 28(4):258-281, 2007.
- [4]. B. Agostini and J. R. Thome. Comparison of an extended database for flow boiling heat transfer coefficients in multi-microchannels: Elements with the three-zone model. *ECI Heat Transfer and Fluid Flow in Microscale*, Castelvechio Pascoli, Italy, Sept. 25–30, 2005.
- [5]. K. Akagawa, K. Sekoguchi, T. Sakaguchi, and S. Kobayashi. Nondimensional expression for the relation between pressure drop and flow rate in steam generating tubes. *Transactions JSME*, 13(58):591-599, 1970.
- [6]. M.K. Akbar, D.A. Plummer, and S.M. Ghiaasiaan. On gas-liquid two-phase flow regimes in microchannels. *International Journal of Multiphase Flow*, 29:855-865, 2003.
- [7]. M.R. Aligoodarz, Y. Yan, and D.B.R. Kenning. Wall temperature and pressure variations during flow boiling in narrow channels. In *Proceedings of 11th International Heat Transfer Conference (IHTC)*, August 23-28, 2:225-230, 1998.
- [8]. Y. Aounallah and D.B.R. Kenning, P.B. Whalley, and G.F. Hewitt. Boiling heat transfer in annular flow. In *Proceedings of Seventh International Heat Transfer Conference*, 5:193-199, 1982.
- [9]. P. Aussillous and D. Quéré. Quick deposition of a fluid on the wall of a tube. *Physics of Fluids*, 12(10):2367-71, 2000.

- [10]. J.R. Baird, Z.Y. Bao, D.F. Fletcher, and B.S. Haynes. Local flow boiling heat transfer coefficients in narrow conduits. In *Bar-Cohen Ed.- A Boiling phenomena and engineering applications*, Anchorage, Alaska, 2:447–466, 2000.
- [11]. Z.Y. Bao, D.F. Fletcher, and B.S. Haynes. Flow boiling heat transfer of Freon R11 and HCFC123 in narrow passages. *International Journal Heat Mass Transfer*, 43: 3347-3358, 2000.
- [12]. D. Barnea, Y. Luninski, and Y. Taitel. Flow pattern in horizontal and vertical two phase flow in small diameter pipes. *The Canadian Journal of Chemical Engineering*, 61(5):617-620, 1983.
- [13]. D.R.H. Beattie and W.J. Green. The existence of nucleate boiling in diabatic two-phase annular flow. *International Journal of Heat Mass Transfer*, 27(2):315-317, 1984.
- [14]. D.R.H. Beattie and K.R. Lawther. Letter to the editor. *AIChE Journal*, 25(2):384, 1979.
- [15]. D.R.H. Beattie and P.B. Whalley. A simple two-phase frictional pressure drop calculation method. *International Journal Multiphase Flow*, 8(1):83-87, 1982.
- [16]. Batchelor, 1967, see b.p. whalley
- [17]. K.M. Becker. An analytical and experimental study of burnout conditions in vertical round ducts. *Nukleonik*, 96:257–270, 1967.
- [18]. A.E. Bergles and S.G. Kandlikar. On the nature of critical heat flux in microchannels. *Journal of Heat Transfer*, 127(1):101-107, 2005.
- [19]. A.E. Bergles, J.H. Lienhard, G.E. Kendall, and P. Griffith. Boiling and evaporation in small diameter channels. *Heat Transfer Engineering*, 24(1):18-40, 2003.
- [20]. A.E. Bergles and W.M. Rohsenow. The determination of forced convection surface boiling heat transfer. *Journal of Heat Transfer*, Transactions of the ASME, 86:365-372, 1964.
- [21]. M.B. Bowers and I. Mudawar. High flux boiling in low flow rate, low pressure drop minichannel and microchannel heat sinks. *International Journal Heat Mass Transfer*, 37(2):321-332, 1994.
- [22]. R.W. Bowring. A simple but accurate round tube uniform heat flux, dryout correlation over the pressure range 0.7–17 Mpa (100–2500 psia). Report, *Atomic Energy Authority AEEW-R 789*, United Kingdom, 1972.

- [23]. H. Boye, Y. Staate, and J. Schmidt. Experimental investigation and modelling of heat transfer during convective boiling in a minichannel. *International Journal Heat Mass Transfer*, 50:208-215, 2007.
- [24]. N. Brauner and D. Barnea. Slug/churn transition in upward gas-liquid flow, *Chemical Engineering Science*, 41(1):159-163, 1986.
- [25]. N. Brauner and D. Moalem-Maron. Identification of the range of small diameter conduits regarding two-phase flow pattern transitions. *International Communications Heat Mass Transfer*, 19:29-39, 1992.
- [26]. G.J. Brereton, R.J. Crilly, and J.R. Spears. Nucleation in small capillary tubes. *Chem. Phys.* 230:253–265, 1998.
- [27]. D. Brutin and L. Tadrist. Pressure drop and heat transfer analysis of flow boiling in a minichannel: influence of the inlet condition on two phase flow stability. *International Journal Heat Mass Transfer*, 47 (10-11):2365-2377, 2004.
- [28]. V.P. Carey, P. Tervo, and K. Shullenberger. Partial dryout in enhanced evaporator tubes and its impact on heat transfer performance. *SAE Technical Paper*, 920551, 1992.
- [29]. A. Cavallini, D.D. Col, L. Doretti, M. Matkovic, L. Rossetto, and C. Zilio. Two-phase frictional pressure gradient of R-236ea, R-134a and R-410a inside multi-port minichannels. *Experimental Thermal Fluid Science*, 29:861–870, 2005.
- [30]. G.P. Celata, M. Cumo and A. Mariani. Assessment of correlations and models for the prediction of CHF in water subcooled flow boiling. *International Journal Heat Mass Transfer*, 37: 237–255, 1994.
- [31]. K.H. Chang and Chin Pan. Two phase flow instability for boiling in a microchannel heat sink. *International Journal Heat Mass Transfer*, 50:2078-2088, 2007.
- [32]. J.C. Chen. A correlation for boiling heat transfer to saturated fluids in convective flow. *Industrial and Engineering Chemistry*, 5:322-329, 1966.
- [33]. L. Chen, Flow patterns in upward two-phase flow in small diameter tubes, PhD thesis, Brunel University, UK, 2006.
- [34]. L. Chen, Y.S. Tian, and T.G. Karayiannis. The effect of tube diameter on vertical two-phase flow regimes in small tubes. *International Journal Heat Mass Transfer*, 49: 4220-4230, 2006.

- [35]. X. Cheng, F.J. Erbacher, U. Muller, and F.G. Pang. Critical heat flux in uniformly heated vertical tubes. *International Journal heat Mass Transfer*, 40(12):2929-2939, 1997.
- [36]. D. Chisholm. *Two-Phase Flow in Pipelines and Heat Exchangers*. Longman, New York, 1983.
- [37]. D. Chisholm. A theoretical basis for the Lockhart–Martinelli correlation for two-phase flow. *International Journal of Heat Mass Transfer*, 10:1767–1778, 1967.
- [38]. D. Chisholm. Pressure gradients due to friction during the flow of evaporating two-phase mixtures in smooth tubes and channels. *International Journal Heat Mass Transfer*, 16:347-358, 1973.
- [39]. S.B. Choi, R.F. Barron, and R.O. Warrington. Fluid flow and heat transfer in microtubes. *Micromechanical Sensors, Actuators and Systems*, ASME DSC, 32:123–128, 1991.
- [40]. K.R. Chun and R.A. Seban. Heat Transfer to evaporating liquid films. *Journal Heat Transfer Trans. ASME*, 93:391-396, 1971.
- [41]. P.M.-Y. Chung and M. Kawaji. The effect of channel diameter on adiabatic two-phase flow characteristics in microchannels. *International Journal of Multiphase Flow*, 30:735-761, 2004.
- [42]. S.W. Churchill and R. Usagi. A general expression for the correlation of rates of transfer and other phenomena. *AIChE Journal*, 18:1121-1128, 1972.
- [43]. J.W. Coleman and S. Garimella. Characterization of two-phase flow patterns in small diameter round and rectangular tubes. *International Journal of Heat and Mass Transfer*, 42:2869-2881, 1999.
- [44]. H.W. Coleman and W.G. Steele. *Experimentation and uncertainty analysis for engineers*, John Wiley & Sons Inc. Second edition, New York, 1999.
- [45]. J.G. Collier and J.R. Thome. *Convective Boiling and Condensation*. Oxford University Press, Oxford, UK, third edition, 1994.
- [46]. M.G. Cooper. Saturated nucleate pool boiling – a simple correlation. In *first UK National Heat Transfer Conference, IChemE Symposium, Series 86*, 2:785-793, 1984.
- [47]. M.G. Cooper. Heat flow rate in saturated nucleate pool boiling – a wide ranging examination using reduced properties, *Advances in Heat Transfer*, Academic Press, Orlando, 16:157-239, 1984.

- [48]. K. Cornwell and P.A. Kew. Boiling in small parallel channels. In *Energy Efficiency in Process Technology, Applied Science*, P.A. Pilavachi (editor), Elsevier, New York, 624-638, 1993.
- [49]. M. Cortina Diaz, H. Boye, I. Hapke, J. Schmidt, Y. Staate, and Z. Zhekov. Flow boiling in mini and microchannels. In *Proceedings of the Second International Conference on Microchannels and Minichannels (ICMM2004)*, 445-452, 2004.
- [50]. M. Cortina Diaz and J. Schmidt. Experimental investigation of transient boiling heat transfer in microchannels. *International Journal of Heat Fluid Flow*, 28:95-102, 2007a.
- [51]. M. Cortina Diaz and J. Schmidt. Flow boiling of n-hexane in small channels: heat transfer measurement and flow pattern observations, *Chemical Engineering and Technology*, 30(3):389-394, 2007b.
- [52]. C.A. Damianides and J.W. Westwater. Two-phase flow patterns in a compact heat exchanger and in small tubes. In *Second UK National Conference on Heat Transfer*, 11:1257-1268, 1988.
- [53]. E.J. Davis and G.H. Anderson. The incipience of nucleate boiling in forced convection flow. *AIChE Journal*, 12(4):774-780:1966.
- [54]. C.E. Dengler and J.N. Addoms. Heat transfer mechanism for vapourization of water in vertical tube. *Chemical Engineering Symposium Series*, 58(18):85-103, 1956.
- [55]. R.T.P. Derbyshire, G. F. Hewitt, and B. Nicholls. X-radiography of two-phase gas-liquid flow. *Chemical Engineering Division, U.K.A.E.A., Research group, Atomic Research Establishment, Harwell, Memorandum, AERE-M 1321*, 1964.
- [56]. A. de Ryck. The effect of weak inertia on the emptying of a tube. *Physics of Fluids*, 14:2102-2108, 2002.
- [57]. V.K. Dhir. Boiling heat transfer. *Annual Review of Fluid Mechanics*, 30:365-401, 1998.
- [58]. F.W. Dittus and L.M.K Boelter. Heat transfer in automobile radiators of tubular type, *Publications in Engineering*, University of California Berkeley, 2(13):443-461:1930.
- [59]. A.E. Dukler and Y. Taitel. Flow pattern transition in gas-liquid systems: measurement and modelling. *Multiphase Science and Technology*, Hemisphere Publishing, New York, 2:1-94, 1986.

- [60]. A.E. Dukler, M. Wicks, and R.G. Cleveland. Pressure drop and hold-up in two-phase flow, part A – a comparison of existing correlations, part B – an approach through similarity analysis. *AIChE Journal*, 10(1):38 – 51, 1964.
- [61]. V. Dupont, J.R. Thome, A.M. Jacobi, Heat transfer model for evaporation in microchannels, Part II: comparison with the database, *International Journal Heat Mass Transfer*, 47:3387-3401, 2004.
- [62]. V. Dupont, J.R. Thome, Evaporation in microchannels: influence of the channel diameter on heat transfer, *Journal of Microfluidics and Nanofluidics*, 1(2):119-127, 2005.
- [63]. F. Durst, S. Ray, B. Unsal, and A.O. Bayoumi. The Development Lengths of Laminar Pipe and Channel Flows. *Journal Fluids Engineering*, 127:1154–1160, 2005.
- [64]. L. Friedel. Improved friction pressure drop correlations for horizontal and vertical two phase pipe flow. In *European Two phase Flow Group Meeting*, Ispara, Italy, E2, 1979.
- [65]. R.G. Frieser and M.D. Reeber. Surface treatments of silicon to enhance thermal nucleation. *Journal Applied Electrochemistry*, 10(4):449-457, 1980.
- [66]. Y. Fujita, Y. Yang, and F. Nami. Flow boiling heat transfer and pressure drop in uniformly heated small tubes. In *Proceedings of the 12th International Heat Transfer Conference*, Grenoble, 3:743-748, 2002.
- [67]. T. Fukano and A. Kariyasaki. Characteristics of gas-liquid two-phase flow in a capillary tube. *Nuclear Engineering and Design*, 141:59-68, 1993.
- [68]. T. Fukano, A. Kariyasaki, M. Kagawa. Flow patterns and pressure drop in isothermal gas–liquid concurrent flow in a horizontal capillary tube. In *ANS Proceedings National Heat Transfer Conference*, 4:153–161, 1989.
- [69]. S. Garimella, J.D. Killion, and J.W. Coleman. An experimental validated model for two-phase pressure drops in the intermittent flow regime for circular channel. *Journal of Fluid Engineering*, 124:205–214, 2002.
- [70]. S.M. Ghiaasiaan and R.C. Chedester. Boiling incipience in microchannels. *International Journal of Heat and Mass Transfer* 45:4599-4606, 2002.
- [71]. V. Gnielinski. New equations for heat transfer in turbulent pipe and channel flow. *International Chemical Engineering*, 16:359–368, 1976.
- [72]. V. Gnielinski. *VDI-Wärmeatlas*, Springer-Verlag, Berlin, Heidelberg, 1997.

- [73]. V.A. Grigoriev. Towards the problem on the determination of the liquid film thickness under bubble during boiling in capillary channels. In *Proceedings of the Moscow Power Engineering Institute*, Trudy MEI, 200:52-56, 1974.
- [74]. A.C. Groeneveld. The onset of dry sheath condition – a new definition of dryout. *Nuclear Engineering and Design*, 92:135-140, 1986.
- [75]. D.C. Groeneveld, S.C. Cheng, and T. Doan. AECL-UO critical heat flux look-up table. *Heat Transfer Engineering* 7(1–2):46–61, 1986.
- [76]. K.E. Gungor, R.H.S. Winterton. A general correlation for flow boiling in tubes and annuli. *International Journal Heat Mass Transfer*, 29:351-358, 1986.
- [77]. D.D. Hall and I. Mudawar. Critical heat flux (CHF) for water flow in tubes—II. Subcooled CHF correlations. *International Journal Heat Mass Transfer*, 43:2605–2640, 2000.
- [78]. I. Hapke, H. Boye, and J. Schmidt. Onset of nucleate boiling in minichannels. *International Journal Thermal Science*, 39:505–513, 2000.
- [79]. G. Hetsroni, M. Gurevich, A. Mosyak, E. Pogrebnyak, R. Rozenblit, and L.P. Yarin. Boiling in capillary tubes. *International Journal of Multiphase Flow*, 29:1551-1563, 2003.
- [80]. G. Hetsroni, A. Mosyak, E. Pogrebnyak, and Z. Segal. Explosive boiling of water in parallel microchannels. *International Journal Multiphase Flow*, 31(4):371-392, 2005.
- [81]. G. Hetsroni, A. Mosyak, E. Pogrebnyak, and Z. Segal. Periodic boiling in parallel micorchannels at low vapour quality. *International Journal Multiphase Flow*, 32:1141-1159, 2006.
- [82]. G.F. Hewitt. *Measurement of two-phase flow parameters*. Academic Press, London, UK, 1978.
- [83]. G.F. Hewitt. Flow regimes. In *Handbook of Multiphase Systems*. McGraw-Hill, G. Hetsroni (editor), New York, 1982.
- [84]. G.F. Hewitt and N.S. Hall-Taylor. *Annular two-phase flow*. Pergamon Press, Oxford, UK, 1970.
- [85]. G.F. Hewitt, H.A. Kersey, P.M.C. Lacey, and D.J. Pulling. Burnout and nucleation in climbing film flow. *International Journal of Heat Mass Transfer*, 8:793- 814, 1965.

- [86]. G. F. Hewitt and D. N. Roberts. Studies of in two-phase flow patterns by simultaneous x-ray and flash photography. Technical report, UKAEA Report AERE-M 2159, 1969.
- [87]. G.F. Hewitt and G.B. Wallis. Flooding and associated phenomena in falling film in vertical tube. In *Proceedings of Multiphase flows Symposium*, Philadelphia, PA, 62-74, 1963.
- [88]. R. Hino, T. Ueda. Studies on heat transfer and flow characteristics in subcooling flow boiling. Part I: boiling characteristics. *International Journal Multiphase Flow*, 11:269–281, 1985.
- [89]. Y.Y. Hsu. On the size range of active nucleation cavities on a heating surface. *Journal of Heat Transfer*, Transactions of the ASME, 84:207-216, 1962.
- [90]. Y.Y. Hsu and R.W. Graham. *Transport processes in boiling and two phase systems*. Hemisphere, Washington, DC, 1976.
- [91]. X. Huo, Experimental study of boiling heat transfer in small diameter tubes, PhD thesis, London South Bank University, London, UK, 2005.
- [92]. X. Huo, L. Chen, Y.S. Tian and T.G. Karayiannis. Flow boiling and flow regimes in small diameter tubes. *Applied Thermal Engineering*, 24:1225-1239, 2004.
- [93]. X. Huo, Y.S. Tian, and T.G. Karayiannis. R134a Flow boiling heat transfer in small diameter tubes. *Advances in compact heat exchangers*, R.T. Edwards, Inc., 5: 95-111, 2007.
- [94]. F. Inasaka and H. Nariai. Critical heat flux and flow characteristics of subcooled flow boiling in narrow tubes. *JSME International Journals*, 30:1595–1600, 1987.
- [95]. M. Ishibashi and K. Nishikawa. Saturated boiling heat transfer in narrow spaces. *International Journal Heat Mass Transfer*, 12:863–894, 1969.
- [96]. A.M. Jacobi and J.R. Thome. Heat transfer model for evaporation of elongated bubble flows in microchannels. *Journal Heat Transfer*, 124(6):1131-1136, 2002.
- [97]. S. Jayanti and G.F. Hewitt. Prediction of the slug to churn flow transition in vertical two-phase flow. *International Journal Multiphase Flow*, 18:847-860, 1992.

- [98]. M.K. Jensen and G.J. Memmel. Evaluation of bubble departure diameter correlations. In *Proceedings of the 8th International Heat Transfer Conference*, San Francisco, CA, USA, 1907-1912, 1986.
- [99]. L. Jiang, J. Mikkelsen, J.M. Koo, D. Huber, S. Yao, L. Zhang, P. Zhou, J.G. Maveety, R. Prasher, J.G. Santiago, T.W. Kenny, and K.E. Goodson. Closed-loop electroosmotic microchannel cooling system for VLSI circuits. *IEEE Transactions on Components and Packaging Technologies*, 25(3):347-355, 2002.
- [100]. D.S. Jung and R. Radermacher. Prediction of pressure drop during horizontal annular flow boiling of pure and mixed refrigerants. *International Journal Heat Mass Transfer*, 32:2435-2446, 1989.
- [101]. F. Kaminaga, B. Sumith, and K. Matsumura. Pressure drop in a capillary tube in boiling two phase flow. In *Proceedings of First International Microchannels and Minichannels*, April 24-25, New York, ICMM2003- 1080, 2003.
- [102]. S.G. Kandlikar. Two-phase flow patterns, pressure drop, and heat transfer during boiling in minichannel flow passages of compact evaporators. *Heat Transfer Engineering*, 23:5-23, 2002.
- [103]. S.G. Kandlikar. A general correlation for saturated two-phase flow boiling heat transfer inside horizontal and vertical tubes. *Journal of Heat Transfer, Transactions of the ASME*, 112:219-228, 1990.
- [104]. S. G. Kandlikar. Effect of liquid-vapour phase distribution on the heat transfer mechanisms during flow boiling in minichannels and microchannels. *Heat Transfer Engineering*, 27(1):4-13, 2006.
- [105]. S. G. Kandlikar. Fundamental issues related to flow boiling in minichannels and microchannels. *Experimental Thermal and Fluid Science* 26:389-407, 2002.
- [106]. S.G. Kandlikar and P. Balasubramanian. An extension of the flow boiling correlation to transition, laminar, and deep laminar flows in minichannels and microchannels. *Heat Transfer Engineering*, 25(3): 86-93, 2004.
- [107]. S.G. Kandlikar, M.D. Cartwright, and V.R. Mizo. A photographic study of nucleation characteristics of cavities in flow boiling. In *Proceedings of the*

- International Conference on Convective Flow Boiling*, Banff, Canada, United Engineering Foundation, NY, 11-1, 1995.
- [108]. S. G. Kandlikar and W.J. Grande. Evolution of microchannel flow passages—thermohydraulic performance and fabrication technology. *Heat Transfer Engineering*, 25 (1): 3-17, 2003.
- [109]. S. G. Kandlikar, W. K. Kuan, D. A. Willistein, and J. Borrelli. Stabilization of flow boiling in microchannels using pressure drop elements and fabricated nucleation sites. *Journal Heat Transfer*, 128:389-396, 2006.
- [110]. I. Kataoka, S. Kodama, A. Tomiyama, and A. Serizawa. Study on analytical prediction of forced convective CHF based on multi-fluid model. *Nuclear Engineering and Design* 175:107-117, 1997.
- [111]. Y. Katto. A generalized correlation of critical heat flux for the forced convection boiling in vertical uniformly heated round tubes. *International Journal Heat Mass Transfer*, 21:1527–1542, 1978
- [112]. Y. Katto and H. Ohno. An improved version of the generalized correlation of critical heat flux for the forced convection boiling in uniformly heated vertical tubes. *International Journal Heat and Mass Transfer* 27:1641–1648, 1984.
- [113]. Y. Katto and M. Yoshiwara. Analytical study of critical heat flux of subcooled flow boiling in round tubes. *Transaction JSME*, series B. 55(519):3515-3522, 1989.
- [114]. A. Kawahara, P.M-Y. Chung, and M. Kawaji. Investigation of two-phase flow patterns, void fraction and pressure drop in a micro-channel. *International Journal Multiphase Flow*, 28(9):1411–1435, 2002.
- [115]. W.M. Kays and M.E. Crawford. *Convective Heat and Mass Transfer*. McGraw-Hill, Second Edition, New York, 1980.
- [116]. D.B.R. Kenning and M.G. Cooper. Flow patterns near nuclei and the initiation of boiling during forced convection heat transfer. In *Symposium on Boiling Heat Transfer in Steam Generating Units and Heat Exchangers*, Manchester, UK, September 1965.
- [117]. D.B.R. Kenning and Y. Yan. Saturated flow boiling of water in a narrow channel: experimental investigation of local phenomena. *ICHEME Transaction A, Chemical Engineering Res. and Design*, 79: 425-436, 2001.

- [118]. D.B.R. Kenning, D.S. Wen, K.S. Dan, and S.K. Wilson. Confined growth of vapour bubble in a capillary tube at initially uniform superheat: Experiments and modeling. *International Journal Heat Mass Transfer*, 49:4653-4671, 2006.
- [119]. T. W. Kenny, K. E. Goodson, J. G. Santiago, E. Wang, J.M. Koo, L. Jiang, E. Pop, S. Sinha, L. Zhang, D. Fogg, S. Yao, R. Flynn, C.H. Chang, and C. H. Hidrovo. Advanced cooling technologies for microprocessors. *International Journal High Speed Electronics Systems*, 16(1):301-313, 2006.
- [120]. P.A. Kew and K. Cornwell. Confined bubble flow and boiling in narrow channels. In *Proceedings of the 10th International Heat Transfer Conference*, Brighton, U.K, 473-478, 1995.
- [121]. P. A. Kew and K. Cornwell. Correlations for the prediction of boiling heat transfer in small diameter channels. *Applied Thermal Engineering*, 17(8-10):705-715, 1997.
- [122]. P.A. Kew and K. Cornwell. Correlations for the prediction of boiling heat transfer in small-diameter channels. *Applied Thermal Engineering*, 17(8):705-715, 1997.
- [123]. P. A. Kew and K. Cornwell. On pressure fluctuations during boiling in narrow channels. In *2nd European Thermal-Science and 14th UIT National Heat Transfer Conference*, Rome, 1323-1327, 1996.
- [124]. R. Khodabandeh. Influence of channel diameter on boiling heat transfer in a closed advanced two-phase thermosiphon loop. In *Proceedings of the 5th International Boiling Conference*, Montego Bay, Jamaica, May 4-8, 2003.
- [125]. M. Kureta, T. Kobayashi, K. Mishima, and H. Nishihara. Pressure drop and heat transfer for flow boiling of water in small diameter tubes, *JSME International Journal, Series B*, 41(4):871-879, 1998.
- [126]. S.S. Kutateladze and A.I. Leont'Ev. Some applications of the asymptotic theory of the turbulent boundary layer. In *Proceedings of the Third International Heat Transfer Conference, American Institute of Chemical Engineers*, New York, 2:1-6, 1966.
- [127]. K. Kuwahara, S. Koyama, and Y. Hashimoto. Characteristics of evaporation heat transfer and flow pattern of pure refrigerant HFC134a in a horizontal

- capillary tube. In *Proceedings of the 4th JSME-KSME Thermal Engineering Conference*, 385–390, 2000.
- [128]. V.V. Kuznestov and A.S. Shamirzaev. Two phase flow pattern and flow boiling heat transfer in non-circular channel with a small gap. In *proceedings of Two-Phase Flow Modelling and Experimentation*, Pisa, 249-253, 1999.
- [129]. G.M. Lazarek and S.H. Black. Evaporative heat transfer, pressure drop and critical heat flux in a small vertical tube with R-113. *International Journal Heat Mass Transfer*, 25(7):945-960, 1982.
- [130]. H. J. Lee and S.Y. Lee. Heat transfer correlation for boiling flows in small rectangular horizontal channels with low aspect ratios. *International Journal Multiphase Flow*, 27:2043-2062, 2001.
- [131]. H. J. Lee and S. Y. Lee. Pressure drop correlation for two-phase flow within horizontal rectangular channels with small height. *International Journal of Multiphase Flow*, 27:783-796, 2001.
- [132]. J. Lee and I. Mudawar. Implementation of microchannel evaporator for high heat flux refrigeration cooling applications. *Transactions of The ASME, Journal Electronic Packaging*, 28(1):30-37, 2006.
- [133]. S. Lin, P.A. Kew, and K. Cornwell. Two-phase flow regimes and heat transfer in small tubes and channels. In *Proceedings of 11th International Heat Transfer Conference*, August 23-28, Kyongju, Korea, 2:45-50, 1998.
- [134]. S. Lin, P.A. Kew, and K. Cornwell. Two-phase heat transfer to a refrigerant in a 1 mm diameter tube. *International Journal of Refrigeration*, 24:51–56, 2001a.
- [135]. S. Lin, P.A. Kew, and K. Cornwell. Flow boiling of refrigerant R141b in small tubes. *Chemical Engineering Research and Design*, 79(4):417-424, 2001b.
- [136]. P.C. Lee, F.G. Tseng, and C. Pan. Bubble dynamics in microchannels. Part I: Single microchannel, *International Journal Heat Mass Transfer* 47:5575–5589, 2004.
- [137]. A.M. Lezzi and A. Niro. Critical heat flux and pressure drop in capillary tubes with high L/D ratio. *ASME, Nuclear Engineering Division*, 311-326, 1994.
- [138]. J. Li and P. Cheng. Bubble cavitation in a microchannel. *International Journal Heat Mass Transfer*, 47: 2689–2698, 2004.

- [139]. D. Liu, P-S. Lee, S.V. Garimella. Prediction of the onset of nucleate boiling in microchannel flow. *International Journal Heat Mass Transfer*, 48:5134- 5149, 2005.
- [140]. Z. Liu and R.H.S. Winterton. A general correlation for saturated and subcooled flow boiling in tubes and annuli, based on a nucleate pool boiling equation. *International Journal Heat Mass Transfer*, 34(11):2759-2766, 1991.
- [141]. R.W. Lockhart and R.C. Martinelli. Proposed correlation of data for isothermal two-phase two-component flow in pipes. *Chemical Engineering Progress*, 45-39, 1949.
- [142]. Z. Lu and X. Zhang. Identification of flow patterns of two-phase flow by mathematical modelling. *Nuclear Engineering and Design*, 149:111-116, 1994.
- [143]. W.J. Marsh and I. Mudawar. Predicting the onset of nucleate boiling in wavy free-falling turbulent liquid films. *International Journal Heat Mass Transfer*, 32(2):361-378, 1989.
- [144]. R.C. Martinelli and D.B. Nelson. Prediction of pressure drop during forced circulation boiling of water. *Transactions of the ASME*, 70:695, 1948.
- [145]. B. Massey and J. Ward-Smith. *Mechanics of Fluids*. Stanley Thornes Ltd, seventh edition, 1998.
- [146]. W.H. McAdams, W.K. Woods, and R.L. Bryan. Vaporization inside horizontal tubes-ii-benzene-oil mixtures. *Trans. ASME*, 64:193, 1942.
- [147]. K.W. McQuillan and P.B. Whalley. Flow patterns in vertical two phase flow. *International Journal Multiphase Flow*, 11:161-175, 1985.
- [148]. S. S. Mehendale, A. M. Jacobi, and R. K. Shah. Fluid flow and heat transfer at micro- and meso-scales with application to heat exchanger design. *Applied Mechanics Reviews*, 53(7):175–193, 2000.
- [149]. R.B. Mesler. An alternate to the dangler and addoms convection concept of forced convection boiling heat transfer. *AIChE Journal*, 23(4):448-453, 1977.
- [150]. B.B. Mikic, W.M. Rohsenow, and P. Griffith. On bubble growth rates. *International Journal Heat Mass Transfer*, 13:657-665, 1970.
- [151]. K. Mishima and T. Hibiki. Some characteristics of air-water two-phase flow in small diameter vertical tubes. *International Journal Multiphase Flow*, 22(4):703 – 712, 1996.

- [152]. K. Mishima, T. Hibiki, and H. Nishihara. Some characteristics of gas–liquid flow in narrow rectangular ducts. *International Journal Multiphase Flow*, 19:115–124, 1993.
- [153]. K. Mishima and M. Ishii. Flow regime transition criteria for two-phase flow in vertical tubes. *International Journal Heat Mass Transfer*, 27:723-734, 1984.
- [154]. K. Moriyama, A. Inoue. Thickness of the liquid film formed by a growing bubble in a narrow gap between two horizontal plates. *Journal Heat Transfer*, 118:132-139, 1996.
- [155]. I. Mudawar. Assessment of high heat flux thermal management schemes. *Transactions on Components and Packaging Technologies*, 24(2):122-140, 2001.
- [156]. I. Mudawar and M.B. Bowers. Ultra-high critical heat flux (CHF) for subcooled water flow boiling: I. CHF data and parametric effects for small diameter tubes. *International Journal Heat Mass Transfer*, 42(8):1405-1428, 1999.
- [157]. A. Mukherjee and S.G. Kandlikar. Numerical simulation of growth of a vapor bubble during flow boiling of water in a microchannel. *Microfluid Nanofluid*, 1:137-145, 2005.
- [158]. H. Muller-Steinhagen and K. Heck. A simple friction pressure drop correlation for two-phase flow in pipes. In *Proceedings of Chemical Engineering*, 20:297–308, 1986.
- [159]. H. K. Oh, M. Katsuta, and K. Shibata. Heat transfer characteristics of R134a in a capillary tube heat exchanger. In *Proceedings of the 11th International Heat Transfer Conference*, 6:131-136, 1998.
- [160]. W. Owhaib, C. Martin-Callizo, and B. Palm. Evaporative heat transfer in vertical circular microchannels. *Applied Thermal Engineering*, 24:1241-1253, 2004.
- [161]. W. Owhaib and B. Palm. Flow boiling heat transfer in a vertical circular microchannel tube. In Eurotherm Seminar, Valencia, Spain, no. 722003, 2003.
- [162]. W. Owhaib, B. Palm, and C. Martin-Callizo. Flow boiling visualization in a vertical circular microchannel at high vapour quality. *Experimental Thermal Fluid Science*, 30(8): 755-763, 2006.

- [163]. B Palm. Review heat transfer in microchannels. *Microscale Thermophysical Engineering*, 5:155-175, 2001.
- [164]. Y.P. Peles and S. Haber. A steady state, one dimensional, model for boiling two phase flow in triangular microchannel. *International Journal Heat Mass Transfer*, 26:1095-1115, 2000.
- [165]. X.F. Peng and G.P. Peterson. Convective heat transfer and flow friction for water flow in microchannel structures. *International Journal Heat Mass Transfer*, 39:2599-2608, 1996.
- [166]. X.F. Peng and B.X Wang. Forced convection and flow boiling heat transfer for liquid flowing through microchannels. *International Journal Heat Mass Transfer*, 26:3421–3427, 1993.
- [167]. X. F. Peng, H. Y. Hu, and B. X. Wang. Boiling nucleation during liquid flow in microchannels. *International Journal Heat Mass Transfer*, 41:101-106, 1998.B.
- [168]. B.S. Petukhov. Heat transfer and friction in turbulent pipe flow with variable physical properties. In *Advances in Heat Transfer*, 6:503–564, 1970.
- [169]. M. Piasecka and M. Poniewski. Hysteresis phenomena at the onset of subcooled nucleate flow boiling in microchannels. *Heat Transfer Engineering*, 25(3):441-451, 2004.
- [170]. M.S. Plesset and S.A. Zwick. The growth of vapour bubbles in superheated liquids. *Journal Applied Physics*, 25:493–500, 1954.
- [171]. W. Qu and I. Mudawar. Flow boiling heat transfer in two phase microchannel heat sinks: I. Experimental investigation and assessment of correlation methods. *International Journal Heat Mass Transfer*, 46:2755-2771, 2003a.
- [172]. W. Qu and I. Mudawar. Flow boiling heat transfer in two phase microchannel heat sinks – II. Annular two phase flow model. *International Journal Heat Mass Transfer*, 46:2773-2784, 2003b.
- [173]. W. Qu and I. Mudawar. Measurement and correlation of critical heat flux in two phase microchannel heat sinks. *International Journal Heat Mass Transfer*, 47:2045–2059, 2004.
- [174]. W. Qu and I. Mudawar. Prediction and measurement of incipient boiling heat flux in microchannel heat sinks. *International Journal Heat and Mass Transfer*, 45:3933-3945, 2002.

- [175]. W. Qu, Y. Seok-Mann, and I. Mudawar. Two phase flow and heat transfer in rectangular microchannels. *Journal Electronic Packaging*, 126(3):288-300, 2004.
- [176]. N. A. Radovich and R. Moissis. The transition from two-phase bubble flow to slug flow. *MIT Report 7-7673-22*, 1962.
- [177]. R. Revellin, V. Dupont, T. Ursenbacher, J.R. Thome, and I. Zun. Characterization of diabatic two phase flows in microchannels: Flow parameter results for R134a in a 0.5 mm channel. *International Journal Multiphase Flow* 32:755-774, 2006.
- [178]. R. Revellin and J.R. Thome. Experimental investigation of R134a and R245fa two-phase flow in microchannels for different flow conditions. *International Journal of Heat and Fluid Flow*, 28(1):63-71, 2007a.
- [179]. R. Revellin and J.R. Thome. A new type of diabatic flow pattern map for boiling heat transfer in microchannels. *Journal of Micromechanics and Microengineering*, 17(4):788-796, 2007b.
- [180]. R. Revellin and J.R. Thome. Adiabatic two-phase frictional pressure drops in microchannels. *Experimental Thermal Fluid Science*, 31(7):673-685, 2007c.
- [181]. S. Saitoh, H. Daiguji, and E. Hihara. Effect of tube diameter on boiling heat transfer of R134a in horizontal small-diameter tubes. *International Journal of Heat Mass Transfer*, 48:4973-4984, 2005.
- [182]. S. Saitoh, H. Daiguji, and E. Hihara. Correlation for boiling heat transfer of R134a in horizontal tubes including effect of tube diameter. *International Journal of Heat Mass Transfer*, 50:5215-5225, 2007.
- [183]. T. Sato and H. Matsumura. On the conditions of incipient subcooled boiling with forced convection, *Bulletin ISME*, 7(26):392-398, 1963.
- [184]. A. Serizawa, Z. Feng, and Z. Kawara. Two phase flow in microchannels. *Experimental Thermal Fluid Science*, 26:703-714, 2002.
- [185]. R. Schmidt. Low temperature CMOS experience at IBM, In *Sixteenth Annual IEEE Semiconductor Thermal Measurement and Management Symposium* (Cat. No 00CH37068), 112-113, 2000.
- [186]. M.M. Shah. Improved general correlation for critical heat flux during up flow in uniformly heated vertical tubes. *Heat and Fluid Flow* 84: 326-335, 1987.

- [187]. M.M. Shah. Chart correlation for saturated boiling heat transfer: equations and further study. *ASHRAE Transactions*, 88:185-196, 1982.
- [188]. R. K. Shah. Classification of heat exchangers. In *Heat Exchangers: Thermal-Hydraulic Fundamentals and Design*, editors, S. Kakac, A. E. Bergles, and F. Mayinger, Hemisphere Publishing Corp., 9-46, 1986.
- [189]. M.M. Shah. A generalized graphical method for predicting CHF in uniformly heated vertical tubes. *International Journal Heat Mass Transfer*, 22:557–568, 1979.
- [190]. R.K. Shah and A.L. London. *Laminar Flow Forced Convection in Ducts: a Source Book for Compact Heat Exchanger Analytical Data*, Supl. 1, Academic press, New York, 1978.
- [191]. D. Shiferaw, X. Huo, T.G. Karayiannis, and D.B.R. Kenning. Examination of heat transfer correlations and a model for flow boiling of R134a in small diameter tubes. *International Journal Heat Mass Transfer*, 50:5177-5193, 2007.
- [192]. S.L. Smith. Void fractions in two phase flow: Part 1, a correlation based upon an equal velocity head model. In *Proceedings of Institute of Mechanical Engineers*, London 184:647–657, 1969.
- [193]. A.L. Souza and M.M. Pimenta. Prediction of pressure drop during horizontal two-phase flow of pure and mixed refrigerants. In *Cavitation and Multiphase Flow Symposium, ASME*, New York, FED-210:161-171, 1995.
- [194]. F.C. Standiford. Letter to the editor. *AIChE Journal*, 24(4):750-751, 1978.
- [195]. D. Steiner and J. Taborek. Flow boiling heat transfer in vertical tubes correlated by an asymptotic model. *Heat Transfer Engineering*, 13(2):43-69, 1992.
- [196]. G. F. Stevens and G. J. Kirby. A quantitative comparison between burn-out data for water at 10001b/in² and Freon-12 at 155 Ib/in² (abs), uniformly heated round tubes, vertical up flow, U.K. *AEA report AEEW-R327*, 1964.
- [197]. B. Sumith, F. Kaminaga, and K. Matsumura. Saturated flow boiling of water in a vertical small diameter tube. *Experimental Thermal Fluid Science*, 27:789–801, 2003.

- [198]. B. Sunden, M. Faghri, and E. J. Kenyon. An overview of fabrication methods and fluid flow and heat transfer characteristics of microchannels. *Advances in Engineering Heat Transfer*, 3-23, 1995.
- [199]. M. Suo and T. Griffith. Two-phase flow in capillary tubes. *Journal Basic Engineering*, 86:576-582, 1964.
- [200]. Y. Taitel, D. Barnea, and A. E. Dukler. Modelling flow pattern transitions for steady upward gas-liquid flow in vertical tubes. *AIChE Journal*, 26:345-354, 1980.
- [201]. Y. Taitel and A. E. Dukler. A model for predicting flow regime transitions in horizontal and near-horizontal flow. *AIChE Journal*, 22:47-55, 1976.
- [202]. Y. Taitel, D. Barnea, and A. E. Dukler. Modelling of flow pattern transitions for steady upward gas-liquid flow in vertical tubes. *AIChE Journal*, 26:345-354, 1980.
- [203]. G.I. Taylor. Deposition of viscous fluid on the wall of a tube. *Fluid Mechanics*, 10(2): 161-165, 1961.
- [204]. J.R.S. Thom. Prediction of pressure drop during forced circulation boiling of water. *International Journal Heat Mass Transfer*, 7:709-724, 1964.
- [205]. J. R. Thome. Boiling in microchannels: a review of experiment and theory. *International Journal of Heat and Fluid Flow*, 25:128-139, 2004.
- [206]. J.R. Thome. State-of-the-art overview of boiling and two-phase flows in microchannels. *Heat Transfer Engineering*, 27(9):4-19, 2006.
- [207]. J.R. Thome, V. Dupont, and A.M. Jacobi. Heat transfer model for evaporation in microchannels, Part I: presentation of the model. *International Journal Heat Mass Transfer*, 47:3375-3385, 2004.
- [208]. W. Tong, A.E. Bergles, and M.K. Jensen. Pressure drop with highly subcooled flow boiling in small-diameter tubes. *Experimental Thermal and Fluid Science*, 15:202-212, 1997.
- [209]. L.S. Tong and Y.S. Tang. *Boiling heat transfer and two-phase flow*. Taylor & Francis, second edition, 1997.
- [210]. T.N. Tran, M.W. Wambsganss, and D.M. France. Small circular- and rectangular-channel boiling with two refrigerants. *International Journal Multiphase Flow*, 22(3): 485-498, 1996.

- [211]. T. N. Tran, M. C. Chyu, M. W. Wambsganss, and D. M. France. Two-phase pressure drop of refrigerants during flow boiling in small channels: an experimental investigation and correlation development. *International Journal Multiphase Flow*, 26:1739 -1754, 2000.
- [212]. K.A. Triplett, S.M. Ghiaasiaan, S.I. Abdel-Khalik, and D.L. Sadowski. Gas-liquid two-phase flow in microchannels, Part I: Two-phase flow patterns. *International Journal of Multiphase Flow*, 25:377-394, 1999.
- [213]. D.B. Tuckerman and R.F.W. Pease. High performance heat sink for VLSI. *IEEE Electronic Device Letters*, 2:126-129, 1981.
- [214]. G. Upadhyaya. Cooligy active micro-structure cooling offers key advanced processor performance and quieter systems. *A White Paper from the Experts in Business-Critical Continuity*, EMERSON Network Power, 2005.
- [215]. V.V. Wadekar. Vertical slug flow heat transfer with nucleate boiling. *Phase change heat transfer, ASME, HTD*, 159:157-161, 1991.
- [216]. V.V. Wadekar and D.B.R. Kenning. Flow boiling heat transfer to slug/churn flow region. In *Proceedings of the 9th International Heat Transfer Conference*, 9:449-454, 1990.
- [217]. G.B. Wallis. *One Dimensional Two-phase Flow*. McGraw-Hill, New York, 1969.
- [218]. G.B. Wallis. Annular two phase flow. II Additional effects. *Journal Basic Engineering*, 92:73-82, 1970.
- [219]. M.W. Wambsganss, D.M. France, J.A. Jendrajczyk, and T.N. Tran. Boiling heat transfer in a horizontal small-diameter tube. *Journal of Heat Transfer*, 115:963-972, 1993.
- [220]. G. R. Warriar, V.K. Dhir, and L. A. Momoda. Heat transfer and pressure drop in narrow rectangular channels. *Experimental Thermal and Fluid Science*, 26:53-64, 2002.
- [221]. J. Weisman and B.S. Pei. Prediction of critical heat flux in flow boiling at low qualities. *International Journal Heat and Mass Transfer*, 26:1463-1477, 1983.
- [222]. D.S. Wen, D.B.R. Kenning, and Y. Yan. Flow boiling of water in a narrow vertical channel at low mass flux: observations of local phenomena. In

- Proceedings of the 12th International Heat Transfer Conference*, Grenoble, 3:773-778, 2002.
- [223]. D.S. Wen, Y. Yan and D.B.R. Kenning. Saturated flow boiling of water in a narrow channel: time-averaged heat transfer coefficients and correlations, *Applied Thermal Engineering*, 24:1207-1223, 2004.
- [224]. D.S. Wen and D.B.R. Kenning. Two-phase pressure drops of water during flow boiling in a vertical narrow channel. *Experimental Thermal and Fluid Science*, 28:131-138, 2004.
- [225]. B.P. Whalley. *Boiling, condensation, and gas – liquid flow*. Oxford University press, 1987.
- [226]. P.B. Whalley, P. Hutchinson, and G.F. Hewitt. The calculation of critical heat flux in forced convection boiling. In *Proceedings of the Fifth International Heat Transfer Conference*, Tokyo, Japan, B6:290–294, 1974.
- [227]. L. Wojtan, R. Revellin, and J. R. Thome. Investigation of saturated critical heat flux in a single, uniformly heated microchannel. *Experimental Thermal Fluid Science*, 30(8):765-774, 2006.
- [228]. H.Y. Wu and P. Cheng. Boiling instability in parallel silicon microchannels at different heat flux. *International Journal Heat Mass Transfer*, 47:3631-3641, 2004.
- [229]. H.Y. Wu and P. Cheng. Visualization and measurements of periodic boiling in silicon microchannels. *International Journal Heat Mass Transfer*, 46: 2603–2614, 2003a.
- [230]. H.Y. Wu and P. Cheng. Liquid/two phase/vapour alternating flow during boiling in microchannels at high heat flux. *International Communications Heat Mass Transfer*, 30(3):295-302, 2003b.
- [231]. C. L. Xia, Z.Y. Guo, and W.L. Hu. Mechanism of boiling heat transfer in narrow channels. *Two phase flow and heat transfer, ASME, HTD*, 197:111-119, 1992.
- [232]. R. Xiong and J. N. Chung. An experimental study of the size effect on adiabatic gas-liquid two-phase flow patterns and void fraction in microchannels. *Physics of Fluids*, 19:033301-1, 2007.

- [233]. J. L. Xu, J.J. Zhou, Y.H. Gan, and Y. Chen. Unsteady flow phenomenon in a heated microchannel at high heat fluxes. *Experimental Heat Transfer*, 17:299-319, 2004.
- [234]. Y. Yan and D.B.R. Kenning. Pressure and temperature fluctuations during boiling in narrow channel. In *Eurotherm, Heat Transfer in Condensation and Evaporation*, Grenoble, 62:107-1223, 1998.
- [235]. Y. Y. Yan and T.F. Lin. Evaporation heat transfer and pressure drop of refrigerant R-134a in a small pipe. *International Journal Heat Mass Transfer*, 41: 4183-4194, 1998.
- [236]. C.Y. Yang and C.C. Shieh. Flow pattern of air-water and two-phase R-134a in small circular tubes. *International Journal of Multiphase Flow*, 27:1163-1177, 2001.
- [237]. Z.L. Yang, B. Palm, and B.R. Sehgal. Numerical simulation of bubbly two phase flow in narrow channel. *International Journal Heat Mass Transfer*, 45:631-639, 2002.
- [238]. T-H. Yen, N. Kasagi, and Y. Suzuki. Forced convective boiling heat transfer in microtubes at low mass and heat fluxes. *International Journal of Multiphase Flow*, 29:1771-1792, 2003.
- [239]. W. Yu, D. M. France, M.W. Wambsganss, and J.R. Hull. Two-phase pressure drop, boiling heat transfer, and critical heat flux to water in a small-diameter horizontal tube. *International Journal of Multiphase Flow*, 28:927 – 941, 2002.
- [240]. R. Yun, Y. Kim, and M. S. Kim. Flow boiling heat transfer of carbon dioxide in horizontal mini tubes. *International Journal Heat and Fluid Flow*, 26:801-809, 2005.
- [241]. L. Zhang, K.E. Goodson, T.W. Kenny. *Silicon microchannel heat sinks, theories and phenomena*. Springer, chap. 5-7, Berlin. 2004
- [242]. L. Zhang, J. Koo, L. Jiang, K.E. Goodson, J.G. Santiago, and T.W. Kenny. Study of boiling regimes and transient signal measurements in microchannels, In *Proceedings of Transducers '01*, Munich, Germany, 1514–1517, 2001.
- [243]. L. Zhang, J-M. Koo, L. Jiang, M. Asheghi, K.E. Goodson, J.G. Santiago, E.N. Wang, and T.W. Kenny. Measurements and modeling of two-phase flow in

- microchannels with nearly constant heat flux boundary conditions. *Journal of Microelectromechanical systems*, 11(1):12-19, 2002.
- [244]. W. Zhang, T. Hibiki, and K. Mishima. Correlation for flow boiling heat transfer in mini-channels. *International Journal Heat Mass Transfer*, 47:5749-5763, 2004.
- [245]. W. Zhang, T. Hibiki, K. Mishima, and Y. Mi. Correlation of critical heat flux for flow boiling of water in minichannels. *International Journal Heat Mass Transfer*, 49(5-6):1058-1072, 2006.
- [246]. L. Zhang, E.N. Wang, K.E. Goodson, T.W. Kenny. *Phase change phenomena in silicon microchannels*. *International Journal Heat Mass Transfer*, 48:1572-1582, 2005.
- [247]. L. Zhang, E.N. Wang, J-M. Koo, L. Jiang, K.E. Goodson, J.G. Santiago, and T.W. Kenny. Enhanced nucleate boiling in microchannels. In *Fifth IEEE International Conference on Micro Electro Mechanical Systems*, 89-92, 2002.
- [248]. M. Zhang and R.L. Webb. Correlation of two-phase friction for refrigerants in small-diameter tubes. *Experimental Thermal Fluid Science*, 25:131–139, 2001.
- [249]. T.S. Zhao and Q.C. Bi. Co-current air-water two-phase flow patterns in vertical triangular microchannels. *International Journal of Multiphase Flow*, 27:765-782, 2001.
- [250]. N. Zuber. Nucleate boiling – the region of isolated bubbles – similarity with natural convection. *International Journal Heat Mass Transfer*, 6:53, 1963.
- [251]. N. Zuber and J. Findlay. Average volumetric concentration in two-phase systems. *Journal of Heat Transfer, ASME*, 86:453-468, 1965.

Appendix A

Operating Instructions for the Experimental Facility

The following are instructions for safe operation of the R22 refrigeration system and R134a main circuit.

R22 Refrigeration System

Before starting-up the R22-cooling system

1. Make a brief visual inspection of the system.
2. Check the refrigerant liquid level using the sight glass located at the R22 tank.
3. Check the system pressure using the Gordon-gauges; it should read the saturation pressure of R22 at the daily ambient temperature.
4. Make sure the compressor crank case heater is on, and the temperature is about 40 °C.
5. Check the compressor oil level. If the oil-level is below the level indicator, use the oil-recovery system to top-up the oil, see instructions below for operating the auxiliary oil recovery circuit.
6. Make sure that the switches for the two solenoid-valves in the lines that connect the R22 tank with hot-gas bypass and liquid receiver are turned on.

Instructions for running the oil-recovery system

1. Open the valve below the R22 tank and all the valves in the oil-recovery line, but close the valve between the oil-tank and the compressor crankcase.

2. Run the small oil pump.
3. Fill the oil-recovery tank up to the level between the upper and lower level indicators.
4. Adjust the thermostat for a temperature of about 50 °C.
5. Switch on the immersion heater inside the oil tank. And slightly open the valve that leads the evaporated refrigerant to the system.
6. Observe for any bubble in oil recovery tank using the sight glasses. This ensures that, the remaining fluid is oil and the refrigerant is returned back to the system.
7. Slightly open the valve between the oil recovery tank and the crankcase and drain the oil to the crank case until it reaches to the oil level indicator of the compressor.

Running R22 system

1. Switch on the primary (main isolator switch at the wall) and the secondary switches at the power box.
2. Turn on the control system including the computer and data loggers to monitor the temperatures of the discharge and suction line and compressor motor.
3. Switch on all the R22 condenser fans and then press the green compressor switch to turn on the compressor.
4. Check the discharge temperature and pressure. Initially it may go slightly over 15 bar, but then it should return back immediately to about 11 bar after the condenser starts cooling effectively.
5. Run the secondary cooling system units in the R134a system, i.e. open the valves at the lines to the heat exchangers between R22 and R134a system and run the R22 pump.
6. Switch off part of the R22 condenser fans to match the cooling load required.
7. Control the cooling to the chiller, R134a condenser, or cooling coil in the R134a tank by using the needle valves at the respective positions.

8. The cooling system is designed with flooded evaporator type so that the compressor can run at all times regardless of the load. Therefore, run the compressor continuously.

R134a Main System

Before starting-up the system

1. Make visual inspection at various connections, especially around the test section.
2. Check the R134a refrigerant level using the sight glass at the R134a tank.
3. See the system pressure using the Gordon gauges; it should read the saturation pressure of R134a at the ambient temperature of the day.
4. Open all the valves in the R134a circuit. Select which flow meter to run using the three-way valve located upstream the flow meters. The selection depends on the range of flow rates. Flow meter 1 is for 0 – 25 kg/hr, while flow meter 2 is for flow rates exceeding 25 kg/hr.
5. Set the PID control for the three controlled parameters. These are inlet pressure to the heating test section (P_3) and visualization section (P_0) and R134a tank temperature.
6. Fill the ice-box for reference temperature with ice, and check that the thermometer reads zero.

Running R134a system

1. Switch on the R134a pump using the switch located at the front panel of the power box.
2. Switch on the R134a tank heater and use the variac to attain the required experimental system pressure. The needle valves in the R22 cooling system can also be used to regulate the system pressure.
3. Adjust the needle valves downstream the flow rate to control the R134a flow rate

4. Depending on the required inlet condition switch on the preheater and control the heat needed using the preheater variac.
5. Use the needle valve at the R22-chiller to regulate the degree of subcooling.
6. All the values needed to control the experimental conditions can be monitored by watching the data acquisition computer screen.
7. Once the required experimental conditions, i.e. flow rate, system pressure, and inlet subcooling are attained and steady, carry out a single phase heat transfer measurement to determine the loss coefficient.
8. Switch on the heater transformer of the test section and adjust the test section variac to the required heat flux. In order to avoid sudden thermal shock and damage to the test section or cause dryout, increase the heat flux in very small steps until the required exit quality is achieved.
9. Perform all the heat flux steps according to the experimental plan, and after the exit quality reaches ~ 0.95 , change the flow rate or the system pressure according to the plan of experiment and repeat all the heat flux steps.

System regular shut-down

1. Turn down the test section variac to zero and switch off the transformer switch at the panel of the power box.
2. Turn down other variacs, i.e. R134a tank heater and preheater variacs and switch off their heaters.
3. Make sure you have saved measured data.
4. Check that the test section wall temperatures and R134a fluid temperature dropped down to near the ambient and saturation temperatures respectively.
5. Switch off the compressor and R22 condenser fan switches.
6. Turn off the R22 and R134a pumps.
7. Switch of the control system, PID controller, power meters and data loggers.

8. Switch off the secondary power switches at the power box panel.
9. Switch off the main isolator switches at the wall.

Emergency shut-down

In case of refrigerant leak or other electrical or system failure,

1. Switch-off the R134a by pressing the red emergency switch at the front panel of the power box.
2. Switch of the compressor
3. Switch off the main primary switches,
4. If any refrigerant leaks isolate part of the system that leaks by the closing the corresponding valves to the rest of the system.
5. Ventilate the room. It is necessary precaution to inform the technicians any malfunctioning component or system immediately.

Appendix B

Single Phase Heat Transfer Correlations Used for Validation

Reference	Correlation	Conditions
Gnielinski (1976)	$Nu_{sp} = \frac{(f/8)[Re-1000]Pr}{1+12.7\sqrt{f/8}(Pr^{2/3}-1)}$ $f = (1.82 \log_{10} Re - 1.64)^{-2}$	Turbulent region $3000 < Re < 5 \times 10^6$ $0.5 < Pr < 2000$
Gnielinski (VDI-1997)	$Nu_{sp} = \frac{(f/8)[Re-1000]Pr}{1+12.7\sqrt{f/8}(Pr^{2/3}-1)} \left[1 + \left(\frac{D}{L(z)} \right)^{2/3} \right]$ $f = (1.82 \log_{10} Re - 1.64)^{-2}$	Transition region and considers thermal entry length effect $2300 < Re < 10^6$ $0.6 < Pr < 10^5$
Adams et al. (1998)	$Nu_{sp} = \frac{(f/8)[Re-1000]Pr}{1+12.7\sqrt{f/8}(Pr^{2/3}-1)} (1+F)$ $f = (1.82 \log_{10} Re - 1.64)^{-2}$ $F = 7.6 \times 10^{-5} Re \left[1 - (D/D_r)^2 \right]; D_r = 1.161$	Turbulent $Re = 2.6 \times 10^3 - 2.3 \times 10^4$ $1.53 < Pr < 6.43$
Choi et al. (1991)	$Nu_{sp} = 0.000972 Re^{1.17} Pr^{1/3} \text{ for } Re < 2000$ $Nu_{sp} = 3.82 \times 10^{-6} Re^{1.96} Pr^{1/3} \text{ for } 2500 < Re < 20 \times 10^3$	Laminar and Transition
Peng and Petron (2000)	$Nu_{sp} = 0.1165 \left(\frac{D_h}{W_c} \right)^{0.81} \left(\frac{H}{W} \right)^{-0.79} Re^{0.62} Pr^{1/3}$ <p>W_c - centre to centre distance between channels H - height of channel W - width of channel</p>	For Microchannels of range $D_h=0.15-0.34$ mm $Re = 50 - 4000$

Appendix C

Selected Existing Flow Boiling Heat Transfer Correlations Used for Comparison with the Current Data

Reference	Correlation	Conditions
Lazarek and Black (1982)	$\alpha_{tp} = 30 Re_l^{0.857} Bo^{0.714} (\lambda_l / D_h)$	$D = 3.1 \text{ mm}$ $G = 125 - 750 \text{ kg/m}^2\text{s}$ $q = 14 - 380 \text{ kW/m}^2$ $P = 1.3 - 4.1 \text{ bar}$ R113
Gungor and Winterton (1986)	$\alpha_{tp} = E\alpha_l + S\alpha_{nb}$ $\alpha_l = 0.023 Re_l^{0.8} Pr_l^{0.4} (\lambda_l / D_h)$ $\alpha_{nb} = 55 P_R^{0.12} (-\log_{10} P_R)^{-0.55} M^{-0.5} q^{0.67}$ $E = 1 + 24000 Bo^{1.16} + 1.37(1/X_{tt})^{0.86}$ $X_{tt} = \left(\frac{1-x}{x}\right)^{0.9} \left(\frac{\rho_v}{\rho_l}\right)^{0.5} \left(\frac{\mu_l}{\mu_v}\right)^{0.1}$ $S = 1 / (1 + 15 \times 10^{-6} E^2 Re_l^{1.17})$ <p>If the tube is horizontal and $Fr < 0.05$, E and S should be multiplied by $Fr^{(0.1-2Fr)}$ and $Fr^{0.5}$, respectively.</p>	$D = 3.05 - 32 \text{ mm}$ $G = 12.4-61518 \text{ kg/m}^2\text{s}$ $q = 1.1 - 91.5 \times 10^3 \text{ kW/m}^2$ $P = 1- 202.6 \text{ bar}$ water, refrigerants, ethylene glycol

<p>Liu and Winterton (1991)</p>	$\alpha_{tp}^2 = (E\alpha_l)^2 + (S\alpha_{nb})^2$ $\alpha_l = 0.023 Re_l^{0.8} Pr_l^{0.4} (\lambda_l / D)$ $\alpha_{nb} = 55 P_r^{0.12} (-\log_{10} P_r)^{-0.55} M^{-0.5} q^{0.67}$ $E = \left[1 + x Pr_l \left(\frac{\rho_l}{\rho_v} - 1 \right) \right]^{0.35}$ $S = (1 + 0.55 E^{0.1} Re_l^{0.16})^{-1}$	<p>$D = 2.95 - 32.0$ mm</p> <p>$G = 12 - 8179$ kg/m²s</p> <p>$q = 0.35 - 2620$ kW/m²</p> <p>$P_R = 0.0023 - 0.895$</p> <p>$Re = 569 - 8.75 \times 10^5$</p> <p>water, refrigerants</p>
<p>Tran et al. (1996)</p>	$\alpha_{tp} = 840000 (Bo^2 We_l)^{0.3} \left(\frac{\rho_l}{\rho_g} \right)^{-0.4}$ $We_l = \frac{G^2 D_h}{\rho_l \sigma}$	<p>$D = 2.4, 2.92$ mm,</p> <p>$G = 44 - 832$ kg/m²s</p> <p>$q = 7.5 - 129$ kW/m²</p> <p>$P_R = 0.045 - 0.2$</p> <p>R12, R113</p>
<p>Kandlikar and Balasubramanian (2004)</p>	$\alpha_{tp} = \max(E_{CBD}, S_{NBD}) (1-x)^{0.8} \alpha_{lo}$ $S_{NBD} = (0.6683 Co^{-0.2} + 1058 Bo^{0.7} F_{Fl})$ $E_{CBD} = 1.136 Co^{-0.9} + 667.2 Bo^{0.7} F_{Fl}$ $\alpha_{lo} = \frac{Re_l Pr_l (f/2) (\lambda_l / d)}{1 + 12.7 (Pr_l^{2/3} - 1) (f_f / 2)^{0.5}}$ <p>for $10^4 \leq Re_l \leq 5 \times 10^6$</p> $\alpha_{lo} = \frac{(Re_l - 1000) Pr_l (f_f / 2) (\lambda_l / d)}{1 + 12.7 (Pr_l^{2/3} - 1) (f_f / 2)^{0.5}}$ <p>for $3000 \leq Re_l \leq 10000$,</p> $Co = \left(\frac{1-x}{x} \right)^{0.8} \left(\frac{\rho_g}{\rho_l} \right)^{0.5}$ <p>For $1600 < Re < 3000$ (transition region), α_{Lo} interpolation at $Re = 1600$ and 3000</p> <p>For $Re < 1600$ (laminar)</p> <p>α_{lo} is calculated from $Nu = \text{constant}$</p> <p>For $Re \leq 100$, $\alpha_{tp} = S_{NBD} (1-x)^{0.8} \alpha_{lo}$</p>	<p>Range of data for the original Kandlikar (1990) correlation</p> <p>$D = 0.19 - 32.0$ mm</p> <p>$G = 13 - 8179$ kg/m²s</p> <p>$q = 0.3 - 2280$ kW/m²</p> <p>$P = 0.4 - 64$ bar</p> <p>water, refrigerants</p>

$$\alpha_{tp} = S\alpha_{nb} + E\alpha_{sp}$$

$$\alpha_{nb} = 0.00122 \left(\frac{\lambda_l^{0.79} C_{p_l}^{0.45} \rho_l^{0.49}}{\sigma^{0.5} \mu_l^{0.29} h_{lg}^{0.24} \rho_g^{0.24}} \right) \Delta T_{sat}^{0.24} \Delta P_{sat}^{0.75}$$

$$S = \left(1 + 2.53 \times 10^{-6} Re_l^{1.17} \right)^{-1}$$

$$E = \text{MAX}(E', 1) \quad E' = 0.64\phi_l$$

$$\phi_l^2 = 1 + \frac{C}{X} + \frac{1}{X^2}$$

for $Re_l < 1000$ and $Re_g < 1000$, $X = X_{vv}$, $C = 5$

for $Re_l > 2000$ and $Re_g < 1000$, $X = X_{tv}$, $C = 10$

for $Re_l < 1000$ and $Re_g > 2000$, $X = X_{vt}$, $C = 12$

for $Re_l > 2000$ and $Re_g > 2000$, $X = X_{tt}$, $C = 20$

Zhang et al.
(2004)

$D = 0.78 - 6.0$ mm
 $G = 23.4 - 2939$ kg/m²s
 $q = 2.95 - 2511$ kW/m²
 $P = 1.01 - 8.66$ bar
Water, refrigerants

For other regions of Re_k ($k = l$ or g) interpolate the above values of C

$$X = \left[\left(\frac{dP}{dz} \right)_l / \left(\frac{dP}{dz} \right)_g \right]^{0.5} = \left(\frac{f_f}{f_g} \right)^{0.5} \left(\frac{1-x}{x} \right) \left(\frac{\rho_g}{\rho_l} \right)^{0.5}$$

$$f_k = \begin{cases} 16/Re_k, & \text{for tubes, } Re_k < 1000 \\ 0.046 Re_k^{-0.2}, & \text{for } Re_k > 2000 \end{cases}$$

$$\alpha_{sp} = (\lambda_l/D) Nu_{sp}$$

$$Nu_{sp} = \begin{cases} \max(4.36, Nu_{Collier}), & \text{for } Re \leq 2000, \\ 0.023 Re_l^{0.8} Pr_l^{0.4}, & \text{for } Re \geq 2300 \end{cases}$$

$$Nu_{Collier} = 0.17 Re_l^{0.33} Pr_l^{0.43} \left(\frac{Pr_l}{Pr_w} \right)^{0.25} \times$$

$$\left[\frac{g\beta\rho_l^2 D_h^3 (T_w - T_l)}{\mu_l^2} \right]^{0.1}$$

<p>Saitoh et al. (2007)</p>	$\alpha_{tp} = S\alpha_{nb} + E\alpha_{sp}$ $\alpha_{nb} = 207 \frac{\lambda_l}{D_b} \left(\frac{qD_b}{\lambda_l T_l} \right)^{0.745} \left(\frac{\rho_g}{\rho_l} \right)^{0.581} Pr_l^{0.533}$ $D_b = 0.512 [\sigma/g(\rho_l - \rho_g)]^{0.5}$ $S = (1 + 0.4 Re_l \times 10^{-4})^{1.4}$ $E = 1 + \left[\left(\frac{1}{X} \right)^{1.05} / 1 + We_g^{-0.4} \right]$ $\alpha_{sp} = \begin{cases} 0.023 \frac{\lambda_l}{D} \left(\frac{G_l D}{\mu_l} \right)^{0.8} \left(\frac{Cp_l \mu_l}{\lambda_l} \right)^{1/3}, & Re > 1000 \\ \frac{4.36 \lambda_l}{D}, & Re < 1000 \end{cases}$ $X = \left(\frac{1-x}{x} \right)^{0.9} \left(\frac{\rho_g}{\rho_l} \right)^{0.5} \left(\frac{\mu_l}{\mu_g} \right)^{0.1},$ <p>for $Re_l > 1000$ & $Re_g > 1000$</p> $X = \left(\frac{f_l}{f_g} \right)^{0.5} (Re_g^{-0.4}) \left(\frac{G_l}{G_g} \right)^{0.5} \left(\frac{\rho_g}{\rho_l} \right)^{0.5} \left(\frac{\mu_l}{\mu_g} \right)^{0.5}$ <p>for $Re_l < 1000$ & $Re_g > 1000$</p>	<p>$D = 0.5 - 11$ mm $G = 150 - 450$ kg/m²s $q = 5 - 39$ kW/m² $P = 3.5 - 5$ bar R134a</p>
-----------------------------	---	--

Appendix D

Selected Existing Two Phase Pressure Drop Correlations Used for Comparison with the Current Data

Reference	Correlation	Conditions
Chisholm et al. (1983), B-coefficient method	$\Delta P_{f,tp} = \Delta P_{f,lo} \bar{\phi}_{lo}^2$ $\bar{\phi}_{lo}^2 = \frac{1}{x_e - x_{in}} \int_{x_{in}}^{x_e} \phi_{lo}^2(x) dx$ $\phi_{lo}^2(x) = 1 + (\Gamma^2 - 1) [Bx^{0.875} (1-x)^{0.875} + x^{1.75}]$ $\Gamma^2 = \left[\frac{(dP/dz)_{go}}{(dP/dz)_{lo}} \right]_f$ $B = \begin{cases} 4.8; & \text{for } G \leq 500 \text{ \& } \Gamma \leq 9.5 \\ 15000/(\Gamma^2 G^{0.5}); & \text{for } \Gamma \geq 9.5 \\ 21/\Gamma; & \text{for } G > 600 \text{ \& } 9.5 < \Gamma < 28 \\ 520/(\Gamma G^{0.5}); & \text{for } G \leq 600 \text{ \& } 9.5 < \Gamma < 28 \\ 2400/G; & \text{for } 500 < G < 1900 \text{ \& } \Gamma \leq 9.5 \\ 55/G^{0.5}; & \text{for } G \geq 1900, \text{ \& } \Gamma \leq 9.5 \end{cases}$ $\varepsilon = \Delta P_{f,lo} \phi_{lo}^2$	G = 500 – 1900 kg/m ² s
Tran et al. (2000)	$\Delta P_{f,tp} = \Delta P_{f,lo} \phi_{lo}^2$ $\phi_{lo}^2 = 1 + (4.3\Gamma^2 - 1) [C_o x^{0.875} (1-x)^{0.875} + x^{1.75}]$ $\Gamma^2 = \left[\frac{(dP/dz)_{go}}{(dP/dz)_{lo}} \right]_f ; C_o = \frac{[\sigma / g(\rho_l - \rho_g)]^{1/2}}{D}$	D = 2.46, 2.92 mm D _h = 2.40 mm G = 33 – 832 kg/m ² s q = 2.2– 91 kW/m ² P _R = 0.04 – 0.23 R134a, R12, R113

<p>Mishima and Hibiki (1996)</p>	$\Delta P_{f,tp} = \Delta P_{f,l} \phi_l^2$ $\phi_l^2 = 1 + \frac{C}{X} + \frac{1}{X^2}, X^2 = \left[\frac{(dP/dz)_l}{(dP/dz)_g} \right]$ $C = 21(1 - e^{0.319D})$	<p>$D = 1.05 - 4 \text{ mm}$</p> <p>$U_{gs} = 0.071 - 49.4 \text{ m/s}$</p> <p>$U_{ls} = 0.071 - 2.33 \text{ m/s}$</p>
<p>Muller Steinhagen</p>	$\left(\frac{dP}{dz} \right)_{f,tp} = F(1-x)^{1/3} + Bx^3$ $F = A + 2(B-A)x$ $A = \left(\frac{dP}{dz} \right)_{lo} = f_{lo} \frac{2G^2}{D\rho_l}$ $B = \left(\frac{dP}{dz} \right)_{go} = f_{go} \frac{2G^2}{D\rho_g}$	<p>$D = 4 - 392 \text{ mm}$</p>

Appendix E

R134a Physical Properties

<i>Pressure</i> (bar)	T_{sat} (°C)	h_l (kJ/kg)	h_g (kJ/kg)	h_{lg} (kJ/kg)	ρ_l (kg/m ³)	ρ_g (kg/m ³)
1	-26.37	17.28	234.4	217.2	1378	5.194
2	-10.09	38.43	244.5	206	1327	10.01
4	8.91	63.94	255.6	191.6	1265	19.53
6	21.55	81.51	262.4	180.9	1220	29.16
8	31.31	95.47	267.3	171.9	1182	38.99
10	39.37	107.3	271	163.7	1149	49.23
12	46.29	117.8	273.9	156.1	1119	59.83
14	52.4	127.2	276.2	148.9	1091	70.83

<i>Pressure</i> (bar)	$\mu_l \times 10^4$ (kg/ms)	$\mu_g \times 10^5$ (kg/ms)	λ_l (W/m K)	λ_g (W/m K)	C_{p_l} (kJ/kg K)	σ (N/m)
1	3.788	0.987	0.1052	0.009496	1.28	0.01548
2	3.027	1.051	0.09884	0.01111	1.315	0.01303
4	2.373	1.127	0.09072	0.01297	1.367	0.01029
6	2.028	1.181	0.08488	0.01422	1.411	0.008546
8	1.798	1.225	0.08014	0.0152	1.452	0.007246
10	1.625	1.265	0.07605	0.01604	1.494	0.006207
12	1.487	1.302	0.07239	0.01678	1.538	0.005342
14	1.372	1.338	0.06906	0.01747	1.585	0.004603

Curriculum Vitae

PERSONAL DATA

Name: Dereje Shiferaw
Address: Flat 10, 196 High Street
UB8 1LW, Uxbridge, Middlesex, UK
Phone: + 44 7852120230 (mobile) +44 1895267196 (office)
Email: dereje.shiferaw@gmail.com

RESEARCH INTEREST

Principal research in the area of two phase flow boiling, which is applicable to thermal energy conversion systems and thermal cooling particularly in the field of compact heat exchangers and electronics cooling.

Experimental and analytical investigation of two phase flow boiling in small- to micro-tubes. Currently engaged in developing models to predict heat transfer coefficient and pressure drop during flow boiling inside small diameter tubes.

EDUCATION

- 2005 - 2008 PhD “Two Phase flow boiling in Small to Micro Diameter Tubes”
School of Engineering and Design, Brunel University, UK
The research is experimental and theoretical study of two phase flow boiling in microchannels – potentially to high heat flux electronics cooling and compact heat exchanger design in automotive and air conditioning systems.
Supervisors: Prof T.G. Karayiannis and Prof. D.B.R Kenning (Oxford University)–Both Leading Professors in Thermal Engineering fundamental research
- 2002 - 2004 M.Sc. in Mechanical Engineering (Sustainable Energy Engineering specialization).
Department of Energy Technology, Royal Institute of Technology (KTH), Sweden.
All courses with Merit
- 1993-1998 B.Sc. Mechanical Engineering
Technology Faculty, Addis Ababa University, Ethiopia
With Distinction in Major GPA

AWARDS AND PRIZES

Sigvard Eklund's Prize for Best M.Sc. Thesis, SKC (Swedish Centre for Nuclear Research), Sweden, 2004

Vice-Chancellor's Travel Prize (2007), for a research student who has had a paper accepted at international research conferences, Brunel University, UK

Vice-Chancellor's Research Poster Prize (2007), for best research poster, Brunel University, UK

School of Engineering and Design PhD Scholarship Award (2005), Brunel University, UK

Swedish International Development Agency (SIDA) Scholarship for MSC study in Sustainable Energy Engineering, Sweden, 2002

TEACHING AND PROFESSIONAL EXPERIENCE

- 2005-2008 **Tutor**- School of Engineering and Design, Brunel University, UK
Handling tutorial classes and help students in ThermoFluid course.
Assist in preparation of Building Heat Transfer Course Booklet (for MSc distance students in Building services Engineering).
- 2004-2005 **Research assistant**-Royal Institute of Technology (KTH), Sweden
Conducting researches in nuclear power safety issues particularly in film boiling studies using Nanofluids for the purpose of mitigating steam explosion
- 2000-2002 **Lecturer** - Bahir Dar University, Ethiopia
Delivering Mechanical Engineering Courses (Power Plant Engineering, Engineering Dynamics, Machine Elements, Machine Design, Equipment Handling,)
Coordinator for Pre-Engineering Department
Organiser and Coordinator of the Thermo-Fluid Laboratory
Supervising final year undergraduate students.
- 1998-2000 **Mechanical Engineer II**- MIDROC Construction Pvt. Ltd Co.
Supervising the maintenance department
Administration of light vehicles, heavy trucks and construction equipment
Participate in computerization of the company's equipment maintenance system

Publications from the work covered in this thesis

Key note papers

T.G. Karayiannis, D. Shiferaw, D.B.R. Kenning and V.V. Wadekar. Flow patterns and heat transfer for flow boiling in small to micro diameter tubes, *HEAT 2008, Fifth International Conference on Transport Phenomena in Multiphase Systems*, June 30 - July 3, 2008 , Bialystok, Poland.

T.G. Karayiannis, D. Shiferaw and D.B.R. Kenning. Flow boiling in small- to micro- diameter tubes: Experimental results and modelling, *ECI International Conference on Heat Transfer and Fluid Flow in Microscale Whistler, Canada 21-26 September, 2008*.

Journals

D. Shiferaw, X. Huo, T. G. Karayiannis and D.B.R. Kenning. Examination of heat transfer correlations and a model for flow boiling of R134a in small diameter tubes. *Int. Journal Heat Mass Transfer*, (50), 5177-5193, 2007.

D. Shiferaw, T.G. Karayiannis and D.B.R. Kenning. Flow boiling in 1.1 mm tube with R134a: Experimental results and comparison with model. *Int. Journal Thermal Science*, THESCI-D-07-00339, 2008.

T.G. Karayiannis, D. Shiferaw, D.B.R. Kenning, and V.V. Wadekar. Flow patterns and heat transfer for flow boiling in small to micro diameter tubes. *submitted to Journal of Heat Transfer Engineering*, 2008.

Peer - Reviewed Conferences

D. Shiferaw, M.M. Bassuny, T.G. Karayiannis and D.B.R. Kenning. Experimental flow boiling study in microtube of 500 μ m diameter. In the *5th European Thermal-Sciences Conference* 18-22 May 2008, Eindhoven, the Netherlands 2008.

D. Shiferaw, T.G. Karayiannis, D.B.R. Kenning. Flow boiling in 1.1 mm tube with R134a: Experimental results and comparison with model. In *Proceedings ASME ICNMM 2007-30038, 5th Int. Conf. of Nano-, Micro- and Mini-channels*, 18-20 June 2007, Puebla, Mexico.

X. Huo, D. Shiferaw, T.G. Karayiannis, D.B.R. Kenning. Boiling two-phase pressure drop in small diameter tubes. In *Proceedings of the 6th Int. Conf. on Enhanced, Compact and Ultra-Compact heat exchangers: Science, Engineering and Technology, CHE 2007*, 16-21 September, 2007, Potsdam, Germany.

D. Shiferaw, T.G. Karayiannis, D.B.R. Kenning. A comparison with the three-zone model for flow boiling heat transfer in small diameter tubes. In *the 13th Int. Heat Transfer Conf. BOI-16*, 13-18 June 2006, Sydney, Australia.

Presentations

D. Shiferaw, T.G. Karayiannis D.B.R. Kenning, Modelling issues for flow boiling of refrigerants in channels of small cross-section, Colloquium Proceedings *IMechE. 1st Int. Micro and Nanoscale Flows: Advancing the Engineering science and design*, 7-8 December 2006, University of Strathclyde, Glasgow.

D. Shiferaw, X. Huo, T.G. Karayiannis D.B.R. Kenning, Flow boiling in small diameter tubes using R134a, presented on *the 44th European Two-Phase group meeting*, 7-9 June 2006, Lausanne, Switzerland.